CRANFIELD UNIVERSITY

COLLEGE OF AERONAUTICS

Material & Structure Technology Group

Ph.D. Thesis

Academic Year 1998-99

Malik Nazir Ahmed

The Constrained Torsional Analysis Of Thin-Walled Variable Cross-Section Multi-Cell Laminated Composite Beams

Supervisor: Dr. J. Loughlan

August 1999

This thesis is submitted in partial fulfilment of the requirements for the degree of Doctor of Philosophy

Proclaim ! (or Read!) In the name of thy Lord and Cherisher. Created man, out of a (mere) clot of congealed blood. Proclaim ! And thy Lord is Most bountiful. He who taught (the use of) the Pen. Taught man that which he knew not.

Al-Qur'an 96:1-5

DEDICATION

This Thesis is dedicated with love to my both parents in Pakistan , their constant prayers and un-ending love made me whatever I am today.

ABSTRACT

A Constrained Torsional Analysis of Thin-Walled Variable Cross-Section Multi-Cell Laminated Composite Beams has been undertaken . The existing Isotopic theory has been modified using the effective engineering elastic constants to cater for the Composite structures under torsional loads. The relevant computer programs for the Composite structure analysis have also been developed. The results are discussed in detail for single-cell and multi-cell prismatic/tapered beams for all $[0/45/-45/90]_s$ lay up in flanges and webs, all $[45/-45]_2]_s$ lay-up in flanges and webs, and for flanges $[0/45/-45/90]_s$ & webs $[45/-45]_2]_s$ lay-up. The theoretical results obtained are then compared with those obtained from a finite element method analysis carried out by the author employing MSC commercial package PATRAN/NASTRAN. This has provided confidence in the validity and capability of the developed Composite theory in handling the Torsional Analysis of Variable Cross-section Single-Cell & Multi-Cell Laminated Composite Beams.

ACKNOWLEDGEMENTS

The author would like to start the acknowledgements by very humbly thanking God Almighty the Exalted for His (s w t) utmost graciousness and compassion to the author throughout his life.

The author would like to thank his parents and his brother (Mr. Munir Ahmed) in Pakistan for their love, constant support and prayers throughout his academic study.

The author is grateful to his academic supervisor Dr. J. Loughlan for his continued supervision, advice, encouragement and friendship throughout this project. His comments and suggestions were very much appreciated.

The author wishes to express his appreciation to his past and present office colleagues , (Dr. Reza Ovesy & Mr. Raja Javed) at College of Aeronautics for their continued support to the author during this project.

The author also wishes to express his appreciation to Dr R.L.Oswald incharge of Computer network services at COA for his continued support during the tenure of study.

The author wishes to thank Pakistan Air Force , for sponsoring subject PhD programme.

Finally, and most importantly, special thanks are extended to the author's wife (Uzma) and three children (Maria Saad and Dania), whose love, unsparing support and never-ending patience made this work possible.

TABLE OF CONTENTS

LIST OF FIGURES

NOMENCLATURE

a	Width of web
a_{11}	Term of reduced compliance matrice
a_{33}	Term of reduced compliance matrice
b	Width of flange
b'	b-2z tan β
d'	d-2z tan α
f	Spanwise variation of axial displacement
n	Number of cells in multi-cell box section
q_{TOTAL}	Total shear flow
r	Radius from the geometric centre to any point on the surface
r_1 & r_2	Roots at any location along z
s	Distance along the box cross section
$t = \delta$	Thickness of box section
t_{eff}	Effective thickness defined in equation 4.9
t_f	Thickness of flange
t_w	Thickness of web
w	Axial displacement component in the z co-ordinate direction
$\overline{w} = w(s)$	Sectorial co-ordinate
x	Cartesian co-ordinate in x direction
y	Cartesian co-ordinate in y direction
z	Cartesian co-ordinate in z direction
A	Constant defined in equation 3.20
A_i	Area of the ith cell
A_{13}	Term of A matrice
A_{23}	Term of A matrice
B	Constant defined in equation 3.20
C	Constant defined in equation 3.20

C_1 & C_2	Coefficient appearing in the equation 3.21
D	Constant defined in equation 3.20
E	Young's modulus
E_w	Young's modulus in web
E_f	Young's modulus in flange
E'	Active Young's modulus $E' = \frac{E}{1-\nu^2}$
E_x^m	Young's modulus in membrane mode
E_x^a	Apparent Young modulus as defined in equation 4.7
E_{eff}	Effective Young modulus as defined in equation 4.10
F = q	Bredt Batho Shear flow
F*	Warping shear flow
G	Shear modulus of elasticity
G_{xy}^m	Shear modulus in membrane mode
G_{eff}	Effective shear modulus defined by equation 4.3
$I_w = \Gamma$	Warping moment of inertia = $\int w(s)^2 tds$
I_c	Second moment of area = $\int P_R^2 tds$
J	Torsion constant
L	Length of the box section
N	Force Intensity
$P_R = r_t$	Perpendicular distance from the Centre of twist to the tangent at any point on the surface
$S_{w,0}(s)$	Sectorial shear flow for open section
$S_{w,c}(s)$	Sectorial shear flow for closed section
T	section torque
$\overline{T}$	Unit torque
V_t	Tangential displacement
Ω	Twice the area of ith cell
σ_x	Normal membrane stress in the x direction
σ_y	Normal membrane stress in the y direction
σ_z	Normal membrane stress in the z direction

$\lambda = \eta^2$	Dimensionless constant defined by equation 2.37
τ	Shear membrane stress
$\bar{\tau}$	Basic transverse distribution
ε_x	Normal membrane strain in the x direction
ε_y	Normal membrane strain in the y direction
γ	Shear membrane strain in $x\,y$ plane
α	Taper angle as shown in figure 3.5
β	Taper angle as shown in figure 3.5
ϕ	Rotation angle
$\theta = \frac{d\phi}{dz}$	Rate of twist
η	Torsion bending constant defined by equation 2.45
ν_{xy}^m	Major Poisson ratio in membrane mode
ν_{yx}^m	Minor Poisson ratio in membrane mode
ν	Poisson's ratio
I_{ceff}	Defined in equation 4.13
λ_{eff}	Defined in equation 4.15

1. INTRODUCTION

1.1 GENERAL INTRODUCTION

The increasing competition in the air transport industry due to de-regulation and the open sky policy all over the globe is narrowing down the profit margins of airlines. This mounts pressure on the commercial aircraft manufacturers to develop more fuel efficient and lighter aircraft with lower Direct Operating Costs (DOC). This has led to the increase in use of composite materials in the aircraft industry in general. The prime reason for using fibrous composites is that, substantial weight savings can be achieved due to their superior strength to weight ratios , as compared with the conventional materials of aerospace vehicle construction such as aluminium alloys.

The composite materials belong to the class of materials called fibre reinforced plastics (FRP), comprising of continuous fibres embedded in a resin (or plastic) matrix. All the structural properties of the composite come from the fibres. The matrix mainly serves to bond the fibres into structural entity. Some of the main attractions of fibrous composites for any aircraft designer are as follows:

- high strength and high stiffness to weight ratio
- capability to create smooth aerodynamic surfaces
- high fatigue resistance
- high corrosion resistance
- mechanical properties can be tailored
- aeroelastic tailoring capabilities

- reduced part-count through co-curing

It is for these advantages that the composites have a potential to achieve weight savings and lower life time costs as compared to conventional light alloy structures. The capability to produce smooth curvature surfaces improves the aerodynamic efficiency and can be equated to reduced fuel consumption or increased pay load.

However the fibre reinforced plastics (FRP) are relatively new materials with many unknown characteristics and disadvantages such as:

- highly orthotropic behaviour
- low bearing strength
- environmental degradation (moisture, temperature and Ultra violet radiation)
- low through thickness strength
- brittle
- difficult to machine
- requirement to inspect for disbonds and delaminations
- environmental protection at all stages of operation
- higher material costs than conventional aluminium alloys
- new manufacturing techniques required
- need for lightning strike protection

These disadvantages have resulted in a slower acceptance of carbon fibre material for use in aircraft structures than expected. This is so as no aircraft manufacturer would favour risking the safety of aircraft and passengers for economical gains , unless all the characteristic properties of composites were fully known. This obviously requires more in depth study and investigations into the composite behaviour under different applied load conditions . Hence the full use of composites in aircraft industry will only be made possible when all the unknowns mentioned above have been successfully tested out and results verified to the satisfaction of the design engineers working in the aircraft manufacturing industry .

Inspite of all the factors mentioned above, today almost all new aircraft designs incorporate significant primary composite structures. Composites are being used by all major aircraft manufacturers like Boeing and Airbus industries. Composite materials make upto 15 % of the structural weight of the Airbus A320. However it is apparent that the full range of applications for composite materials is at this stage only beginning to be discovered. Hence it is required that the design engineers using FRP should remain aware of its advantages and disadvantages at all times during and after the design process.

The aluminium alloy aircraft structure design engineer has usually access to a large data base of information and guidelines due to many years of experience of aircraft manufacturing companies in having dealt with metal structures. Metals are isotropic and homogeneous whereas FRPs consist of high strength, high stiffness continuous fibres which are held together by a relatively weak matrix material and exhibit a highly orthotropic behaviour. This difference in the material properties makes the experience gained over the years with metal structures in the aircraft industry generally non-transferable to FRPs.

With the advancements in the computer field and the computer power becoming cheaper and readily available, Finite Element Analysis (FEA) is being commonly used by stress engineers. However it needs to be kept in mind that the quality of results achieved from FEA depend directly upon the quality of the created FE model, and how closely does it resemble the real structure under application of load. Errors in the FE modelling may lead to errors in the analysis , without the stress engineer being aware of them. It is hence considered a good practise for a stress engineer to get some analytical analysis results on a simplified structure to establish the expected approximate FE results. This enables a suggestive figure to the solution required to be obtained, against which, the results from FE analysis can be compared. The correlation of the results would confirm the validity of the FE model and hence will give confidence into using the FE analysis results obtained for required problem.

Human beings have been using metals since thousands of years, and our mastery and confidence in their usage stems from this long experience . On the other hand it has not been more than just 50 years that fibrous composite materials have been introduced to the industry. It is hence considered that this age of ours is just the beginning of life for the composite materials.

Thin walled single-cell and multi-cell beams manufactured from isotropic materials have been used in the aircraft industry extensively. Manufacturing of these beams using laminated fibrous composite materials can result in further weight reductions over conventional metal thin beams. There is an ever increasing tendency in the aircraft industry for using such thin walled composite beams as structural members.

1.1.1 REQUIREMENT OF TORSIONAL ANALYSIS

Torsional loading causes warping displacements in the thin walled beams. Warping is defined as the axial displacements taking place in a thin walled beam due to a non-axial loading. The torsional analysis of thin walled beams forms a basis in determining the longitudinal behaviour of beams which are either restrained against warping or that induce warping. If a thin walled beam in any way is restrained against warping than this would always lead to warping stresses, which are axial and direct in nature.

In the actual aircraft wing structure the requirement for the torsional analysis of tapered boxes stems from the fact that the bending moment is maximum at the root of the aircraft wing . Hence the root of the wing is required to be kept strong and thus requires maximum area to manage the maximum moment at root. As the bending moment on the aircraft wing structure decreases when moving towards wing tip , subsequently the requirement for large wing area as required at the root diminishes slowly. This decrease in wing area requirement due to decreased bending moment leads to the taper design of the wing thus avoiding unnecessary weight of wing structure.

Torsional load on an aircraft wing is caused due to the distance between wing Centre of Pressure (CP) and wing Centre of Gravity (CG). If these two points existed on same location on the wing then the requirement of torsional analysis for the tapered wing could have been avoided. However due to practical limitations and aerodynamic requirements these two points are invariably located at different locations on the wing structure thus giving rise to torsional load on the aircraft wing structure. Hence the requirement to analyse the tapered multi-cell box beams under torsional loads exists.

1.2 LITERATURE SURVEY

1.2.1 GENERAL INTRODUCTION

J.Hadji Argyris & Dunne P.C[10] in their torsional analysis of open and closed section beams published in The Royal Aeronautical Society Journal in 1947 while dealing with the stressing of single or multi cell tubes particularly of the type encountered in wing structures had adopted an idealisation in which all the shear stresses acting on the cross section were assumed to be resisted by shear walls and all the axial stresses by the booms or stringers. The theory had been developed for conical or cylindrical tubes of arbitrary cross section whose shape was maintained by the use of closely spaced system of diaphragms which were rigid in their plane and parallel to the root section. However in case of thin walled sections without stiffeners this method is not readily applicable as in such cases both the shear and axial loading has to be resisted by the walls.

Vlasov[11] is generally considered to be the first who presented a rigorous treatment of thin-walled open sections. He considered a thin-walled beam which in its unloaded form has the shape of a cylindrical shell or a prismatic hipped section. These shapes were

considered as a continuous spatial system composed of plates capable of bearing, in each point of the middle surface, not only axial stresses but also moments as well. Instead of analysing deformation of the beam on the basis of the usual hypothesis of plane sections , Vlasov[11] used the more general and natural hypothesis of an inflexible section contour and the absence of shear stresses in the middle surface. This constituted the basis for a new law of distribution of longitudinal stresses in the cross section.

This law, which Vlasov[11] calls the law of sectorial areas and which includes the law of plane sections as a particular case, permits the computation of stresses in the most general cases of flexural-torsional equilibrium of a beam.

Vlasov[11] method has been summarised by Zbirohowski-Koscia, K[12] in the following two theorems:

The stress, $\sigma_B(r)$, in a longitudinal fibre of a thin-walled beam due to a bimoment, B, is equal to the product of this bimoment and the principal sectorial co-ordinate, $\omega(r)$, of this fibre divided by the principal sectorial moment of inertia , I_w , of its cross section, i.e.

$$\sigma_B(r) = \frac{B\ \omega(r)}{I_w}$$

Also:

The shear stress in a fibre of a thin-walled beam caused by a flexural twisting moment, T_w, is equal to the product of this moment and the statical moment, $S_w(r)$, of this point divided by the principal sectorial moment of inertia and the wall thickness (of this point) of its cross-section, i.e.

$$\tau_w(r) = \frac{T_w S_w(r)}{t I_w}$$

The bimoment, B , and the flexural twisting moment, T_w , at any section of a thin-walled beam are obtained from the solution of a differential equation and the relationship $T_w = \frac{dB}{dz}$ (reference Zbirohowski-Koscia, K[12]) . The boundary condition used in the solution of this differential equation usually involves the angle of twist and the representation of the applied loads or support reactions as an external bimoment. A bimoment may be generally defined as the product of a pair of equal and opposite moments M and the distance , d , between them, thus B = Md. Zbirohowski-Koscia, K[12] has given the procedure for the determination of bimoments corresponding to different loading conditions.

Wagner and Kappus[13] in their torsion bending theory for the open sections have proposed a rather specific approach to the restrained torsion problem of open sections. They have proposed their theory to be applicable in case of application of pure torsional load only. They obtained an expression for primary warping by considering the distortion produced by shear stresses in a rectangular element of an open section beam. In comparison to Wagner and Kappus[13] torsion bending theory the method of Vlasov[11] is more general and has the added advantage of allowing applied loading systems (extensional , bending, etc) other than just pure torsion to be considered. However the resulting governing equations of Vlasov's approach for a pure torsional loading of thin walled open section isotropic beam is the same as the Wagner and Kappus theory.

The primary and secondary warping and associated axial constraint stresses , in an open-section beam subjected to torsion and completely restrained from warping , can be determined by either of the two methods , the Wagner and Kappus torsion bending theory or Vlasov's method. However in secondary warping, sectorial moment of inertia is determined in a different manner. Oden[14] and Gjelsvik[15] have given the method of calculation of secondary warping sectorial moment of inertia for open sections.

1.2.2 CLOSED SECTIONS

Von Karman and Christensen[4] provided an analysis for an unstiffened beam with arbitrary multi-cell cross-section. Using the mathematical arguments they arrived at a transverse distribution of axial displacements and normal stresses proportional to the axial displacements of St Venant torsion (free torsion). They also obtained correct basic transverse distributions of primary and secondary shear flows. The spanwise variation of stresses and rotations obtained by Von Karman and Christensen[4] was not accurate. This in-accuracy was the result of their failure to consider the effect of shearing strains upon deflections. Von Karman and Christensen[4] gave practical methods for computing the basic stress distributions by introducing the use of a beam analogy.

An analysis method for the special case of a cantilever beam of infinite length with torque applied at the tip was presented by Fine and Williams[3] . They considered a single-cell cross-section of arbitrary shape with, or without, stiffeners and assumed the transverse distribution of axial stress to be proportional to the axial displacements of free torsion. They also assumed the spanwise variation to be given by an exponential function with an unknown rate of decay determined by the theory of least work. The method is very similar to one used by Timoshenko[16] for solid sections and thin-walled open sections. They came up with accurate formulas for computing the axial displacements of free torsion and showed that such computations yield the co-ordinates of the centre of twist. They also showed, for a single-cell section, that, this centre of twist coincides with the shear centre. However the special case solved by these authors does not offer any suggestion as to how to formulate a differential equation relating the stresses or rotations to the applied loads.

Both the above mentioned approaches of Von Karman and Christensen[4] and Fine and Williams[3] assume that, the shear strain due to warping is zero, and, only the St. Venant shear strain is significant. This means that the stress-strain relationship between warping shear stress and strain cannot be used to obtain the warping shear stress, and hence it must be derived by considering the equilibrium in the longitudinal direction. This is similar to that used in the simple beam theory where the Bernoulli assumption implies zero shear strain and the shear stress must be obtained from equilibrium of an element in the longitudinal direction. However in certain cases, where the warping stresses are large and change rapidly, this assumption leads to inaccurate results.

Beskin[17] in a paper presented an analysis for a single-cell unstiffened section. He used method similar to Von Karman and Christensen[4] , and derived an equation relating the spanwise variation of normal stress to the applied load. However he did not provide any direct relation between rotations and the applied load. The spanwise distribution of stress given by Beskin[17] does not agree with Fine and Williams[3] and Benscoter[2] . Beskin[17] gave the location of the centre of twist and also proved, for a single-cell unstiffened section, that the centre of twist coincides with the shear centre. In the method of solution given by Beskin[17] and also by Fine and Williams[3] , the designer is required to calculate an additional section property which is not required in the Benscoter[2] theory.

Benscoter[2] theory provides a more accurate analysis to overcome the problem in finding warping shear stress as faced by Von Karman and Christensen[4] and Fine and Williams[3], by starting with developing assumed forms for the components of deformation. Benscoter[2] then finds the strains by simple differentiation and then obtains direct and shear stresses due to warping by using the stress-strain relationship, in this way Benscoter[2] provided a more direct approach to the problem.

Benscoter[2] considered the loading, end conditions, and cross-sectional shape of the beam to be arbitrary. He assumed the beam to be non-uniform and of multi-cell design. His theory is applicable to mono-coque, or unstiffened, sections . Benscoter[2] theory rests on the basic assumption that the axial displacements leading to normal stresses have the same transverse distribution at a section of an arbitrary beam as would occur in Saint Venant torsion of a uniform beam with that section. He developed differential equations which relate the spanwise variation of warping displacements to the applied torsional load and also which relate the rotation (angle of twist) to the load. Benscoter[2] provided methods for the calculation of various stress distributions.

The final solution of Benscoter[2] bears a close resemblance to that of Von Karman and Christensen[4] . Infact the governing equations are identical except for section properties and it can be shown that the method of analysis used by Von Karman and Christensen[4] will lead to a solution in complete agreement with Benscoter[2] if appropriate modifications are introduced to correct their spanwise variations of stresses and rotations. Benscoter[2] theory has the added advantage of being able to handle different geometric shapes of multi-cell closed section beams with special application use in the aircraft industry of incorporating various taper angles in the geometry of the beam.

Waldron[1] has given a sectorial method of analysis for thin walled beams with open or closed cross-section subjected to torsional loading. This method enables warping restraint effects due to non-uniform torsion to be incorporated into a general beam theory covering all solid, thick walled and thin-walled beams of non-deformable cross-section. The distribution of warping restraint stresses around the section is defined in a similar way as for bending by a system of sectorial co-ordinates and several additional geometric terms. The difficulty in this analysis is the requirement of calculating the various sectorial functions which becomes quite tedious when performed by using hand calculation method. However a computer programme can solve this problem and make the analysis very useful tool.

1.2.3 COMPOSITE BEAMS

During the course of literature survey no attempt has been encountered which relate to the torsional analysis of single cell composite tapered beam, multi-cell composite prismatic beam and multi-cell composite tapered beam. The torsional analysis of various open section composite beams and single cell composite beam was undertaken by ATA[7] . However other direct analytical methods which have been formulated for torsional analysis of thin-walled composite beams are basically for specific composite box sections such as helicopter blades.

Reissner and Tsai[18] developed shell analysis for bending stretching and twisting of composite cylindrical shell structures. Mansfield and Sobey[19] developed a simple thin-walled contour analysis and introduced the concept of the aeroelasticity tailored composite helicopter blade. Using a simple composite beam model, Hong and Chopra[20,21] formulated comprehensive analysis for aeroelastic stability of advanced composite rotor systems. Panda and Chopra[22] extended this analysis from hover to the forward flight condition, and demonstrated the potential for composite tailoring to increase aeroelastic stability and reduce blade vibration. Rehfield[23] developed a thin-walled contour analysis for tailored composite beams and applied this formulation to a variety of beam problems.

Bauchau[24] developed a thin-walled contour formulation using a refined approach to warping. Variations of this work have been incorporated into a finite element method[25]. Bicos and Springer[26] investigated the minimum weight design of a semi-monocoque

(stringers and webs) composite box beam using a reduced plate model. Libove and Chang[27] have also developed a thin-walled contour analysis which is similar to the work of Mansfield and Sobey[19]. Klang and Kuo[28] developed a method using plates and corner springs to model the composite box beam. Minguet and Dugundji[29] used a reduced plate formulation to investigate coupled composite beams. The main focus of this experimental and analytical study was on solid section beams under large deflections.

Smith and Chopra[30] proposed an analytical method for predicting the effective elastic stiffness and corresponding load deformation behaviour of composite box beams by representing the walls of the beam as four laminated plates which are built up from layers of orthotropic plies. Barrau and Laroze[31] used a finite difference method to calculate torsion stiffness, locate the shear stresses and shear centre of a composite box beam undergoing free torsion.

Chai Hong Yoo & Samir[34] applied a numerical procedure to determine the torsional and flexural properties of multi-cellular cross sections which are used frequently in modern curved highway bridge girders. The solution of shear flow in multi-cellular sections becomes indeterminate and hence requires as many number of equations as the number of cells. Chai Hong Yoo & Samir[34] developed an algorithm to evaluate these indeterminate shear flows and incorporated it into a computer programme. They examined two hypothetical multi-cellular sections and presented the numerical results along with input preparation. Their computer programme SECP provides an opportunity for an automatic evaluation of cross sectional properties of a cross section with a large number of cells.

Steen Krenk & Bo Jeppesen[35] have formulated the torsion and shear load problems of elastic beam cross-sections of moderate wall thickness in terms of finite elements with warping function as primary unknown variable. They concluded that by introduction of

suitable internal degrees of freedom in the shear problem the stiffness matrices of both problems become identical. Their method is applicable to both open and closed cross-sections. An example was provided for efficient PC implementation. Moderate thickness of 4 mm to 20 mm were discussed in the examples presented .

J Jonsson[36] used simple one dimensional finite elements in the plane of cross-section to model the axial displacement modes of thin-walled beams. He determined the axial shear displacement modes, and the torsional and distortional warping functions based on the weak formulation of axial equilibrium of an infinitesimal section cut out. He then used the axial displacement functions to determine the shear stress distributions and the section properties. J Jonsson[36] method is applicable to open , closed and multi-celled cross sections. He found the transverse distortional modes by the use of a frame model in the plane of cross section.

J Jonsson[32]. states that in the analysis of thin-walled beams it is often necessary to consider the effects of distortion of the cross-section. The distortion in the plane of the cross-section generates axial warping displacements. On the basis of a known in-plane distortional displacement mode it is possible to derive a unique warping function and the related stress distributions. J Jonsson[32] used the local axial equilibrium to derive the main differential equation for determination of the distortional warping function and shear distributions. J Jonsson[32] stated that in closed single or multi-celled cross-sections it was necessary to introduce circulation shear force flows around the cells to achieve compatibility of the axial displacement. He generalised the methods for analysis of closed single or multi-celled cross-sections to include distortional displacement modes. J Jonsson[32] showed that axial extension, flexure and torsional warping are included as special cases of distortion. J Jonsson[32] also presented a generalisation of the conventional orthogonalization procedure and a normalisation technique for distortional modes. A triple cell cross-section was used to illustrate the generalised calculation procedure and computed results. His approach includes the effects of distortion and hence can be used in cases where the distortion is occurring in actual practise. However Jonsson [32] has not

dealt with the theory of composite thin-walled single-cell and multi-cell box beams with prismatic and tapered geometries. Also he has not validated his theoretical isotropic results with any experimental or finite element analysis.

J Jonsson[33] has generalised the classic thin-walled beam theory for open and closed cross-sections to include one distortional mode of deformation. J Jonsson[33] introduced distortional cross-section parameters and gave the new orthogonality conditions for uncoupling of the axial displacement modes. His normalisation technique for the distortional modes leads to unique distortional cross-section properties. Since the theoretical formulations for torsion and distortion are nearly similar , therefore they result in nearly identical equilibrium equations. J Jonsson[33] study of the order of magnitude of the governing torsional and distortional parameters shows the difference between open and closed cross-sections and the related solution types. Also the difference in the order of magnitude of the governing cross-section parameters leads to approximate solution techniques.

J.Loughlan & M. Ata[37] presented a detailed experimental work which examines the constrained torsional response of carbon fibre composite beams for the cantilevered configuration with torque applied at the free end. J.Loughlan & M. Ata[37] reported and discussed the behaviour of open-section beams and that of single-cell closed-section box beams and showed that the experimental findings corroborate simple engineering theoretical approaches. They carried out tests on zed and angle-section beams and thus examined the effects of primary and secondary warping restraint respectively on the torsional response of open section beams. They determined the stress distribution along the beams and around the cross-sections from the measured strains during test obtained from surface bonded strain gauges and showed that the comparison of these results with theory was in good agreement.

J.Loughlan & M. Ata[38] presented a simple analytical procedure for determining the constrained torsional response of a specific class of carbon fibre composite box beams. Their analysis approach essentially makes use of the existing theories of torsion appropriate to isotropic construction and these are then suitably modified to account for the non-isotropic nature of typical carbon fibre composite material. The composite box beams are devoid of overall elastic couplings through the use of constituent laminates which are symmetrically laid-up about their own mid-planes and which possess in-plane orthotropy. The thin walls of the box beam can have different lay-up configurations provided the stiffness distribution around the sections is of symmetrically disposed nature. It was thus possible in the analysis to have different lay-up configurations in flanges and webs. The constrained torsion considered by J.Loughlan & M. Ata[38] is that of the cantilevered box-beam with torque applied at the free end and the torsional and warping rigidities of the composite box-sections being determined through the use of the appropriate equivalent engineering elastic constants of the individual thin composite walls. J.Loughlan & M. Ata[38] showed that the comparison between finite element and theory was in close agreement and also that the use of appropriate equivalent engineering elastic material constants in the theory was able to predict the actual behaviour very closely.

J.Loughlan & M. Ata[39] gave the details of a simple analytical procedure for determining the constrained torsional response of a specific class of carbon fibre composite box-beams. They have given the comparison of the theoretical results for a composite single-cell box section using the Benscoter and Waldron approaches vis a vis the finite element results. It is shown that the Benscoter results are closer to the finite element results and depict the actual behaviour of the structure. The theoretical results for the various composite configurations of single cell box section have also been compared by J.Loughlan & M. Ata[39] against their experimental results and found to be in good agreement.

J.Loughlan & M. Ata[40] presented a simple engineering theoretical approach in this paper to predict the initial constrained torsional response of open and closed section composite beams. The flat walls of the composite beams are symmetrically laminated about their own mid-planes and possess membrane orthotropy. The analysis approach of J.Loughlan & M. Ata[40] simply makes use of the existing theories of torsion appropriate to isotropic construction and these are then suitably modified to account for the non-isotropic nature of the composite material. The torsional and warping rigidities for use in the analysis of the composite beams are thus duly determined through the use of the appropriate equivalent engineering elastic constants of the individual thin composite walls and the concept of effective thickness is employed to account for the different stiffnesses of the walls. The stress systems set up in open-section and single-cell closed-section carbon fibre composite beams when subjected to torsion with variable twist are examined in the paper. The comparison between open and closed section beam theoretical results vis a vis the finite element results and the experimental results show good comparison.

Grant[41] applied the network theory to the problem of Saint-Venant torsion in thin-walled multi-cell sections by treating the section as a network of interconnected limbs. The method has considerable advantages over traditional methods of calculation since it exploits the topological independence of a network from its physical characteristics. Only routine matrix operations are required to set up and solve a system of linear algebraic equations. Four distinct network methods are identified, i.e., circuit, cutset, node and face analysis. Each method requires the solution of far fewer equations than the total number of problem variables. It is possible to select the appropriate method to minimise the number of equations.

Shakourzadeh[42] formulated finite element for the torsion problems of thin-walled beams. He based the element on Benscoter's beam theory, which is valid for open and also closed cross-sections. The non-polynomial interpolation presented in his paper allows the exact static solution to be obtained with only one element. Numerical results have been

presented for three thin-walled cantilever beams, one with channel cross-section and the two others with rectangular cross-sections. The influence of the transverse shear strain has been investigated and the different models of torsion compared. The results obtained with one-dimensional torsion elements were compared with those obtained using shell elements.

Kaiser[43] presented a theory for linear analysis of thin-walled beams with a multi-celled closed cross section made up of general composite laminates containing elastic couplings. Kaiser[43] modified theory is based on the Vlasov type theory of Chandra and Chopra[49] , which includes non-classical effects, such as transverse-shear deformation and torsional warping, and includes an approach to take in-plane warping effects into account . The in-plane warping is caused by the effects of elastic coupling of the laminated branches of the cross-section and by the strains in the direction of the contour line of the cross section. Kaiser[43] was able to achieve good correlation between analytical numerical and experimental results for the case of a two-celled anisotropic composite beam.

Rodriguez[44] presented a study of a special case of symmetric laminated composite cantilever beams. His approach models beams that are tapered both in depth and in width and investigates the effect of the ply lay-up angle and ply taper on bending and interlaminar shearing stresses. Rodriguez[44] expressed the beam stiffness matrices as linear functions of the beam length for the determination of stresses and deflections. Using classical lamination theory the stiffness matrices are determined and assembled at all the points of interest along the length of the beam. The stiffness matrices are then inverted by Rodriguez[44] and necessary stiffness parameters numerically extracted for determination of design information at each chosen location. He investigated several ply lay-up configurations, and presented his design considerations based on the findings. Rodriguez[44] also presented the recommendations for the design of these beams and also a means to anticipate the location of highest stresses encountered on beam.

Chandra & Chopra[45] fabricated symmetric and antisymmetric lay-up graphite-epoxy composite beams with thin-walled rectangular cross sections using autoclave moulding technique and tested these under bending, torsional, and extensional loads. The bending slope and elastic twist at any location were measured using an optical system, and the results were correlated with predicted values from a simple beam analysis as well as finite element analysis. For symmetric lay-up beams, the bending-induced twist and torsion-induced bending slope are predicted satisfactorily using simple analytical solution. The correlation with measured experimental data however generally improved using finite element solution.

Rehfield[46] focused on two non-classical effects in the linear theory of thin-walled composite beams i.e., torsional warping and elastic coupling between bending and transverse shear. Rehfield[46] clarified and analysed these non-classical effects with some simple examples involving cantilever beams. Torsional warping is shown to be important in box beams having a thin-walled, closed cross section and loaded with a twisting moment applied at the end. Bending-transverse shear coupling is shown to be important in the analysis of a beam designed for extension-twist coupling and with a distributed lateral load. The importance of including these effects in a complete theory has also been discussed .

Bauchau[47] stated that when simple beam theory was applied to the composite beams, its accuracy became questionable due to the fact that shearing and warping deformations become more significant, as the shearing stiffness of the composite laminates is often very low. Also several elastic couplings can occur that strongly influence the behaviour of composite beams. The torsional behaviour of thin walled composite beams which have important implications for aeronautical structures are deeply modified due to these non-classical effects. Bauchau[47] presents two analysis methodologies for composite beams and describes experimental results obtained from thin walled, rectangular cross sectional

beam. Bauchau[47] suggests that the out of plane torsional warping of the cross section is the key factor for an accurate modelling of the torsional behaviour of such composite structures.

Wu[48] derived the governing equations for composite thin-walled beams. His theory is suitable for open-section or closed section beams of any shape and laminate stacking sequence. Using more general assumptions than Vlasov, Wu[48] equilibrium equations consist of seven ordinary differential equations. These seven equations were further reduced to four coupled ordinary differential equations, which govern the shear deformation of the middle surface. Wu[48] considered the numerical example of displacements of channel beams of composite laminates according to his beam theory and compared his results against finite elements and other existing theories.

Chandra[49] analysed the structural behaviour of coupled, thin walled, composite beams of open as well as closed section using Vlasov theory, and validated the results by experiment. Chandra[49] analysis modelled the walls of beams as general composite laminates and accounted for the transverse shear deformation of the cross-section. The out of plane warping deformation of the cross-section was included implicitly in this formulation. In order to validate the analysis, graphite epoxy beams of various cross sections such as solid rectangular, I-section, single-cell rectangular and two cell airfoil were fabricated and tested for their structural response under bending, torsional and extensional loads. Chandra[49] observed good correlation between theoretical and experimental results.

Barbero[50] developed a simple methodology for the analysis of thin walled composite beams subjected to bending, torque, shear, and axial forces. He considered members with open and closed cross-section. Each laminated segment is modelled with the constitutive equations of classical lamination theory accounting for a linear distribution of normal and

shear strains through the thickness of the walls, thus allowing for greater accuracy than classical thin walled theory when the walls are moderately thick. Barbero[50] did not use the geometrical properties used in the classical beam theory such as area, first moment of area, centre of gravity etc , due to the variability of the material properties in the cross section. Instead he used mechanical properties such as axial stiffness, mechanical first moment of area, mechanical centre of gravity etc. , which were defined to incorporate both the geometry and the material properties. Barbero[50] finally presented comparison of theoretical results with the experimental results.

1.3 THE OBJECTIVE OF RESEARCH

Although a lot of work is nowadays being undertaken to understand the true nature and response of the composite materials under various loading conditions. However it still remains an area which will need to be looked into by researchers for years to come before it can finally be brought at par with their older metallic partners. Also none of the aforementioned literature fully investigates the torsional response of multi-cell prismatic and tapered composite box beams.

Rodriguez[44] has dealt with study of a special case of symmetrical laminated cantilever beam and used his approach for determination of stresses and deflections in these cantilever beams. However he did not present any study for multi-cell prismatic & tapered box beams. Moreover he did not verify his single cantilever theory against finite element or experimental results.

Kaiser[43] presented a theory for linear analysis of thin-walled beams with multi-celled closed cross-section. He gave example of two-celled composite beam and compared the results from his theory with the experimental results. Kaiser[43] has however not given any

comparisons for a three celled composite beam. Moreover he did not include the analysis of multi-celled tapered composite box beam in his theory.

Jonsson [32,33] has given his theory for the multi-cell thin-walled box beams. He has also shown results for multi-celled tapered box beams. However his paper was presented in April 1999 in Thin walled journals and by that time the author of this Thesis had already finished the research work and was in the process of final submission. His approach includes the effects of distortion and hence can be used in cases where the distortion is occurring in actual practise. However Jonsson [32,33] has not dealt with the theory of composite thin-walled single-cell and multi-cell box beams with prismatic and tapered geometries. Also he has not validated his theoretical isotropic results with any experimental or finite element analysis.

The objective of this research is to develop a generalised straightforward analytical analysis method for restrained torsional problem of thin-walled multi-cell composite box beams with prismatic and tapered geometrical configuration by incorporating the complications emerging from the use of such materials into the existing isotropic theories. This theory assumes no distortion of the box beams and hence can be applied to structures where either there is no distortion at all or having negligible distortional effect.

To validate the proposed theory, a series of finite element analysis is aimed to be performed on isotropic box beams , and a wide range of single-cell and multi-cell prismatic and tapered composite box beams under restrained torsion.

2 BASIC TORSION THEORY

2.1 DEVELOPMENT OF THE FUNDAMENTAL DIFFERENTIAL EQUATION GOVERNING THE CONSTRAINED TORSIONAL RESPONSE OF THIN-WALLED VARIABLE CROSS-SECTION BEAMS.

The fundamental differential equations being developed in this chapter were presented by Benscoter[2] for generic beams when the general shape of the cross section does not change rapidly.

Shear stress is related to shear strain by

$$\tau = G\,\gamma \qquad (2.1)$$

Axial Stress is related to strain by

$$\sigma = E'\,\varepsilon \qquad (2.2)$$

Two dimensional Stress Strain relationship is given by

$$\sigma_z = \frac{E}{1-\nu^2}\,(\varepsilon_z + \nu\,\varepsilon_s)$$

Strain ε_s is assumed to be zero , since no deformation of the box takes place.
Hence we have

$$\sigma_z = \frac{E}{1-\nu^2}(\varepsilon_z)$$

$$\text{Here } E' = \frac{E}{1-\nu^2} \qquad (2.3)$$

Strains are expressed in terms of displacement by following two equations
Eq. 2.4 and Eq. 2.5 (Reference figure 2.2)

Shear Strain $\gamma = \phi_1 + \phi_2$

$$\gamma = \frac{\partial w}{\partial s} + \frac{\partial V_t}{\partial z} \qquad (2.4)$$

here "w" is axial displacement and "V_t" is tangential displacement.

and

Normal Strain $\varepsilon = \frac{\partial w}{\partial z}$ (2.5)

Shear Flow

$q = \tau\ t$ (2.6)

Normal Stress Flow

$N = \sigma\ t$ (2.7)

Equation of equilibrium for a differential element of web is given by considering figure 2.1 showing the forces acting on the element.

Following can be deduced from the figure considering the force equilibrium in the z direction.

$$\sigma_z\ t\ ds - \sigma_z\ t\ ds - \frac{\partial \sigma_z}{\partial z}\ dz\ t\ ds + q\ dz - q\ dz - \frac{\partial q}{\partial s} ds\ dz = 0$$

$$\frac{\partial \sigma_z}{\partial z}\ dz\ t\ ds + \frac{\partial q}{\partial s} ds\ dz = 0$$

Since Force Intensity $N = \sigma\ t$

Therefore the equation of equilibrium of a differential element is given by

$$\frac{\partial N}{\partial z} + \frac{\partial q}{\partial s} = 0 \qquad (2.8)$$

Equation of equilibrium relating internal shear flows to section torque is given by

$$\int_a qr\,ds = T \qquad (2.9)$$

where r is the radius for any point on the surface measured from the geometric centre.

Condition of Continuity of axial displacements is given by

$$\oint_n \frac{\partial w}{\partial s} ds = 0 \qquad (2.10)$$

This is so as there is No Axial load applied i.e. $P_{Axial} = 0$ and hence axial displacement variation around the box section is self balancing.

Substituting Eq. (2.2) into (2.7) and (2.1) into (2.6) we get Eqs (2.11) and (2.12) respectively.

$$N = (E' \varepsilon)\, t \qquad (2.11)$$

$$q = (G \gamma)\, t \qquad (2.12)$$

Next substituting Eq. (2.5) into (2.11) and (2.4) into (2.12) we get Eqs (2.13) and (2.14) respectively.

$$N = (E' \frac{\partial w}{\partial z})\, t \qquad (2.13)$$

$$q = G\, (\frac{\partial w}{\partial s} + \frac{\partial V_t}{\partial z})\, t \qquad (2.14)$$

Putting values of N and q from above in the equation of equilibrium Eq (2.8), we have

$$E' \frac{\partial}{\partial z} (t \frac{\partial w}{\partial z}) + G \frac{\partial}{\partial s} (t \frac{\partial w}{\partial s}) + G \frac{\partial}{\partial s} (t \frac{\partial V_t}{\partial z}) = 0 \qquad (2.15)$$

Warping displacement may be expressed as the product of a basic transverse distribution (the unit warping function) and the rate of twist

$$w = \overline{w}\, \theta \qquad (2.16)$$

The unit warping function $\overline{w}$ is referred as sectorial co-ordinate w(s) in chapter 3 and chapter 4.

Substituting Eq (2.4) into Eq (2.1)

$$\tau = G (\frac{\partial w}{\partial s} + \frac{\partial V_t}{\partial z}) \qquad (2.17)$$

As spanwise derivative of tangential displacement is given by the product $r_t \theta$

$$\frac{\partial V_t}{\partial z} = r_t \theta$$

Here r_t is the perpendicular distance from shear centre to the tangent at any point in the mid-plane of the beam section. This r_t is referred to as P_R in chapter 3 .

so Eq 2.17 above becomes

$$\tau = G \frac{\partial w}{\partial s} + G r_t \theta \qquad (2.18)$$

Also Shear stress may be expressed as product of a basic transverse distribution and $G\theta$

Hence

$$\tau = \bar{\tau} G \theta \qquad (2.19)$$

Here $\bar{\tau}$ is the basic transverse distribution and is defined as the transverse distribution for unit rate of twist,
where
Unit rate of twist is defined as $G\theta = 1$

Substituting Eq 2.16 and 2.19 into 2.18 we get

$$\bar{\tau} G \theta = G \frac{\partial \bar{w}}{\partial s} \theta + G r_t \theta$$

$$\bar{\tau} = \frac{\partial \bar{w}}{\partial s} + r_t$$

$$\frac{\partial \bar{w}}{\partial s} = \bar{\tau} - r_t \qquad (2.20)$$

Integrating Eq (2.20)

$$\bar{w} = \int_{s_0}^{s} (\bar{\tau} - r_t)\, ds + C_1 \qquad (2.21)$$

Warping displacement may be expressed as follows

$$w = \bar{w} f(z) \qquad (2.22)$$

Eq of equilibrium Eq. (2.15) is multiplied by $\bar{w}$ and then solved by Glerikan's method
Integrating over cross section , 1st , 2nd and 3rd integrals of the equation are evaluated and finally the equation of equilibrium reaches the form below

$$\frac{d}{dz}(E^{l}I_{w}\frac{df}{dz}) - G\int_{a} t\,(\bar{\tau} - r_t)\frac{\partial w}{\partial s}ds - G\int_{a} t\,(\bar{\tau} - r_t)\frac{\partial V_t}{\partial z}ds = 0 \quad (2.23)$$

I_w is warping moment of inertia given by

$$I_w = \int_{a} w(s)^2\, t\, ds$$

where w(s) is the Sectorial coordinate
and "t" is thickness

Now
Substituting Eq.(2.14) into (2.9) we have

$$\int_{a} (G\,t\frac{\partial w}{\partial s} + G\,t\frac{\partial V_t}{\partial z})\, r_t ds = T$$

$$G\int_{a} t\, r_t \frac{\partial w}{\partial s}ds + G\int_{a} t\, r_t \frac{\partial V_t}{\partial z}\, ds = T \quad (2.24)$$

Opening equation of equilibrium Eq. (2.23) we can write as

$$\frac{d}{dz}(E^{l}I_{w}\frac{df}{dz}) - G\int_{a} t\,\bar{\tau}\frac{\partial w}{\partial s}ds - G\int_{a} t\,\bar{\tau}\frac{\partial V_t}{\partial z}ds$$

$$+ (G\int_{a} t\, r_t \frac{\partial w}{\partial s}ds + G\int_{a} t\, r_t \frac{\partial V_t}{\partial z}ds) = 0 \quad (2.25)$$

Substituting the value of Torque T from Eq. (2.24) into (2.25) we have

$$\frac{d}{dz}(E^{l}I_{w}\frac{df}{dz}) - G\int_{a} t\,\bar{\tau}\frac{\partial w}{\partial s}ds - G\int_{a} t\,\bar{\tau}\frac{\partial V_t}{\partial z}ds = -T \quad (2.26)$$

Since $\bar{q} = t\,\bar{\tau}$ (2.27)

The 2nd Integral of Eq. (2.26) becomes

$$\int_{a} t\,\bar{\tau}\frac{\partial w}{\partial s}ds = \int_{a}\bar{q}\frac{\partial w}{\partial s}ds = \sum_{n}\bar{q}_n \oint_{n}\frac{\partial w}{\partial s}ds \quad (2.28)$$

The RHS of Eq. 2.28 becomes zero using the continuity equation Eq (2.10)

Hence

$$\int_a t\ \bar{\tau}\ \frac{\partial w}{\partial s} \mathrm{ds} = 0 \qquad (2.29)$$

Now substituting Eq. 2.29 in Eq. 2.26, the 2nd Integral of 2.26 becomes zero and we have

$$\frac{d}{dz}(E^{/} I_w \frac{df}{dz}) - \mathrm{G} \int_a t\ \bar{\tau}\ \frac{\partial V_t}{\partial z} \mathrm{ds} = -\mathrm{T} \qquad (2.30)$$

This equation 2.30 is the equation of equilibrium

Now for the solutions of Eq. 2.24 and 2.30 we consider

$$V_t = r_t\ \phi \qquad (2.31)$$

Substituting Eq. (2.22) $w = \bar{w}\ f(z)$ and (2.31) into Eq. (2.24) we have

$$\mathrm{G} \int_a \mathrm{t}\ r_t \frac{\partial}{\partial s}(\bar{\mathrm{w}}\ \mathrm{f})\ \mathrm{ds} + \mathrm{G} \int_a \mathrm{t}\ r_t (\frac{\partial}{\partial z}(\mathrm{r_t}\ \phi))\ ds = \mathrm{T}$$

$$\mathrm{G\,f} \int_a \mathrm{t}\ r_t \frac{\partial \bar{\mathrm{w}}}{\partial s}\ \mathrm{ds} + \mathrm{G} \int_a \mathrm{t}\ r_t (\frac{\partial}{\partial z}(\mathrm{r_t}\ \phi))\ ds = \mathrm{T} \qquad (2.32)$$

Substituting $\frac{\partial \bar{w}}{\partial s} = \bar{\tau} - r_t$

and $\frac{\partial \phi}{\partial z} = \theta$ into Eq. 2.32 we have

$$\mathrm{G\,f} \int_a \mathrm{t}\ r_t (\bar{\tau} - r_t)\ \mathrm{ds} + \mathrm{G}\ \theta \int_a \mathrm{t}\ r_t^{\,2}\ ds = \mathrm{T} \qquad (2.33)$$

Second Moment of Area introduced by Benscoter $I_c = \int_a \mathrm{t}\ r_t^{\,2} ds \qquad (2.34)$

Putting (2.34) into (2.33) we have

$$G f \int_a t \bar{\tau} r_t \, ds - G I_c f + G I_c \theta = T \qquad (2.35)$$

Since we have $\tau = \bar{\tau} G \theta$ (2.19)

Multiplying both sides by $r_t t \, ds$ and integrating over the cross section we have

$$\int_a \tau r_t t \, ds = \int_a \bar{\tau} G \theta r_t t \, ds$$

Left hand side above is the definition of Torque, hence we have

$$T = \int_a \bar{\tau} r_t t \, ds \; G \theta$$

Here $\int_a \bar{\tau} r_t t \, ds$ is defined as Unit Torque = $\bar{T}$

Hence

$$T = \bar{T} G \theta$$

Hence Unit Torque $\bar{T} = \frac{T}{G\theta}$

We know that $T = G J \theta$

Therefore $J = \frac{T}{G\theta}$

So we can conclude that Torsion constant J = Unit Torque $\bar{T}$

$$J = \bar{T}$$

Hence we can write J as below

$$J = \int_a t \bar{\tau} r_t \, ds$$

we have Eq. (2.35) as

$$G f (J - I_c) + G I_c \theta = T \qquad (2.36)$$

A dimension-less section constant has been defined by Benscoter[2] as follows

$$\eta^2 = 1 - \frac{J}{I_C} \qquad (2.37)$$

where

J is the torsion constant

and

I_c is Second Moment of Area

This constant η^2 indicates the slenderness of the cross section or the amount by which the section is non regular. For a regular polygon it is zero. For a very thin supersonic wing it approaches unity. For a subsonic aeroplane with a fairly thick wing the value of η^2 will be in the neighbourhood of 0.5.

Substituting Eq. 2.37 into Eq. 2.36 we have

$$- G f I_c \left(1 - \frac{J}{I_c} \right) + G I_c \theta = T \qquad (2.38)$$

$$- G f I_c \eta^2 + G I_c \theta = T \qquad (2.39)$$

Rate of twist θ is given by Benscoter as follows

$$\theta = \frac{T}{GI_C} + \eta^2 f \qquad (2.40)$$

where "f" is the spanwise variation of axial displacements

The first term here gives the rate of twist due to shearing strains and the second term gives the rate of twist due to axial warping displacements.

f can be written as below

$$f = \frac{\theta}{\eta^2} - \frac{T}{\eta^2 G I_c} \qquad (2.41)$$

Now substituting Eq. 2.31 into Equation of equilibrium 2.30 we get

$$\frac{d}{dz}(E' I_w \frac{df}{dz}) - G \int_a t \; \bar{\tau} \; \frac{\partial}{\partial z}(r_t \phi) \; ds = - T$$

$$\frac{d}{dz}(E' I_w \frac{df}{dz}) - G \theta \int_a t \; \bar{\tau} \; r_t \; ds = - T$$

Since $\theta = \frac{\partial}{\partial z}(\phi)$

Torque "T" is given by Benscoter as follows

$$\frac{d}{dz}(E' I_w \frac{df}{dz}) - GJ\theta = - T \qquad (2.42)$$

Here $E' = \frac{E}{1-\nu^2}$

Now putting value of f into Eq. 2.42 we have

$$\frac{d}{dz}(E' I_w \frac{d}{dz}(\frac{\theta}{\eta^2} - \frac{T}{\eta^2 G I_c})) - GJ\theta = - T$$

$$\frac{d}{dz}(E' I_w \frac{d}{dz}(\frac{\theta}{\eta^2})) - \frac{d}{dz}(E' I_w \frac{d}{dz}(\frac{T}{\eta^2 G I_c})) - GJ\theta = - T$$

$$\frac{d}{dz}(E^{/}I_w\frac{d}{dz}(\frac{\theta}{\eta^2})) - GJ\theta = - T + \frac{d}{dz}(E^{/}I_w\frac{d}{dz}(\frac{T}{\eta^2 GI_c}))$$

where $\theta_0 = \frac{T}{GI_C}$

Hence we have

$$\frac{d}{dz}[E^{/}I_w\frac{d}{dz}(\frac{\theta}{\eta^2})] - GJ\theta = - T + \frac{d}{dz}[E^{/}I_w\frac{d}{dz}(\frac{\theta_0}{\eta^2})] \qquad (2.43)$$

In solving equation 2.43 , $\frac{\theta}{\eta^2}$ may be regarded as unknown.

Equation 2.37 suggests that η will have only a small variation along span if the general shape of the cross section does not change rapidly. The section properties J and I_c are both properties of the shear carrying area. If the variation of "η" along "z" is neglected then equation 2.43 takes the form

$$\frac{d}{dz}[E^{/}C\frac{d\theta}{dz}] - GJ\theta = - T + \frac{d}{dz}[E^{/}C\frac{d\theta_0}{dz}] \qquad (2.44)$$

where Torsion bending constant has been defined below by Eq. 2.45

$$C = \frac{I_w}{\eta^2} \qquad (2.45)$$

The differential equation 2.44 being presented here can be used for analysing torsional response of single-cell and multi-cell isotropic prismatic and tapered box beams. The solution procedure for using this equation in the analysis of isotropic materials and composite materials has been discussed in chapter 3 and chapter 4 respectively.

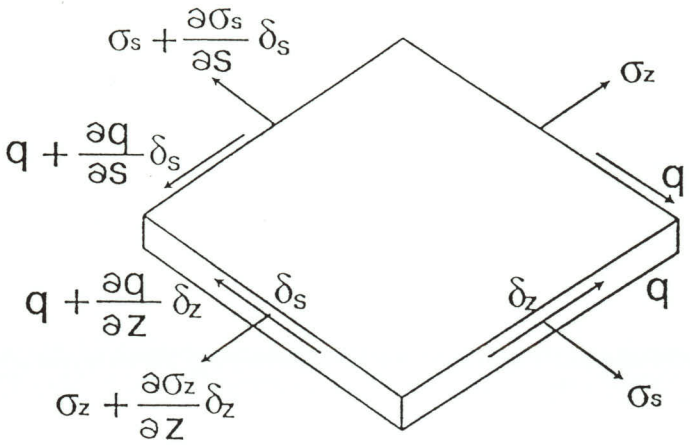

Fig 2.1 Direct stress and shear flow system on an element of a closed section

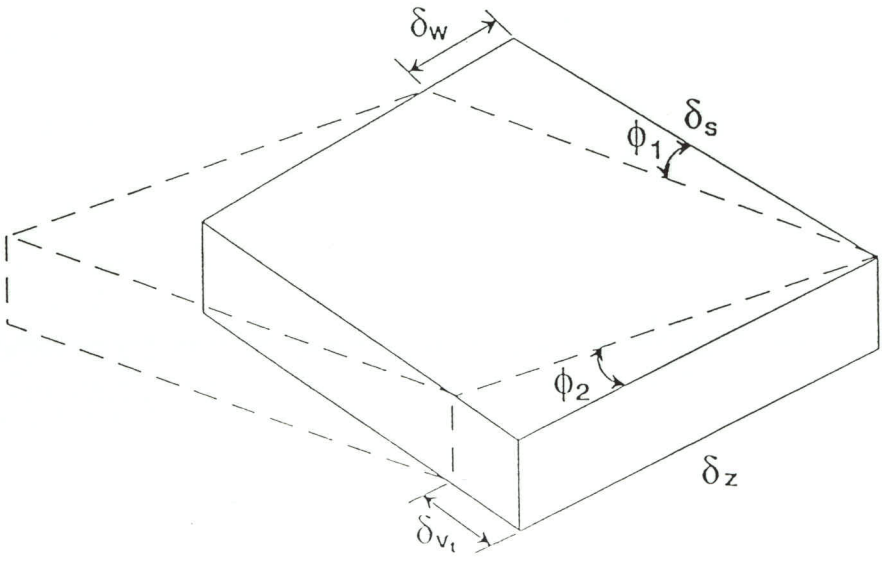

Fig 2.2 Distorted shape of element due to shear stresses in an element of the beam section wall

3 TORSION THEORY OF MULTI-CELL THIN -WALLED ISOTROPIC BEAMS

3.1 INTRODUCTION

Warping is considered to be the most significant effect of the application of torsion on single cell and multi-cell thin walled beams. When there are no axial restraints applied on the beam i.e. **free torsion** case , the beam is not restrained at any end then according to the classical St.Venant's theory the only stress that could exist in the thin walled beam under such conditions is the shear stress. However if the beam is restrained axially at an end then under such **restrained torsion** case direct (axial) stresses do exist on the torsionally loaded beam.

The reason for the existence of these direct (axial) stresses is simple, since the beam wants to warp due to the application of torsional load and is not allowed to warp at the restrained end then this gives rise to direct (axial) stresses in the beam. These direct (axial) stresses are a maximum at the restrained end and drop down to zero at the free end. The rate of twist which is constant along the length of the beam in free torsion case of prismatic uniform beam does no longer remain constant in the restrained torsion case due to the existence of the warping restraint , which produces variable twist and also gives rise to the direct (axial) stresses.

Thin walled beams subjected to torsion experience two types of warping. Primary warping is the warping of the mid-plane of the cross-section which is constant across the wall thickness. Secondary warping is the warping of the section across its wall thickness . In such sections which posses primary warping the effects of secondary warping are

usually neglected as they are generally much less than primary warping. However if a section only exhibits secondary warping then this must be accounted for.
The assumptions in the evaluation of the theory of torsion of thin walled beams are listed below.

(a) Cross-section of any beam, is stiffened against distortion, i.e. , it remains undistorted in its own plane after loading.

(b) Shear stresses normal to beam surface are neglected.

(c) It is generally agreed that thin wall theory may be applied with reasonable accuracy to sections for which the ratio

$$t_{max} / b \leq 0.1$$

where t_{max} is the maximum thickness in the section and b is the typical cross-sectional dimension. A general view of thin walled multi-cell box beam cross section is shown in figure 3.1 .

3.2 TORSIONAL ANALYSIS OF MULTI-CELL SECTION

By considering the connectivity condition of a single cell, an expression may be derived in terms of constant shear flow "F" and the rate of twist 'θ' which has been given by Waldron[1] as follows

$$\oint (F/\delta)ds = G \Omega \theta$$

For multi cellular sections it can be restated as

$$\theta = \frac{1}{G\Omega_i} \oint_i \frac{F_i}{\delta i} ds$$

Here G is the shear modulus , δ is the thickness and 'θ' refers to rate of twist of complete section about its shear centre. The contour integral is evaluated around the entire perimeter of the ith cell only. The area of the ith cell is $\Omega_i/2$. When pure torque is applied, the shear flow 'F_i' around each of the separate cells is constant , and in the shared walls it is the difference in shear flow of both adjacent cells. When applying the above equation to 'n' cells we get 'n' simultaneous equations of the general form

$$\theta G \Omega_i = - F_{i-1} \frac{s_{i-1,i}}{\delta_{i-1,i}} + F_i \oint \frac{ds}{\delta_i} - F_{i+1} \frac{s_{i,i+1}}{\delta_{i,i+1}} \qquad (3.1)$$

here $s_{i,i+1}$, $\delta_{i,i+1}$ are the length and thickness respectively of the shared wall connecting cells i and i+1.

For the single cell an extra expression is available from the Torsion equilibrium condition

$T = 2AF_i$ (Bredt Batho Formula)

we may write above for multi-cell sections as follows

$$T = \sum_{i=1}^{n} F_i \Omega_i \qquad (3.2)$$

Hence it is now possible to solve for the shear flows ' F_i ' and rate of twist 'θ' for the multi cellular box section using equations 3.1 and 3.2 .

Example

The following example refers to figures 3.6 and 3.7, and shows the application of equations 3.1 and 3.2 in calculating the rate of twist and the Bredt Batho shear flows in each of the three cells for a multi- cell box with given dimensions as shown in referred figure.

First we set up three equations using eq. 3.1 , one for each of the three cells.

$$\theta G \Omega_i = - F_{i-1} \frac{s_{i-1,i}}{\delta_{i-1,i}} + F_i \oint \frac{ds}{\delta_i} - F_{i+1} \frac{s_{i,i+1}}{\delta_{i,i+1}} \qquad (3.1)$$

Here we have

T= 1,000,000 Nmm

Ω_i = 2*Area = 2*(200*150)= 60,000 mm^2 for each of the three cells

G = 80700 N/mm^2 (steel)

thickness δ = 1 mm for each cell

Hence for cell i-1 we have

θ*(80700)*(60,000) = + F_{i-1} *(700) - F_i *(150)

and for cell i we have

θ*(80700)*(60,000) = - F_{i-1} *(150) + F_i *(700) - F_{i+1} *(150)

finally for cell i+1 we have

θ*(80700)*(60,000) = - F_i *(150) + F_{i+1} *(700)

Next the fourth equation is written from eq. 3.2 as below

$$T = \sum_{i=1}^{n} F_i \, \Omega_i \qquad (3.2)$$

T= 1,000,000 = 60,000 *F_{i-1} + 60,000 *F_i + 60,000 *F_{i+1}

Now solving above four equations we get the following rate of twist θ , and the Bredt Batho shear flows in the three cells i-1 , i and i+1 as shown in figure 3.7 .

θ = 5.673 E - 7 rad/mm

F_{i-1} = 5.25 N/mm

F_i = 6.17 N/mm

F_{i+1} = 5.25 N/mm

3.2.1 SECTORIAL CO-ORDINATE w(s)

Sectorial co-ordinate around the isotropic single-cell box section is given by M.Fine &Williams D[3] as follows

$$w(s) = \int_0^s (P_R - \frac{\Psi}{t}) ds \qquad (3.3)$$

where $\Psi = \dfrac{2A}{\oint \frac{ds}{t}}$ for closed section (3.4)

Hence

$$w(s) = \int_0^s \left[P_R - \frac{\frac{2A}{\oint \frac{ds}{t}}}{t} \right] ds$$

$$w(s) = \int_0^s P_R \, ds - \int_0^s \frac{2A}{(\oint \frac{ds}{t} * t)} ds$$

Since $q = \tau\ t$

Here "q" is shear flow and "τ" is shear stress

"T" is applied Torque and "t" is thickness

also $q = \frac{T}{2A}$

therefore $\tau t = \frac{T}{2A}$

or $2A = \frac{T}{\tau t}$

hence

$$w(s) = \int_0^s P_R\, ds - \int_0^s \frac{\frac{T}{\tau t}}{(\oint \frac{ds}{t} * t)} ds$$

since rate of twist $\theta = \Phi' = \frac{d\Phi}{dz} = \frac{1}{2A}\oint \frac{q}{Gt} ds = \frac{T}{GJ}$ (3.5)

therefore

$$T = \frac{GJ}{2A}\oint \frac{q}{Gt} ds$$

using above T , w(s) becomes

$$w(s) = \int_0^s P_R\,ds - \int_0^s \frac{\frac{GJ}{2A}\oint\frac{q}{Gt}ds}{\frac{\pi t}{(\oint\frac{ds}{t}*t)}}ds$$

$$w(s) = \int_0^s P_R\,ds - \int_0^s \frac{\frac{GJ}{2A\pi t}\oint\frac{q}{Gt}ds}{(\oint\frac{ds}{t}*t)}ds$$

$$w(s) = \int_0^s P_R\,ds - \int_0^s \frac{\frac{GJ}{T}\oint\frac{q}{Gt}ds}{(\oint\frac{ds}{t}*t)}ds$$

since $\theta = \Phi' = \frac{d\Phi}{dz} = \frac{T}{GJ}$

therefore

Sectorial co-ordinate is given as follows

$$w(s) = \int_0^s P_R\,ds - \frac{q}{\theta G}\int_0^s \frac{ds}{t} \qquad (3.6)$$

Here $\oint \frac{ds}{t}$ has cancelled out top and bottom and thus "q" and "G" are considered constant for the single cell box , but we can have different thickness "t" .

This can be written for multi cellular sections as follows

$$w(s) = \int_0^s P_R \, ds - \frac{1}{\theta G} \int_0^s \frac{F_i}{t_i} \, ds \qquad (3.7)$$

Since the integration must be started at point of zero warping , therefore an imaginary cut is made in the closed box section for this reason. Above formula for w(s) takes into consideration the effect of imaginary cut in the closed section.

Warping distribution for a multi-cell box beam is shown in figure 3.2 .

Example

Referring to figures 3.6 and 3.8 , and the example mentioned in section 3.2 for the calculation of the rate of twist and shear flows for a three cell box, now the same example is being extended for calculation of the w(s) at each location of the multi-cell box section using equation 3.7

We have defined w(s) for multi-cell section as

$$w(s) = \int_0^s P_R \, ds - \int_0^s \frac{1}{\theta} \frac{F_i}{G t_i} \, ds \qquad (3.7)$$

Now calculating the 1st and 2nd integral of eq. 3.7 for each of the three cells of the multi-cell section we have as follows.

1st Integral

cell i-1

P_R is considered positive when going around Shear centre in Anti-Clockwise direction.

$$w(s)_{A\text{-}B} = \int_0^s P_R\,ds = \int 300\,ds = 22500 \text{ at B}$$

$$w(s)_{B\text{-}C} = \int_0^s P_R\,ds = 22500 + \int 75\,ds = 37500 \text{ at C}$$

$$w(s)_{C\text{-}D} = \int_0^s P_R\,ds = 37500 - \int 100\,ds = 22500 \text{ at D}$$

$$w(s)_{D\text{-}E} = \int_0^s P_R\,ds = 22500 + \int 75\,ds = 37500 \text{ at E}$$

$$w(s)_{E\text{-}F} = \int_0^s P_R\,ds = 37500 + \int 300\,ds = 60000 \text{ at F}$$

1st Integral

cell i

$$w(s)_{G\text{-}H} = \int_0^s P_R\,ds = 7500 \text{ at H}$$

$$w(s)_{H\text{-}I} = \int_0^s P_R\,ds = 22500 \text{ at I}$$

$$w(s)_{I\text{-}J} = \int_0^s P_R\,ds = 37500 \text{ at J}$$

$$w(s)_{J\text{-}K} = \int_0^s P_R\,ds = 52500 \text{ at K}$$

$$w(s)_{K\text{-}L} = \int_0^s P_R\,ds = 60000 \text{ at L}$$

1st Integral

cell i+1

$$w(s)_{M\text{-}N} = \int_0^s P_R\,ds = \int 300\,ds = 22500 \text{ at N}$$

$$w(s)_{N\text{-}O} = \int_0^s P_R\,ds = 22500 + \int 75\,ds = 37500 \text{ at O}$$

$$w(s)_{O\text{-}P} = \int_0^s P_R\,ds = 37500 - \int 100\,ds = 22500 \text{ at P}$$

$$w(s)_{P\text{-}Q} = \int_0^s P_R\,ds = 22500 + \int 75\,ds = 37500 \text{ at Q}$$

$$w(s)_{Q\text{-}R} = \int_0^s P_R\,ds = 37500 + \int 300\,ds = 60000 \text{ at R}$$

Now 2nd Integral

cell i-1

$$w(s)_{A\text{-}B} = \int_0^s \frac{1}{\theta}\frac{F_i}{Gt_i}\,ds = \frac{5.25}{(5.67E-11)*(80700)}\int_0^s ds = 114.60(s) = 8595.5 \text{ at B}$$

$w(s)_{B\text{-}C}$ = 8595.5 + (114.60 * s) = 31516.83 at C

$w(s)_{C\text{-}D}$ = 31516.83 - (20.22 * s) = 28483 at D

(F_i is -ve when going from C to D as actually +ve shear flow of 6.17-5.25 = 0.92 is flowing from D to C)

$w(s)_{D\text{-}E}$ = 28483 + (114.60 * s) = 51404.5 at E

$w(s)_{E\text{-}F}$ = 51404.5 + (114.60 * s) = 60,000 at F

2nd Integral

cell i

$$w(s)_{G\text{-}H} = \int_0^s \frac{1}{\theta}\frac{F_i}{Gt_i}\,ds = \frac{6.17}{(5.67E-11)*(80700)}\int_0^s ds = 134.83(s) = 13483 \text{ at H}$$

$w(s)_{H\text{-}I}$ =13483 + (20.22 * s) = 16516.8 at I

$w(s)_{I\text{-}J}$ = 16516.8 + (134.83 * s) = 43483 at J

$w(s)_{J\text{-}K}$ = 43483 + (20.22 * s) = 46516.7 at K

$w(s)_{K\text{-}L}$ = 46516.7 + (134.83 * s) = 60,000 at L

2nd Integral

cell i+1

$$w(s)_{M\text{-}N} = \int_0^s \frac{1}{\theta}\frac{F_i}{Gt_i}\,ds = \frac{5.25}{(5.67E-11)*(80700)}\int_0^s ds = 114.60(s) = 8595.5 \text{ at N}$$

$w(s)_{N\text{-}O}$ =8595.5 + (114.60 * s) = 31516.83 at O

$w(s)_{O\text{-}P}$ = 31516.83 - (20.22 * s) = 28483 at P

(F_i is -ve when going from O to P as actually +ve shear flow of 6.17-5.25 = 0.92 is flowing from P to O)

$w(s)_{P\text{-}Q}$ = 28483 + (114.60 * s) = 51404.5 at Q

$w(s)_{Q\text{-}R}$ = 51404.5 + (114.60 * s) = 60,000 at R

Net effect of w(s) i.e. 1st Integral - 2nd Integral for all the three cells is shown in figure 3.9.

3.2.2 WARPING RIGIDITY $(E\ \Gamma)_s$

Warping rigidity according to Von Karman and Christnesen[4] is given as follows

$$(E\ \Gamma)_s = \oint w^2(s) E_x^a\ t\ ds \qquad (3.8)$$

From figure 3.3 showing Sectorial Co-ordinate distribution,
for single cell plate element we have w(s) as follows

$$w(s) = \frac{(w_k - w_i)s}{L} + w_i$$

It satisfies conditions at all points along s

If s=0 we have $w(s) = w_i$

If s=L we have $w(s) = w_k$

If $s=\frac{L}{2}$ we have $w(s) = (\frac{w_k + w_i}{2})$

Hence above equation is valid at all points along s

So we have

$$w^2(s) = [\ (\frac{w_k - w_i}{L})s + w_i\ ]^2$$

$$w^2(s) = \left(\frac{w_k - w_i}{L}\right)^2 s^2 + w_i^2 + 2\left(\frac{w_k - w_i}{L}\right) s * w_i$$

$$w^2(s) = \frac{s^2}{L^2}(w_k^2 + w_i^2 - 2w_k w_i) + w_i^2 + \frac{2s}{L}(w_k w_i - w_i^2)$$

Now for a single plate element we have

$$\int_0^L w^2(s)\, ds = \frac{1}{L^2}(w_k^2 + w_i^2 - 2w_k w_i) * \frac{s^3}{3} + w_i^2 * s + \frac{2}{L}(w_k w_i - w_i^2)\frac{s^2}{2}$$

Putting limits we have

$$\int_0^L w^2(s)\, ds = \frac{L}{3}(w_k^2 + w_i^2 - 2w_k w_i) + w_i^2 * L + (w_k w_i - w_i^2) * L$$

$$\int_0^L w^2(s)\, ds = \frac{L}{3}(w_k^2 + w_i^2 - 2w_k w_i + 3w_i^2 + 3w_k w_i - 3w_i^2)$$

$$\int_0^L w^2(s)\, ds = \frac{L}{3}(w_k^2 + w_i^2 + w_k w_i) \qquad (3.9)$$

Hence the Warping Rigidity $(E\ \Gamma)_s$ defined above as

$$(E\ \Gamma)_s = \oint w^2(s) E_x^a\ t\ ds$$

can now be written as follows

$$(E\ \Gamma)_s = \frac{1}{3}\sum_{i=1}^{N} L_n t_n E^a_{x_n} \quad (w^2_{k_n} + w^2_{i_n} + w_{k_n} w_{i_n}) \qquad (3.10)$$

Example

Referring to figures 3.6, 3.8 and 3.9 , and the example mentioned in section 3.2 for calculation of the rate of twist and shear flows for a three cell box, now the same example is being extended for calculation of $(E\ \Gamma)_s$ for the multi-cell box beam.

$$(E\ \Gamma)_s = \frac{1}{3}\ \{\ (2*(150)*(1)*(2.30769E5)*(13904)^2\ ) +$$
$$(\ 2*(150)*(1)*(2.30769E5)*(5983)^2\ ) +$$
$$(\ 2*(200)*(1)*(2.30769E5)*(5983)^2\ ) +$$
$$(\ 4*(200)*(1)*(2.30769E5)*(\ (13904)^2 + (5983)^2 + (13904*5983)\ )\ \}$$

$(E\ \Gamma)_s = 2.560917534638936\ E\ 16$

3.2.3 SECTORIAL SHEAR FUNCTION $S_w(s)$

Sectorial shear function for open sections is defined as

$$S_w(s) = S_{w,0}(s) = \int_0^s w(s)tds$$

in which case the integration must be started at a free edge.

However for closed section , we do not have any free edge and hence starting point must be chosen arbitrarily. Therefore first an imaginary cut at any point of the section is assumed and SSF (Sectorial shear function) distribution $S_{w,0}(s)$ of this quasi isotropic

section is calculated by above equation. Afterwards it is modified by a constant to provide final reduced value of the closed section SSF distribution $S_{w,c}(s)$. The $S_{w,c}(s)$ for a single cell box section is as follows.

$$S_{w,c}(s) = S_{w,0}(s) - \frac{1}{2A}\int_s S_{w,0}(s)P_R ds \qquad (3.11)$$

Here the second term on the RHS of the equation gives the constant which modifies the final SSF distribution.

However in case of multi-cell box section the final reduced value of the closed section SSF distribution $S_{w,c}(s)$ is given as

$S_{w,c}(s)$ at any location of cell i-1 = F^*_{i-1} - $S_{w,0}(s)$ of the given location

$S_{w,c}(s)$ at any location of cell i = F^*_{i} - $S_{w,0}(s)$ of the given location

$S_{w,c}(s)$ at any location of cell i+1 = F^*_{i+1} - $S_{w,0}(s)$ of the given location

Here F^*_{i-1} , F^*_{i} & F^*_{i+1} are the warping shear flows under constrained torsion in each of the three cells and are calculated using following set of equations defined by Waldron[1] .

$$\theta^* G\Omega_i = -F^*_{i-1}\frac{s_{i-1,i}}{\delta_{i-1,i}} + F^*_{i}\oint\frac{ds}{\delta_i} - F^*_{i+1}\frac{s_{i,i+1}}{\delta_{i,i+1}} - \oint_i \frac{S_{w,0}}{t_i}ds \qquad (3.12)$$

Three set of equations i.e. one for each of the cells are obtained from eq. 3.12 and the fourth equation is obtained using eq. 3.13

$$T = \oint F_w P_R ds = \sum_{i=1}^{n} F^*_{i}\,\Omega_i - \oint S_{w,0}P_R ds = 0 \qquad (3.13)$$

(F_w in eq. 3.13 is the self equilibrating shear flow)

Solving these four equations , the four unknowns θ^*, F^*_{i-1} , F^*_i & F^*_{i+1} are obtained and used to get the final reduced value of $S_{w,c}(s)$ at all required locations in the multi-cell box section. The detailed procedure showing the calculation of $\oint_i \frac{S_{w,0}}{t_i} ds$ & $\oint S_{w,0} P_R ds$ and hence the calculation of final reduced value of $S_{w,c}(s)$ is shown in the following example in detail.

In case of restrained torsion , the shear flow consists of two factors Bredt Batho shear flow and warping shear flow. The applied torque on the beam is balanced by the Bredt Batho shear flow , where as the warping shear flow does not take any part in the balancing of the applied torque. Warping shear flow comes into effect only for the case of restrained torsion, when the restraint applied at the end of the beam stops the warping displacement of the beam at this end and hence gives rise to axial stresses all along the length of the beam. In addition to the axial stresses , there exists a warping shear flow which is self equilibrating around the beam cross-section. The reason for warping shear flow being self equilibrating is that since no axial force is being applied on the beam therefore $\oint_n \frac{\partial w}{\partial s} ds = 0$, which means that axial displacement variation around the box surface is self equilibrating. Therefore warping shear flow must also be self equilibrating and should balance itself out on its own at any given cross-section of the beam.

Example

Referring figures 3.6, 3.8 and 3.9 , and the example mentioned above in section 3.2 for calculation of the rate of twist and shear flows for a three cell box, now the same example is being extended for calculation of $S_{w,c}(s)$ for the multi-cell box beam.

We need to first calculate $S_{w,0}(s)$ for each of the three cells and then later on it will be modified to $S_{w,c}(s)$

We know that

$$w(s) = \frac{(w_k - w_i)s}{L} + w_i$$

and

$$S_{w,0}(s) = \int_0^s w(s)tds$$

For Cell i-1 we have as follows

$$w(s)_{AB} = \frac{(13904 - 0)}{75} * s + 0$$

$$w(s)_{AB} = 185.38 * s$$

$$S_{w,0}(s)_{AB} = \int_0^s w(s)tds = \int_0^s (185.38 * s) * (1)\ ds$$

s = 75 for A-B

$S_{w,0}(s)_{AB}$ = 521418 is the value at point B

Next

$$w(s)_{BC} = w(s)_B + \frac{(5983 - 13904)}{200} * s$$

$$w(s)_{BC} = 13904 - 39.60 * s$$

$$S_{w,0}(s)_{BC} = S_{w,0}(s)_B + \int_0^s w(s)tds$$

$$= 521418 + \int_0^s (13904 - 39.60 * s) * (1)\ ds$$

s = 200 for B-C

$S_{w,0}(s)_{BC}$ = 2510182 is the value at point C

Similarly for other points we find $S_{w,0}(s)$ as below

$S_{w,0}(s)$ at D = 2510182

$S_{w,0}(s)$ at E = 521418

$S_{w,0}(s)$ at F = 0

Now for cell i we have as follows

$S_{w,0}(s)$ at H = - 299157

$S_{w,0}(s)$ at I = - 299157

$S_{w,0}(s)$ at J = - 299157

$S_{w,0}(s)$ at K = - 299157

$S_{w,0}(s)$ at L = 0

Next for cell i+1 we have as follows

$S_{w,0}(s)$ at N = 521418

$S_{w,0}(s)$ at O = 2510182

$S_{w,0}(s)$ at P = 2510182

$S_{w,0}(s)$ at Q = 521418

$S_{w,0}(s)$ at R = 0

Now after finding $S_{w,0}(s)$ for all the three cells above , next we need to find $\oint \frac{S_{w,0}}{t_i} ds$ for each of the three cells.

For cell i-1 ,

$$\oint \frac{S_{w,0}}{t_i} ds = \int_O^B \frac{S_{w,0}}{t_i} ds + \int_B^C \frac{S_{w,0}}{t_i} ds + \int_C^D \frac{S_{w,0}}{t_i} ds + \int_D^E \frac{S_{w,0}}{t_i} ds + \int_E^F \frac{S_{w,0}}{t_i} ds$$

$$\int_O^B \frac{S_{w,0}}{t_i} ds = \int_0^{75} \frac{S_{w,0}}{1} ds$$

Now we know $S_{w,0}(s)_{AB}$ from above calculation as

$$S_{w,0}(s)_{AB} = \int_0^s w(s) t ds = \int_0^s (185.38 * s) * (1)\ ds = 185.38 * \frac{s^2}{2}$$

So we have

$$\int_O^B \frac{S_{w,0}}{t_i} ds = \int_0^{75} \frac{S_{w,0}}{1} ds = 13034942.0646067$$

next

$$\int_B^C \frac{S_{w,0}}{t_i} ds = \int_0^{200} \frac{S_{w,0}}{1} ds$$

$$S_{w,0}(s)_{BC} = S_{w,0}(s)_B + \int_0^s w(s) t ds = 521418 + \int_0^s (13904 - 39.60 * s) * (1)\ ds$$

$$S_{w,0}(s)_{BC} = 521418 + 13904 * s - 39.60 * \frac{s^2}{2}$$

Hence we have

$$\int_B^C \frac{S_{w,0}}{t_i} ds = \int_0^{200} \frac{S_{w,0}}{1} ds = 329566719.101124$$

Similarly we calculate

$$\int_C^D \frac{S_{w,0}}{t_i} ds = 398965980.337079$$

$$\int_{D}^{E} \frac{S_{w,0}}{t_i} ds = 329566719.101124$$

$$\int_{E}^{F} \frac{S_{w,0}}{t_i} ds = 13034942.0646067$$

Hence for complete cell i+1 we have $\oint \frac{S_{w,0}}{t_i} ds = 1084169302.66854$

Now for cell i ,

$$\oint \frac{S_{w,0}}{t_i} ds = \int_{G}^{H} \frac{S_{w,0}}{t_i} ds + \int_{H}^{I} \frac{S_{w,0}}{t_i} ds + \int_{I}^{J} \frac{S_{w,0}}{t_i} ds + \int_{J}^{K} \frac{S_{w,0}}{t_i} ds + \int_{K}^{L} \frac{S_{w,0}}{t_i} ds$$

so we have

$$\int_{G}^{H} \frac{S_{w,0}}{t_i} ds = -9971511.23595506$$

$$\int_{H}^{I} \frac{S_{w,0}}{t_i} ds = -67328342.6966292$$

$$\int_{I}^{J} \frac{S_{w,0}}{t_i} ds = -19911910.1123595$$

$$\int_{J}^{K} \frac{S_{w,0}}{t_i} ds = -67328342.6966292$$

$$\int_K^L \frac{S_{w,0}}{t_i} ds = -9967921.34831457$$

For complete cell i we have $\oint \frac{S_{w,0}}{t_i} ds = -174508028.089888$

We calculate and find that $\oint \frac{S_{w,0}}{t_i} ds$ for cell i-1 and cell i+1 are same ,

hence we have

$\oint \frac{S_{w,0}}{t_i} ds$ for cell i+1 = 1084169302.66854

Now

Next we need to find $\oint S_{w,0} P_R ds$ for the complete three cell box , which will be the addition of $\oint S_{w,0} P_R ds$ for all the three cells i-1, i and I+1.

Hence first we find $\oint S_{w,0} P_R ds$ for cell i-1 which will be the addition of $\oint S_{w,0} P_R ds$ for all the sides of this cell.

For cell i-1 we have

$\int_A^B S_{w,0} P_R ds =$ 3910482619.38202 (P_R for side AB is 300)

$\int_B^C S_{w,0} P_R ds =$ 24717503932.5843 (P_R for side BC is 75)

$\int_{C}^{D} S_{w,0} P_R ds$ = -39896598033.7079 (P_R for side CD is -100)

$\int_{D}^{E} S_{w,0} P_R ds$ = 24717503932.5843 (P_R for side DE is 75)

$\int_{E}^{F} S_{w,0} P_R ds$ = 3910482619.38202 (P_R for side EF is 300)

Hence $\oint S_{w,0} P_R ds$ for complete cell i-1 is addition of all above =17359375070.2247

Similarly $\oint S_{w,0} P_R ds$ for complete cell i is calculated as =-16454519241.5730

and $\oint S_{w,0} P_R ds$ for complete cell i +1 is calculated as =17359375070.2247

Hence $\oint S_{w,0} P_R ds$ for complete three-cell box is calculated by adding all the three cells $\oint S_{w,0} P_R ds$ and is found to be = 18264230898.8764

Next we need to calculate warping shear flows for restrained torsion F^*_{i-1} , F^*_i & F^*_{i+1} in each cell of the three-cell box and also the restrained rate of twist θ^* using Waldron[1] equation mentioned below by setting up three equations i.e. one for each cell.

$$\theta^* G \Omega_i = - F^*_{i-1} \frac{s_{i-1,i}}{\delta_{i-1,i}} + F^*_i \oint \frac{ds}{\delta_i} - F^*_{i+1} \frac{s_{i,i+1}}{\delta_{i,i+1}} - \oint_i \frac{S_{w,0}}{t_i} ds$$

Here we have

T= 1000,000 Nmm

Ω_i = 2*Area = 2*(200*150)= 60,000 mm^2 for each of the three cells

G = 80700 N/mm^2 (steel)

thickness δ = 1 mm for each cell

Hence for cell i-1 we have

θ^**(80700)*(60,000) = + F^*_{i-1} *(700) - F^*_i *(150) - 1084169302.66854

and for cell i we have

θ^**(80700)*(60,000) = - F^*_{i-1} *(150) + F^*_i *(700)-F^*_{i+1} *(150)+ 174508028.0898

finally for cell i+1 we have

θ^**(80700)*(60,000) = - F^*_i *(150) + F^*_{i+1} *(700) - 1084169302.66854

the fourth equation is written from considering following equation

$$\sum_{i=1}^{n} F^*_i \, \Omega_i - \oint S_{w,0} P_R ds = 0$$

60,000 * F^*_{i-1} + 60,000 * F^*_i + 60,000 * F^*_{i+1} - 18264230898.8764 = 0

Now solving above four equations we get the following rate of twist θ^* , and the warping shear flows in the three cells i-1 , i and i+1 .

θ^* = -0.117270187858295 rad/mm

F^*_{i-1} = 562007.630305868 N/mm

F^*_i = -819611.412297129 N/mm

F^*_{i+1} = 562007.630305868 N/mm

Now we need to finally get the $S_{w,c}(s)$ at each location around the three cell box by using following relation

$S_{w,c}(s)$ at point B = F^{*}_{i-1} - $S_{w,0}(s)$ at point B

and similarly for all other points around the three cells i-1,i and I+1.

Hence for cell i-1, we get the $S_{w,c}(s)$ values as follows

$S_{w,c}(s)_B$ = 40589.0909800251

$S_{w,c}(s)_C$ = -1948174.95396380

$S_{w,c}(s)_D$ = -1948174.95396380

$S_{w,c}(s)_E$ = 40589.0909800249

$S_{w,c}(s)_F$ = 562007.630305868

and for cell i, we get the $S_{w,c}(s)$ values as follows

$S_{w,c}(s)_H$ = -520454.108926342

$S_{w,c}(s)_I$ = -520454.108926342

$S_{w,c}(s)_J$ = -520454.108926342

$S_{w,c}(s)_K$ = -520454.108926342

$S_{w,c}(s)_L$ = -819611.412297129

Cell i+1 has same $S_{w,c}(s)$ results as that of cell i+1, results of $S_{w,0}(s)$ and $S_{w,c}(s)$ for the three cell box is shown in figures 3.10 and 3.11.

3.2.4 BENSCOTER[2] APPROACH

Ata[7] has shown that the spanwise variation of stresses and rotations obtained by Von Karman and Christnesen[4] was NOT accurate as they did not consider accurately the effect of warping shearing strains upon deflections. A more accurate analysis was provided by Benscoter[2] to overcome this problem in Von Karman and Christnesen[4] approach due to neglecting of γ_{Γ} .

Hence Benscoter[2] gave his "λ" (Benscoter factor) which when multiplied by warping rigidity $(E\Gamma)$ changes it to $(E\Gamma)_B$ thus making it accurate.

Benscoter factor "λ"has been defined by Benscoter[2] to modify the Sectorial moment of inertia "Γ" as below. It has been defined as η^2 in chapter 2.

$$\eta^2 = \lambda = 1 - \frac{J}{I_C} \qquad (3.14)$$

where I_c is named as polar constant and is defined as follows

$$I_c = \oint P_R^2 t ds = \sum_{i=1}^{N} P_{R_n}^2 t L_n \qquad (3.15)$$

and J is the torsion constant, defined for single cell as

$$J = \frac{4A^2}{\oint \frac{ds}{t}} \qquad (3.16)$$

$T = GJ\ \theta$

$$\text{hence } J = \frac{T}{G\theta} \qquad (3.17)$$

and its sample calculation is shown in next example.

and hence after calculating η^2, then $(E\ \Gamma)_s$ is modified by using Benscoter factor as follows

$$(E\ \Gamma)_{s\ \text{BENSCOTER}} = \frac{(E\Gamma)_s}{\lambda} \qquad (3.18)$$

Example

Referring to figures 3.6 and 3.8 , and the example mentioned in section 3.2 for calculation of the rate of twist and shear flows for a three cell box, now the same example is being extended for calculation of the I_c and J for the multi-cell box.

Here in this example we have

P_{R1} = 300 mm (Perpendicular distance from line MN to shear centre of box)

P_{R2} = 75 mm (Perpendicular distance from line NO to shear centre of box)

P_{R3} = 100 mm (Perpendicular distance from line OP to shear centre of box)

Hence we have for complete multi-cell box

$$I_c = \oint P_R^2 tds = \sum_{i=1}^{N} P_{R_n}^2 tL_n$$

$$I_c = 2^*\ (P_{R1}{}^2 * t_w * W) + 6^*\ (P_{R2}{}^2 * t_f * F) + 2^*\ (P_{R3}{}^2 * t_w * W)$$

$I_c = 2* [(300)^2*(1)*(150)] + 6* [(75)^2*(1)*(200)] + 2* [(100)^2*(1)*(150)]$

$I_c = 3.675$ E 7

Example

Calculation of Torsion constant J for multi-cell box beam

We know that

$T = GJ\theta$

Therefore

Since we know the applied Torque T, and also the rate of twist θ

$$J = \frac{T}{G\theta} = \frac{10^6}{80700*(5.673^{-7})} = 2.1843070 \text{ E } 7$$

Also J for multi-cell section can be defined as follows

$$J = \frac{T}{G\theta}$$

We may write θG using eq 3.1 , hence expression for J becomes

$$J = \frac{\sum_{i=1}^{n} F_i \Omega_i}{\left(\left(-F_{i-1} \frac{s_{i-1,i}}{\delta_{i-1,i}} + F_i \oint \frac{ds}{\delta_i} - F_{i+1} \frac{s_{i,i+1}}{\delta_{i,i+1}} \right) / \Omega_i \right)}$$

which can be re stated as

$$J = \frac{4 * A_i^2 \sum_{i=1}^{n} F_i}{\left(- F_{i-1} \frac{s_{i-1,i}}{\delta_{i-1,i}} + F_i \oint \frac{ds}{\delta_i} - F_{i+1} \frac{s_{i,i+1}}{\delta_{i,i+1}} \right)}$$

This can be used to evaluate J for any number of cells in a multi-cell beam.

However in case when all the three cells have same dimensions then it takes the form as shown below

$$J = 2 * A^2_i \sum_{i=1}^{n} F_i \quad / \quad \left(F_i * \left(\frac{b}{\delta} + \frac{d}{\delta}\right) - F_{i+1} \frac{d}{\delta} \right)$$

$$J = \frac{2 * A_i^2 \sum_{i=1}^{n} F_i}{\left(+ F_i * \left(\frac{b}{\delta} + \frac{d}{\delta}\right) - F_{i+1} \frac{d}{\delta} \right)}$$

Using this expression to calculate J for our example we have as follows

$$J = \{ 2 * [(200*150)^2] * [5.24+6.17+5.24] \} / \{ 6.17 * [\frac{200}{1} + \frac{150}{1}] - 5.24 * \frac{150}{1} \}$$

$$J = 21828114$$

This J for multi-cell box beam is approximately same as the one calculated using

$$J = \frac{T}{G\theta}$$

The difference in both values of J is approximately only 0.06 %

3.3 Mathematical solution using Benscoter approach to get Warping, Axial stress and Shear stress for a Multi-cell Tapered / Prismatic Box.

The differential equation 2.44 presented in chapter 2 can be used for analysing torsional response of single-cell and multi-cell isotropic prismatic and tapered box beams. The solution procedure for using this equation in the analysis of isotropic materials is being discussed below .

Equation 2.44 is now written as 3.19 .

$$\frac{d}{dz}[E'C\frac{d\theta}{dz}] - GJ\theta = -T + \frac{d}{dz}[E'C\frac{d\theta_0}{dz}] \qquad (3.19)$$

Equation 3.19 can be written in the general form given below as 3.20 at any particular location z along length of beam and then this standard form can have a solution θ as given in equation 3.21.

In order to write equation 3.19 in the general form given below by 3.20

$$A\frac{d^2\theta}{dz^2} + B\frac{d\theta}{dz} + C\theta = D \qquad (3.20)$$

we define following terms

$$\theta_0 = \frac{T}{GI_C}$$

$$f_1 = \frac{d}{dz}(\theta_0)$$

$$f_2 = \frac{d}{dz}(f_1)$$

$$f_5 = (E\Gamma)_{BENSCOTER}$$

$$f_6 = \frac{d}{dz}(f_5)$$

$$f_7 = G * J$$

A = 1.0

B = $((\frac{1}{f_5}) * f_6)$

C = $- (\frac{f_7}{f_5})$

D = $- (\frac{T}{f_5})$ + (f_2) + $((\frac{1}{f_5}) * (f_6) * (f_1))$

The general form of equation 3.20 has the solution as given by equation 3.21 below

$$A \frac{d^2\theta}{dz^2} + B \frac{d\theta}{dz} + C\,\theta = D \qquad (3.20)$$

$$\theta = \frac{D}{C} + C_1 e^{r_1 z} + C_2 e^{r_2 z} \qquad (3.21)$$

The Boundary condition at the restraint end (z=0) is

$\theta = 0$ at z = 0 mm

So we have at the restraint end

$$\theta = \frac{D}{C}(0) + C_1 + C_2$$

$$C_1 + C_2 = - \frac{D}{C}(0) \qquad (3.22)$$

The Boundary condition at the Free end (z=L) is

$\frac{dw}{dz} = 0$ at z = L

since w = - w(s) θ

therefore

$$\frac{dw}{dz} = -w(s)\frac{d\theta}{dz} + \theta\frac{d}{dz}(-w(s))$$

At z = L we have

$$\frac{dw}{dz} = -w(s)\frac{d\theta}{dz} + \theta\frac{d}{dz}(-w(s)) = 0$$

Inserting value of θ from equation 3.21 we can write

$$\frac{dw}{dz} = -\mathrm{w(s)} * \left[\frac{d}{dz}\left(\frac{D}{C}\right) + C_1\frac{d}{dz}(r_1 z)e^{r_1 z} + C_2\frac{d}{dz}(r_2 z)e^{r_2 z} \right] + \left[\frac{D}{C} + C_1 e^{r_1 z} + C_2 e^{r_2 z} \right] * \frac{d}{dz}(-w(s)) = 0 \qquad (3.23)$$

3.3.1 SOLUTION PROCEDURE

Following functions are required to be evaluated analytically in order to solve equations 3.22 and 3.23.

$$\theta_0 = \frac{T}{GI_C}$$

$$\mathrm{f_1} = \frac{d}{dz}(\theta_0)$$

$$\mathrm{f_2} = \frac{d}{dz}(f_1)$$

$$\mathrm{f_5} = (\mathrm{E}\Gamma)_{\mathrm{BENSCOTER}}$$

$$\mathrm{f_6} = \frac{d}{dz}(f_5)$$

The analytical procedure for evaluating above mentioned functions is outlined below

$$\theta_0 = \frac{T}{GI_C}$$

$$I_c = 2*[\ ((\frac{3b'}{2})**2)\ *t_w*d'\ ] + 2*[\ ((\frac{b'}{2})**2)\ *t_w*d'\ ]$$
$$+\ 2*[\ ((\frac{d'}{2})**2)\ *t_f*\ 3\ *b'\ ]$$

Here b and d are the lengths for flange and web of each cell at the root of the restrained multi-cell box beam and b' and d' are the respective lengths at any location z from the restrained end. Figure 3.5 shows side elevation and Plan of the box , showing angles α & β , and b' & d'.

$b' = b - 2z\tan\beta$

$d' = d - 2z\tan\alpha$

hence

$$\theta_0 = \frac{T}{GI_C}$$

$$\theta_0 = \frac{2*T}{G*((b'**2)*t_w*d' + (d'**2)*t_f*b')}$$

Next $f_1 = \frac{d}{dz}(\theta_0)$ and $f_2 = \frac{d}{dz}(f_1)$ are shown in Appendix "B".

$$E\Gamma = \frac{1}{3}((2*d'*t_w*E_w'*w(s)_B^2) + (2*d'*t_w*E_w'*w(s)_C^2)$$
$$+\ (2*b'*t_f*E_f'*w(s)_C^2)$$
$$+\ 4*(b'*t_f*E_f'*w(s)_B^2) + (w(s)_B*w(s)_C) + (w(s)_C^2)\ \ )$$

Here $E' = \frac{E}{1-\nu^2}$

Since $\eta^2 = 1 - \frac{J}{I_C}$

therefore $(E\Gamma)_{BENSCOTER} = \frac{E\Gamma}{\eta^2}$

$\frac{d}{dz}(E\Gamma)_{BENSCOTER}$ is defined in Appendix "B" as f_6.

All above mentioned factors are required to be evaluated analytically and then using following factors which shall be evaluated numerically, the required equations can be solved.

The solution of equation 3.22 and 3.23 in order to evaluate values of C_1 and C_2 also requires evaluation of various functions by numerical methods. Moreover during the evaluation of warping , axial stresses and shear stresses in later sections these functions will be required to be evaluated again. It is therefore considered appropriate to highlight the procedure for numerical evaluation of following functions in this section.

$$\frac{d}{dz}(r_1 z)$$

$$\frac{d^2}{dz^2}(r_1 z)$$

$$\frac{d}{dz}(r_2 z)$$

$$\frac{d^2}{dz^2}(r_2 z)$$

$$\frac{d}{dz}(\frac{D}{C})$$

$$\frac{d^2}{dz^2}(\frac{D}{C})$$

$$\frac{d}{dz}(w(s))$$

The procedure for evaluating $\frac{d}{dz}(r_1 z)$ by numerical method is being highlighted here , same procedure can be adopted for evaluating other functions mentioned above.

Figure 3.12 shows a plot of "r1*z " Vs "z". In order to evaluate the slope of this curve, we need to take any two points on X axis, say x=500 mm and x=600 mm are the two points selected. The corresponding values of Y co-ordinate or "r1*z " at these two locations are noted to be 18.58682 and 23.77683 . Now in order to evaluate the slope of this curve at the mid-point of these two given locations, i.e. the slope at x=550 mm will be determined by following formula.

Slope at x=550 mm =

$$\tan\theta = \frac{\text{(Value of Y Co-ordinate at x=600) - (Value of Y Co-ordinate at x=500)}}{\text{(Distance on X axis between x=600 and x=500)}}$$

Therefore, in this example

Slope at x=550 mm =

$$\tan\theta = \frac{23.77683 - 18.58682}{100} = 0.0519001$$

Hence the slope of "r1*z " at x = 550 mm , which is referred to as $\frac{d}{dz}(r_1 z)$ at x = 550 mm , is found to be 0.0519001 .

Now after calculating the slope of "r1*z " at x = 550 mm , we may look at figure 3.14 , which shows the variation of $\frac{d}{dz}(r_1 z)$ Vs Z , it can be seen that the Y value of this curve at x = 550 mm is 0.0519001, which is infact the value of slope of "r1*z " at x = 550 mm calculated from figure 3.12 using above numerical technique.

In order to get accurate values of slope at all locations along the X axis , the length of box beam (x=600mm) was divided into 6000 equal divisions of 0.1 mm each. Hence in order to get slope at x=550 mm , we use the corresponding two points on its either sides x=550.1 mm and x=549.9 mm , and divide the difference of their Y co-ordinate values by 0.2 mm which is the distance between these points on x axis .

This in turn would result in getting very accurate slopes at all locations along the length of the box beams. As is obvious the manual calculations of such slopes at all 6000 points along the length would become very tedious, it therefore becomes necessary to use the computer power for getting these slopes with such desired high accuracy . A computer programme was used to evaluate all above mentioned functions numerically using above mentioned technique.

All the required functions $\frac{d}{dz}(r_1 z)$, $\frac{d^2}{dz^2}(r_1 z)$, $\frac{d}{dz}(r_2 z)$, $\frac{d^2}{dz^2}(r_2 z)$, $\frac{d}{dz}(\frac{D}{C})$, $\frac{d^2}{dz^2}(\frac{D}{C})$ and $\frac{d}{dz}(w(s))$ can be obtained in similar fashion applying numerical method and using data from figures 3.12 to 3.22.

Hence solving above equations 3.22 and 3.23 we get the two unknowns C_1 and C_2. The values of C_1 and C_2 depend upon the geometry of beam and also its material properties "E" and "G", i.e. change of taper angle or change in dimensions/ characteristic properties of beam will change the values of C_1 and C_2

Hence after the two unknowns C_1 and C_2 have been found the solution θ of the general equation 3.20 is known

$$A \frac{d^2\theta}{dz^2} + B \frac{d\theta}{dz} + C\,\theta = D \qquad (3.20)$$

and its solution θ is

$$\theta = \frac{D}{C} + C_1 e^{r_1 z} + C_2 e^{r_2 z} \qquad (3.21)$$

here r_1 and r_2 are the two roots at each location along the length of the box and are defined as

$$r_1 = \frac{-B + \sqrt{B^2 - 4AC}}{2A}$$

$$r_2 = \frac{-B - \sqrt{B^2 - 4AC}}{2A}$$

3.3.2 WARPING

Hence once we know θ from equation 3.21 above, we can find warping at any point along the length and across the cross section of beam by using following relation .

$$w = - w(s) * \theta$$

where w(s) is the Sectorial Co-ordinate at any given location and has been defined above.

3.3.3 AXIAL STRESS

Since

$$\theta = \frac{D}{C} + C_1 e^{r_1 z} + C_2 e^{r_2 z} \qquad (3.21)$$

therefore

$$\frac{d\theta}{dz} = \frac{d}{dz}\left(\frac{D}{C}\right) + C_1 \frac{d}{dz}(r_1 z) * e^{r_1 z} + C_2 \frac{d}{dz}(r_2 z) * e^{r_2 z}$$

Since Axial Stress $\sigma_\Gamma = E \frac{\partial w}{\partial z}$

$$\sigma_\Gamma = E \frac{\partial}{\partial z} [\, w(s) * \theta \,]$$

$$\sigma_\Gamma = \left[\frac{d\theta}{dz} * w(s) + \theta * \frac{d}{dz}(w(s)) \right] * E$$

$$\sigma_\Gamma = [\{\frac{d}{dz}(\frac{D}{C}) + C_1\frac{d}{dz}(r_1 z)*e^{r_1 z} + C_2\frac{d}{dz}(r_2 z)*e^{r_2 z}\}* w(s) + \{\frac{D}{C}+C_1 e^{r_1 z}+C_2 e^{r_2 z}\}*\frac{d}{dz}(w(s))\ ] * E \quad (3.24)$$

Above equation 3.24 can be used to get Axial stress at any location along length and across the cross-section of the beam by using the respective value of Sectorial Co-ordinate w(s) , r_1 and r_2 at that particular location along "z" .

3.3.4 SHEAR STRESS

Shear stress is defined as follows

$$\frac{\partial q_\Gamma}{\partial s} = -t\ \frac{\partial \sigma_\Gamma}{\partial z} \quad (3.25)$$

$$\frac{\partial q_\Gamma}{\partial s} = -t\ [\ \frac{\partial}{\partial z}(E\ \frac{dw}{dz})\ ]$$

$$\frac{\partial q_\Gamma}{\partial s} = -t\ [\ \frac{\partial}{\partial z}\{E\ \frac{d}{dz}\ (-\ w(s)\ *\ \theta\ )\}\ ]$$

Since $\sigma_\Gamma = E\ \frac{\partial w}{\partial z}$

and

$w = -\ w(s)\ *\ \theta$

hence

$$\sigma_{\Gamma} = E \frac{\partial}{\partial z} [- w(s) * \theta]$$

$$\sigma_{\Gamma} = [\frac{d\theta}{dz} * - w(s) + \theta * \frac{d}{dz}(-w(s))] * E$$

Therefore

$$\frac{\partial \sigma_{\Gamma}}{\partial z} = \frac{\partial}{\partial z} \{ E * - w(s) * \frac{d\theta}{dz} + \theta * \frac{d}{dz}(-w(s)) \}$$

$$\frac{\partial \sigma_{\Gamma}}{\partial z} = - E * [w(s) * \frac{d^2\theta}{dz^2} + \frac{d\theta}{dz} * \frac{d}{dz}(w(s)) + \theta * \frac{d^2}{dz^2}(w(s)) + \frac{d}{dz}(w(s)) * \frac{d\theta}{dz}]$$

since

$$\frac{\partial q_{\Gamma}}{\partial s} = - t \frac{\partial \sigma_{\Gamma}}{\partial z}$$

Therefore integrating we get

$$q_{\Gamma} = E \frac{d^2\theta}{dz^2} \int_0^s w(s) t ds$$

Sectorial shear function $S_w(s)$ is defined as

$$S_w(s) = \int_0^s w(s) t ds$$

Therefore

$$q_{\Gamma} = E \frac{d^2\theta}{dz^2} S_w(s)$$

Since

$$\frac{d\theta}{dz} = \frac{d}{dz}\left(\frac{D}{C}\right) + C_1 \frac{d}{dz}(r_1 z) * e^{r_1 z} + C_2 \frac{d}{dz}(r_2 z) * e^{r_2 z}$$

therefore

$$\frac{d^2\theta}{dz^2} = \frac{d^2}{dz^2}\left(\frac{D}{C}\right) + C_1 * \{ \left(\frac{d}{dz}(r_1 z) * \frac{d}{dz}(r_1 z) * e^{r_1 z}\right) + \left(e^{r_1 z} * \frac{d^2}{dz^2}(r_1 z)\right) \}$$

$$+ C_2 * \{ \left(\frac{d}{dz}(r_2 z) * \frac{d}{dz}(r_2 z) * e^{r_2 z}\right) + \left(e^{r_2 z} * \frac{d^2}{dz^2}(r_2 z)\right) \}$$

Since $q_\Gamma = E \frac{d^2\theta}{dz^2} S_w(s)$

Hence Shear flow is given by equation 3.26 below as

$$q_\Gamma = E * S_w(s) *$$

$$[\frac{d^2}{dz^2}\left(\frac{D}{C}\right) + C_1 * \{ \left(\frac{d}{dz}(r_1 z) * \frac{d}{dz}(r_1 z) * e^{r_1 z}\right) + \left(e^{r_1 z} * \frac{d^2}{dz^2}(r_1 z)\right) \}$$

$$+ C_2 * \{ \left(\frac{d}{dz}(r_2 z) * \frac{d}{dz}(r_2 z) * e^{r_2 z}\right) + \left(e^{r_2 z} * \frac{d^2}{dz^2}(r_2 z)\right) \}] \qquad (3.26)$$

Equation 3.26 can be used to get shear flow at any location along length and across the cross section of the beam by using the respective value of Sectorial shear function $S_w(s)$ at that particular location.

Once the warping shear flow has been calculated using above equation, total shear flow is obtained adding warping shear flow to the Bredt Batho shear flow. Figure 3.4 shows shear flow patterns across the thickness of the thin walled box beam.

$q_{TOTAL} = q_\Gamma + q_{BREDT\ BATHO}$

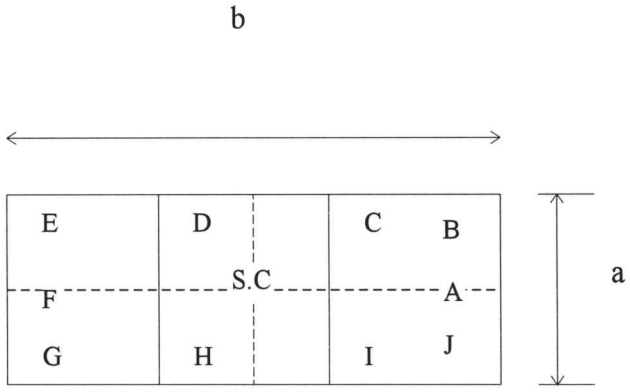

Figure 3.1 Thin walled multi-cell box beam cross section

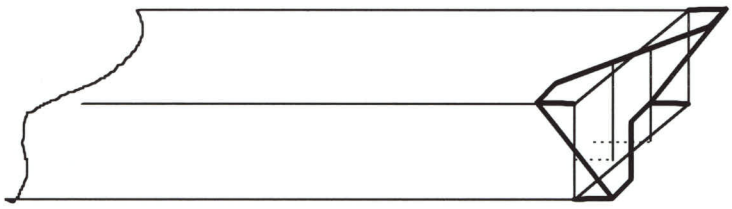

Figure 3.2 warping distribution for a multi-cell box

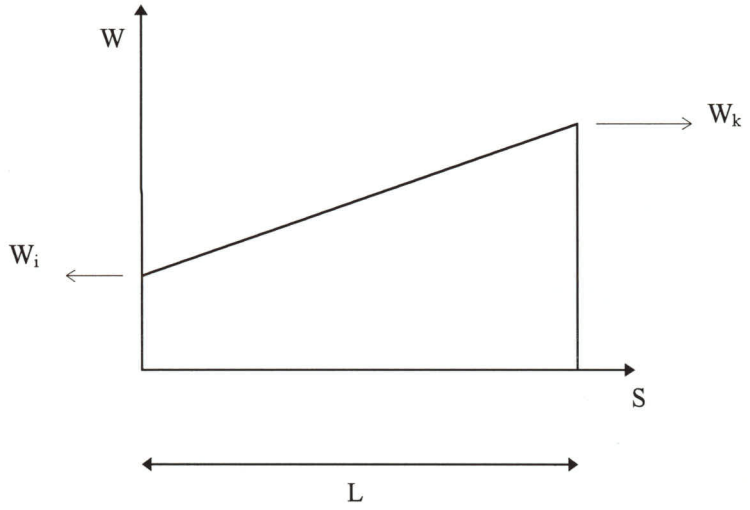

Figure 3.3 Sectorial Coordinate Distribution

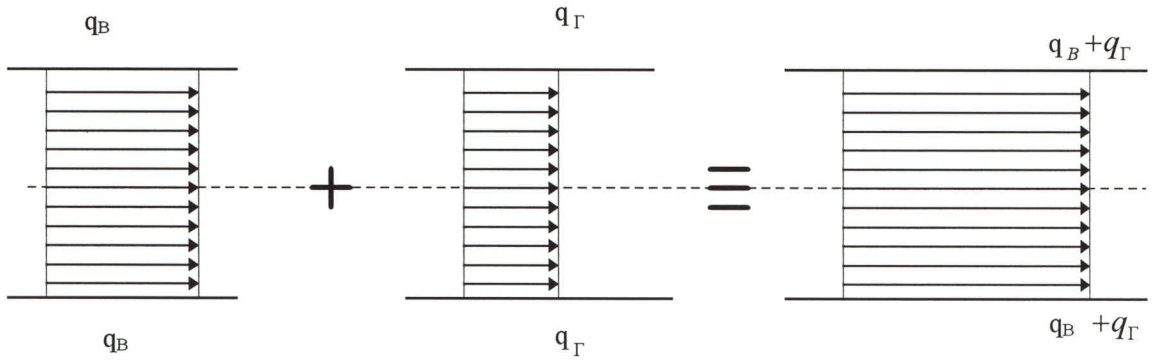

Figure 3.4 Shear flow patterns across the thickness of thin walled box beam

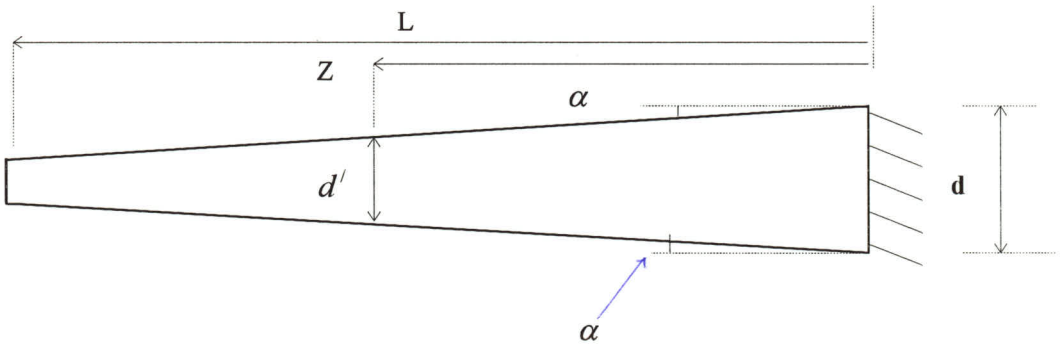

(a) Side Elevation

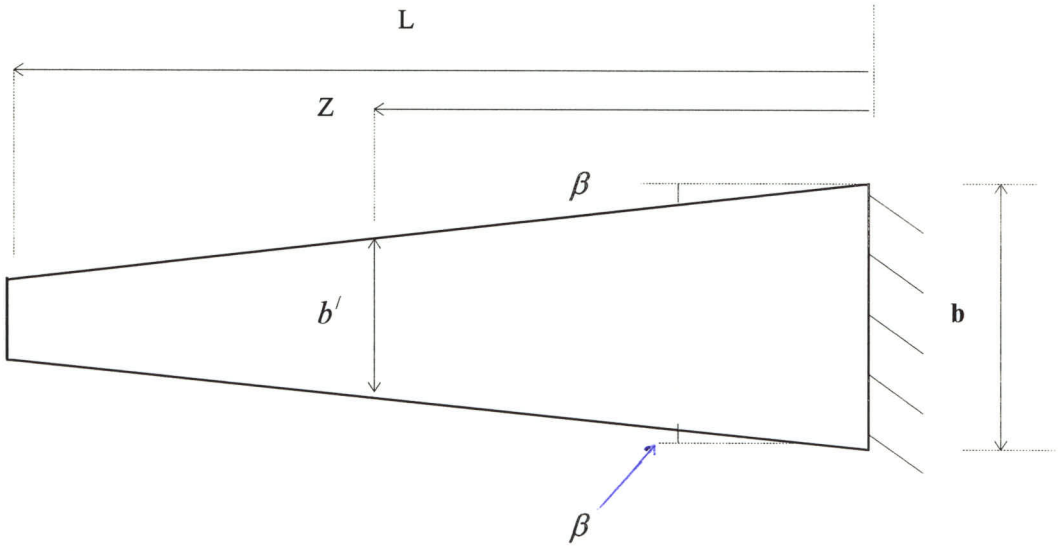

(b) Plan

Figure 3.5 Side Elevation and Plan of Box showing angles α and β

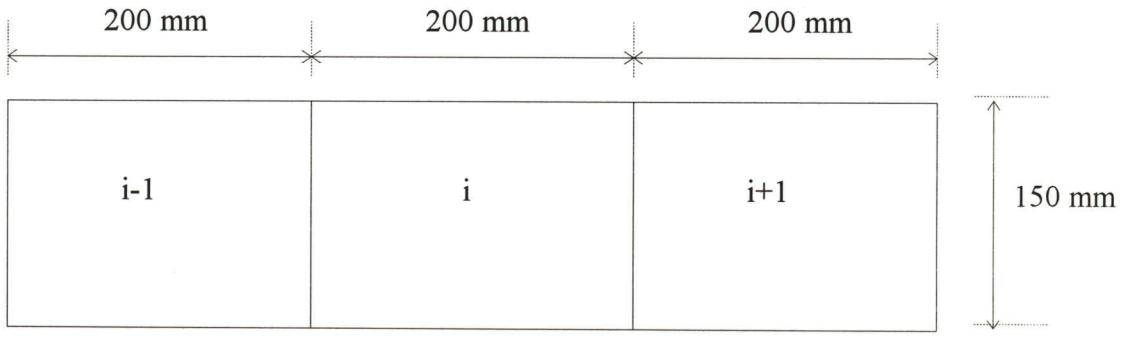

Figure 3.6 Dimensions of example isotropic three-cell box

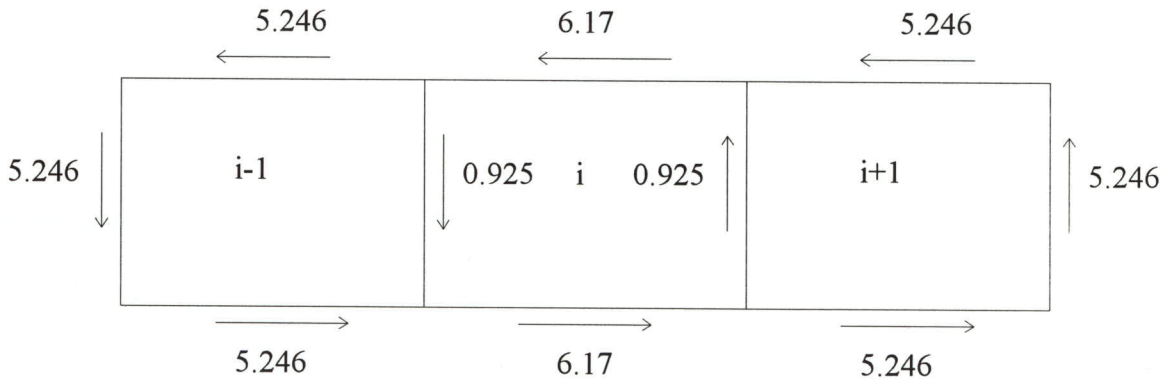

Figure 3.7 Bredt Batho Shear Flows in each of the 3 cells of example isotropic three-cell box

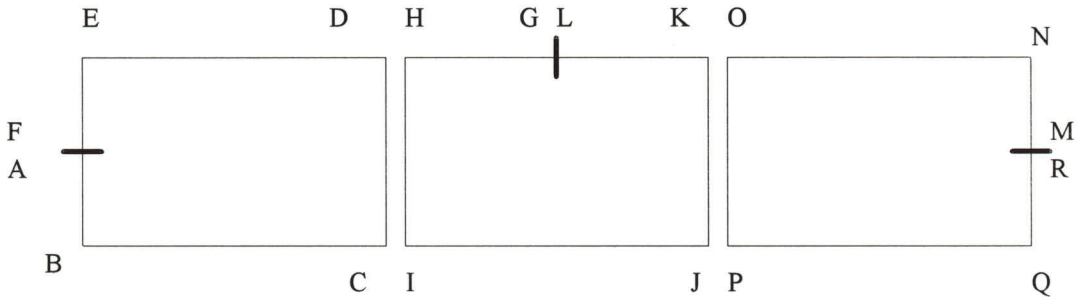

Figure 3.8 Three cells shown separately for calculation of w(s)

Figure 3.9 w(s) final distribution in each of the 3 cells of example isotropic three-cell box

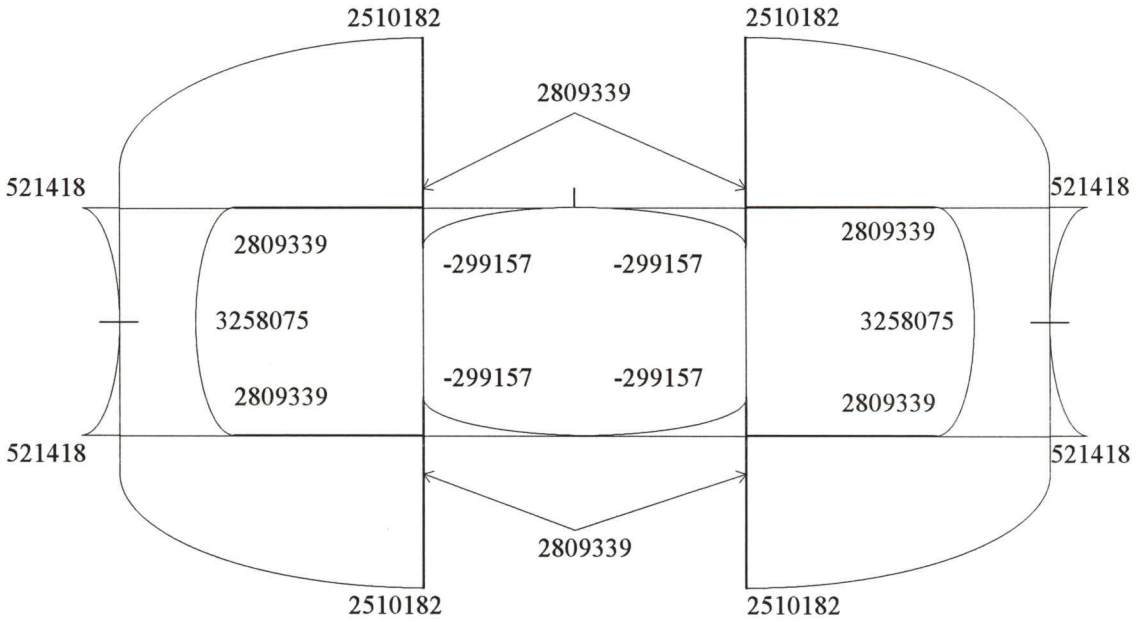

Figure 3.10 $S_{w,0}(s)$ distribution for the isotropic three cell box

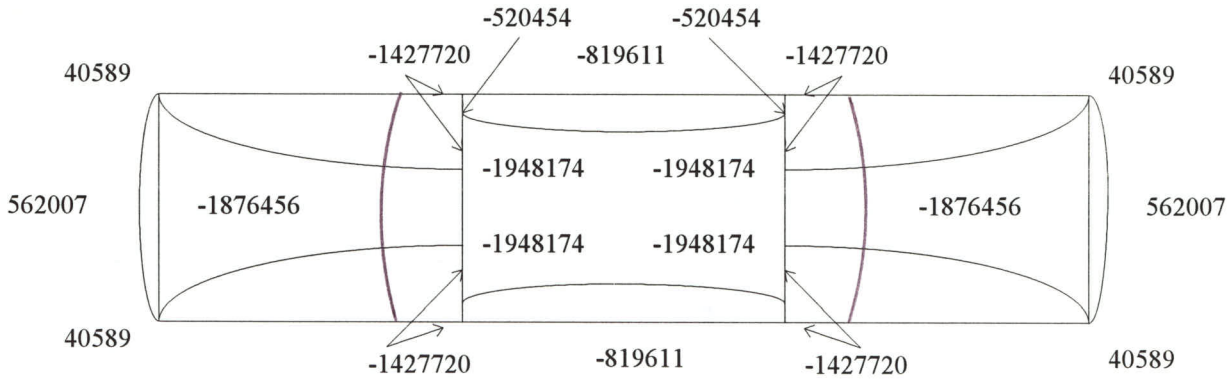

Figure 3.11 $S_{w,c}(s)$ distribution for the isotropic three cell box

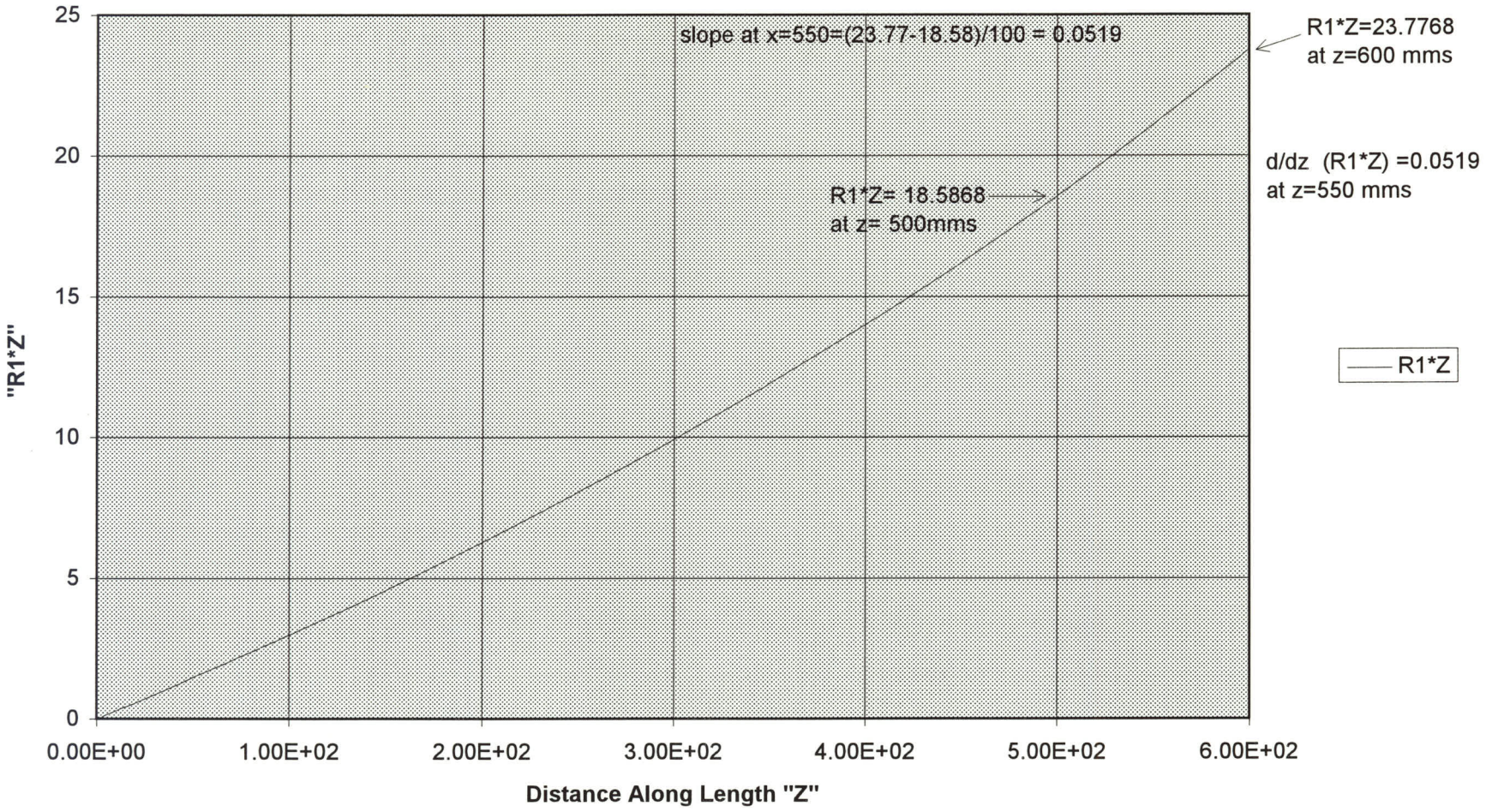

Figure 3.12 PLOT SHOWING R1*Z VS "Z"

Figure 3.13 PLOT SHOWING R2*Z VS "Z"

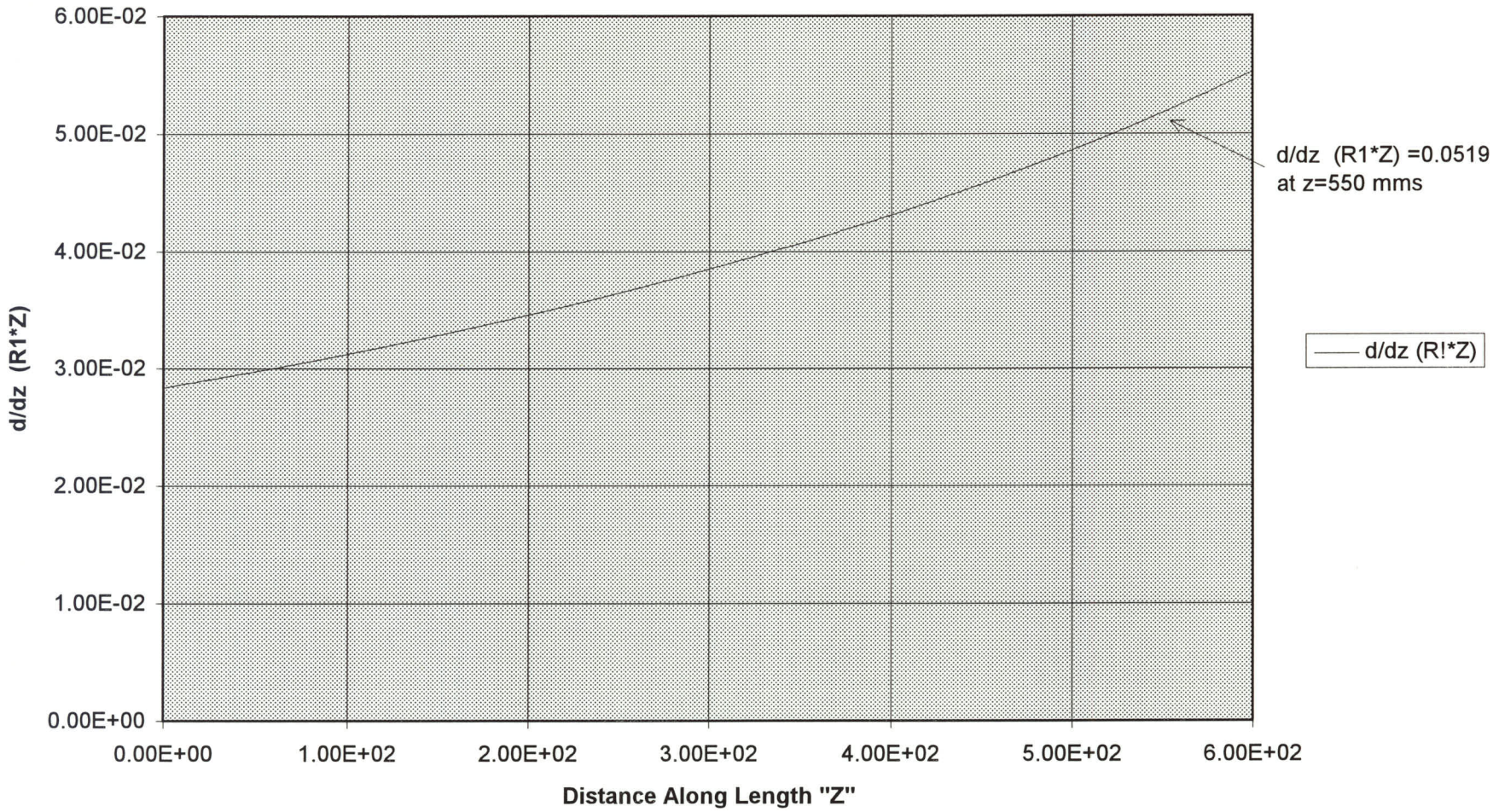

Figure 3.14 PLOT SHOWING d/dz (R1*Z) VS "Z"

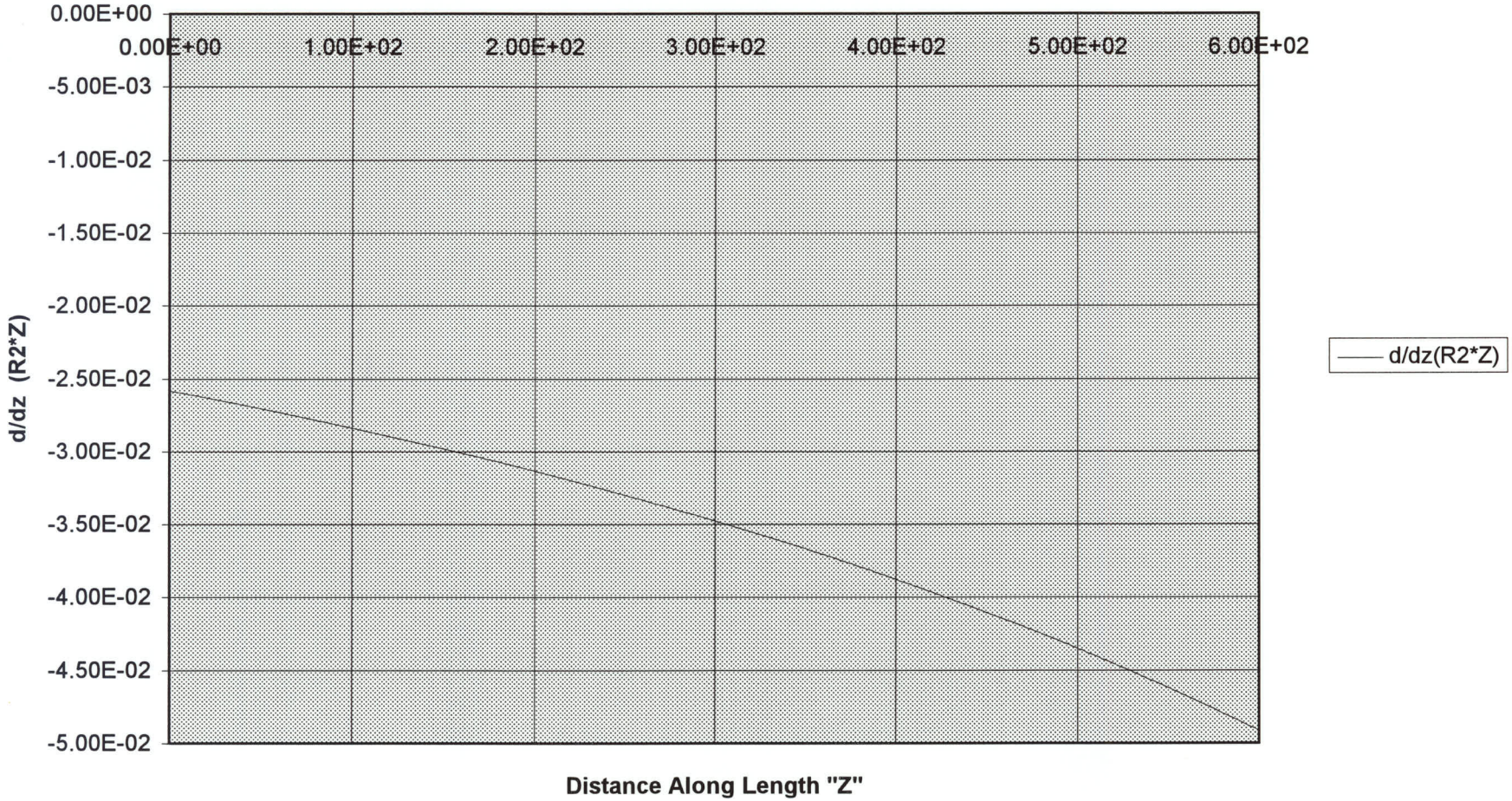

Figure 3.15 PLOT SHOWING d/dz (R2*Z) VS "Z"

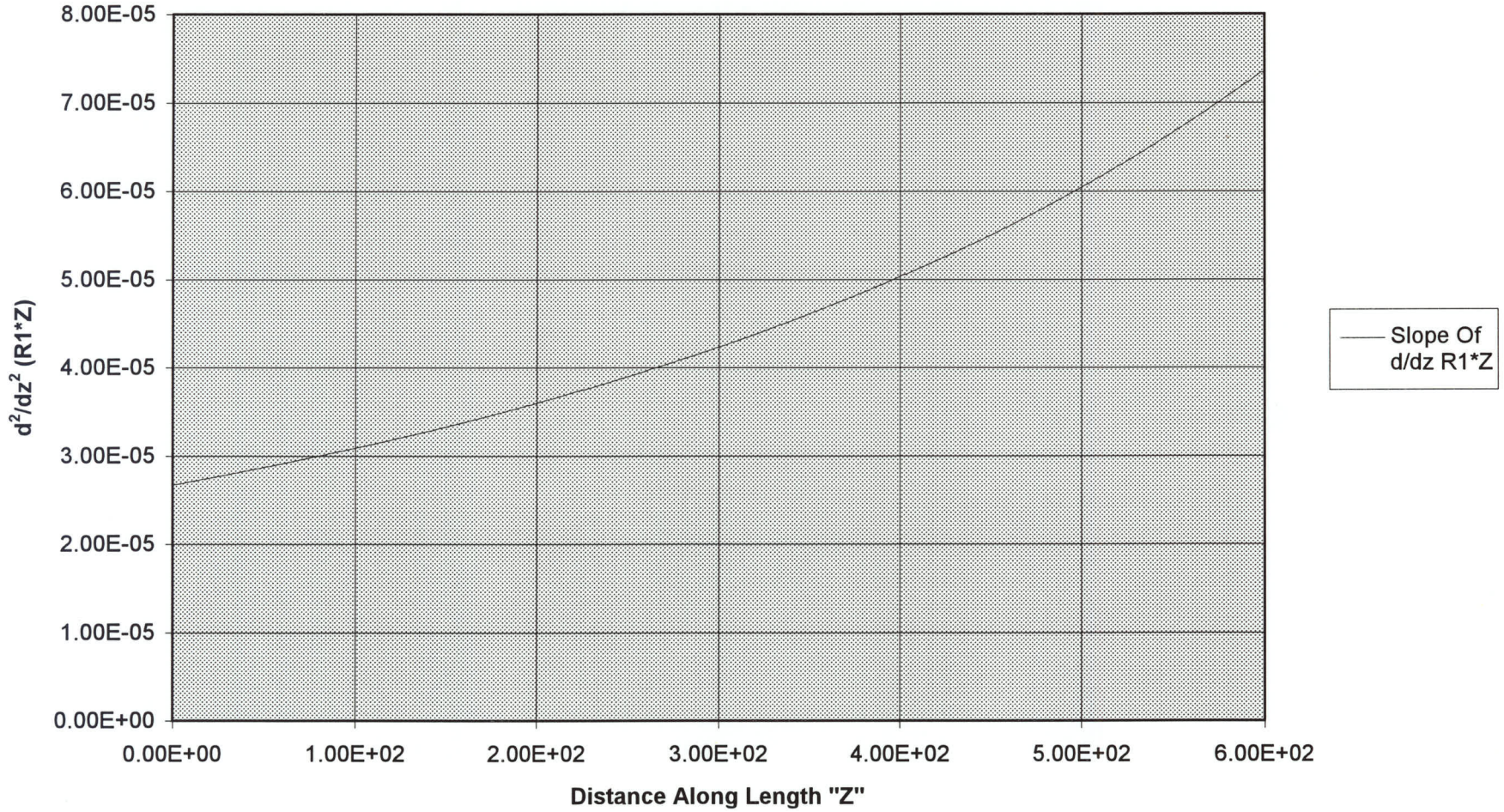

Figure 3.16 PLOT SHOWING d^2/dz^2 (R1*Z) VS "Z"

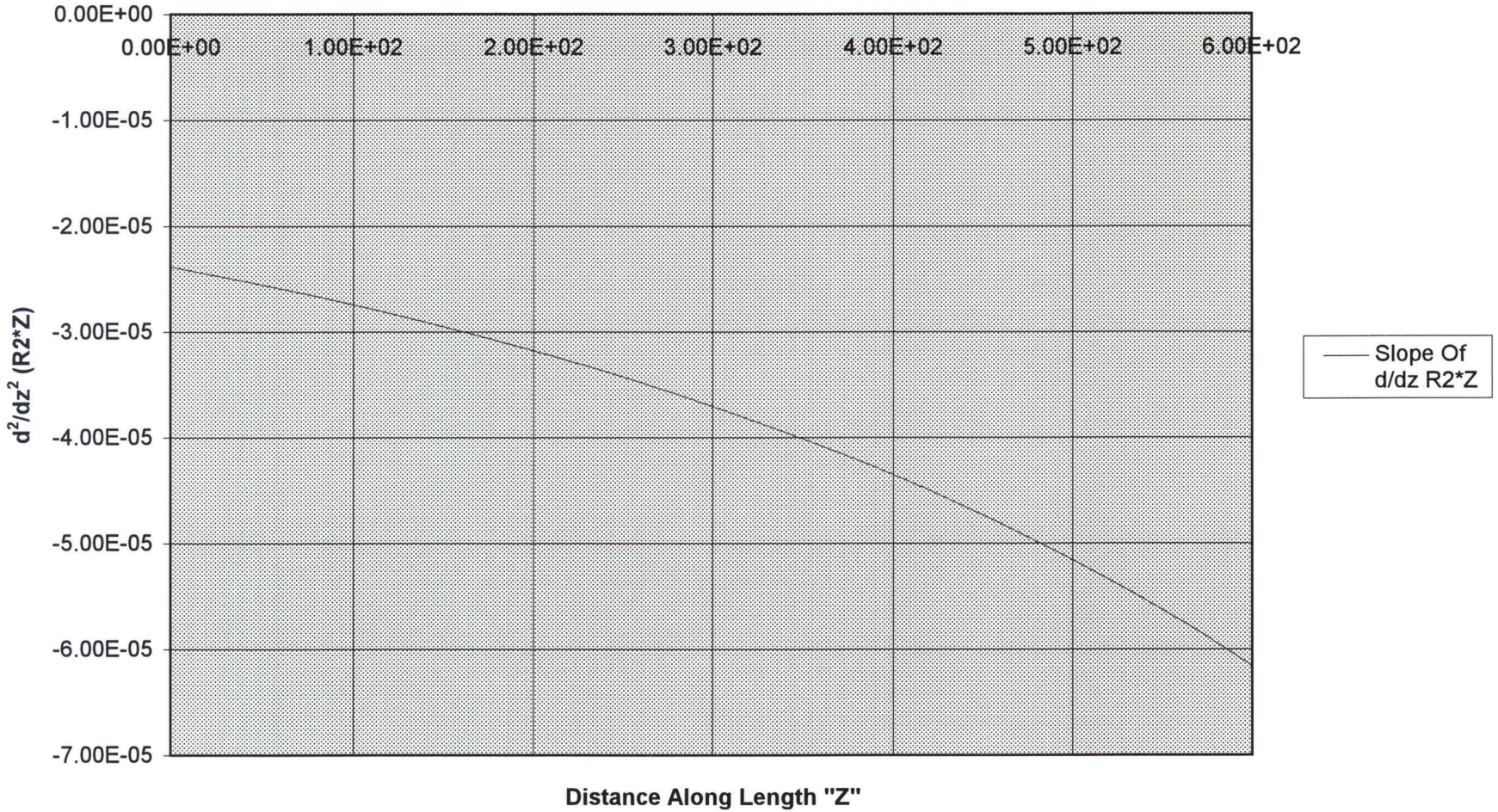

Figure 3.17 PLOT SHOWING d^2/dz^2 (R2*Z) VS "Z"

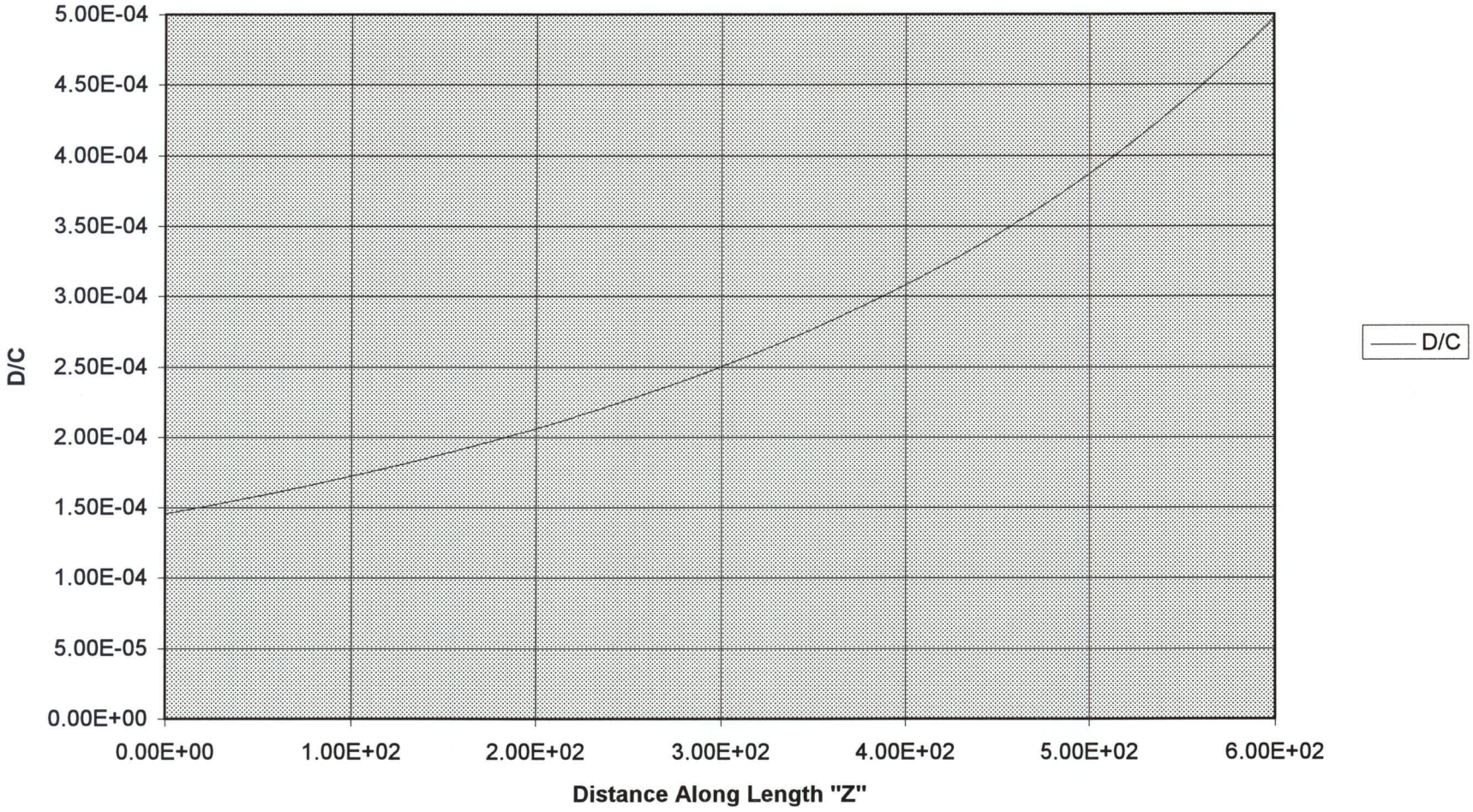

Figure 3.18 PLOT SHOWING (D/C) VS "Z"

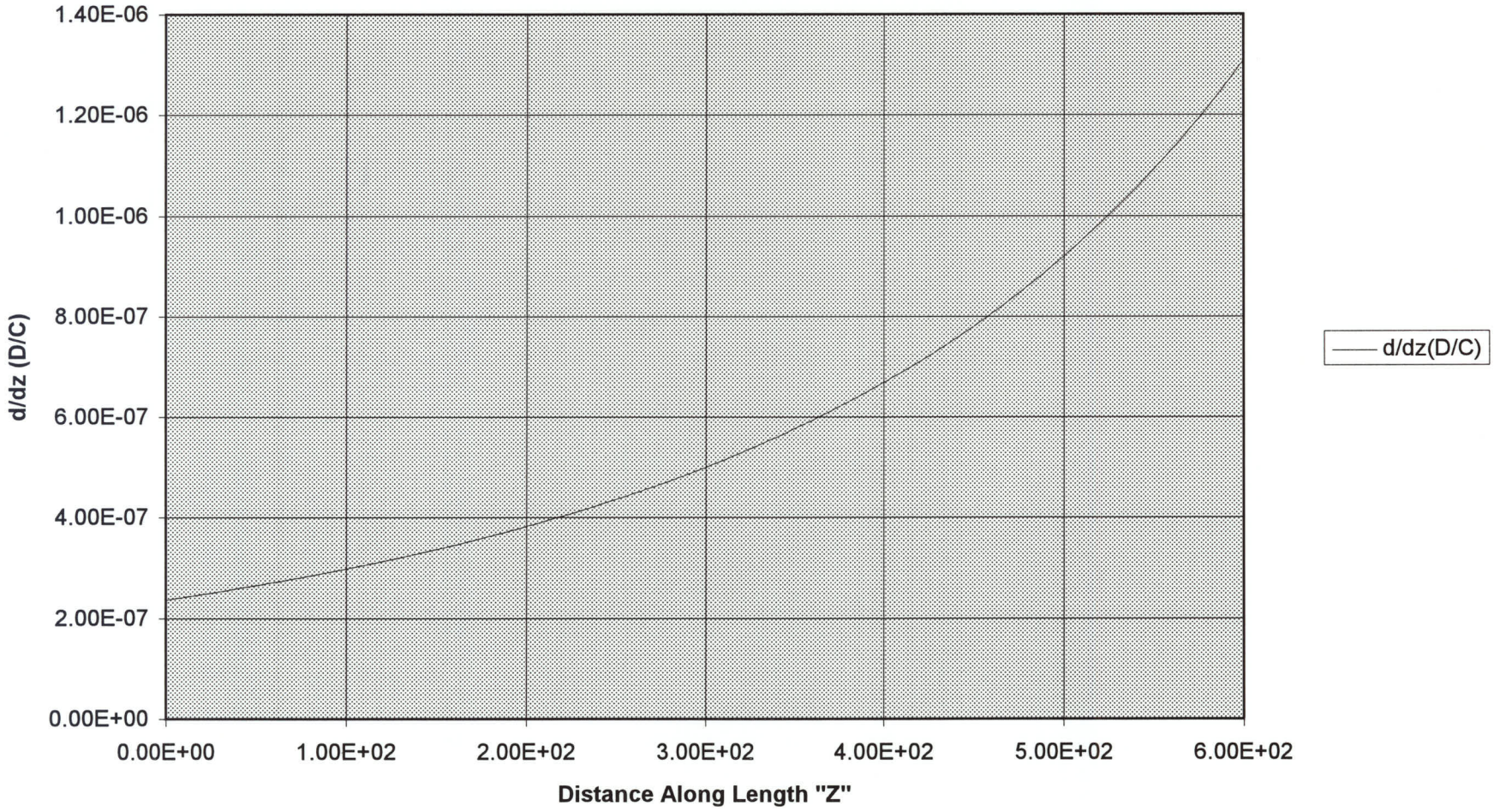

Figure 3.19 PLOT SHOWING d/dz (D/C) VS "Z"

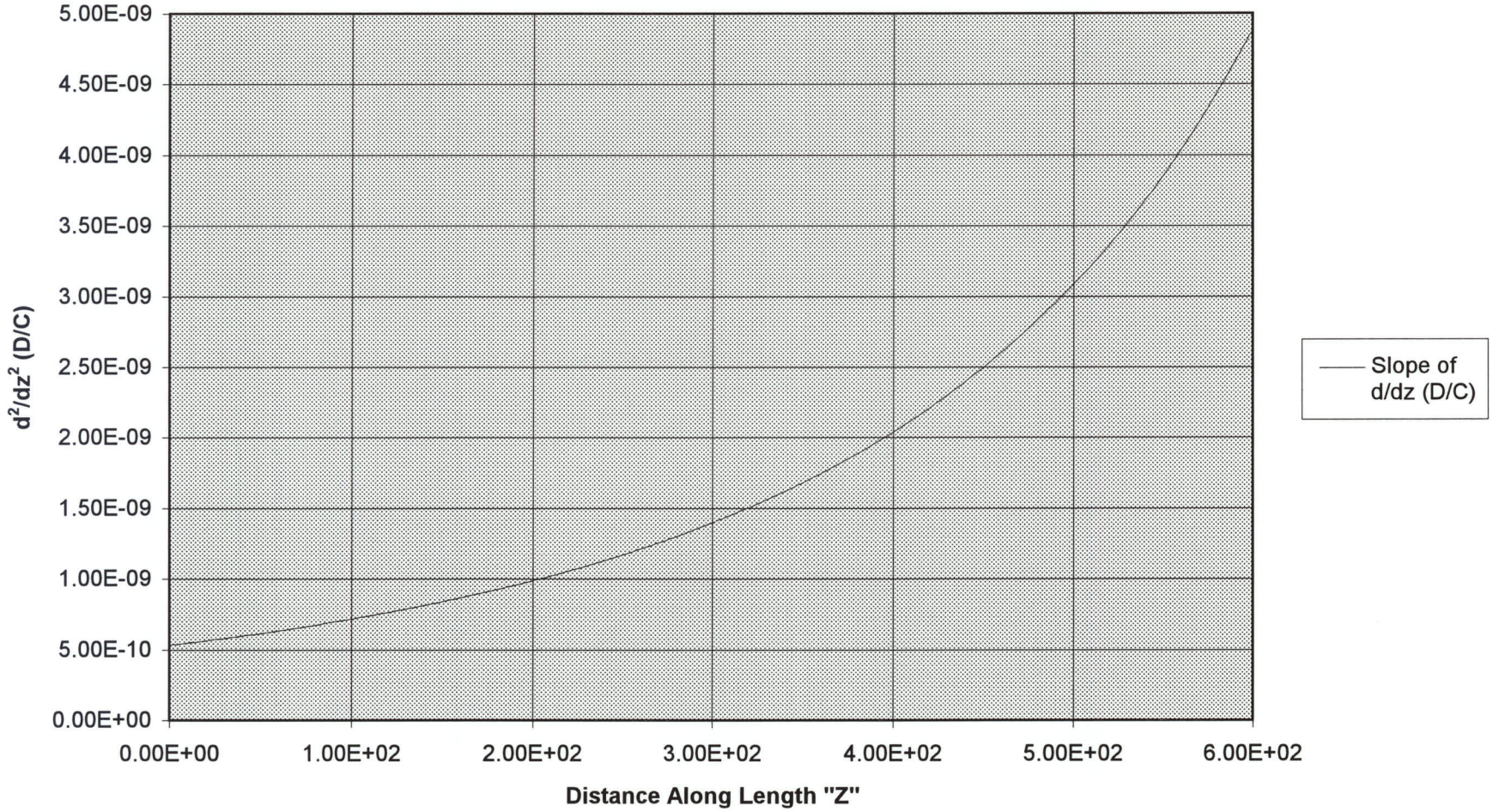

Figure 3.20 PLOT SHOWING d^2/dz^2 (D/C) VS "Z"

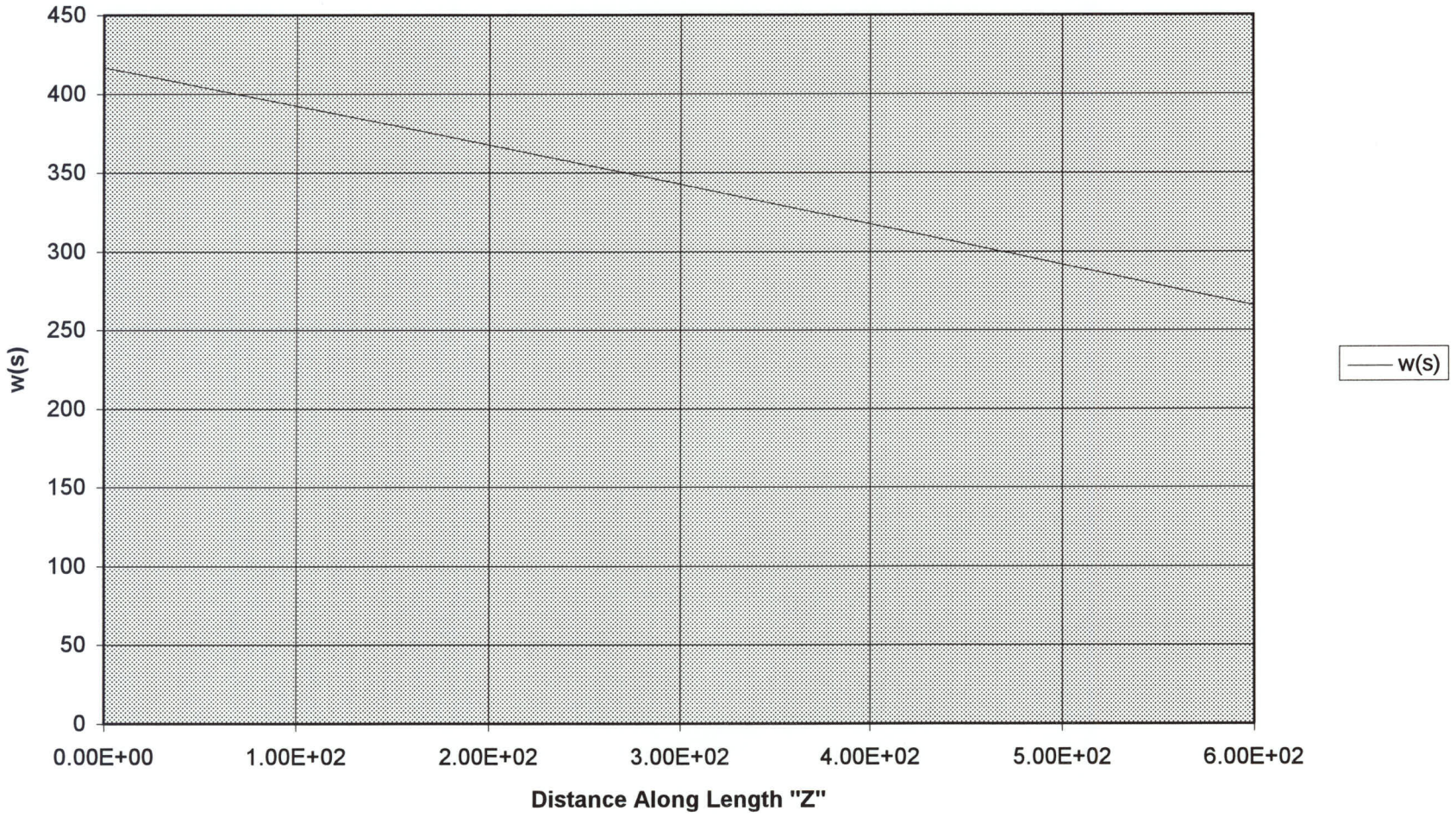

Figure 3.21 PLOT SHOWING w(s) VS "Z"

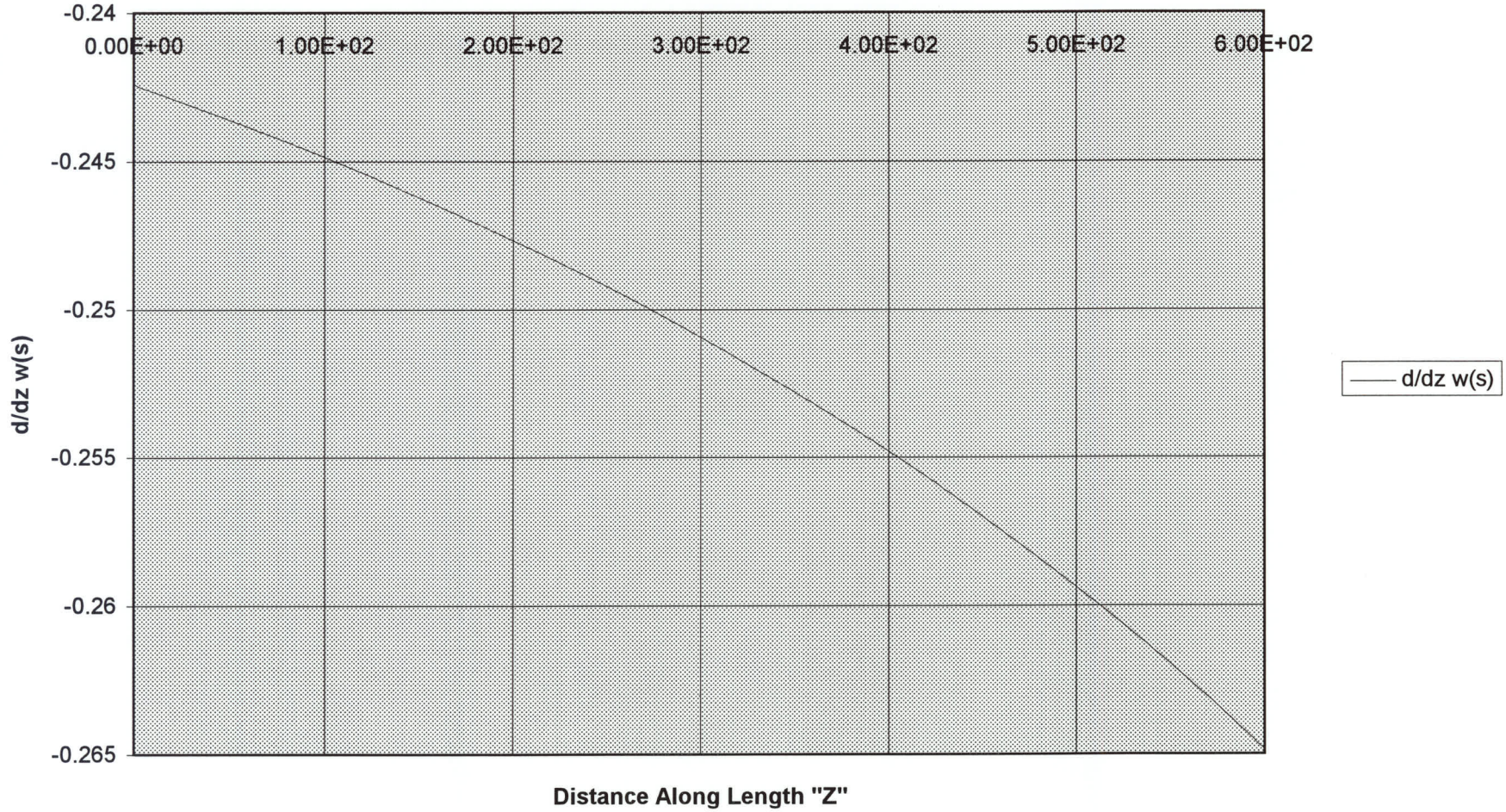

Figure 3.22 PLOT SHOWING d/dz w(s) VS "Z"

4 PROPOSED TORSION THEORY OF THIN WALLED MULTI-CELL COMPOSITE BEAMS

4.1 INTRODUCTION

The proposed theory being presented in this chapter is basically intended for symmetric laminates which have membrane orthotropy , i.e. $A_{13}=A_{23}=0$. The proposed analysis method will use the existing isotropic theory by relating the isotropic properties to the equivalent laminate properties.

A section is considered to consist of a number of connected thin plate walls. Since the warping related properties depend directly on the thickness of each of the walls of a beam section, therefore the proposed theory uses the isotropic equations given in chapter 3 with the wall thickness factored to take into account the wall laminate properties.

In case of composites the elastic modulus "E" and shear modulus "G" have different values in the membrane and bending modes. Since warping is basically a membrane deformation therefore elastic modulus "E" and shear modulus "G" come from the membrane mode for the composites.

4.2 PROPOSED COMPOSITE THEORY

The torsion constant of a multi-cell box beam section has been defined previously in chapter 3 . This relationship is applicable to any isotropic & composite lay-up multi cell

box beam. The shear flows used in eq. 4.1 are obtained using actual values of shear modulus "G" and thickness "t" in equations 3.1 and 3.2 .

$$J = \frac{\sum_{i=1}^{n} F_i \Omega_i}{((-F_{i-1} \frac{s_{i-1,i}}{\delta_{i-1,i}} + F_i \oint \frac{ds}{\delta_i} - F_{i+1} \frac{s_{i,i+1}}{\delta_{i,i+1}}) / \Omega_i)}$$

which can be restated as

$$J = \frac{4 * A_i^2 \sum_{i=1}^{n} F_i}{(- F_{i-1} \frac{s_{i-1,i}}{\delta_{i-1,i}} + F_i \oint \frac{ds}{\delta_i} - F_{i+1} \frac{s_{i,i+1}}{\delta_{i,i+1}})} \qquad (4.1)$$

The torsional rigidity of a multi-cell composite box beam is

$$GJ = \frac{T}{\theta}$$

where θ is obtained from eq 3.1 below

$$\theta G \Omega_i = - F_{i-1} \frac{s_{i-1,i}}{\delta_{i-1,i}} + F_i \oint \frac{ds}{\delta_i} - F_{i+1} \frac{s_{i,i+1}}{\delta_{i,i+1}}$$

and Torque T comes from eq. 3.2 below

$$T = \sum_{i=1}^{n} F_i \Omega_i$$

Hence

when the flanges and webs consist of same isotropic or composite material , we have

$$(GJ)_s = \frac{G \sum_{i=1}^{n} F_i \Omega_i}{((-F_{i-1} \frac{s_{i-1,i}}{\delta_{i-1,i}} + F_i \oint \frac{ds}{\delta_i} - F_{i+1} \frac{s_{i,i+1}}{\delta_{i,i+1}}) / \Omega_i)}$$

In general case when the lay-up in flanges and webs is different it can be stated as

$$(GJ)_s = \frac{4 * A_i^2 \sum_{i=1}^{n} F_i}{\left(- F_{i-1} \frac{s_{i-1,i}}{G_{i-1,i}\delta_{i-1,i}} + F_i \oint \frac{ds}{G_i \delta_i} - F_{i+1} \frac{s_{i,i+1}}{G_{i,i+1}\delta_{i,i+1}} \right)} \qquad (4.2)$$

Hence the effective shear modulus of composite multi-cell box section will be

$$G_{eff} = \frac{(GJ)_s}{J}$$

$$G_{eff} = \frac{\left(- F_{i-1} \frac{s_{i-1,i}}{\delta_{i-1,i}} + F_i \oint \frac{ds}{\delta_i} - F_{i+1} \frac{s_{i,i+1}}{\delta_{i,i+1}} \right)}{\left(- F_{i-1} \frac{s_{i-1,i}}{G_{i-1,i}\delta_{i-1,i}} + F_i \oint \frac{ds}{G_i \delta_i} - F_{i+1} \frac{s_{i,i+1}}{G_{i,i+1}\delta_{i,i+1}} \right)} \qquad (4.3a)$$

This eq. 4.3a can be used to calculate G_{eff} for any multi-cell section consisting of any isotropic or composite material.

where as G_{eff} for the single cell box is as follows

$$G_{eff} = \frac{\oint \frac{ds}{t}}{\oint \frac{ds}{Gt}} \qquad (4.3b)$$

In the present study G_{eff} for the multi-cell box has been calculated using equation 4.3b, by considering the entire cross section of the three cell box. The actual relation for calculating the G_{eff} for the multi-cell box section is given by eq. 4.3a. This resulted in an error of 12.8 % in the value of G_{eff} for the multi-cell box sections where the lay-up in flanges and webs was different. However this G_{eff} error did not occur for any multi-cell beam section where the lay-up in flanges and webs was same.

In case of multi-cell box beam section when the lay-up in webs is $[0/45/-45/90]_s$ and the lay-up in flanges is $[[45/-45]_2]_s$, the comparison of theoretical results Vs Finite Element

results along the length of the beam section for Force Intensity at locations B and C, Warping at point B and C and Shear flow at location s=0 and s=100 mm are calculated based on both G_{eff} (i.e. G_{eff} calculated on basis of single cell theory and multi-cell beam section theory) and are shown in figures 6.16 to 6.21.

These results show that the use of actual G_{eff} as compared to the G_{eff} used on basis of single cell theory has following affects:
In case of FI along the length of the multi-cell beam section the curves for actual G_{eff} are shifted upwards near the restrained end where the stresses are maximum.

In case of Warping along the length of the multi-cell beam section the curves for actual G_{eff} are shifted upwards near the restrained end , and thus result in closer coherence to the FE results. However there is not much significant affect.

In case of Shear Flow along the length of the multi-cell beam section at location s=0 mm and s=100 mm the curves for actual G_{eff} are shifted upwards and downwards respectively near the restrained end, and thus result in greater coherence to the FE results.

Example

Following example relates to figure 4.1 and is being used here to show the calculation of G_{eff} for a three cell box section consisting of $[0/45/-45/90]_s$ lay-up in flanges and $[[45/-45]_2]_s$ lay-up in webs by using two different techniques mentioned above, (i.e. eq. 4.3a and 4.3b)

Using equation 4.3b for the complete three-cell box we have as follows

$$G_{eff} = \frac{(\frac{50}{1}*6)+(\frac{50}{1}*4)}{(\frac{50}{20616*1}*6)+(\frac{50}{36233*1}*4)}$$

$$G_{eff} = \frac{500}{0.020071634} = 24910.77 \text{ N/mm}^2$$

Hence a G_{eff} value of 24910.77 N/mm^2 is obtained for the three-cell composite box using the single-cell G_{eff} relation of eq. 4.3b applied to complete three cell box.

Now using the G_{eff} relation for multi-cell box beam section (eq. 4.3a)we use the actual G_{FLANGE} = 20616 N/mm^2 and G_{WEB} = 36233 N/mm^2 and thickness as the actual thickness of each Web and Flange (t=1 mm for all Flanges and Webs in this case) and hence solving the four equations obtained from eqs 3.1 and 3.2 get Bredt Batho shear flows and the rate of twist θ in the three cells as follows

F_{i-1}=63.42 N/mm

F_i=73.15 N/mm

F_{i+1}= 63.42 N/mm

θ= 7.6349 E-5

Now using the relation for G_{eff} of multi-cell section we have

$$G_{eff} = \frac{\left(- F_{i-1} \frac{s_{i-1,i}}{\delta_{i-1,i}} + F_i \oint \frac{ds}{\delta_i} - F_{i+1} \frac{s_{i,i+1}}{\delta_{i,i+1}} \right)}{\left(- F_{i-1} \frac{s_{i-1,i}}{G_{i-1,i}\delta_{i-1,i}} + F_i \oint \frac{ds}{G_i\delta_i} - F_{i+1} \frac{s_{i,i+1}}{G_{i,i+1}\delta_{i,i+1}} \right)} \qquad (4.3a)$$

$$G_{eff} = \frac{\{-63.42 * \frac{50}{1} + 73.15 * (\frac{50}{1}) * 4 - 63.42 * (\frac{50}{1})\}}{[-63.42 * \frac{50}{36233} + 73.15 * (\frac{50}{36233} + \frac{50}{20616} + \frac{50}{36233} + \frac{50}{20616}) - 63.42 * (\frac{50}{36233})]}$$

G_{eff} = 21715 N/mm^2

This is the G_{eff} for the three-cell box beam using eq. 4.3a for multi-cell box beam, its value is lower than the one calculated using the single cell relation of eq. 4.3b applied to the complete multi-cell box. The difference between the two G_{eff} is 12.8 % .

For the purposes of this study G_{eff} was calculated using eq. 4.3b and the close co-relation between the FE results and theoretical results has shown that it did not have any adverse affect on the theoretical results thus calculated.

As pointed out earlier since warping is basically a membrane deformation therefore elastic modulus "E" and shear modulus "G" come from the membrane mode

$$G = G^{m}_{xy} = \frac{1}{a_{33}t} \qquad (4.4)$$

Therefore putting value of G^{m}_{xy} from equation 4.4 into equation 4.2 we have

$$(GJ)_s = \frac{4 * A_i^2 \sum_{i=1}^{n} F_i}{(- F_{i-1}\ a_{33_{i-1,i}} s_{i-1,i} + F_i \oint a_{33i} ds \ - F_{i+1}\ a_{33i,i+1}\ s_{i,i+1}\ )} \qquad (4.5)$$

and putting value of G^{m}_{xy} from equation 4.4 into equation 4.3a , for the multi-cell box we have

$$G_{eff} = \frac{\left(- F_{i-1} \frac{s_{i-1,i}}{\delta_{i-1,i}} + F_i \oint \frac{ds}{\delta_i} - F_{i+1} \frac{s_{i,i+1}}{\delta_{i,i+1}} \right)}{\left(- F_{i-1} a_{33_{i-1,i}} s_{i-1,i} + F_i a_{33_i} ds - F_{i+1} a_{33_{i,i+1}} s_{i,i+1} \right)} \qquad (4.6)$$

The active elastic modulus , E_x^a is given as

$$E_x^a = \frac{E_x^m}{1 - \nu_{xy}^m \nu_{yx}^m} \qquad (4.7)$$

where $E_x^m = \frac{1}{t a_{11}}$ (4.8)

Effective thickness for ith wall is defined as

$$t_{eff\,i} = \frac{G_{xyi} t_i}{G_{eff}} \qquad (4.9)$$

The effect of active elastic modulus of each wall on the overall behaviour of the section has been reflected by defining an effective elastic modulus as follows

$$E^a_{x_{eff}} = \frac{\oint E_x^a t ds}{\oint t_{eff} ds} = \frac{\sum E^a_{x_i} t_i s_i}{\sum t_{eff_i} s_i} \qquad (4.10)$$

Sectorial co-ordinate distribution for multi-cell beam is defined previously in chapter 3. This relationship is valid for all isotropic and composite lay-up multi-cell box beams.

$$w(s) = \int_0^s P_R \, ds - \frac{1}{\theta} \int_0^s \frac{F_i}{G_i t_i} \, ds \qquad (4.11)$$

Warping rigidity according to VK&C approach is

$$(E\Gamma)_s = \oint w^2(s) E_x^a t_{eff} \, ds \qquad (4.12)$$

Warping rigidity according to Benscoter approach can be found by defining effective polar constant $I_{c_{eff}}$, and effective Benscoter factor λ_{eff} ,

$$I_{c_{eff}} = \oint P_R^2 t_{eff} \, ds = \sum_{i=1}^{N} P_R^2 t_{eff} L_n \qquad (4.13)$$

and

$$\lambda_{eff} = 1 - \frac{J}{I_{c_{eff}}} \qquad (4.14)$$

and hence warping rigidity $(E\ \Gamma)_{B_s}$ according to Benscoter[2] is as follows

$$(E\ \Gamma)_{s\ \text{BENSCOTER}} = \frac{\oint w^2(s) E_x^a t_{eff} \, ds}{\lambda_{eff}} \qquad (4.15)$$

The sectorial shear function distribution of any isotropic or composite single-cell box section is given as

$$S_{w,c}(s) = S_{w,0}(s) - \frac{1}{2A}\int_s S_{w,0} P_R ds \qquad (4.16)$$

where

$$S_{w,0}(s) = \int_0^s w(s) t ds \qquad (4.17)$$

However in case of multi-cell box section the final reduced value of the closed section SSF distribution $S_{w,c}(s)$ is given as

$S_{w,c}(s)$ at any location of cell i-1 = F^*_{i-1} - $S_{w,0}(s)$ of the given location

$S_{w,c}(s)$ at any location of cell i = F^*_{i} - $S_{w,0}(s)$ of the given location

$S_{w,c}(s)$ at any location of cell i+1 = F^*_{i+1} - $S_{w,0}(s)$ of the given location

Here F^*_{i-1} , F^*_{i} & F^*_{i+1} are the warping shear flows in each of the three cells and are calculated using equations 3.12 and 3.13 as explained in Chapter 3. The actual application of these equations and calculation of the final reduced value of the closed section SSF distribution $S_{w,c}(s)$ for a composite multi-cell section is explained in an example at the end of current chapter.

It is to be noted that while calculating the quasi-open section sectorial shear function distribution $S_{w,0}$ using equation 4.17 above, the thickness is taken as normal thickness and NOT the effective thickness. The logic behind this is that effective thickness is based on closed section idea and the effect of the effective thickness has already been included by $w(s)$ term in the above equation.

Equations for Warping , Axial Stress and Shear stress modified for multi-cell tapered and prismatic composite beams will be defined below, however the solution procedure remains same as already described in detail for multi-cell isotropic beams in chapter 3 , and hence shall NOT be repeated here.

WARPING

Hence once we know θ from equation 3.21 (as detailed in chapter 3 for multi-cell isotropic beams), we can find warping at any point along the length and across the cross section of beam by using following relation .

$$w = - w(s) * \theta \qquad (4.18)$$

where w(s) is the Sectorial Co-ordinate at any given location and has been defined above previously in chapter 3 .

AXIAL STRESS

$$\sigma_x = [\{\frac{d}{dz}(\frac{D}{C}) + C_1\frac{d}{dz}(r_1 z)*e^{r_1 z} + C_2\frac{d}{dz}(r_2 z)*e^{r_2 z}\}* w(s) + \{\frac{D}{C}+C_1 e^{r_1 z}+C_2 e^{r_2 z}\}*\frac{d}{dz}(w(s))\ ] * E^{a}_{x_{eff}} \qquad (4.19)$$

Above equation 4.19 can be used to get Axial stress at any location along length and across the cross-section of the multi-cell composite beam by using the respective value of Sectorial Co-ordinate w(s) , r_1 and r_2 at that particular location along "z" .

SHEAR FLOW

$$q_{\Gamma} = E^{a}_{x_{eff}} * S_{w}(s) *$$

$$[\quad \frac{d^2}{dz^2}(\frac{D}{C}) + C_1 * \{ (\frac{d}{dz}(r_1 z) * \frac{d}{dz}(r_1 z) * e^{r_1 z}) + (e^{r_1 z} * \frac{d^2}{dz^2}(r_1 z)) \}$$

$$+ C_2 * \{ (\frac{d}{dz}(r_2 z) * \frac{d}{dz}(r_2 z) * e^{r_2 z}) + (e^{r_2 z} * \frac{d^2}{dz^2}(r_2 z)) \}] \qquad (4.20)$$

Equation 4.20 can be used to get shear flow at any location along length and across the cross section of the multi-cell composite beam by using the respective value of Sectorial shear function $S_{w}(s)$ at that particular location.

Once the warping shear flow has been calculated using above equation, total shear flow is obtained adding warping shear flow to the Bredt Batho shear flow.

$$q_{TOTAL} = q_{\Gamma} + q_{BREDT\ BATHO}$$

Example

Following example relates to figures 4.1 to 4.4 and the example discussed above for calculation of G_{EFF} and is being used here to show the calculation of w(s) for a three cell box section consisting of $[0/45/-45/90]_s$ lay-up in flanges and $[[45/-45]_2]_s$ lay-up in webs.

We have defined w(s) for multi-cell section as

$$w(s) = \int_0^s P_R\,ds - \frac{1}{\theta}\int_0^s \frac{F_i}{G_i t_i}\,ds \qquad (4.11)$$

Now calculating the 1st and 2nd integral of eq. 4.11 for each of the three cells of the multi-cell section we have as follows.

1st Integral

cell i-1

P_R is considered positive when going around Shear centre in Anti-Clockwise direction.

$$w(s)_{A\text{-}B} = \int_0^s P_R\,ds = \int 75\,ds = 1875 \text{ at B}$$

$$w(s)_{B\text{-}C} = \int_0^s P_R\,ds = 1875 + \int 25\,ds = 3125 \text{ at C}$$

$$w(s)_{C\text{-}D} = \int_0^s P_R\,ds = 3125 - \int 25\,ds = 1875 \text{ at D}$$

$$w(s)_{D\text{-}E} = \int_0^s P_R\,ds = 1875 + \int 25\,ds = 3125 \text{ at E}$$

$$w(s)_{E\text{-}F} = \int_0^s P_R\,ds = 3125 + \int 75\,ds = 5000 \text{ at F}$$

1st Integral

cell i

$$w(s)_{G\text{-}H} = \int_0^s P_R\,ds = 625 \text{ at H}$$

$$w(s)_{H\text{-}I} = \int_0^s P_R\,ds = 1875 \text{ at I}$$

$$w(s)_{I\text{-}J} = \int_0^s P_R\,ds = 3125 \text{ at J}$$

$$w(s)_{J\text{-}K} = \int_0^s P_R \, ds = 4375 \quad \text{at K}$$

$$w(s)_{K\text{-}L} = \int_0^s P_R \, ds = 5000 \quad \text{at L}$$

1st Integral

cell i+1

$$w(s)_{M\text{-}N} = \int_0^s P_R \, ds = \int 75 \, ds = 1875 \quad \text{at N}$$

$$w(s)_{N\text{-}O} = \int_0^s P_R \, ds = 1875 + \int 25 \, ds = 3125 \quad \text{at O}$$

$$w(s)_{O\text{-}P} = \int_0^s P_R \, ds = 3125 - \int 25 \, ds = 1875 \quad \text{at P}$$

$$w(s)_{P\text{-}Q} = \int_0^s P_R \, ds = 1875 + \int 25 \, ds = 3125 \quad \text{at Q}$$

$$w(s)_{Q\text{-}R} = \int_0^s P_R \, ds = 3125 + \int 75 \, ds = 5000 \quad \text{at R}$$

Now 2nd Integral

cell i-1

$$w(s)_{A\text{-}B} = \int_0^s \frac{1}{\theta} \frac{F_i}{Gt_i} ds = \frac{63.42}{(7.6349E-5)*(36233)} \int_0^s ds = 22.92(s) = 573.19 \quad \text{at B}$$

$w(s)_{B\text{-}C}$ $= 573.19 + (40.29 * s) = 2587.97$ at C

$w(s)_{C\text{-}D}$ $= 2587.97 - (3.51 * s) = 2412$ at D

(F_i is -ve when going from C to D as actually +ve shear flow of 73.15-63.42 = 9.73 is flowing from D to C)

$w(s)_{D\text{-}E}$ = 2412 + (40.29 * s) = 4426 at E

$w(s)_{E\text{-}F}$ = 4426 + (22.92 * s) = 5000 at F

2nd Integral

cell i

$$w(s)_{G\text{-}H} = \int_0^s \frac{1}{\theta}\frac{F_i}{Gt_i}\,ds = \frac{73.15}{(7.6349E-5)*(20616)}\int_0^s ds = 46.47(s) = 1161.75 \text{ at H}$$

$w(s)_{H\text{-}I}$ =1161.75 + (3.51 * s) = 1337.25 at I

$w(s)_{I\text{-}J}$ = 1337.25 + (46.47 * s) = 3662 at J

$w(s)_{J\text{-}K}$ = 3662 + (3.51 * s) = 3838 at K

$w(s)_{K\text{-}L}$ = 3838 + (46.47 * s) = 5000 at L

2nd Integral

cell i+1

$$w(s)_{M\text{-}N} = \int_0^s \frac{1}{\theta}\frac{F_i}{Gt_i}\,ds = \frac{63.42}{(7.6349E-5)*(36233)}\int_0^s ds = 22.92(s) = 573.19 \text{ at N}$$

$w(s)_{N\text{-}O}$ = 573.19 + (40.29 * s) = 2587.97 at O

$w(s)_{O\text{-}P}$ = 2587.97 - (3.51 * s) = 2412 at P

(F_i is -ve when going from O to P as actually +ve shear flow of 73.15-63.42 = 9.73 is flowing from P to O)

$w(s)_{P\text{-}Q}$ = 2412 + (40.29 * s) = 4426 at Q

$w(s)_{Q\text{-}R}$ = 4426 + (22.92 * s) = 5000 at R

Net effect of w(s) i.e. 1st Integral - 2nd Integral for all the three cells is shown in figure 4.4.

Example

Referring to figures 4.1 to 4.4 , and the example mentioned above, now the same example is being extended for calculation of $(E\ \Gamma)_s$ for the composite multi-cell box beam.

$E_{Flange} = 54067$

$E_{web} = 17740$

$E^a_{Flange} = 59856$

$E^a_{web} = 44247$

$t_{eff_{Flange}} = 0.9493$

$t_{eff_{Web}} = 1.6685$

$$(E\ \Gamma)_s = \frac{1}{3}\sum_{i=1}^{N} L_n t_{eff} E_x^a \quad (w_{k_n}^2 + w_{i_n}^2 + w_{k_n} w_{i_n}) \qquad (4.12)$$

$$(E\ \Gamma)_s = \frac{1}{3}\{ (2*(50)*(1.6685)*(44247)*(1301)^2) +$$
$$(2*(50)*(1.6685)*(44247)*(537)^2) +$$
$$(2*(50)*(0.9493)*(59856)*(537)^2) +$$
$$(4*(50)*(0.9493)*(59856)*((1301)^2+(537)^2+(1301*537)) \}$$

$(E\ \Gamma)_s = 1.5588109\ E\ 13$

Example

Referring to figures 4.1 to 4.4 , and the example mentioned above , now the same example is being extended for calculation of $S_{w,c}(s)$ for the composite multi-cell box beam.

We need to first calculate $S_{w,0}(s)$ for each of the three cells and then later on it will be modified to $S_{w,c}(s)$

We know that

$$w(s) = \frac{(w_k - w_i)s}{L} + w_i$$

and

$$S_{w,0}(s) = \int_0^s w(s)tds$$

For Cell i-1 we have as follows

$$w(s)_{AB} = \frac{(1301-0)}{25} * s + 0$$

$$w(s)_{AB} = 52.04 * s$$

$$S_{w,0}(s)_{AB} = \int_0^s w(s)tds = \int_0^s (52.04 * s) * (1)\ ds$$

s = 25 for A-B

$S_{w,0}(s)_{AB} = 16272.60$ is the value at point B

Next

$$w(s)_{BC} = w(s)_B + \frac{(537 - 1301)}{50} * s$$

$$w(s)_{BC} = 1301 - 15.28 * s$$

$$S_{w,0}(s)_{BC} = S_{w,0}(s)_B + \int_0^s w(s)tds$$

$$= 16272.6 + \int_0^s (1301 - 15.28 * s) * (1)\ ds$$

$s = 50$ for B-C

$S_{w,0}(s)_{BC} = 62243.33$ is the value at point C

Similarly for other points we find $S_{w,0}(s)$ as below

$S_{w,0}(s)$ at D = 62243.33

$S_{w,0}(s)$ at E = 16272.60

$S_{w,0}(s)$ at F = 0

Now for cell i we have as follows

$S_{w,0}(s)$ at H = - 6712

$S_{w,0}(s)$ at I = - 6712

$S_{w,0}(s)$ at J = - 6712

$S_{w,0}(s)$ at K = - 6712

$S_{w,0}(s)$ at L = 0

Next for cell i+1 we have as follows

$S_{w,0}(s)$ at N = 16272.60

$S_{w,0}(s)$ at O = 62243.33

$S_{w,0}(s)$ at P = 62243.33

$S_{w,0}(s)$ at Q = 16272.60

$S_{w,0}(s)$ at R = 0

Now after finding $S_{w,0}(s)$ for all the three cells above , next we need to find $\oint \frac{S_{w,0}}{t_i} ds$ for each of the three cells.

For cell i-1 ,

$$\oint \frac{S_{w,0}}{t_i} ds = \int_O^B \frac{S_{w,0}}{t_i} ds + \int_B^C \frac{S_{w,0}}{t_i} ds + \int_C^D \frac{S_{w,0}}{t_i} ds + \int_D^E \frac{S_{w,0}}{t_i} ds + \int_E^F \frac{S_{w,0}}{t_i} ds$$

$$\int_O^B \frac{S_{w,0}}{t_i} ds = \int_0^{25} \frac{S_{w,0}}{1} ds$$

Now we know $S_{w,0}(s)_{AB}$ from above calculation as

$$S_{w,0}(s)_{AB} = \int_0^s w(s) t ds = \int_0^s (52.04 * s) * (1)\ ds = 52.04 * \frac{s^2}{2}$$

So we have

$$\int_O^B \frac{S_{w,0}}{t_i} ds = \int_0^{25} \frac{S_{w,0}}{1} ds = 135599$$

next

$$\int_B^C \frac{S_{w,0}}{t_i} ds = \int_0^{50} \frac{S_{w,0}}{1} ds$$

$$S_{w,0}(s)_{BC} = S_{w,0}(s)_B + \int_0^s w(s)tds = 16272.60 + \int_0^s (1301 - 15.28 * s) * (1)\ ds$$

$$S_{w,0}(s)_{BC} = 16272.60 + 1301 * s - 15.28 * \frac{s^2}{2}$$

Hence we have

$$\int_B^C \frac{S_{w,0}}{t_i} ds = \int_0^{50} \frac{S_{w,0}}{1} ds = 2122242$$

Similarly we calculate

$$\int_C^D \frac{S_{w,0}}{t_i} ds = 3335943$$

$$\int_D^E \frac{S_{w,0}}{t_i} ds = 2122242$$

$$\int_E^F \frac{S_{w,0}}{t_i} ds = 135599$$

Hence for complete cell i+1 we have $\oint \frac{S_{w,0}}{t_i} ds = 7851626$

Now for cell i ,

$$\oint \frac{S_{w,0}}{t_i} ds = \int_G^H \frac{S_{w,0}}{t_i} ds + \int_H^I \frac{S_{w,0}}{t_i} ds + \int_I^J \frac{S_{w,0}}{t_i} ds + \int_J^K \frac{S_{w,0}}{t_i} ds + \int_K^L \frac{S_{w,0}}{t_i} ds$$

so we have

$$\int_G^H \frac{S_{w,0}}{t_i} ds = -55937$$

$$\int_H^I \frac{S_{w,0}}{t_i} ds = -559575$$

$$\int_I^J \frac{S_{w,0}}{t_i} ds = -111700$$

$$\int_J^K \frac{S_{w,0}}{t_i} ds = -559575$$

$$\int_K^L \frac{S_{w,0}}{t_i} ds = -55917$$

For complete cell i we have $\oint \frac{S_{w,0}}{t_i} ds = -1342705$

We calculate and find that $\oint \frac{S_{w,0}}{t_i} ds$ for cell i-1 and cell i+1 are same ,

hence we have

$\oint \frac{S_{w,0}}{t_i} ds$ for cell i+1 = 7851626

Now

Next we need to find $\oint S_{w,0} P_R ds$ for the complete three cell box , which will be the addition of $\oint S_{w,0} P_R ds$ for all the three cells i-1, i and I+1.

Hence first we find $\oint S_{w,0} P_R ds$ for cell i-1 which will be the addition of $\oint S_{w,0} P_R ds$ for all the sides of this cell.

For cell i-1 we have

$\int_A^B S_{w,0} P_R ds$ = 10169973 (P_R for side AB is 75)

$\int_B^C S_{w,0} P_R ds$ = 53056056 (P_R for side BC is 25)

$\int_C^D S_{w,0} P_R ds$ = -83398575 (P_R for side CD is -25)

$\int_D^E S_{w,0} P_R ds$ = 53056056 (P_R for side DE is 25)

$\int_E^F S_{w,0} P_R ds$ = 10169973 (P_R for side EF is 75)

Hence $\oint S_{w,0} P_R ds$ for complete cell i-1 is addition of all above = 43053484

Similarly $\oint S_{w,0} P_R ds$ for complete cell i is calculated as = -33567625

and $\oint S_{w,0} P_R ds$ for complete cell i +1 is calculated as = 43053484

Hence $\oint S_{w,0} P_R ds$ for complete three-cell box is calculated by adding all the three cells $\oint S_{w,0} P_R ds$ and is found to be = 52539342

Next we need to calculate warping shear flows for restrained torsion F^*_{i-1} , F^*_i & F^*_{i+1} in each cell of the three-cell box and also the restrained rate of twist θ^* using Waldron[1] equation mentioned below by setting up three equations i.e. one for each cell.

$$\theta^* G \Omega_i = - F^*_{i-1} \frac{s_{i-1,i}}{\delta_{i-1,i}} + F^*_i \oint \frac{ds}{\delta_i} - F^*_{i+1} \frac{s_{i,i+1}}{\delta_{i,i+1}} - \oint_i \frac{S_{w,0}}{t_i} ds$$

Here we have

T= 1000,000 Nmm

Ω_i = 2*Area = 2*(50*50)= 5,000 mm^2 for each of the three cells

G_{FLANGE} = 20616 N/mm^2

G_{WEB} = 36233 N/mm^2

thickness δ = 1 mm for each of the lay-ups used

Hence for cell i-1 we have

$$\theta^* *(5{,}000) = F^*_{i-1} *(\frac{50}{36233} + \frac{50}{20616} + \frac{50}{36233} + \frac{50}{20616}) - F^*_i *(\frac{50}{36233}) - 7851626$$

and for cell i we have

$$\theta^{*}*(5{,}000) = -\ F^{*}_{i-1}*\left(\frac{50}{36233}\right) + F^{*}_{i}*\left(\frac{50}{36233}+\frac{50}{20616}+\frac{50}{36233}+\frac{50}{20616}\right)-F^{*}_{i+1}*\left(\frac{50}{36233}\right) + 1342705$$

finally for cell i+1 we have

$$\theta^{*}*(5{,}000) = -\ F^{*}_{i}*\left(\frac{50}{36233}\right) + F^{*}_{i+1}*\left(\frac{50}{36233}+\frac{50}{20616}+\frac{50}{36233}+\frac{50}{20616}\right) - 7851626$$

the fourth equation is written from considering following equation

$$\sum_{i=1}^{n} F^{*}_{i}\ \Omega_{i} - \oint S_{w,0} P_{R} ds = 0$$

$$5{,}000 * F^{*}_{i-1} + 5{,}000 * F^{*}_{i} + 5{,}000 * F^{*}_{i+1} - 52539342 = 0$$

Now solving above four equations we get the following rate of twist θ^{*} , and the warping shear flows in the three cells i-1 , i and i+1 .

θ^{*} = -3.632542587318928E-002 rad/mm
F^{*}_{i-1} = 14776.6237200010 N/mm
F^{*}_{i} = -19045.3788754630 N/mm
F^{*}_{i+1} = 14776.6237200010 N/mm

Now we need to finally get the $S_{w,c}(s)$ at each location around the three cell box by using following relation

$S_{w,c}(s)$ at point B = F^{*}_{i-1} - $S_{w,0}(s)$ at point B

and similarly for all other points around the three cells i-1,i and I+1.

Hence for cell i-1, we get the $S_{w,c}(s)$ values as follows

$S_{w,c}(s)_B = -1495$

$S_{w,c}(s)_C = -47466$

$S_{w,c}(s)_D = -47466$

$S_{w,c}(s)_E = -1495$

$S_{w,c}(s)_F = 14776$

and for cell i, we get the $S_{w,c}(s)$ values as follows

$S_{w,c}(s)_H = -12332$

$S_{w,c}(s)_I = -12332$

$S_{w,c}(s)_J = -12332$

$S_{w,c}(s)_K = -12332$

$S_{w,c}(s)_L = -19045$

Cell i+1 has same $S_{w,c}(s)$ results as that of cell i+1, results of $S_{w,0}(s)$ and $S_{w,c}(s)$ for the multi-cell composite three cell box is shown in figures 4.5 and 4.6.

Example

Referring to figures 4.1 to 4.4 , and the example mentioned above , now the same example is being extended for calculation of the I_c for the multi-cell box.

Here in this example we have

P_{R1} = 75 mm (Perpendicular distance from line MN to shear centre of box)

P_{R2} = 25 mm (Perpendicular distance from line NO to shear centre of box)

P_{R3} = 25 mm (Perpendicular distance from line OP to shear centre of box)

Hence we have for composite multi-cell box

$$I_{c\,eff} = \oint P_R^2 t_{eff}\, ds = \sum_{i=1}^{N} P_R^2 t_{eff} L_n \qquad (4.13)$$

$t_{eff_{Flange}} = 0.9493$

$t_{eff_{Web}} = 1.6685$

$$I_{c\,eff} = 2^* (P_{R1}{}^2 * t_{eff_{Web}} * W) + 6^* (P_{R2}{}^2 * t_{eff_{Flange}} * F) + 2^* (P_{R3}{}^2 * t_{eff_{Web}} * W)$$

$$I_{c\,eff} = 2^* [(75)^2*(1.6685)*(50)] + 6^* [(25)^2*(0.9493)*(50)] + 2^* [(25)^2*(1.6685)*(50)]$$

$I_{c\,eff} = 1220866$

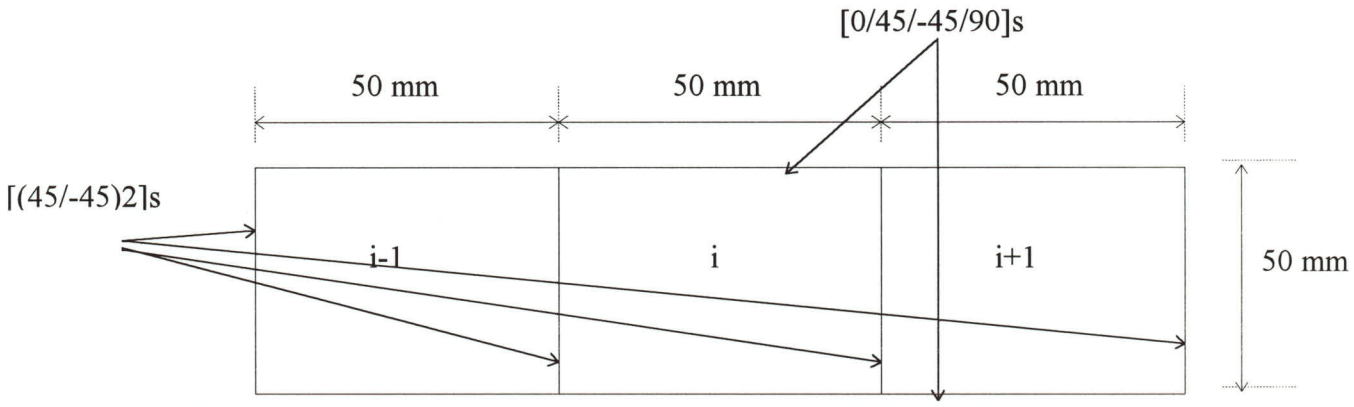

Figure 4.1 Dimensions of example composite three-cell box

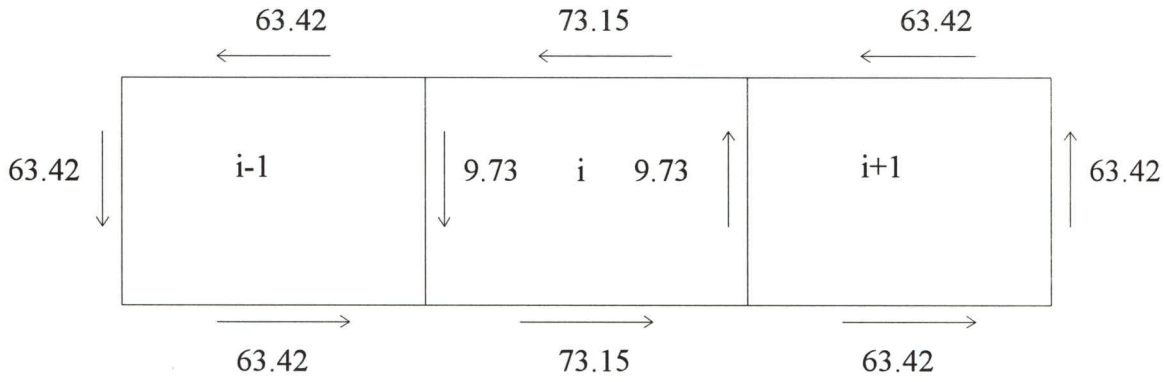

Figure 4.2 Bredt Batho Shear Flows in each of the 3 cells of composite three-cell box

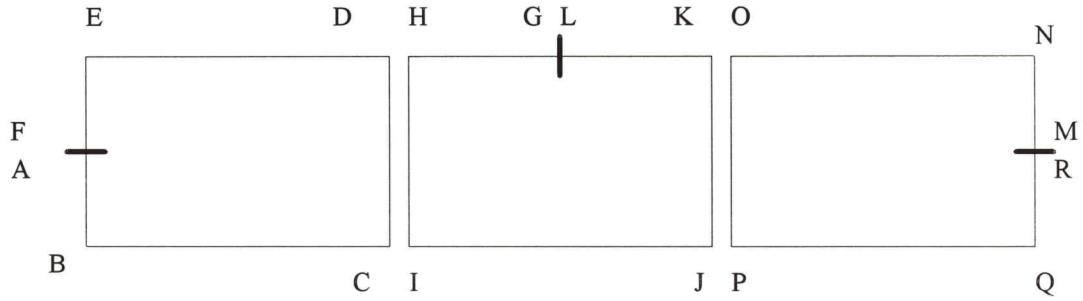

Figure 4.3 Three cells shown separately for calculation of w(s)

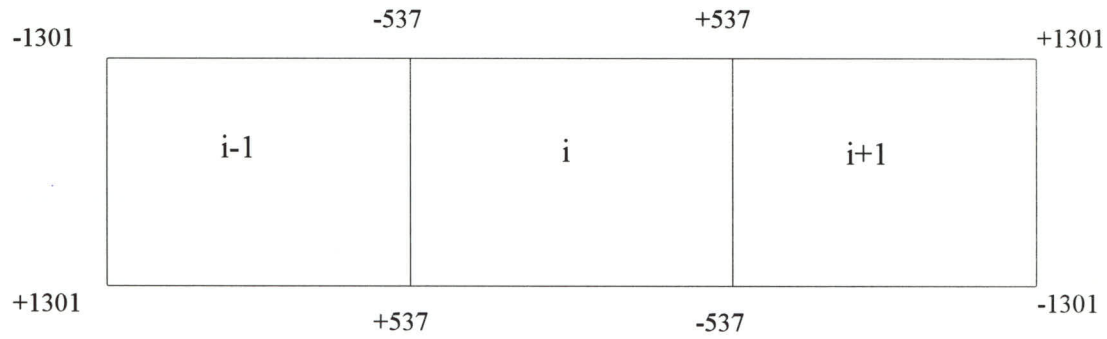

Figure 4.4 w(s) final distribution in each of the 3 cells of composite three-cell box

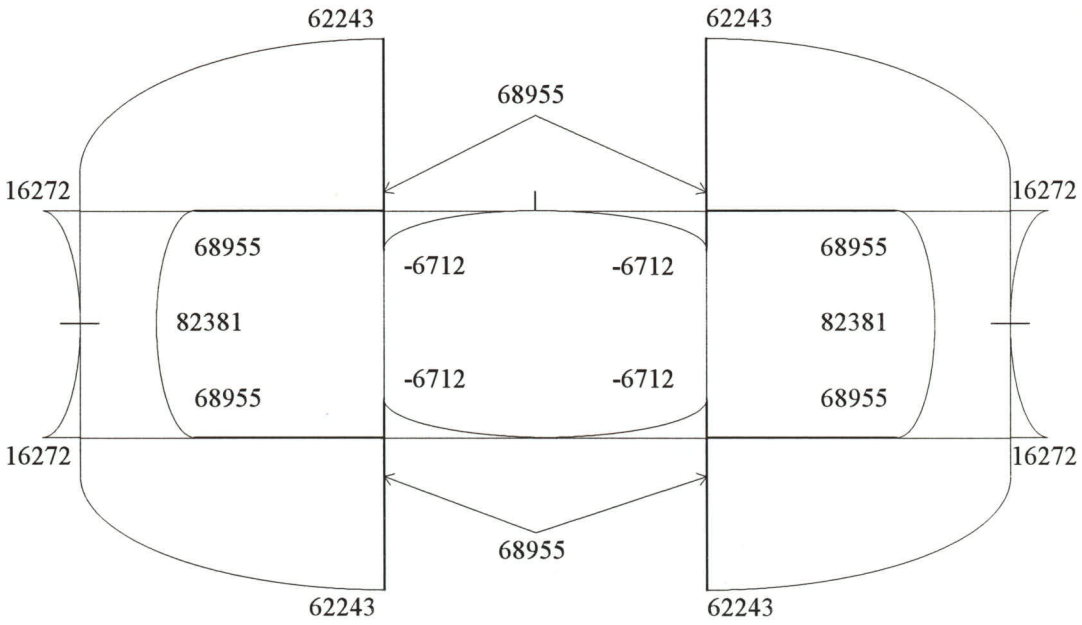

Figure 4.5 $S_{w,0}(s)$ distribution for the composite three cell box

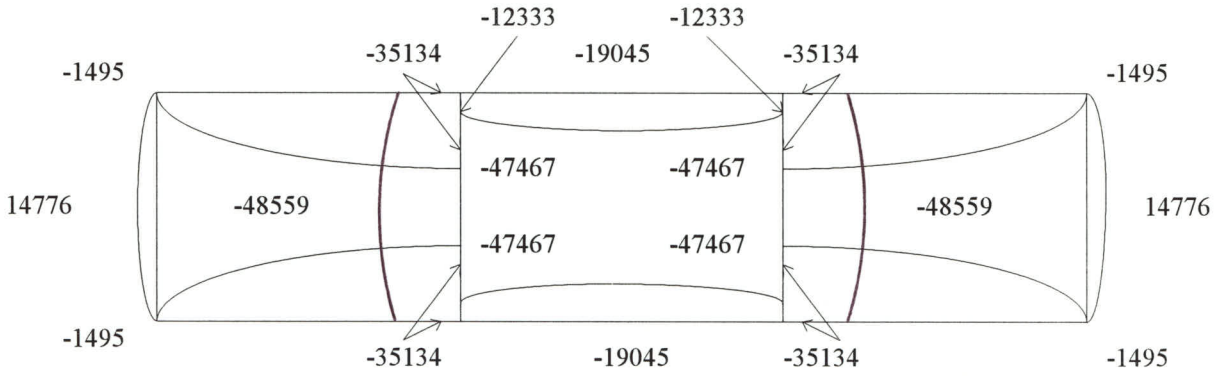

Figure 4.6 $S_{w,c}(s)$ distribution for the composite three cell box

5 FINITE ELEMENT ANALYSIS

5.1 INTRODUCTION

Finite Element (FE) Analysis of structures has over the years turned into a very useful , important and un-avoidable tool for the engineers working in industry and academic institutions all over the world due to its inherent flexibility , speed and ease of use. Although the mathematical modelling of the element behaviour has been available for many years , however , it was only possible with the not so distant advances in the computer power that the analysis method has turned out to be the most popular design tool of today. This is so as the advance computers have tremendously reduced the time taken to solve the very large number of equations that are required to be solved for any Finite Element Model.

FE analysis of a structure is achieved by examining the behaviour of a number of its constituent well defined elements. Suitable stiffness equations are used to model the behaviour of these constituent elements under given applied load conditions. The stiffness equations are in a matrix form and the element stiffness matrix is termed as the local stiffness matrix. Once these local stiffness matrices for the elements have been formed then they are combined together according to their relation to one another and thus global stiffness matrix for the complete structure is formed. This global stiffness matrix is then used to solve for the loads , displacements and stresses acting on the structure according to the requirement of each problem.

The main advantage of using FEM (Finite Element Method) is its time and cost effectiveness vis a vis any experimental work being under taken to determine the results of the application of required load conditions on the structure under consideration. The experimental work as is obvious can take many hours in its construction and preparation phase and is also expected to be very costly. FEM on the other hand allows the structure to be analysed relatively quickly without any hassle with the prime cost being that of computer system and software being used for the subject analysis. However probably the biggest advantage of the FEM is its ability to modify the problem with relatively much ease and very little effort without having to start the work from the beginning as is the case with any experimental set up. This ability becomes very significant when analysing different variations in lay-up configurations of composite laminates where for each new case the problem can be modified by simply modifying the laminate properties of the structure.

5.2 FEM ANALYSIS

5.2.1 INTRODUCTION TO MSC/NASTRAN

MSC/NASTRAN is a computer program for structural analysis that is based on the finite element method. It is an advanced version of the NASTRAN program that was developed under the sponsorship of the National Aeronautics and space administration popularly known as NASA. The NASTRAN development which was based on the requirements of the aerospace industry , began in 1966. The name of NASTRAN is derived from NAsa STRuctural ANalysis. The MacNeal-Schwendler Corporation (MSC) was involved with NASTRAN from the beginning , and MSC has been marketing their own advanced version, MSC/NASTRAN, since 1972. This undertaking involved the extension of the program to provide for the needs of general industry. MSC/NASTRAN,

is the worlds most comprehensive and a large scale general purpose digital program , which solves a wide variety of engineering problems by the finite element method. The program uses a finite element structural model, wherein disturbed physical properties of a structure are represented by a finite number of structural elements which are interconnected at a finite number of grid points to which the loads are applied and for which the displacements are calculated. The program capabilities include linear and non linear static and dynamic structural analysis.

5.2.2 FEM ANALYSIS USING MSC/NASTRAN

The FEM analysis of single-cell and multi-cell prismatic and tapered boxes was carried out employing the general purpose MSC/NASTRAN package developed by the MacNeal Schwendler Corporation, and incorporated into the College of Aeronautics Sun Sparc server 630MP computer system.

For a number of years, the above-mentioned package has been used successfully by research students to perform a variety of analysis, e.g. linear static, non-linear static and dynamic analysis. The capability of performing different types of analysis is provided by different *"solution sequences"* in MSC/NASTRAN. Each of these solution sequences is designed for a specific application.

The torsional behaviour of single-cell and multi-cell prismatic and tapered boxes was studied by performing geometric linear analysis, using the linear static solution sequence.

A detailed description of the theory of MSC/NASTRAN geometric linear FEM analysis is given in the MSC/NASTRAN handbook for linear static analysis[5] . However, for

completeness, the salient features of the aforementioned theory are briefly outlined below.

- The whole region of the structure under study is divided into a number of well defined elements which have simple geometrical shapes. The shape, size and position of the elements are defined by nodes (i.e. by grid points).

- The admissible displacement field within each element is expressed in terms of nodal displacements (i.e. nodal degrees of freedom) using interpolation functions known as shape functions.

- For a given set of loading or for a given set of enforced displacements, the governing equilibrium equations of each element are obtained through variational process by invoking the principle of Minimum Potential Energy. The element equilibrium equations are in a matrix form, and termed local equilibrium equations.

- The global equilibrium equations, which are also in a matrix form, are constructed for the whole structure by assembling all of the element matrices according to their relation to one another. These equations are modified by applying the appropriate boundary conditions.

- Having applied the boundary conditions, the global equilibrium equations are then solved for all nodal displacements.

- Using the strain-displacement and stress-strain relations, the state of all elements are determined (i.e. the strains and stresses are calculated for the computed displacements).

5.2.3 DESCRIPTION OF NASTRAN

All the information required by NASTRAN to perform a Finite Element Analysis must be available in an input data file (.bdf) written in ASCII format. The input data file is usually made up of three parts, the executive section, the case control section and the bulk data section. The executive section specifies values for executive system operational parameters called cells, i.e. memory settings. The case control section selects loads and constraints, requests printing or plotting of input and output data and defines the subcase structure for the analysis. The bulk data section contains entries that specify the meshed structure, element connectivity, element and material properties, constraints and loads. The input data file can be modified and amended with a text-editor.

The progress of the analysis and additional information about the modules NASTRAN executes can be observed in .log and .f04 files. The .f04 file also contains valuable information about the maximum number of rows (Degree of Freedom) in the stiffness matrix[k] and the amount of computer memory used in the analysis.

The results of the finite element analysis are written in the .f06 and .op2 file. The .f06 file contains all calculated results and is in readable ASCII format. The file is quite large and not suitable to visualise and understand the analysis results. However this file is used for noting the data by hand and then later on plotting for required results using some other software available in market i.e. XL from Microsoft Word. This method is quite tedious and consumes a lot of time in getting each plot. All the plots shown in this Thesis containing FE results have been prepared using this .f06 file. The other output file .op2 is in binary format and is utilised for viewing different stresses, strains and displacements acting along the length of the model in a multi-coloured format. The colour at each location shows the value of stress/strain/displacement at that particular location along length of the model. This provides good visualisation to the user as to what is going on in the model at various locations.

5.2.4 FEM MODELLING USING PATRAN

The computer program "PATRAN" distributed by the MSC and specifically designed for use as pre and post-processor for NASTRAN has been used to create the geometrical model, to discretisize the structure (meshing), to assign the boundary conditions, to apply the loading and to define the material properties. After finishing the model and defining the executive and case control sections, PATRAN writes an ASCII NASTRAN input data file (.bdf), containing executive control, case control and bulk data section. The NASTRAN analysis can then be started on the SUN sparc station to get the required output files

.

For geometric-linear analysis and for that matter all types of FEM analysis, the accuracy of the results are very dependent on the finite element model developed for the structure. An incorrect model can sometimes lead to completely meaningless results. Therefore, it is necessary to pay a great deal of attention to the modelling process in order to ensure that the developed FEM model will represent the true behaviour of the structure as closely as possible.

In order to use the FEM effectively , the application of users engineering knowledge to the structure is mandatory. It is also required to be decided that how much detail is required to be put in the model, i.e., the size and the number of elements. Although more detail in a model results in more accurate solution but it costs more in terms of computer resources. Ideally it is required to create an accurate, yet cost effective model. A better understanding of structure, applied loads and MSC/NASTRAN solution process provides an effective way in finding solution to the required problem.

As far as the FEM modelling of the single-cell and multi-cell prismatic and tapered boxes under consideration was concerned, the pre & post-processor P3/PATRAN software produced by PDA Engineering was used as a tool to construct the FEM models. For the successful implementation of finite element modelling, some necessary considerations were taken into account. These considerations included the element type, mesh size, boundary conditions and applied torque.

The single-cell prismatic boxes had a cross sectional size of 100 mm x 50 mm at the restraint end of the box. This cross-sectional dimension was maintained constant all along the 600 mm length of the single cell box beam as is shown in figure 5.1.

In case of single cell tapered boxes, the cross sectional size of 100 mm x 50 mm at the restraint end of the box started to reduce steadily along the length of the beam .This was due to the effect of taper angle α (Alpha) and β (Beta). The cross sectional size of the beam reached its minimum values at the free end of the beam at a distance of 600 mm from the restraint end as is shown in figure 5.2.

The three-cell prismatic boxes had a cross sectional size of 150 mm x 50 mm at the restraint end of the box. Each cell had a dimension of 50 mm x 50 mm at the root. This cross-sectional dimension was maintained constant all along the 600 mm length of the three cell box beam as is shown in figure 5.3.

In case of three cell tapered boxes, the cross sectional size of 150 mm x 50 mm at the restraint end of the box started to reduce steadily along the length of the beam .This was due to the effect of taper angle α (Alpha) and β (Beta). The cross sectional size of the beam reached its minimum values at the free end of the beam at a distance of 600 mm from the restraint end as is shown in figure 5.4.

5.2.4.1 TYPE OF ELEMENT USED

The MSC/NASTRAN software has a wide range of elements for the analysis of different types of structures. Scalar (zero dimensional), One-dimensional, two- dimensional and three-dimensional elements are included in the element library.

According to the MSC/NASTRAN Linear Static Analysis Guide[6] , two-dimensional elements, commonly referred to as plate and shell elements, are used to represent areas of model where one of the dimensions is small in proportion to the other two. As shown in figure 5.5 , the thickness of the model is substantially less than the other two dimensions a and b.

For the type of problem under consideration, it was necessary to use two-dimensional thin shell elements for two main reasons. One reason was that the thickness of the boxes was very small compared to their other dimensions, thus the boxes were required to be represented by two-dimensional elements. The other reason was that the boxes responded to the applied torque with a combination of membrane and bending action. Thus, the boxes were required to be modelled using thin shell elements which had the bending-membrane capability.

It may be noted that the MSC/NASTRAN element library contains only two type of shell elements suitable for the geometric linear analysis of this kind which are capable of carrying inplane force, bending force and transverse shear force. One is a quadrilateral element called CQUAD4, and the other is called CQUAD8 . The CQUAD8 are higher order elements that are useful for modelling curved surfaces with less elements than are required if CQUAD4 was used. According to the MSC/NASTRAN handbook, in general, CQUAD4 element is more reliable than the CQUAD8 element. An element CQUADR is also defined in the library which is complementary to CQUAD4. It may be mentioned here that the other two types of triangular elements CTRIA3 and CTRIA6 mentioned in the MSC/NASTRAN library of 2-D elements have not been recommended

for use by MSC/NASTRAN User guide[6] due to the inherent errors associated with the triangular elements.

It is worth noting that the CQUAD4 element is a general purpose element, capable of carrying inplane force, bending forces and transverse shear force. This is the most commonly used 2-D element in the MSC/NASTRAN element library. CQUAD4 is a quadrilateral flat plate connecting four grid points. This element is elastically connected to only five of the six degrees of freedom at each of its grid points (i.e. it is connected to three translational and two rotational degrees of freedom at each grid point). The element does not provide direct elastic stiffness to the sixth degree of freedom which corresponds to the rotation about the normal to the surface of the element. The CQUAD4 element caters for shear contribution out of the element's plane. However, this facility was not of any exceptional importance in the current FEM analysis as the boxes were very thin.

5.2.4.2 FINITE ELEMENT MESH

The number of elements per unit area in a structure should be carefully arranged so as to obtain optimum results. In general, a refined mesh should be used in regions of high stress gradients and a course mesh in region of low stress gradients. Initially in an analysis, different mesh arrangements should be tried to determine the effect on displacement and stresses. Generally, displacements and stresses converge as the mesh is refined.

A typical FE mesh is shown in figure 5.6. In this figure, node **n** is a common node of elements E-1, E-2 , E-3 and E-4. When the FE model is analysed using NASTRAN we get the .f06 output file which shall have four stress outputs for a certain direction (for example direction Z along the length of box) for node **n** . This is so as the stresses are

calculated by NASTRAN on an element basis. Ideally , the values of stresses coming out from all four elements for node **n** should be same. This is actually an indicator of the reliability of the FE model. A huge discrepancy in a certain stress or strain value of node **n** shared by four elements would mean that FE model is not quite accurate and needs to be modified further. This normally results in a finer mesh. As the mesh is refined, the values of node **n** coming from the sharing elements converge. The point where the refining should be stopped depends upon the computer capability and also the computing time, as it is evident that a finer mesh demands increase in both the computer capability and the computing time.

A nodal discrepancy of around 5% is considered as reasonable in verification of a certain FE model for the case of present study. However it needs to be stated that the nodal discrepancy may not converge to 5% limit around the restraint and loading region. This is so due to the Poisson's effect at the restraint end and a sudden concentrated torque in the loading region.

The other important consideration in the FE modelling is the aspect ratio of elements within the mesh. Aspect ratio is defined as the ratio of the longer side of an element to the shorter side. Although it is generally agreed that, it is better to keep the aspect ratio upto or below 3.0 . However this is very much dependant on the theoretical formulation of the finite element model being used. The MSC/NASTRAN guide does not place any restriction on the upper limit of aspect ratio required to be used in the FEA. However in case of this study a maximum aspect ratio limit of upto 2.0 has been maintained in all of the FE models .

Fine mesh with element size of 5 mm x 5 mm was used in the first 100 mm from the restraint end. This was done to get better understanding of the results in the area of high stress concentration near the restraint end. However in the later 500 mm length of the box beam with a decrease in the stress gradient an element size of 10 mm x 5 mm was considered quiet adequate. Thus in case of single cell prismatic/tapered box beams a total of 4200 elements were used with this mesh density . However a total of 7000 elements constituted the FE model for the three cell prismatic/tapered box beams. The Computer

time utilised in the analysis of these FE models by NASTRAN was approximately 4 minutes . Finite Element Meshing for Single-cell box, Single-cell tapered box, Three cell box and Three cell tapered box are shown in figures 5.7, 5.8 , 5.9 and 5.10 respectively.

5.2.4.3 BOUNDARY CONDITIONS

The influence of the torque being applied at the free end while other edge of the tapered /prismatic box being fully clamped has been considered in this FEA. The restrained end had all the six degrees of freedom fully restrained for all the nodes at that end. This implied putting $u = 0$, $v = 0$, $w = 0$, $\theta_x = 0$, $\theta_y = 0$ and $\theta_z = 0$, for all the nodes at the restraint end.

A moment of 1000,000 Nmm was applied about Z Axis of the box beam on an independent node located at the centre of free edge. The applied Boundary Conditions on the box beam are shown in figure 5.11 .

5.2.4.4 LAMINATE PROPERTIES

Laminate properties of all the composites used in the FE analysis of single-cell and multi-cell composite beams are calculated by MSc PATRAN using the following input properties of carbon ply :

E_1=140000 N/mm^2
E_2=10000 N/mm^2
G_{12}=5000 N/mm^2
ν_{12}=0.3

5.3 USE OF DIAPHRAGMS TO AVOID DISTORTION OF BOX BEAMS

In order to avoid the cross sectional deformation in the box beam , initially it was proposed to use 5 diaphragms located at regular intervals across the cross section of the beam. Following diaphragm properties were used

$E_d = 210 \times 10^{10}$ N/mm^2

$t_d = 0.001$ mm

Membrane stiffness $E_d t_d = 210 \times 10^7$ N/mm

Bending Stiffness $E_d t_d^3 / 12 = 175$ N mm

The value of "E" modulus was chosen high in order to keep high membrane stiffness which was considered imperative for the maintenance of cross sectional shape of the box beam under subject loading conditions. However it was observed that the cross sectional deformations were still taking place at the locations between any two adjacent diaphragms. It was thus decided to increase the number of diaphragms initially to 10 and then subsequently to 20 along the length of box beam with diaphragms located at every 30 mm along the length of beam (length of box beam being 600 mm) . An extreme case of having 50 diaphragms i.e. a diaphragm after every 12 mm along the length was also considered to see the effect of such a large number of diaphragms on the box deformation.

It was observed that the deformation was still taking place at the locations in between the two adjacent diaphragms. Moreover use of such high number of diaphragms is also considered to be a false representation of the FE model. It was hence concluded that the

diaphragm concept as used in the past by ATA[7] and Wooley[8] could not be of much use in the torsional analysis of single-cell and multi-cell prismatic and tapered box beams. It was thus time to bring in a new concept to avoid the cross sectional deformation of the box beam.

It was at this stage that a study was undertaken to consider all the elements available in the MSC/NASTRAN library which could be potentially used to avoid the deformation of the box beam without increasing the stiffness of the model. R-type elements which are a type of Multi Point Constraints (MPCs) available in the MSC/NASTRAN library were considered in this regard and found suitable for use . A detail of the R-type elements are given below.

5.3.1 R-TYPE ELEMENTS

An R-type element is an element which imposes fixed constraints between components of motions at the grid points or scalar points to which they are connected. The three most commonly used R-type elements in the MSC/NASTRAN library are RBAR , RBE-2 and RBE-3 elements. When using an R-type element it is required to specify which degrees of freedom are independent and which degrees of freedom are dependant. The simplest way to describe this is to say that the motion of a dependent degree of freedom is expressed as a linear combination of one or more of the independent degrees of freedom. All dependent degrees of freedom are placed in what is referred to as the m-set. The independent degrees of freedom are temporarily placed in an n-set, which is the set that is not made dependant by the MPCs or R-type elements. A constraint equation (an internal MPC equation) is generated for each of the dependant degrees of freedom.

5.3.2 RBE-2 ELEMENT

The RBE-2 (Rigid Body Element type 2) provides a very convenient tool for rigidly connecting the same components of several grid points together. Multiple RBARs or an RBE-1 can be used where ever RBE-2 is used . However according to the MSC NASTRAN user guide it is more convenient to use the RBE-2 elements. The use of RBE-2 element is recommended by MSC/NASTRAN user guide when the aim is to maintain the cross sectional shape of the model while applying torque about the axis of the cross section under consideration .

RBE-2 elements are described as the rigid body connected to an arbitrary number of grid points. The independent degrees of freedom are the six components of motion at a single grid point. The dependant degrees of freedom at the other grid points all have the same user selected component numbers according to the requirement of the model.

In the case of this study all the slave or dependant nodes at each of the 70 RBE-2 element locations along the length of box beam were coupled to the master or independent node at the centre of the beam at that location in directions Ux, Uy, and Rz. This was done to avoid cross sectional deformation of the beam, and allow warping of the box in the Z direction along the length of box beam. To achieve this objective the independent or master nodes of all 70 RBE-2 elements were restricted by application of single point constraints in the directions X, Y, Z, Rx and Ry.

5.4 CONVERGENCE STUDY

The validity and accuracy of the finite element results is not only dependant on element type (shell, volume, number of nodes) but also on element quality (distortions), the

number of elements used to model the structure (mesh density) and if the correct solution sequence for the type of analysis has been selected.

If the FE analyst has the required experience and knowledge in FEA (Finite Element Analysis) and has sufficient structural analysis background then it is usually not difficult to chose the correct element type and solution sequence. However it is quite difficult to estimate the required minimum number of elements to obtain sufficient accurate results and to know how increasing or decreasing the number of elements influences the analysis results. It is usually considered that the more the number of finite elements used in a model the better the accuracy, but the increased computing time to obtain a solution is also an important factor which has to be considered.

It is therefore of great importance to analyse the same structure repeatedly using different density finite element meshes and to compare the results obtained. If the influence on the results is negligible than it can usually be assumed that the finite element solution is accurate and the finite element mesh is sufficiently fine. It might be possible to reduce the mesh density and to reduce the analysis time without reducing the accuracy of FEA. On the contrary if the results show significant differences than the results are unreliable and a finer mesh might be required to obtain a more accurate solution.

The convergence study for FEA of this case was carried out by considering a three cell composite box using all $[45/-45]_2]_s$ lay-up in flanges and webs . The Finite Element modelling was initially carried out using 1500 elements. The results obtained for axial displacements (warping), force intensity (FI) and shear flow all along the length of box at points "B" and "C" and around the box at different locations from the restraint end of box were plotted and compared with another finite element model using 7000 elements. The results in both cases were found to be exactly same with in an accuracy of upto 1%. However after the convergence study it was decided to continue using 7000 elements for all future models as it provided more data points required for plotting the response of

model in axial displacements (warping), force intensity (FI) and shear flow all along the length of box and also around the cross section of the box due to availability of more nodal points. The convergence study was repeated for single-cell and multi-cell prismatic/tapered all $[0/45/-45/90]_s$ lay up in flanges and webs, and also for flanges $[0/45/-45/90]_s$ & webs $[45/-45]_2]_s$ lay-up. The results in all these cases were found to be in total agreement for both models made from 1500 elements and 7000 elements in each case. This provided enough confidence that the number of elements being used for the FE models were adequate for the type of analysis being carried out in this study.

5.5 RESULTS OF FINITE ELEMENT ANALYSIS

The results obtained from FEA were compared with the theoretical results for the case of an isotropic material. This was done using the already existing isotropic theories in use. The excellent agreement between the two results gave the confidence for the change of lay-ups in the Finite Element Model from existing isotropic lay-up to the required composite lay-ups to take place. The composite models for prismatic and tapered boxes for single cell and multi-cell boxes were compared against the proposed composite theory of torsion and were found to be in very close agreement , thus giving confidence in the proposed composite theory of torsion for the single cell and multi-cell prismatic and tapered boxes.

The results from FEA have been presented in Chapter 6 in comparison with the theoretical results. Some of the fringe plots showing coloured depiction of warping and Axial stresses along the length of the single cell and multi-cell prismatic/tapered boxes have been shown in figures 5.12 to figures 5.19. Deformed shapes under application of the applied Torque 1000,000 Nmm at the free end for the single cell and multi-cell prismatic/tapered boxes are shown in figures 5.20 to 5.23.

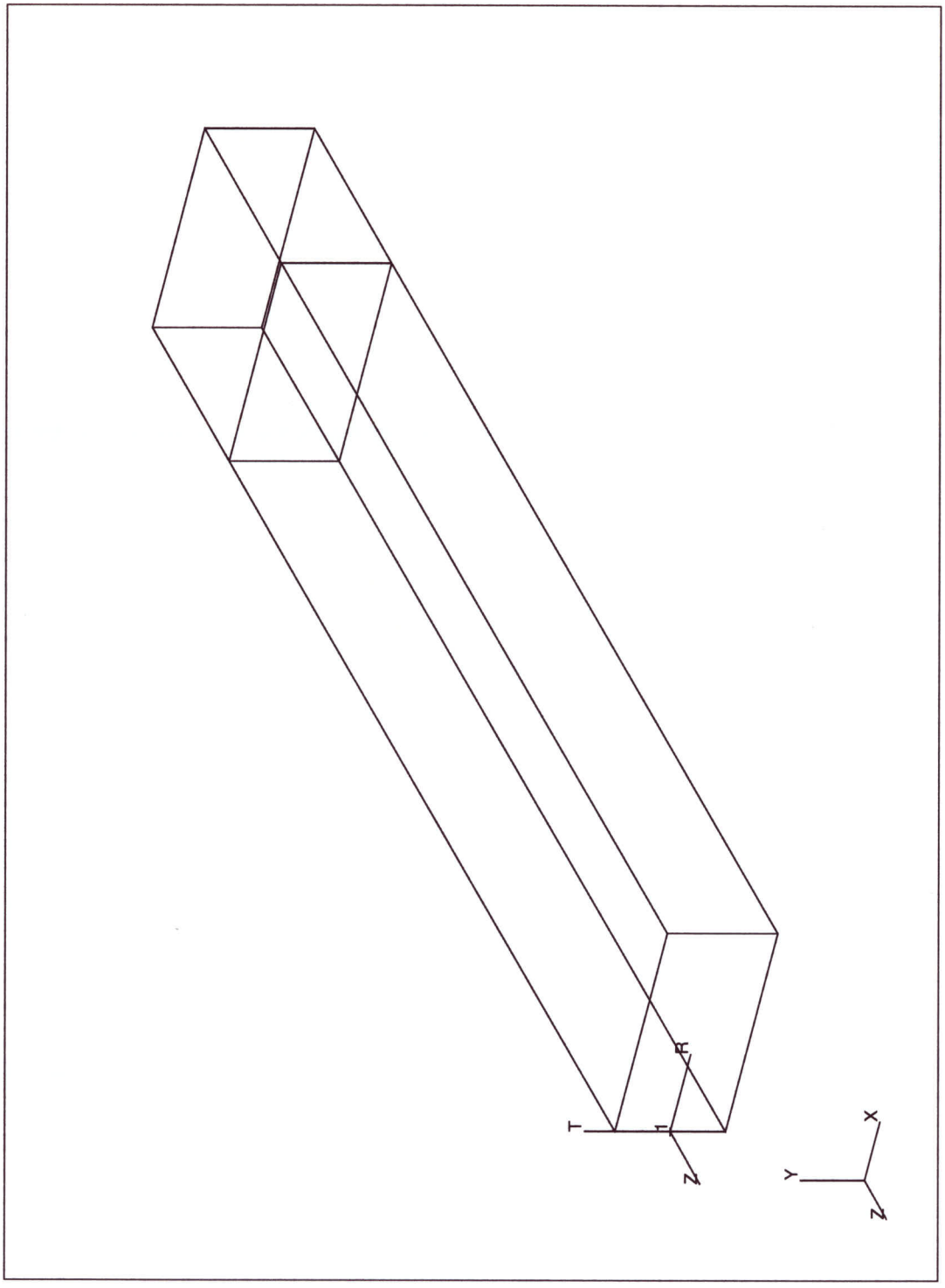

Figure5.1SingleCellBoxGeometry

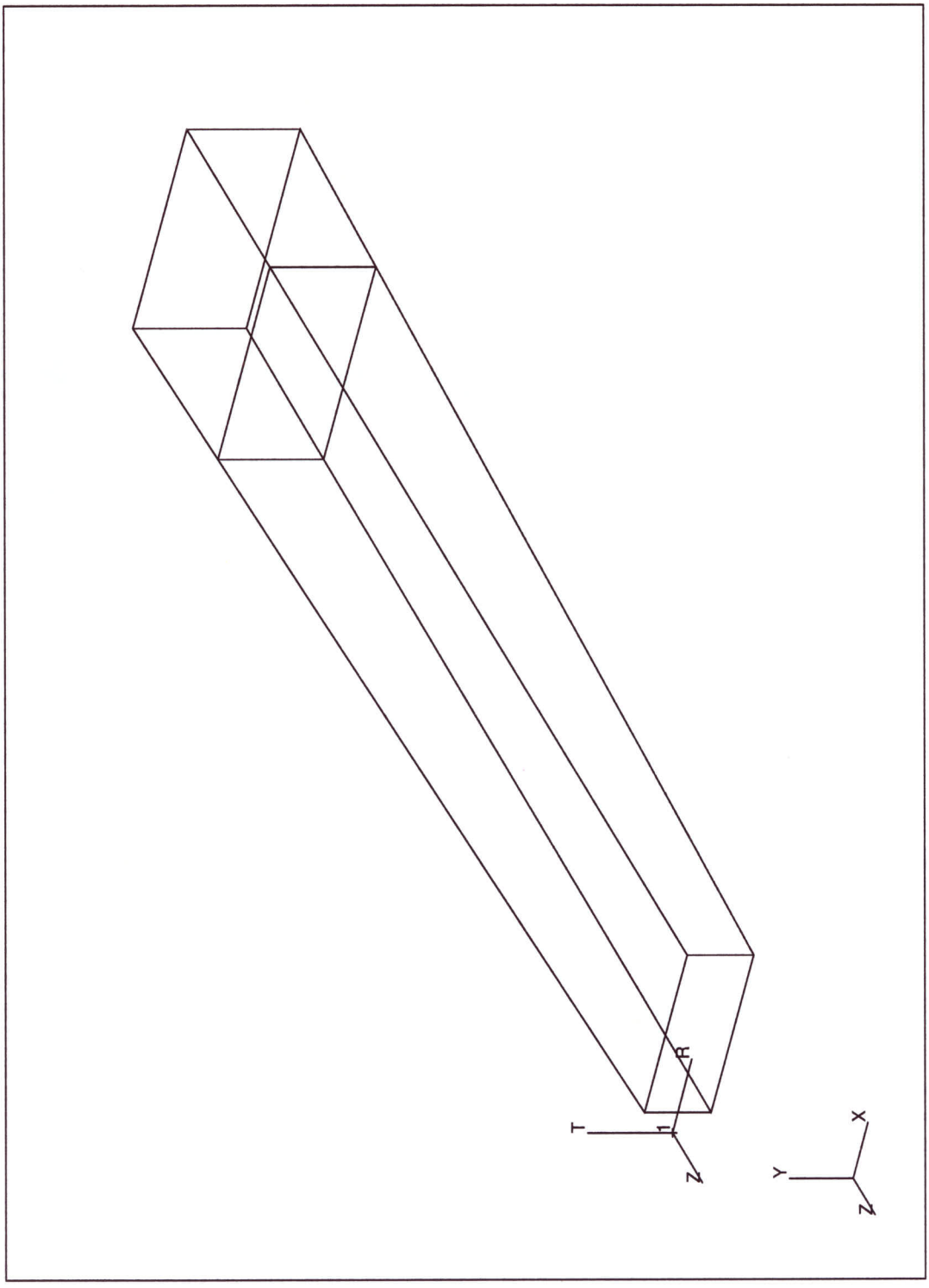

Figure 5.2 Geometry of Single Cell Taper Box

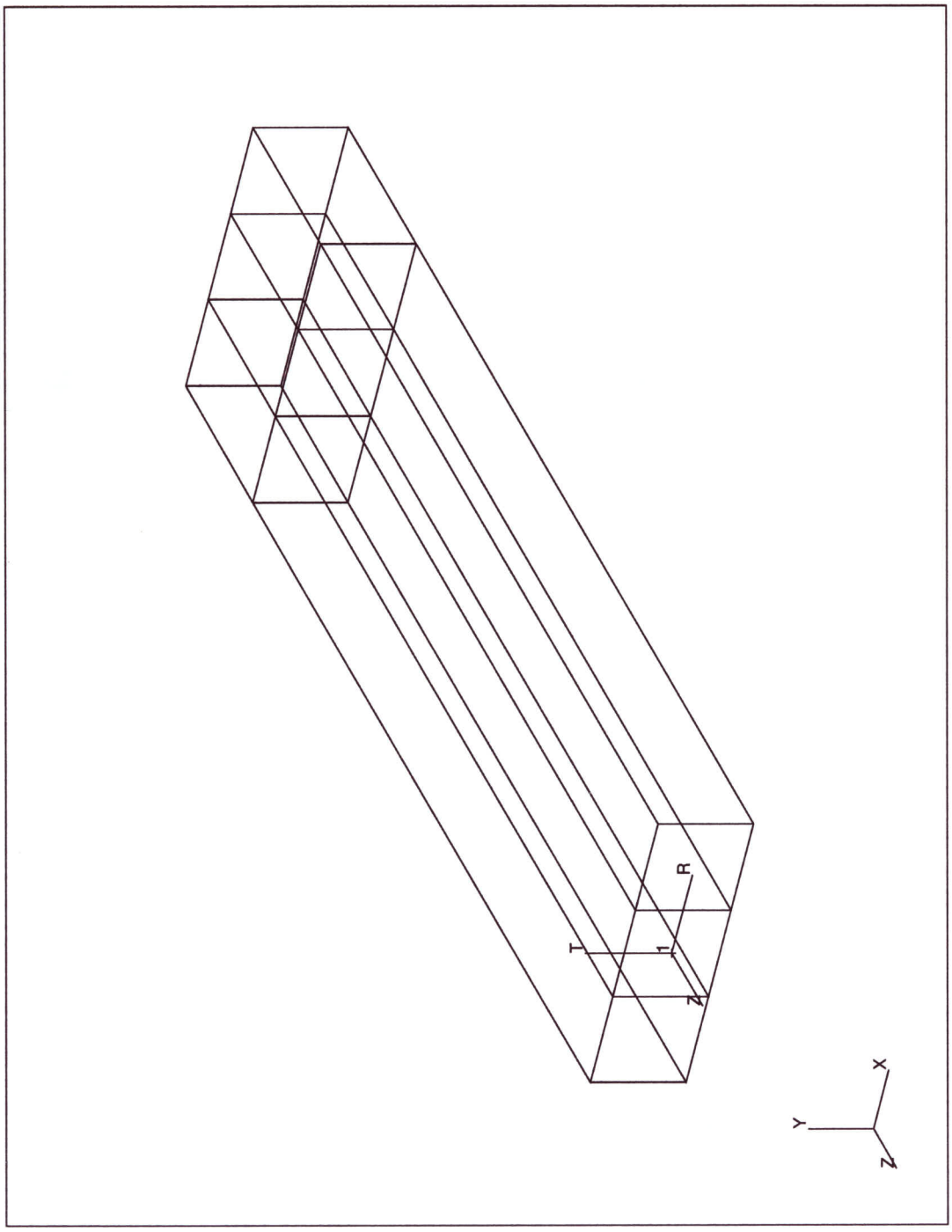

Figure5.3ThreeCellBoxGeometry

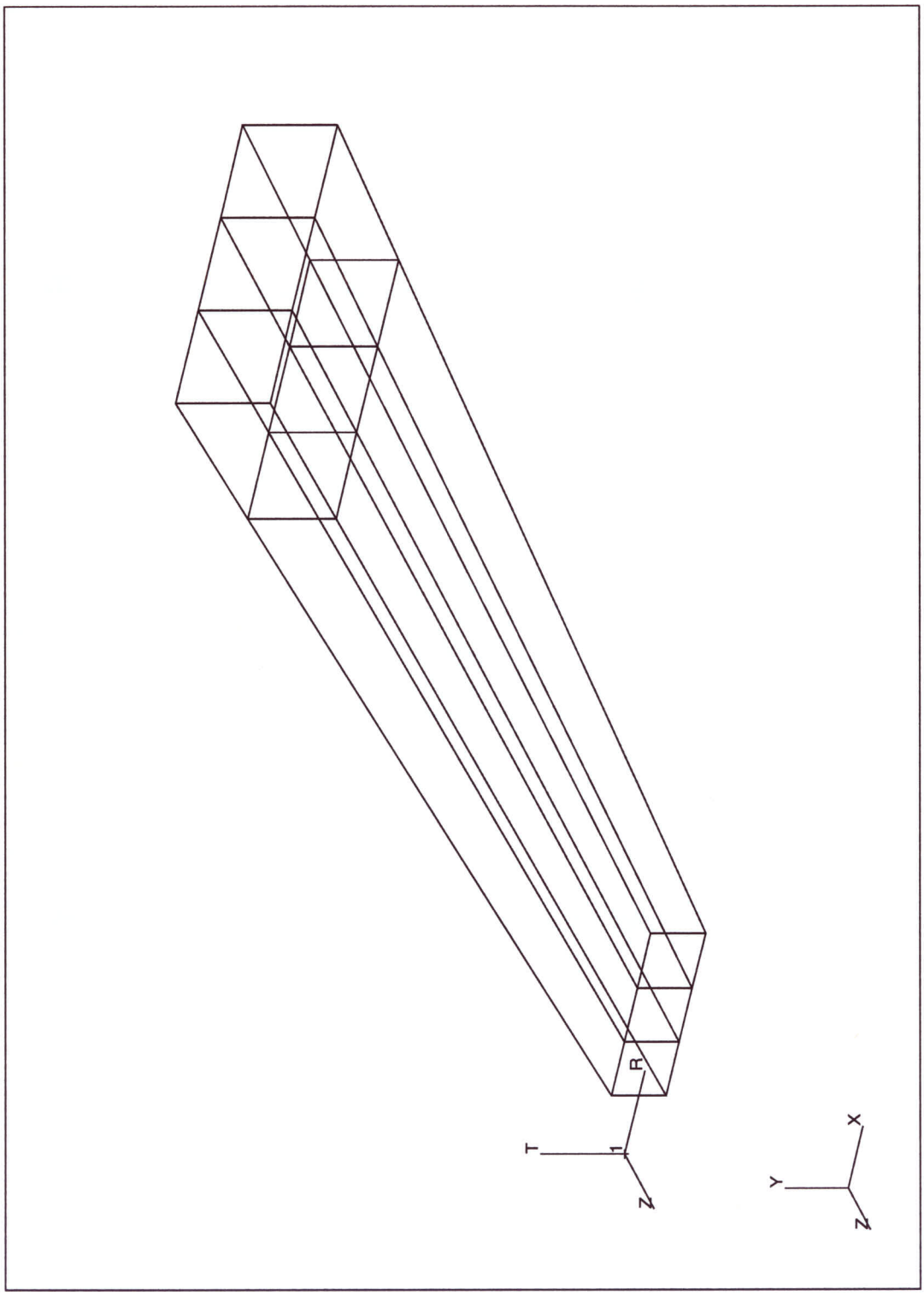

Figure5.4ThreeCellTaperBoxGeometry

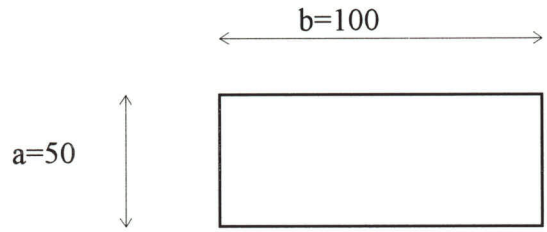

Figure 5.5a Cross-sectional dimension of Single-cell Box thickness "t" = 1

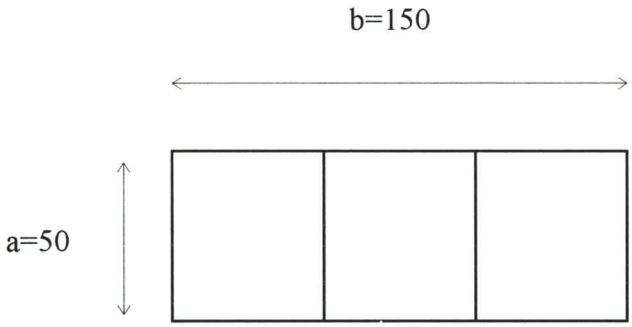

Figure 5.5b Cross-Sectional Dimension of Three-cell Box thickness "t" = 1

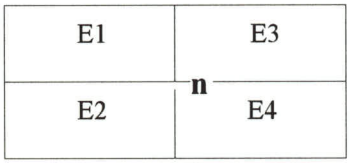

Figure 5.6a 4 CQUAD4 elements having common node "n"

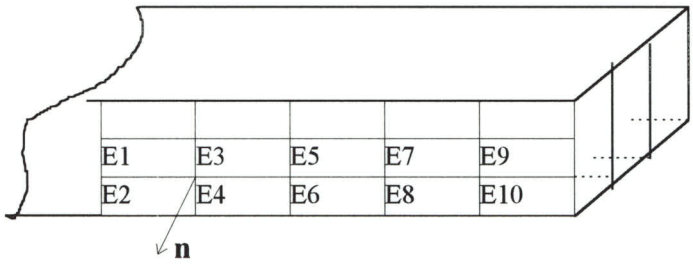

Figure 5.6b Typical FE Mesh with node "n" connected to 4 Elements

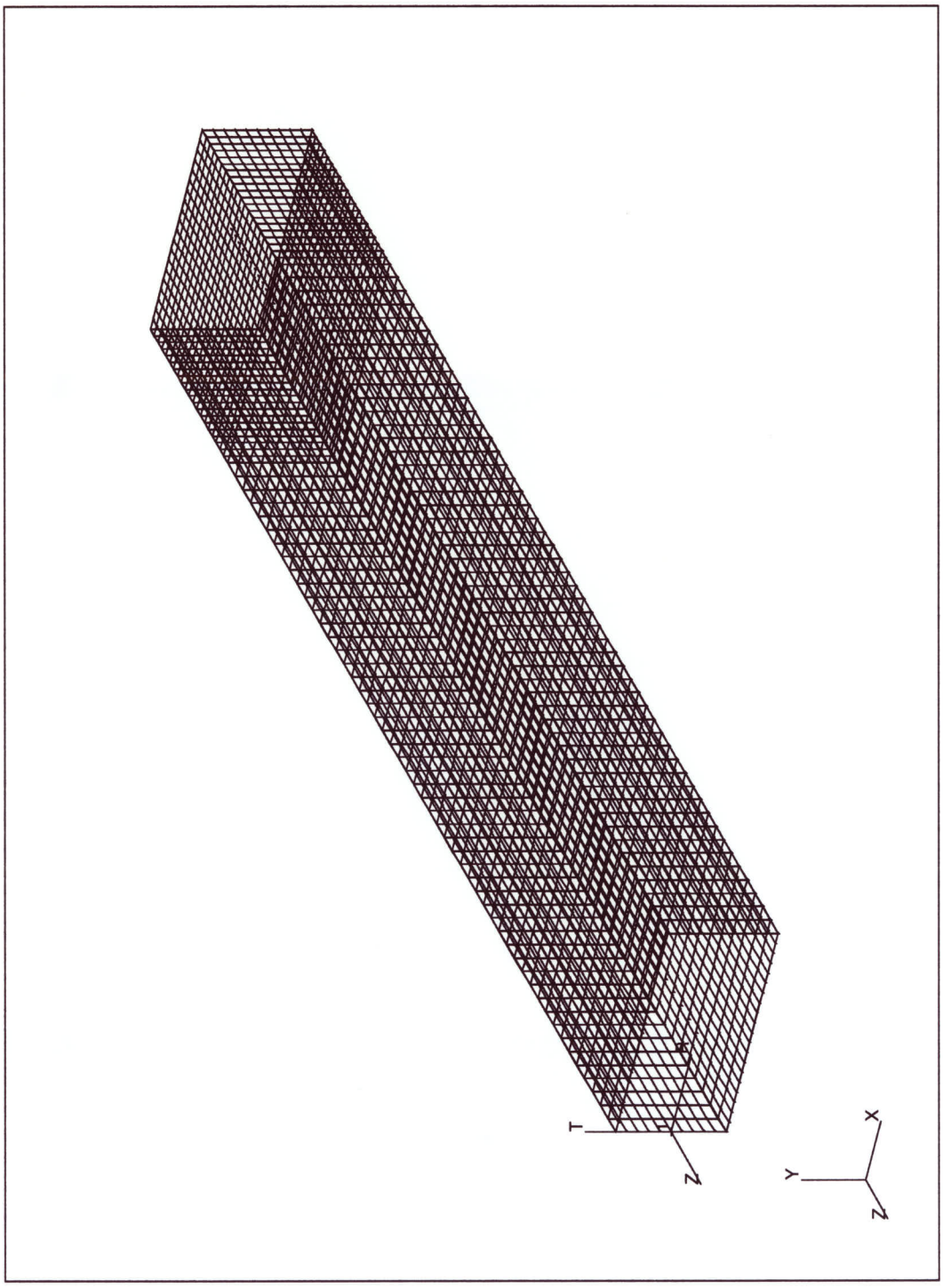

Figure 5.7 Single Cell Box FE Mesh

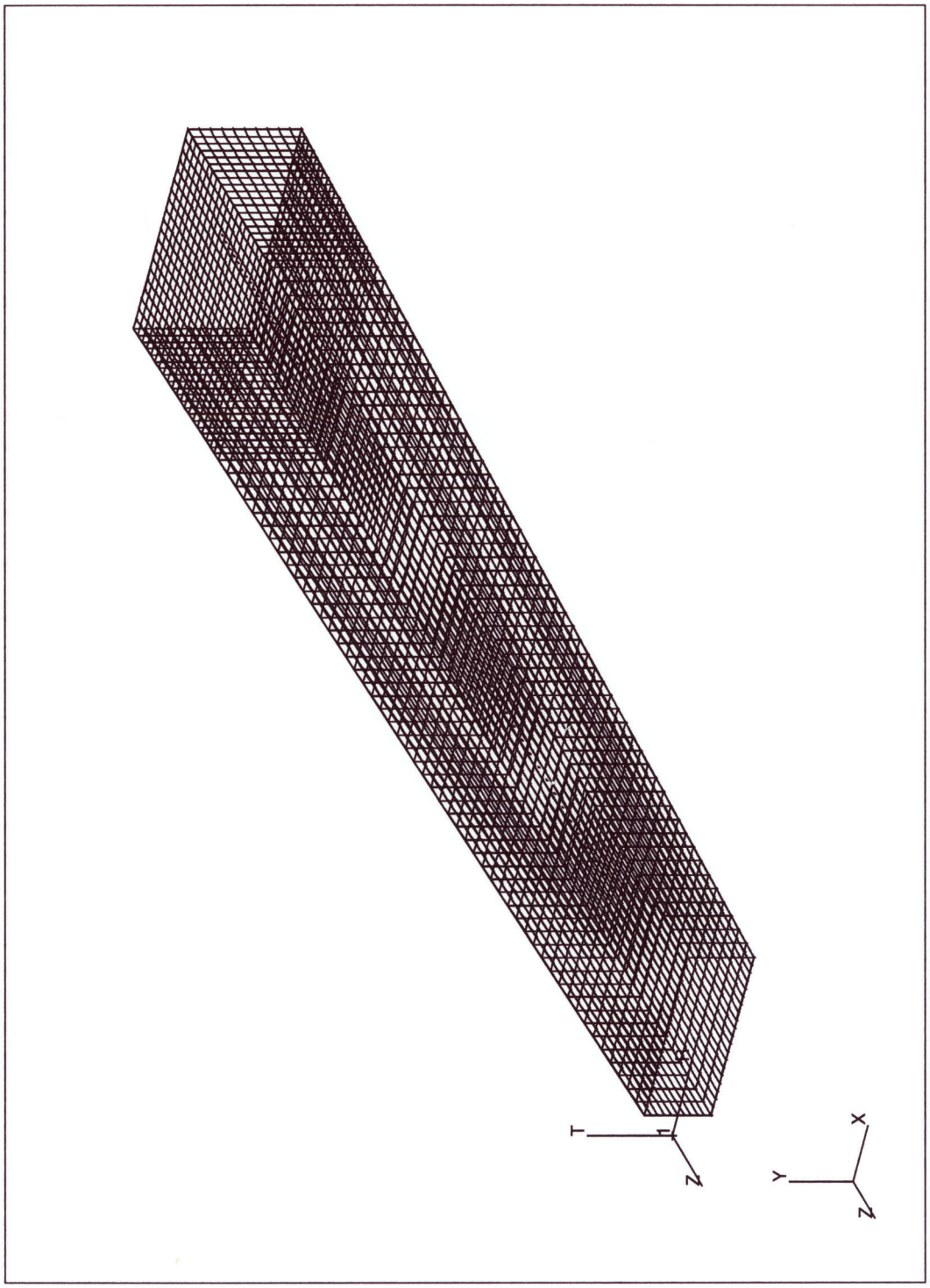

Figure 5.8 Single-Cell Taper Box Finite Element Mesh

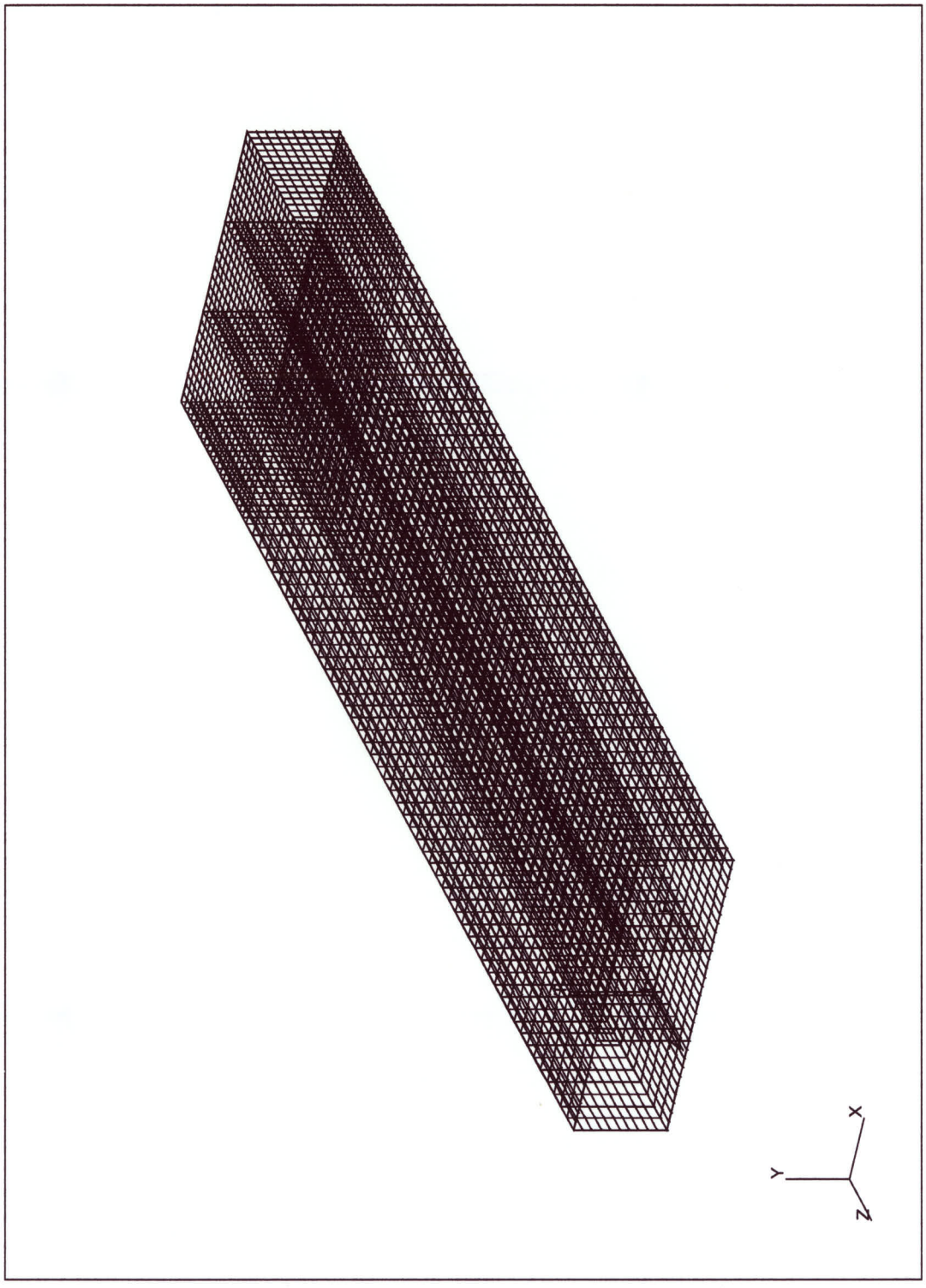

Figure5.9ThreeCellBoxFEMesh

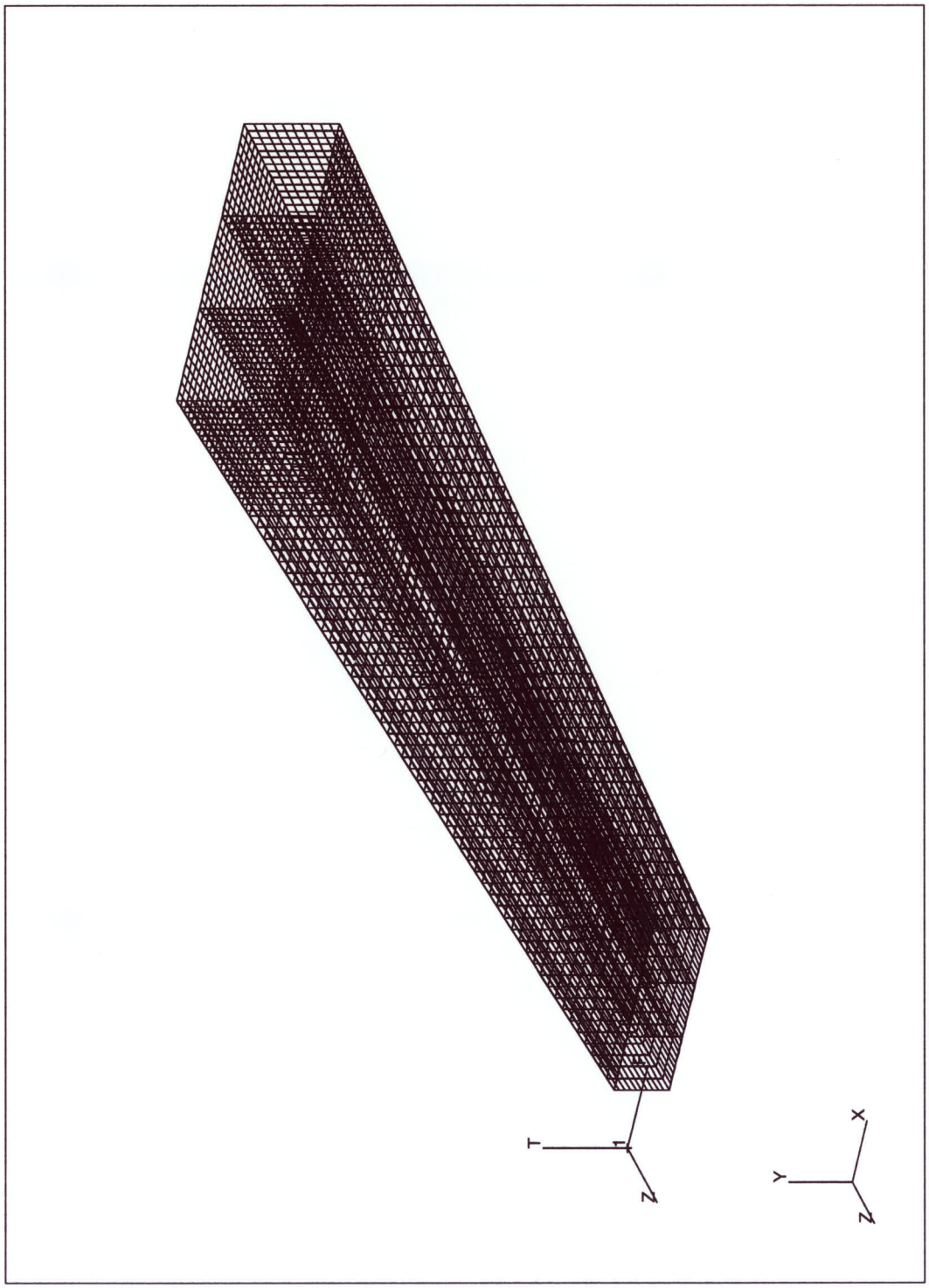

Figure 5.10 Three cell taper Box FE Mesh

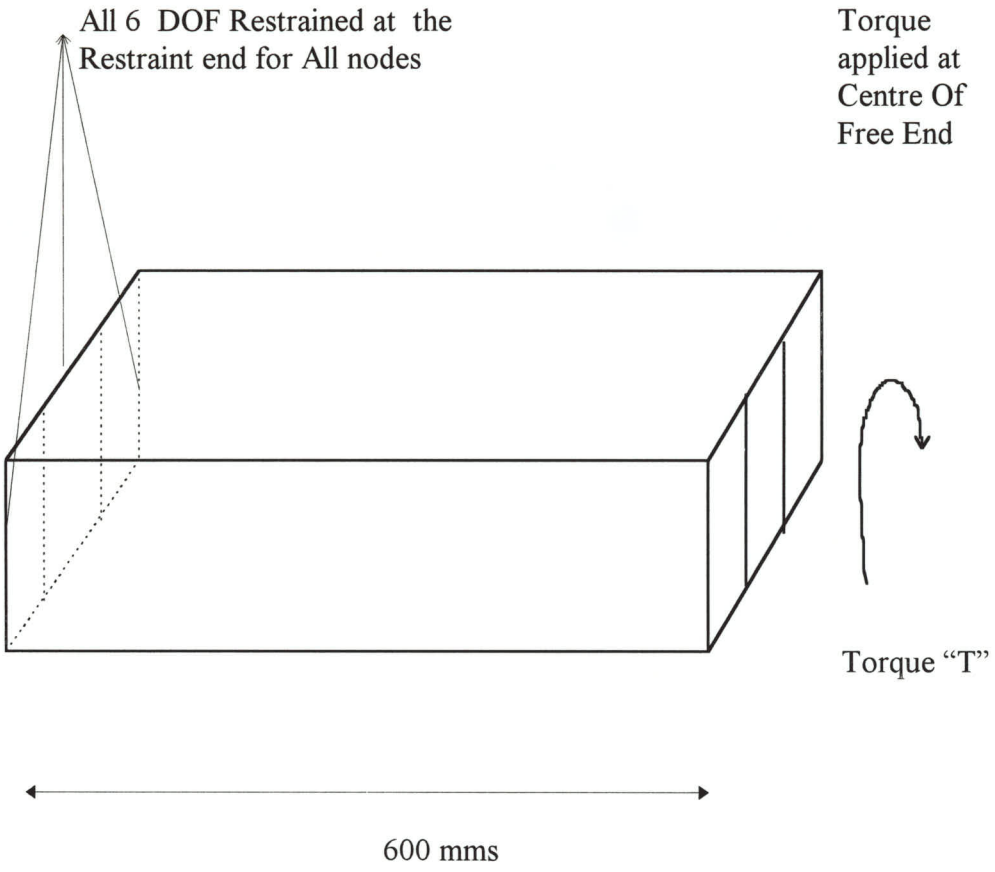

Figure 5.11 Boundary Conditions at Free and Restraint Ends

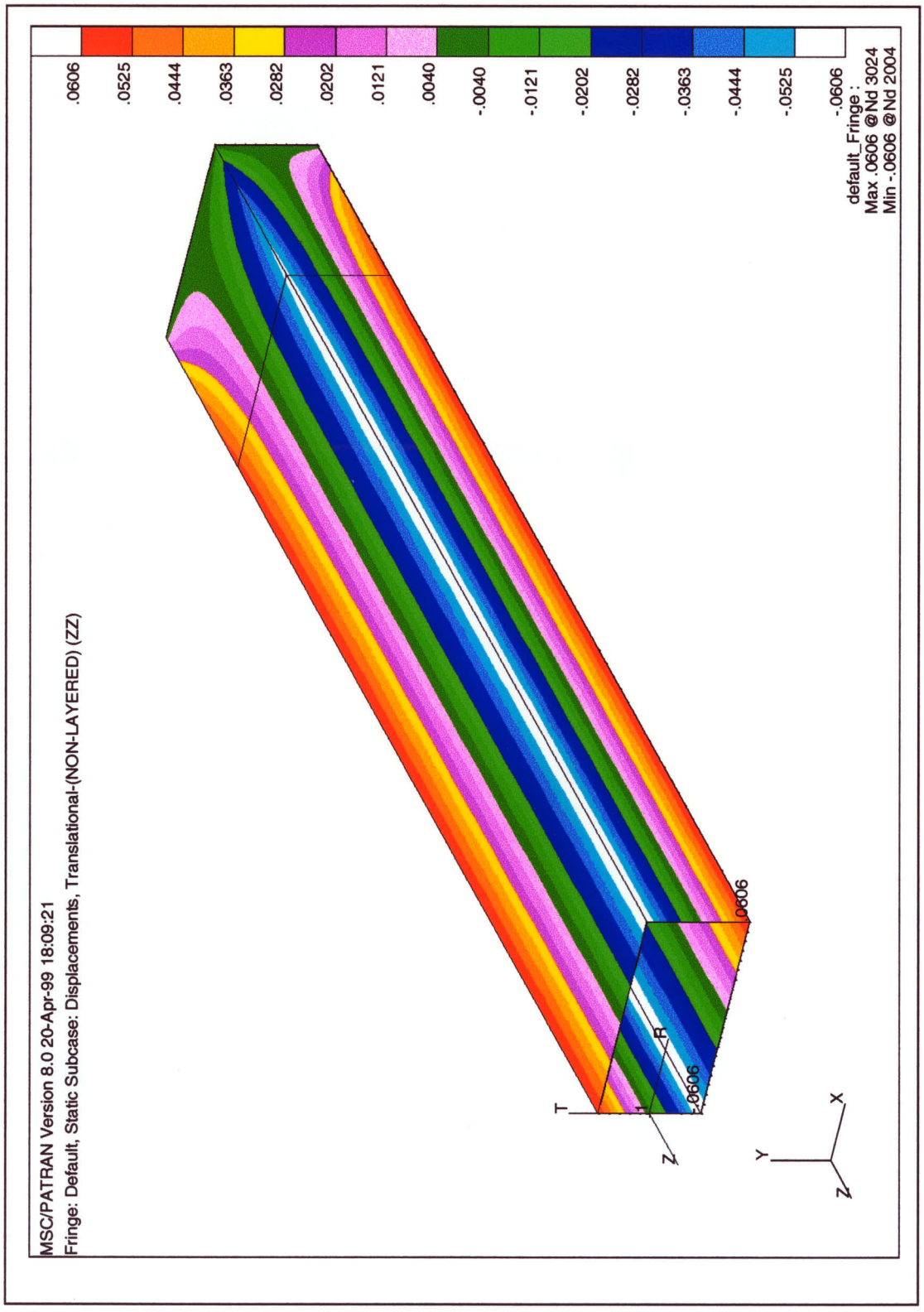

Figure 5.12 Single Cell Box Warping Along Length

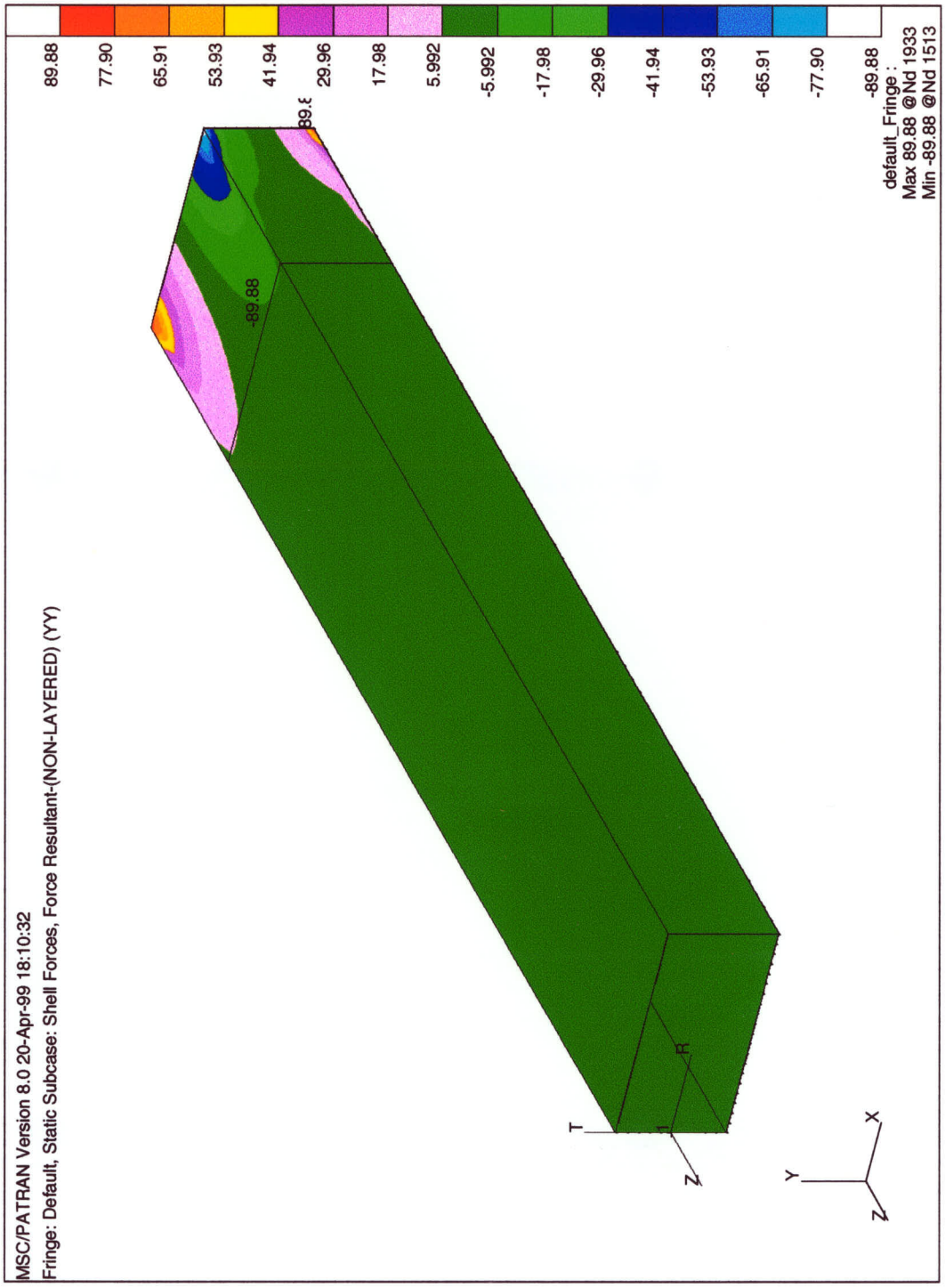

Figure 5.13 Single Cell Box FI Along Length

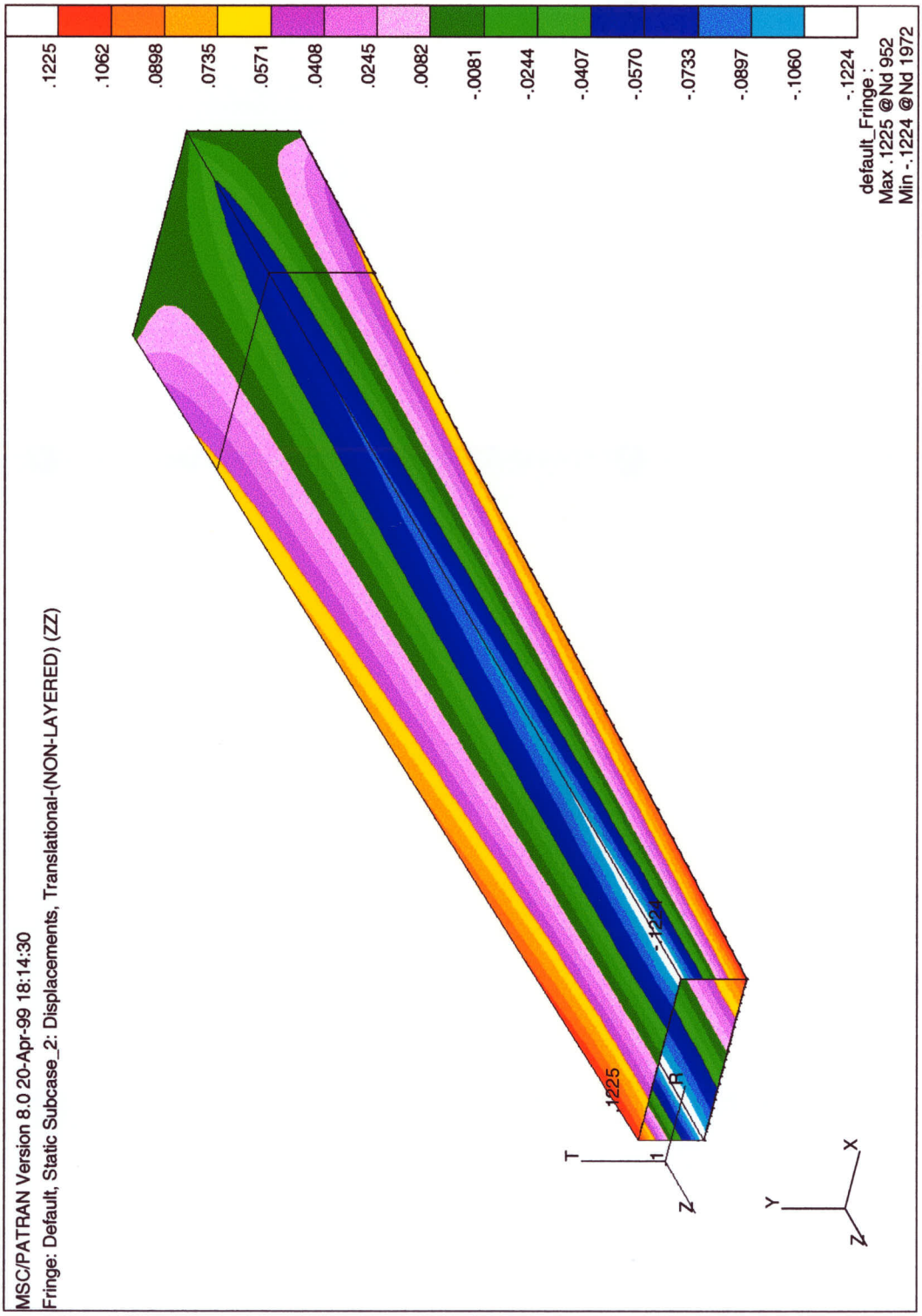

Figure 5.14 Single Cell Tapered Box Warping Along Length

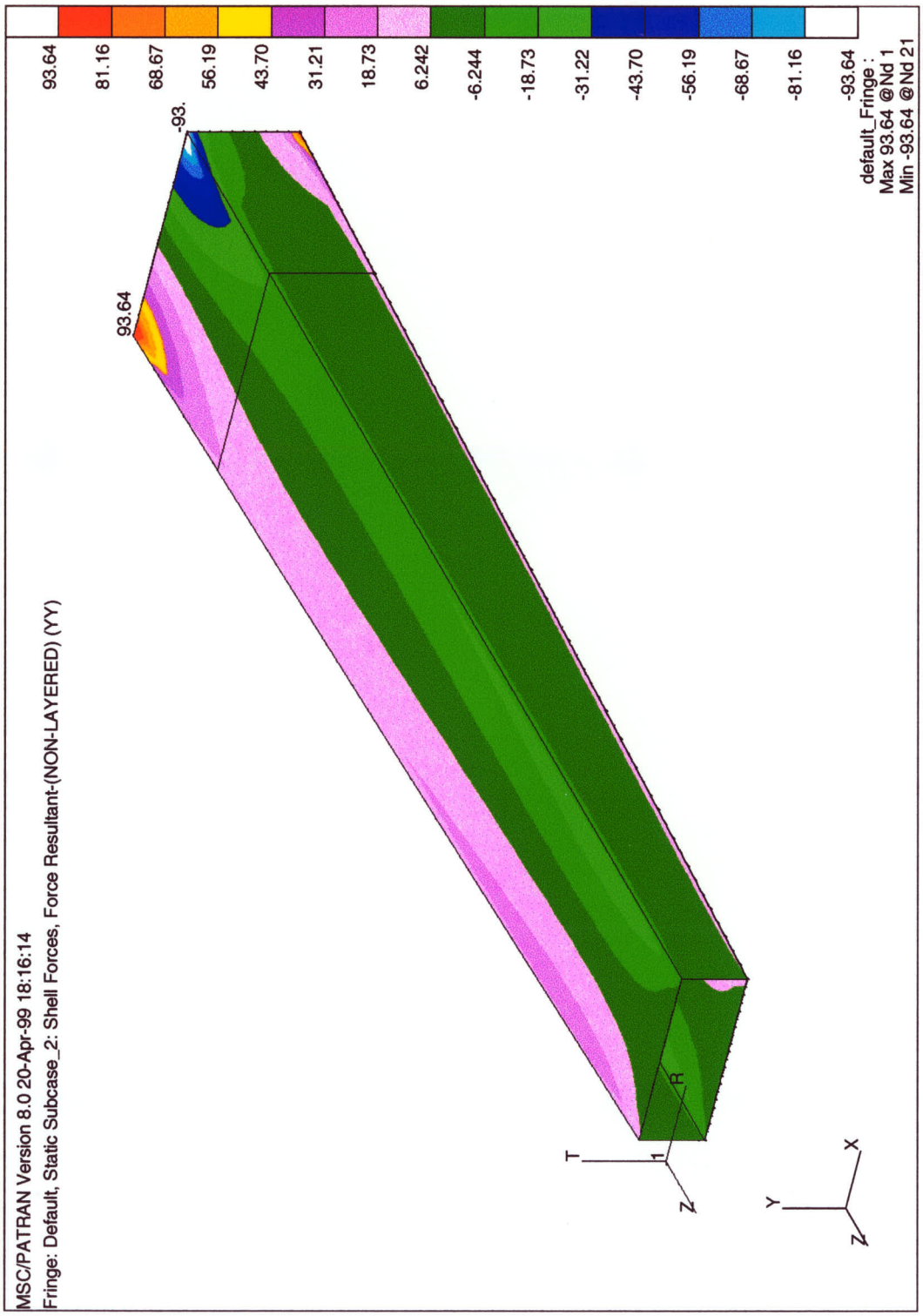

Figure 5.15 Single Cell Tapered Box FI Along Length

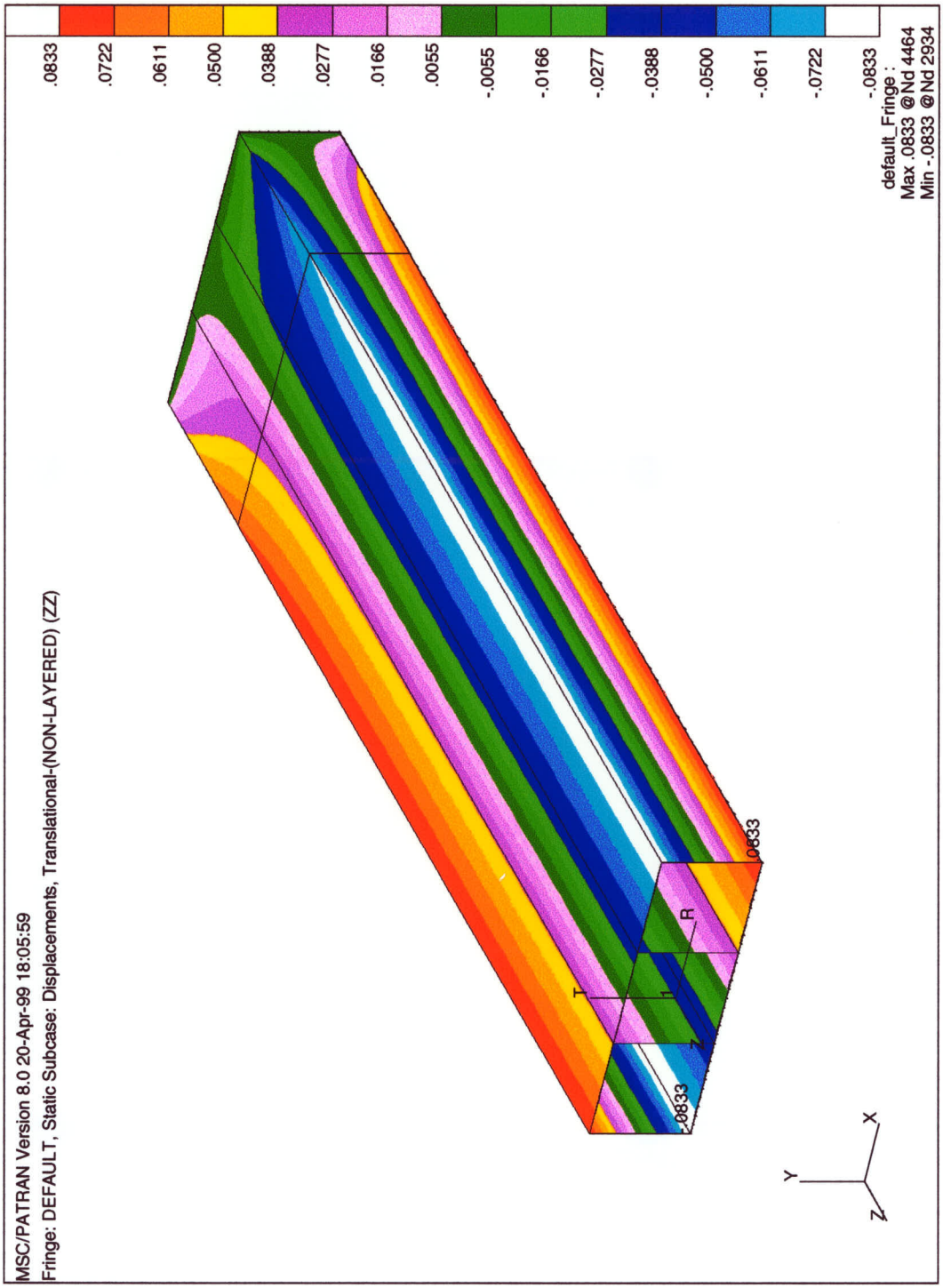

Figure 5.16 Three Cell Box Warping Along Length

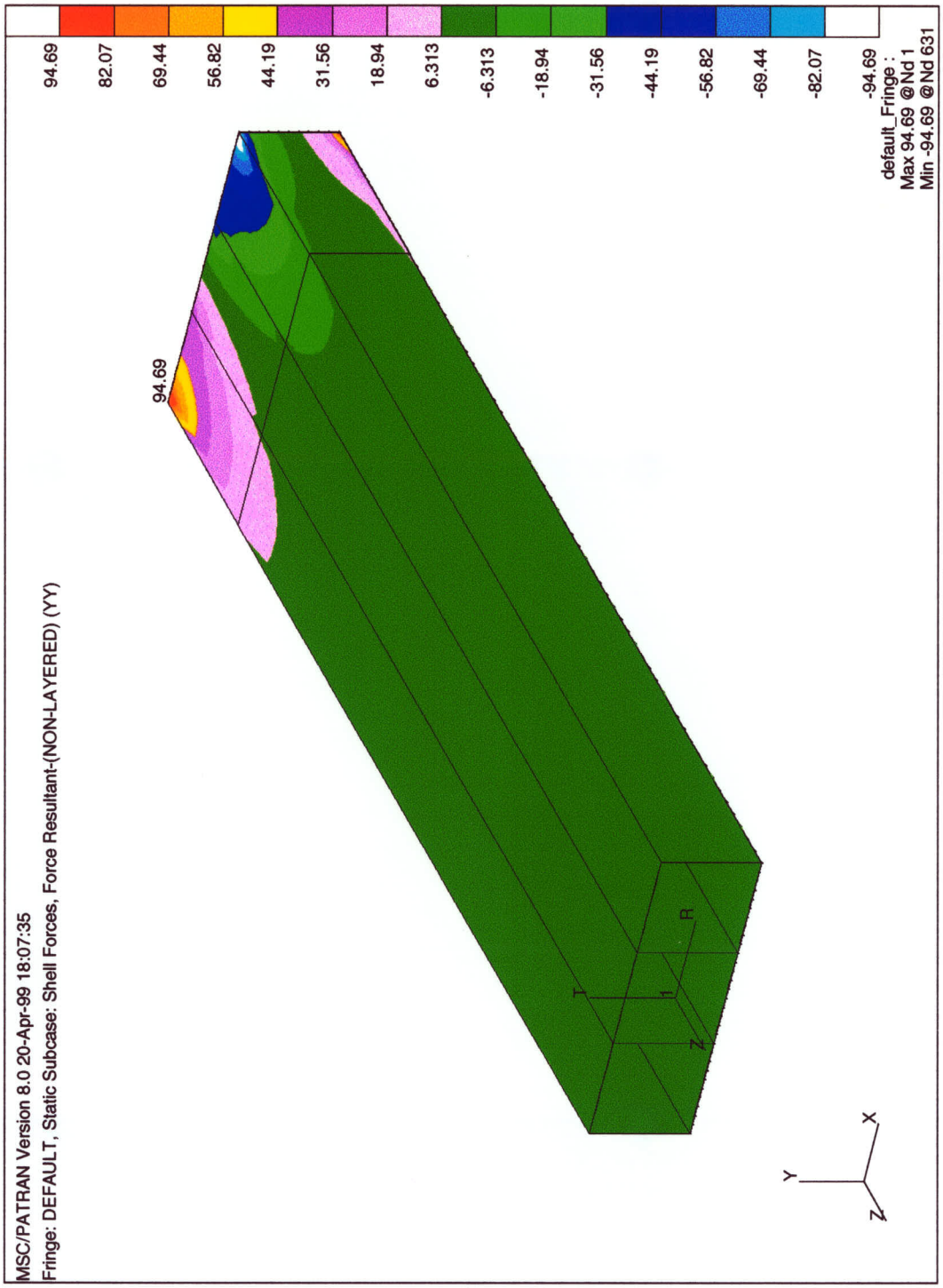

Figure 5.17 Three Cell Box FI Along Length

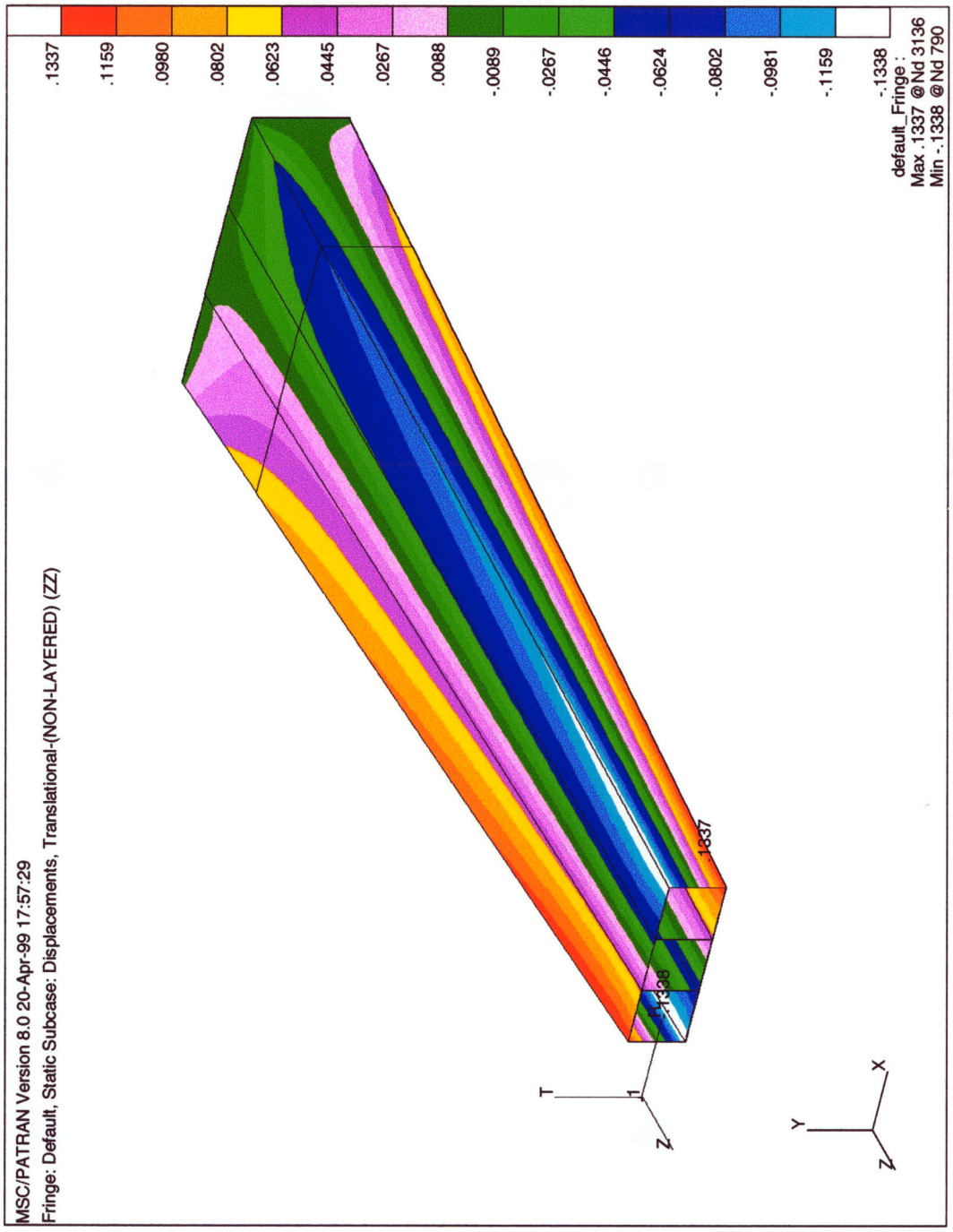

Figure 5.18 Three Cell Tapered Box Warping Along Length

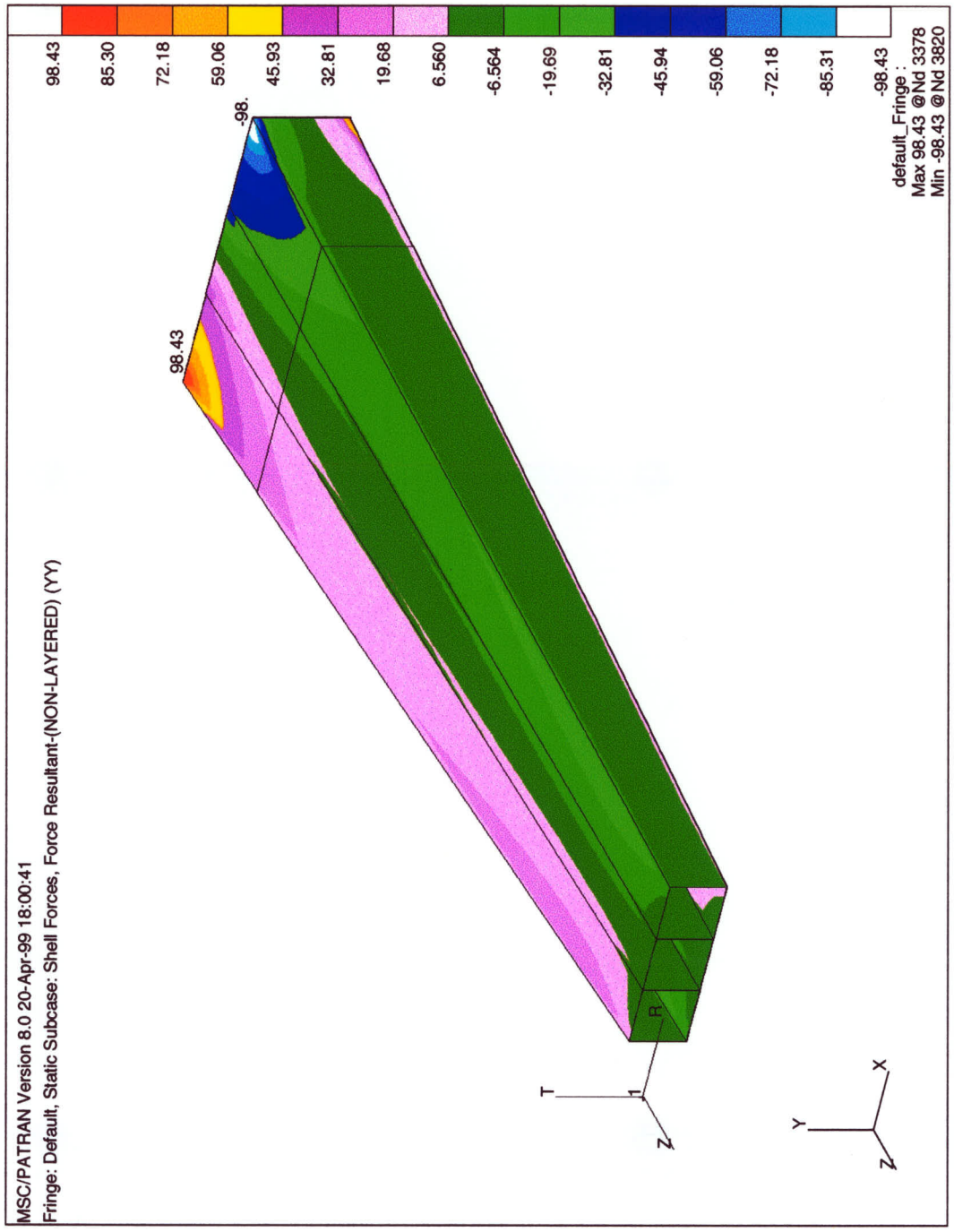

Figure 5.19 Three Cell Tapered Box FI Along Length

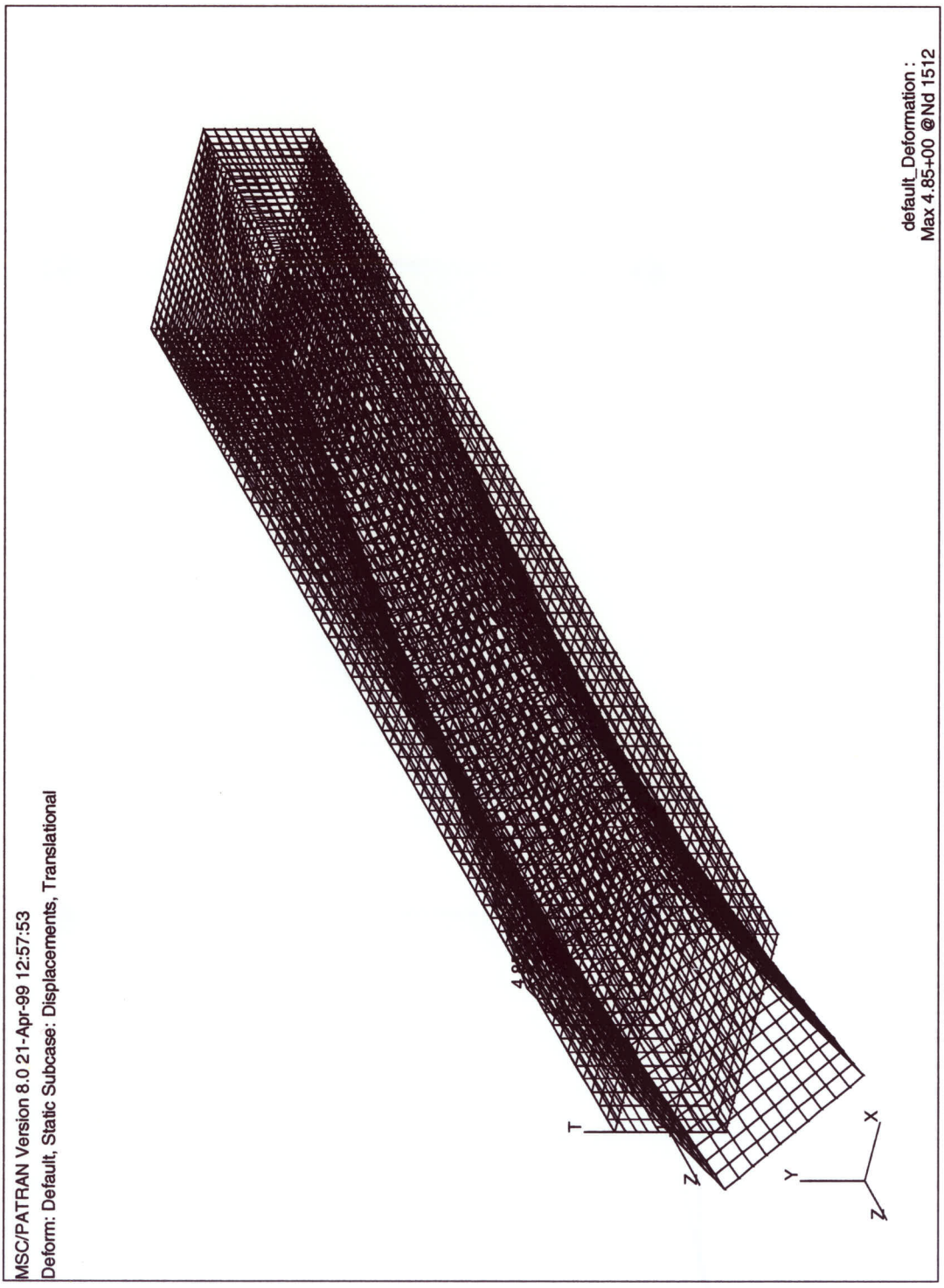

Figure 5.20 Deformed Shape of Single-Cell Box under Torque

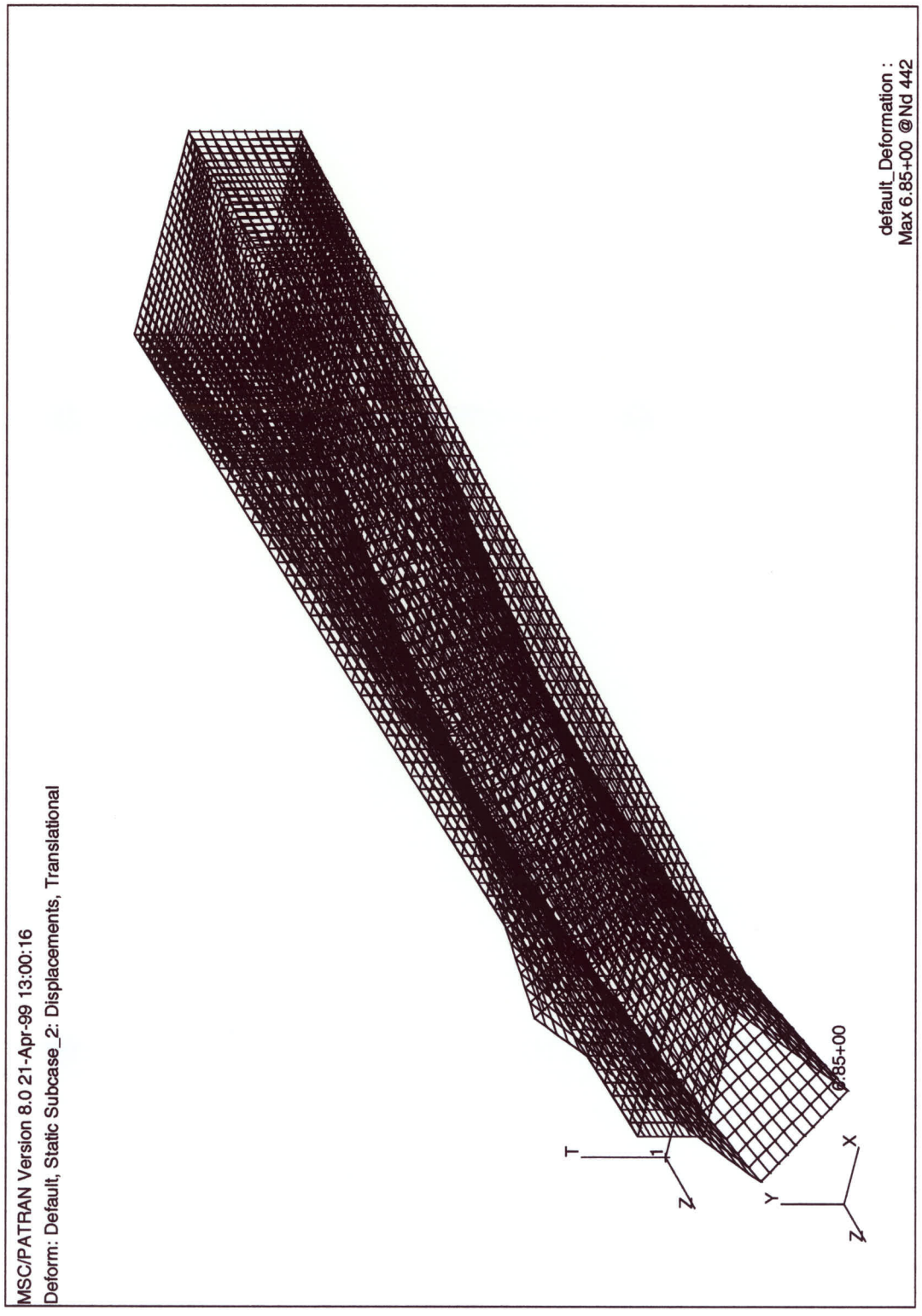

Figure 5.21 Deformed Shape of Single-Cell Taper Box under Torque

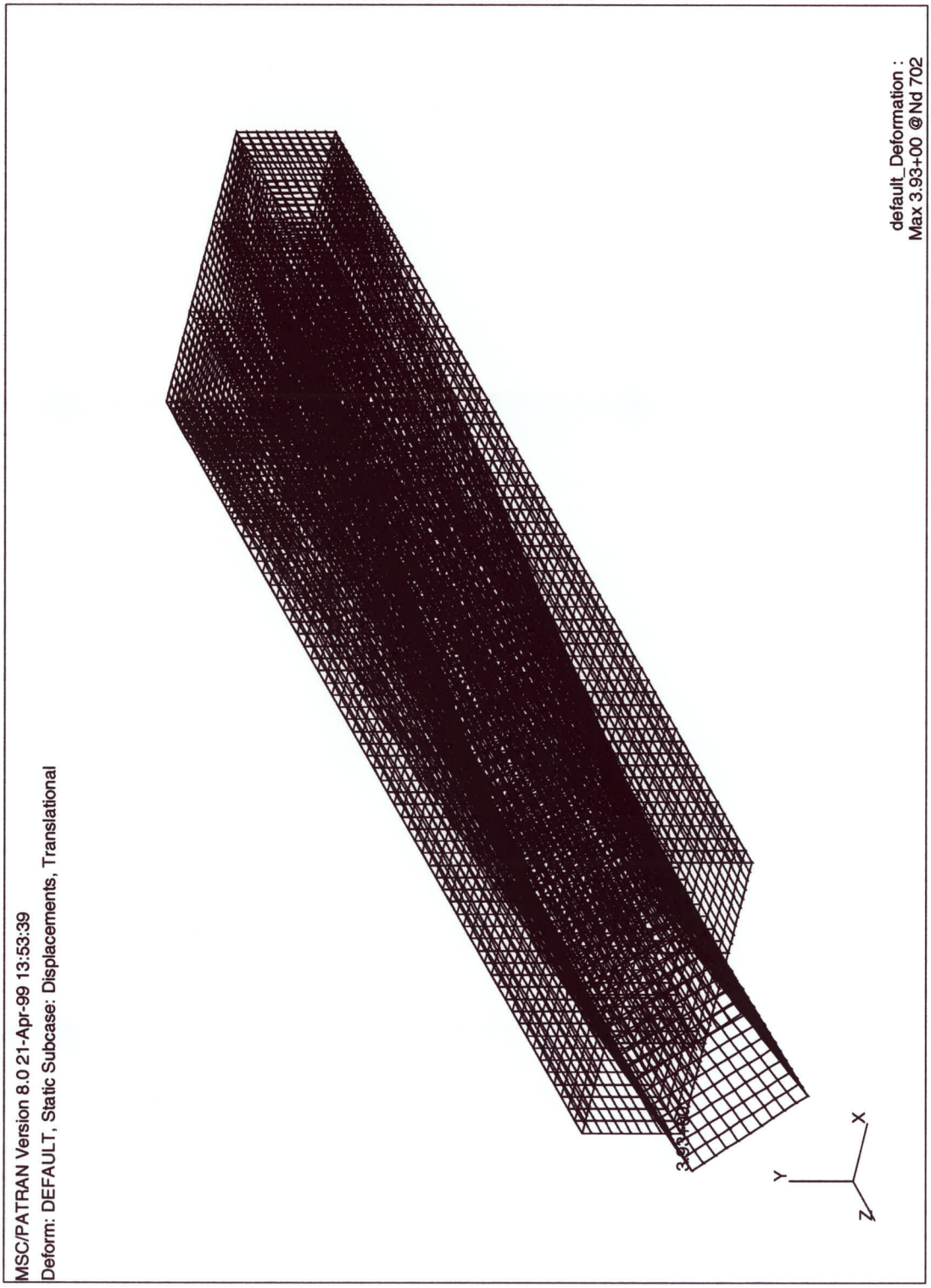

Figure 5.22 Deformed Shape of Three-Cell Box under Torque

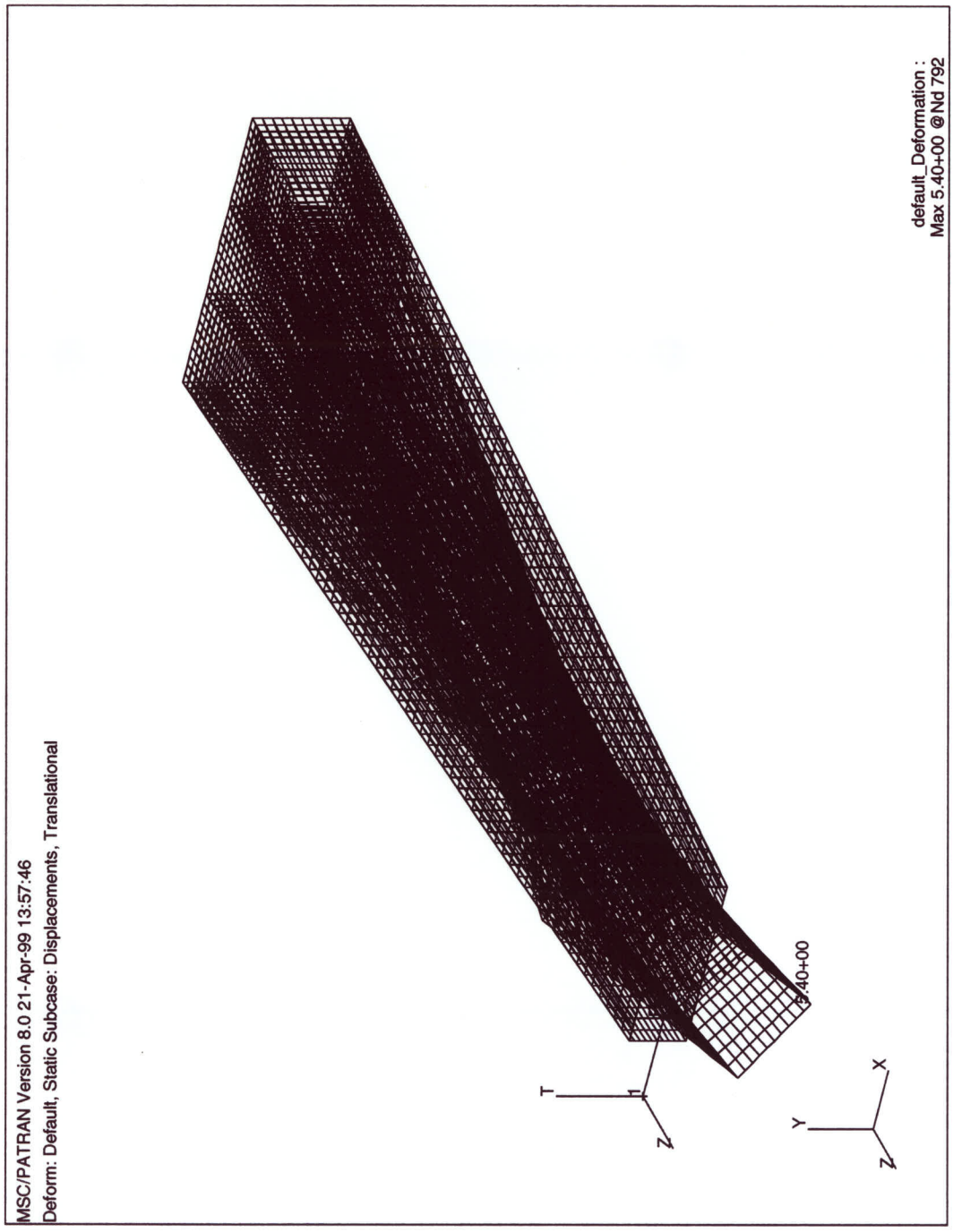

Figure 5.23 Deformed Shape of Three-Cell Taper Box under Torque

6 COMPARISON OF FE RESULTS WITH THE PROPOSED THEORY

The results from the FE analysis are shown to be in close agreement with the Composite theory being proposed in this thesis for the Single-Cell and Multi-Cell Prismatic and Tapered Boxes. The comparison of theoretical results with FE is being shown for quarter models in all given cases for ease of presentation . FE Analysis of Composite beams from a wide range of laminate configurations was performed during the course of research, however only some of the typical results are being presented here in this chapter.

6.1 SINGLE CELL PRISMATIC BOX

A Single cell prismatic box FE model for constrained torsion has been compared with the existing Single cell composite theory by Ata[7] for flanges and webs [0/45/-45/90]s lay-up at an applied Torque of 1000,000 Nmm. As expected the effect of axial restraint on a closed section box beam undergoing torsional loading is quite local close to the restraint end. This is verified in Fig 6.1 that shows the comparison between FE and theory for FI (Force intensity) along length at the corner point "B". There is an overall good agreement between theory and FE and the FI starting from a peak value of around 100 N/mm at the restraint end drops to zero at a distance of approximately 200 mm from the restraint end. Fig 6.2 shows the comparison between FE and theory for warping along length at point "B". The warping is seen to increase from zero at the restraint end to a peak value of around 0.06 mm at the Free end. Both the FI and the warping displacement distributions along the length of the beam undergoing restrained torsion are hyperbolic and the curves are very steep near the restraint end. FI vanishes between z=100 mm and z=200 mm in composite beams depending upon the laminate configuration of the beams, more over the warping displacement converges to its peak value at the location where the FI vanishes. Figs 6.3 and 6.4 show the comparison for warping around the box section at a distance of 200 mm from the restraint end and FI around box section at a distance of 20 mm from the restraint end respectively. Warping around box section is

seen to have an excellent comparison between FE and theory whereas in case of FI around the box section a maximum error of around 8% is observed between theory and FE at the peak value of FI at point "B". The difference between theory and FE at all other locations around the box section is less than 8%. This error is considered well within the acceptable limit and hence the FE and theory are found to be in overall agreement in the case of FI variation around the box section. Shear Flow along length at s=0 mm (centre of web on the box section) and s=75 mm (centre of flange on the box section) are shown in Figs 6.5 and 6.6 respectively. Shear flow along length at s=0 mm drops from a peak value of 145 N/mm at the restraint end to the Bredt Batho value of 100 N/mm at a distance of 200 mm from the restraint end. It is apparent from Figure 6.5 that the warping shear flow decays quickly as the curve moves away from the restraint end and the only shear flow after that is the contribution from Bredt Batho, which is 100 N/mm. The comparison between FE and theory is in agreement and a maximum difference between the two is observed at the restraint end where the error is only 3.4%. Shear flow along the length at s=75 mm increases from the starting value of 45 N/mm at the restraint end to the Bredt Batho value of 100 N/mm at a distance of 200 mm from the restraint end. Here again the FE and theory are in agreement along the length, however there is a difference between the two at the restraint end which decreases as the curve moves away from the restraint end and both FE and theory become synonymous at around 70 mm from restraint end and remain so till the free end. The maximum error between the two occurs at the restraint end that is 28%. The reason for this error is the difference in the way in which both FE and theory calculate their respective shear flows. FE following the strain energy method does not calculate the exact solution whereas the proposed torsion-bending theory is of approximately the same accuracy as engineering bending theory and hence the difference occurs between the two in the variation of Shear flow along the length. The error quickly dies off as curve moves away from the restraint end and then theory and FE become synonymous.

6.2 MULTI-CELL PRISMATIC BOX

Comparison of theoretical results with FE for three-cell Prismatic Box all [0/45/-45/90]s lay-up with flanges 150 mm and webs 50 mm is shown from Fig 6.7 to Fig 6.15. Force intensity along length at "B" and "C" decreases from its peak value at the restraint end to zero within 300 mm of the restraint end (Fig 6.7 & 6.8).Warping along the length at point "B" and "C" increases from zero at the restraint end to its peak value with in a distance of 300 mm from the restraint end when the effect of axial restraint has died out (Fig 6.9 & 6.10).The comparison of FE Vs theory shows good validation of the theory for the cases of FI and warping variation along the length of box. Shear Flow along length at s=0 mm (centre of web) decreases from the peak value at the restraint end to the Bredt Batho value within a distance of 200 mm from the restraint end as the warping shear flow dies out with in that distance.(Fig 6.11). Shear flow along length at s=100 mm (centre of flange) increases from the restraint end value to the Bredt Batho value within a distance of 200 mm from the restraint end (Fig 6.12).The comparison of FE Vs theory for shear flows at s=0 mm and s=100 mm along length show some difference at the restraint end which decreases as we move away from the restraint end and FE synchronises with the theoretical results at a distance of 200 mm from the restraint end and continues to do so all along the length till the free end. Warping around the box section at z=200 mm (Fig 6.13) shows an excellent comparison between FE and theory where the warping starting from zero at the zero warping point (centre of web s=0 mm) rises to its peak value at the corner point "B" of the box that is situated at s=25 mm from the centre of web and then drops down all the way along till it reaches a zero value again at the next zero warping point (centre of flange s=100 mm). The comparison between FE and theory for FI around the box section at z=20 mm from restraint end is shown in Fig 6.14 where it is seen that the force intensity starting from zero at the centre of web (s=0 mm) rises to its peak value at s=25 mm (corner point "B") and then drops down steadily till it reaches zero at the centre of flange s=100 mm. The FI in the inner web rises from zero at the centre of inner web to the value of point "C" that is the common point of flange and inner web at s=75 mm. The comparison between FE and theory shows good

coherence and a maximum difference of 4.6% occurs between them at point "B". Fig 6.15 shows the comparison between FE and theory for Shear flow around the box section at z=60 mm from restraint end. Here again the FE and theory supplement each other.

Comparison of theoretical results with FE for three cell Prismatic Box with flanges [[45/-45]2]s and webs [0/45/-45/90]s lay-up is shown in Fig 6.16 to Fig 6.24. The FI along length for points "B" and "C" drops to zero within 200 mm from the restraint end (Fig 6.16 & Fig 6.17).The warping at points "B" and "C" increases from zero to maximum value at around 200 mm from restraint end (Fig 6.18 & Fig 6.19). A good coherence is observed between FE and theory for all these plots. The shear flow along length at s=0 mm and s=100 mm decreases/increases respectively to the Bredt Batho value within 200 mm from the restraint end (Fig 6.20 & Fig 6.21). The comparison between FE and theory for the shear flow along length is good however there is a difference between the two near the restraint end that decreases steadily as the curve moves away from restraint end and vanishes at a distance of 200 mm from the restraint end for reasons already explained above. Warping around the box section (Fig 6.22) shows an excellent coherence between the theory and FE. Force intensity around the box section (Fig 6.23) shows a jump in FI at point "B" and point "C" where the lay-up changes from [0/45/-45/90]s in the webs to [[45/-45]2]s in the flanges hence a sudden decrease in the FI is seen occurring at these two locations. Shear flow around the box section at z=60 mm (Fig 6.24) shows a good comparison between theory and FE as the curve moves from s=0 mm to s=100 mm.

Comparison of theoretical results with FE for three cell Prismatic Box all [[45/-45]2]s lay-up is shown from Fig 6.25 to Fig 6.33. FI along length at points "B" and "C" decreases from a maximum value at the restraint end to zero at a distance of approximately 170 mm from the restraint end (Fig 6.25 & Fig 6.26). Warping along length at points "B" and "C" increases from zero warping at the restraint end to a maximum warping value at a distance of 170 mm from the restraint end (Fig 6.27 & Fig 6.28).Shear flow along length at s=0 mm and s=100 mm (Fig 6.29 & Fig 6.30)

decreases/increases respectively to the Bredt Batho value at a distance of 170 mm from the restraint end. FE and theory have some difference at the restraint end that decreases as the two curves move away from the restraint end and reach the Bredt Batho value. Warping around the box section at z=200 mm (Fig 6.31) starts from zero warping at s=0 mm and reaches a maximum warping value at s=25 mm and then drops down steadily reaching zero warping value at the next zero warping point at s=100 mm. The warping in the inner web rises from zero warping at the centre of inner web to warping value at s=75 mm (point "C") that is common point for the flange and the inner web. Force intensity around the box section at z=20 mm (Fig 6.32) starts from zero FI value at s=0 mm and reaches a maximum value at point "B" (s=25 mm) and then steadily drops down to zero value at centre of flange (s=100 mm). Shear flow around the box section at z=100 mm (Fig 6.33) shows the shear flow variation around the box section from s=0 mm to s=100 mm. The three shear flows at point "C" follow the principle of shear flow in at any point is equal to shear flow out at that point, hence at point "C" the shear flow going out towards s=100 mm from the point "C" is the combination of the two shear flows (shear flow coming in from point "B" and shear flow coming in from inner web). The FE and theory show coherence in all the plots for the three-cell box beam having all angle ply lay-up.

6.3 SINGLE-CELL TAPERED BOX

The FE analysis of Single cell tapered box all [0/45/-45/90]s lay-up was started initially with a tapered box having Alpha and Beta equal to 0.1 degree. The dimensions at the restraint end were 100 mm and 50 mm for flanges and webs respectively. These dimensions reduced continuously as the distance from the restraint end increased and reached their minimum value of 97.90 mm and 47.90 mm respectively at the free end (600 mm from the restraint end). Figures 6.34 to 6.37 show the variation of force intensity, warping and shear flows at s=0 mm and s=75 mm along the length of Single cell tapered box respectively. Force intensity drops from the peak value of 100N/mm at

the restraint end to zero at around 200 mm from the restraint end. Warping increases from zero at the restraint end to a peak value of 0.064 mm at around 200 mm from the restraint end. Shear flow at s=0 drops from 140 N/mm at the restraint end to the Bredt Batho value at around 200 mm from the restraint end when the warping shear flow has gradually dropped to zero. Shear flow at s=75 mm increases from 50 N/mm to the Bredt Batho value of at a distance of 200 mm from the restraint end. The comparison of FE Vs Theory for all these plots show a good coherence.

The next tapered model considered for comparison with FE was a Single cell tapered box all [0/45/-45/90]s lay-up with Alpha and Beta equal to 0.5 degree. The dimensions of flanges and webs reduce to 89.52 mm and 39.52 mm respectively at a distance of 600 mm from the restraint end. Figures 6.38 to 6.41 show the variation of force intensity, warping and shear flows at s=0 mm and s=75 mm along the length of Single cell tapered box respectively. Force intensity drops from the peak value of 100 N/mm at the restraint end to 5 N/mm at around 190 mm from the restraint end and then continues to follow a smooth line up to around 550 mm when it starts to drop down and reaches the zero value at 600 mm from the restraint end. Warping increases steeply from zero at the restraint end to a value of 0.06 mm at around 100 mm from the restraint end and then the slope of the curve becomes smoother as it continues to increase steadily and reaches the peak value of warping 0.085 mm at the free end. Shear flow at s=0 drops from 140 N/mm at the restraint end to 110 N/mm at a distance of 100 mm from the restraint end as the warping shear flow starts to reduce steadily and ultimately goes to zero . On the other hand the Bredt Batho value of 100 N/mm at the restraint end starts to increase when the effective area of the box is continuously reduced due to the taper angle as the curve moves away from the restraint end . This increase in the Bredt Batho value increases the total shear flow and a steady increase in shear flow is hence witnessed along the length of box till it reaches the peak value of around 150 N/mm at the free end. Shear flow at s=75 mm increases from 50 N/mm at the restraint end to its peak value of 140 N/mm at the free end due to constant increase in the Bredt Batho shear flow along the length of beam affected due to a continuous decrease in the area along the length.

The comparison of FE Vs Theory for all these plots show a good coherence for all these cases.

In case of Single cell tapered box having [0/45/-45/90]s lay-up in flanges and webs ,with Alpha & Beta equal to 1.0 degree. The dimensions of flanges and webs reduce to 79.06 mm and 29.05 mm respectively at a distance of 600 mm from the restraint end. Figures 6.42 to 6.45 show the variation of force intensity, warping and shear flows at s=0 mm and s=75 mm along the length of box and Figures 6.46 to 6.48 show variation of warping, force intensity and shear flow around the box section respectively. Force intensity drops from the peak value of 100 N/mm at the restraint end to 5 N/mm at around 190 mm from the restraint end and then starts to increase continuously reaching 15N/mm at around 570 mm from restraint end when it starts to drop down and reaches the zero value at the free end (600 mm from the restraint end). Warping increases from zero at the restraint end to a value of 0.06 mm at around 100 mm from the restraint end and then the slope of the curve becomes smoother as it continues to increase steadily and reaches the peak value of warping 0.13 mm at the free end. Shear flow at s=0 drops from 139 N/mm at the restraint end to 114 N/mm at a distance of 100 mm from the restraint end as the warping shear flow starts to reduce steadily. On the other hand the Bredt Batho value of 100 N/mm at the restraint end starts to increase when the effective area of the box is continuously reduced due to the taper angle as the curve moves away from the restraint end This increase in the Bredt Batho value increases the total shear flow and a steady increase in shear flow is hence witnessed along the length of box till it reaches the peak value of around 224 N/mm at the free end. Shear flow at s=75 mm increases from 52 N/mm at the restraint end to its peak value of 209 N/mm at the free end due to a general decrease in the warping shear flow at the centre of flange and more significantly due to a constant increase in the Bredt Batho shear flow caused by continuous decrease of cross sectional area of beam as the curve moves away from the restrained end . The comparison of FE Vs Theory for all these plots show a good coherence for all these cases. Warping around the box section at z=200 mm from restraint end is shown to increase from zero warping at s=0 mm (centre of web) to a peak value of warping 0.075 mm at point "B"(corner of box) and then again drops steadily along the flange reaching a

zero warping value at s=75 mm (centre of flange). Force intensity around the box section at z=20 mm from the restraint end (Figure 6.47) is shown to increase from a zero force intensity value at s=0 mm(centre of web) to a peak value at point "B" (s=25 mm corner of box), the FI starts to reduce steadily after this point and reaches a zero FI value at centre of flange (s=75 mm).The maximum error between FE and theory for this case occurs at the corner point "B" where it is 6%. All other points show conformity between FE and theory. Figure 6.48 shows the comparison between FE and theory for the shear flow around box section at z=20 mm from restrained end. Total Shear flow at s=0 mm (centre of web) is around 125 N/mm that is the addition of warping shear flow and Bredt Batho at this location. The total shear flow reduces steadily due to the gradual decrease in the warping shear flow as the curve moves around the box section from the centre of web to the corner point "B" (s=25 mm). After moving away from the corner point "B", the total shear flow starts to reduce as the direction of warping shear flow in the flange now becomes opposite to that of the Bredt Batho shear flow, hence the addition of these two shear flows in fact now results in subtraction of warping shear flow from the Bredt Batho giving a lower value for total shear flow all along the length of flange till the curve reaches the centre of flange (s=75 mm) and the total shear flow reaches its minimum value of 76 N/mm.

The results for the case of Single cell tapered box having [[45/-45]2]s lay-up in flanges & webs , with Alpha & Beta equal to 1.0 degree are shown in Figures 6.49 to 6.55 The variations of force intensity, warping and shear flows at s=0 mm and s=75 mm along the length of box are shown from Figure 6.49 to Figure 6.52 respectively. Figures 6.53 to 6.55 show variation of warping, force intensity and shear flow around the box section respectively. Force intensity drops from the peak value of 65 N/mm at the restraint end to 4 N/mm at around 150 mm from the restraint end and then starts to increase continuously reaching 10 N/mm at around 570 mm from restraint end when it starts to drop down and reaches the zero value at the free end (600 mm from the restraint end). Warping increases from zero at the restraint end to a value of 0.038 mm at around 100 mm from the restraint end and then the slope of the curve becomes smoother as it continues to increase steadily and reaches the peak value of warping 0.073 mm at the

free end. Shear flow at s=0 drops from 140 N/mm at the restraint end to 113 N/mm at a distance of 100 mm from the restraint end as the warping shear flow starts to reduce steadily . On the other hand the Bredt Batho value of 100 N/mm at the restraint end starts to increase when the effective area of the box is continuously reduced due to the taper angle as the curve moves away from the restraint end . This increase in the Bredt Batho value increases the total shear flow and a steady increase in shear flow is hence witnessed along the length of box till it reaches the peak value of around 224 N/mm at the free end. Shear flow at s=75 mm increases from 50 N/mm at the restraint end to its peak value of 209 N/mm at the free end due to constant increase in the Bredt Batho shear flow along the length of beam affected due to a continuous decrease in the area along the length. The comparison of FE Vs Theory for all these plots show a good coherence for all these cases. Warping around the box section at z=200 mm from restraint end (Figure 6.53) is shown to increase from zero warping at s=0 mm (centre of web) to a peak value of warping 0.043 mm at point "B"(corner of box) and then again drops steadily along the flange reaching a zero warping value at s=75 mm (centre of flange). Force intensity around the box section at z=20 mm from the restraint end (Figure 6.54) is shown to increase from a zero force intensity value at s=0 mm(centre of web) to a peak value at point "B" (s=25 mm corner of box), the FI starts to reduce steadily after this point and reaches a zero FI value at centre of flange (s=75 mm).The maximum error between FE and theory for this case occurs at the corner point "B" where it is 6.5%. All other points show conformity between FE and theory. Figure 6.55 shows the comparison between FE and theory for the shear flow around box section at z=20 mm from restrained end. Total Shear flow at s=0 mm (centre of web) is around 122 N/mm that is the addition of warping shear flow and Bredt Batho at this location. The total shear flow reduces steadily due to the gradual decrease in the warping shear flow as the curve moves around the box section from the centre of web to the corner point "B" (s=25 mm). After moving away from the corner point "B", the total shear flow starts to reduce as the direction of warping shear flow in the flange now becomes opposite to that of the Bredt Batho shear flow, hence the addition of these two shear flows now results in subtraction of warping shear flow from the Bredt Batho giving a lower value for total shear flow all along the length of flange till the curve reaches the centre of flange (s=75

mm) and the total shear flow reaches its minimum value of 79 N/mm. The theory compares well with FE for all the above mentioned cases.

The results for the case of Single cell tapered box having [[45/-45]2]s lay-up in flanges & [0/45/-45/90]s lay-up in webs with Alpha & Beta equal to 1.0 degree are shown in Figures 6.56 to 6.62 . The variations of force intensity, warping and shear flows at s=0 mm and s=75 mm along the length of box are shown from Figure 6.56 to Figure 6.59 respectively. Figures 6.60 to 6.62 show variation of warping, force intensity and shear flow around the box section respectively. Force intensity drops from the peak value of 19 N/mm at the restraint end to 4 N/mm at around 150 mm from the restraint end and then starts to increase continuously reaching 10N/mm at around 570 mm from restraint end when it starts to drop down and reaches the zero value at the free end (600 mm from the restraint end). Warping increases from zero at the restraint end to a value of 0.011 mm at around 100 mm from the restraint end and then the slope of the curve becomes smoother as it continues to increase steadily and reaches the peak value of warping 0.036 mm at the free end. Shear flow at s=0 drops from 107 N/mm at the restraint end to 105 N/mm at a distance of 30 mm from the restraint end as the warping shear flow starts to reduce slowly . On the other hand the Bredt Batho value of 100 N/mm at the restraint end starts to increase when the effective area of the box is continuously reduced due to the taper angle as the curve moves away from the restraint end . This increase in the Bredt Batho value increases the total shear flow and a steady increase in shear flow is hence witnessed along the length of box till it reaches the peak value of around 221 N/mm at the free end. Shear flow at s=75 mm increases from 93 N/mm at the restraint end to its peak value of 209 N/mm at the free end due to constant increase in the Bredt Batho shear flow along the length of beam affected due to a continuous decrease in the area along the length. The comparison of FE Vs Theory shows a good coherence for all these cases. Warping around the box section at z=200 mm from restraint end (Figure 6.60) is shown to increase from zero warping at s=0 mm (centre of web) to a peak value of warping 0.015 mm at point "B"(corner of box) and then again drops steadily along the flange reaching a zero warping value at s=75 mm (centre of flange). Force intensity around the box section at z=20 mm from the restraint end (Figure 6.61) is shown to increase from a zero force

intensity value at s=0 mm(centre of web) to a peak value at point "B" (s=25 mm corner of box), the FI starts to reduce steadily after this point and reaches a zero FI value at centre of flange (s=75 mm). The maximum level of FI for this case is quite low (10 N/mm) at the corner point "B" (s=25 mm). The maximum error between FE and theory for this case occurs at the corner point "B" where it is less than 10%. All other points show conformity between FE and theory. Figure 6.62 shows the comparison between FE and theory for the shear flow around box section at z=20 mm from restrained end. Total Shear flow at s=0 mm (centre of web) is around 106 N/mm that is the addition of warping shear flow and Bredt Batho at this location. The total shear flow reduces steadily due to the gradual decrease in the warping shear flow as the curve moves around the box section from the centre of web to the corner point "B" (s=25 mm). After moving away from the corner point "B", the total shear flow starts to reduce as the direction of warping shear flow in the flange now becomes opposite to that of the Bredt Batho shear flow, hence the addition of these two shear flows now results in subtraction of warping shear flow from the Bredt Batho giving a lower value for total shear flow all along the length of flange till the curve reaches the centre of flange (s=75 mm) and the total shear flow reaches its minimum value of 97 N/mm. The theory compares well with FE for all the above mentioned cases.

The results for the case of Single cell tapered box having [0/45/-45/90]s lay-up in flanges & [[45/-45]2]s lay-up in webs with Alpha & Beta equal to 1.0 degree are shown in Figures 6.63 to 6.69 The variations of force intensity, warping and shear flows at s=0 mm and s=75 mm along the length of box are shown from Figure 6.63 to Figure 6.66 respectively. Figures 6.67 to 6.69 show variation of warping, force intensity and shear flow around the box section respectively. Force intensity drops from the peak value of 136 N/mm at the restraint end to 9 N/mm at around 200 mm from the restraint end and then starts to increase continuously reaching 15 N/mm at around 550 mm from restraint end when it starts to drop down and reaches the zero value at the free end (600 mm from the restraint end). Warping increases from zero at the restraint end to a value of 0.09 mm at around 100 mm from the restraint end and then the slope of the curve becomes smoother as it continues to increase steadily and reaches the peak value of warping 0.16

mm at the free end. Shear flow at s=0 drops from 160 N/mm at the restraint end to 114 N/mm at a distance of 100 mm from the restraint end as the warping shear flow starts to reduce steadily . On the other hand the Bredt Batho value of 100 N/mm at the restraint end starts to increase when the effective area of the box is continuously reduced due to the taper angle as the curve moves away from the restraint end . This increase in the Bredt Batho value increases the total shear flow and a steady increase in shear flow is hence witnessed along the length of box till it reaches the peak value of around 223 N/mm at the free end. Shear flow at s=75 mm increases from 30 N/mm at the restraint end to its peak value of 205 N/mm at the free end due to constant increase in the Bredt Batho shear flow along the length of beam affected due to a continuous decrease in the area along the length. The comparison of FE Vs Theory for all these plots show a good coherence for all these cases. Warping around the box section at z=200 mm from restraint end (Figure 6.67) is shown to increase from zero warping at s=0 mm (centre of web) to a peak value of warping 0.10 mm at point "B"(corner of box) and then again drops steadily along the flange reaching a zero warping value at s=75 mm (centre of flange). Force intensity around the box section at z=20 mm from the restraint end (Figure 6.68) is shown to increase from a zero force intensity value at s=0 mm(centre of web) to a peak value at point "B" (corner of box). The FI at this corner point jumps up from 68 N/mm in the webs having [[45/-45]2]s lay-up to 92 N/mm in the flanges having [0/45/-45/90]s lay-up. FI starts to reduce steadily after this point and reaches a zero FI value at centre of flange (s=75 mm).The maximum error between FE and theory for this case occurs at the corner point "B" in web location where it is 10% . The error between FE and theory in flanges at same location "B" reduces to 4%. All other points show conformity between FE and theory. Figure 6.69 shows the comparison between FE and theory for the shear flow around box section at z=20 mm from restrained end, total Shear flow at s=0 mm (centre of web) is around 137 N/mm that is the addition of warping shear flow and Bredt Batho at this location. The total shear flow reduces steadily due to the gradual decrease in the warping shear flow as the curve moves around the box section from the centre of web to the corner point "B" (s=25 mm). After moving away from the corner point "B", the total shear flow starts to reduce as the direction of warping shear flow in the flange now becomes opposite to that of the Bredt Batho shear

flow, hence the addition of these two shear flows in fact now results in subtraction of warping shear flow from the Bredt Batho giving a lower value for total shear flow all along the length of flange till the curve reaches the centre of flange (s=75 mm) and the total shear flow reaches its minimum value of 58 N/mm. The theory compares well with FE for all the above mentioned cases.

6.4 MULTI-CELL TAPERED BOX

In case of Multi cell tapered box having [0/45/-45/90]s lay-up in flanges and webs, with Alpha & Beta equal to 1.0 degree, the dimensions of flanges and webs reduce from 150 mm & 50 mm to 87.15 mm & 29.05 mm respectively at a distance of 600 mm from the restraint end. Figures 6.70 to 6.75 show the variation of force intensity at point "B" and "C" along length, warping at point "B" and "C" along length and shear flows at s=0 mm and s=75 mm along the length of box. Figures 6.76 to 6.78 show variation of warping, force intensity and shear flow around the box section respectively. Force intensity along length at point "B" drops from the peak value of 100 N/mm at the restraint end to 5 N/mm at around 250 mm from the restraint end and then starts to increase slowly reaching 9 N/mm at around 570 mm from restraint end when it starts to drop down and reaches the zero value at the free end (600 mm from the restraint end). Force intensity along length at point "C" drops from the peak value of 45 N/mm at the restraint end to 2 N/mm at around 250 mm from the restraint end and then starts to increase slowly reaching 4 N/mm at around 570 mm from restraint end when it starts to drop down and reaches the zero value at the free end . Warping along length at point "B" increases from zero at the restraint end to a value of 0.08 mm at around 100 mm from the restraint end and then the slope of the curve becomes smoother as it continues to increase steadily and reaches the peak value of 0.14 mm at the free end. Warping along length at point "C" increases from zero at the restraint end to a value of 0.035 mm at around 100 mm from

the restraint end and then the slope of the curve becomes smoother as it continues to increase steadily and reaches the peak value of 0.06 mm at the free end . Shear flow at s=0 drops from 91 N/mm at the restraint end to 72 N/mm at a distance of 70 mm from the restraint end as the warping shear flow starts to reduce steadily. On the other hand the Bredt Batho starts to increase when the effective area of the box is continuously reduced due to the taper angle as the curve moves away from the restraint end . This increase in the Bredt Batho value increases the total shear flow and a steady increase in shear flow is hence witnessed along the length of box till it reaches the peak value of around 187 N/mm at the free end. Shear flow at s=100 mm increases from 40 N/mm at the restraint end to its peak value of 208 N/mm at the free end due to steady decrease in the warping shear flow and more so due to the constant increase in the Bredt Batho shear flow affected due to a continuous decrease in the area along the length of the beam. The comparison of FE Vs theory for all these plots show a good coherence for all cases. Warping around the box section at z=200 mm from restraint end (Figure 6.76)is shown to increase from zero warping at s=0 mm (centre of web) to a peak value of warping 0.095 mm at point "B"(corner of box) and then again drops steadily along the flange reaching zero warping value at s=100 mm (centre of flange).Warping in the internal web is shown to start from a zero warping value at the centre of web to the value of 0.0434 mm warping at point "C" (common point of internal web and flange) . Force intensity around the box section at z=20 mm from the restraint end (Figure 6.77) is shown to increase from a zero force intensity value at s=0 mm(centre of web) to a peak value of 74 N/mm at point "B" (corner of box), the FI starts to reduce steadily after this point and reaches a zero FI value at centre of flange (s=100 mm). FI in the internal web is shown to increase from a zero FI value at the centre of web to the FI value of 31 N/mm at point "C"(common point of internal web and flange) . The maximum error between FE and theory for this case occurs at the corner point "B" where it is 8%. All other points show conformity between FE and theory. Figure 6.78 shows the comparison between FE and theory for the shear flow around box section at z=60 mm from restrained end. Total Shear flow at s=0 mm (centre of web) is around 73 N/mm that is the addition of warping shear flow and Bredt Batho at this location. The total shear flow reduces steadily due to the gradual decrease in the warping shear flow as the curve

of web) is around 73 N/mm that is the addition of warping shear flow and Bredt Batho at this location. The total shear flow reduces steadily due to the gradual decrease in the warping shear flow as the curve moves around the box section from the centre of web to the corner point "B" (s=25 mm). After moving away from the corner point "B", the total shear flow starts to reduce this reduction occurs due to the gradual increase in the value of warping shear flow as the direction of warping shear flow in the flange now becomes opposite to that of the Bredt Batho shear flow, hence the addition of these two shear flows in fact now results in subtraction of warping shear flow from the Bredt Batho giving a lower value for total shear flow all along the length of flange till the curve reaches the junction point "C" which is the common point of the internal web and the flange. It is at this point "C" that the shear flow coming from the inner web adds up to the shear flow coming from the point "B" direction and hence the out flow of shear flow from this point towards the centre of the flange becomes the addition of these two shear flows. Hence a jump in shear flow value from 50 N/mm to 77 N/mm is seen at this location (point "C" s=75 mm). The total shear flow beyond point "C" keeps reducing steadily due to the gradual increase in the warping shear flow as the curve then moves towards the centre of flange (s=100 mm) where the total shear flow reaches the value of 69 N/mm. The FE shows goods coherence with theory for all these cases.

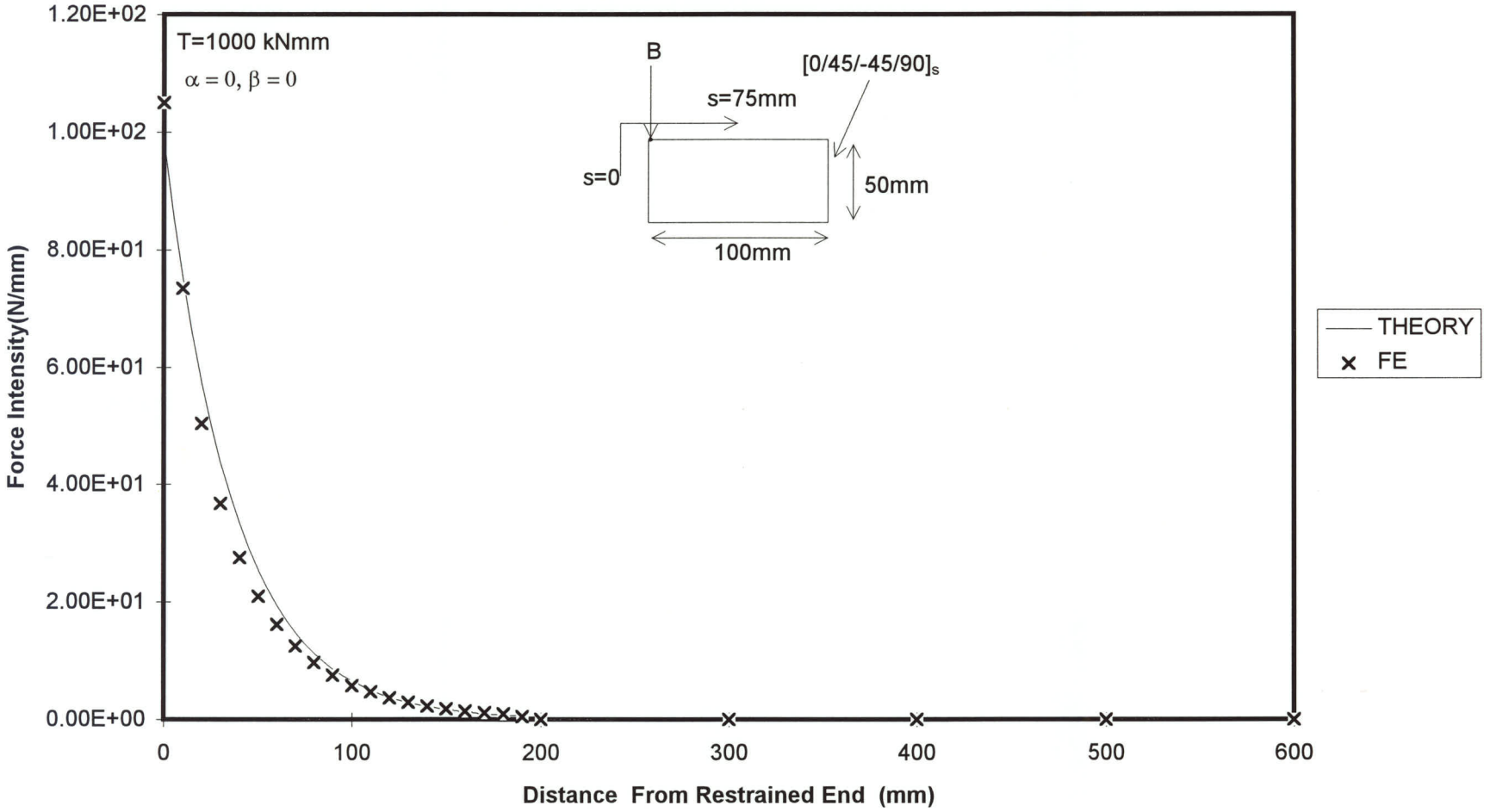

Figure 6.1 FORCE INTENSITY ALONG LENGTH OF BOX AT POINT "B"

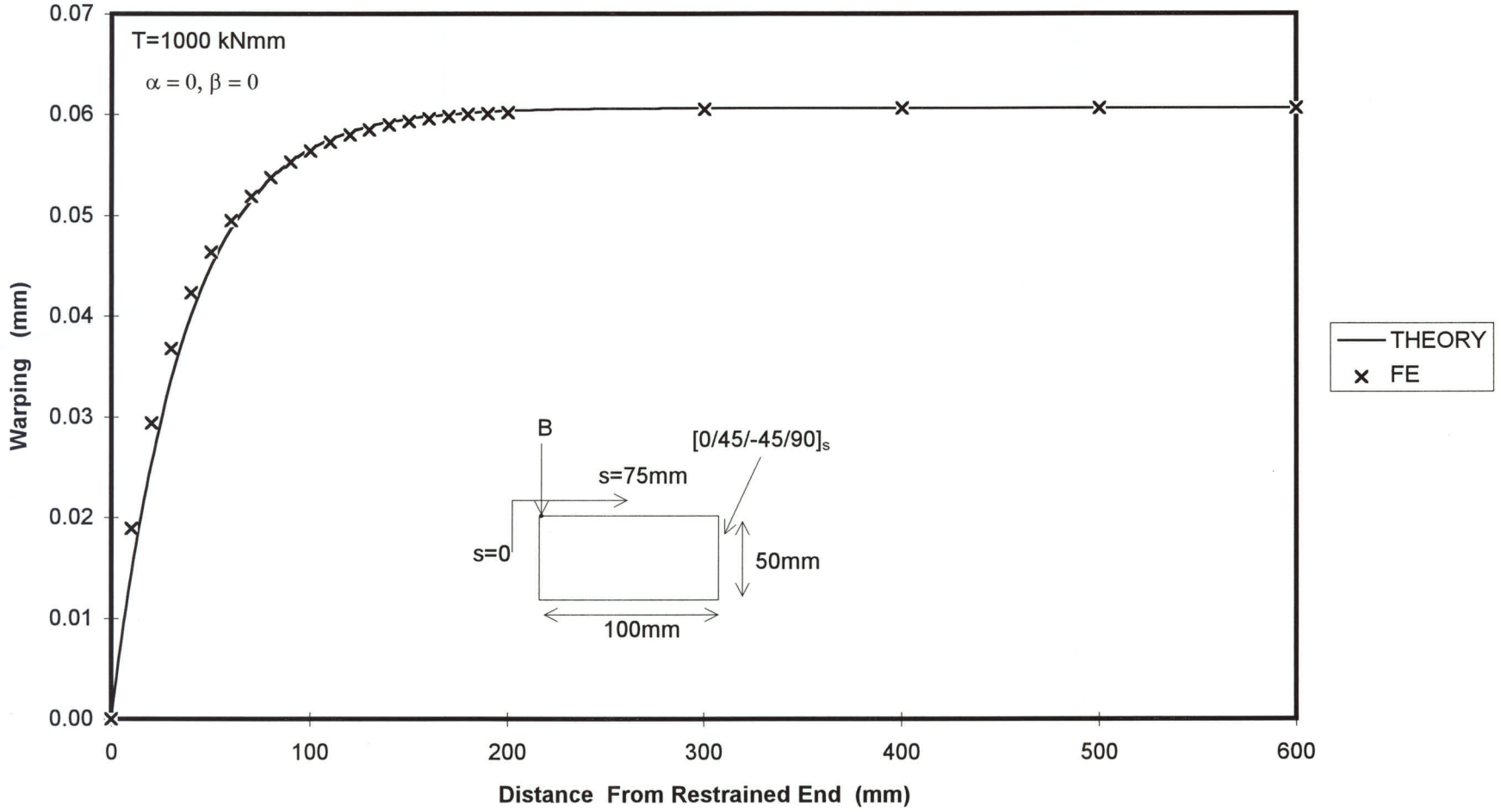

Figure 6.2 WARPING ALONG LENGTH OF BOX AT POINT "B"

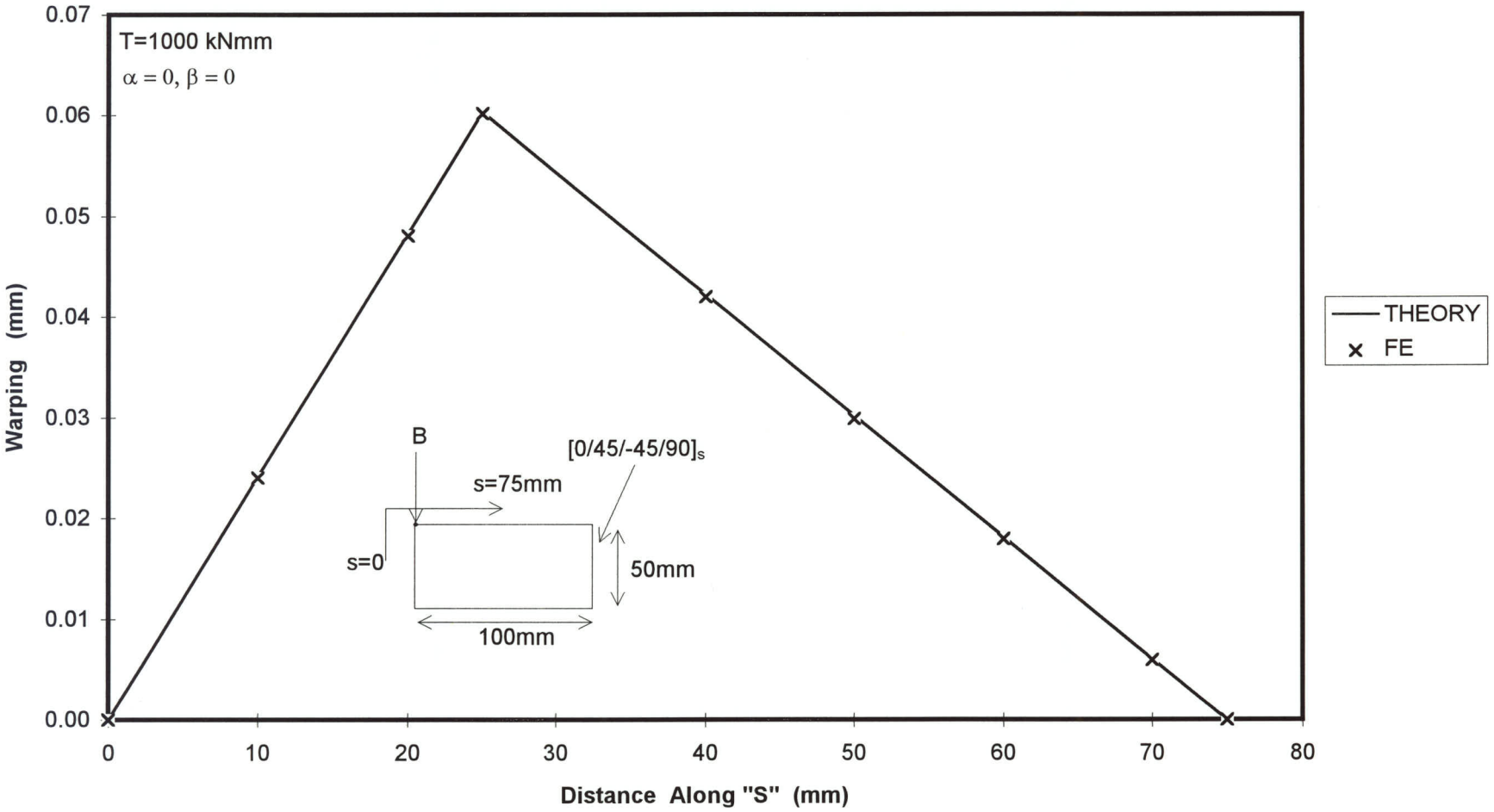

Figure 6.3 WARPING AROUND BOX AT Z=200mm

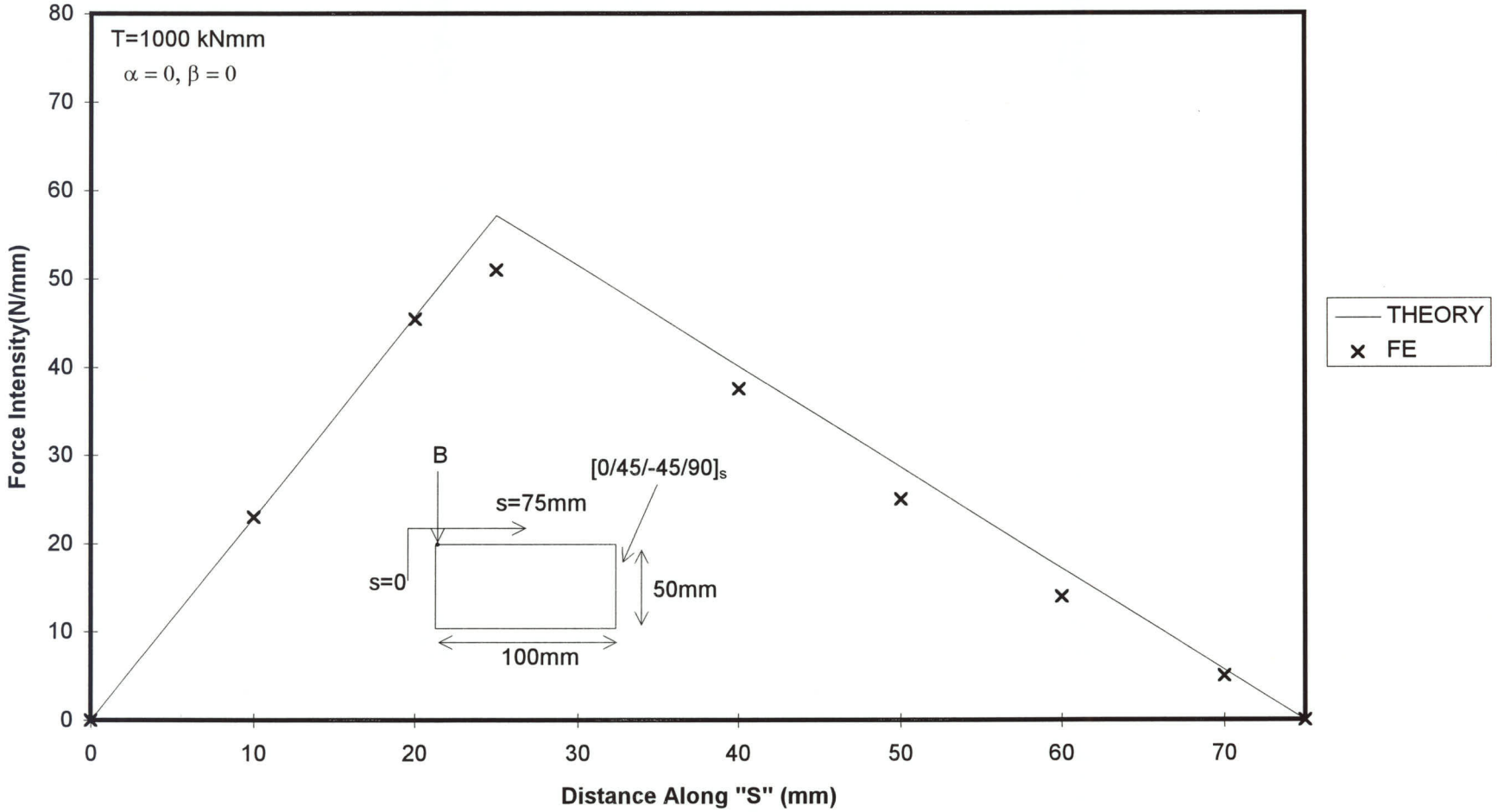

Figure 6.4 FORCE INTENSITY AROUND BOX AT Z=20mm

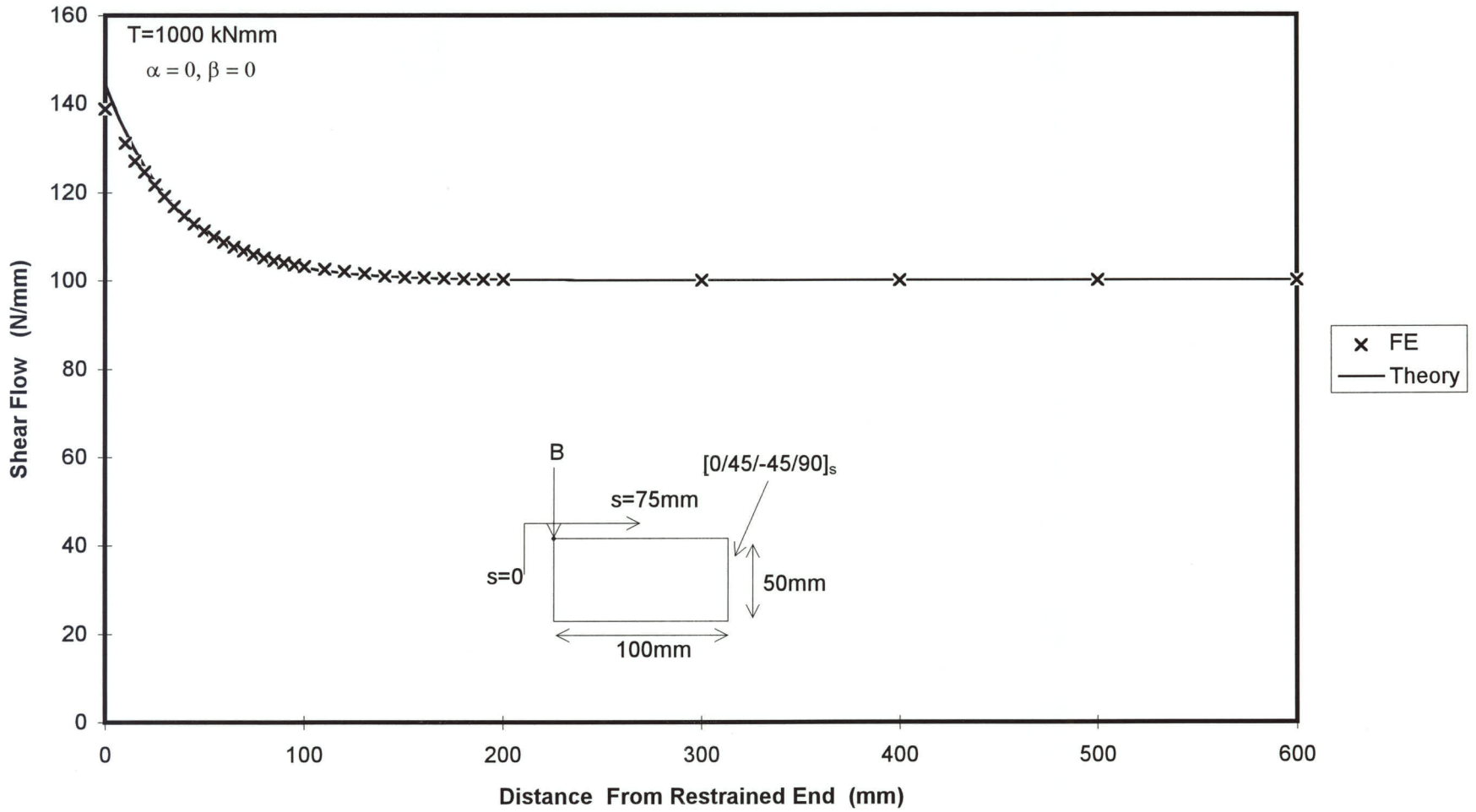

Figure 6.5 SHEAR FLOW ALONG LENGTH OF BOX AT S=0 mm

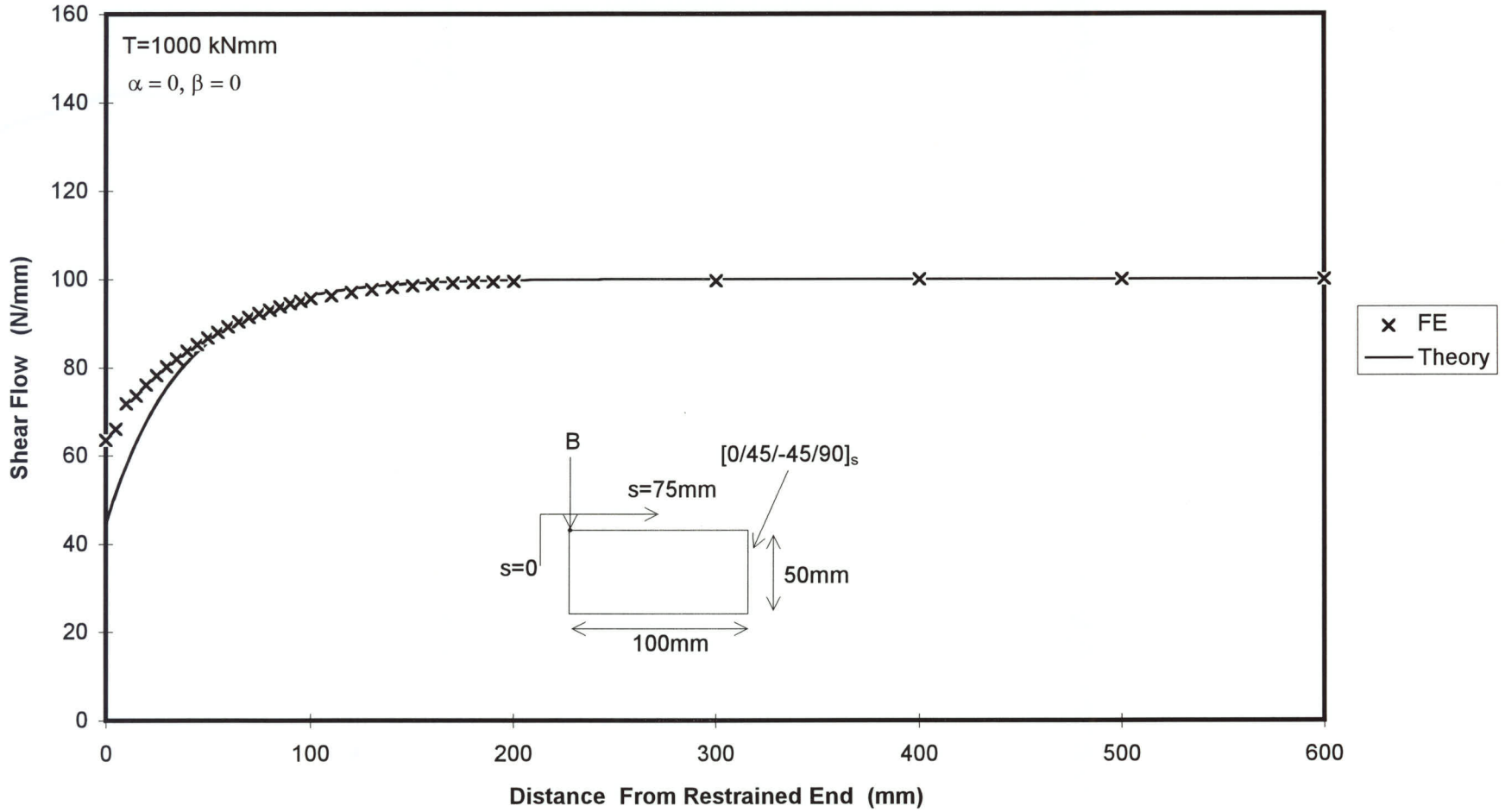

Figure 6.6 SHEAR FLOW ALONG LENGTH OF BOX AT S=75 mm

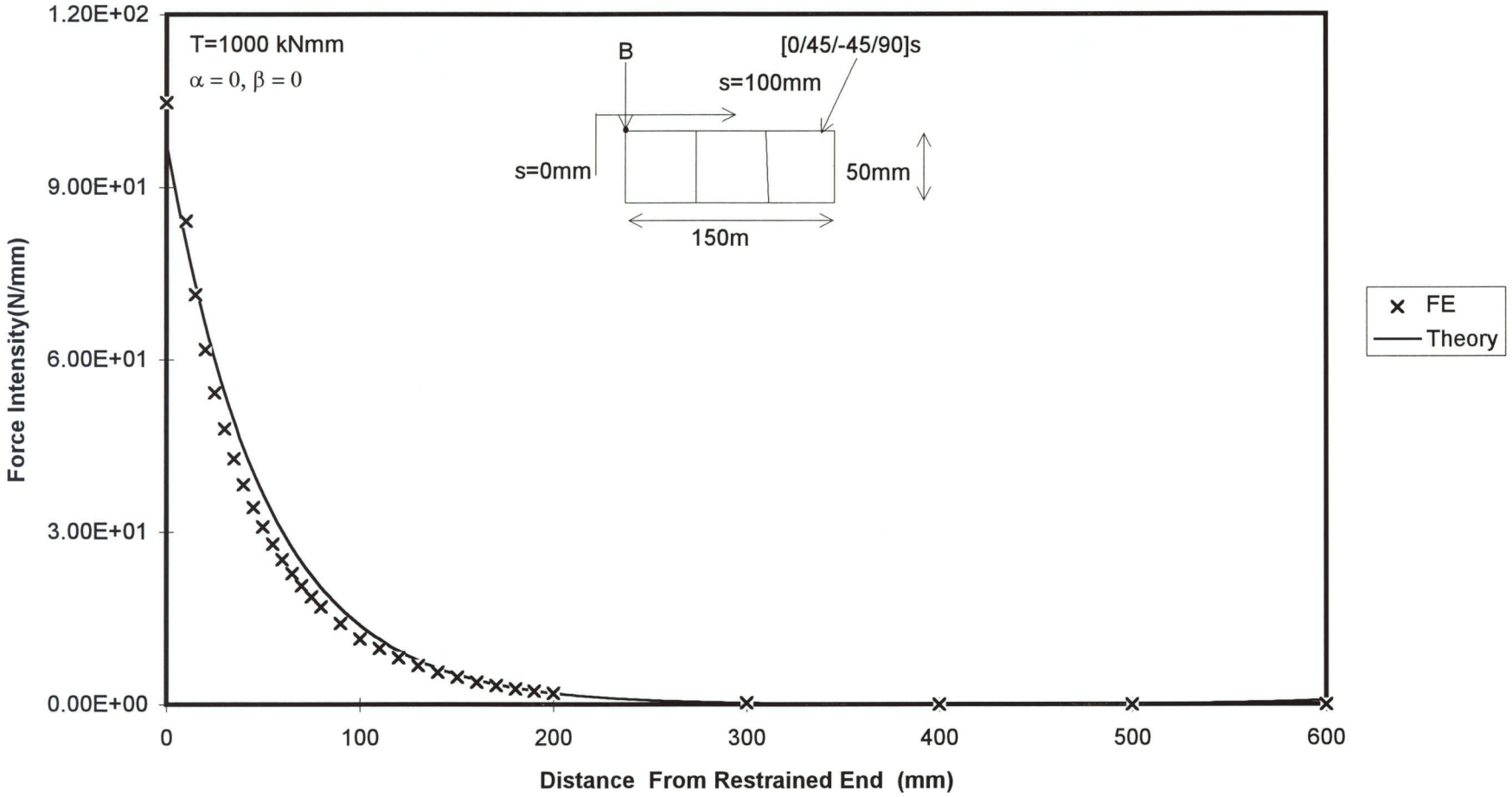

Figure 6.7 FORCE INTENSITY ALONG LENGTH OF BOX AT POINT "B"

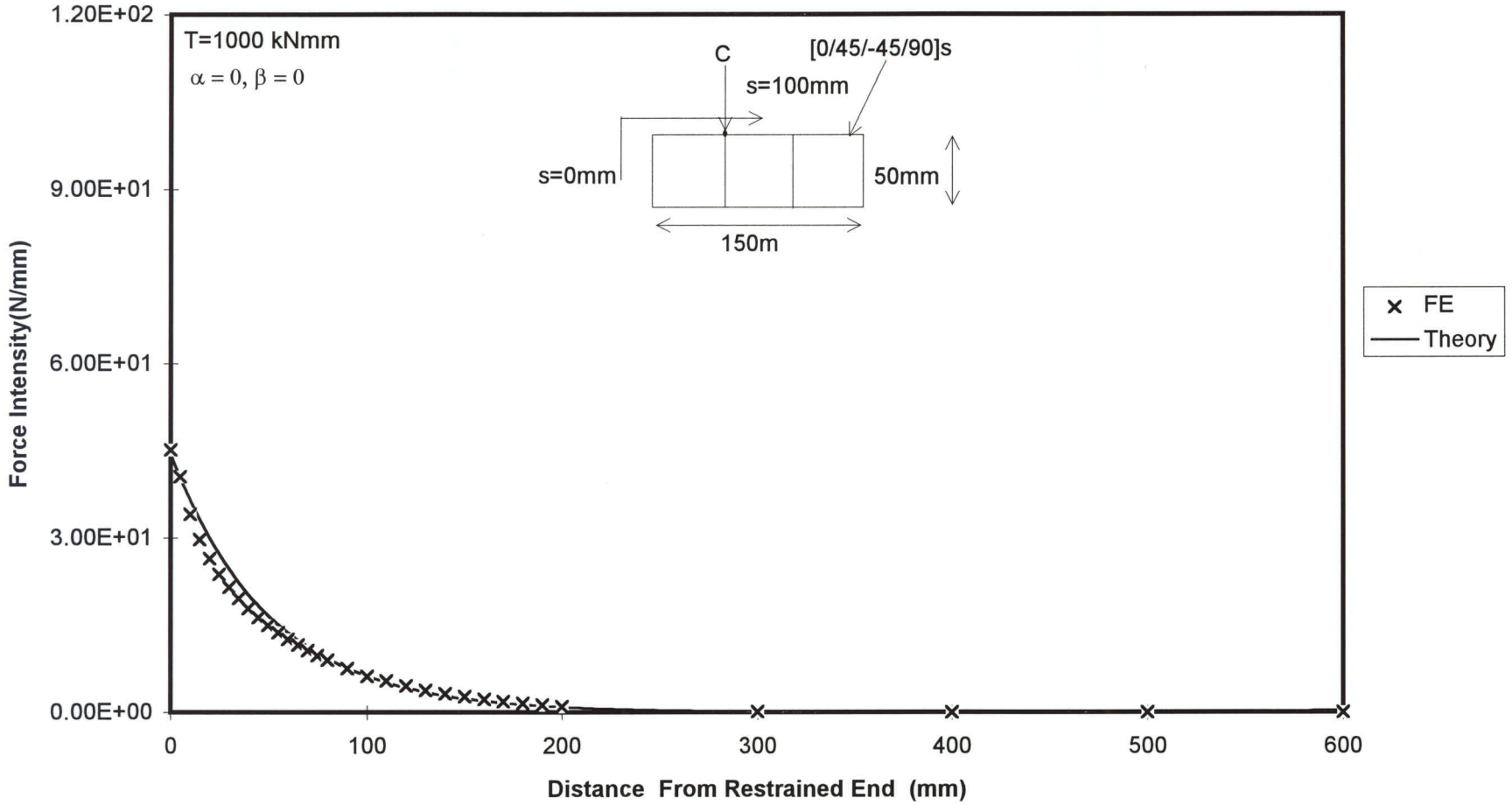

Figure 6.8 FORCE INTENSITY ALONG LENGTH OF BOX AT POINT "C"

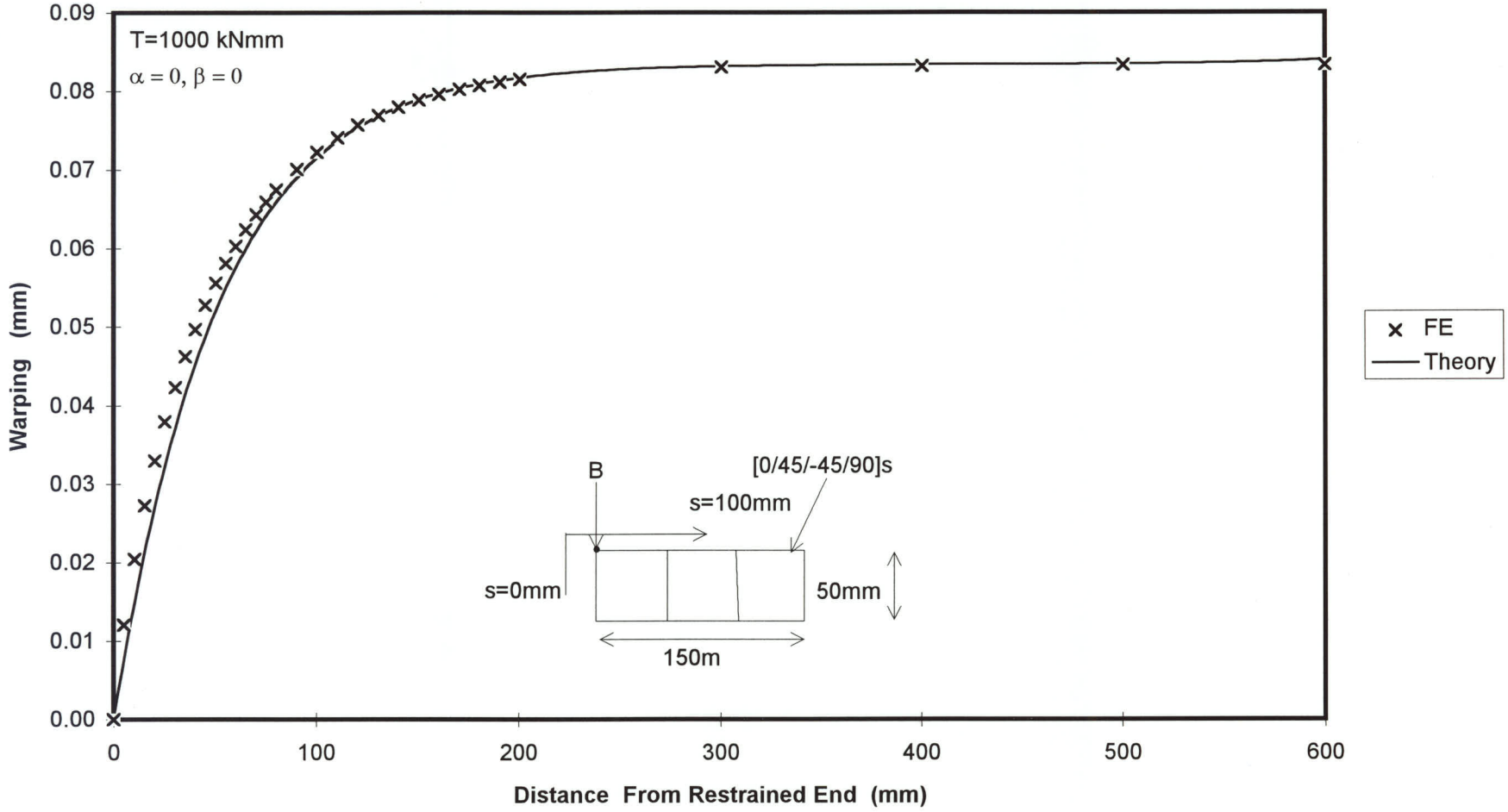

Figure 6.9 WARPING ALONG LENGTH OF BOX AT POINT "B"

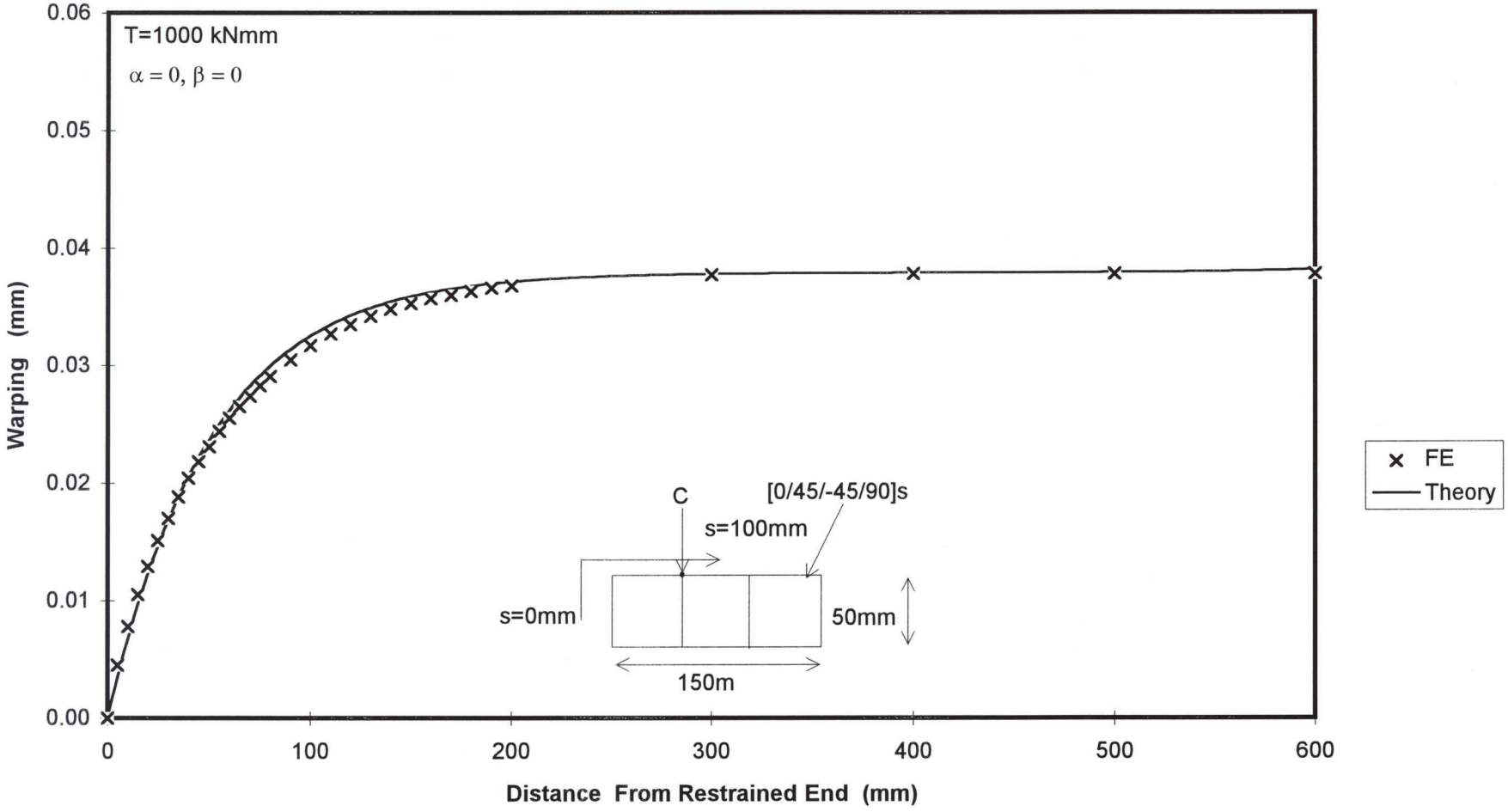

Figure 6.10 WARPING ALONG LENGTH OF BOX AT POINT "C"

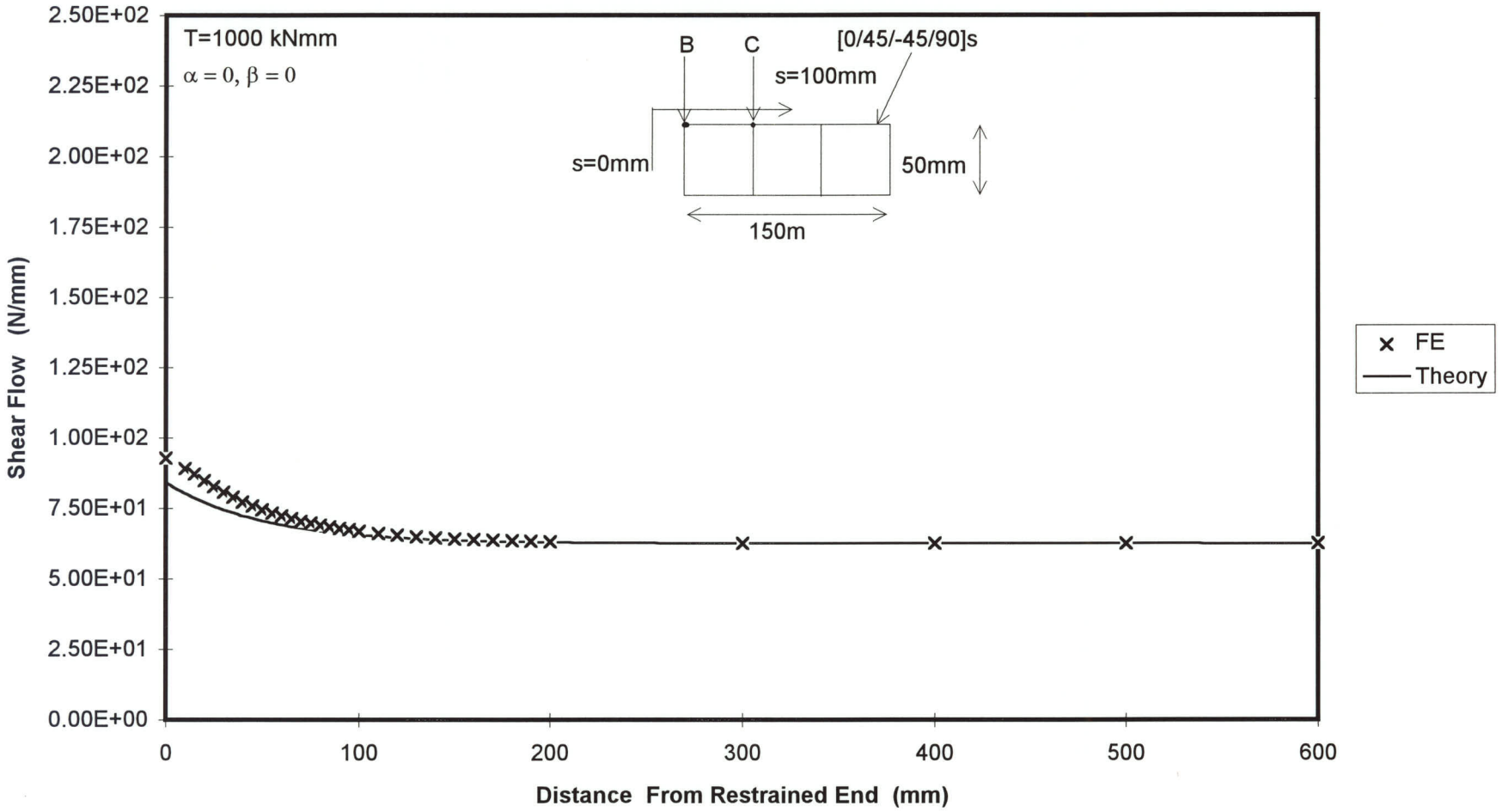

Figure 6.11 SHEAR FLOW ALONG LENGTH OF BOX AT S=0 mm

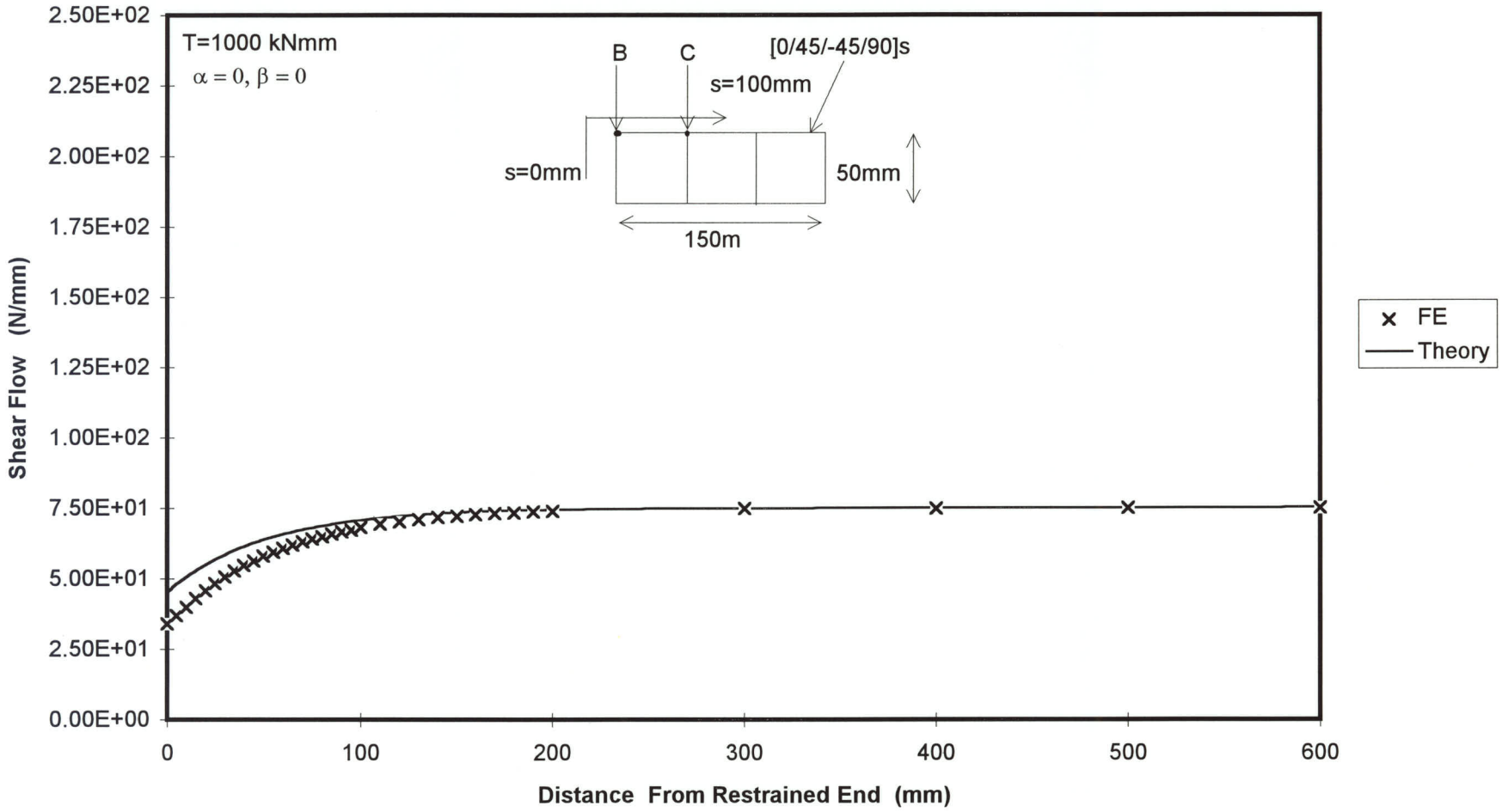

Figure 6.12 SHEAR FLOW ALONG LENGTH OF BOX AT S=100 mm

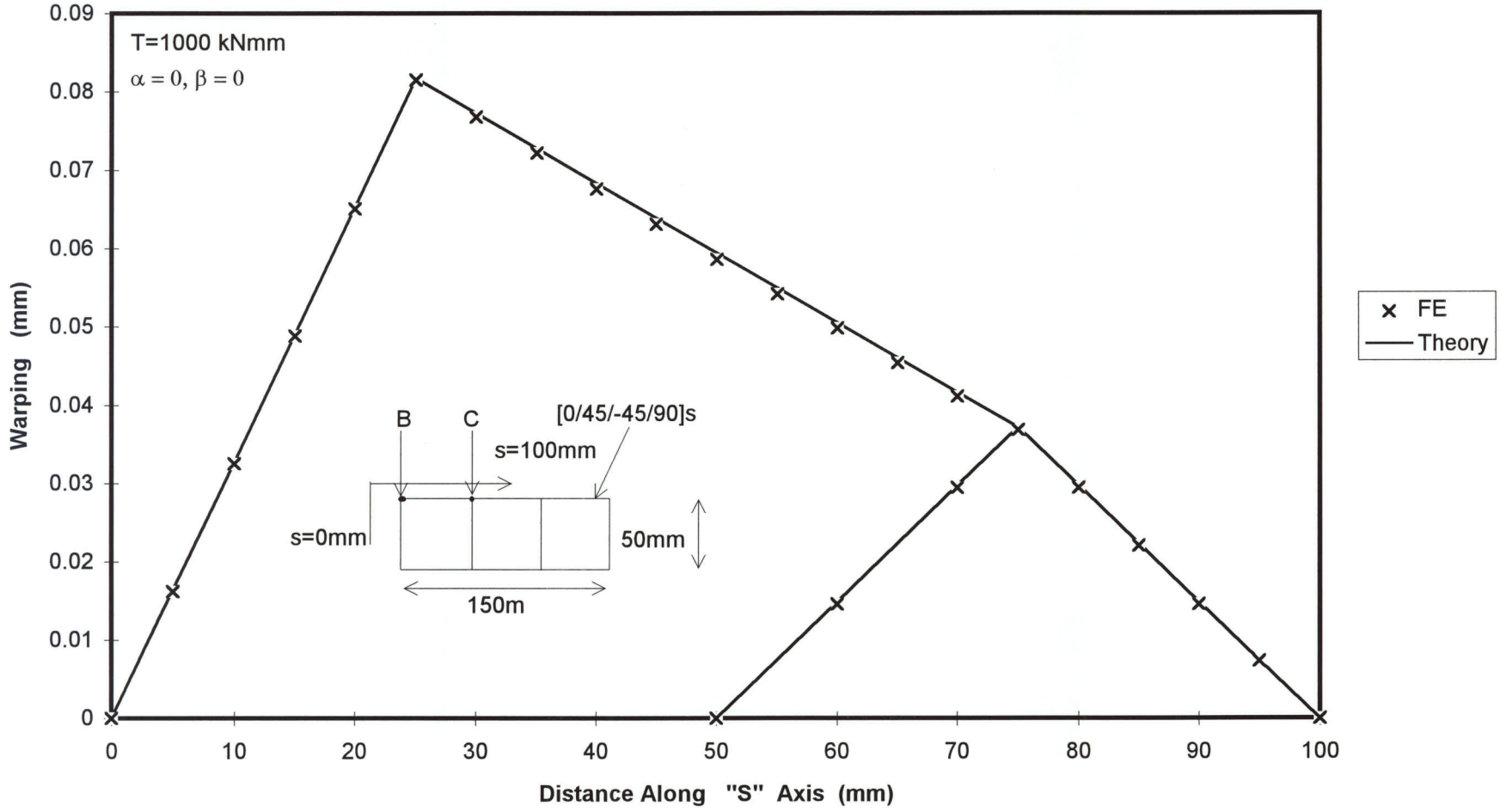

Figure 6.13 WARPING AROUND BOX AT Z=200mm

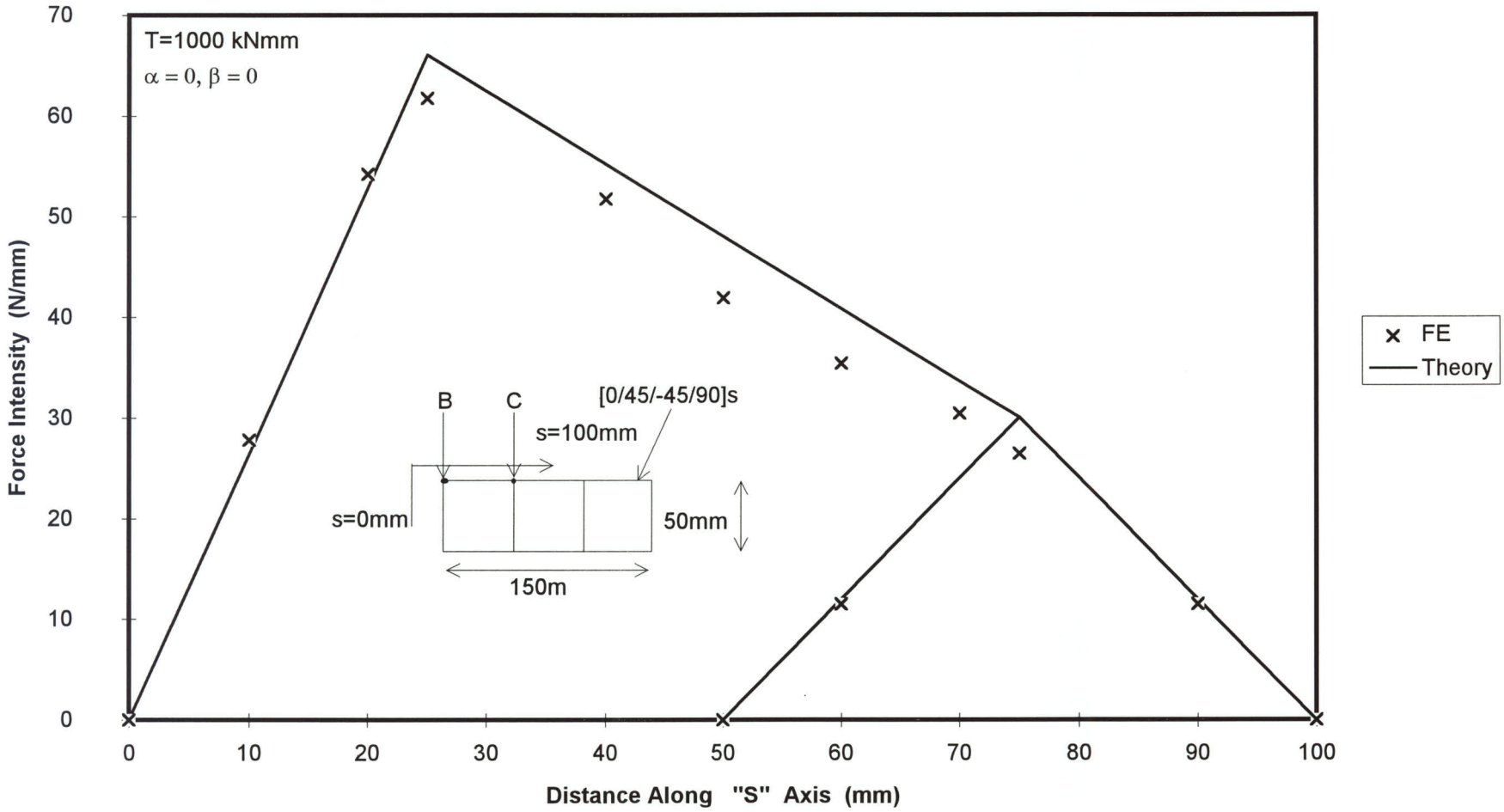

Figure 6.14 FORCE INTENSITY AROUND BOX AT Z=20mm

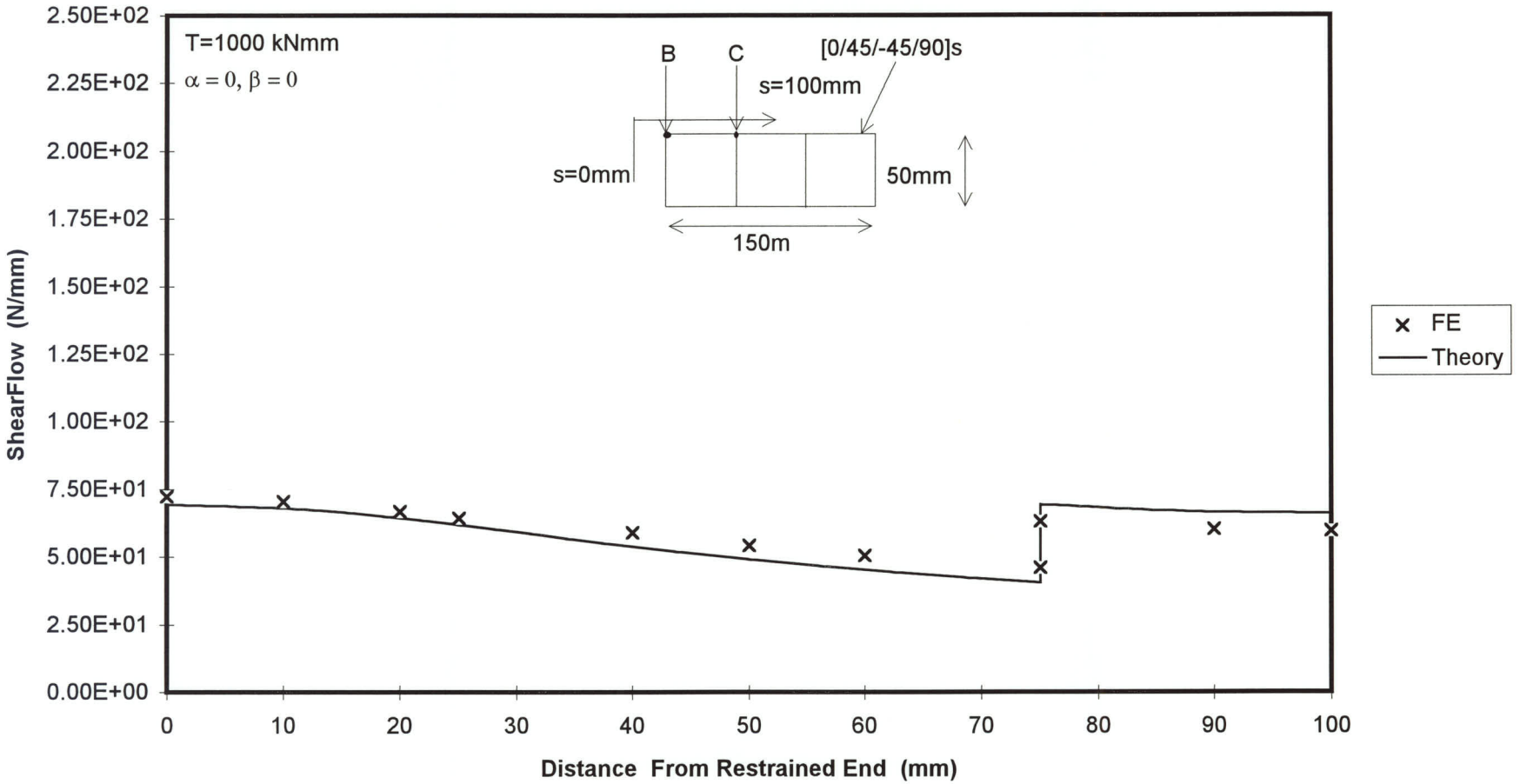

Figure 6.15 SHEAR FLOW AROUND BOX AT Z=60mm

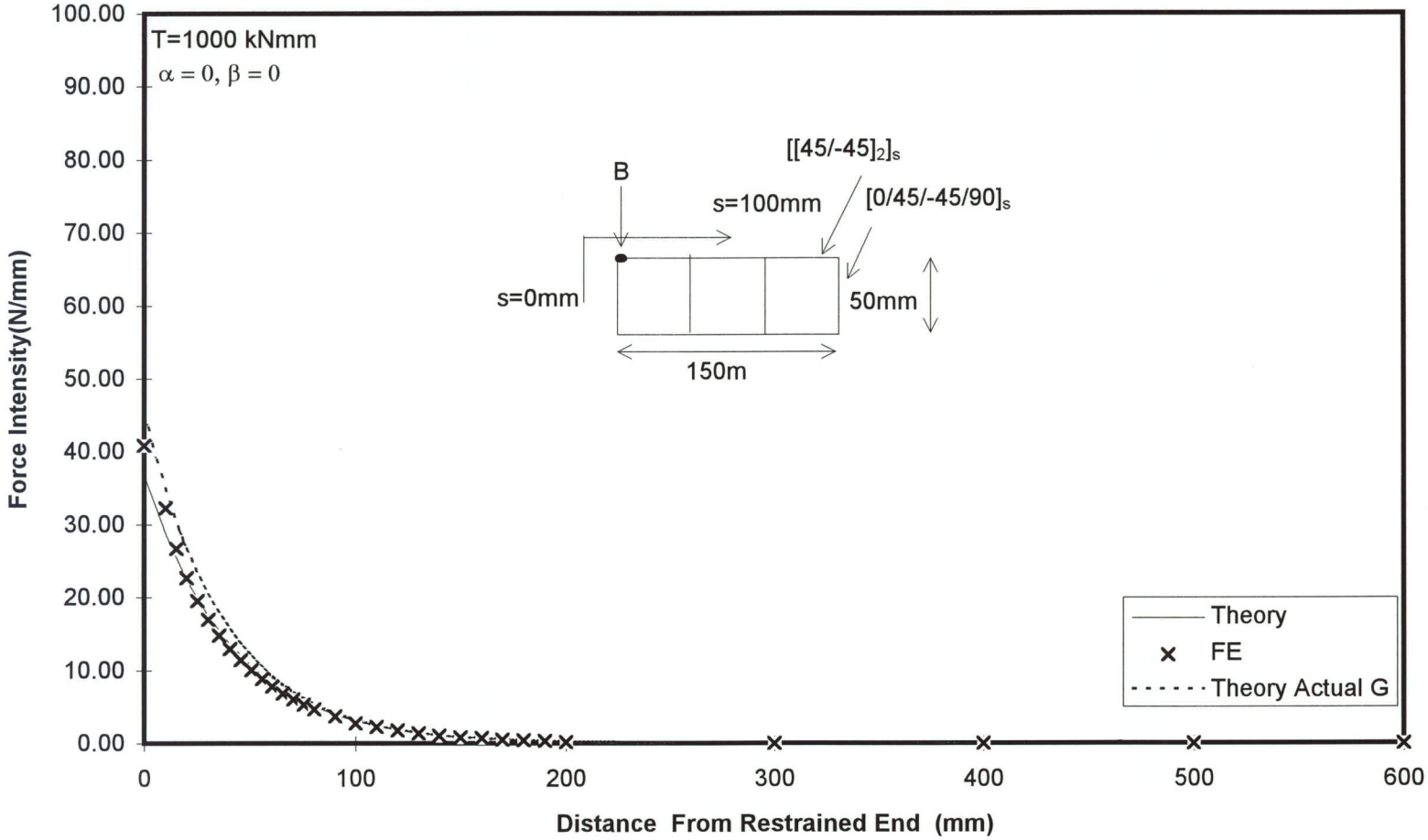

Figure 6.16 FORCE INTENSITY ALONG LENGTH OF BOX AT POINT "B"

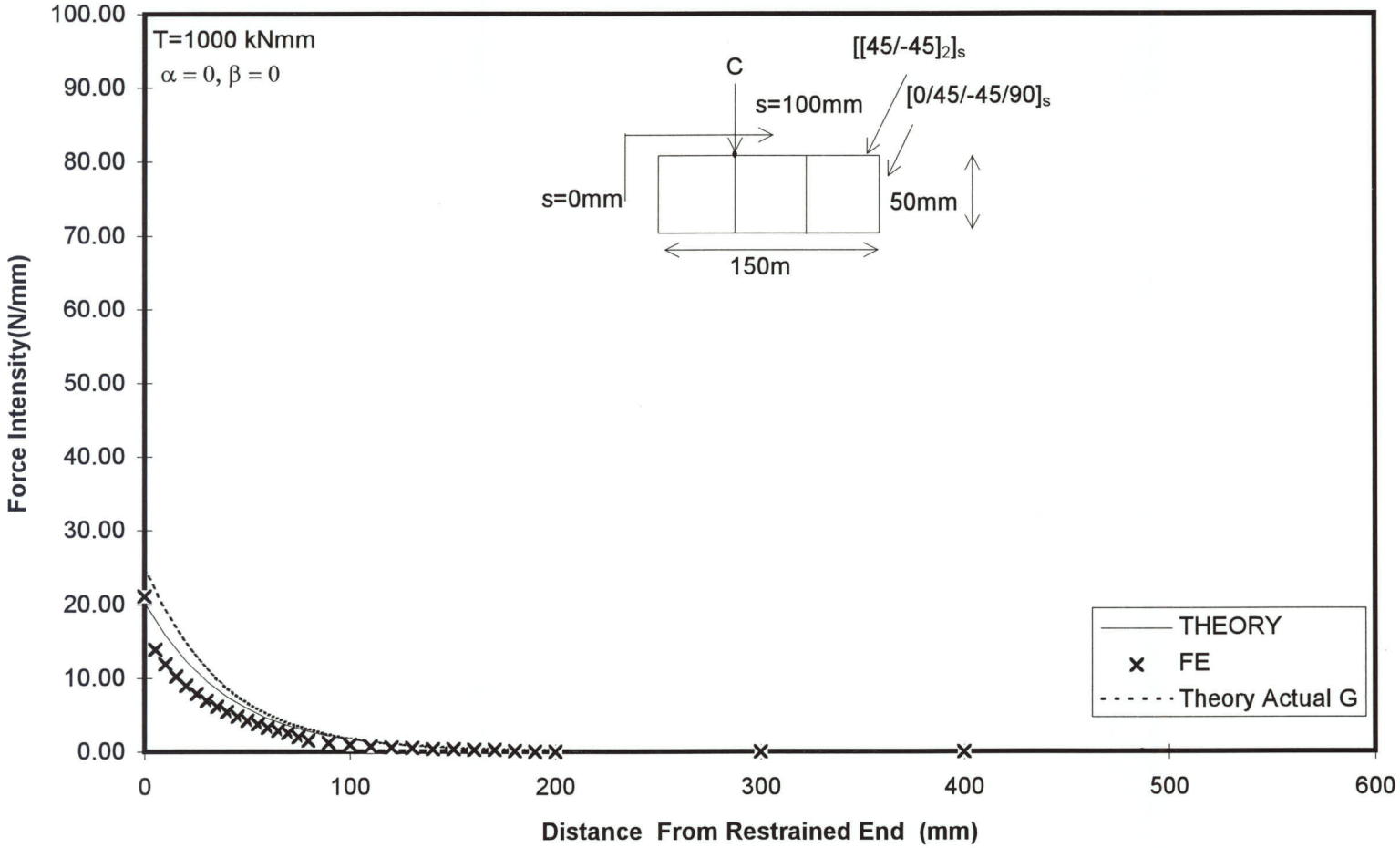

Figure 6.17 FORCE INTENSITY ALONG LENGTH OF BOX AT POINT "C"

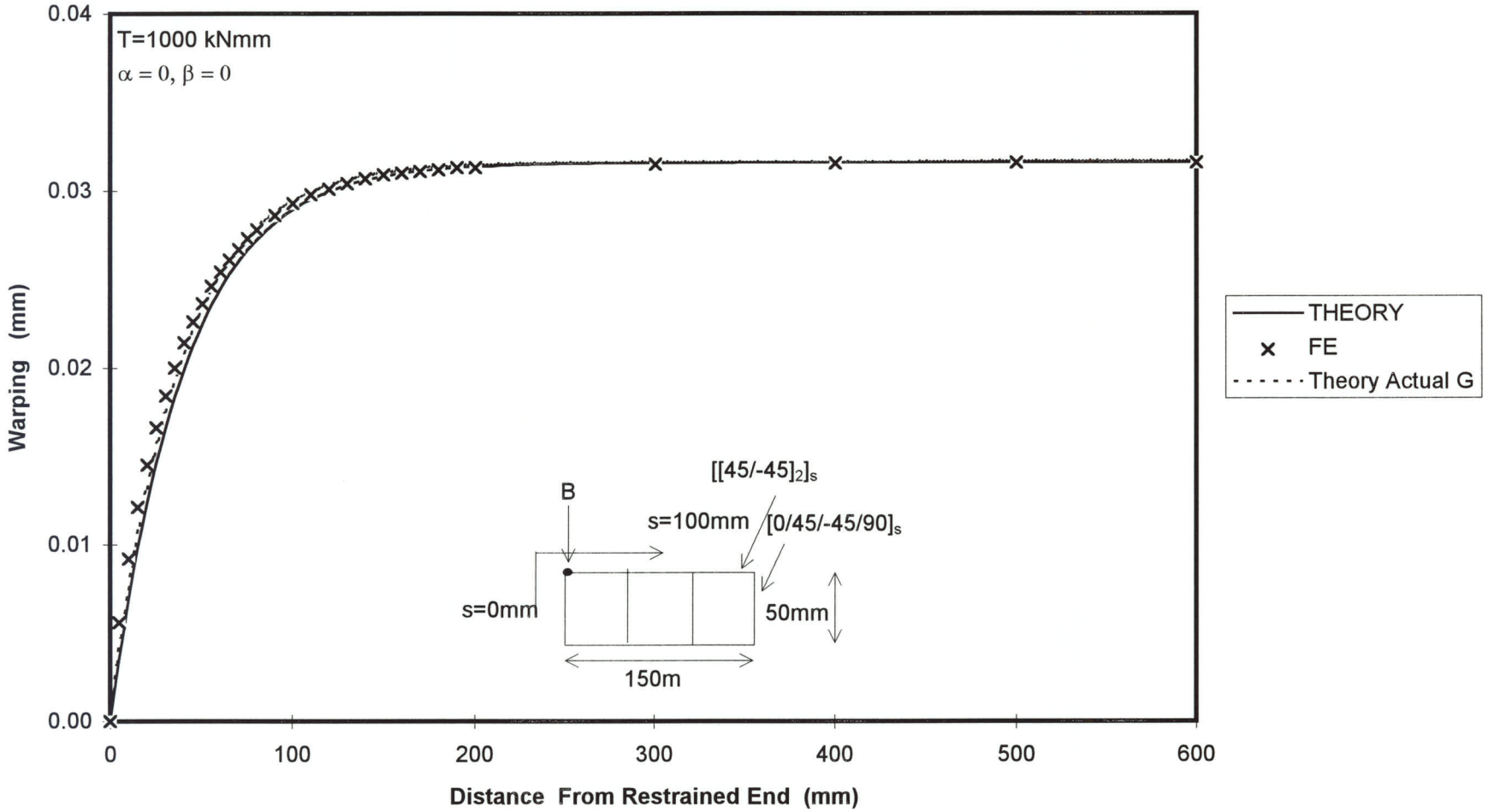

Figure 6.18 WARPING ALONG LENGTH OF BOX AT POINT "B"

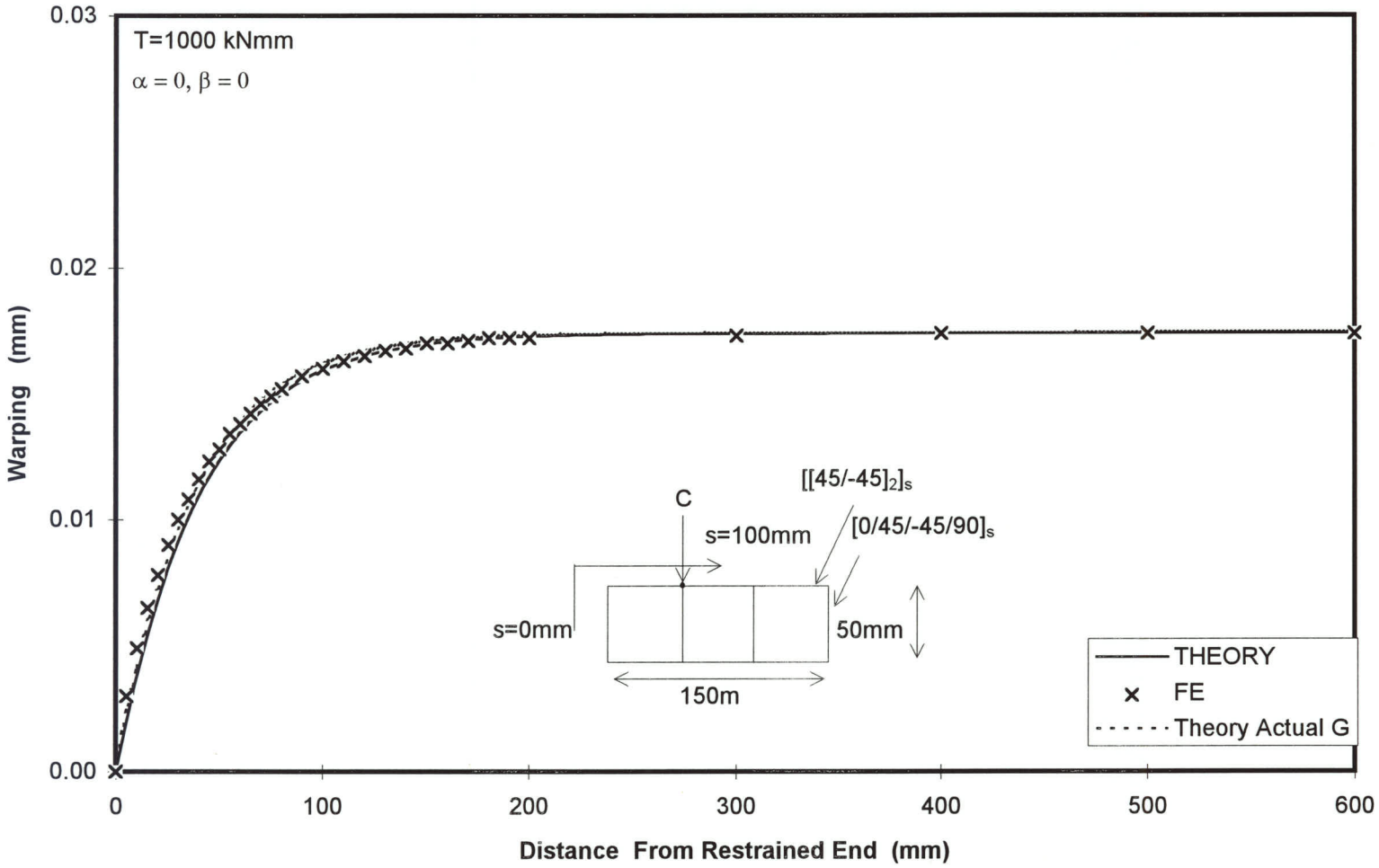

Figure 6.19 WARPING ALONG LENGTH OF BOX AT POINT "C"

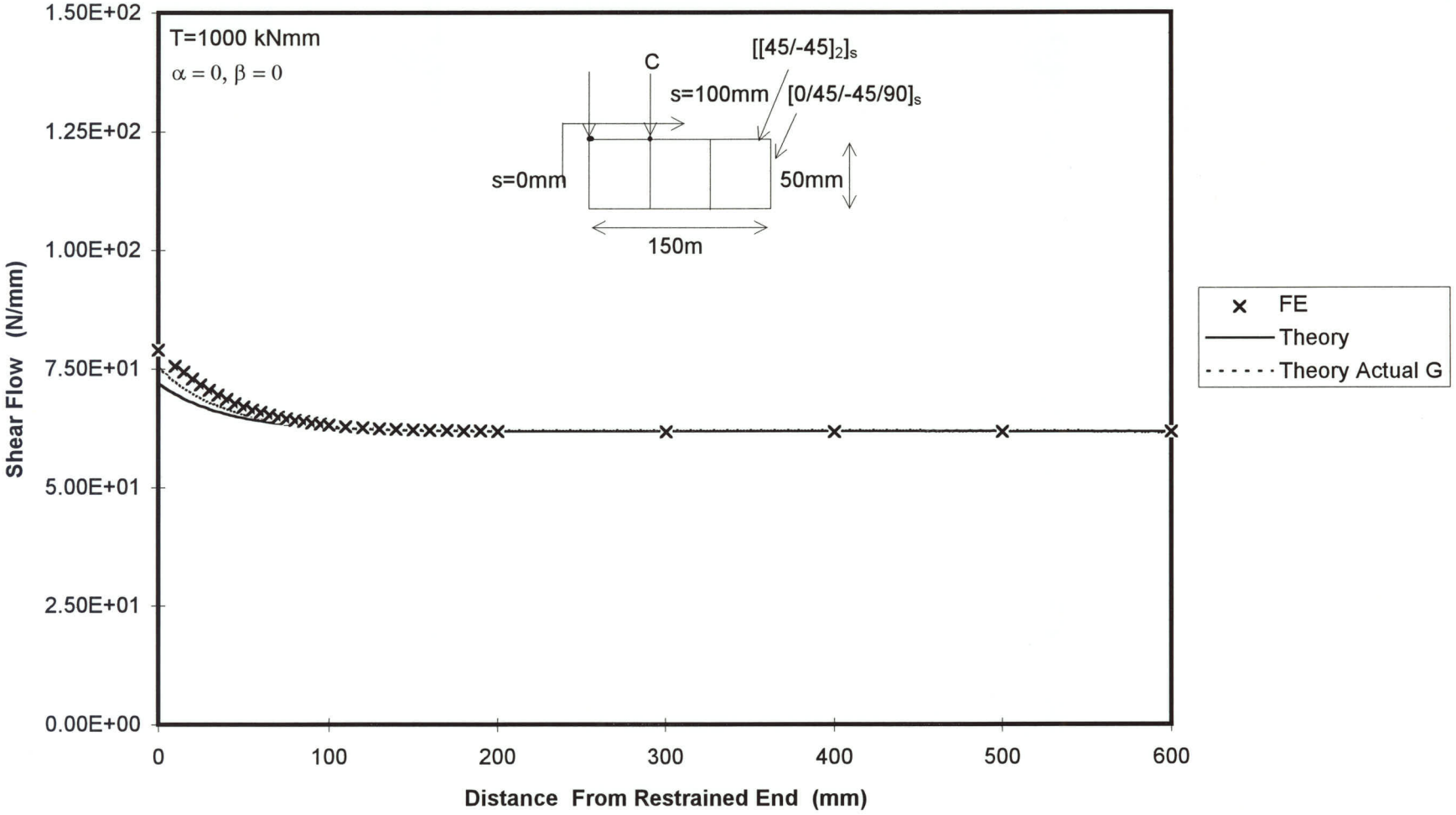

Figure 6.20 SHEAR FLOW ALONG LENGTH OF BOX AT S=0 mm

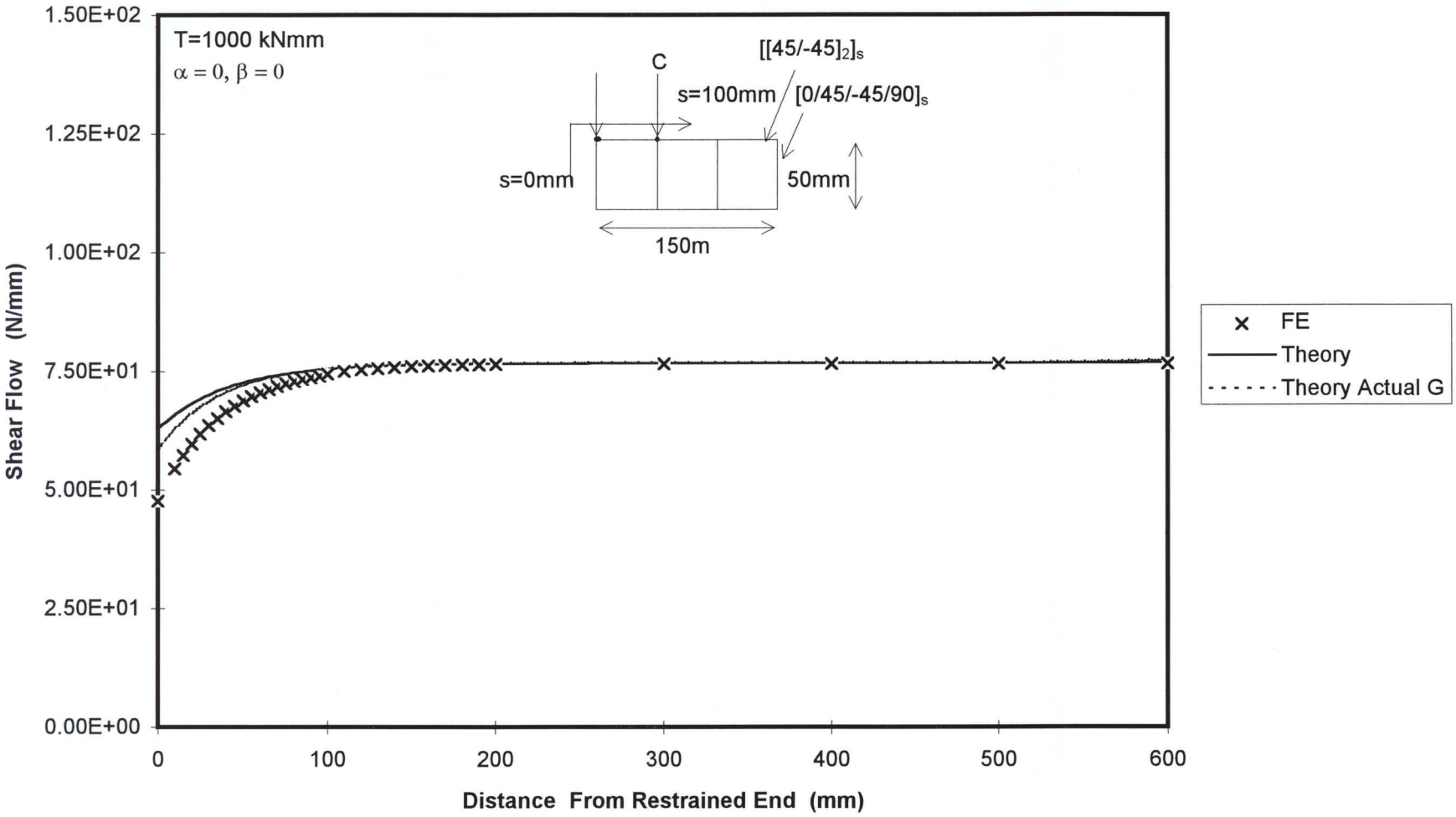

Figure 6.21 SHEAR FLOW ALONG LENGTH OF BOX AT S=100 mm

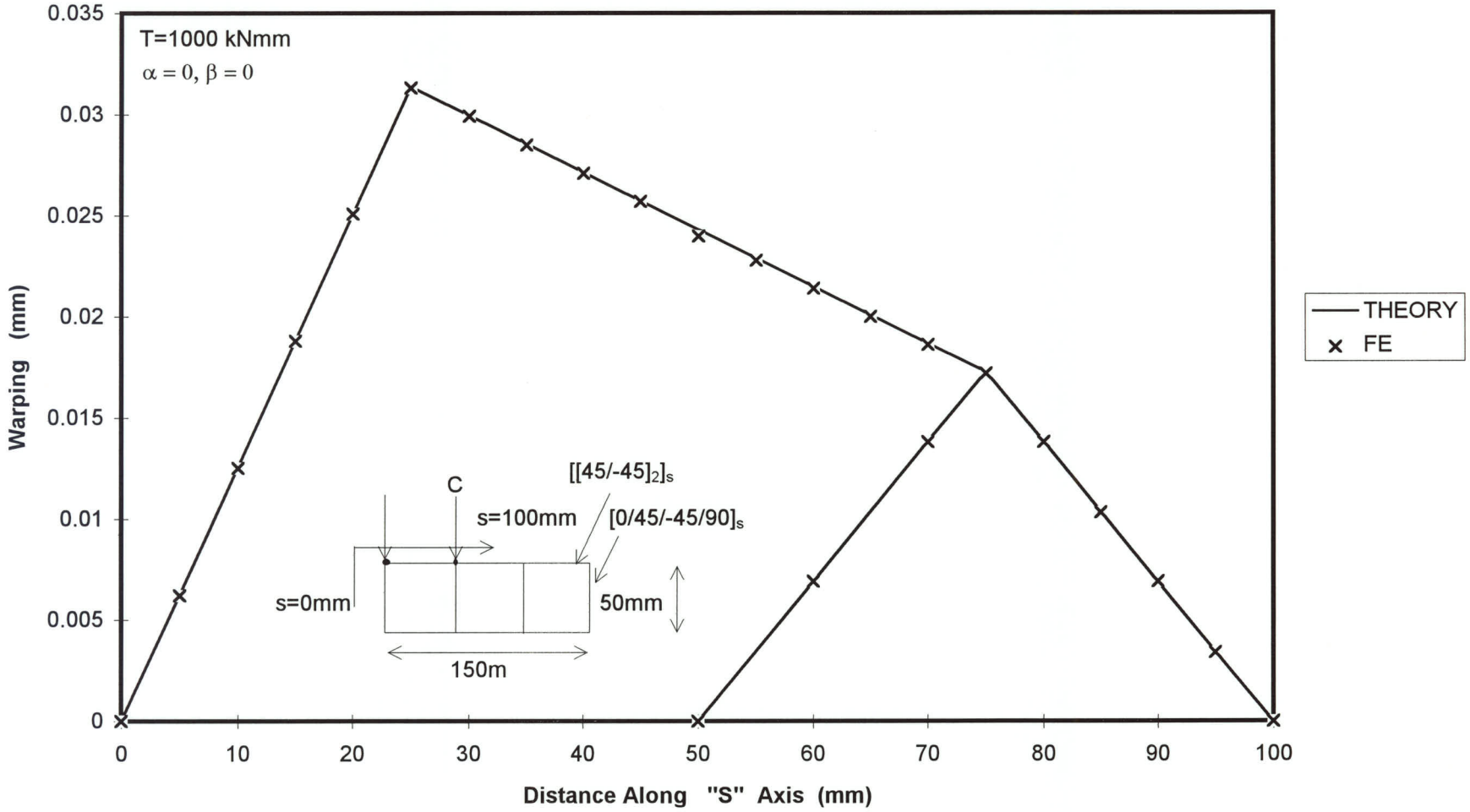

Figure 6.22 WARPING AROUND BOX AT Z=200mm

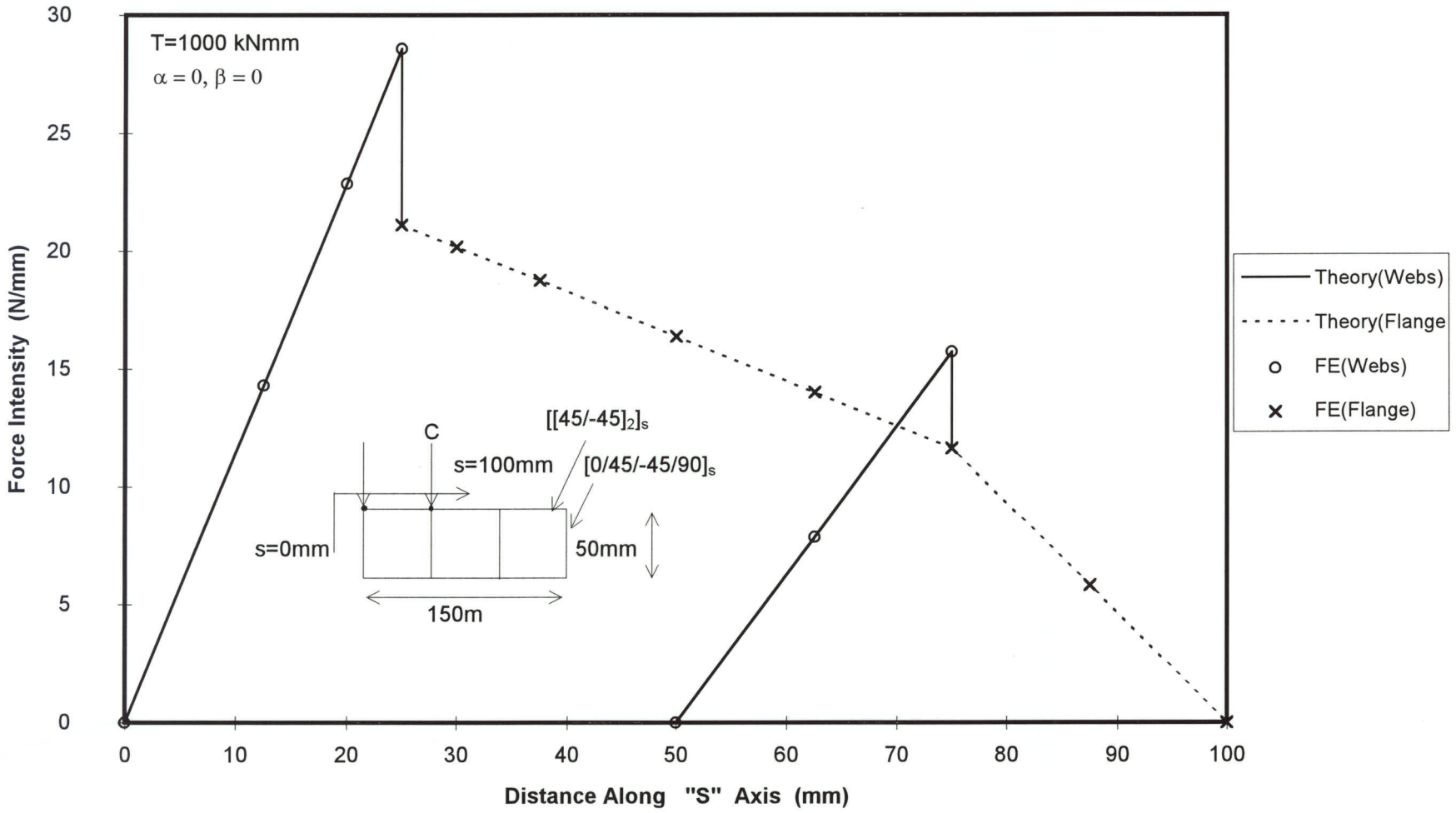

Figure 6.23 FORCE INTENSITY AROUND BOX AT Z=20mm

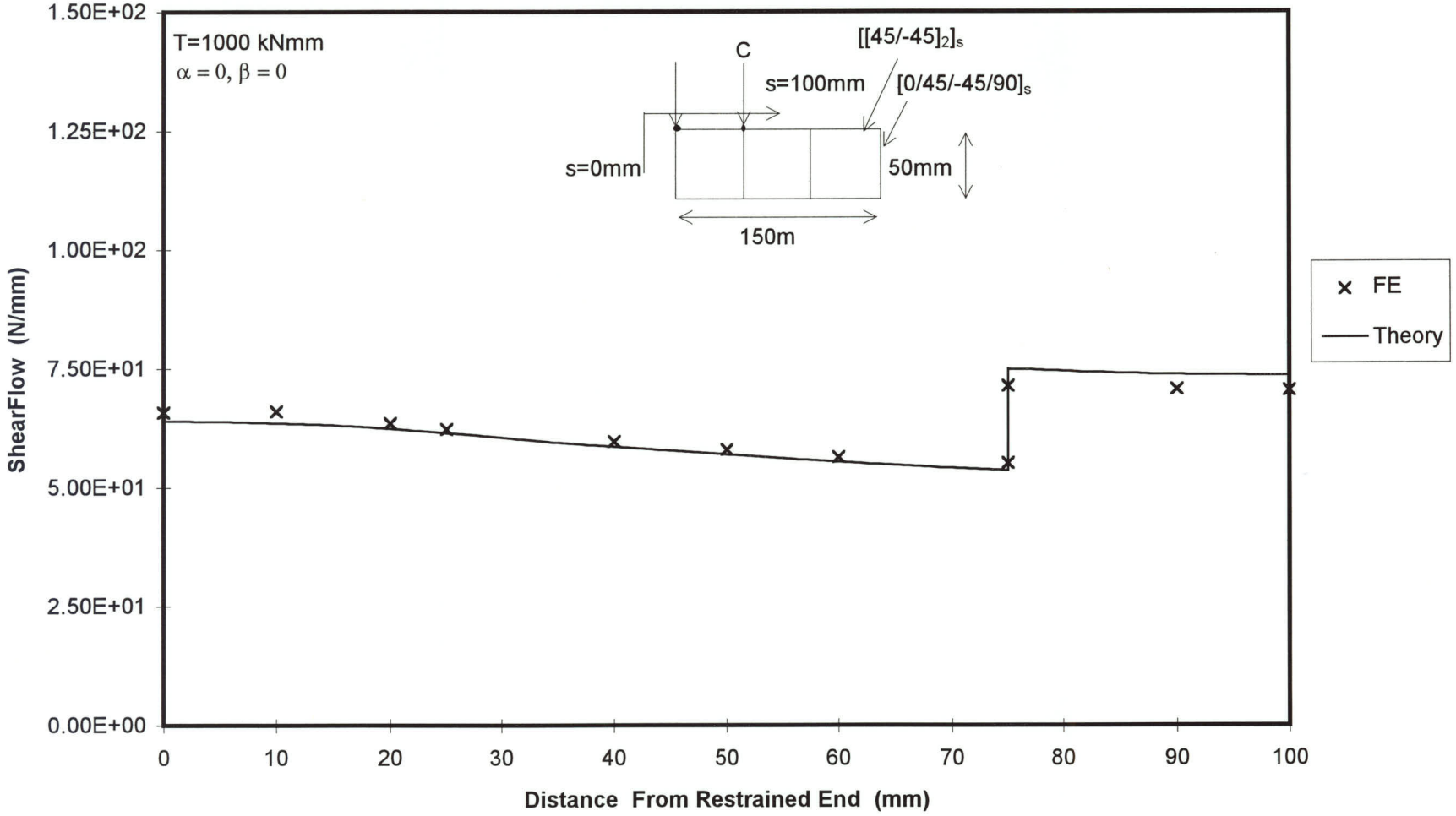

Figure 6.24 SHEAR FLOW AROUND BOX AT Z=60mm

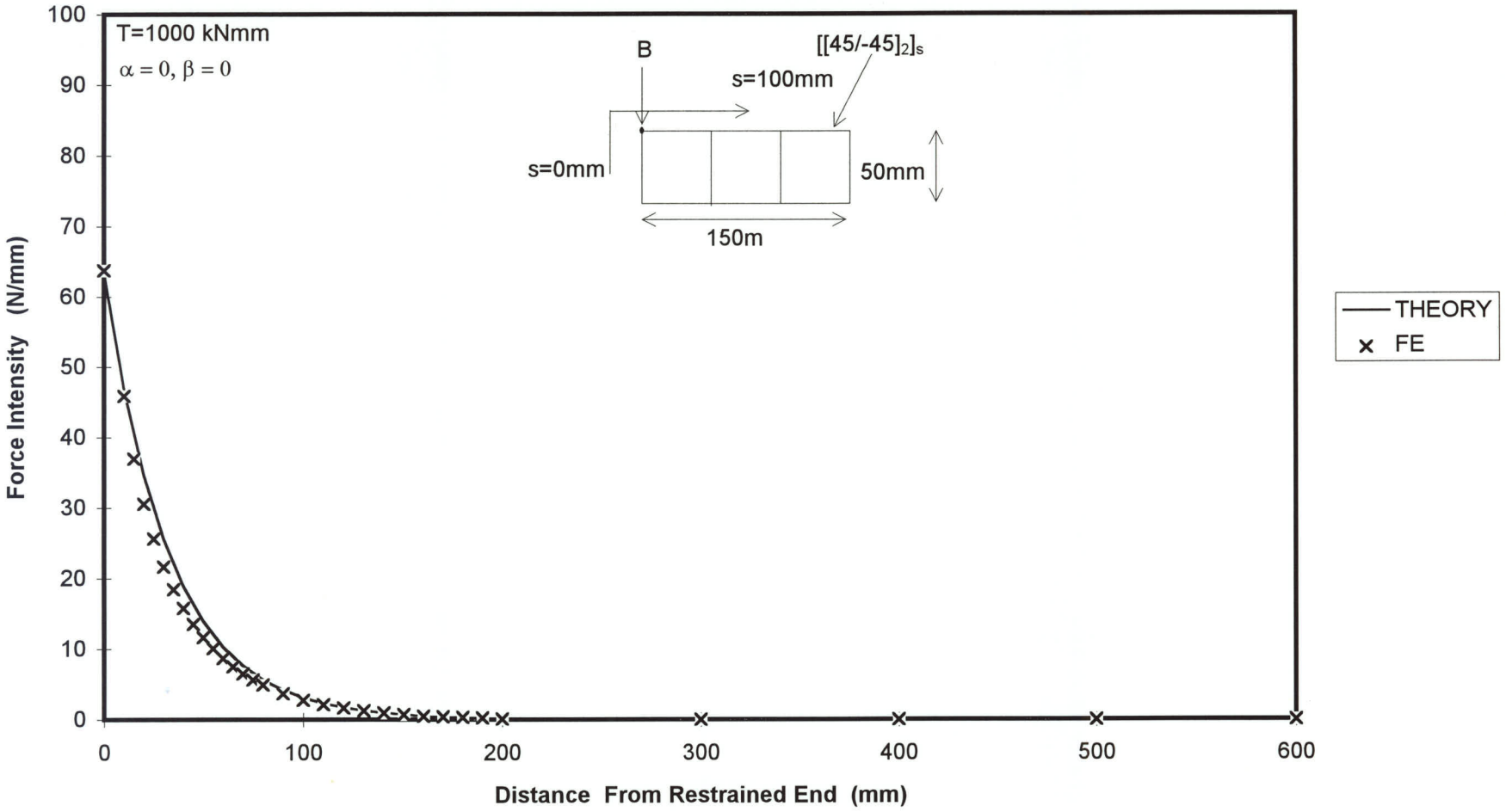

Figure 6.25 FORCE INTENSITY ALONG LENGTH OF BOX AT POINT "B"

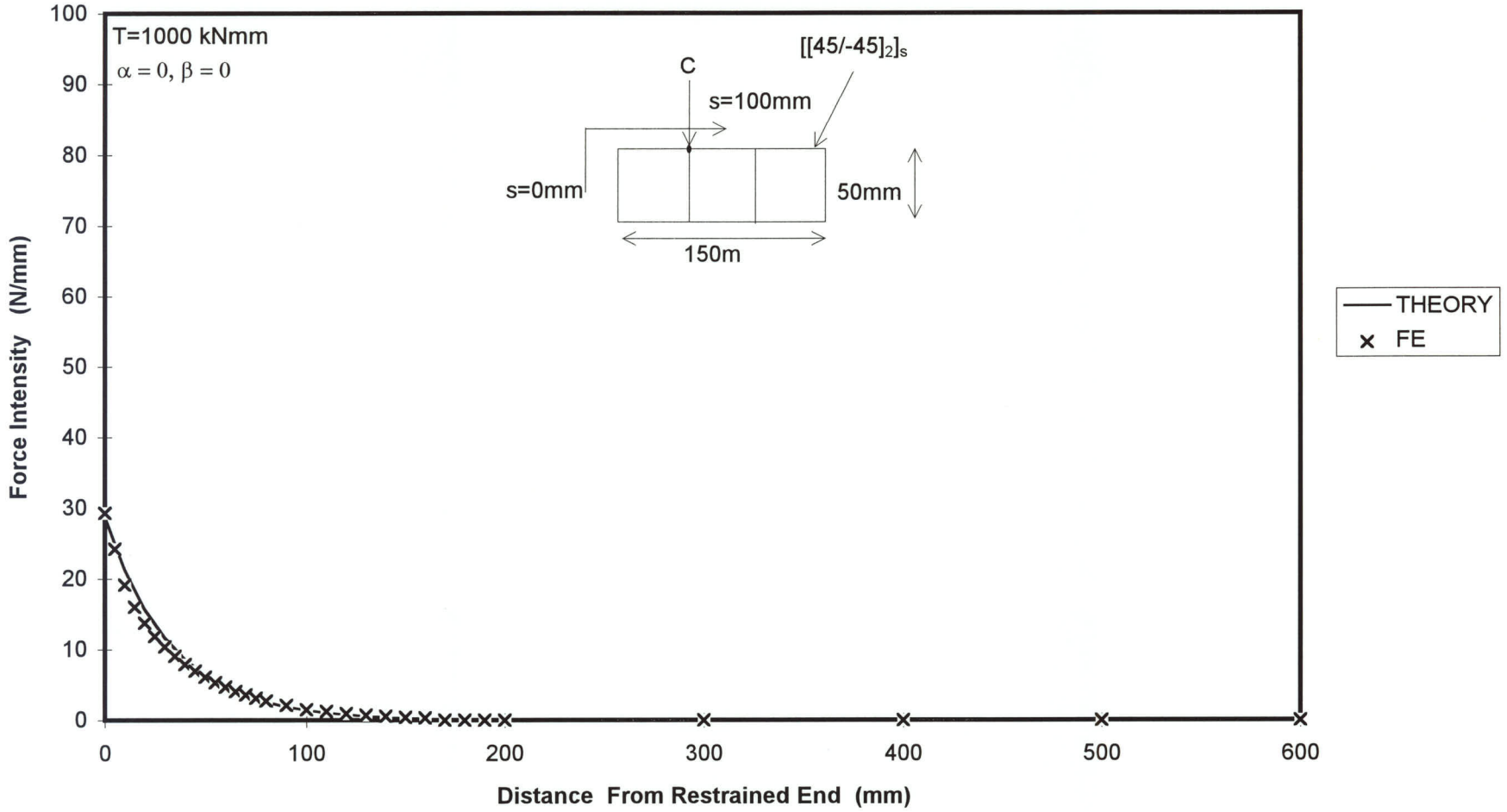

Figure 6.26 FORCE INTENSITY ALONG LENGTH OF BOX AT POINT "C"

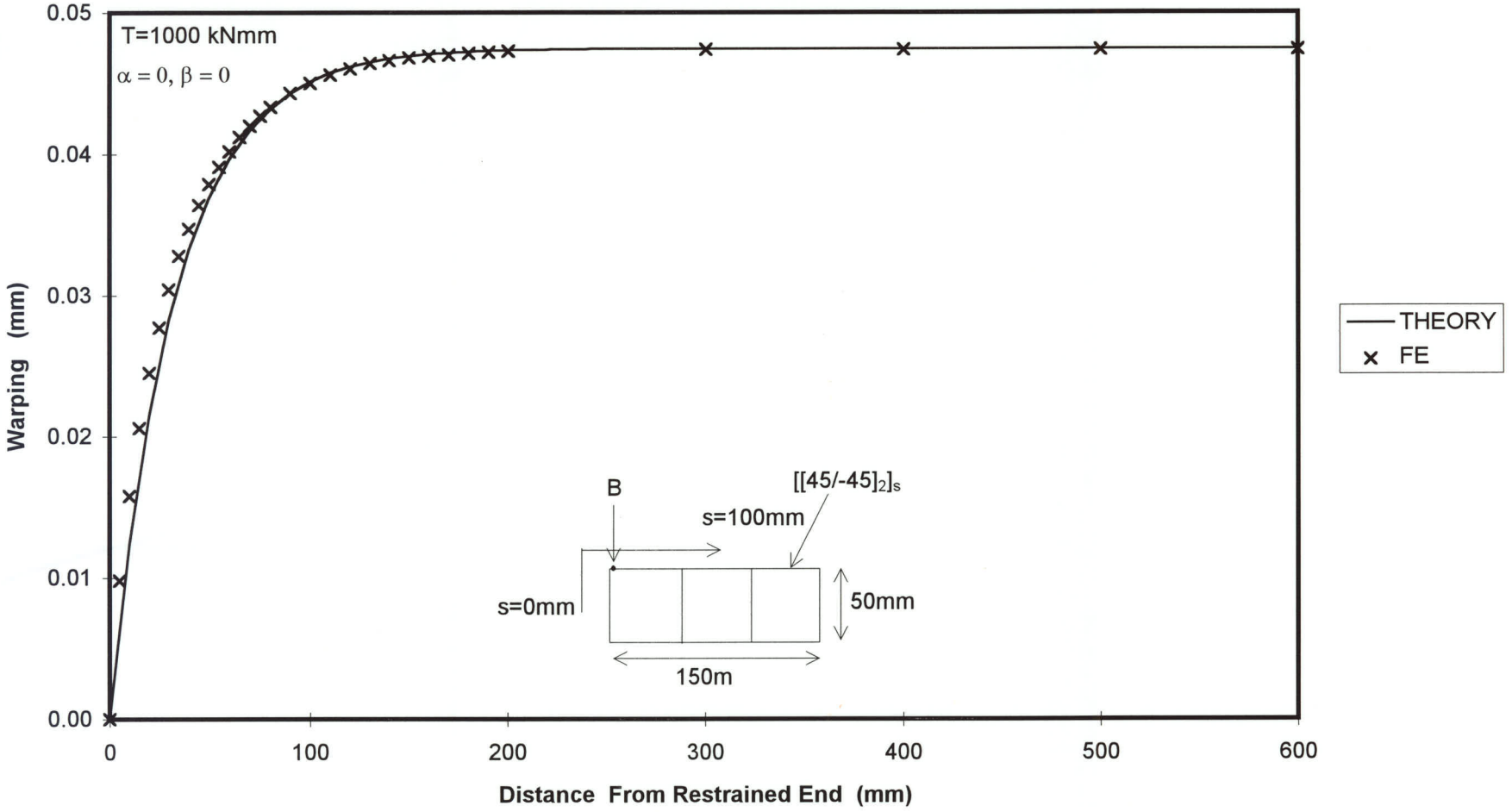

6.27 WARPING ALONG LENGTH OF BOX AT POINT "B"

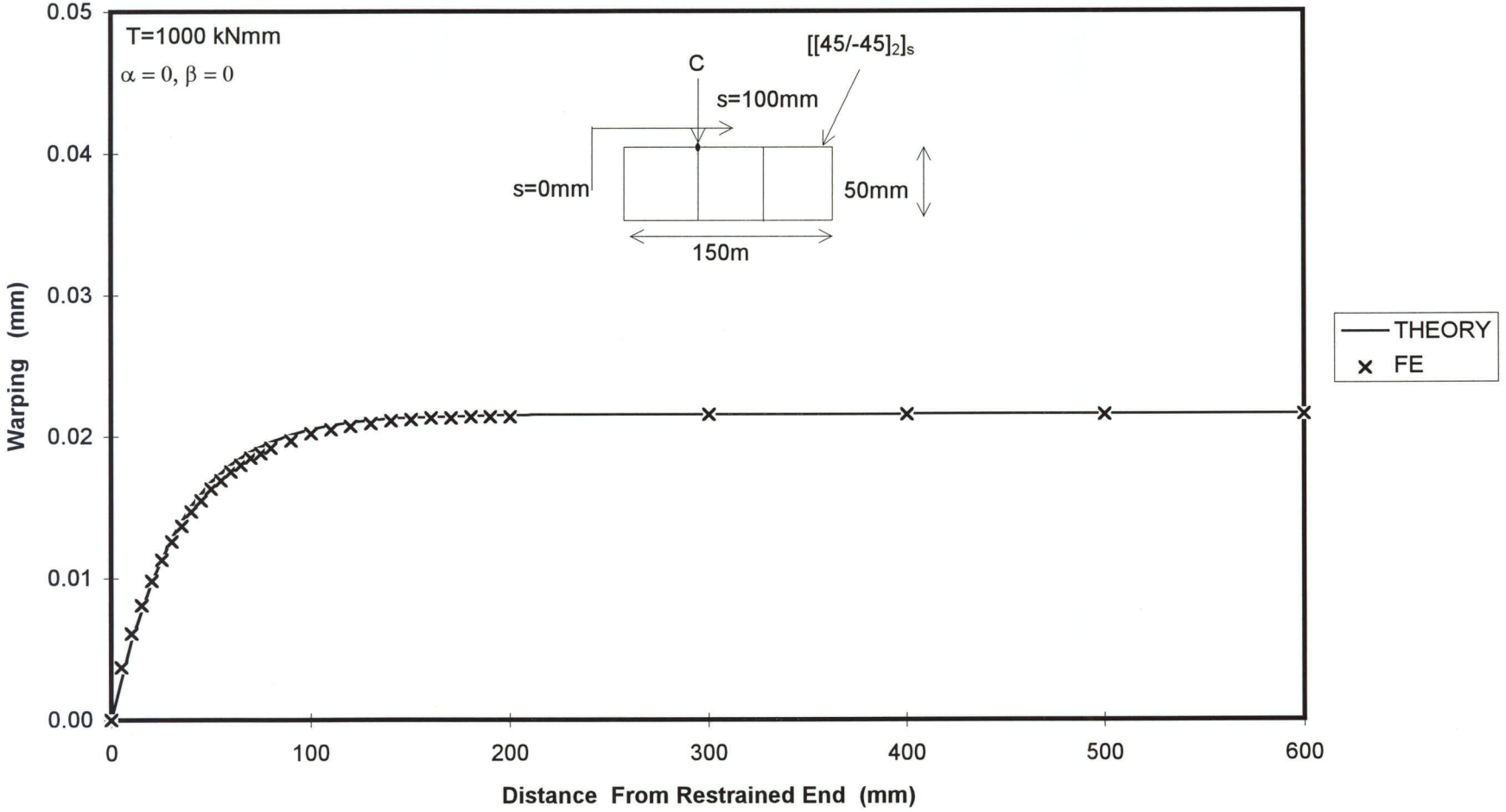

6.28 WARPING ALONG LENGTH OF BOX AT POINT "C"

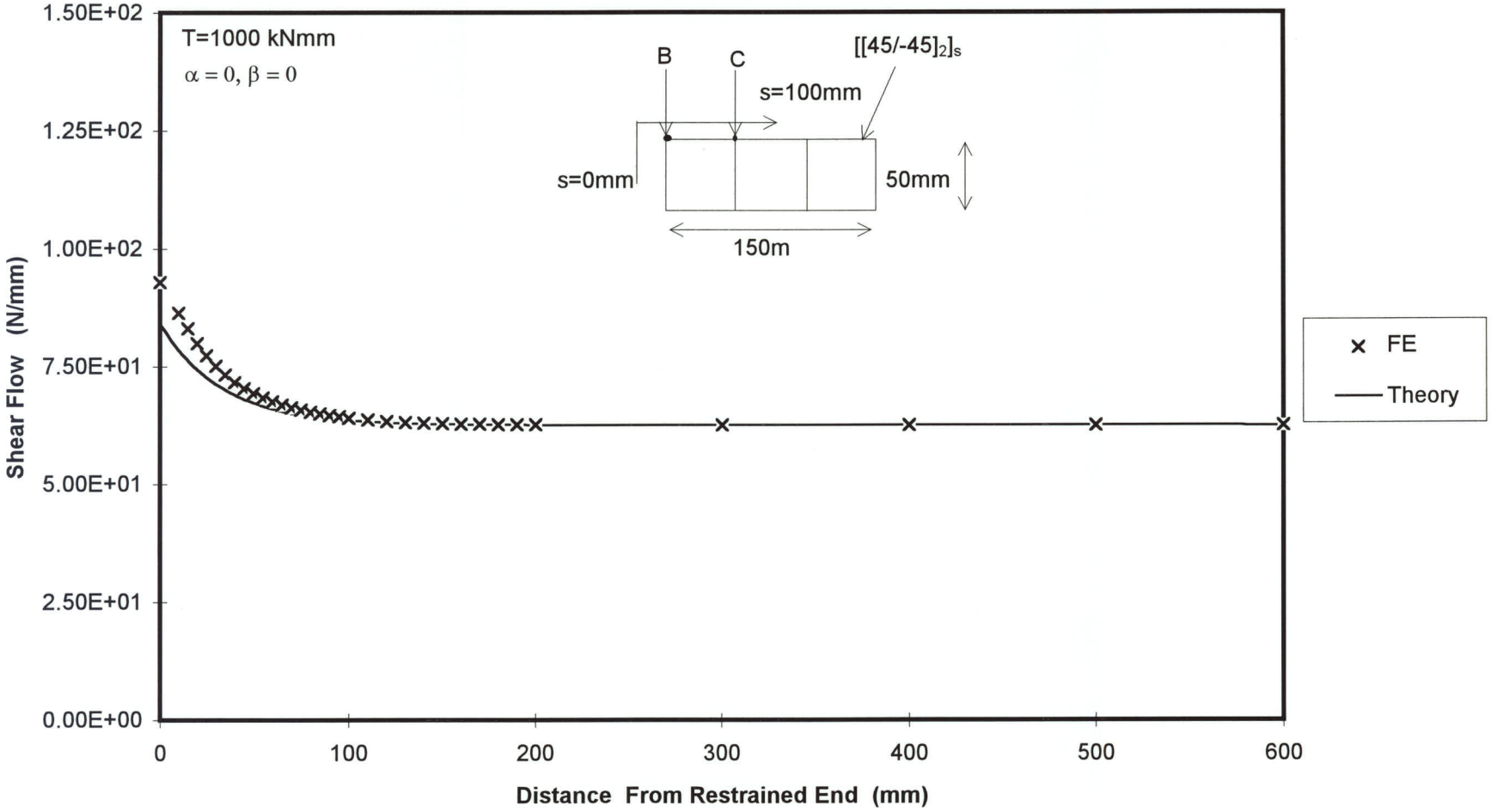

Figure 6.29 SHEAR FLOW ALONG LENGTH OF BOX AT S=0 mm

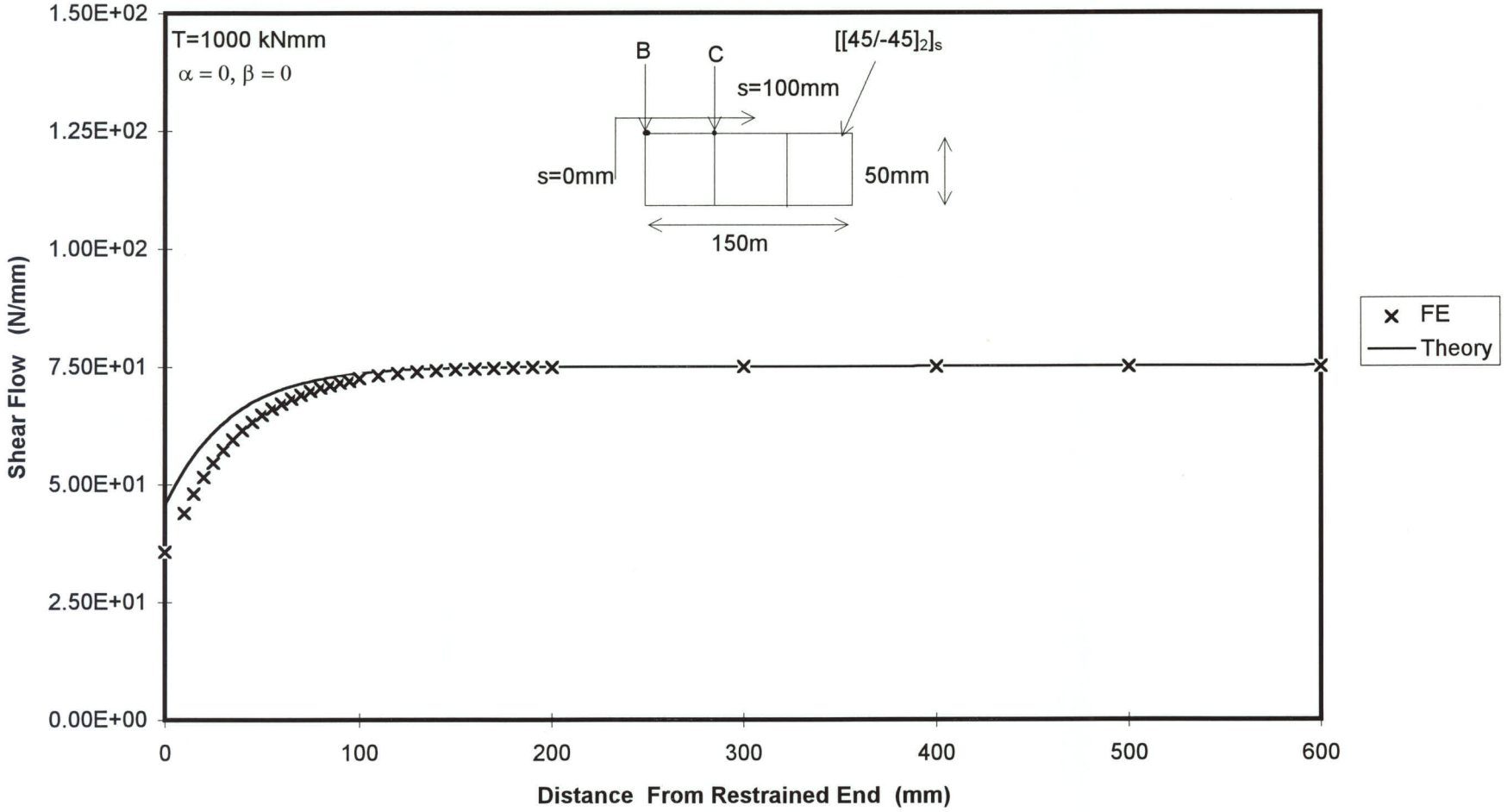

Figure 6.30 SHEAR FLOW ALONG LENGTH OF BOX AT S=100 mm

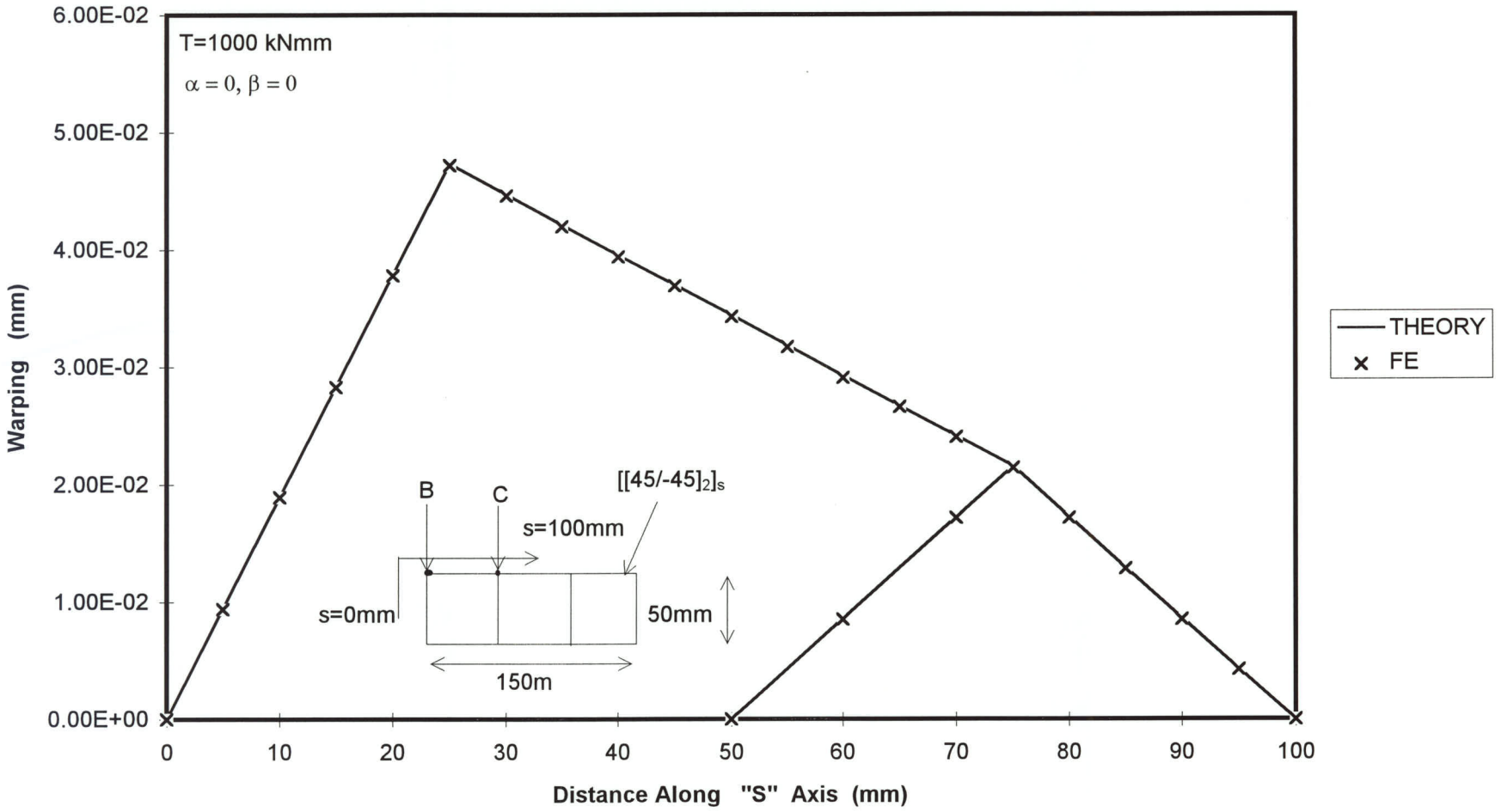

Figure 6.31 WARPING AROUND BOX AT Z=200mm

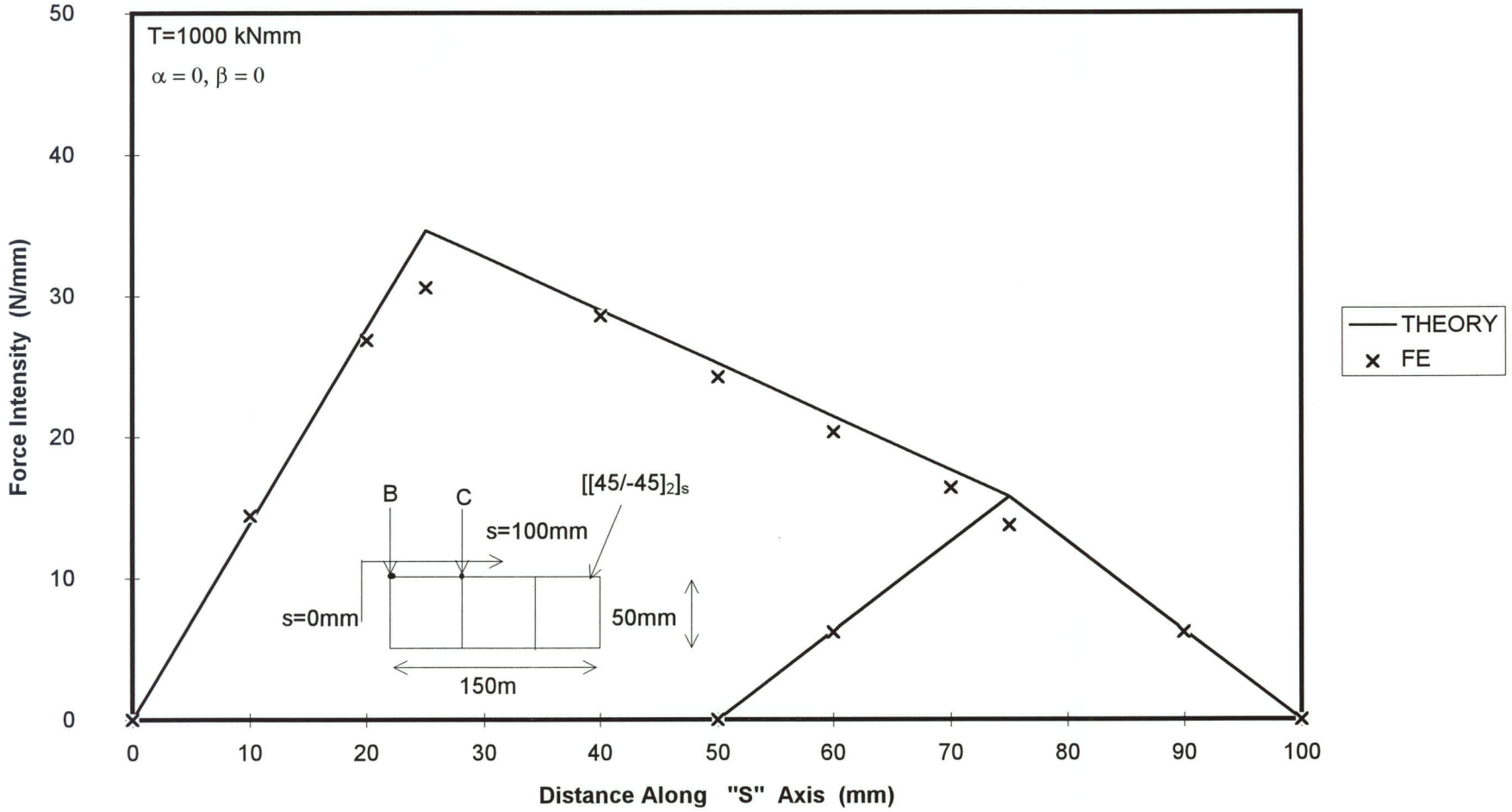

Figure 6.32 FORCE INTENSITY AROUND BOX AT Z=20mm

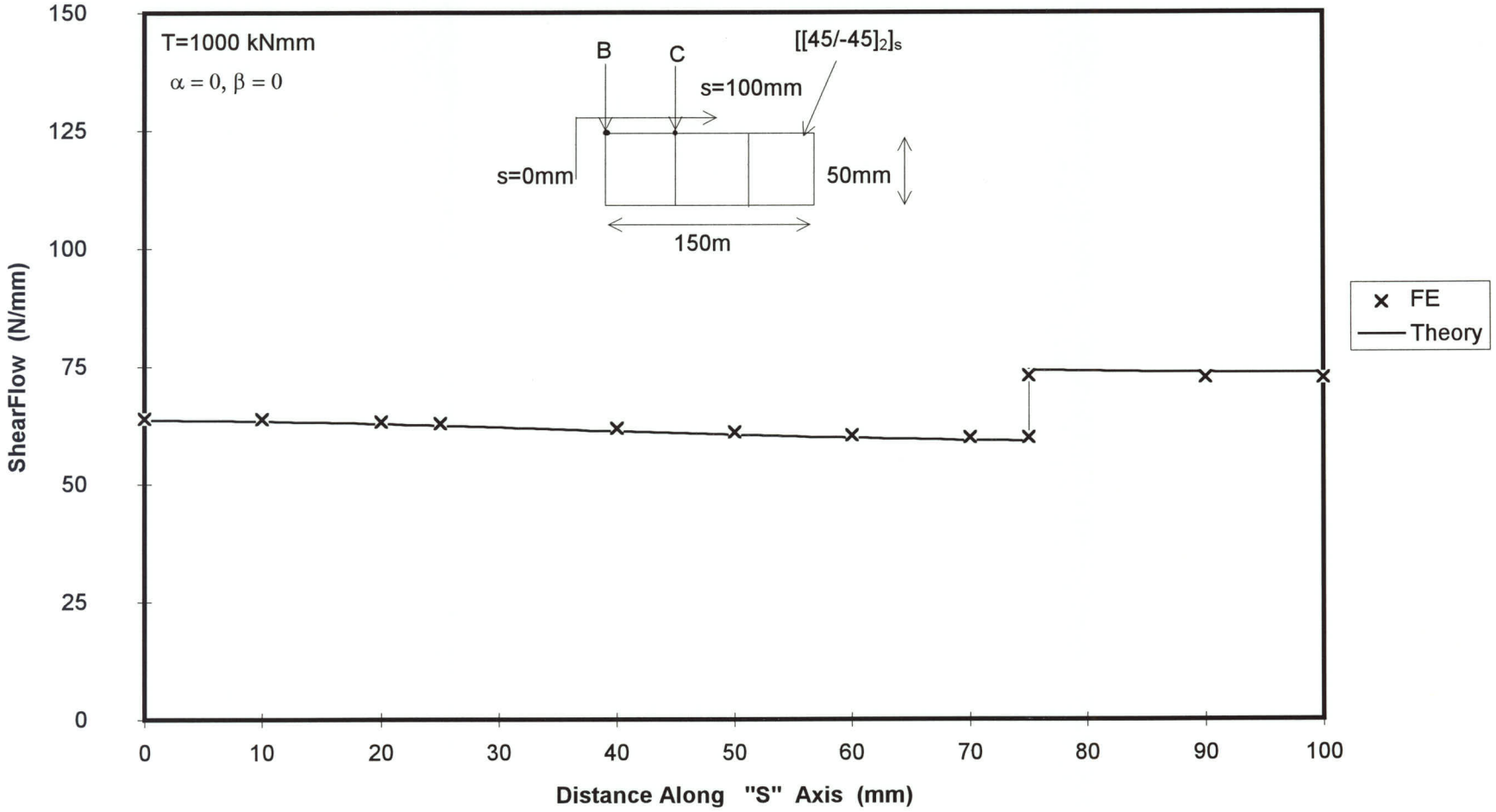

Figure 6.33 SHEAR FLOW AROUND BOX AT Z=100mm

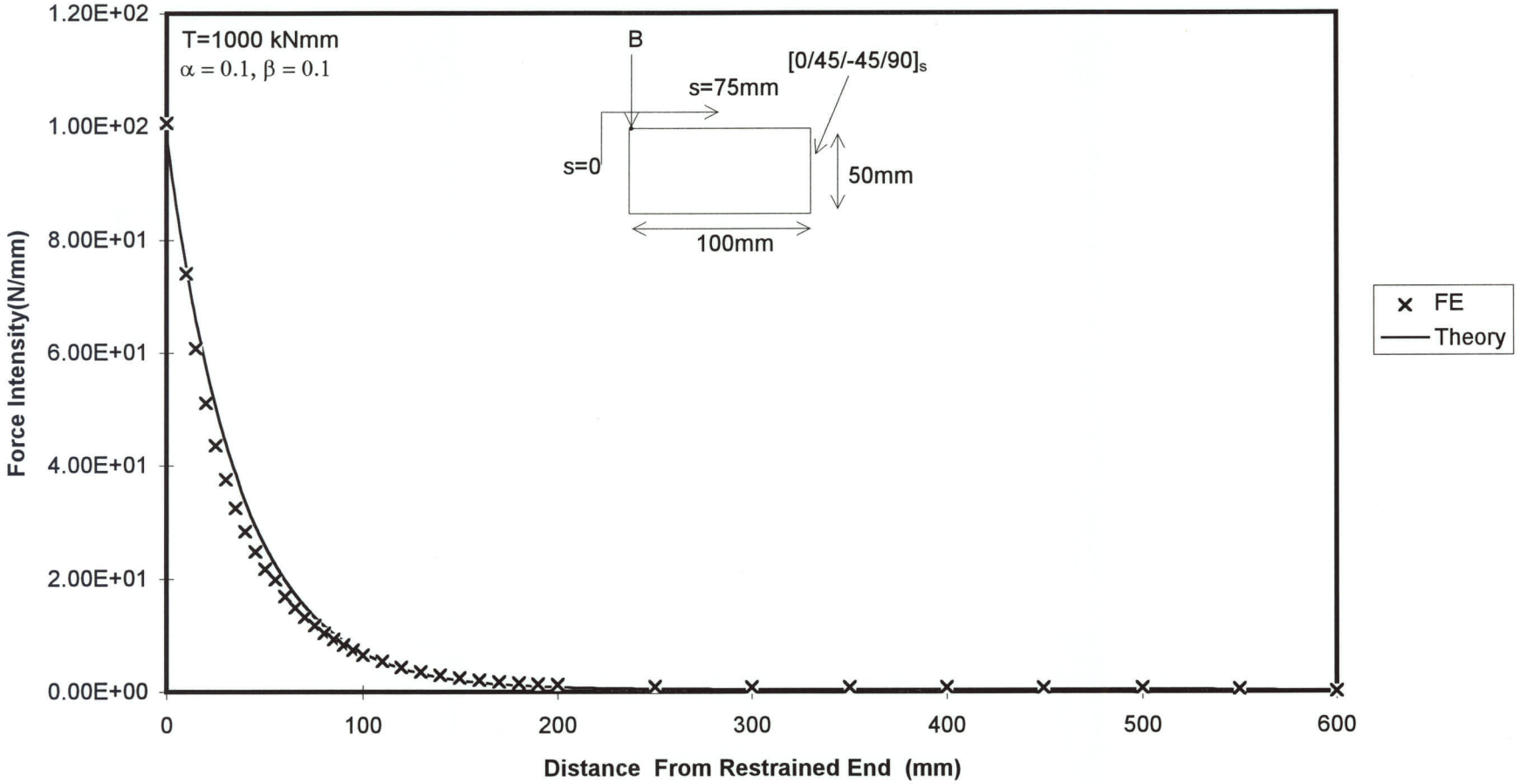

Figure 6.34 FORCE INTENSITY ALONG LENGTH OF TAPERED BOX AT POINT "B"

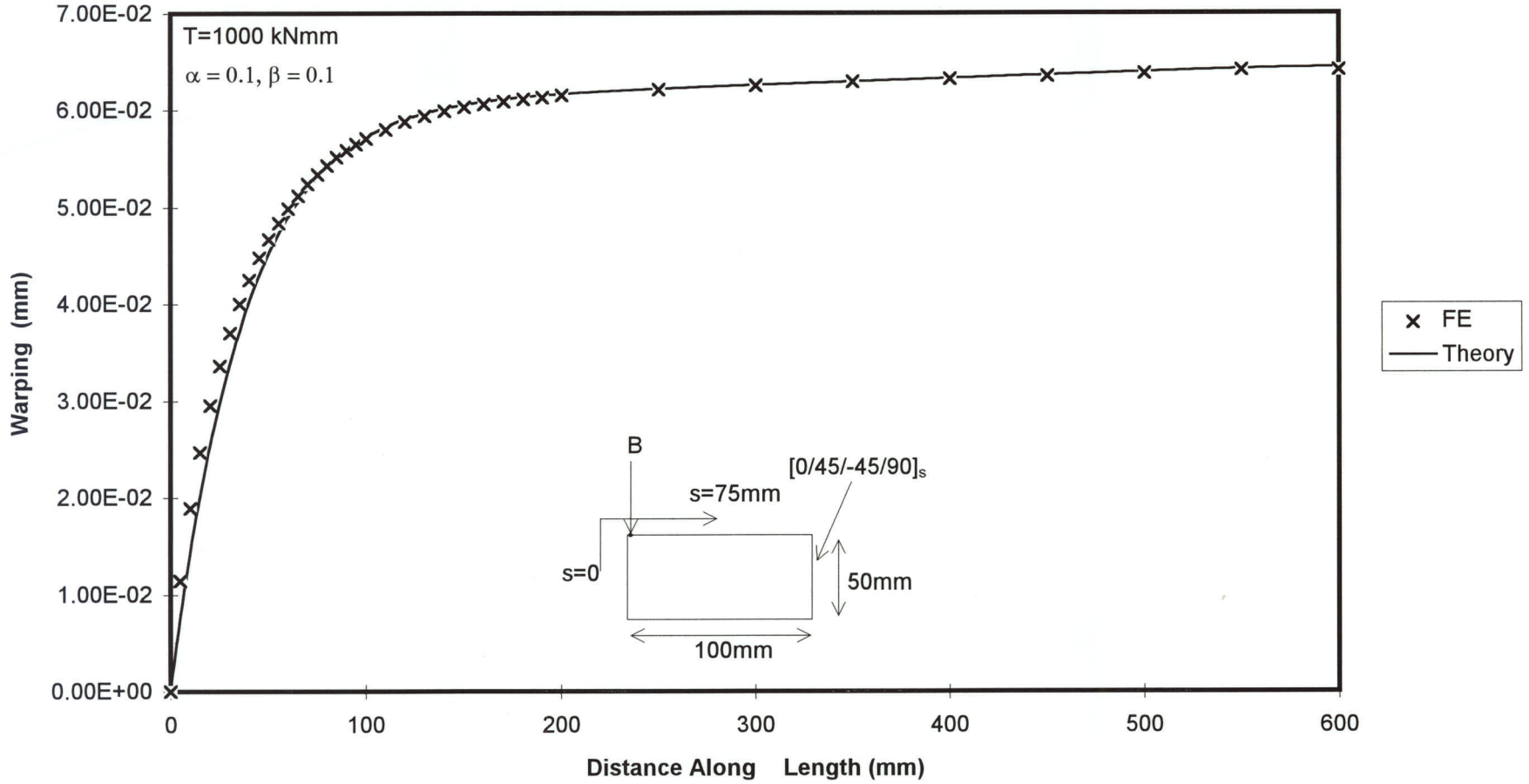

Figure 6.35 WARPING ALONG LENGTH OF TAPERED BOX AT "B"

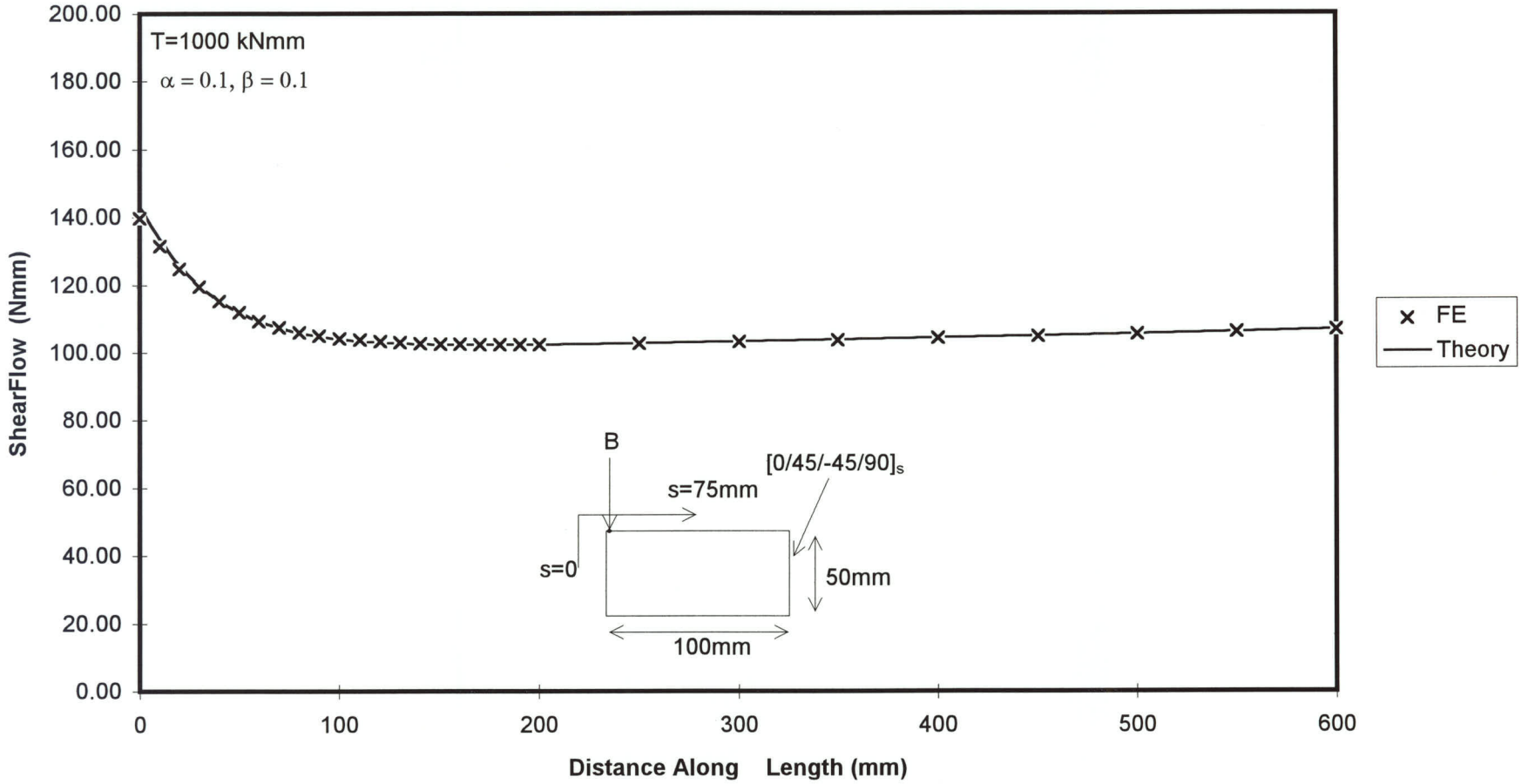

Figure 6.36 SHEAR FLOW ALONG LENGTH OF TAPERED BOX AT S=0 mm

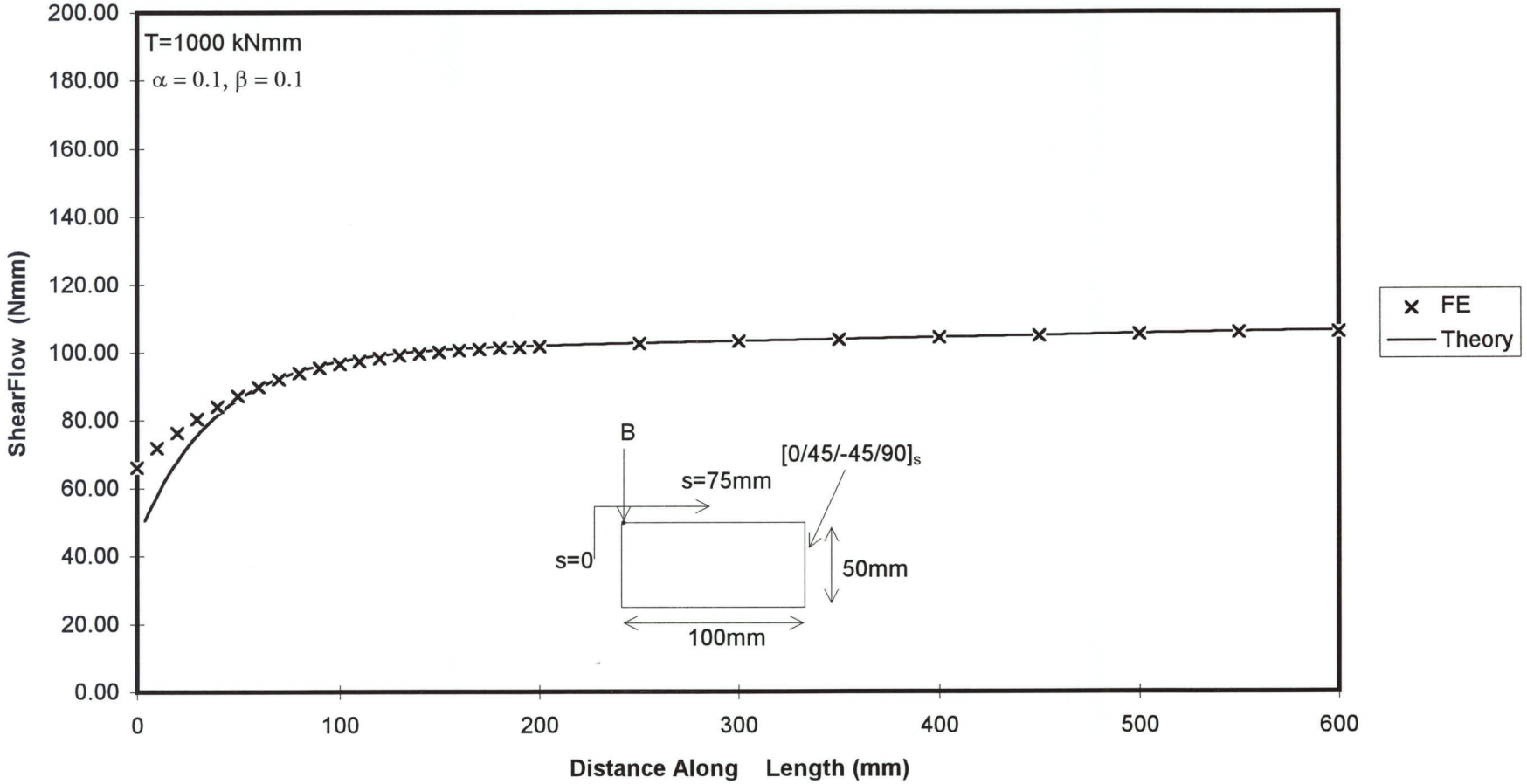

Figure 6.37 SHEAR FLOW ALONG LENGTH OF TAPERED BOX AT S=75 mm

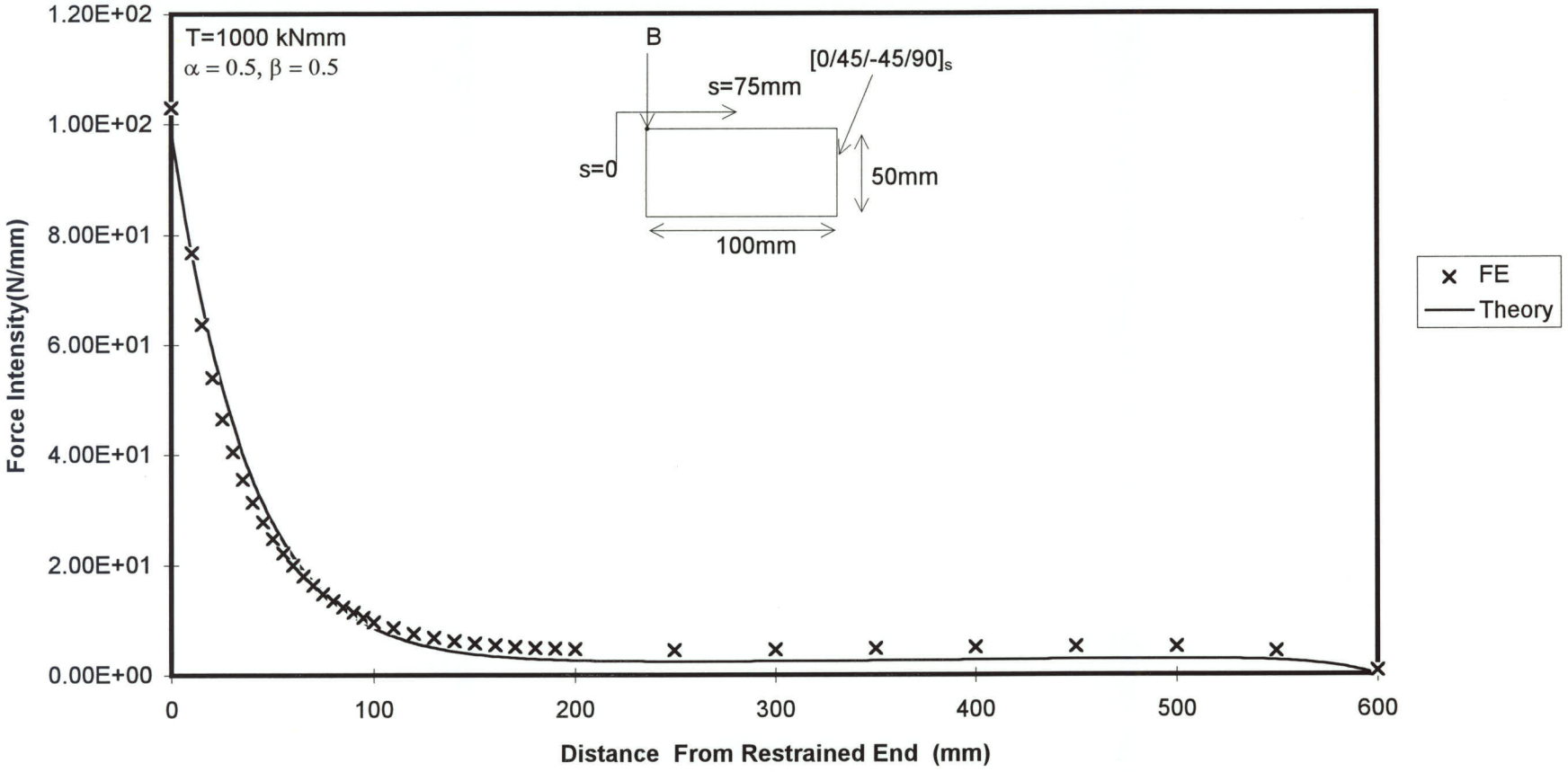

Figure 6.38 FORCE INTENSITY ALONG LENGTH OF TAPERED BOX AT POINT "B"

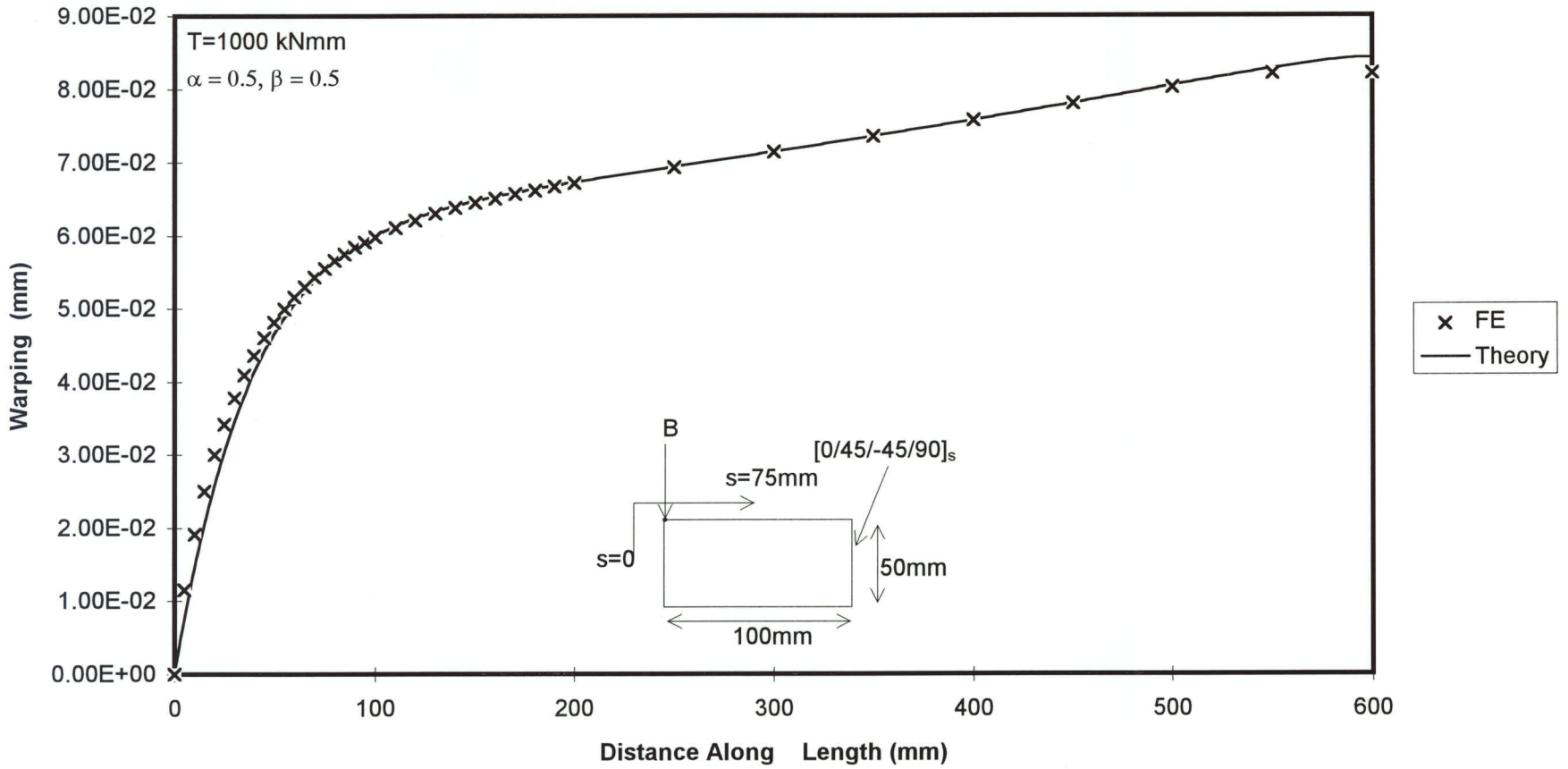

Figure 6.39 WARPING ALONG LENGTH OF TAPERED BOX AT "B"

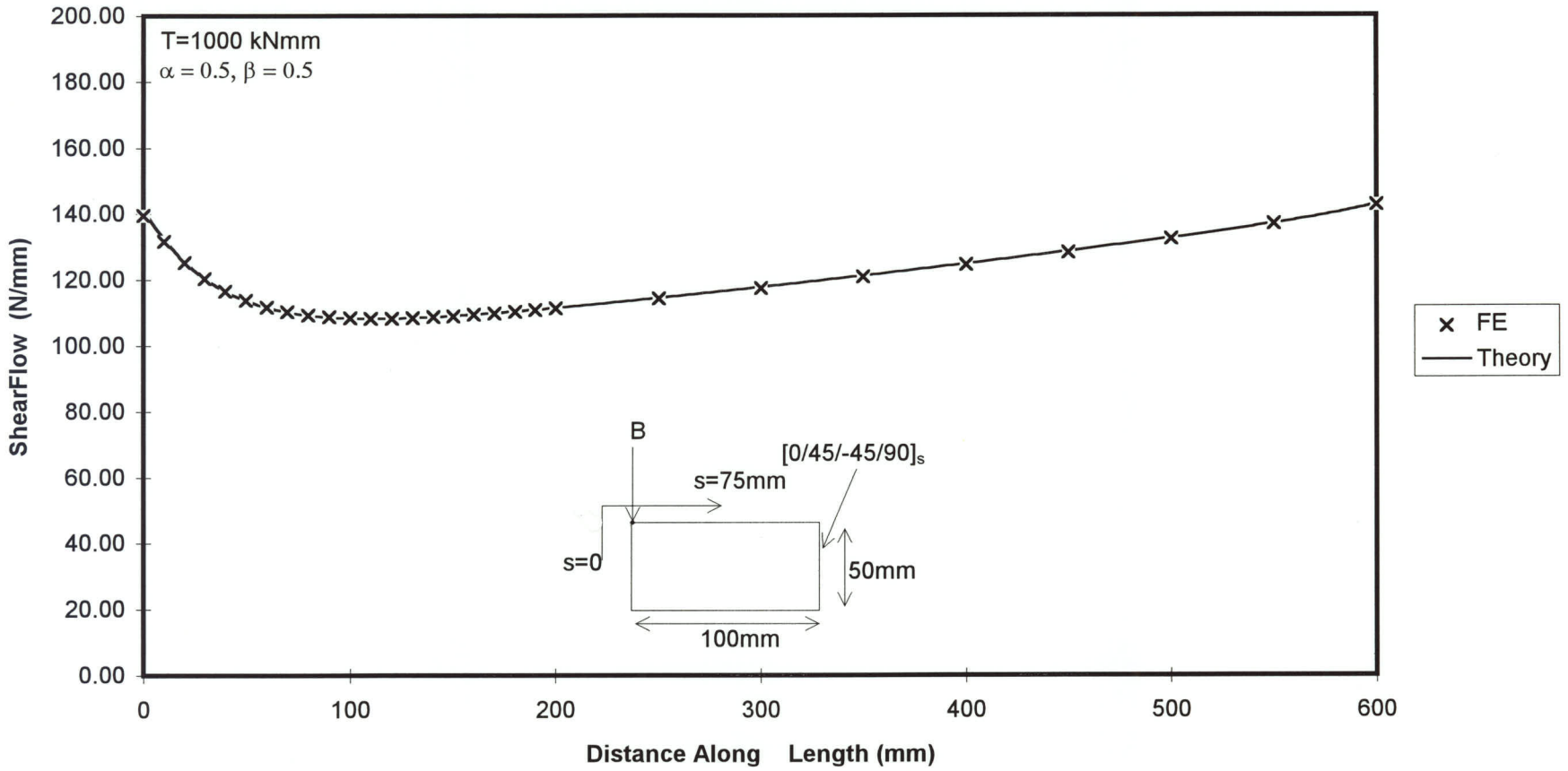

Figure 6.40 SHEAR FLOW ALONG LENGTH OF TAPERED BOX AT S=0 mm

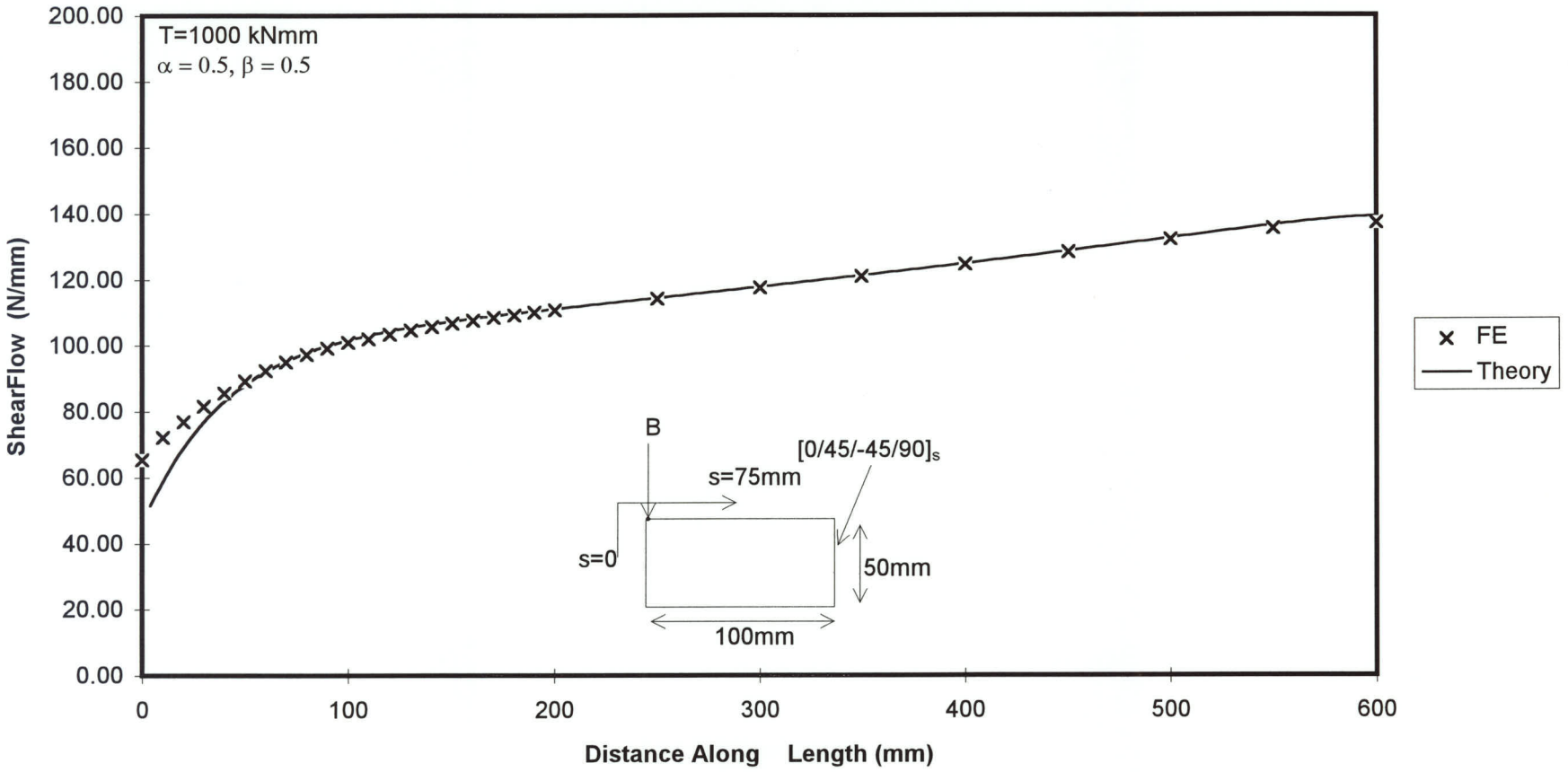

Figure 6.41 SHEAR FLOW ALONG LENGTH OF TAPERED BOX AT S=75 mm

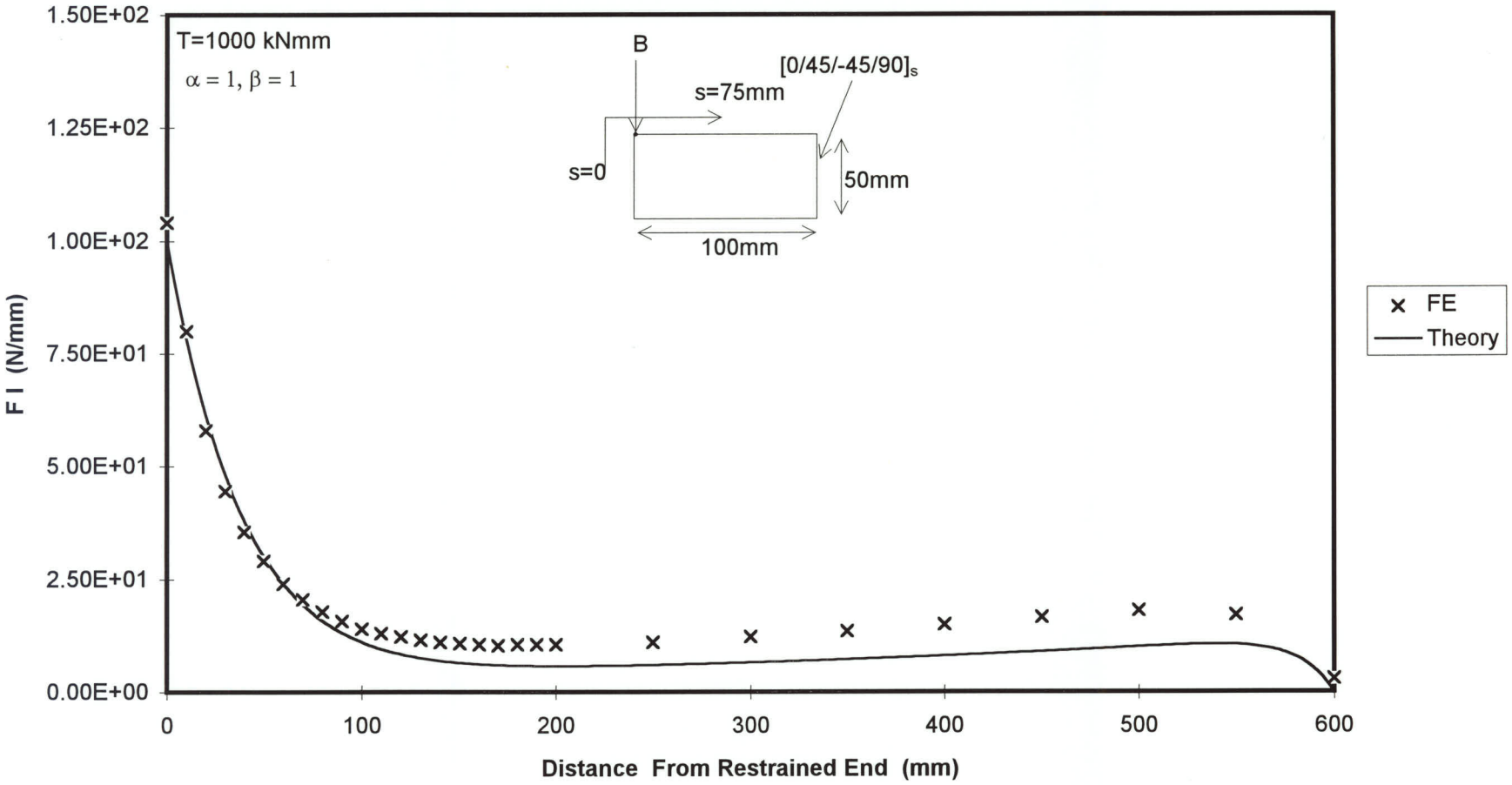

Figure 6.42 FORCE INTENSITY ALONG LENGTH OF TAPERED BOX AT "B"

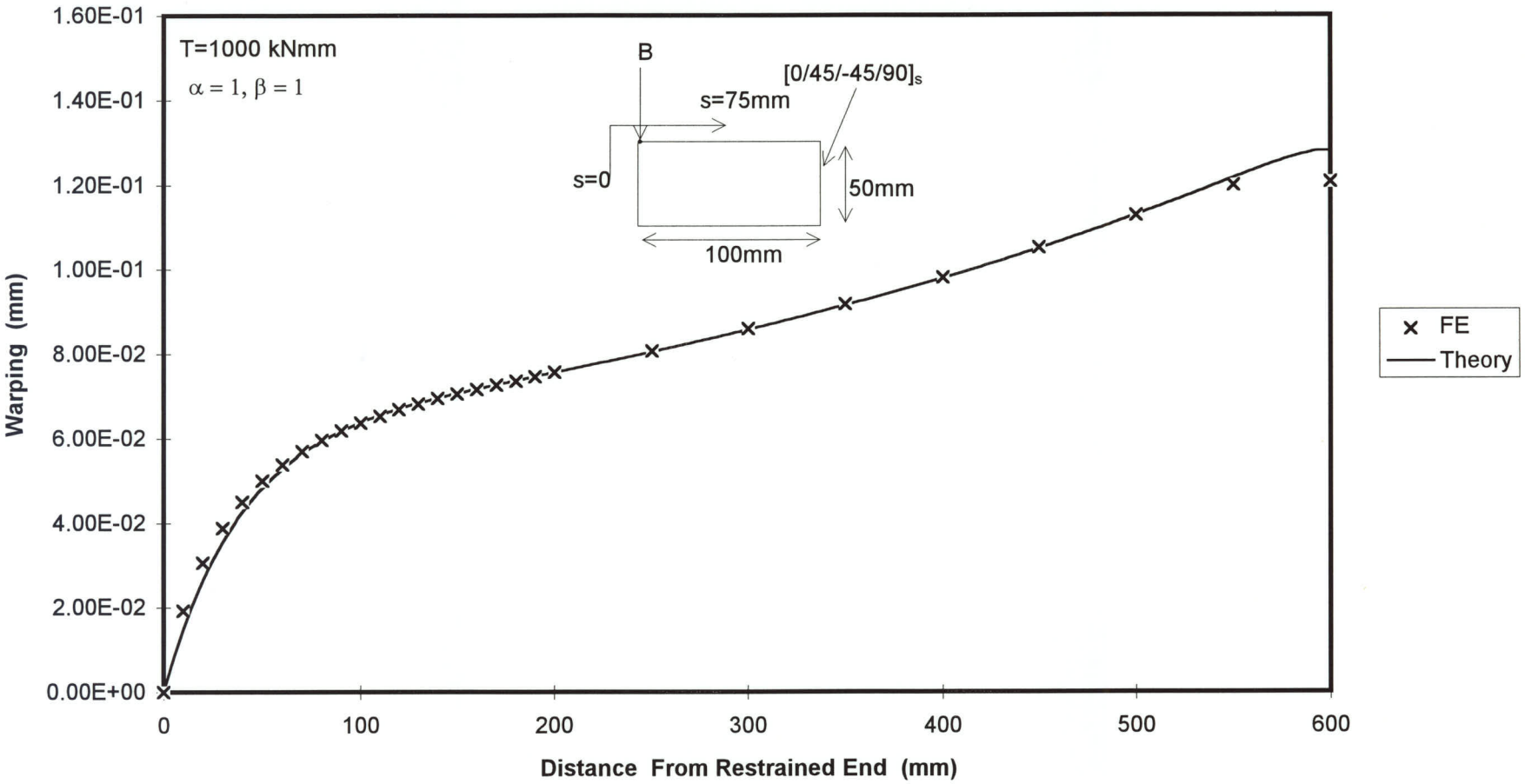

Figure 6.43 WARPING ALONG LENGTH OF TAPERED BOX AT POINT "B"

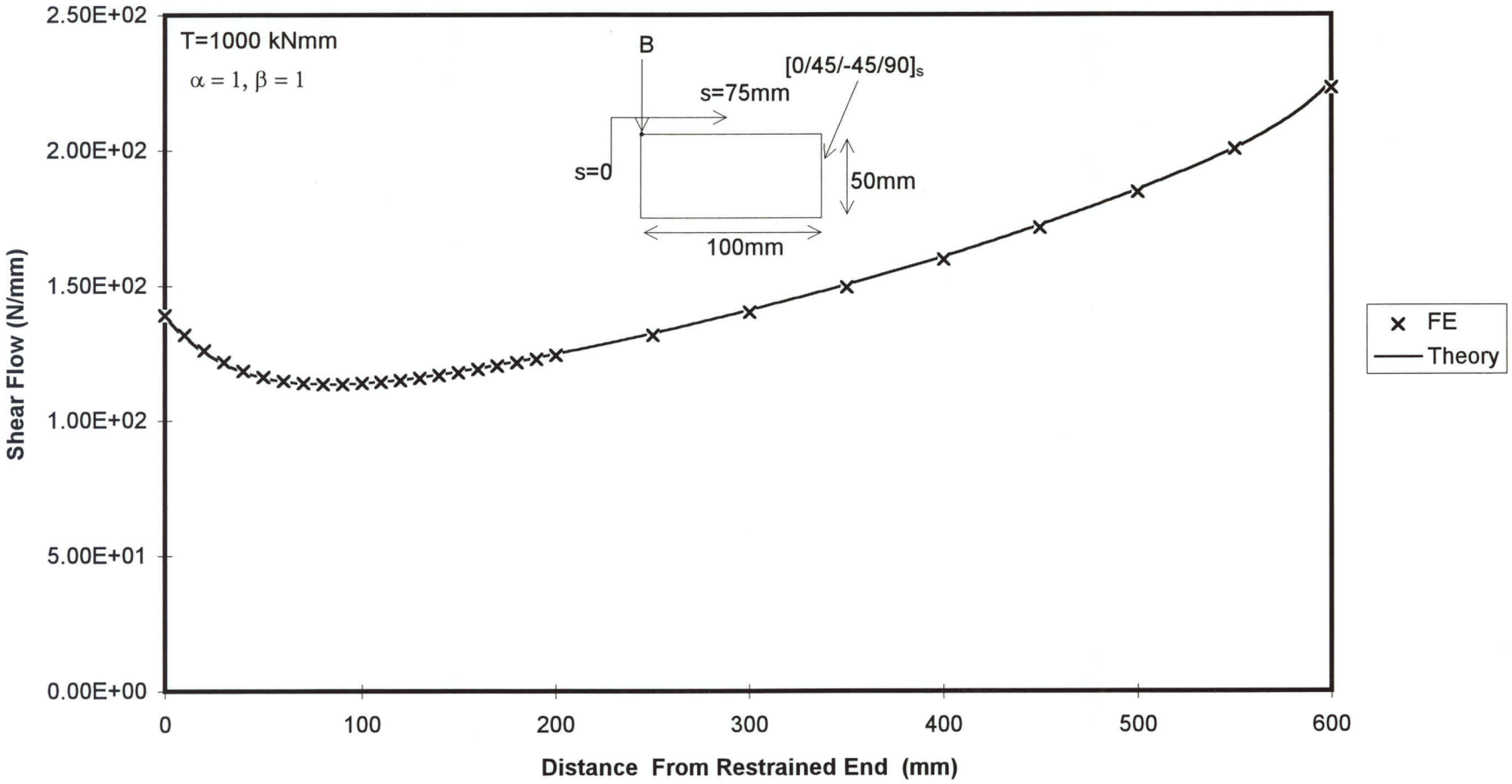

Figure 6.44 SHEAR FLOW ALONG LENGTH OF TAPERED BOX AT S=0

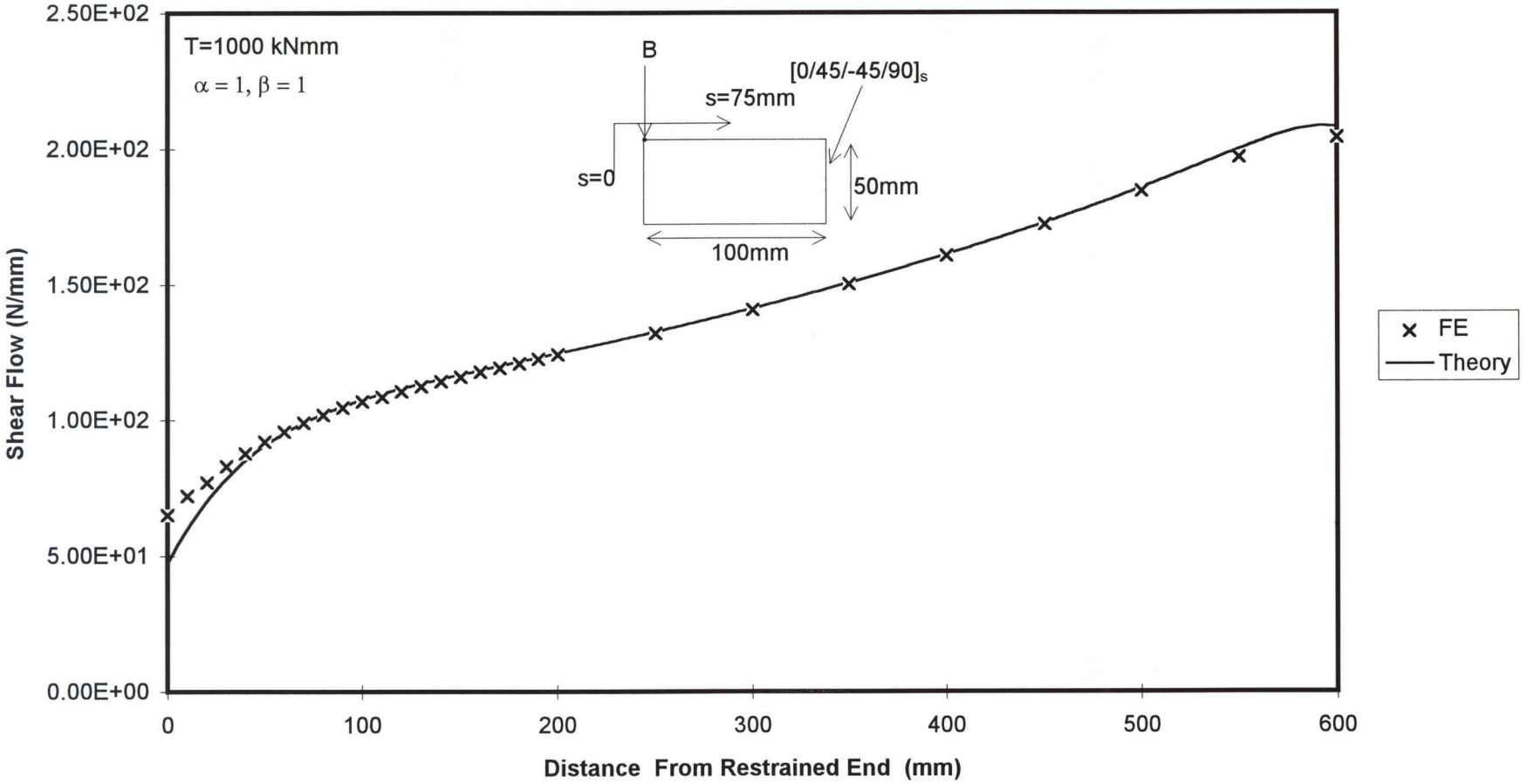

Figure 6.45 SHEAR FLOW ALONG LENGTH OF TAPERED BOX AT S=75

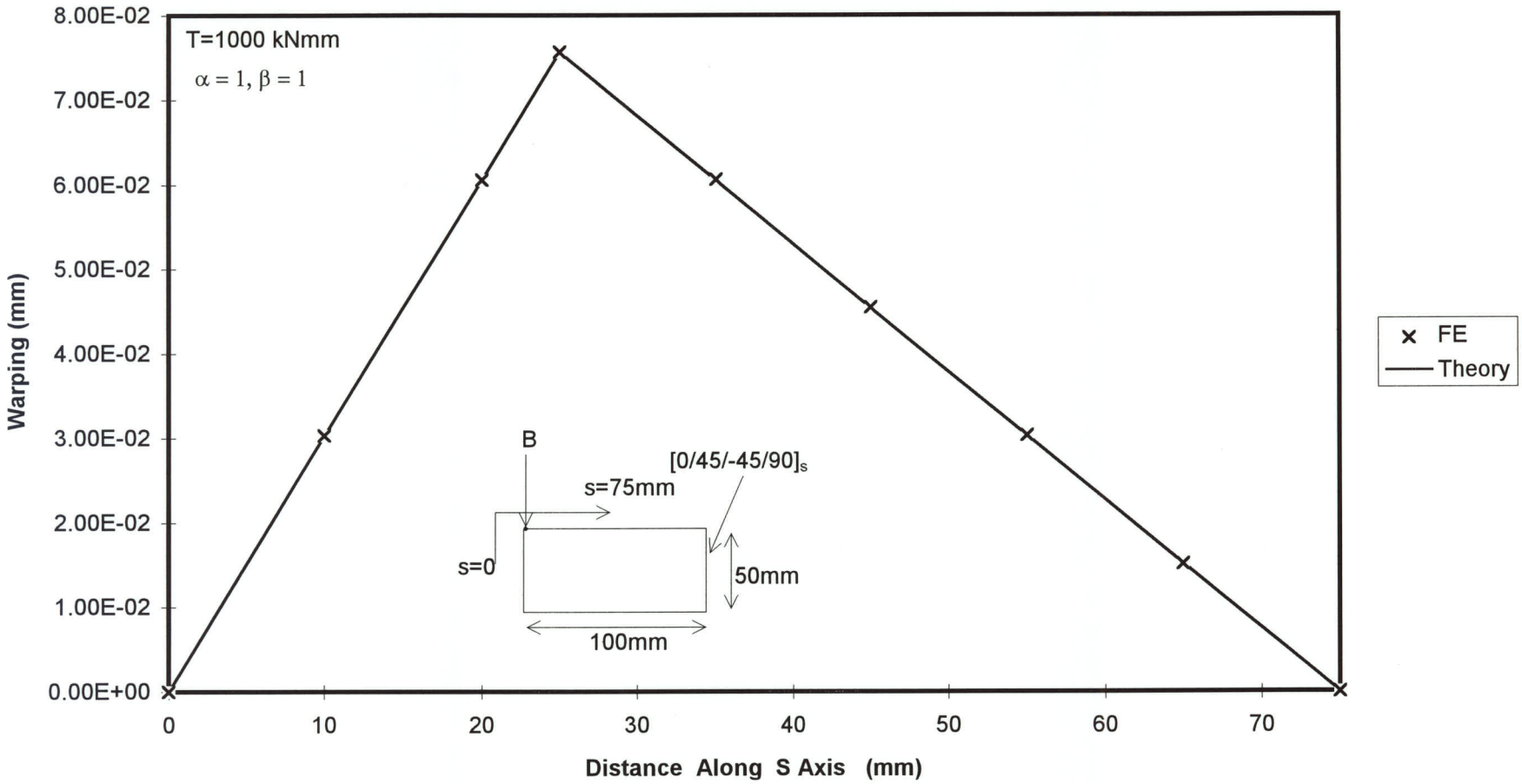

Figure 6.46 WARPING AROUND TAPERED BOX AT Z = 200 mm

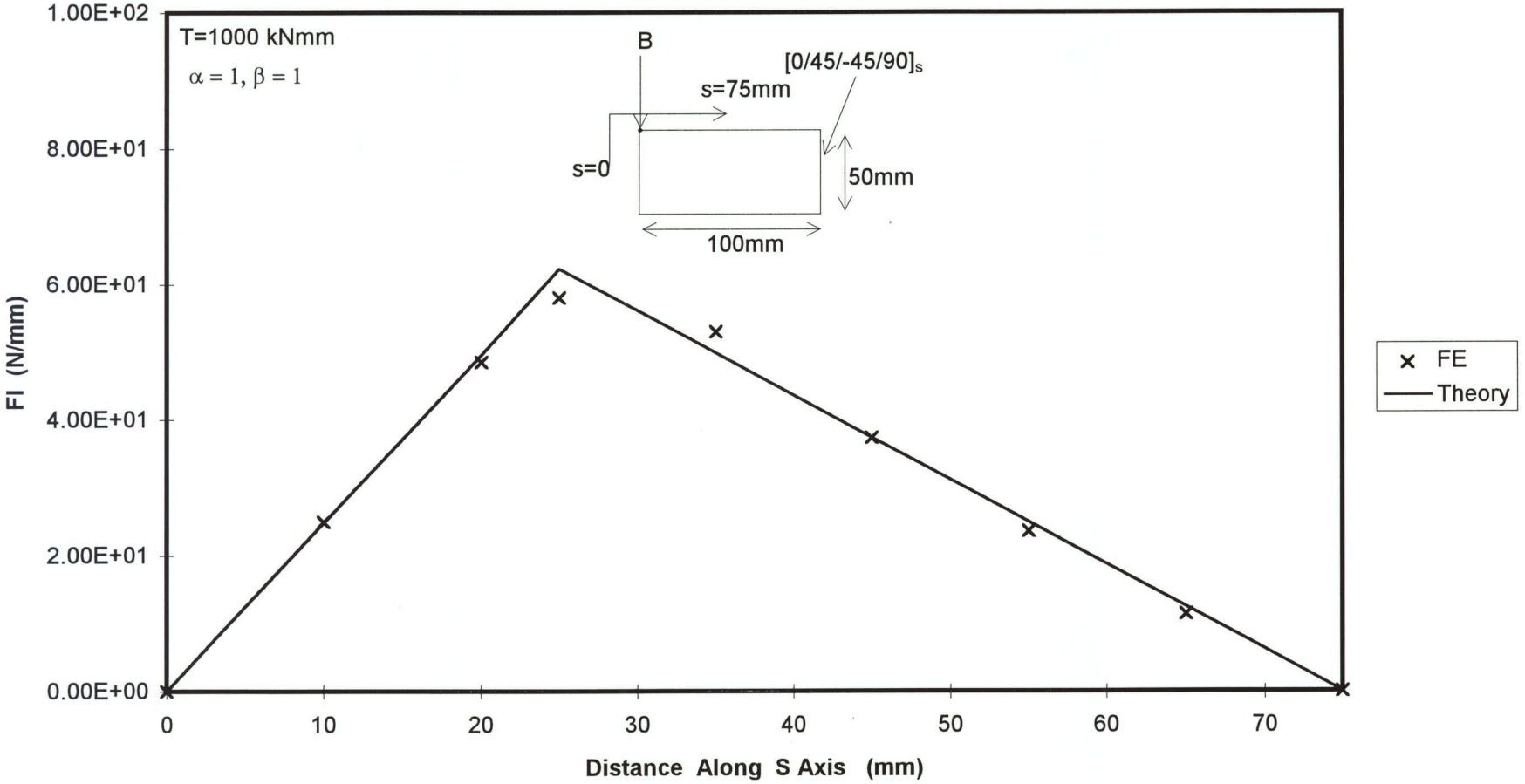

Figure 6.47 F I AROUND TAPERED BOX AT Z = 20mm

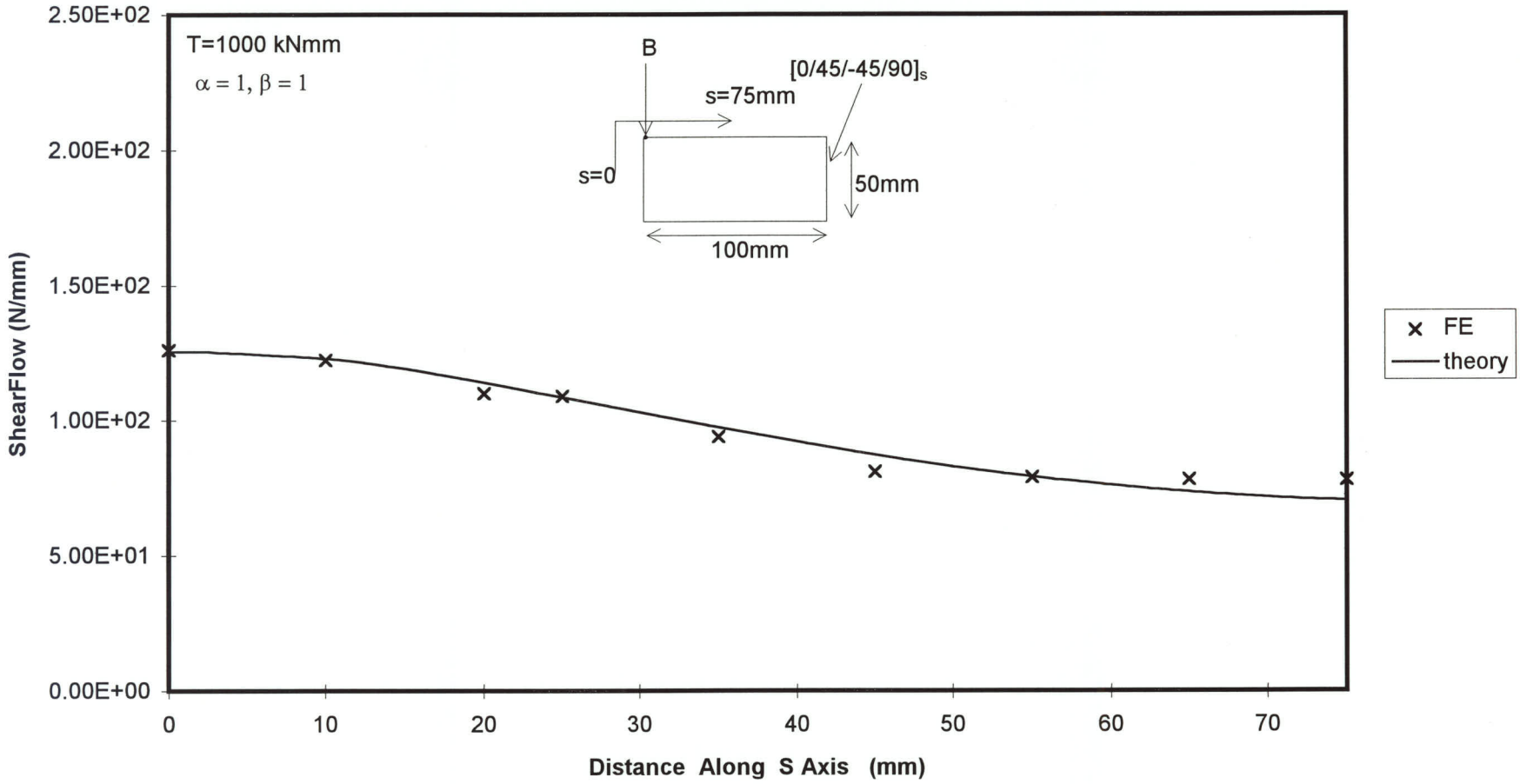

Figure 6.48 TOTAL SHEAR FLOW AROUND TAPERED BOX AT Z = 20 mm

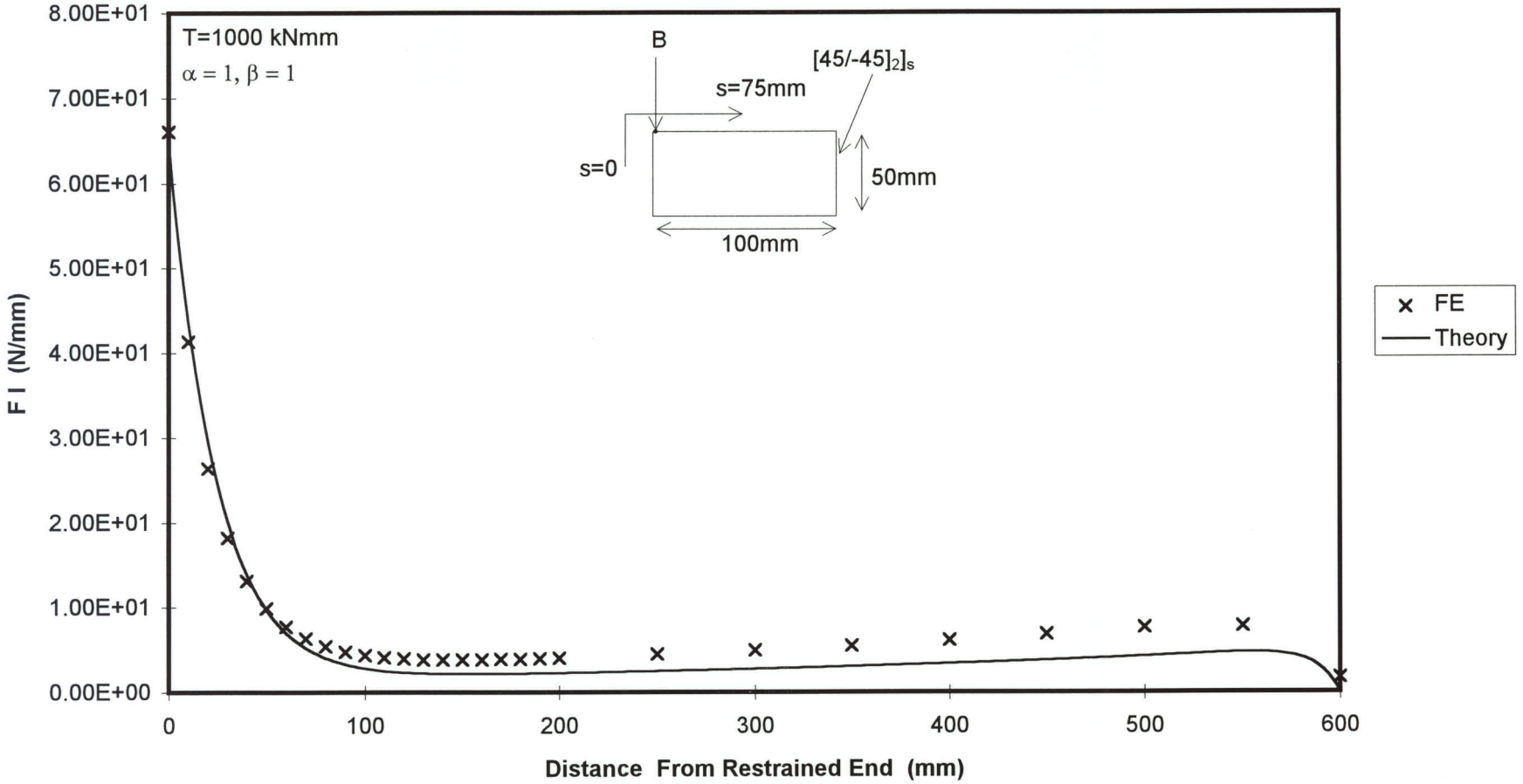

Figure 6.49 FORCE INTENSITY ALONG LENGTH OF TAPERED BOX AT "B"

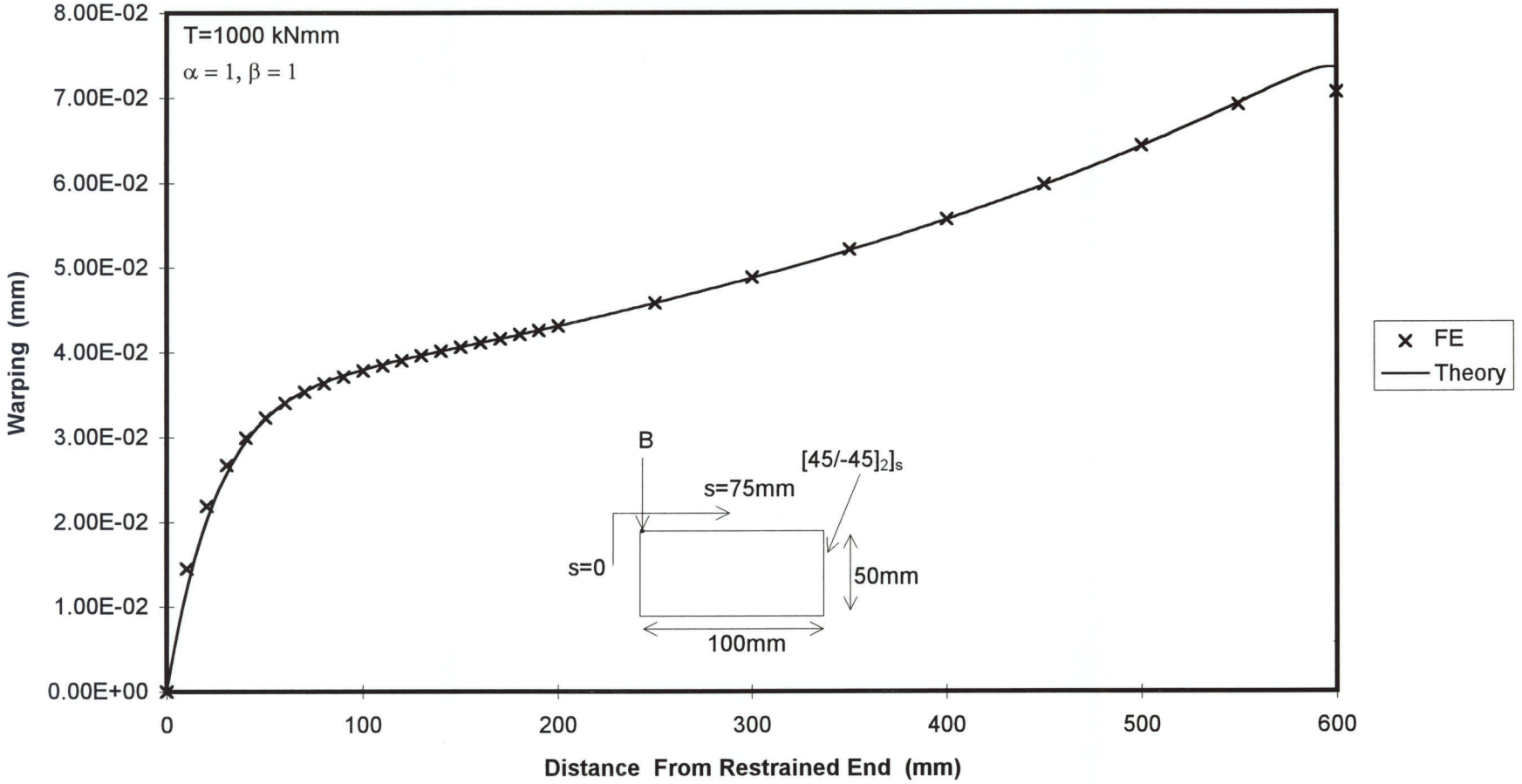

Figure 6.50 WARPING ALONG LENGTH OF TAPERED BOX AT POINT "B"

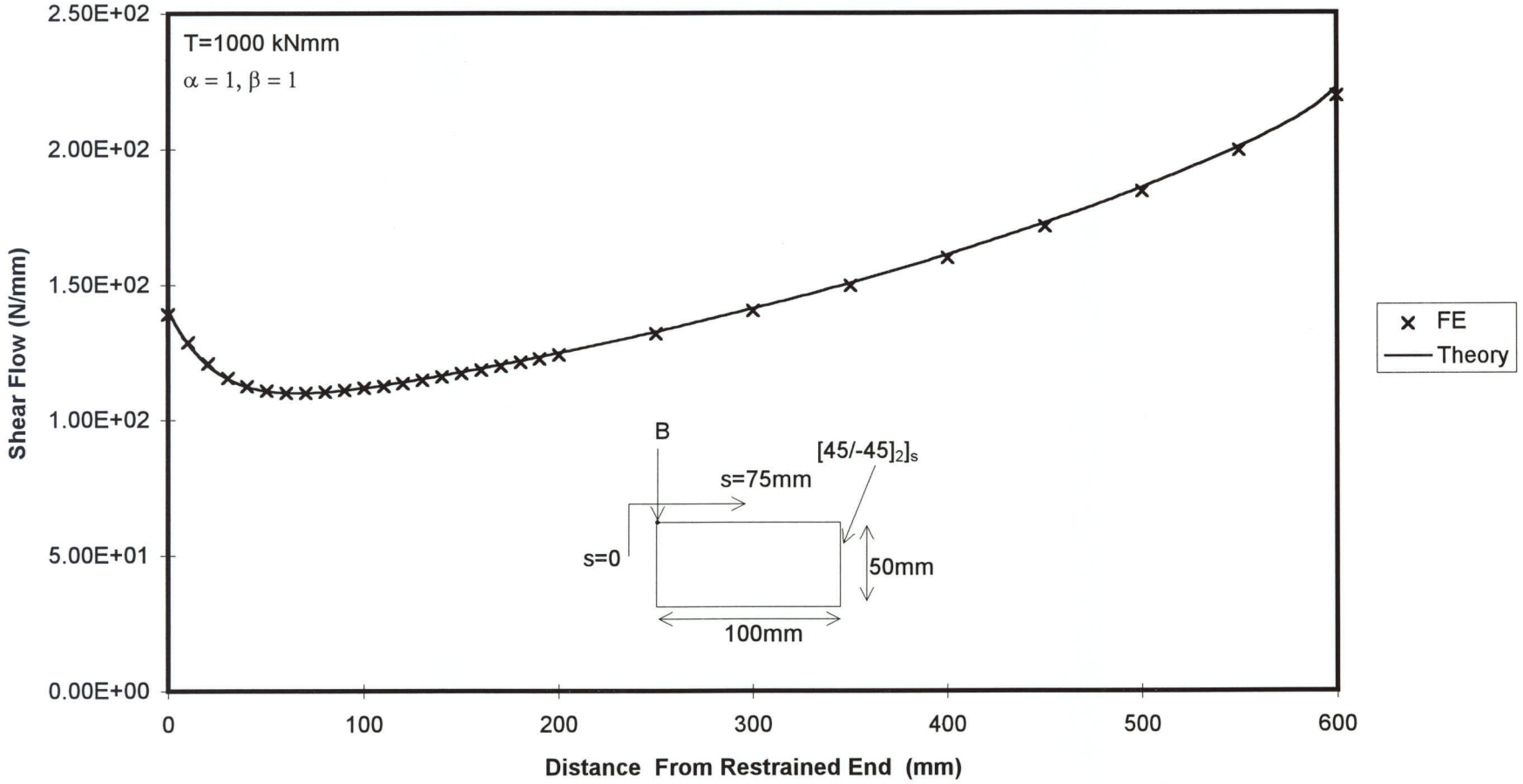

Figure 6.51 SHEAR FLOW ALONG LENGTH OF TAPERED BOX AT S=0

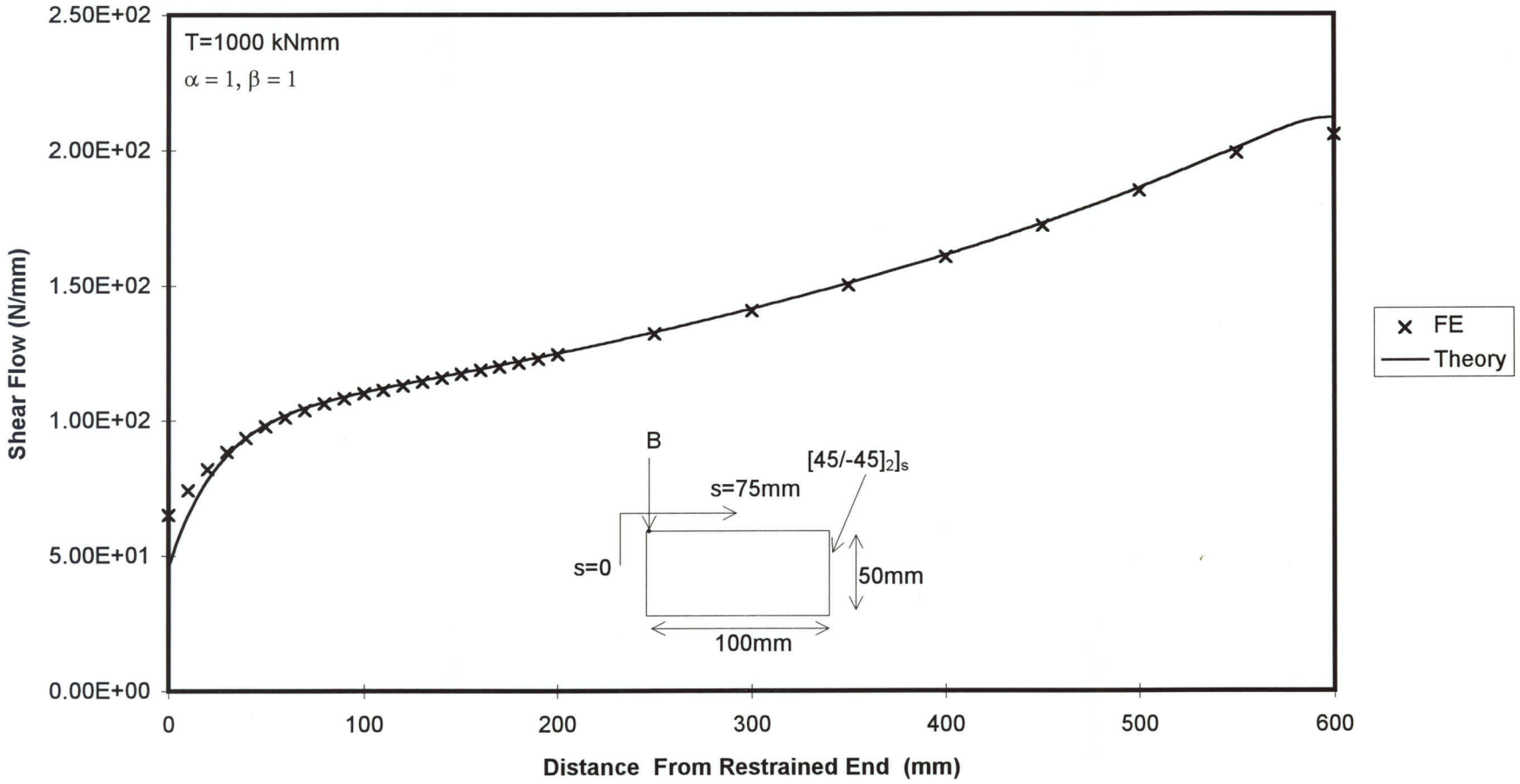

Figure 6.52 SHEAR FLOW ALONG LENGTH OF TAPERED BOX AT S=75

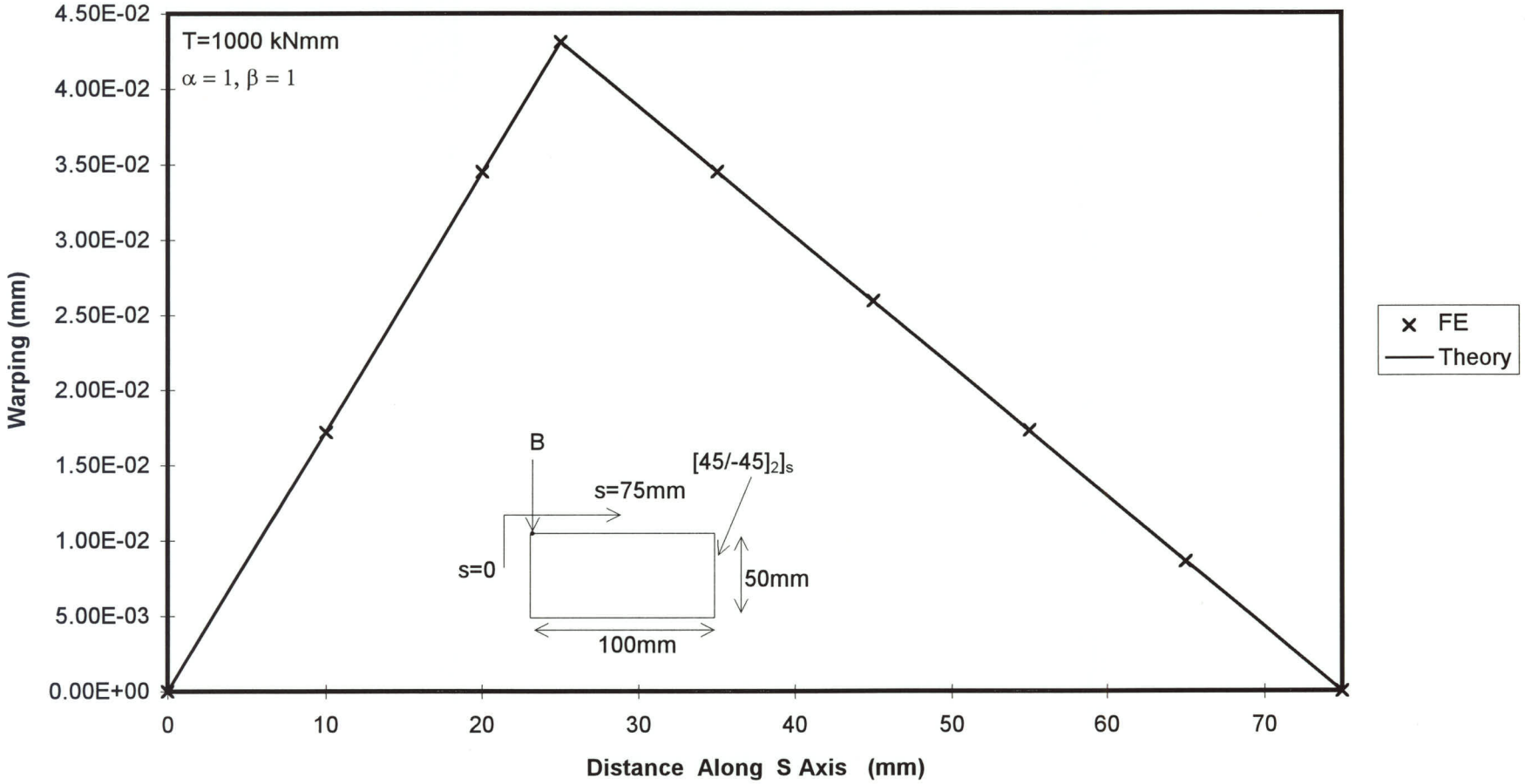

Figure 6.53 WARPING AROUND TAPERED BOX AT Z = 200 mm

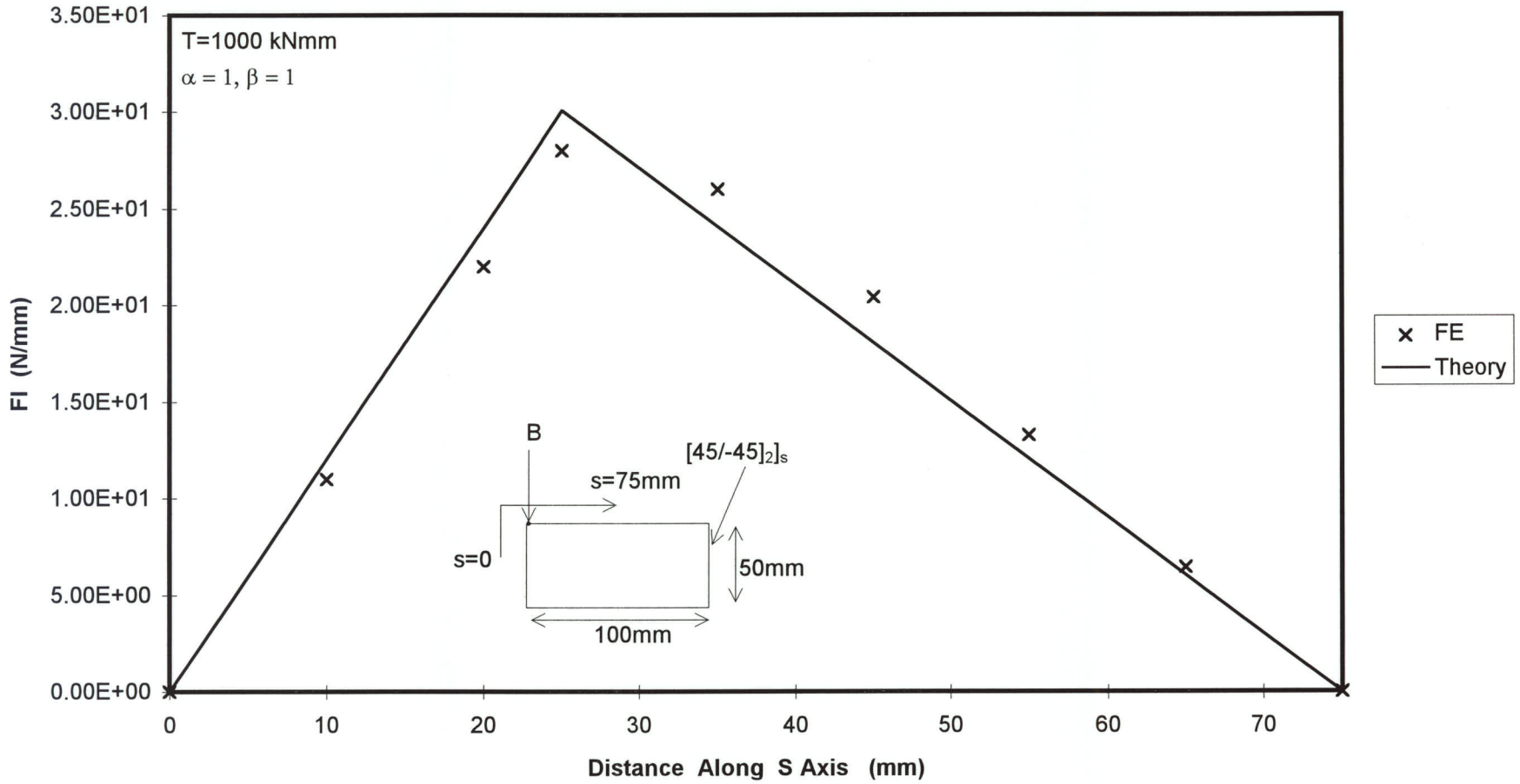

Figure 6.54 F I AROUND TAPERED BOX AT Z = 20mm

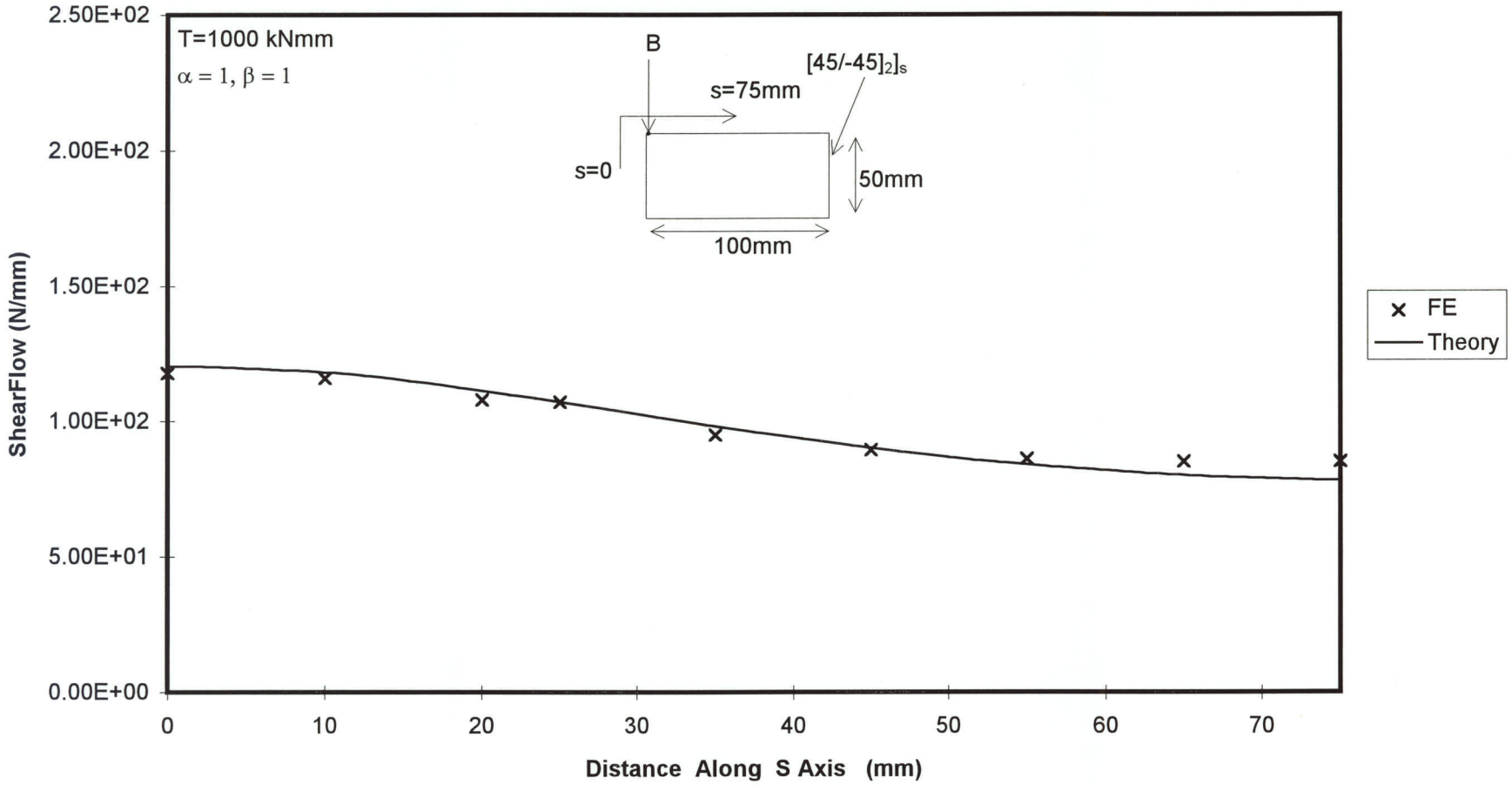

Figure 6.55 TOTAL SHEAR FLOW AROUND TAPERED BOX AT Z = 20 mm

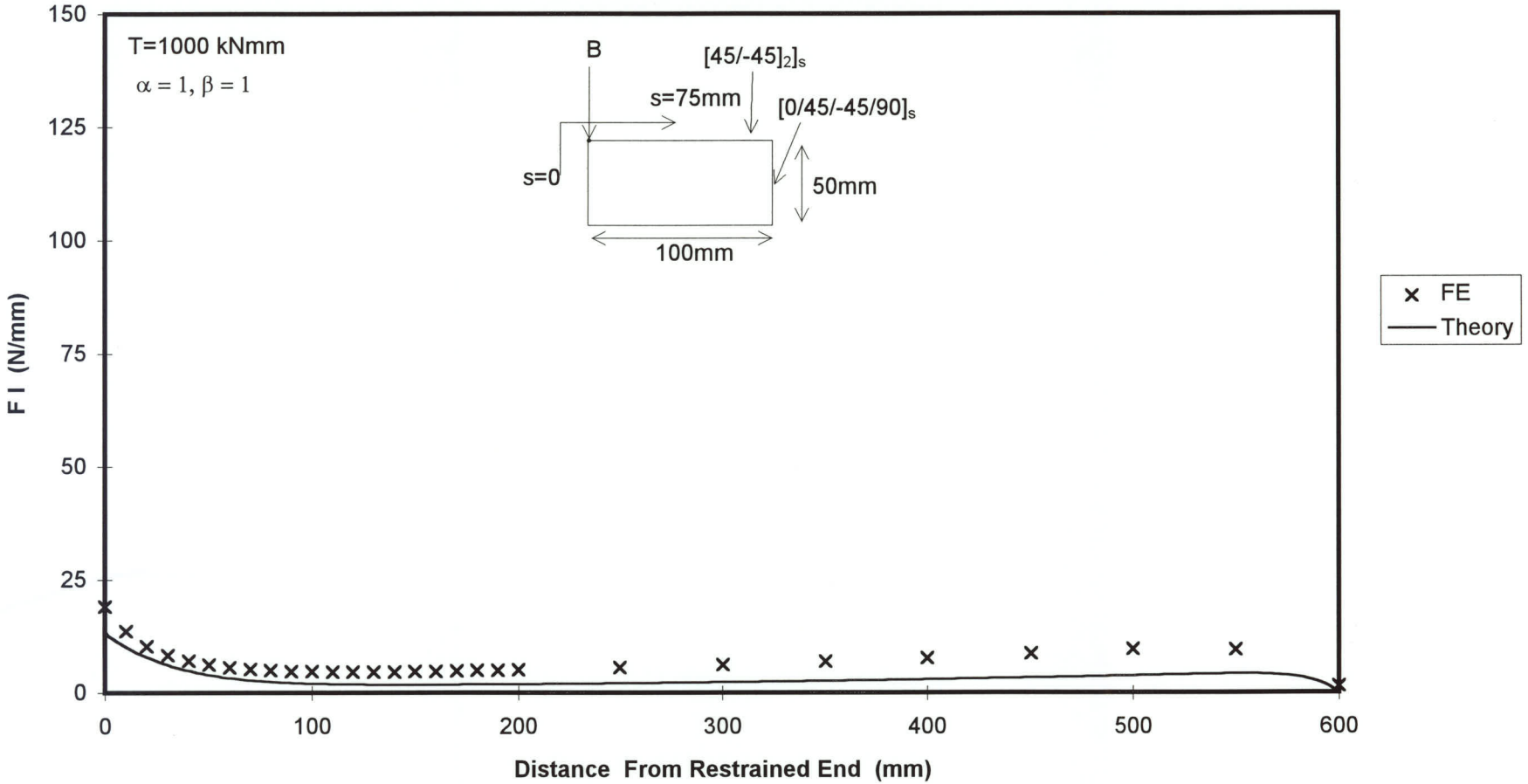

Figure 6.56 FORCE INTENSITY ALONG LENGTH OF TAPERED BOX AT "B"

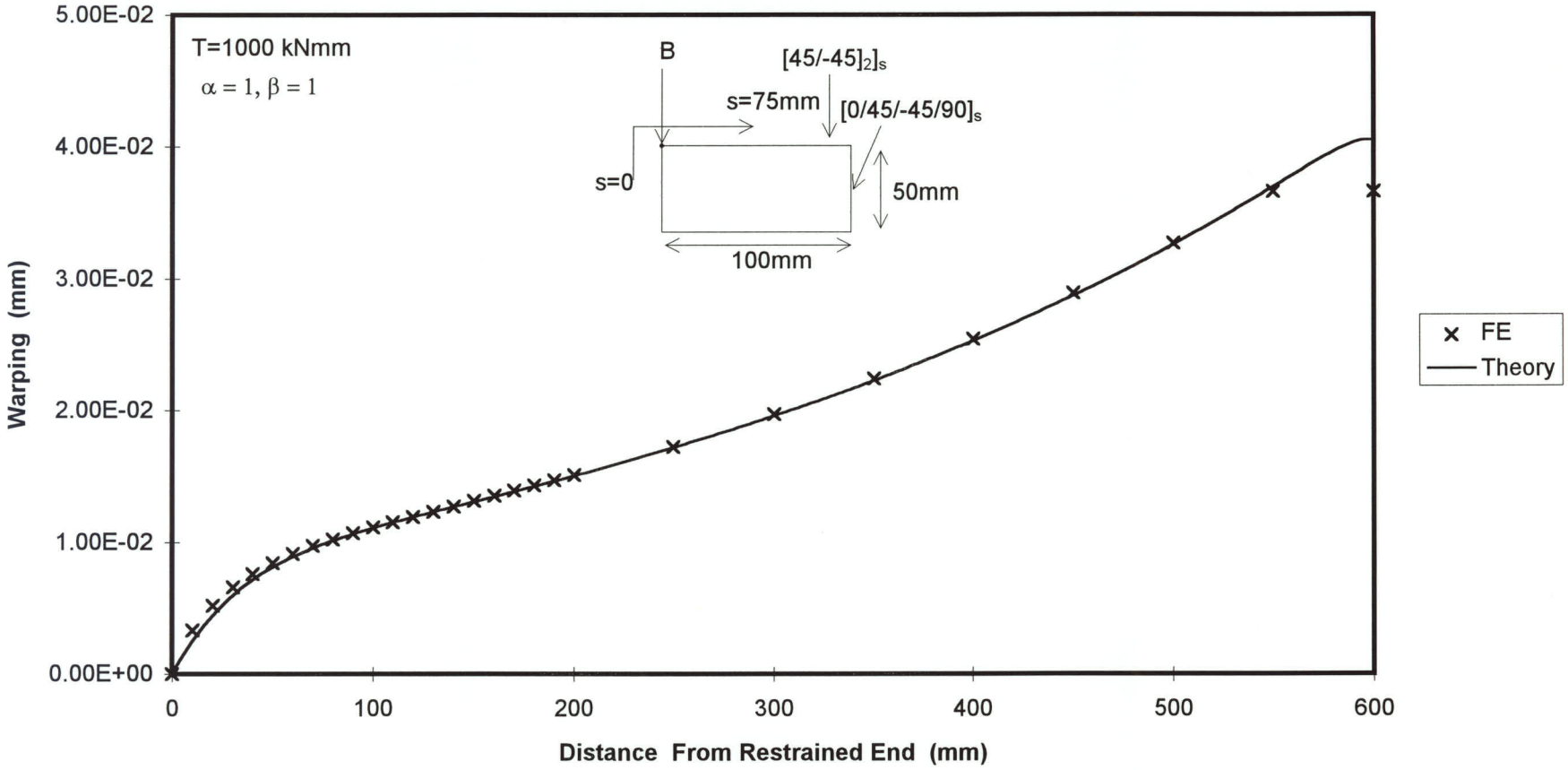

Figure 6.57 WARPING ALONG LENGTH OF TAPERED BOX AT POINT "B"

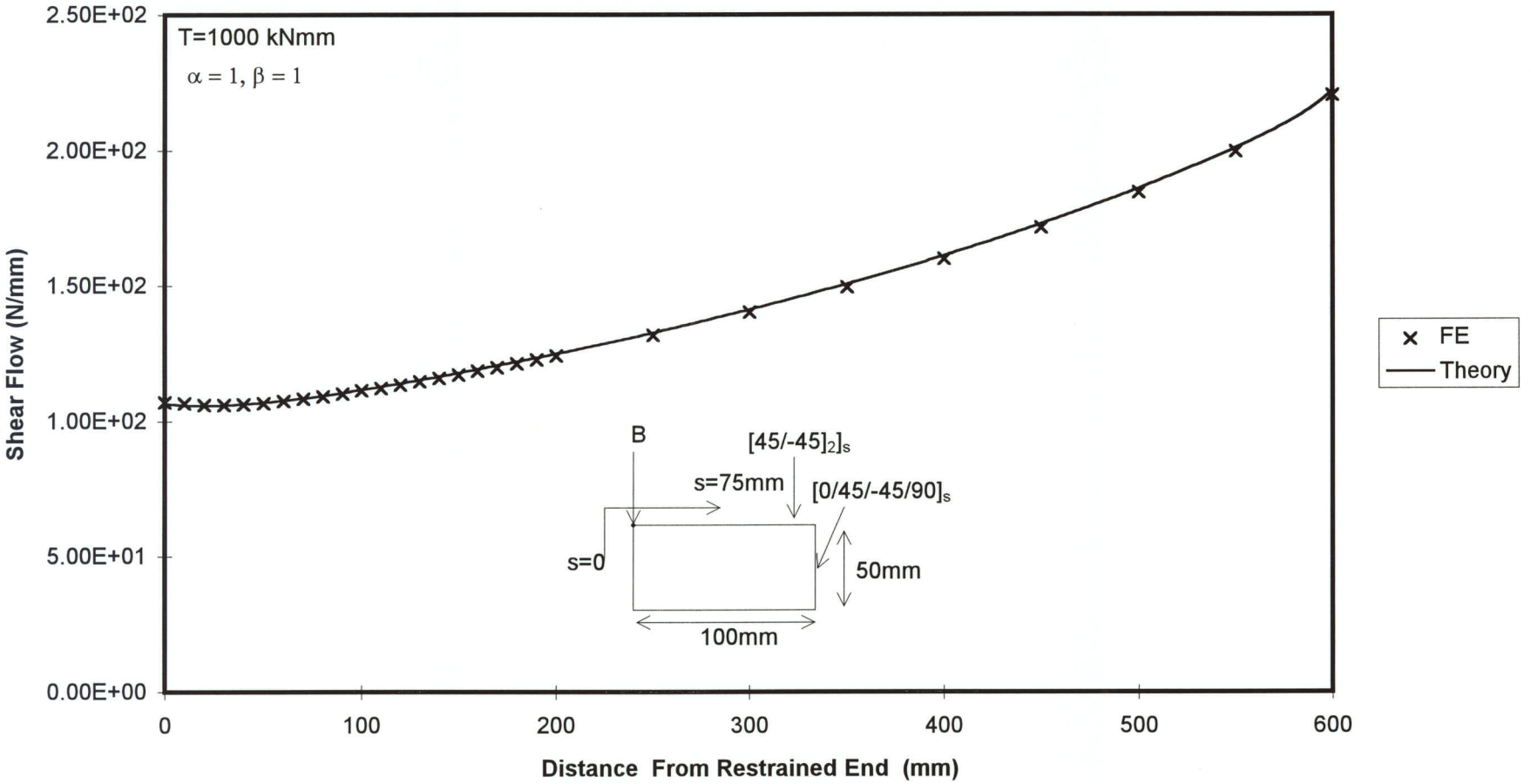

Figure 6.58 SHEAR FLOW ALONG LENGTH OF TAPERED BOX AT S=0

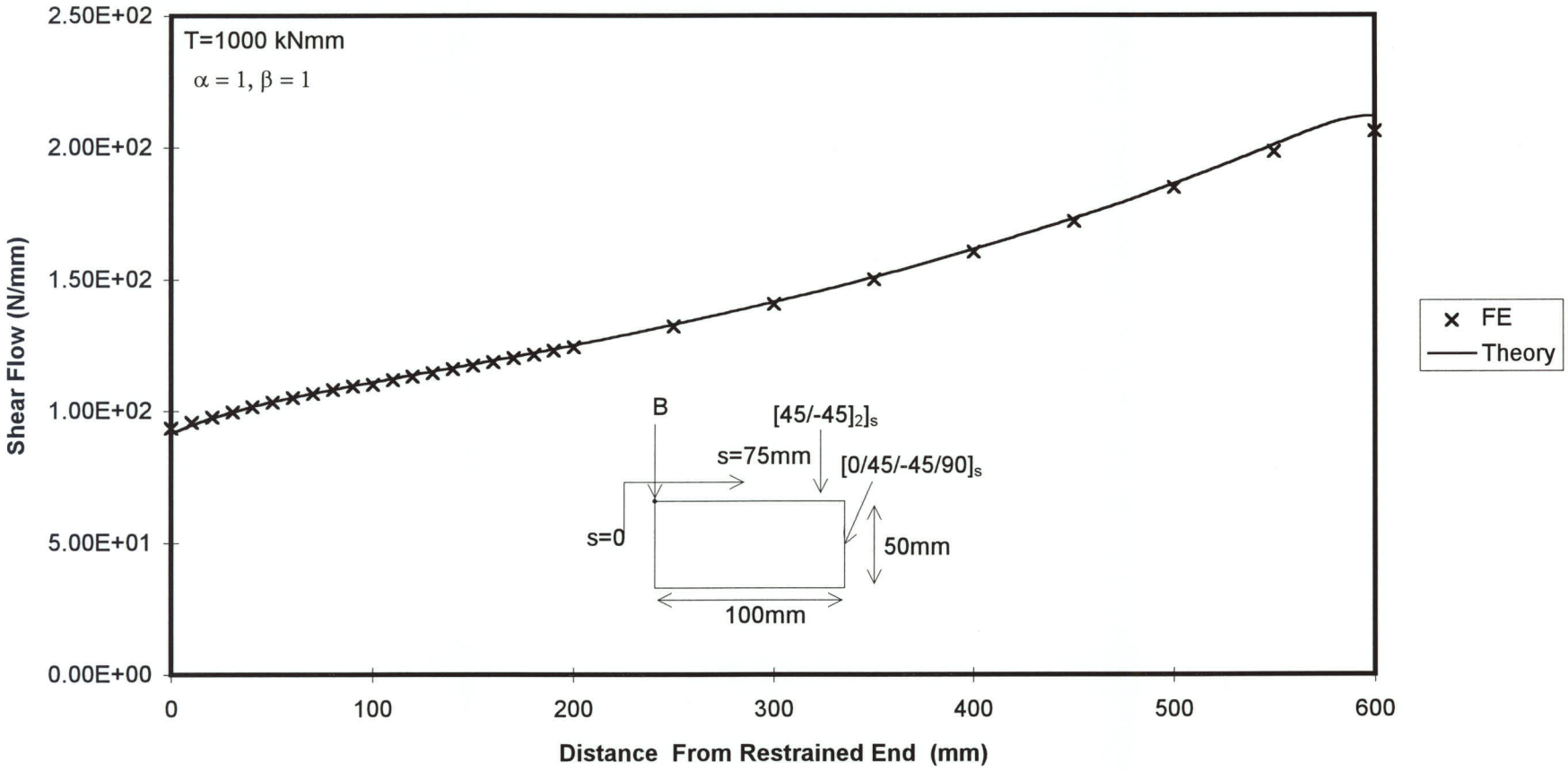

Figure 6.59 SHEAR FLOW ALONG LENGTH OF TAPERED BOX AT S=75

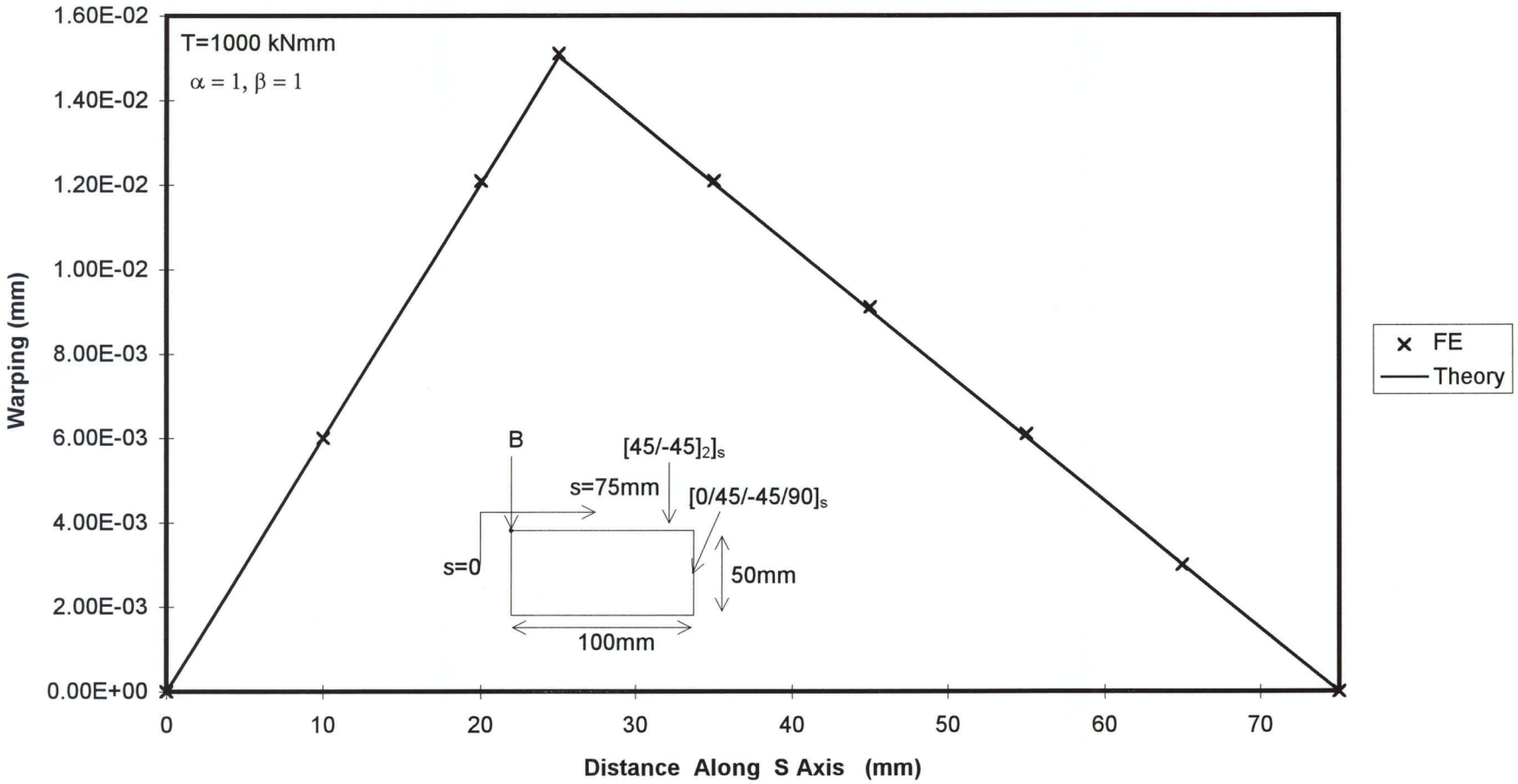

Figure 6.60 WARPING AROUND TAPERED BOX AT Z = 200 mm

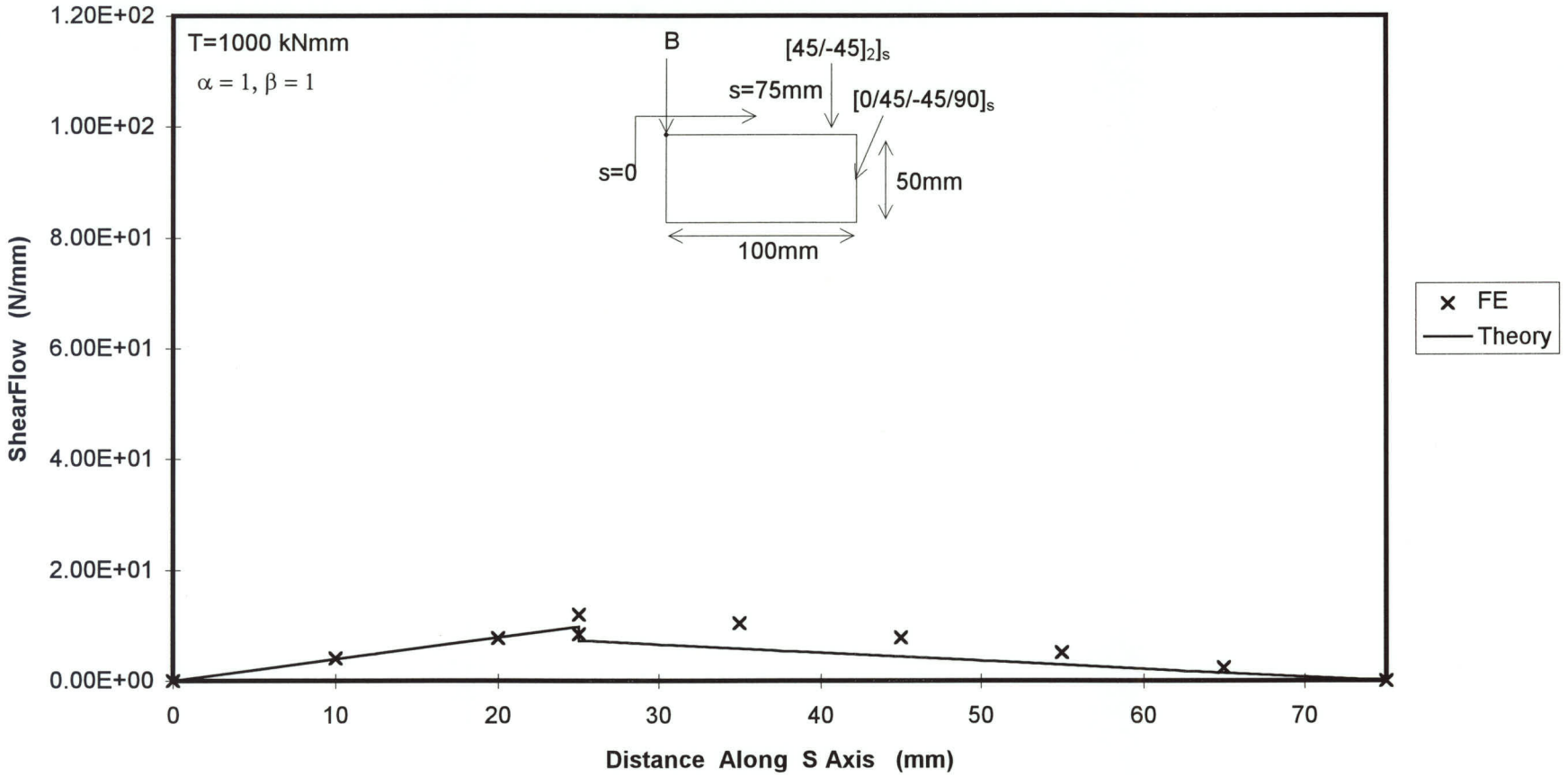

Figure 6.61 FI AROUND TAPERED BOX AT Z = 20mm

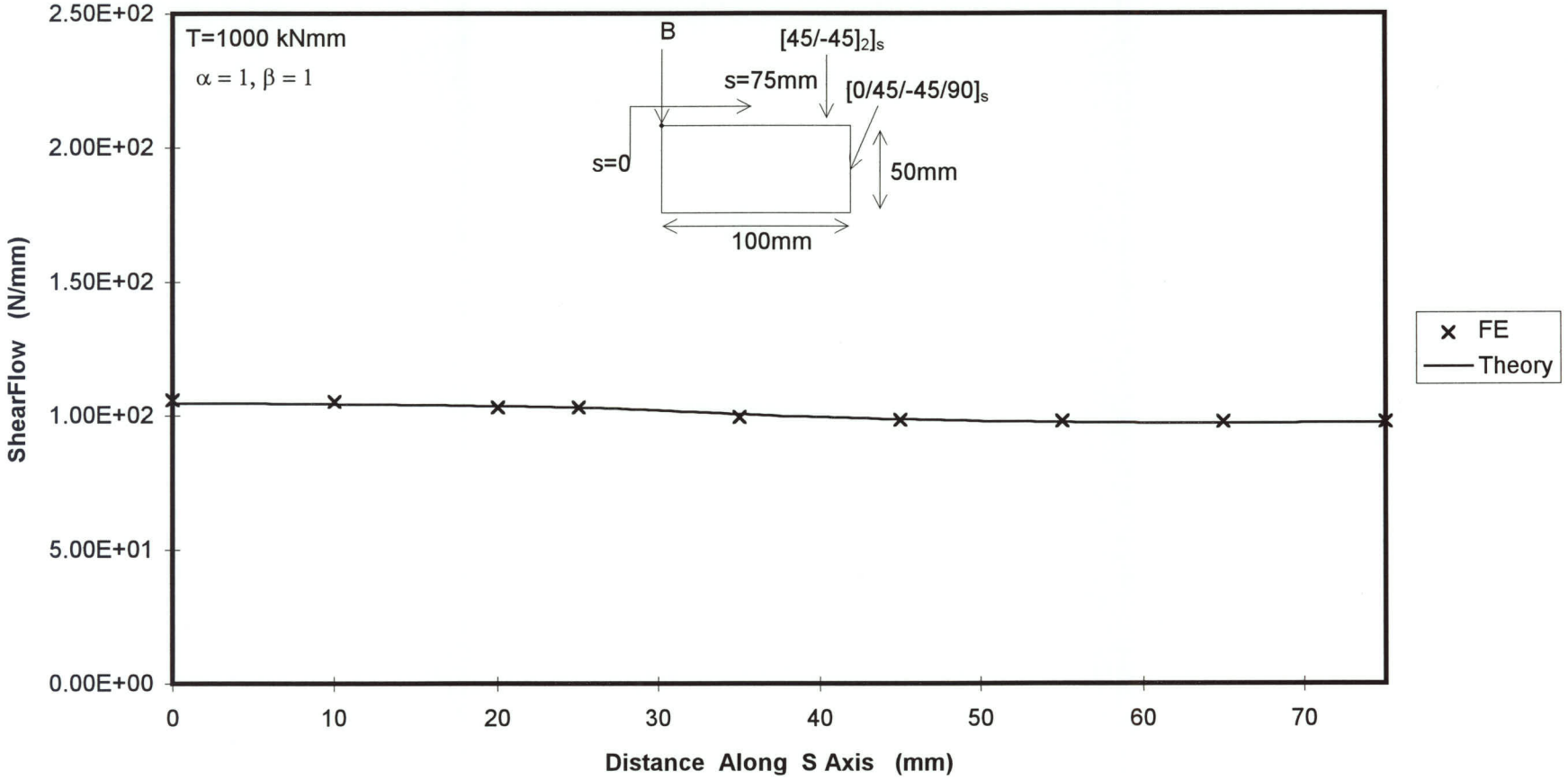

Figure 6.62 SHEAR FLOW AROUND TAPERED BOX AT Z = 20mm

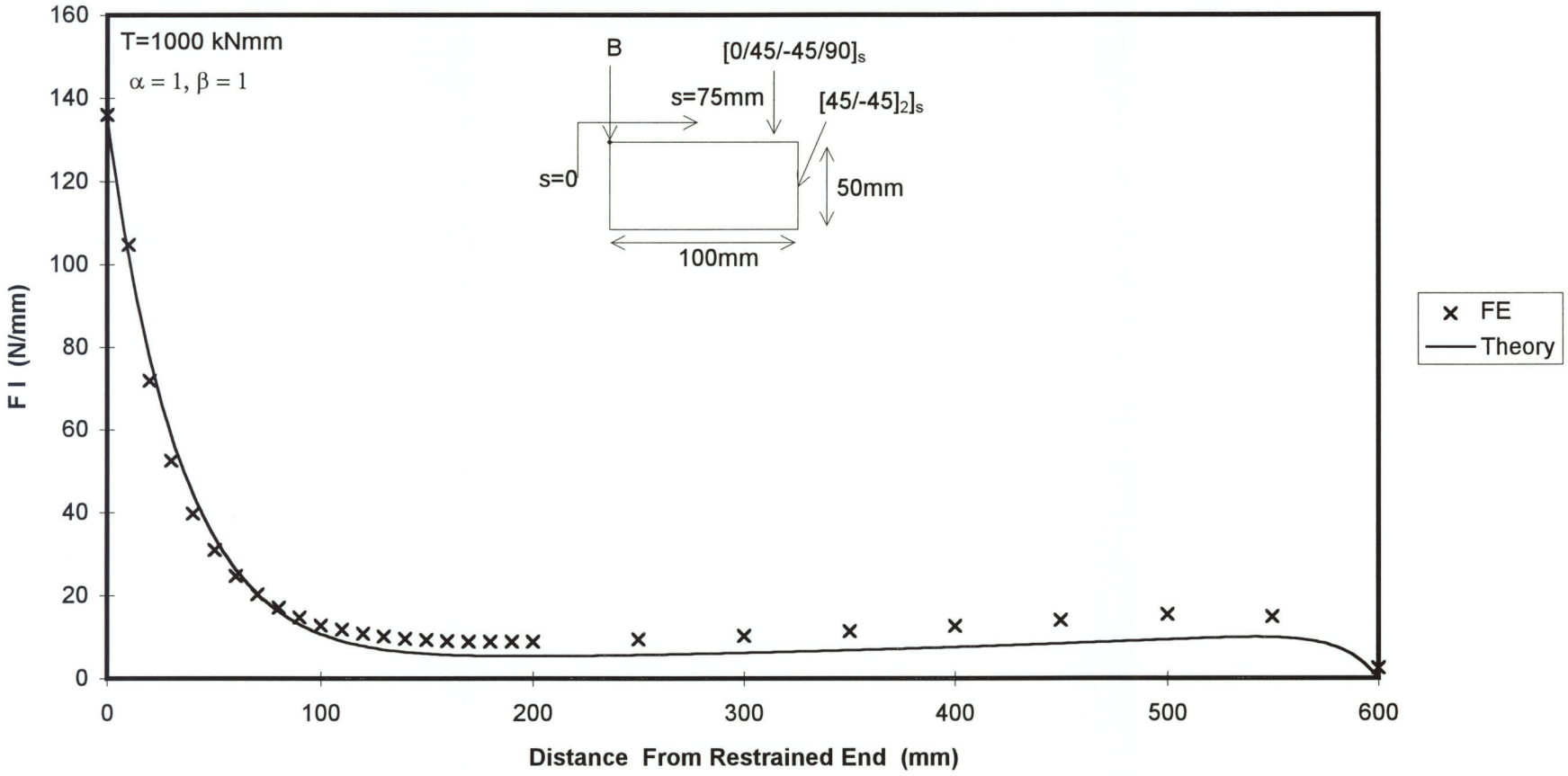

Figure 6.63 FORCE INTENSITY ALONG LENGTH OF TAPERED BOX AT "B"

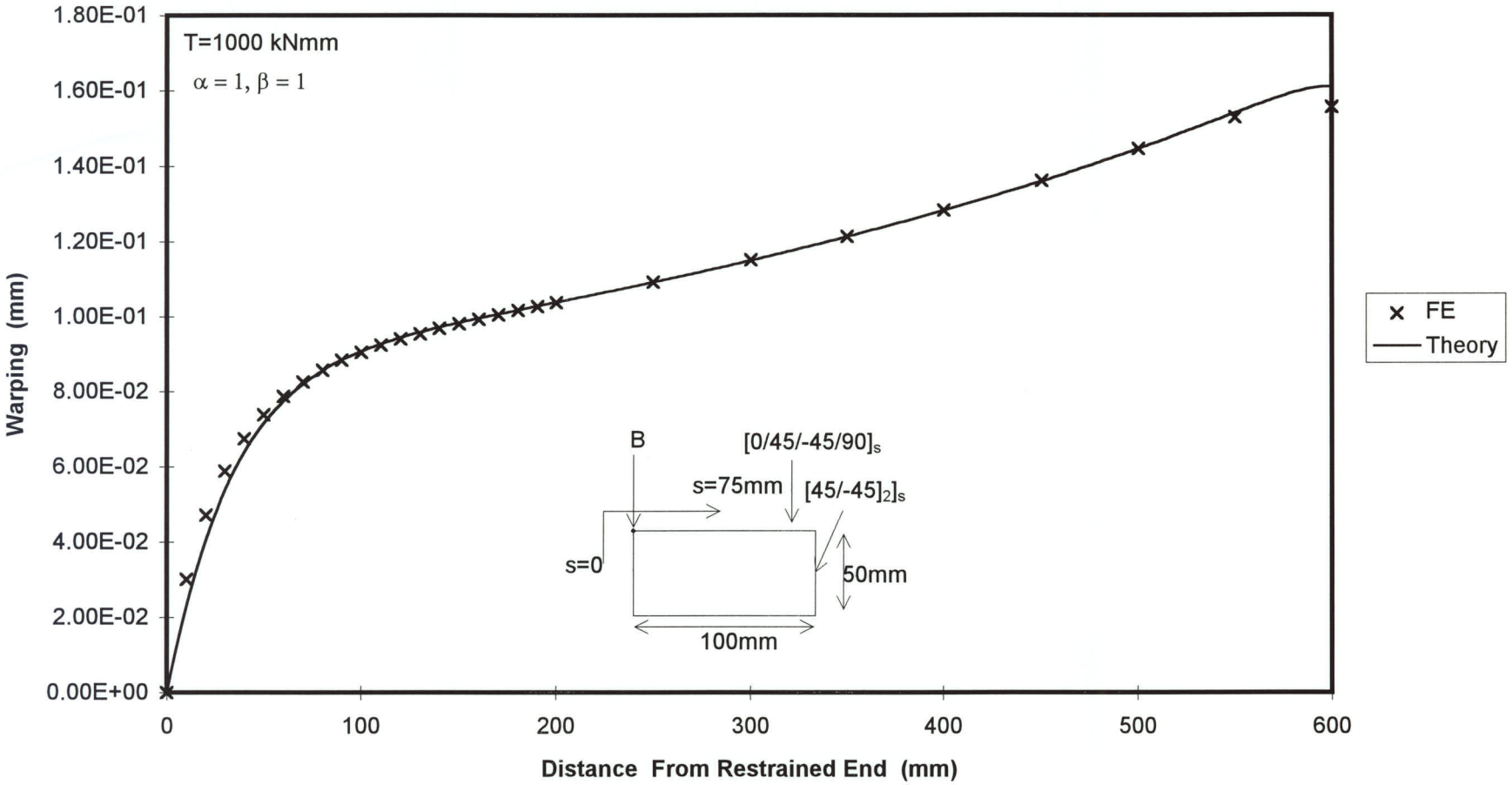

Figure 6.64 WARPING ALONG LENGTH OF TAPERED BOX AT POINT "B"

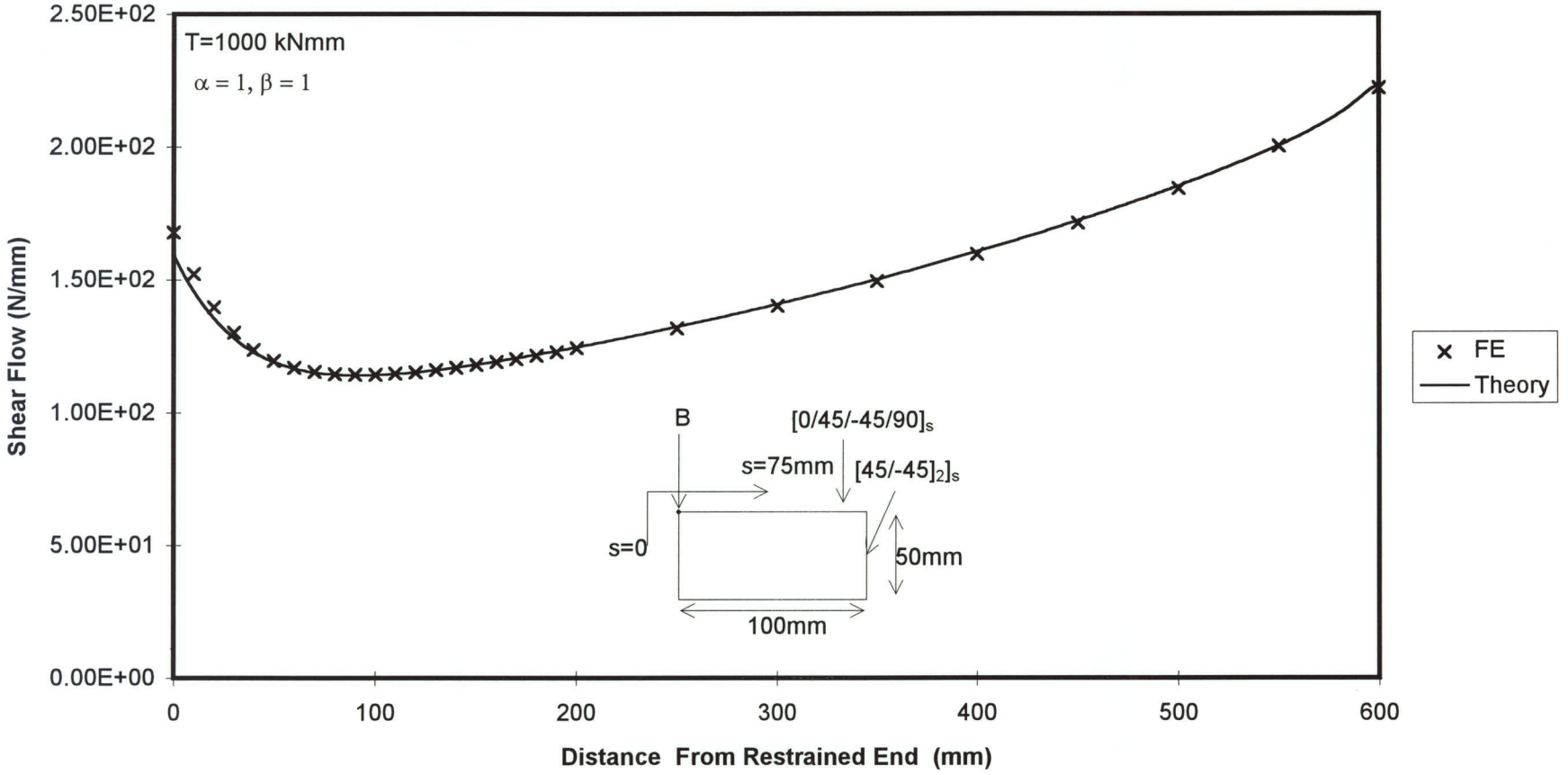

Figure 6.65 SHEAR FLOW ALONG LENGTH OF TAPERED BOX AT S=0

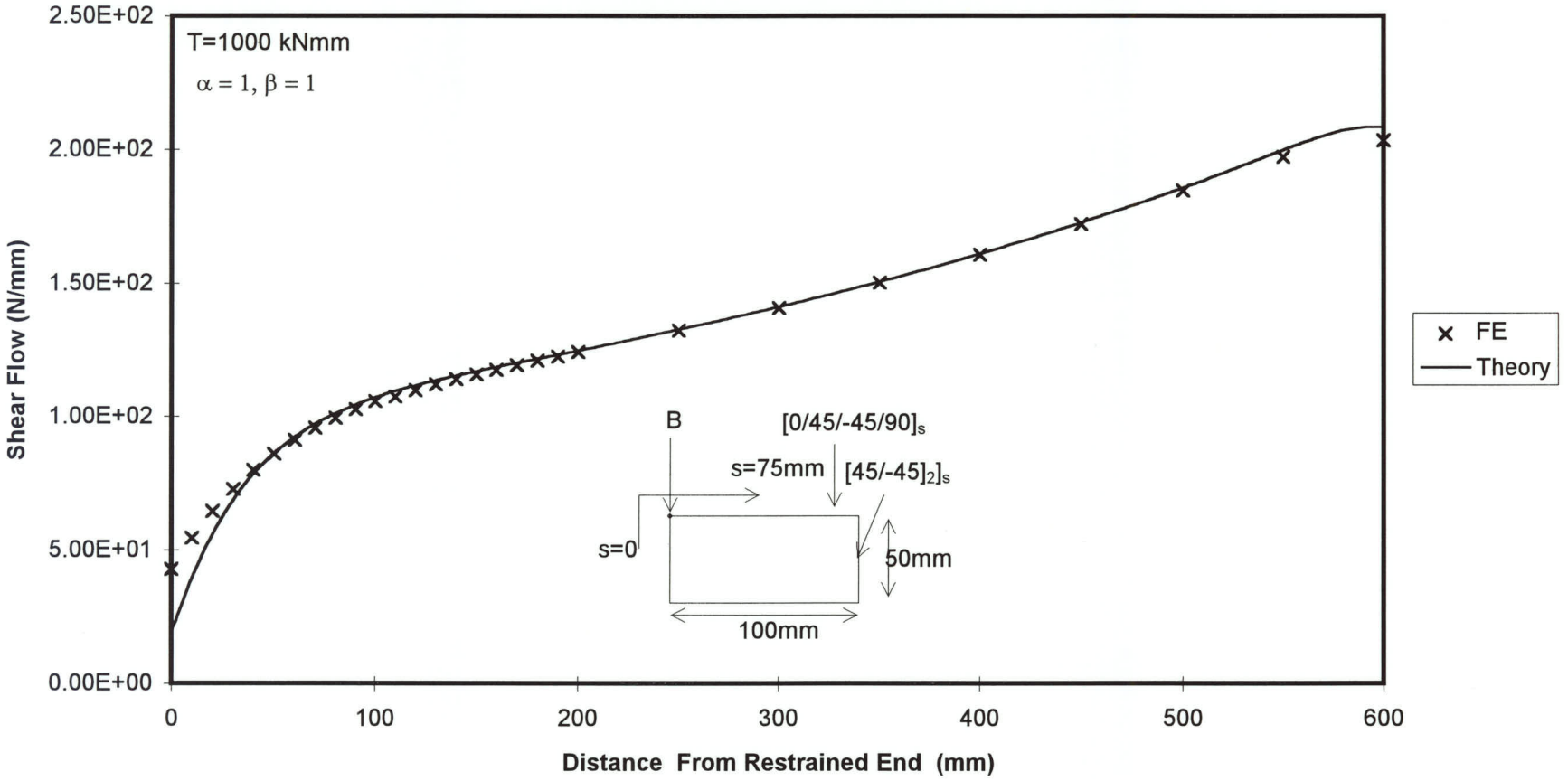

Figure 6.66 SHEAR FLOW ALONG LENGTH OF TAPERED BOX AT S=75

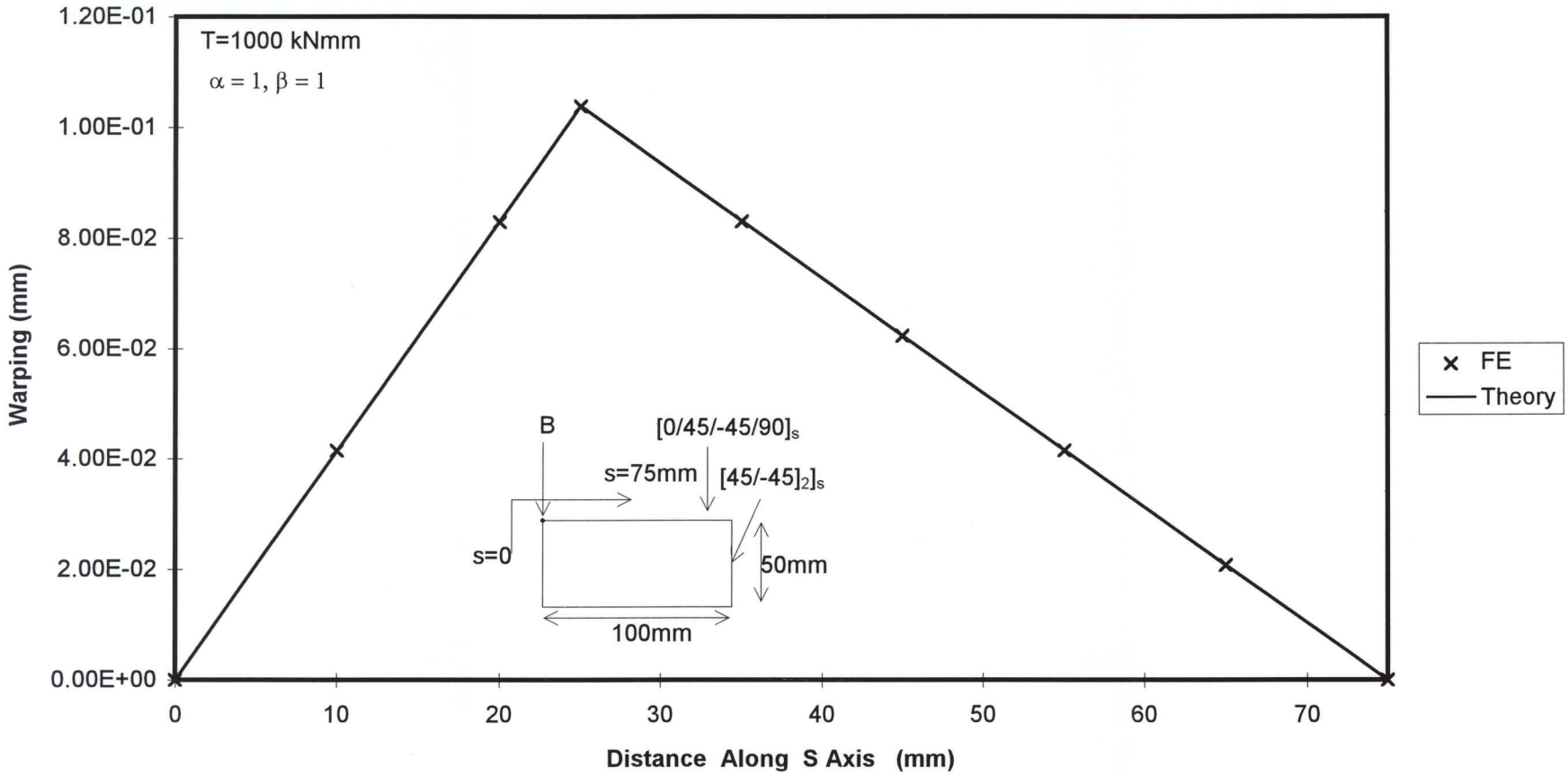

Figure 6.67 WARPING AROUND TAPERED BOX AT Z = 200 mm

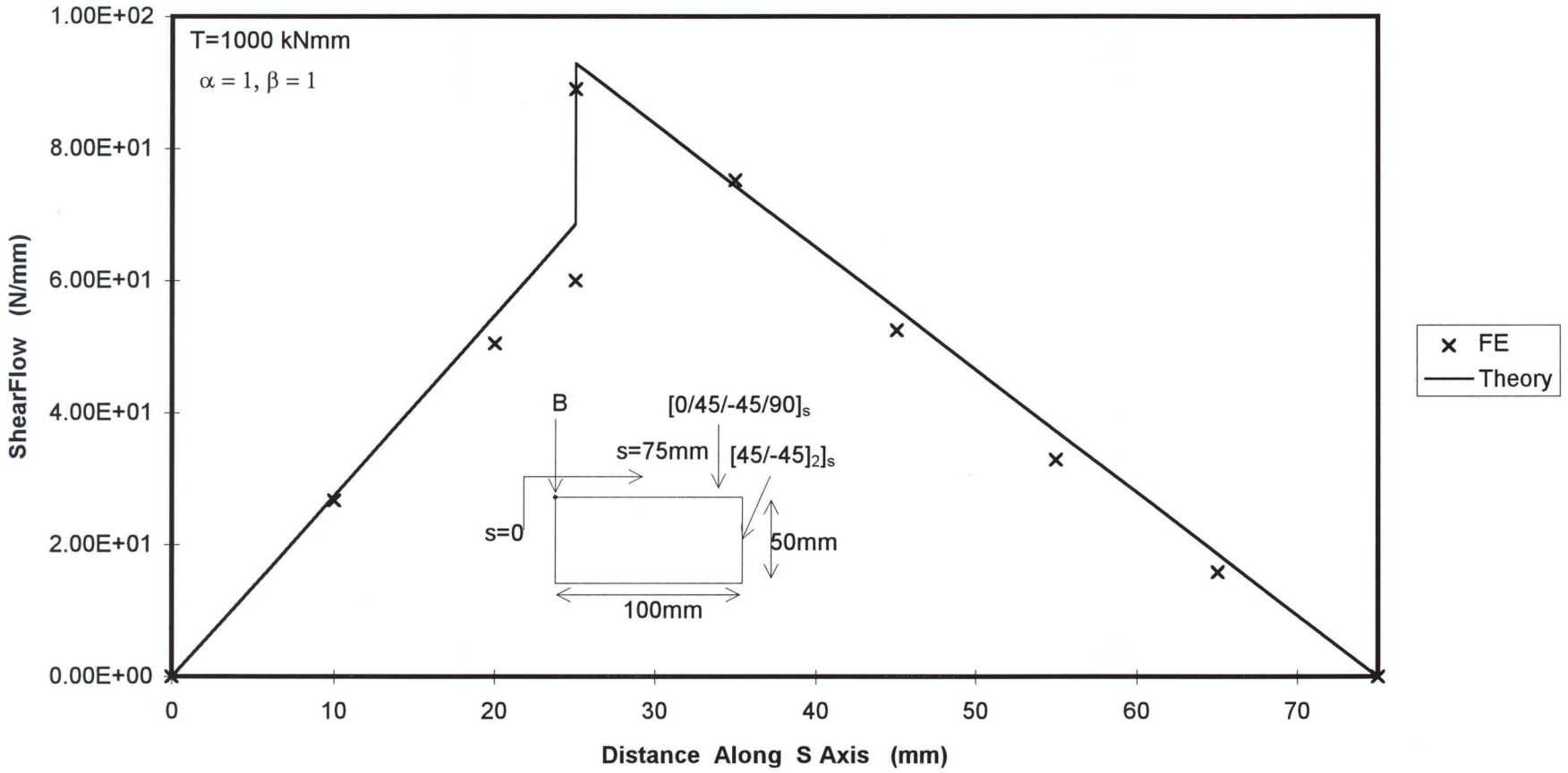

Figure 6.68 FI AROUND TAPERED BOX AT Z = 20mm

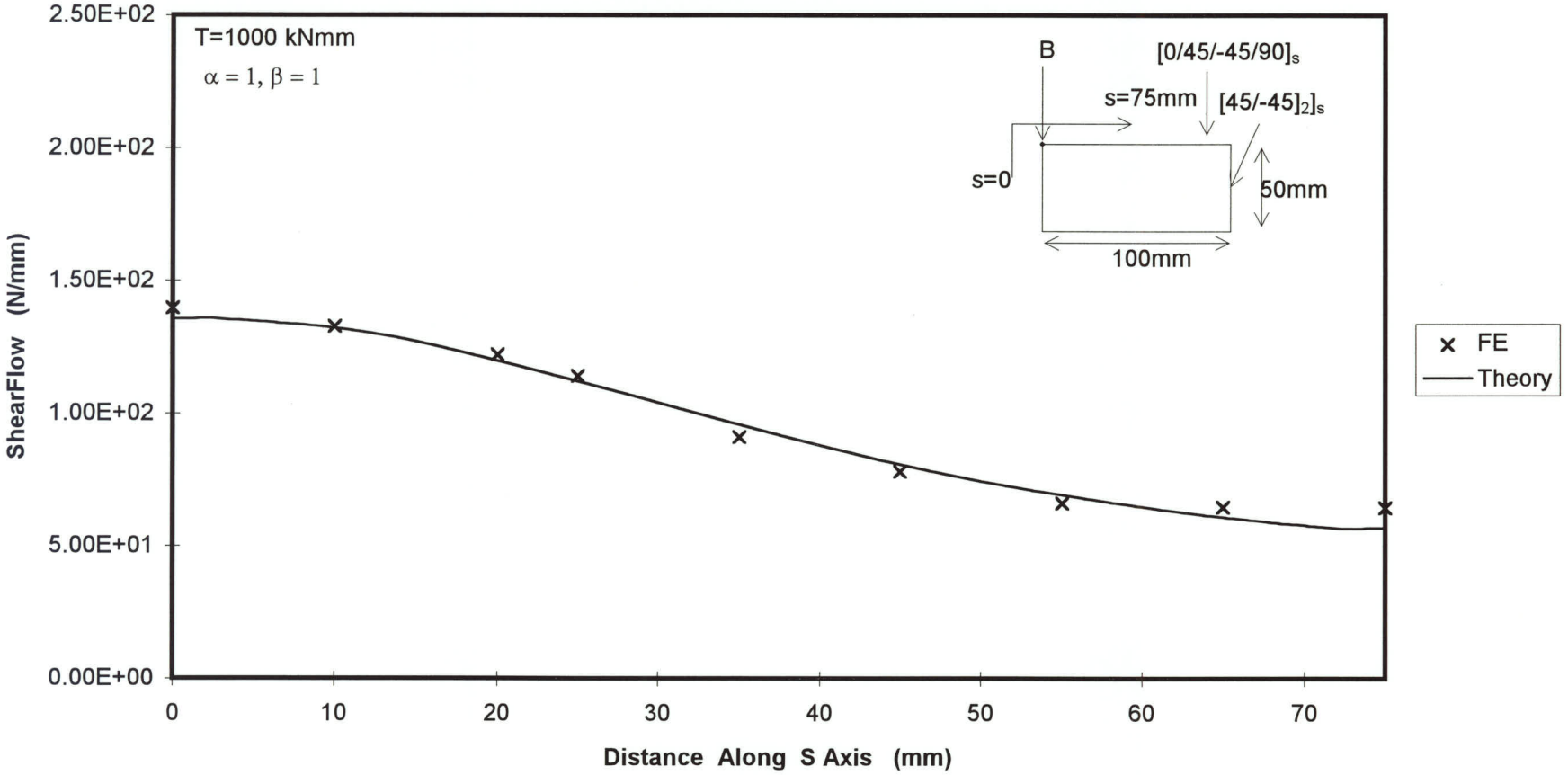

Figure 6.69 SHEAR FLOW AROUND TAPERED BOX AT Z = 20mm

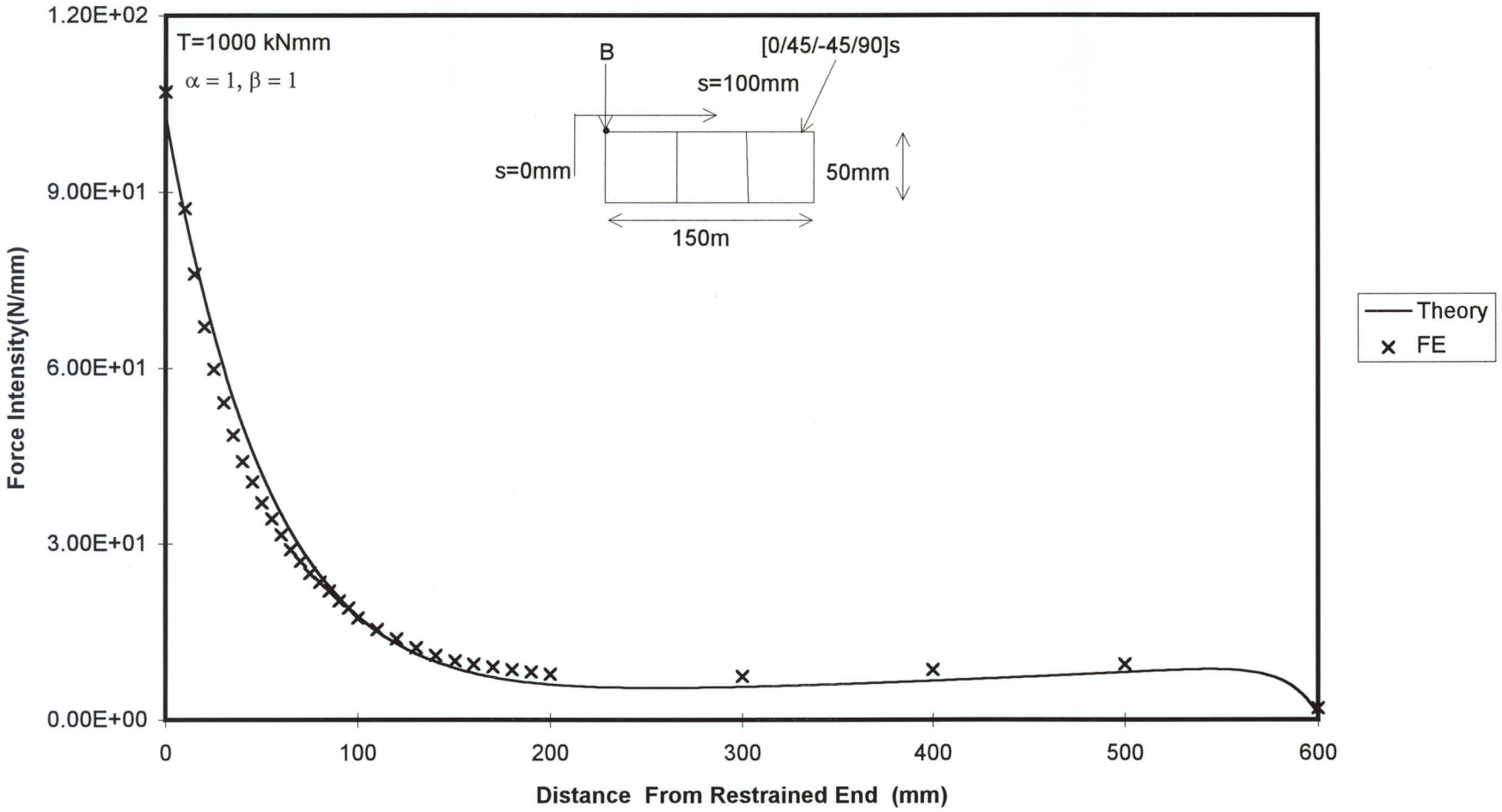

Figure 6.70 FORCE INTENSITY ALONG LENGTH OF BOX AT "B"

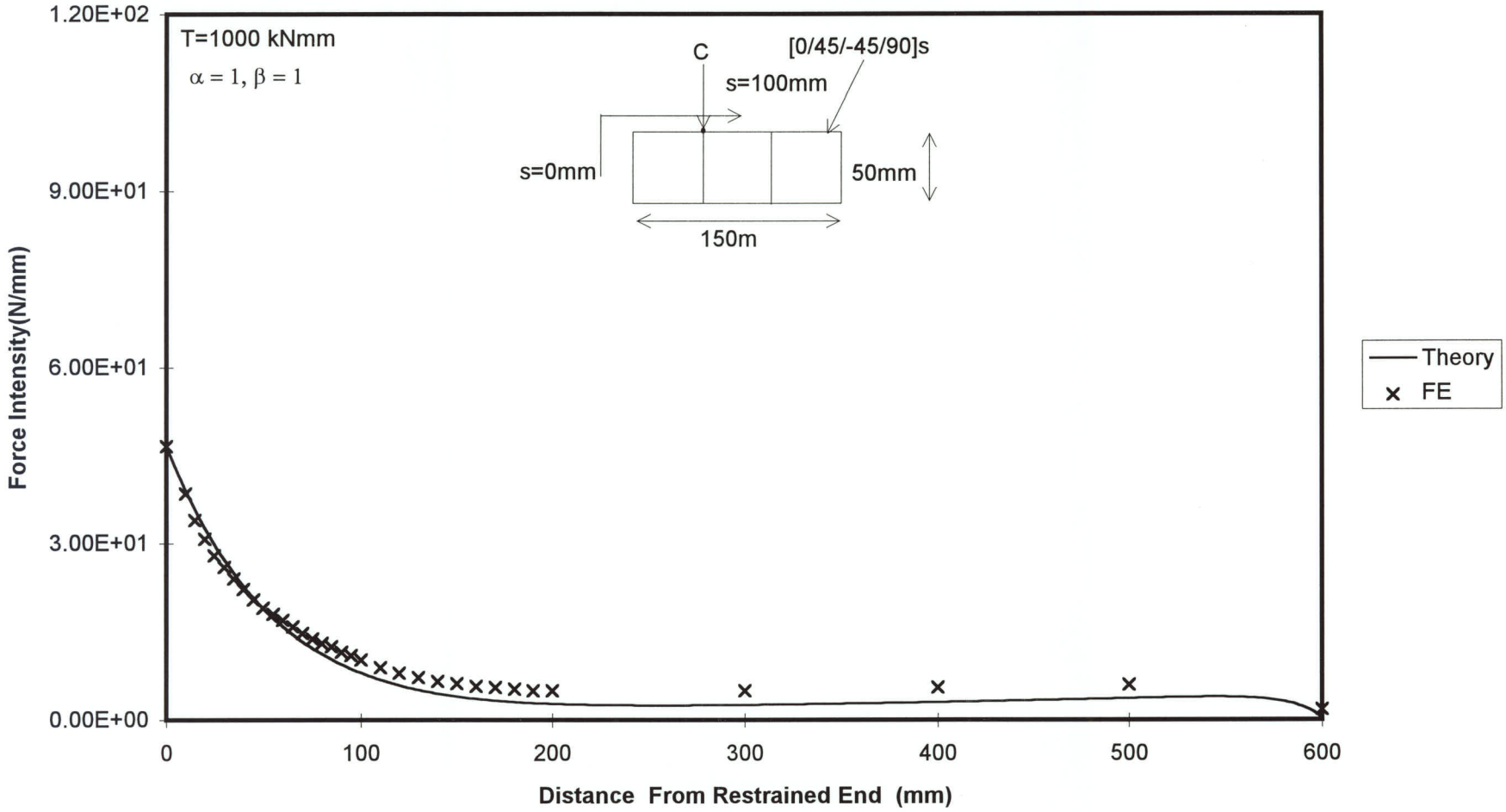

Figure 6.71 FORCE INTENSITY ALONG LENGTH OF BOX AT "C"

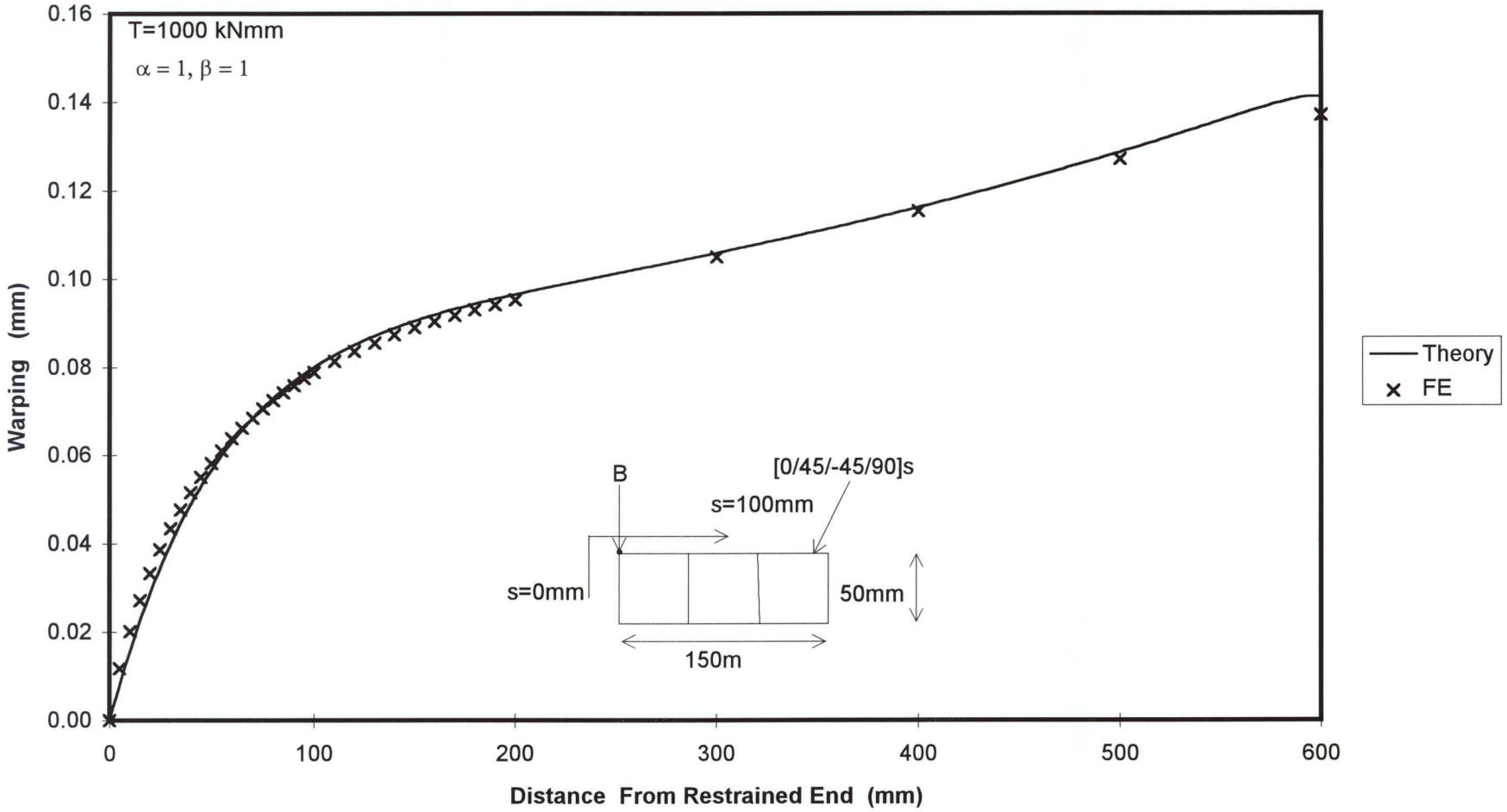

Figure 6.72 WARPING ALONG LENGTH OF BOX AT POINT "B"

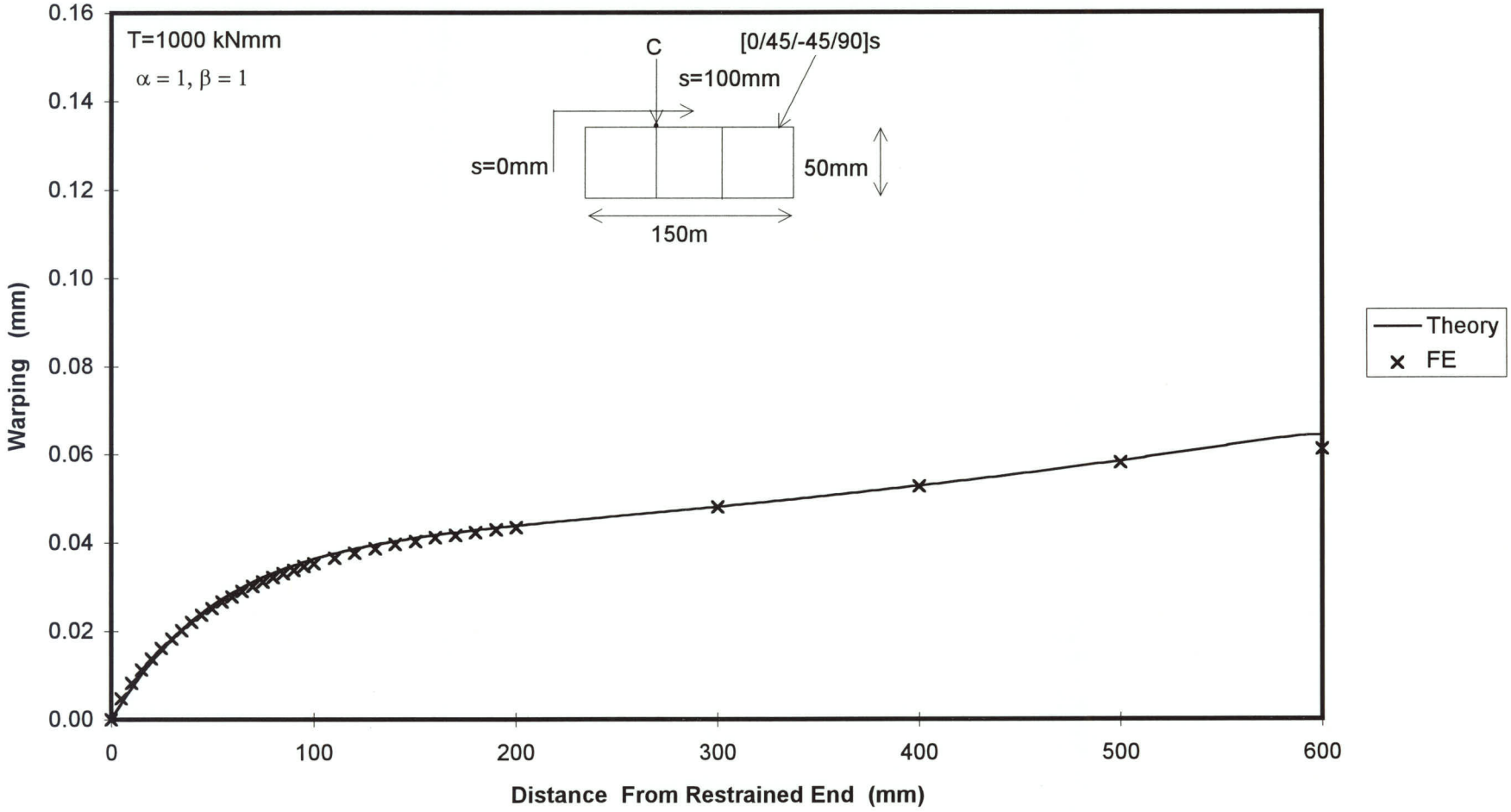

6.73 WARPING ALONG LENGTH OF BOX AT POINT "C"

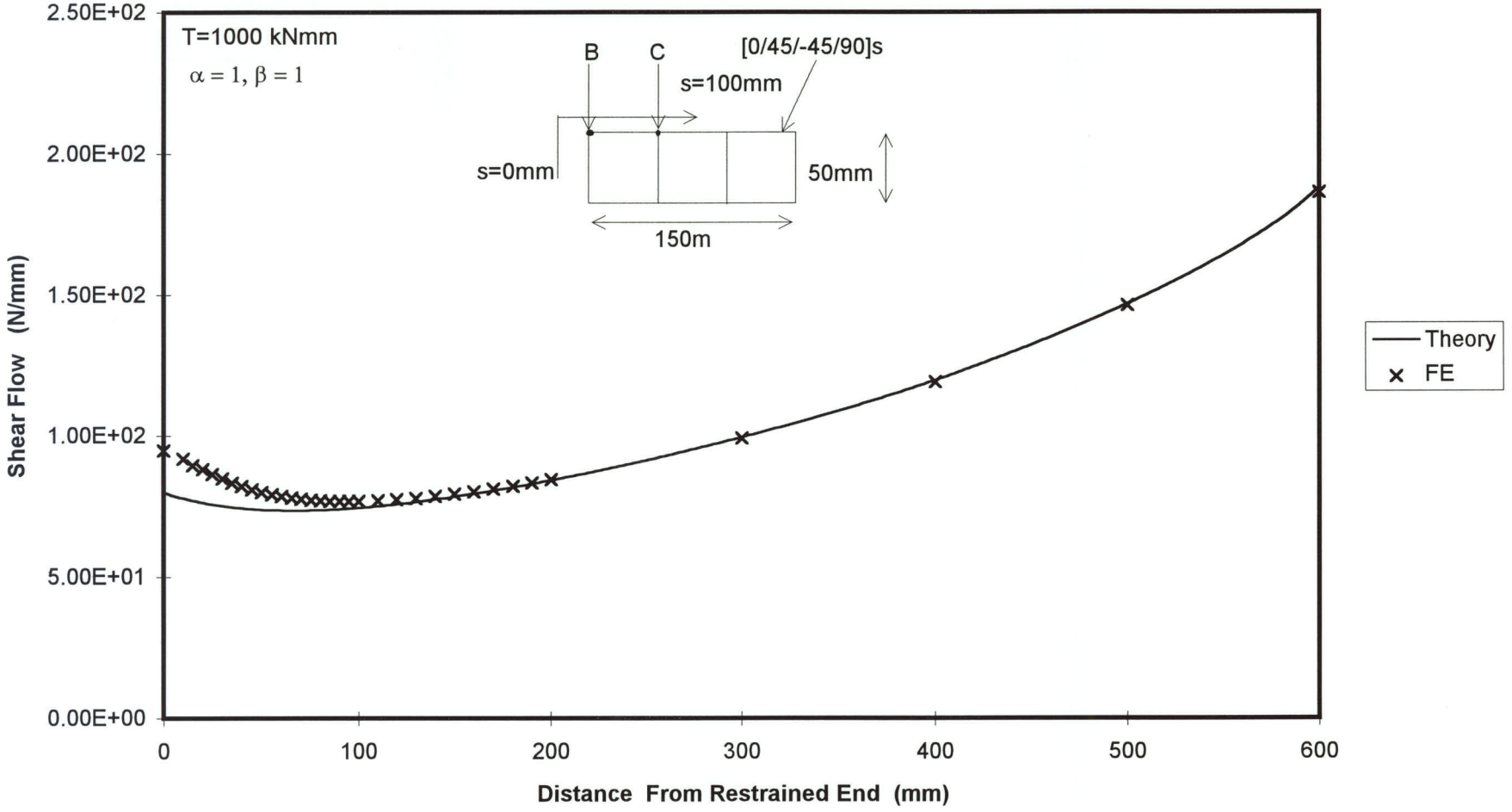

Figure 6.74 SHEAR FLOW ALONG LENGTH OF BOX AT S=0 mm

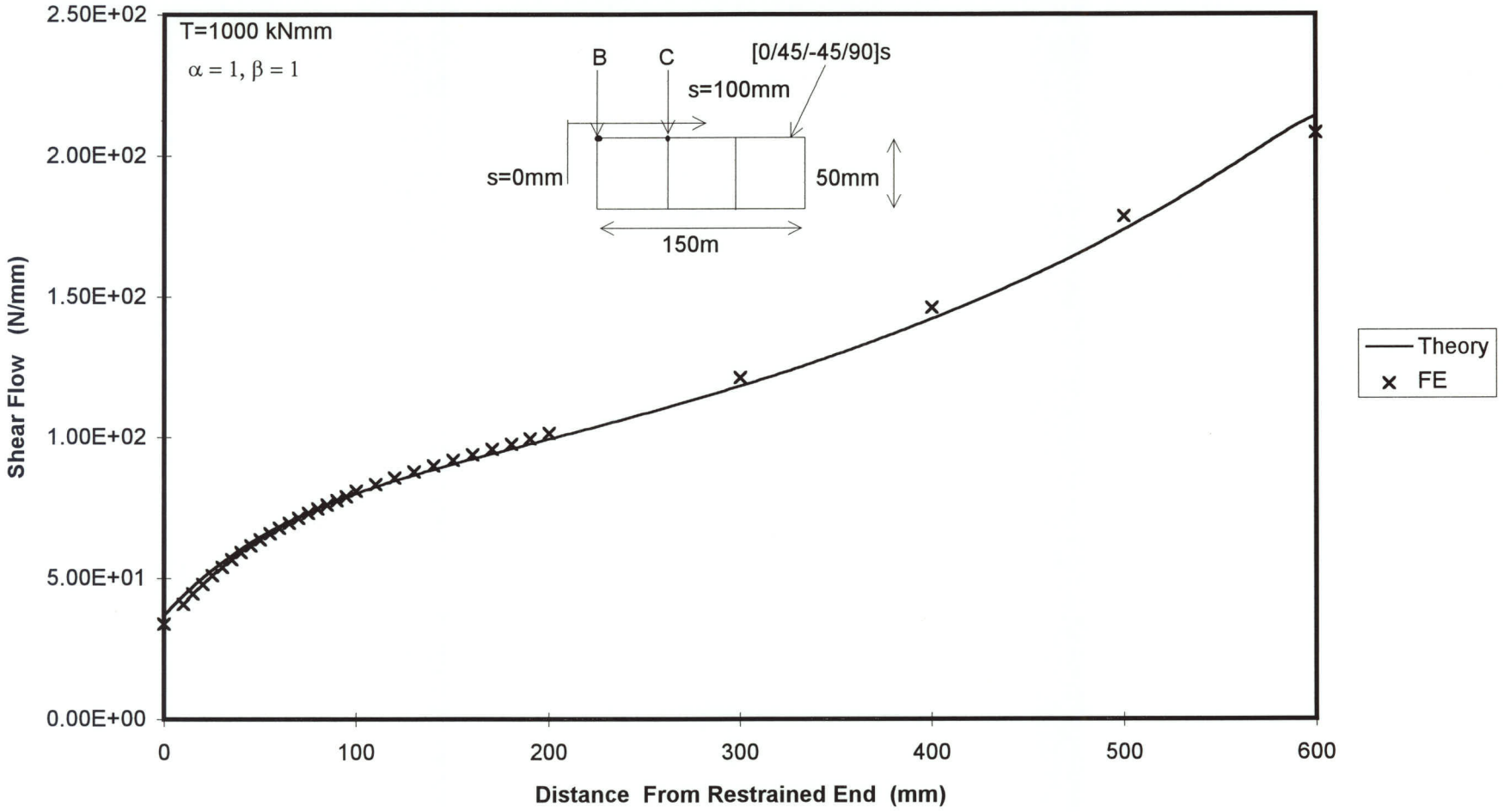

Figure 6.75 SHEAR FLOW ALONG LENGTH OF BOX AT S=100 mm

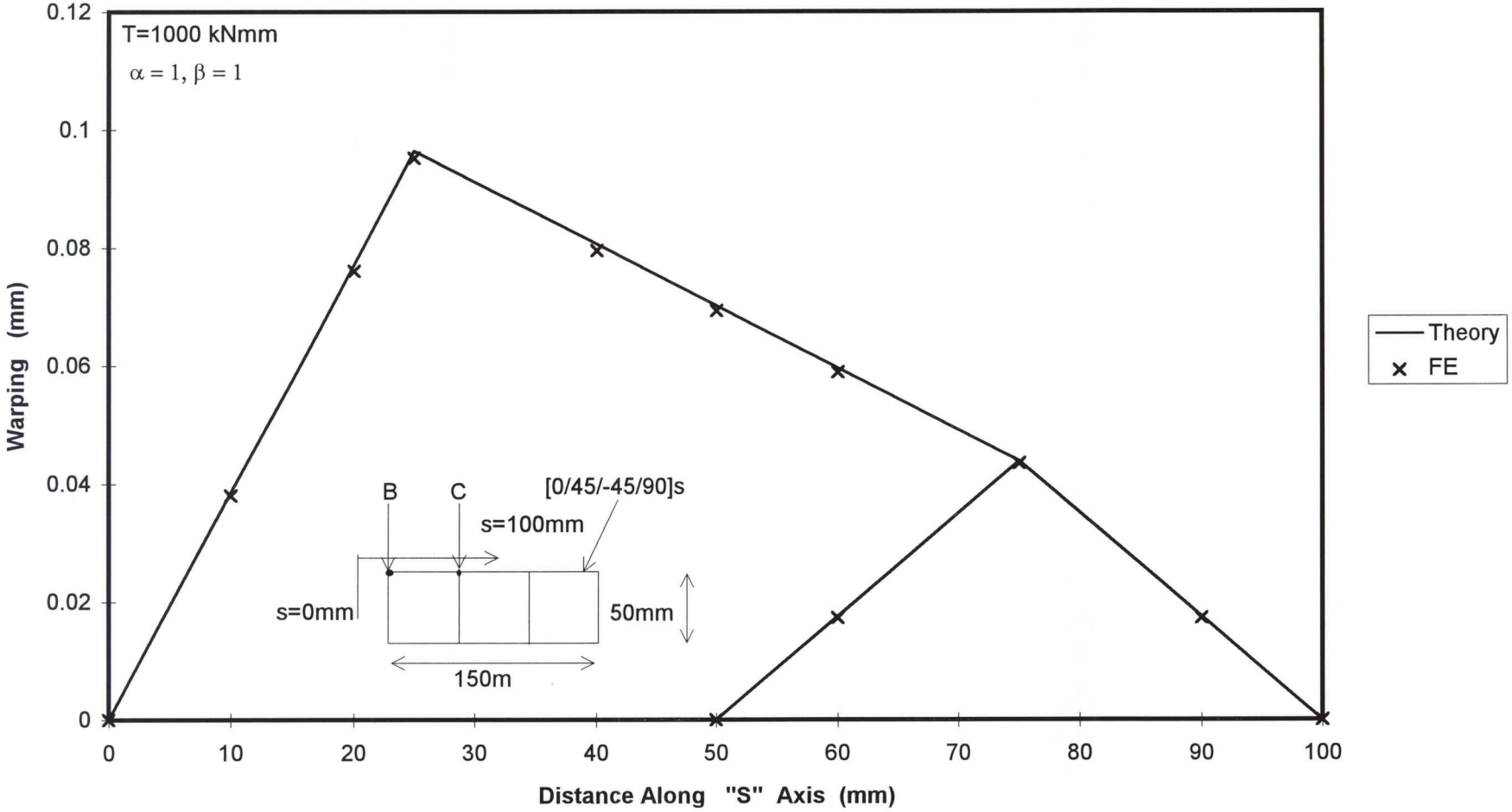

Figure 6.76 WARPING AROUND BOX AT Z=200mm

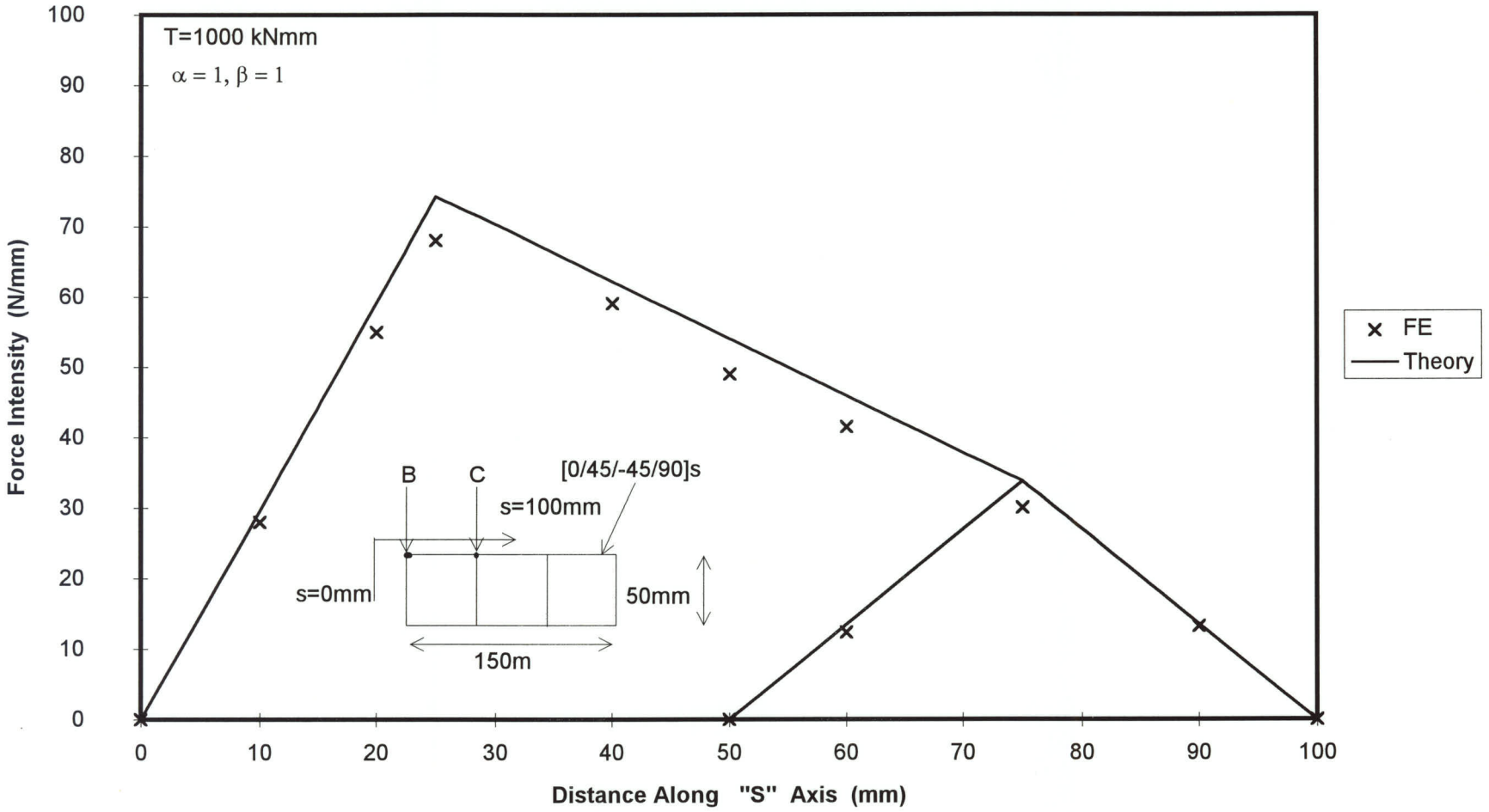

Figure 6.77 FORCE INTENSITY AROUND BOX AT Z=20mm

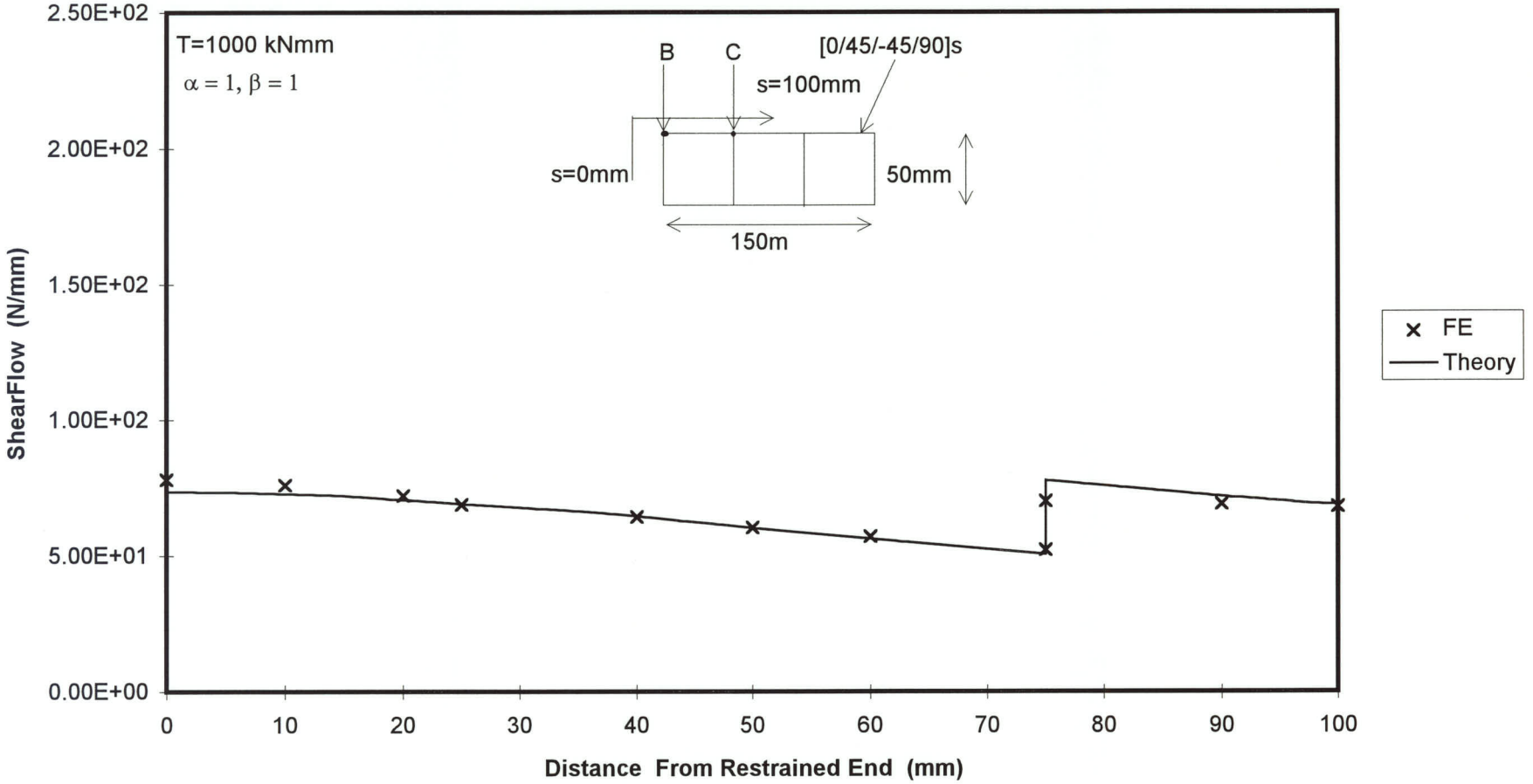

Figure 6.78 SHEAR FLOW AROUND TAPERED BOX AT Z=60mm

7 THEORETICAL RESULTS

The theoretical results for a variety of composite lay-ups in respect of Single-cell and Multi-cell tapered boxes encompassing various taper angles Alpha and Beta are shown in this chapter.

7.1 SINGLE CELL TAPERED BOX

The theoretical results for a variety of composite lay-ups for Single cell tapered box for various Alpha and Beta are shown in this section.

7.1.1 COMPARISON OF RESULTS FOR VARIOUS ALPHA & BETA FLANGES & WEBS ALL [0/45/-45/90]s LAY-UP

The comparison of results for taper angles , Alpha and Beta equal to 0.25, Alpha and Beta equal to 0.50, Alpha and Beta equal to 0.75, Alpha and Beta equal to 1.0, Alpha equal to zero and Beta equal to 1.0, Alpha equal to 1.0 and Beta equal to zero, having all [0/45/-45/90]s lay-up are shown from Figures 7.1 to 7.7 . Force Intensity variation along length is shown (figure 7.1) to have a FI peak value of around 98 N/mm to 100 N/mm at the restrained end for the different taper angles being discussed here. This peak value of FI drops to 7.5 N/mm, 8.6 N/mm, 9.8 N/mm, 11 N/mm, 4.9 N/mm, 12.7 N/mm at a distance of 100 mm from the restrained end for all the above mentioned taper angles respectively. The curves in each case then start to increase slowly reaching a peak value between 500 mm to 575 mm from the restrained end. All the curves then drop down to zero value at the free end. A general tendency of the FI curves shifting up with the increase in taper angle Alpha and Beta is witnessed here. The drop from peak value to

minimum FI value decreases with the increase in taper angles and also the maximum FI value reached between 500 mm to 575 mm before the curve finally drops to zero increases with the increase in taper angles. The curve for Alpha equal to zero and Beta equal to 1.0 shows a different trend than all other taper angles discussed here. The FI curve for this case drops from a peak value of 98 N/mm to zero within a distance of 150 mm from the restrained end , the curve then moves down to negative FI value implying a change in direction of the Force Intensity. The FI negative value reaches a minimum value of -1.8 N/mm at 500 mm from the restrained end, and then finally the slope of the curve becomes positive and the curve reaches the FI value of zero at the free end.

Warping variation along length is shown (figure 7.2) to start from zero warping value at the restrained end increasing steeply to 0.058 mm, 0.06 mm, 0.062 mm, 0.0638 mm, 0.0564 mm and 0.066 mm for all the taper angles mentioned above respectively within the first 100 mm from the restrained end. The curves then increase steadily beyond that point reaching the respective maximum warping values at the free end. The slope of the curves beyond first 100 mm of the restrained end varies with the increase in the taper angle Alpha and Beta. The higher the taper angle Alpha and Beta the higher is the curve pushed up in its warping value as it moves beyond the first 100 mm towards the free end. The curve for Alpha equal to zero and Beta equal to 1.0 degree shows different results from all other taper angles discussed here. The curve in this case starts to drop down after 100 mm from the restrained end and keeps the steady negative slope till reaching its minimum value of 0.045 mm at the free end.

Shear flow at s=0 mm is shown (figure 7.3) to decrease from an initial shear flow value ranging from 140 N/mm to 143 N/mm for all of the taper angles mentioned above to 105 N/mm, 108 N/mm, 111 N/mm, 114 N/mm, 106 N/mm and 110 N/mm respectively in the first 100 mm from the restrained end. The shear flow curves starts to rise after this point and the higher the taper angle Alpha and Beta the higher is the curve pushed up as it moves towards the free end . The curves reach their respective maximum values at the free end. The reason for this behaviour of the shear flows to occur is the steady reduction in the warping shear flow as the curve moves away from the restrained end. As the total

shear flow at location s=0 mm is the addition of the Bredt Batho shear flow and warping shear flow , therefore the reduction of warping shear flow results in reduction of the total shear flow in the first 100 mm from restrained end. On the other hand the Bredt Batho value of 100 N/mm at the restrained end starts to increase when the effective area of the box is continuously reduced due to the taper angle as the curves moves away from the restrained end . This increase in the Bredt Batho value increases the total shear flow and a steady increase in shear flows is hence witnessed along the length of box till the curves reach their respective peak values at the free end

Shear flow at s=75 mm is shown (figure 7.4) to increase continuously from the initial value between 46 N/mm to 52 N/mm for all of the taper angles mentioned above to peak values of 117 N/mm, 139 N/mm, 168 N/mm, 209 N/mm, 127 N/mm and 163 N/mm respectively. The higher the taper angle Alpha and Beta the more steeper the curve becomes beyond first 100 mm of restrained end as it moves on towards the free end. The maximum values of the Shear flow for each curve are reached at the free end. This increase in the shear flow happens due to constant increase in the Bredt Batho shear flow along the length of beam affected due to a continuous decrease in the area along the length. The increase in total shear flow along length is also affected by the continuous decrease in the warping shear flow as the total shear flow at location s=75 mm is the difference of Bredt Batho shear flow and the warping shear flow. Hence the reduction in warping shear flow also results in the increase in total shear flow along length at this location .

Warping around box at z=200 mm from restrained end is shown (figure 7.5) to increase from the initial zero value at the zero warping point s=0 mm (centre of web) for all the taper angles mentioned above to their respective peak values at the corner point "B" (s=25 mm) . The peak value of warping at point "B" is seen to jump up with the increase in the taper angle Alpha and Beta . Also the curves are seen to shift up with the increase in the respective taper angles Alpha and Beta. However in case of Alpha equal to zero and Beta equal to 1.0 degree the curve is seen to be at the bottom of all other taper angle curves, thus having a minimum value of warping at the corner point "B". All the curves

show a steep decrease in the warping value after moving beyond point "B" onto the flange and finally reach the zero warping value at the centre of flange (s=75 mm).

FI (Force Intensity) around box at z=20 mm from restrained end is shown (figure 7.6) to increase from the initial zero value at the zero warping point s=0 mm (centre of web) for all the taper angles mentioned above to their respective peak values at the corner point "B" (s=25 mm) . The peak value of warping at point "B" is seen to jump up with the increase in the taper angle Alpha and Beta . Also the curve is seen to shift up with the increase in the respective taper angles Alpha and Beta. However in case of Alpha equal to zero and Beta equal to 1.0 degree the curve is seen to be at the bottom of all other taper angle curves, thus having a minimum value of FI at the corner point "B". All the curves show a steep decrease in the FI value after moving beyond point "B" onto the flange and finally reach the zero value at the centre of flange (s=75 mm).

Shear flow around box at z=20 mm from the restrained end (figure 7.7) shows the total Shear flow at s=0 mm (centre of web) to be around 125 N/mm for all the taper angles mentioned above. This is the addition of warping shear flow and Bredt Batho at this location. The total shear flow curves then reduce steadily due to the gradual decrease in the warping shear flow as the curves move around the box section from the centre of web (s=0 mm) to the corner point "B" (s=25 mm). After moving away from the corner point "B", the total shear flow curves continue to reduce as the direction of warping shear flow in the flange now becomes opposite to that of the Bredt Batho shear flow, hence the addition of these two shear flows in fact now results in subtraction of warping shear flow from the Bredt Batho giving a lower value for total shear flow all along the length of flange till the curves reach their respective minimum values at the centre of flange (s=75 mm).

7.1.2 COMPARISON OF RESULTS FOR VARIOUS ALPHA & BETA FLANGES & WEBS ALL [[45/-45]2]s LAY-UP

The comparison of results for taper angles , Alpha and Beta equal to 0.25, Alpha and Beta equal to 0.50, Alpha and Beta equal to 0.75, Alpha and Beta equal to 1.0, Alpha equal to zero and Beta equal to 1.0, Alpha equal to 1.0 and Beta equal to zero, having all [[45/-45]2]s lay-up are shown from Figures 7.8 to 7.14 . Force Intensity variation along length is shown (figure 7.8) to have a FI peak value of around 63 N/mm to 64 N/mm at the restrained end for the different taper angles being discussed here. This peak value of FI drops to 1.58 N/mm, 1.81 N/mm, 1.55 N/mm, 2.81 N/mm, 0.0 N/mm, 2.77 N/mm at a distance of 100 mm from the restrained end for all the above mentioned taper angles respectively. The curves in each case then start to increase slowly reaching a peak value between 500 mm to 575 mm from the restrained end. All the curves then drop down to zero value at the free end. A general tendency of the FI curves shifting up with the increase in taper angle Alpha and Beta is witnessed here. The drop from peak value to minimum FI value decreases with the increase in taper angles and also the maximum FI value reached between 500 mm to 575 mm before the curve finally drops to zero increases with the increase in taper angles. The curve for Alpha equal to zero and Beta equal to 1.0 shows a different trend than all other taper angles discussed here. The FI curve for this case drops from a peak value of 63 N/mm to zero within a distance of 110 mm from the restrained end , the curve then moves down to negative FI value implying a change in direction of the Force Intensity. The FI negative value reaches a minimum value of - 0.8 N/mm at 540 mm from the restrained end, and then finally the slope of the curve becomes positive and the curve reaches the FI value of zero at the free end.

Warping variation along length is shown (figure 7.9) to start from zero warping value at the restrained end increasing steeply to 0.0349 mm, 0.0359 mm, 0.0369 mm, 0.0380 mm, 0.0328 mm and 0.0391 mm for all the taper angles mentioned above respectively within the first 100 mm from the restrained end. The curves then increase steadily beyond that point reaching the respective maximum warping values at the free end. The

slope of the curves beyond first 100 mm of the restrained end varies with the increase in the taper angle Alpha and Beta. The higher the taper angle Alpha and Beta the higher is the curve pushed up in its warping value as it moves beyond the first 100 mm towards the free end. The curve for Alpha equal to zero and Beta equal to 1.0 degree shows different results from all other taper angles discussed here. The curve in this case starts to drop down after 100 mm from the restrained end and keeps the steady negative slope till reaching its minimum value of 0.0257 mm at the free end.

Shear flow at s=0 mm is shown (figure 7.10) to decrease from an initial shear flow value ranging from 140 N/mm to 143 N/mm for all of the taper angles mentioned above to 103 N/mm, 106 N/mm, 109 N/mm, 112 N/mm, 104 N/mm and 108 N/mm respectively in the first 100 mm from the restrained end. The shear flow curve starts to rise after this point and the higher the taper angle Alpha and Beta the higher is the curve pushed up as it moves towards the free end . The curves reach their respective maximum values at the free end.

Shear flow at s=75 mm is shown (figure 7.11) to increase continuously from the initial value between 46 N/mm to 49 N/mm for all of the taper angles mentioned above to peak values of 117 N/mm, 140 N/mm, 170 N/mm, 212 N/mm, 127 N/mm and 166 N/mm respectively. The higher the taper angle Alpha and Beta the more steeper the curve becomes beyond first 100 mm of restrained end as it moves on towards the free end. The maximum values of the Shear flow for each curve are reached at the free end.

Warping around box at z=200 mm from restrained end is shown (figure 7.12) to increase from the initial zero value at the zero warping point s=0 mm (centre of web) for all the taper angles mentioned above to their respective peak values at the corner point "B" (s=25 mm) . The peak value of warping at point "B" is seen to jump up with the increase in the taper angle Alpha and Beta . Also the curves are seen to shift up with the increase in the respective taper angles Alpha and Beta. However in case of Alpha equal to zero and Beta equal to 1.0 degree the curve is seen to be at the bottom of all other taper angle curves, thus having a minimum value of warping at the corner point "B". All the curves

show a steep decrease in the warping value after moving beyond point "B" onto the flange and finally reach the zero warping value at the centre of flange (s=75 mm).

FI (Force Intensity) around box at z=20 mm from restrained end is shown (figure 7.13) to increase from the initial zero value at the zero warping point s=0 mm (centre of web) for all the taper angles mentioned above to their respective peak values at the corner point "B" (s=25 mm) . The peak value of FI at point "B" is seen to jump up with the increase in the taper angle Alpha and Beta . Also the curve is seen to shift up with the increase in the respective taper angles Alpha and Beta. However in case of Alpha equal to zero and Beta equal to 1.0 degree the curve is seen to be at the bottom of all other taper angle curves, thus having a minimum value of FI at the corner point "B". All the curves show a steep decrease in the FI value after moving beyond point "B" onto the flange and finally reach the zero value at the centre of flange (s=75 mm).

Shear Flow around box at z=20 mm from restrained end is shown (figure 7.14) to start from the initial shear value of around 120 N/mm at s=0 mm (centre of web) for all the taper angles mentioned above . All the curves then have a decrease in the shear flow as explained previously while going from s=0 mm towards corner point "B" and then onto the flange moving towards the centre of flange (s=75 mm) where all the curves reach their respective minimum shear flow value ranging between 75.66 N/mm and 78.28 N/mm.

7.1.3 COMPARISON OF RESULTS FOR VARIOUS ALPHA & BETA FLANGES [0/45/-45/90]s & WEBS [[45/-45]2]s LAY-UP

The comparison of results for taper angles , Alpha and Beta equal to 0.25, Alpha and Beta equal to 0.50, Alpha and Beta equal to 0.75, Alpha and Beta equal to 1.0, Alpha equal to zero and Beta equal to 1.0, Alpha equal to 1.0 and Beta equal to zero, having flanges [0/45/-45/90]s and webs [[45/-45]2]s lay-up are shown from Figures 7.15 to 7.21

. Force Intensity variation along length is shown (figure 7.15) to have a FI peak value of around 132 N/mm to 135 N/mm at the restrained end for the different taper angles being discussed here. This peak value of FI drops to 1.29 N/mm, 2.44 N/mm, 3.75 N/mm, 5.3 N/mm, 0.0 N/mm, 6.20 N/mm at a distance of 200 mm from the restrained end for all the above mentioned taper angles respectively. The curves in each case then start to increase slowly reaching a peak value between 500 mm to 575 mm from the restrained end. All the curves then drop down to zero value at the free end. A general tendency of the FI curves shifting up with the increase in taper angle Alpha and Beta is witnessed here. The drop from peak value to minimum FI value decreases with the increase in taper angles and also the maximum FI value reached between 500 mm to 575 mm before the curve finally drops to zero increases with the increase in taper angles. The curve for Alpha equal to zero and Beta equal to 1.0 shows a different trend than all other taper angles discussed here. The FI curve for this case drops from a peak value of 132 N/mm to zero within a distance of 170 mm from the restrained end , the curve then moves down to negative FI value implying a change in direction of the Force Intensity. The FI negative value reaches a minimum value of - 0.8 N/mm at 510 mm from the restrained end, and then finally the slope of the curve becomes positive and the curve reaches the FI value of zero at the free end.

Warping variation along length is shown (figure 7.16) to start from zero warping value at the restrained end increasing steeply to 0.0845 mm, 0.0865 mm, 0.0886 mm, 0.0908 mm, 0.0816 mm and 0.0916 mm for all the taper angles mentioned above respectively within the first 100 mm from the restrained end. The curves then increase steadily beyond that point reaching the respective maximum warping values at the free end. The slope of the curves beyond first 100 mm of the restrained end varies with the increase in the taper angle Alpha and Beta. The higher the taper angle Alpha and Beta the higher is the curve pushed up in its warping value as it moves beyond the first 100 mm towards the free end. The curve for Alpha equal to zero and Beta equal to 1.0 degree shows different results from all other taper angles discussed here. The curve in this case starts to drop down after 100 mm from the restrained end and keeps the steady negative slope till reaching its minimum value of 0.0781 mm at the free end.

Shear flow at s=0 mm is shown (figure 7.17) to decrease from an initial shear flow value ranging from 153 N/mm to 158 N/mm for all of the taper angles mentioned above to 105 N/mm, 108 N/mm, 111 N/mm, 114 N/mm, 106 N/mm and 110 N/mm respectively in the first 100 mm from the restrained end. The shear flow curve starts to rise after this point and the higher the taper angle Alpha and Beta the higher is the curve pushed up as it moves towards the free end . The curves reach their respective maximum values at the free end.

Shear flow at s=75 mm is shown (figure 7.18) to increase continuously from the initial value between 16 N/mm to 20 N/mm for all of the taper angles mentioned above to peak values of 117 N/mm, 139 N/mm, 168 N/mm, 208 N/mm, 127 N/mm and 163 N/mm respectively. The higher the taper angle Alpha and Beta the more steeper the curve becomes beyond first 100 mm of restrained end as it moves on towards the free end. The maximum values of the Shear flow for each curve are reached at the free end.

Warping around box at z=200 mm from restrained end is shown (figure 7.19) to increase from the initial zero value at the zero warping point s=0 mm (centre of web) for all the taper angles mentioned above to their respective peak values at the corner point "B" (s=25 mm) . The peak value of warping at point "B" is seen to jump up with the increase in the taper angle Alpha and Beta . Also the curves are seen to shift up with the increase in the respective taper angles Alpha and Beta. However in case of Alpha equal to zero and Beta equal to 1.0 degree the curve is seen to be at the bottom of all other taper angle curves, thus having a minimum value of warping at the corner point "B". All the curves show a steep decrease in the warping value after moving beyond point "B" onto the flange and finally reach the zero warping value at the centre of flange (s=75 mm).

FI (Force Intensity) around box at z=20 mm from restrained end is shown (figure 7.20) to increase from the initial zero value at the zero warping point s=0 mm (centre of web) for all the taper angles mentioned above to their respective peak values for webs and flanges at the corner point "B" (s=25 mm) . The peak value of FI at point "B" is seen to

jump up with the increase in the taper angle Alpha and Beta . Also the curve is seen to shift up with the increase in the respective taper angles Alpha and Beta. However in case of Alpha equal to zero and Beta equal to 1.0 degree the curve is seen to be at the bottom of all other taper angle curves, thus having a minimum value of FI at the corner point "B". All the curves show a steep decrease in the FI value after moving beyond point "B" onto the flange and finally reach the zero value at the centre of flange (s=75 mm).

Shear Flow around box at z=20 mm from restrained end is shown (figure 7.21) to start from the initial shear value of around 136 N/mm at s=0 mm (centre of web) for all the taper angles mentioned above . All the curves then have a decrease in the shear flow as explained previously while going from s=0 mm towards corner point "B" and then onto the flange moving towards the centre of flange (s=75 mm) where all the curves reach their respective minimum shear flow value ranging between 54 N/mm and 56.6 N/mm.

7.1.4 COMPARISON OF RESULTS FOR ALL [0/45/-45/90]s , ALL [[45/-45]2]s AND FLANGES [0/45/-45/90]s WEBS [[45/-45]2]s LAY-UPS WITH ALPHA & BETA EQUAL TO 1.0 DEGREE

The comparison of all [0/45/-45/90]s , all [[45/-45]2]s and Flanges [0/45/-45/90]s Webs [[45/-45]2]s lay-ups with Alpha & Beta Equal to 1.0 degree is shown from figures 7.22 to 7.28. Force Intensity (FI) variation along length at point "B" shows (figure 7.22) a steep decline from the initial maximum FI values of 100 N/mm, 64 N/mm and 135 N/mm at the restrained end to the minimum values of 5.7 N/mm , 2.81 N/mm and 5.3 N/mm respectively with in the first 100 to 200 mm from the restrained end. The FI values then start to increase slightly from this minimum point onwards as the curve moves towards the free end and reach their maximum values of 10.5 N/mm, 4.7 N/mm and 9.95 N/mm respectively at a distance of around 540 mm from the restrained end. All

the curves then drop to zero FI value at the free end. The FI curve for all angle ply lay-up is at the bottom of the figure with all quasi lay-up curve above it and the quasi flanges web angle ply lay-up at the top . This indicates the higher warping rigidity of all angle ply lay-up resulting in lower Force Intensity value for this lay-up than the other two lay-ups being compared with here.

Warping along length of box at point "B" is shown (figure 7.23) to start from zero warping value at the restrained end for all the three lay-ups mentioned above. The warping curves reach 0.0638 mm , 0.038 mm and 0.0908 mm respectively for all above mentioned lay-ups at 100 mm from the restrained end. The curve for all angle lay-up remains at the bottom of all curves, the curve for all quasi lay-up is the next higher curve in the figure and curve achieving maximum warping all along the length is the curve with flanges quasi and web angle ply lay-up. This indicates a strong torsional rigidity in the all angle lay-up beam due to the presence of 45/-45 plies in the lay-up giving it more torsional rigidity than the other two lay-ups.

Shear flow along length at s=0 mm is shown (figure 7.24) to drop from the initial restrained end shear flow values of 139 N/mm , 140 N/mm and 153.6 N/mm for all the three lay-ups mentioned above to 114 N/mm , 112 N/mm and 114 N/mm respectively within a distance of first 100 mm from the restrained end. The three shear flow curves then almost superimpose as they continuously increase while moving towards the free end and reach the common maximum shear flow value of 224 N/mm at the free end.

Shear flow along length at s=75 mm is shown (figure 7.25) to start from the initial restrained end shear flow values of 52 N/mm , 49 N/mm and 20 N/mm for all the three lay-ups mentioned above respectively . All the three curves become synonymous between z=100 mm to z=200 mm from the restrained end as they move towards the free end and reach the maximum shear flow value of 209 N/mm 212 N/mm and 208.26 N/mm respectively at the free end.

Warping around the box section at z=200 mm from the restrained end is shown (figure 7.26) to start from the initial warping value of zero at the centre of web (s=0 mm) for all the three lay-ups rising to maximum warping value of 0.0757 mm , 0.0431 mm and 0.103 mm respectively. It is obvious from the figure that the all angle ply lay-up has the minimum warping curve and is at the bottom of other two lay-up curves. The curve for all quasi lay-up is the next higher curve and the curve for flanges quasi web angle ply lay-up is at the top with maximum warping around the box section. This indicates a strong torsional rigidity in all angle lay-up beam due to the presence of [45/-45] plies in the lay-up giving it more torsional rigidity than the other two lay-ups.

Force Intensity (FI) around the box section at z=20 mm from the restrained end is shown (figure 7.27) to start from the initial FI value of zero at the centre of web (s=0 mm) for all the three lay-ups to their maximum values of 62.2 N/mm , 30 N/mm and 68.66 N/mm in web and 93 N/mm in flanges respectively at point "B" (s= 25 mm) . All the curves then drop to zero FI value at the centre of flange (s=75 mm). The curve for all angle ply lay-up is seen to be at the bottom in the figure indicating minimum Force Intensity value around the box section with curve for all quasi lay-up above it and the curve for flanges quasi web angle ply lay-up at the top. This indicates a strong warping rigidity in all angle lay-up beam due to the presence of [45/-45] plies in the lay-up giving it more warping rigidity than the other two lay-ups.

Shear flow around the box section at z=20 mm is shown (figure 7.28) to start from initial shear flow values of 125 N/mm , 120 N/mm and 135.5 N/mm respectively at centre of web (s=0 mm). The curves then drop to 108.5 N/mm, 107 N/mm and 112 N/mm at the corner point "B". The three lay-up curves then continue to decrease beyond this corner point "B" reaching their respective minimum shear flow values of 73 N/mm 78 N/mm and 57 N/mm at the centre of flange (s=75 mm).

7.2 MULTI CELL TAPERED BOX

The theoretical results for a variety of composite lay-ups for Multi- cell tapered box for various Alpha and Beta are shown in this section.

7.2.1 COMPARISON OF RESULTS FOR VARIOUS ALPHA & BETA FLANGES & WEBS ALL [0/45/-45/90]s LAY-UP

The comparison of results for taper angles , Alpha and Beta equal to 0.25, Alpha and Beta equal to 0.50, Alpha and Beta equal to 0.75, Alpha and Beta equal to 1.0, Alpha equal to zero and Beta equal to 1.0, Alpha equal to 1.0 and Beta equal to zero, having all [0/45/-45/90]s lay-up are shown from Figures 7.29 to 7.37 . Force Intensity variation along length at point "B" is shown (figure 7.29) to have a FI peak value of around 95 N/mm to 104 N/mm at the restrained end for the different taper angles being discussed here. This peak value of FI drops to 14.66 N/mm, 15.6 N/mm, 16.6 N/mm, 17.7 N/mm, 10.6 N/mm, 20.7 N/mm at a distance of 100 mm from the restrained end for all the above mentioned taper angles respectively. The curves in each case then start to increase slowly reaching a peak value between 500 mm to 575 mm from the restrained end. All the curves then drop down to zero value at the free end. A general tendency of the FI curves shifting up with the increase in taper angle Alpha and Beta is witnessed here. The drop from peak value to minimum FI value decreases with the increase in taper angles and also the maximum FI value reached between 500 mm to 575 mm before the curve finally drops to zero increases with the increase in taper angles. The curve for Alpha equal to zero and Beta equal to 1.0 shows a different trend than all other taper angles discussed here. The FI curve for this case drops from a peak value of 104 N/mm to zero within a distance of 175 mm from the restrained end , the curve then moves down to negative FI value implying a change in direction of the Force Intensity. The FI negative

value reaches a minimum value of -3.5 N/mm at 520 mm from the restrained end, and then finally the slope of the curve becomes positive and the curve reaches the FI value of zero at the free end.

Force Intensity variation along length at point "C" is shown (figure 7.30) to have a FI peak value of around 43 N/mm to 47 N/mm at the restrained end for the different taper angles being discussed here. This peak value of FI drops to 6.66 N/mm, 7.09 N/mm, 7.54 N/mm, 8.03 N/mm, 5.25 N/mm, 8.95 N/mm at a distance of 100 mm from the restrained end for all the above mentioned taper angles respectively. The curves in each case then start to increase slowly reaching a peak value between 500 mm to 575 mm from the restrained end. All the curves then drop down to zero value at the free end. A general tendency of the FI curves shifting up with the increase in taper angle Alpha and Beta is witnessed here. The drop from peak value to minimum FI value decreases with the increase in taper angles and also the maximum FI value reached between 500 mm to 575 mm before the curve finally drops to zero increases with the increase in taper angles. The curve for Alpha equal to zero and Beta equal to 1.0 shows a different trend than all other taper angles discussed here. The FI curve for this case drops from a peak value of 47 N/mm to zero within a distance of 200 mm from the restrained end , the curve then moves down to negative FI value implying a change in direction of the Force Intensity. The FI negative value reaches a minimum value of - 0.95 N/mm at 500 mm from the restrained end, and then finally the slope of the curve becomes positive and the curve reaches the FI value of zero at the free end.

Warping variation along length at point "B" is shown (figure 7.31) to start from zero warping value at the restrained end increasing steeply to 0.0736 mm, 0.0756 mm, 0.0777 mm, 0.08 mm, 0.0715 mm and 0.0795 mm for all the taper angles mentioned above respectively within the first 100 mm from the restrained end. The curves then increase steadily beyond that point reaching the respective maximum warping values at the free end. The slope of the curves beyond first 100 mm of the restrained end varies with the increase in the taper angle Alpha and Beta. The higher the taper angle Alpha and Beta the higher is the curve pushed up in its warping value as it moves beyond the first 100

mm towards the free end. The curve for Alpha equal to zero and Beta equal to 1.0 degree shows different results from all other taper angles discussed here. The curve in this case starts to drop down after 100 mm from the restrained end and keeps the steady negative slope till reaching the minimum value of warping 0.0585 mm at the free end.

Warping variation along length at point "C" is shown (figure 7.32) to start from zero warping value at the restrained end increasing steeply to 0.0334 mm, 0.0344 mm, 0.0353 mm, 0.0364 mm, 0.0330 mm and 0.0356 mm for all the taper angles mentioned above respectively within the first 100 mm from the restrained end. The curves then increase steadily beyond that point reaching the respective maximum warping values at the free end. The slope of the curves beyond first 100 mm of the restrained end varies with the increase in the taper angle Alpha and Beta. The higher the taper angle Alpha and Beta the higher is the curve pushed up in its warping value as it moves beyond the first 100 mm towards the free end. The curve for Alpha equal to zero and Beta equal to 1.0 degree shows different results from all other taper angles discussed here. The curve in this case starts to drop down after 100 mm from the restrained end and keeps the steady negative slope till reaching the minimum value of warping 0.0316 mm at the free end.

Shear flow at s=0 mm is shown (figure 7.33) to decrease from an initial shear flow value ranging from 80 N/mm to 84 N/mm for all of the taper angles mentioned above to 67.7 N/mm, 69.8 N/mm, 72 N/mm, 74.5 N/mm, 69.7 N/mm and 70 N/mm respectively in the first 100 mm from the restrained end. The shear flow curves start to rise after this point and the higher the taper angle Alpha and Beta the higher is the curve pushed up as it moves towards the free end . The curves reach their respective maximum values at the free end. This behaviour of shear flow occurs as the warping shear flow starts to reduce steadily as the curve moves away from the restrained end. As the total shear flow at location s=0 mm is the addition of the Bredt Batho shear flow and warping shear flow therefore the reduction of warping shear flow results in reduction of the total shear flow in the first 100 mm from restrained end. On the other hand the Bredt Batho shear flow at the restrained end starts to increase when the effective area of the box is continuously reduced due to the taper angle as the curve moves away from the restrained end . This

increase in the Bredt Batho value increases the total shear flow and a steady increase in shear flow is hence witnessed along the length of box till the curves reach the peak value at the free end.

Shear flow at s=100 mm is shown (figure 7.34) to increase continuously from the initial value between 45 N/mm to 51 N/mm for all of the taper angles mentioned above to peak values of 74 N/mm, 77 N/mm, 80 N/mm, 83 N/mm, 77 N/mm and 76.5 N/mm respectively. The higher the taper angle Alpha and Beta the more steeper the curve becomes beyond first 100 mm of restrained end as it moves on towards the free end. The maximum values of the Shear flow for each curve are reached at the free end. This behaviour of shear flow occurs due to constant increase in the Bredt Batho shear flow along the length of beam affected due to a continuous decrease in the area along the length. The increase in total shear flow along length is also affected by the continuous decrease in the warping shear flow as the total shear flow at location s=100 mm is the difference of Bredt Batho shear flow and the warping shear flow. Hence the reduction in warping shear flow results in the increase in total shear flow along length at this location

Warping around box at z=200 mm from restrained end is shown (figure 7.35) to increase from the initial zero value at the zero warping point s=0 mm (centre of web) for all the taper angles mentioned above to their respective peak values at the corner point "B" (s=25 mm) . The warping curve drops down steeply from point "B" onwards as it moves towards point "C" (s=75 mm). The peak values of warping at point "B" and point "C" are seen to jump up with the increase in the taper angle Alpha and Beta . Also the curves are seen to shift up with the increase in the respective taper angles Alpha and Beta. However in case of Alpha equal to zero and Beta equal to 1.0 degree the curve is seen to be at the bottom of all other taper angle curves, thus having a minimum value of warping at the corner point "B" and junction point "C". All the curves show a steep decrease in the warping value after moving further onto the flange beyond point "B" towards point "C" (s=75 mm) and then finally reach the zero warping value at the centre of flange (s=100 mm).

FI (Force Intensity) around box at z=20 mm from restrained end is shown (figure 7.36) to increase from the initial zero value at the zero warping point s=0 mm (centre of web) for all the taper angles mentioned above to their respective peak values at the corner point "B" (s=25 mm) . The peak value of FI at point "B" is seen to jump up with the increase in the taper angle Alpha and Beta . Also the curve is seen to shift up with the increase in the respective taper angles Alpha and Beta. However in case of Alpha equal to zero and Beta equal to 1.0 degree the curve is seen to be at the bottom of all other taper angle curves, thus having a minimum value of FI at the corner point "B". All the curves show a steep decrease in the FI value after moving beyond point "B" onto the flange towards junction point "C" and finally reach the zero value at the centre of flange (s=100 mm).

Shear Flow around box at z=20 mm from restrained end is shown (figure 7.37) to start from the initial shear value of around 77 N/mm at s=0 mm (centre of web) for all the taper angles mentioned above , that is the addition of warping shear flow and Bredt Batho at this location.. All the curves have a decrease in the shear flow while moving from centre of web (s=0 mm) to corner point "B" (s=25 mm) .This is due to the fact that total shear flow reduces steadily because of the gradual decrease in the warping shear flow as the curve moves around the box section from the centre of web to the corner point "B" (s=25 mm). After moving away from the corner point "B", the total shear flow starts to reduce as the direction of warping shear flow in the flange now becomes opposite to that of the Bredt Batho shear flow, hence the addition of these two shear flows in fact now results in subtraction of warping shear flow from the Bredt Batho giving a lower value for total shear flow all along the length of flange till the curve reaches point "C" which is the junction point of flange and inner web. All the curves have a sudden upwards jump in shear flow at junction point "C" (s=75 mm) due to the addition of the shear flow coming from the centre of inner web adding into the shear flow coming from the direction of point "B" . At junction point "C" the shear flow values are seen to be shifting upwards with the increase in the taper angle Alpha and Beta. After moving beyond point "C" the curves continue to decrease steadily due to above mentioned reason as they move onto the flange moving towards the centre of flange

(s=100 mm) where all the curves reach their respective minimum shear flow values ranging between 48 N/mm and 57 N/mm.

7.2.2 COMPARISON OF RESULTS FOR VARIOUS ALPHA & BETA FLANGES & WEBS ALL [[45/-45]2]s LAY-UP

The comparison of results for taper angles , Alpha and Beta equal to 0.25, Alpha and Beta equal to 0.50, Alpha and Beta equal to 0.75, Alpha and Beta equal to 1.0, Alpha equal to zero and Beta equal to 1.0, Alpha equal to 1.0 and Beta equal to zero, having all [[45/-45]2]s lay-up are shown from Figures 7.38 to 7.46 . Force Intensity variation along length at point "B" is shown (figure 7.38) to have a FI peak value of around 62 N/mm to 66 N/mm at the restrained end for the different taper angles being discussed here. This peak value of FI drops to 3.40 N/mm, 3.74 N/mm, 4.10 N/mm, 4.50 N/mm, 1.80 N/mm, 5.82 N/mm at a distance of 100 mm from the restrained end for all the above mentioned taper angles respectively. The curves in each case then start to increase slowly reaching a peak value between 530 mm to 560 mm from the restrained end. All the curves then drop down to zero FI value at the free end. A general tendency of the FI curves shifting up with the increase in taper angle Alpha and Beta is witnessed here. The drop from peak value to minimum FI value decreases with the increase in taper angles and also the maximum FI value reached between 530 mm to 560 mm before the curve finally drops to zero increases with the increase in taper angles. The curve for Alpha equal to zero and Beta equal to 1.0 shows a different trend than all other taper angles discussed here. The FI curve for this case drops from a peak value of 66 N/mm to zero within a distance of 130 mm from the restrained end , the curve then moves down to negative FI value implying a change in direction of the Force Intensity. The FI negative value reaches a minimum value of -1.6 N/mm at 540 mm from the restrained end, and then finally the

slope of the curve becomes positive and the curve reaches the FI value of zero at the free end.

Force Intensity variation along length at point "C" is shown (figure 7.39) to have a FI peak value of around 28 N/mm to 30 N/mm at the restrained end for the different taper angles being discussed here. This peak value of FI drops to 1.54 N/mm, 1.70 N/mm, 1.86 N/mm, 2.04 N/mm, 0.99 N/mm, 2.45 N/mm at a distance of 100 mm from the restrained end for all the above mentioned taper angles respectively. The curves in each case then start to increase slowly reaching a peak value between 520 mm to 560 mm from the restrained end. All the curves then drop down to zero value at the free end. A general tendency of the FI curves shifting up with the increase in taper angle Alpha and Beta is witnessed here. The drop from peak value to minimum FI value decreases with the increase in taper angles and also the maximum FI value reached between 520 mm to 560 mm before the curve finally drops to zero increases with the increase in taper angles. The curve for Alpha equal to zero and Beta equal to 1.0 shows a different trend than all other taper angles discussed here. The FI curve for this case drops from a peak value of 30 N/mm to zero within a distance of 150 mm from the restrained end , the curve then moves down to negative FI value implying a change in direction of the Force Intensity. The FI negative value reaches a minimum value of - 0.44 N/mm at 540 mm from the restrained end, and then finally the slope of the curve becomes positive and the curve reaches the FI value of zero at the free end.

Warping variation along length at point "B" is shown (figure 7.40) to start from zero warping value at the restrained end increasing steeply to 0.0461 mm, 0.0471 mm, 0.0482 mm, 0.0493 mm, 0.0441 mm and 0.0501 mm for all the taper angles mentioned above respectively within the first 100 mm from the restrained end. The curves then increase steadily beyond that point reaching the respective maximum warping values at the free end. The slope of the curves beyond first 100 mm of the restrained end varies with the increase in the taper angle Alpha and Beta. The higher the taper angle Alpha and Beta the higher is the curve pushed up in its warping value as it moves beyond the first 100 mm towards the free end. The curve for Alpha equal to zero and Beta equal to 1.0

degree shows different results from all other taper angles discussed here. The curve in this case starts to drop down after 100 mm from the restrained end and keeps the steady negative slope till reaching the minimum value of warping 0.0331 mm at the free end.

Warping variation along length at point "C" is shown (figure 7.41) to start from zero warping value at the restrained end increasing steeply to 0.021 mm, 0.0214 mm, 0.0219 mm, 0.0224 mm, 0.0204 mm and 0.0224 mm for all the taper angles mentioned above respectively within the first 100 mm from the restrained end. The curves then increase steadily beyond that point reaching the respective maximum warping values at the free end. The slope of the curves beyond first 100 mm of the restrained end varies with the increase in the taper angle Alpha and Beta. The higher the taper angle Alpha and Beta the higher is the curve pushed up in its warping value as it moves beyond the first 100 mm towards the free end. The curve for Alpha equal to zero and Beta equal to 1.0 degree shows different results from all other taper angles discussed here. The curve in this case starts to drop down after 100 mm from the restrained end and keeps the steady negative slope till reaching the minimum value of warping 0.0179 mm at the free end.

Shear flow at s=0 mm is shown (figure 7.42) to decrease from an initial shear flow value ranging from 81 N/mm to 84 N/mm for all of the taper angles mentioned above to 65.7 N/mm, 68.0 N/mm, 70 N/mm, 73.0 N/mm, 67.9 N/mm and 68 N/mm respectively in the first 100 mm from the restrained end. The shear flow curves start to rise after this point and the higher the taper angle Alpha and Beta the higher is the curve pushed up as it moves towards the free end . The curves reach their respective maximum values at the free end.

Shear flow at s=100 mm is shown (figure 7.43) to increase continuously from the initial value between 45 N/mm to 49 N/mm for all of the taper angles mentioned above to peak values of 93 N/mm, 119 N/mm, 158 N/mm, 218 N/mm, 132 N/mm and 123 N/mm respectively. The higher the taper angle Alpha and Beta the more steeper the curve becomes beyond first 100 mm of restrained end as it moves on towards the free end . The maximum value of the Shear flow for each of the curves is reached at the free end.

Warping around box at z=200 mm from restrained end is shown (figure 7.44) to increase from the initial zero value at the zero warping point s=0 mm (centre of web) for all the taper angles mentioned above to their respective peak values at the corner point "B" (s=25 mm) . The warping curve drops down steeply from point "B" onwards as it moves towards point "C" (s=75 mm). The peak values of warping at point "B" and point "C" are seen to jump up with the increase in the taper angle Alpha and Beta . Also the curves are seen to shift up with the increase in the respective taper angles Alpha and Beta. However in case of Alpha equal to zero and Beta equal to 1.0 degree the curve is seen to be at the bottom of all other taper angle curves, thus having a minimum value of warping at the corner point "B" and junction point "C". All the curves show a steep decrease in the warping value after moving further onto the flange beyond point "B" towards point "C" (s=75 mm) and then finally reach the zero warping value at the centre of flange (s=100 mm).

FI (Force Intensity) around box at z=20 mm from restrained end is shown (figure 7.45) to increase from the initial zero value at the zero warping point s=0 mm (centre of web) for all the taper angles mentioned above to their respective peak values at the corner point "B" (s=25 mm) . The peak value of FI at point "B" is seen to jump up with the increase in the taper angle Alpha and Beta . Also the curve is seen to shift up with the increase in the respective taper angles Alpha and Beta. However in case of Alpha equal to zero and Beta equal to 1.0 degree the curve is seen to be at the bottom of all other taper angle curves, thus having a minimum value of FI at the corner point "B". All the curves show a steep decrease in the FI value after moving beyond point "B" onto the flange towards junction point "C" and finally reach the zero value at the centre of flange (s=100 mm).

Shear Flow around box at z=20 mm from restrained end is shown (figure 7.46) to start from the initial shear flow value of around 75 N/mm at s=0 mm (centre of web) for all the taper angles mentioned above . All the curves have a decrease in the shear flow while moving from centre of web (s=0 mm) to corner point "B" (s=25 mm) as explained in

previously. All the curves have a sudden upwards jump in shear flow at junction point "C" (s=75 mm) due to the addition of the shear flow coming from the centre of inner web adding into the shear flow coming from the direction of point "B" . At junction point "C" the shear flow values are seen to be shifting upwards with the increase in the taper angle Alpha and Beta. After moving beyond point "C" the curves continue to decrease as they move onto the flange moving towards the centre of flange (s=100 mm) where all the curves reach their respective minimum shear flow values ranging between 56 N/mm and 60 N/mm.

7.2.3 COMPARISON OF RESULTS FOR VARIOUS ALPHA & BETA FLANGES [0/45/-45/90]s & WEBS [[45/-45]2]s LAY-UP

The comparison of results for taper angles , Alpha and Beta equal to 0.25, Alpha and Beta equal to 0.50, Alpha and Beta equal to 0.75, Alpha and Beta equal to 1.0, Alpha equal to zero and Beta equal to 1.0, Alpha equal to 1.0 and Beta equal to zero, having flanges [0/45/-45/90]s and webs [[45/-45]2]s lay-up are shown from Figures 7.47 to 7.55 . Force Intensity variation along length at point "B" is shown (figure 7.47) to have a FI peak value of around 108 N/mm to 115 N/mm at the restrained end for the different taper angles being discussed here. This peak value of FI drops to 12.8 N/mm, 13.6 N/mm, 14.5 N/mm, 15.5 N/mm, 9.80 N/mm, 17.7 N/mm at a distance of 100 mm from the restrained end for all the above mentioned taper angles respectively. The curves in each case then start to increase slowly reaching a peak value between 500 mm to 560 mm from the restrained end. All the curves then drop down to zero FI value at the free end. A general tendency of the FI curves shifting up with the increase in taper angle Alpha and Beta is witnessed here. The drop from peak value to minimum FI value decreases with the increase in taper angles and also the maximum FI value reached between 500 mm to 560 mm before the curve finally drops to zero increases with the increase in taper angles. The curve for Alpha equal to zero and Beta equal to 1.0 shows a different trend than all other taper angles discussed here. The FI curve for this case drops

from a peak value of 115 N/mm to zero within a distance of 190 mm from the restrained end , the curve then moves down to negative FI value implying a change in direction of the Force Intensity. The FI negative value reaches a minimum value of -1.7 N/mm at 530 mm from the restrained end, and then finally the slope of the curve becomes positive and the curve reaches the FI value of zero at the free end.

Force Intensity variation along length at point "C" is shown (figure 7.48) to have a FI peak value of around 44 N/mm to 48 N/mm at the restrained end for the different taper angles being discussed here. This peak value of FI drops to 5.27 N/mm, 5.62 N/mm, 5.99 N/mm, 6.39 N/mm, 4.29 N/mm, 7 N/mm at a distance of 100 mm from the restrained end for all the above mentioned taper angles respectively. The curves in each case then start to increase slowly reaching a peak value between 500 mm to 550 mm from the restrained end. All the curves then drop down to zero value at the free end. A general tendency of the FI curves shifting up with the increase in taper angle Alpha and Beta is witnessed here. The drop from peak value to minimum FI value decreases with the increase in taper angles and also the maximum FI value reached between 500 mm to 550 mm before the curve finally drops to zero increases with the increase in taper angles. The curve for Alpha equal to zero and Beta equal to 1.0 shows a different trend than all other taper angles discussed here. The FI curve for this case drops from a peak value of 47.5 N/mm to zero within a distance of 220 mm from the restrained end , the curve then moves down to negative FI value implying a change in direction of the Force Intensity. The FI negative value reaches a minimum value of - 0.36 N/mm at 530 mm from the restrained end, and then finally the slope of the curve becomes positive and the curve reaches the FI value of zero at the free end.

Warping variation along length at point "B" is shown (figure 7.49) to start from zero warping value at the restrained end increasing steeply to 0.0907 mm, 0.0931 mm, 0.0955 mm, 0.0981 mm, 0.0894 mm and 0.0967 mm for all the taper angles mentioned above respectively within the first 100 mm from the restrained end. The curves then increase steadily beyond that point reaching the respective maximum warping values at the free end. The slope of the curves beyond first 100 mm of the restrained end varies with the

increase in the taper angle Alpha and Beta. The higher the taper angle Alpha and Beta the higher is the curve pushed up in its warping value as it moves beyond the first 100 mm towards the free end. The curve for Alpha equal to zero and Beta equal to 1.0 degree shows different results from all other taper angles discussed here. The curve in this case starts to drop down after 150 mm from the restrained end and keeps the steady negative slope till reaching the minimum value of warping 0.0848 mm at the free end.

Warping variation along length at point "C" is shown (figure 7.50) to start from zero warping value at the restrained end increasing steeply to 0.0374 mm, 0.0384 mm, 0.0394 mm, 0.0405 mm, 0.0373 mm and 0.0395 mm for all the taper angles mentioned above respectively within the first 100 mm from the restrained end. The curves then increase steadily beyond that point reaching the respective maximum warping values at the free end. The slope of the curves beyond first 100 mm of the restrained end varies with the increase in the taper angle Alpha and Beta. The higher the taper angle Alpha and Beta the higher is the curve pushed up in its warping value as it moves beyond the first 100 mm towards the free end. The curve for Alpha equal to zero and Beta equal to 1.0 degree shows different results from all other taper angles discussed here. The curve in this case starts to drop down after 100 mm from the restrained end and keeps the steady negative slope till reaching the minimum value of warping 0.0383 mm at the free end.

Shear flow at s=0 mm is shown (figure 7.51) to decrease from an initial shear flow value ranging from 86 N/mm to 90 N/mm for all of the taper angles mentioned above to 68.7 N/mm, 71 N/mm, 73 N/mm, 75.6 N/mm, 70.6 N/mm and 71 N/mm respectively in the first 100 mm from the restrained end. The shear flow curves start to rise after this point and the higher the taper angle Alpha and Beta the higher is the curve pushed up as it moves towards the free end . The curves reach their respective maximum values at the free end.

Shear flow at s=100 mm is shown (figure 7.52) to increase continuously from the initial value between 38 N/mm to 42.6 N/mm for all of the taper angles mentioned above to peak values of 91 N/mm, 116 N/mm, 153 N/mm, 211 N/mm, 129 N/mm and 119 N/mm

respectively. The higher the taper angle Alpha and Beta the more steeper the curve becomes beyond first 100 mm of restrained end as it moves on towards the free end . The maximum value of the Shear flow for each of the curves is reached at the free end.

Warping around box at z=200 mm from restrained end is shown (figure 7.53) to increase from the initial zero value at the zero warping point s=0 mm (centre of web) for all the taper angles mentioned above to their respective peak values at the corner point "B" (s=25 mm) . The warping curve drops down steeply from point "B" onwards as it moves towards point "C" (s=75 mm). The peak values of warping at point "B" and point "C" are seen to jump up with the increase in the taper angle Alpha and Beta . Also the curves are seen to shift up with the increase in the respective taper angles Alpha and Beta. However in case of Alpha equal to zero and Beta equal to 1.0 degree the curve is seen to be at the bottom of all other taper angle curves, thus having a minimum value of warping at the corner point "B" and junction point "C". All the curves show a steep decrease in the warping value after moving further onto the flange beyond point "B" towards point "C" (s=75 mm) and then finally reach the zero warping value at the centre of flange (s=100 mm).

FI (Force Intensity) around box at z=20 mm from restrained end is shown (figure 7.54) to increase from the initial zero value at the zero warping point s=0 mm (centre of web) for all the taper angles mentioned above to their respective peak values at the corner point "B" (s=25 mm) in web where an upward jump is experienced by all curves as the lay-up changes from [[45/-45]2]s in webs to [0/45/-45/90]s in flanges. The peak value of FI at point "B" is seen to jump up with the increase in the taper angle Alpha and Beta . Also the curve is seen to shift up with the increase in the respective taper angles Alpha and Beta. All the curves show a steep decrease in the FI value after moving beyond point "B" onto the flange towards junction point "C" and finally reach the zero value at the centre of flange (s=100 mm).

Shear Flow around box at z=20 mm from restrained end is shown (figure 7.55) to start from the initial shear value of around 81 N/mm at s=0 mm (centre of web) for all the

taper angles mentioned above . All the curves have a decrease in the shear flow while moving from centre of web (s=0 mm) to corner point "B" (s=25 mm) as explained in previously. All the curves have a sudden upwards jump in shear flow at junction point "C" (s=75 mm) due to the addition of the shear flow coming from the centre of inner web adding into the shear flow coming from the direction of point "B" . At junction point "C" the shear flow values are seen to be shifting upwards with the increase in the taper angle Alpha and Beta. After moving beyond point "C" the curves continue to decrease as they move onto the flange moving towards the centre of flange (s=100 mm) where all the curves reach their respective minimum shear flow values ranging between 43 N/mm and 48.5 N/mm.

7.2.4 COMPARISON OF RESULTS FOR ALL [0/45/-45/90]s , ALL [[45/-45]2]s AND FLANGES [0/45/-45/90]s WEBS [[45/-45]2]s LAY-UPS WITH ALPHA & BETA EQUAL TO 1.0 DEGREE

The comparison of all [0/45/-45/90]s , all [[45/-45]2]s and Flanges [0/45/-45/90]s Webs [[45/-45]2]s lay-ups with Alpha & Beta Equal to 1.0 degree is shown from figures 7.56 to 7.64.

Force Intensity (FI) variation along length at point "B" shows (figure 7.56) a steep decline from the initial maximum FI values of 102 N/mm, 65 N/mm and 113 N/mm at the restrained end to the minimum values of 5.4 N/mm , 2.03 N/mm and 5.19 N/mm respectively with in the first 100 to 200 mm from the restrained end. The FI values then start to increase slightly from this minimum point onwards as the curves move towards the free end and reach their maximum values of 8.59 N/mm, 3.78 N/mm and 8.6 N/mm respectively at a distance of around 560 mm from the restrained end. All the curves then drop to zero FI value at the free end. The FI curve for all angle ply lay-up is at the bottom of the figure with all quasi lay-up curve above it and the quasi flanges web angle ply lay-up at the top . This indicates the higher warping rigidity of all angle ply lay-up

resulting in lower Force Intensity value for this lay-up than the other two lay-ups being compared with here.

Force Intensity (FI) variation along length at point "C" shows (figure 7.57) a shallow decline from the initial maximum FI values of 46.5 N/mm, 29.6 N/mm and 47 N/mm at the restrained end to the minimum values of 2.47 N/mm , 0.925 N/mm and 2.14 N/mm respectively with in the first 200 to 250 mm from the restrained end. The FI values then start to increase slightly from this minimum point onwards as the curves move towards the free end and reach their maximum values of 3.90 N/mm, 1.72 N/mm and 3.55 N/mm respectively at a distance of around 560 mm from the restrained end. All the curves then drop to zero FI value at the free end. The FI curve for all angle ply lay-up is at the bottom of the figure with all quasi lay-up curve above it and the quasi flanges web angle ply lay-up at the top.

Warping along length of box at point "B" is shown (figure 7.58) to start from zero warping value at the restrained end for all the three lay-ups mentioned above. The warping curves reach 0.08 mm , 0.0493 mm and 0.098 mm respectively for all above mentioned lay-ups at 100 mm from the restrained end. All the three curves reach their respective peak warping values of 0.1411 mm, 0.0804 mm and 0.1679 mm at the free end. The curve for all angle lay-up remains at the bottom of all curves, the curve for all quasi lay-up is the next higher curve in the figure and curve achieving maximum warping all along the length is the curve with flanges quasi and web angle ply lay-up. This indicates a strong torsional rigidity in the all angle lay-up beam due to the presence of (45/-45) plies in the lay-up giving it more torsional rigidity than the other two lay-ups.

Warping along length of box at point "C" is shown (figure 7.59) to start from zero warping value at the restrained end for all the three lay-ups mentioned above. The warping curves reach 0.0364 mm , 0.0224 mm and 0.0405 mm respectively for all above mentioned lay-ups at 100 mm from the restrained end. All the three curves reach their respective peak warping values of 0.0641 mm, 0.0366 mm and 0.0693 mm at the free end. The curve for all angle lay-up remains at the bottom of all curves, the curve for all

quasi lay-up is the next higher curve in the figure and curve achieving maximum warping all along the length is the curve with flanges quasi and web angle ply lay-up. This indicates a strong torsional rigidity in the all angle lay-up beam due to the presence of (45/-45) plies in the lay-up giving it more torsional rigidity than the other two lay-ups.

Shear flow along length at s=0 mm is shown (figure 7.60) to drop from the initial restrained end shear flow values of 80 N/mm , 81 N/mm and 87 N/mm for all the three lay-ups mentioned above to 74.5 N/mm , 73 N/mm and 75.5 N/mm respectively in the first 100 mm from the restrained end. The three shear flow curves then almost superimpose as they move towards the free end and reach their maximum shear flow values of 188 N/mm, 187 N/mm and 191 N/mm respectively at the free end.

Shear flow along length at s=100 mm is shown (figure 7.61) to start from the initial restrained end shear flow values of 51 N/mm , 49 N/mm and 42 N/mm for all the three lay-ups mentioned above respectively . All quasi and all angle ply lay-up curves become synonymous between z=100 mm to z=200 mm from the restrained end . Flanges quasi & webs angle ply lay up curve remains at the bottom of other two curves till they reach the free end where all the three curves reach their maximum shear flow values of 217 N/mm 218 N/mm and 211 N/mm respectively at the free end.

Warping around the box section at z=200 mm from the restrained end is shown (figure 7.62) to start from the initial warping value of zero at the centre of web (s=0 mm) for all the three lay-ups rising to maximum warping value of 0.0965 mm , 0.0552 mm and 0.1152 mm respectively at pint "B" (s=25 mm) . The three warping curves drop to .0439 mm, .0251 mm and .0475 mm respectively at the junction point "C" (s=75 mm). It is obvious from the figure that the all angle ply lay-up has the minimum warping curve and is at the bottom of other two lay-up curves. The curve for all quasi lay-up is the next higher curve and the curve for flanges quasi & web angle ply lay-up is at the top with maximum warping around the box section. This indicates a strong torsional rigidity in all angle ply lay-up beam due to the presence of (45/-45) plies in the lay-up giving it more torsional rigidity than the other two lay-ups.

Force Intensity (FI) around the box section at z=20 mm from the restrained end is shown (figure 7.63) to start from the initial FI value of zero at the centre of web (s=0 mm) for all the three lay-ups to their maximum values of 74 N/mm , 38 N/mm and 70 N/mm in web & 95 N/mm in flanges respectively at point "B" (s= 25 mm) . All the three lay-ups then drop to the values of 34 N/mm , 17.5 N/mm and 29 N/mm in web & 39 N/mm in flanges respectively at point "C" (s= 75 mm) . All the curves finally drop to zero FI value at the centre of flange (s=100 mm). The curve for all angle ply lay-up is seen to be at the bottom in the figure indicating minimum Force Intensity value around the box section with curve for all quasi lay-up above it and the curve for flanges quasi web angle ply lay-up at the top. This indicates a strong warping rigidity in all angle lay-up beam due to the presence of [45/-45] plies in the lay-up giving it more warping rigidity than the other two lay-ups.

Shear flow around the box section at z=20 mm is shown (figure 7.64) to start from initial shear flow values of 76 N/mm , 75 N/mm and 81 N/mm respectively at centre of web (s=0 mm). The curves then drop to 25.5 N/mm, 30 N/mm and 19 N/mm at the junction point "C". A sudden jump in shear flow is witnessed at this location for all the three curves as the shear flow coming from the direction of inner web now joins in and adds up to the shear flow coming from the direction of corner point "B". Hence we witness a jump in the value of shear flows at this location to 68 N/mm , 69 N/mm and 61 N/mm respectively for all the three curves. The three lay-up curves then continue to decrease beyond this junction point "C" reaching their respective minimum shear flow values of 51 N/mm 58 N/mm and 44 N/mm at the centre of flange (s=100 mm).

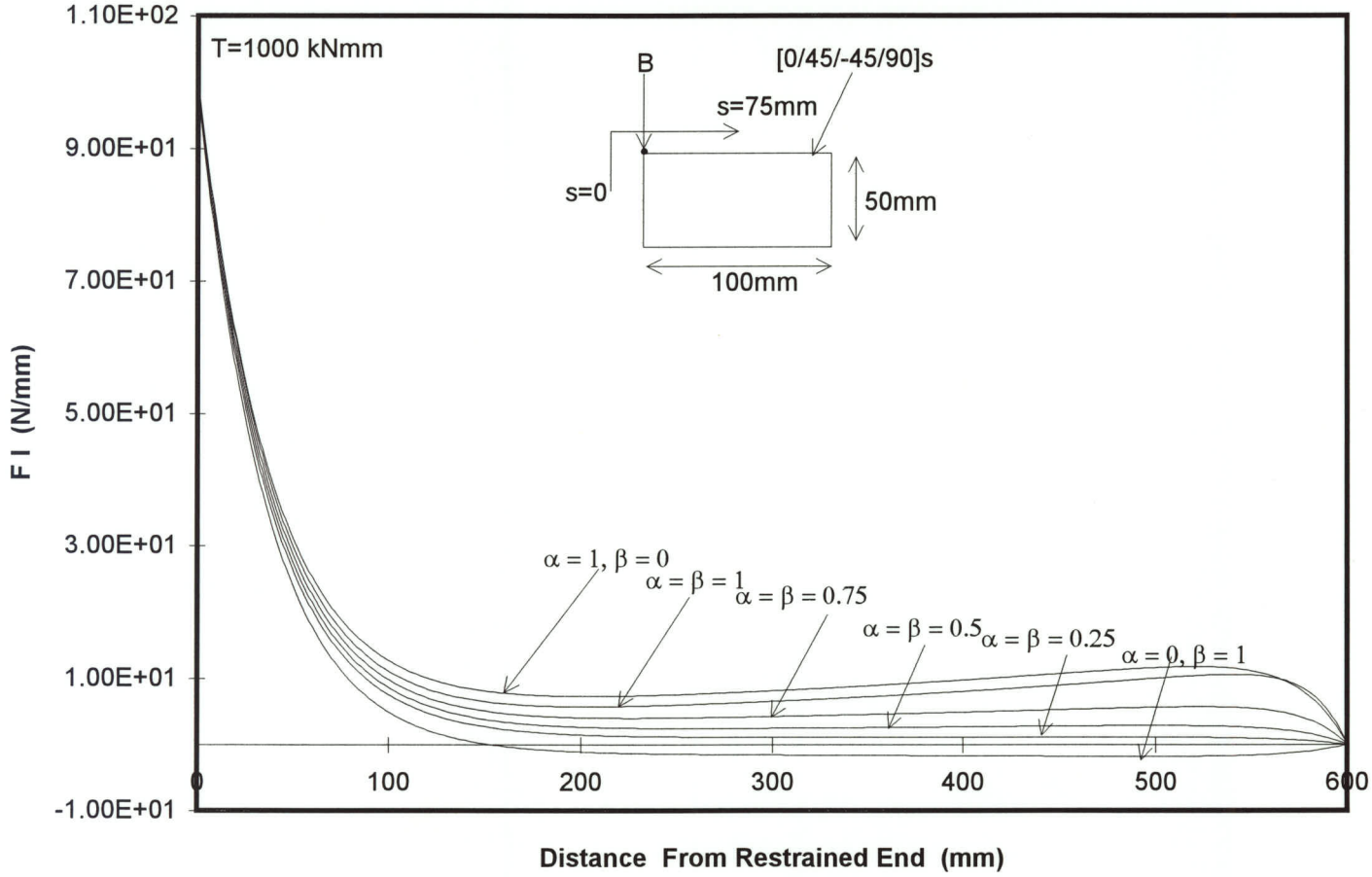

Figure 7.1 FORCE INTENSITY ALONG LENGTH OF BOX AT "B"

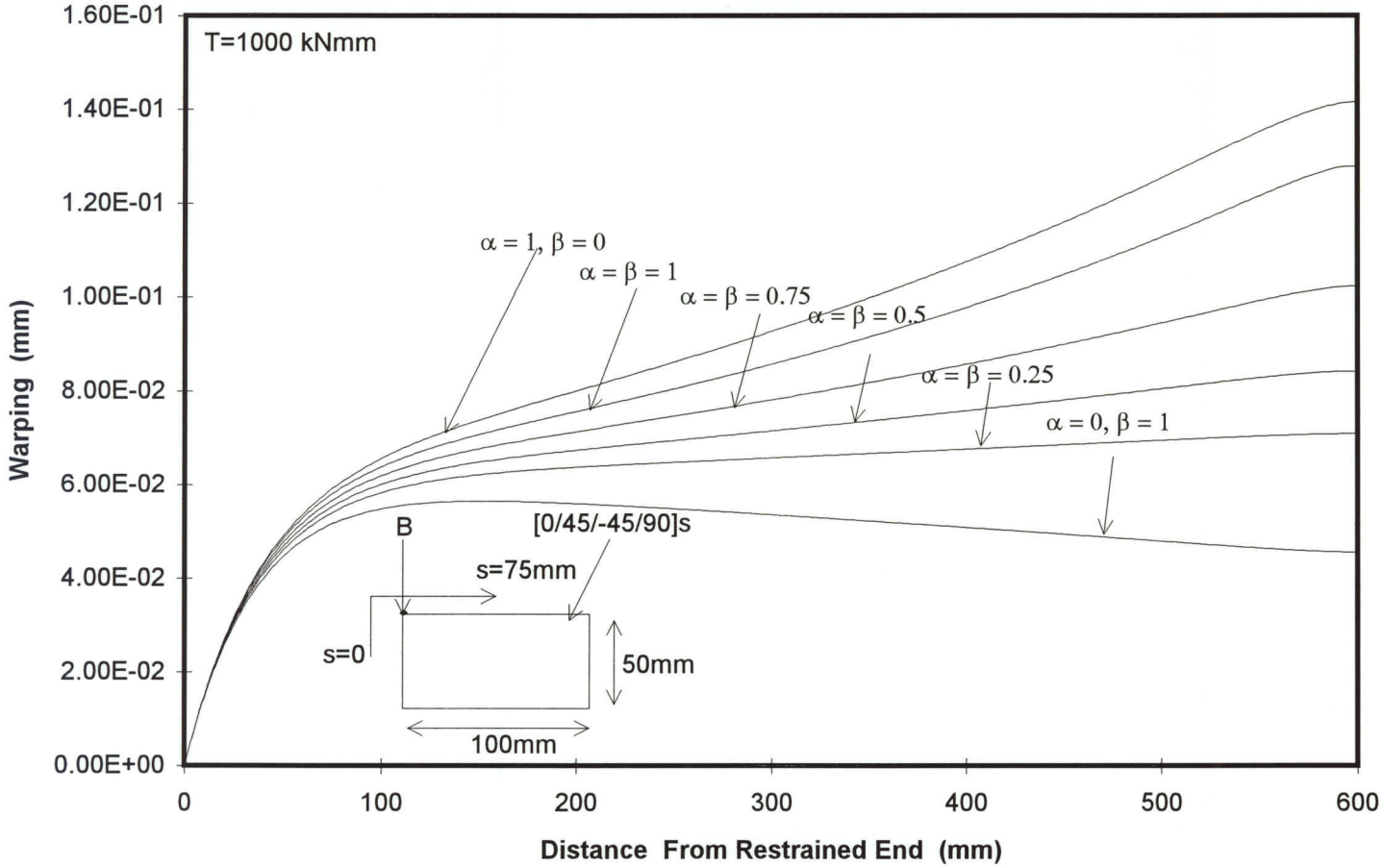

Figure 7.2 WARPING ALONG LENGTH OF BOX AT POINT "B"

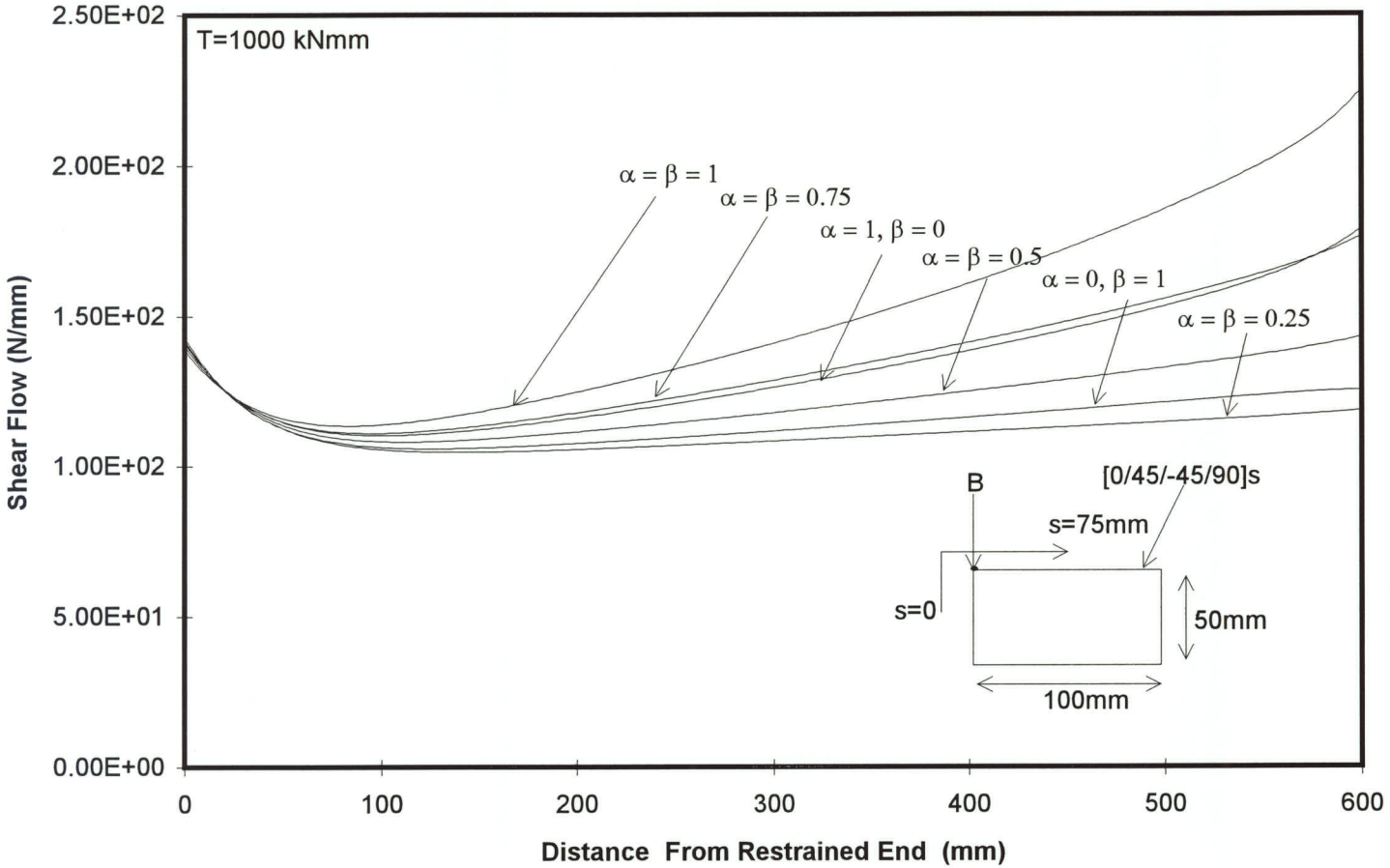

Figure 7.3 SHEAR FLOW ALONG LENGTH OF BOX AT S=0

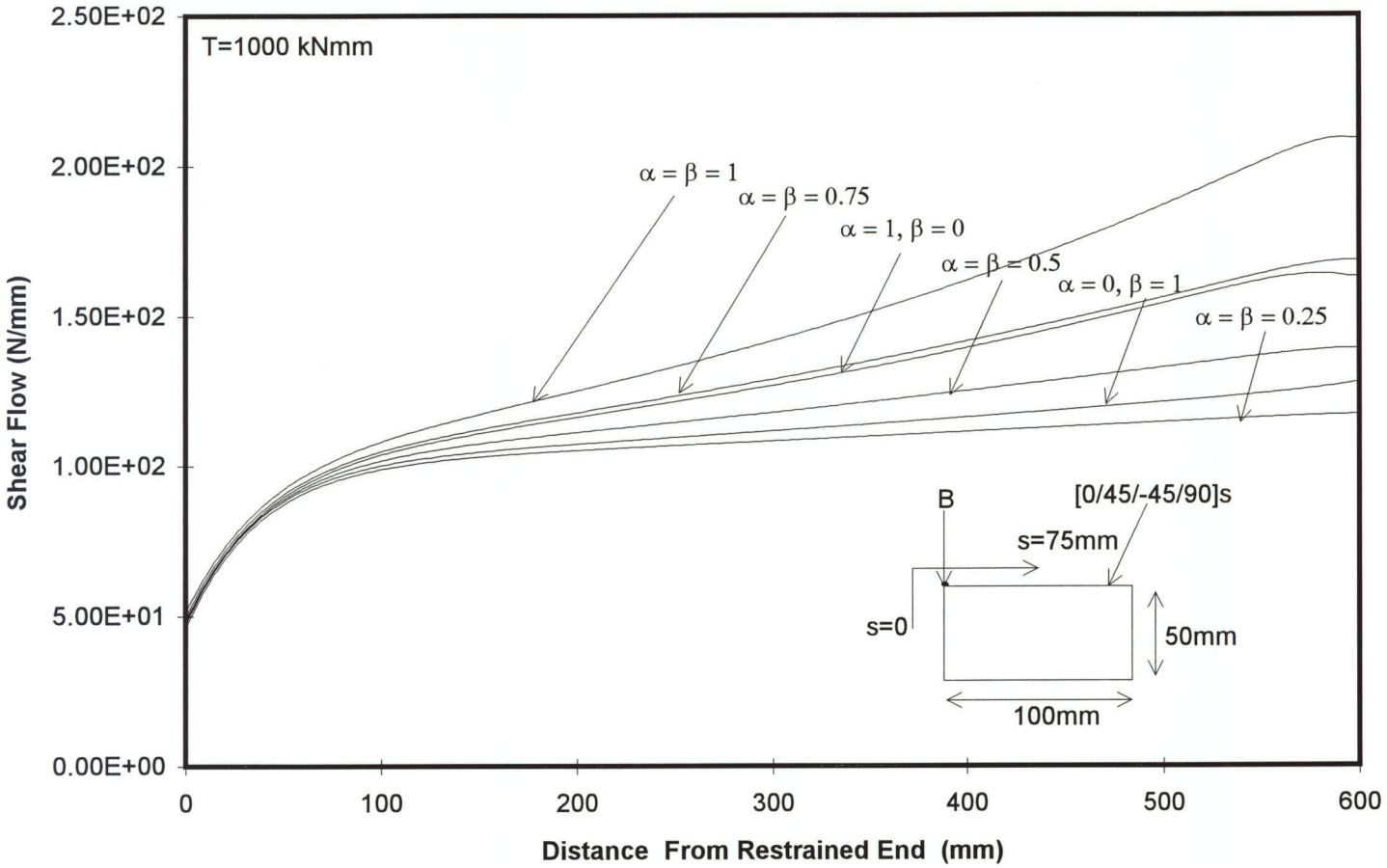

Figure 7.4 SHEAR FLOW ALONG LENGTH OF BOX AT S=75

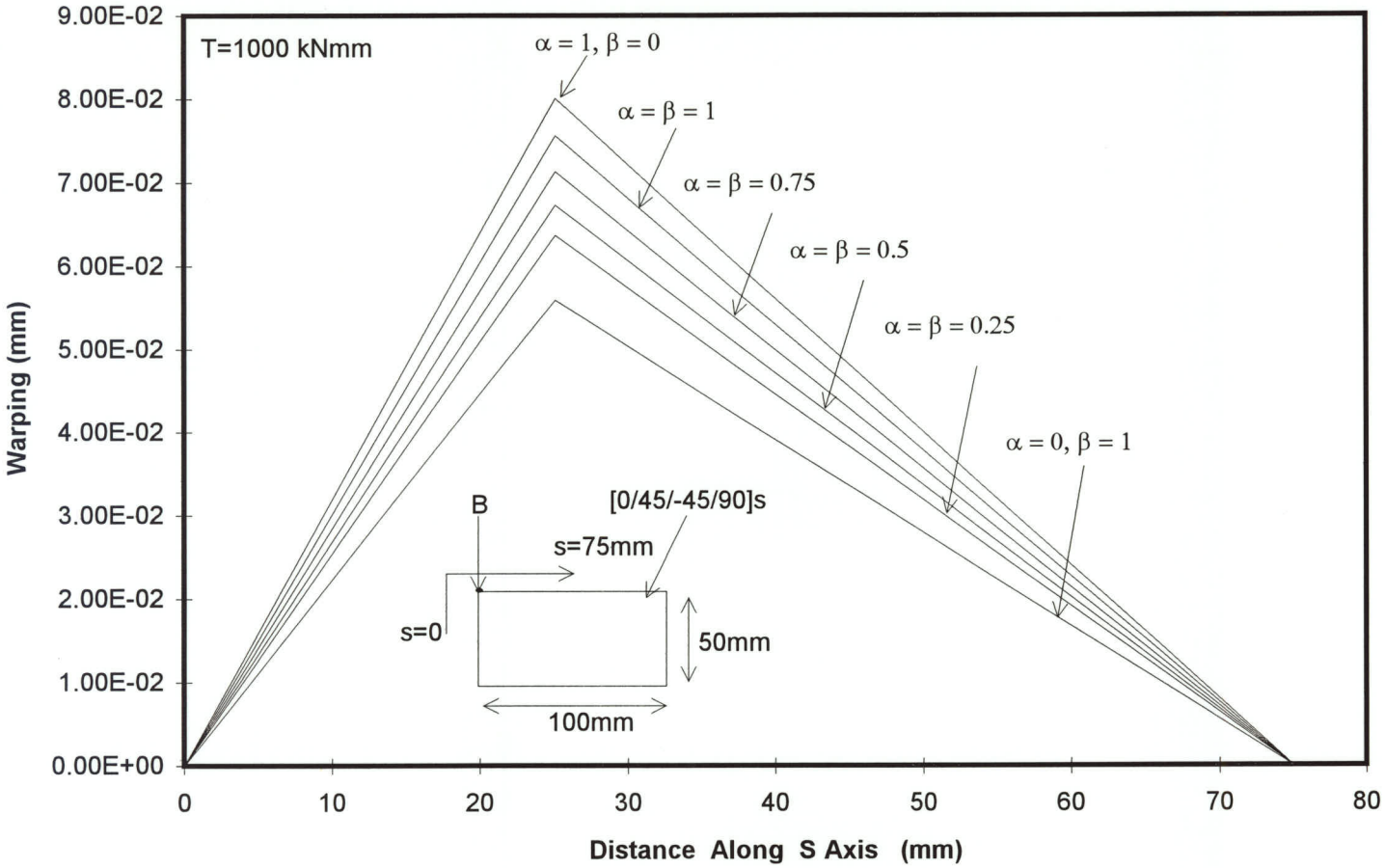

Figure 7.5 WARPING AROUND BOX AT Z = 200 mm

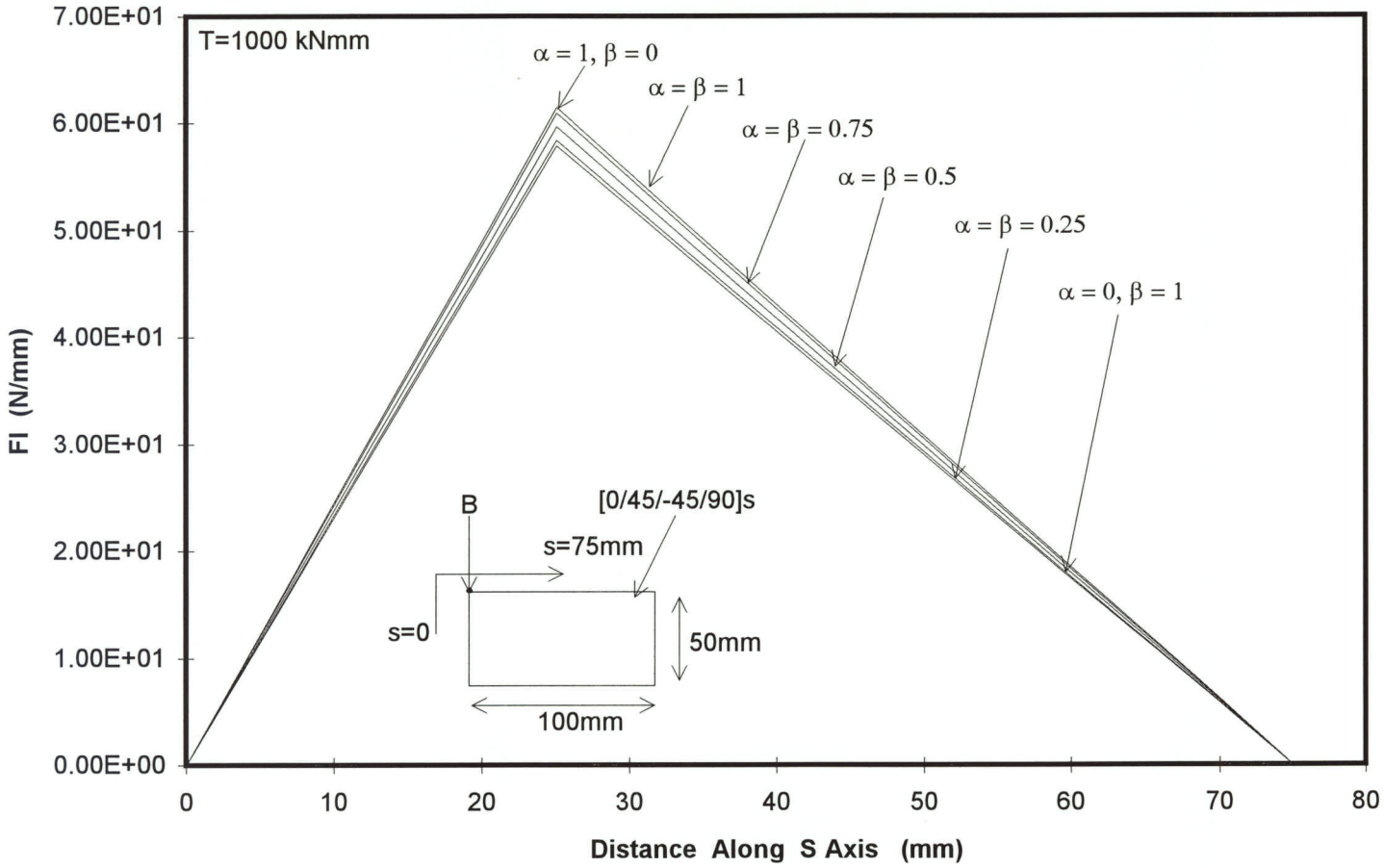

Figure 7.6 F I AROUND BOX AT Z = 20mm

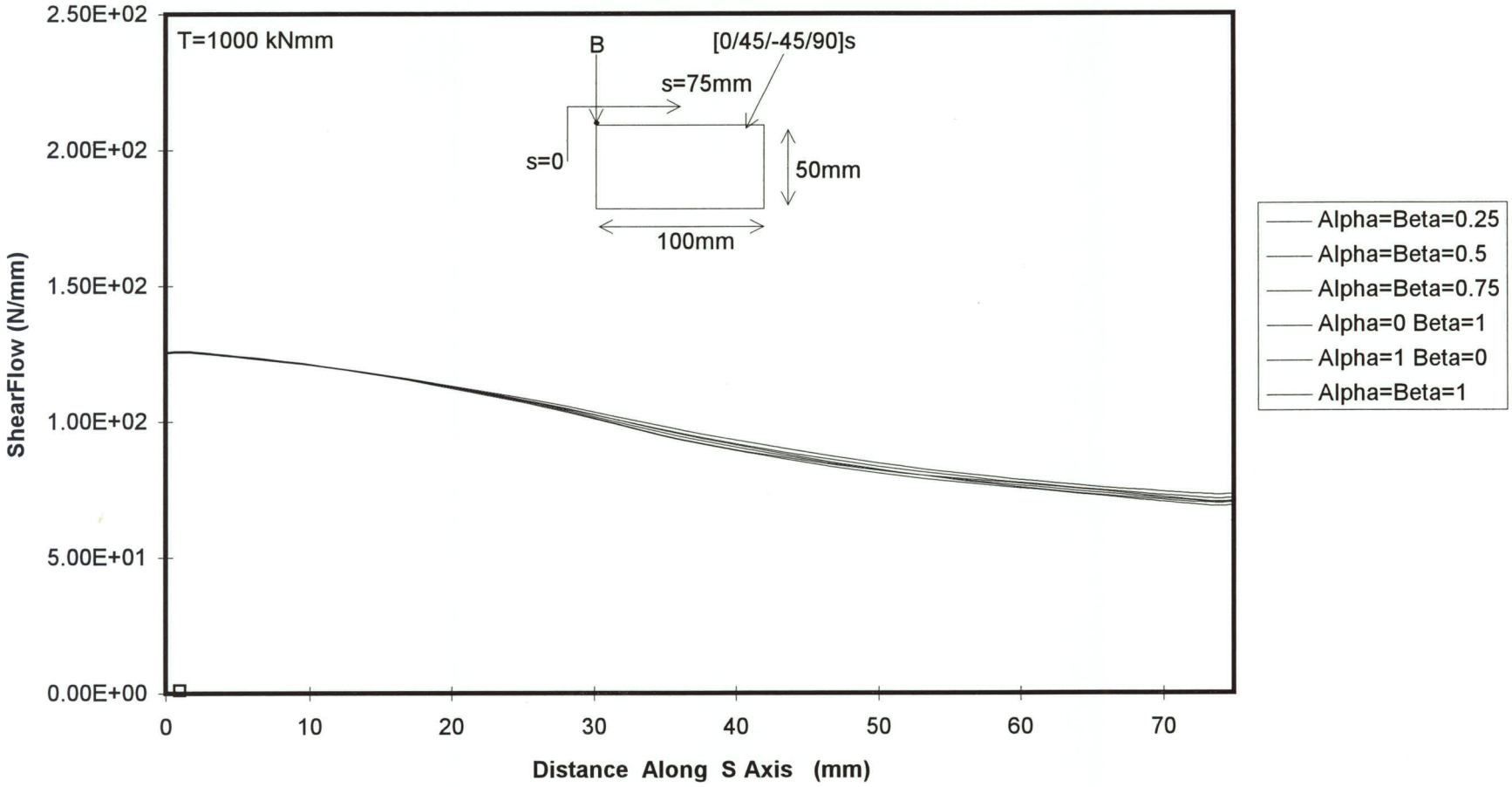

Figure 7.7 TOTAL SHEAR FLOW AROUND BOX AT Z = 20 mm

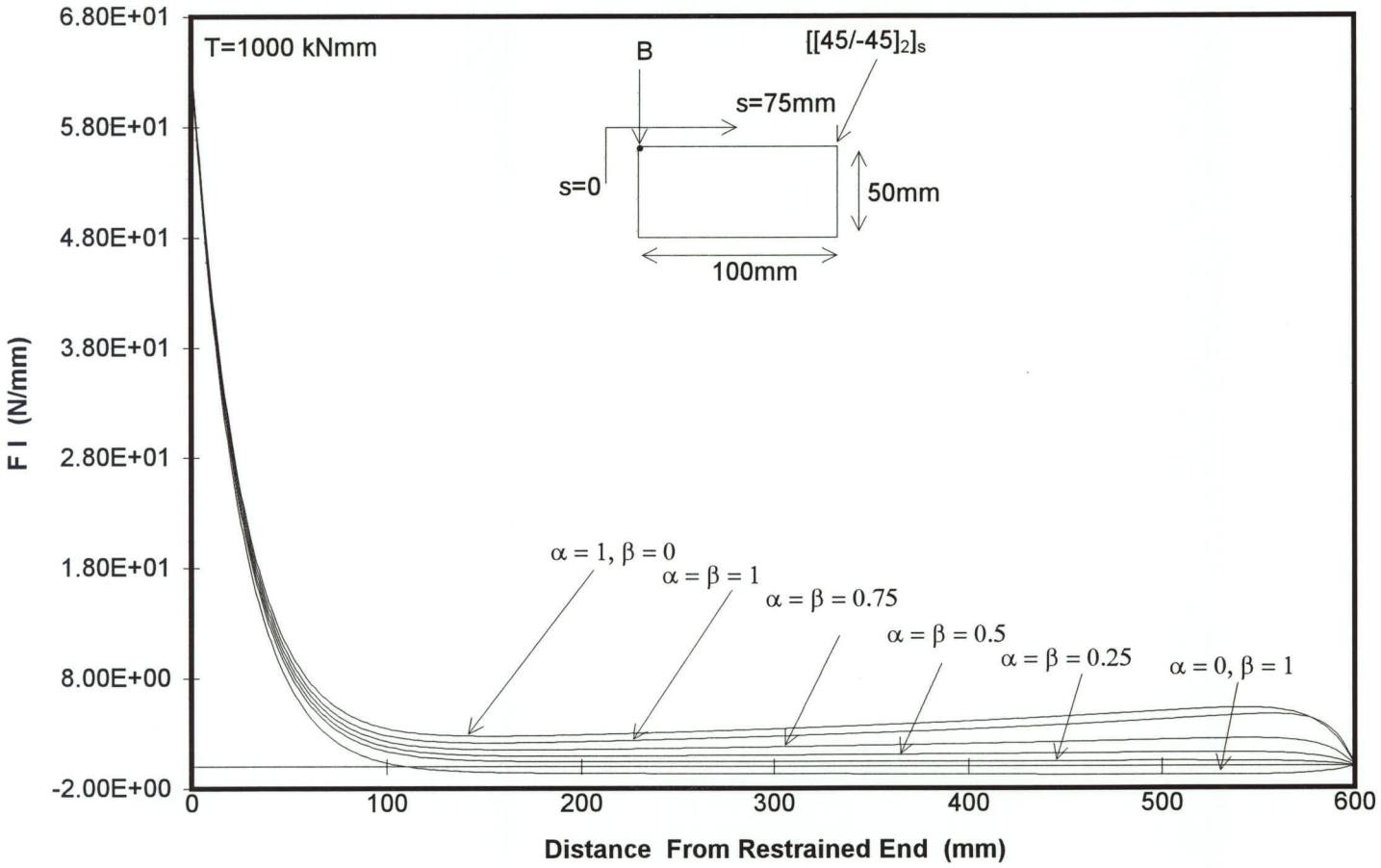

Figure 7.8 FORCE INTENSITY ALONG LENGTH OF BOX AT "B"

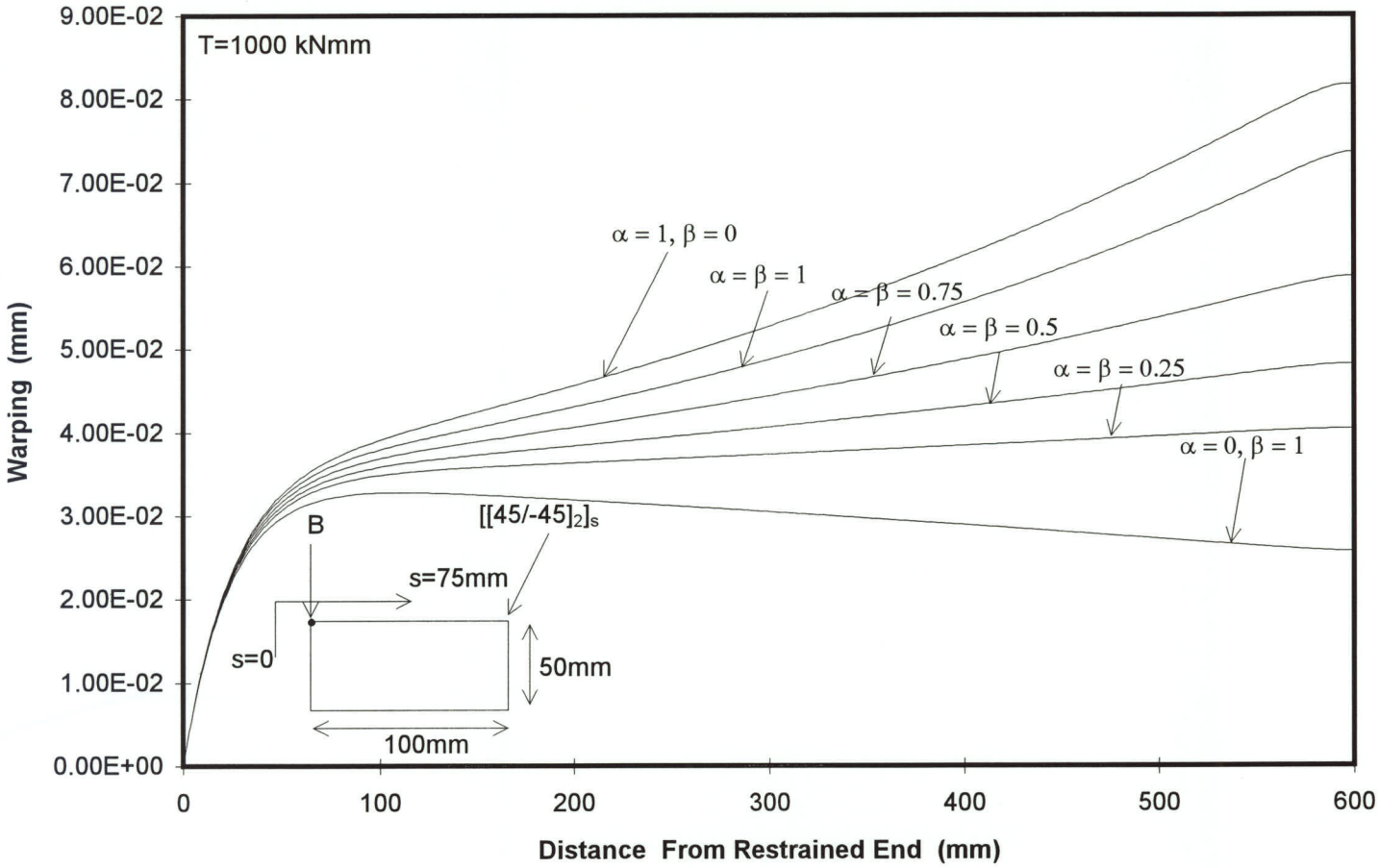

Figure 7.9 WARPING ALONG LENGTH OF BOX AT POINT "B"

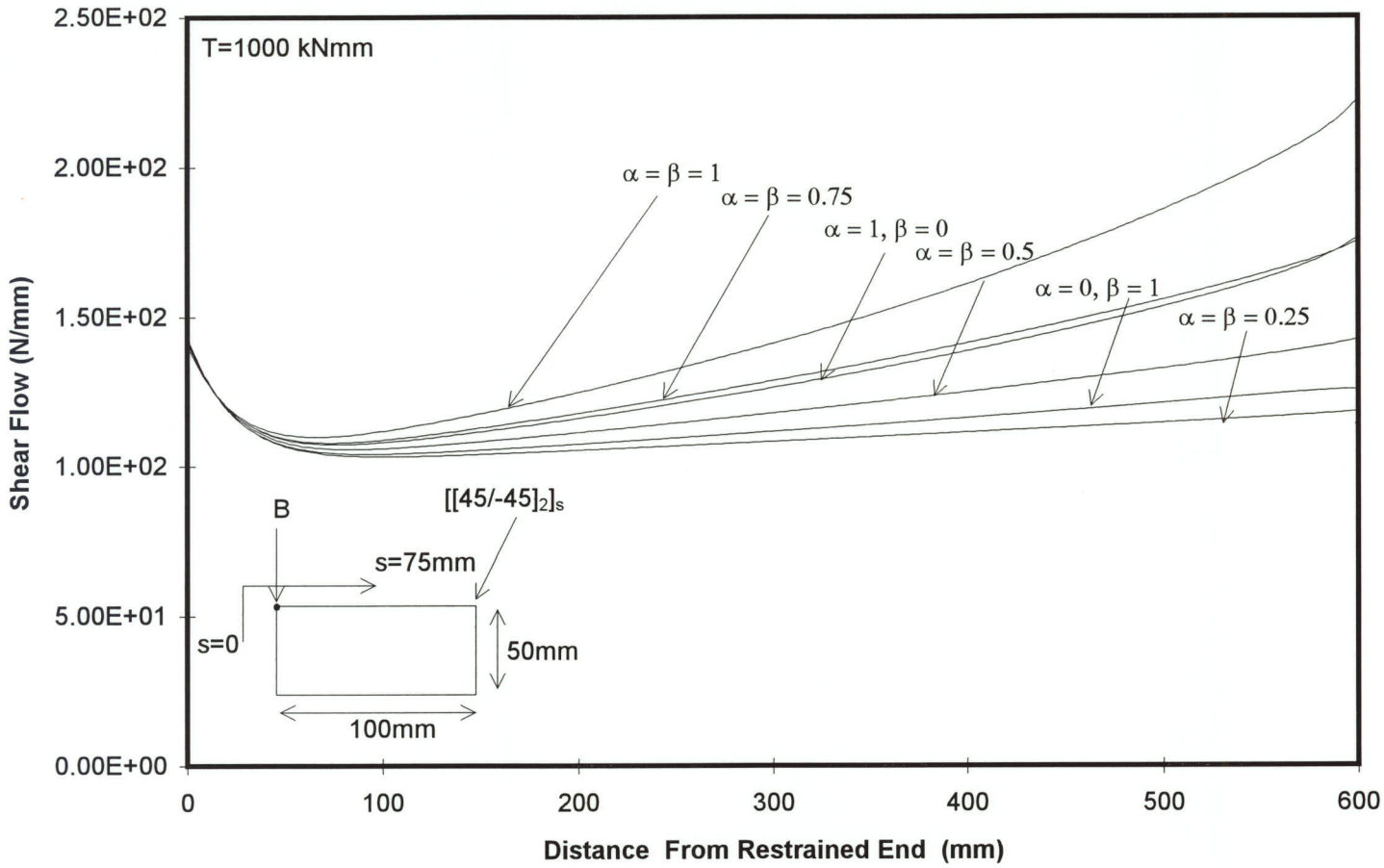

Figure 7.10 SHEAR FLOW ALONG LENGTH OF BOX AT S=0

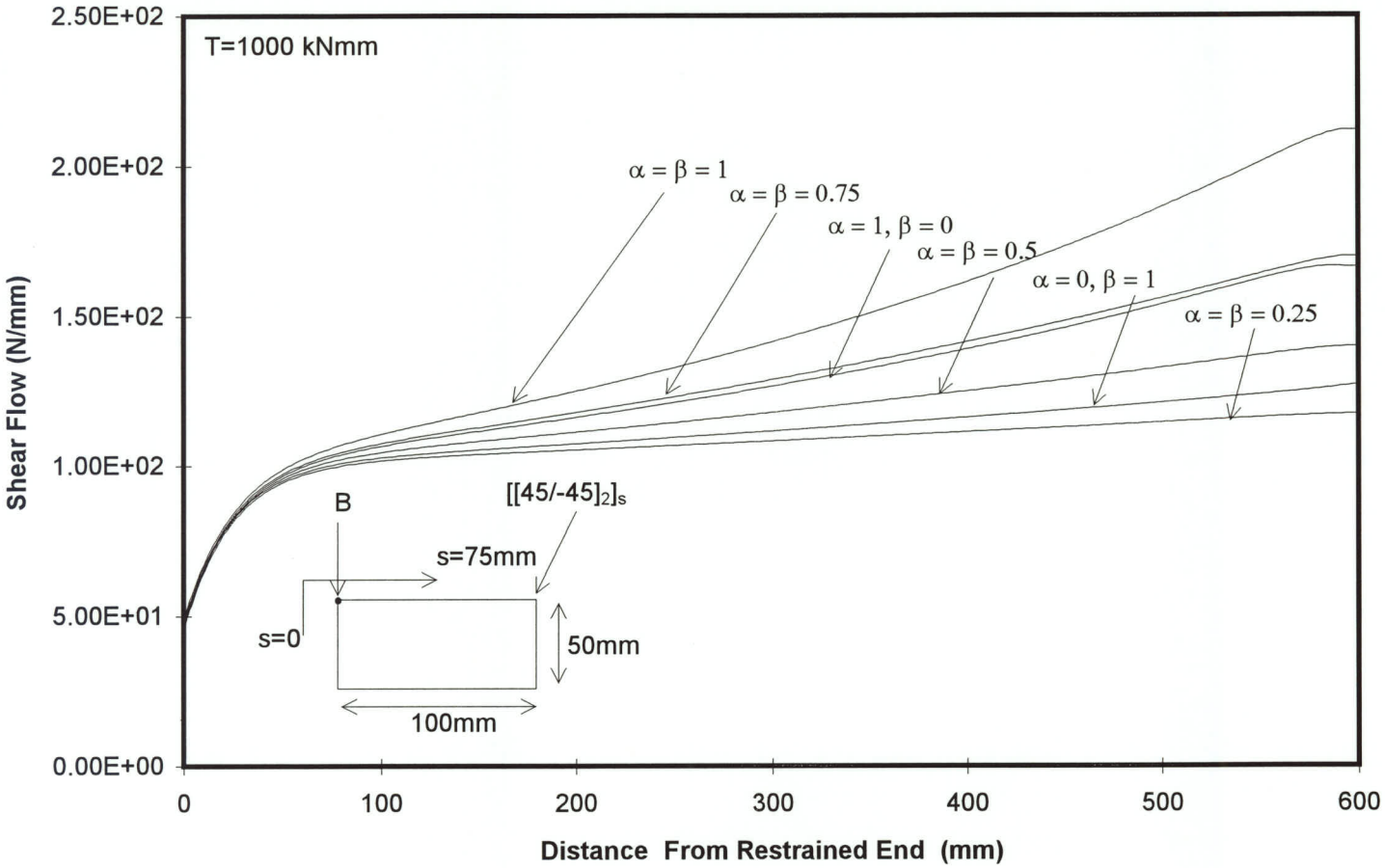

Figure 7.11 SHEAR FLOW ALONG LENGTH OF BOX AT S=75

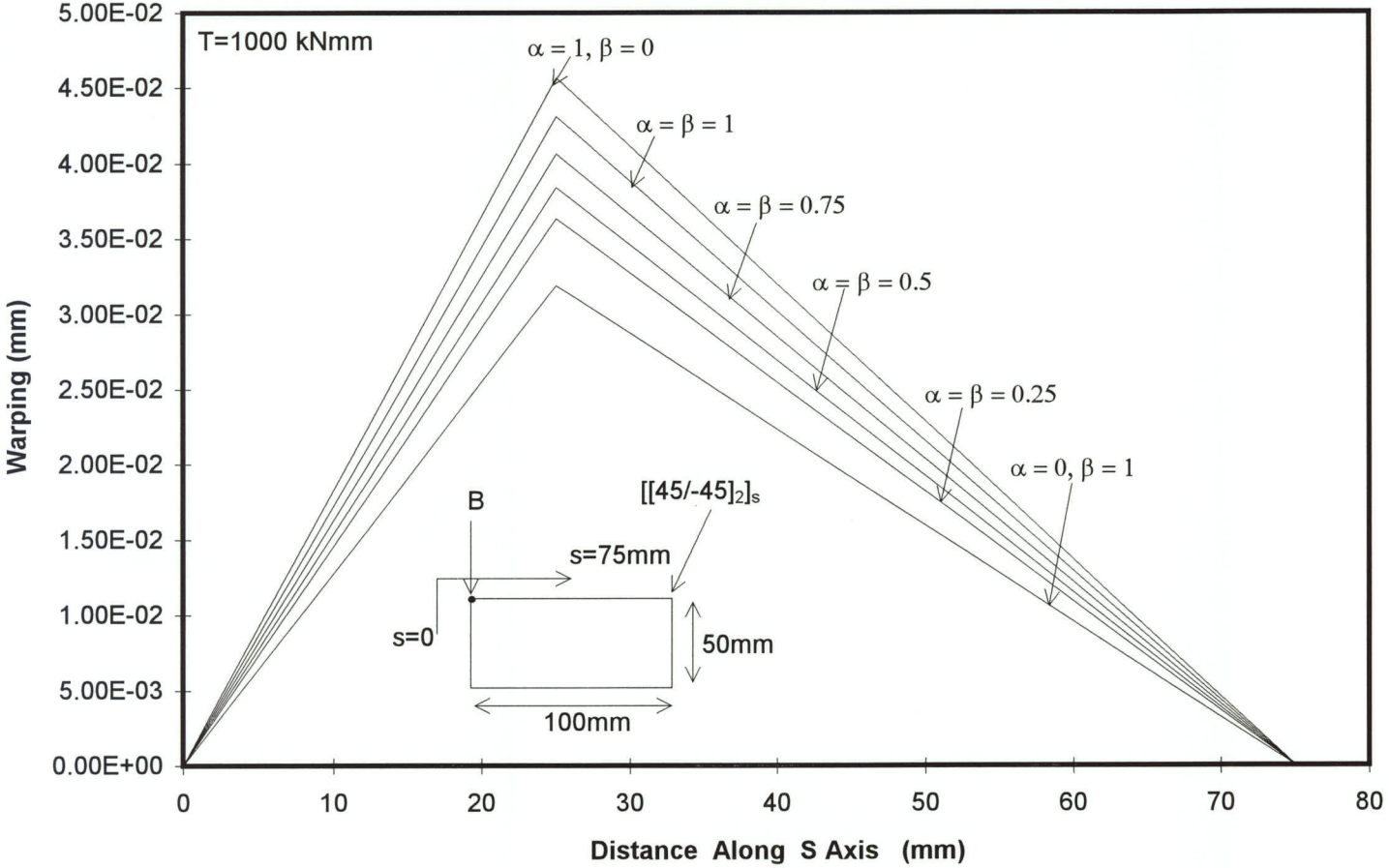

Figure 7.12 WARPING AROUND BOX AT Z = 200 mm

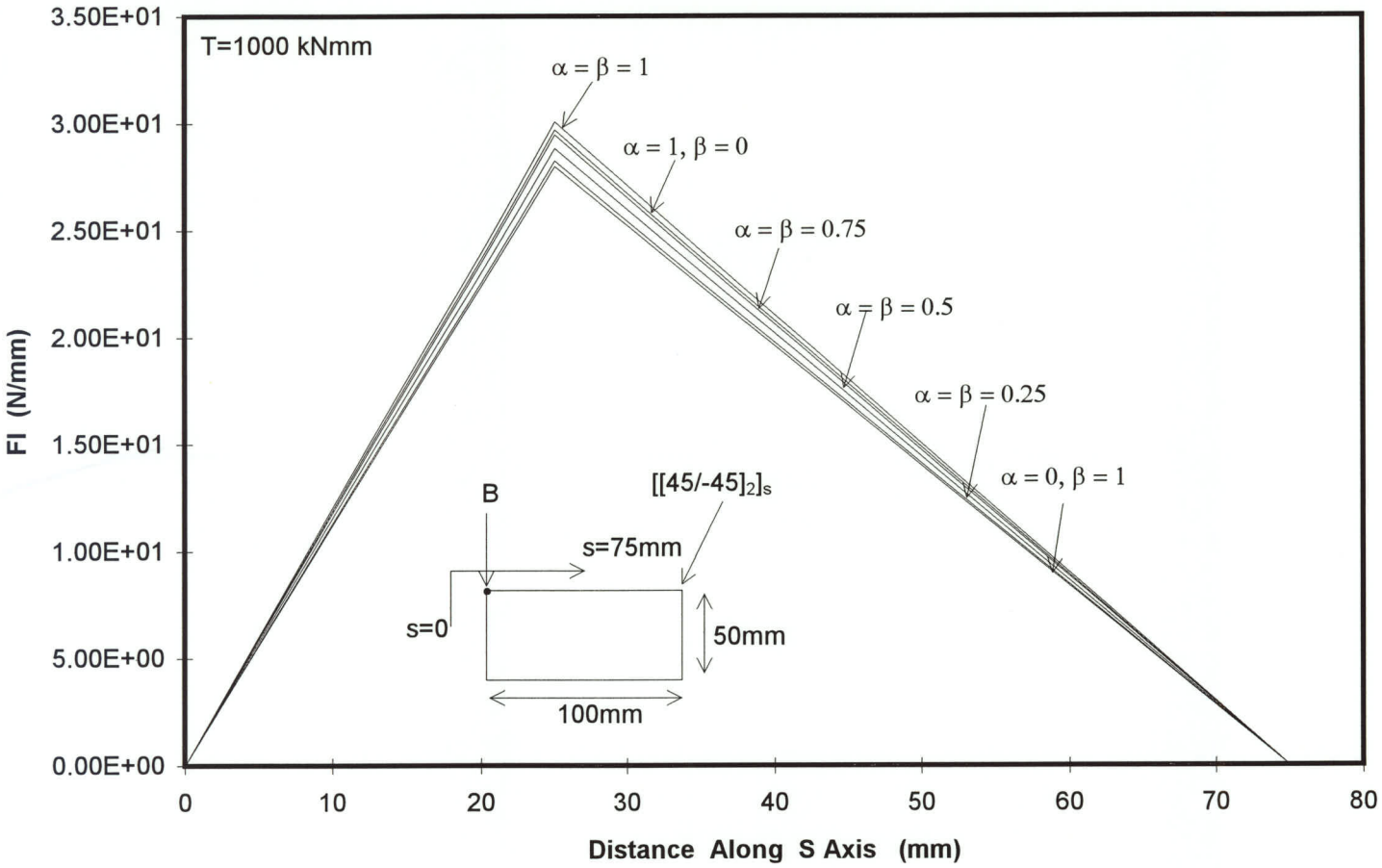

Figure 7.13 F I AROUND BOX AT Z = 20mm

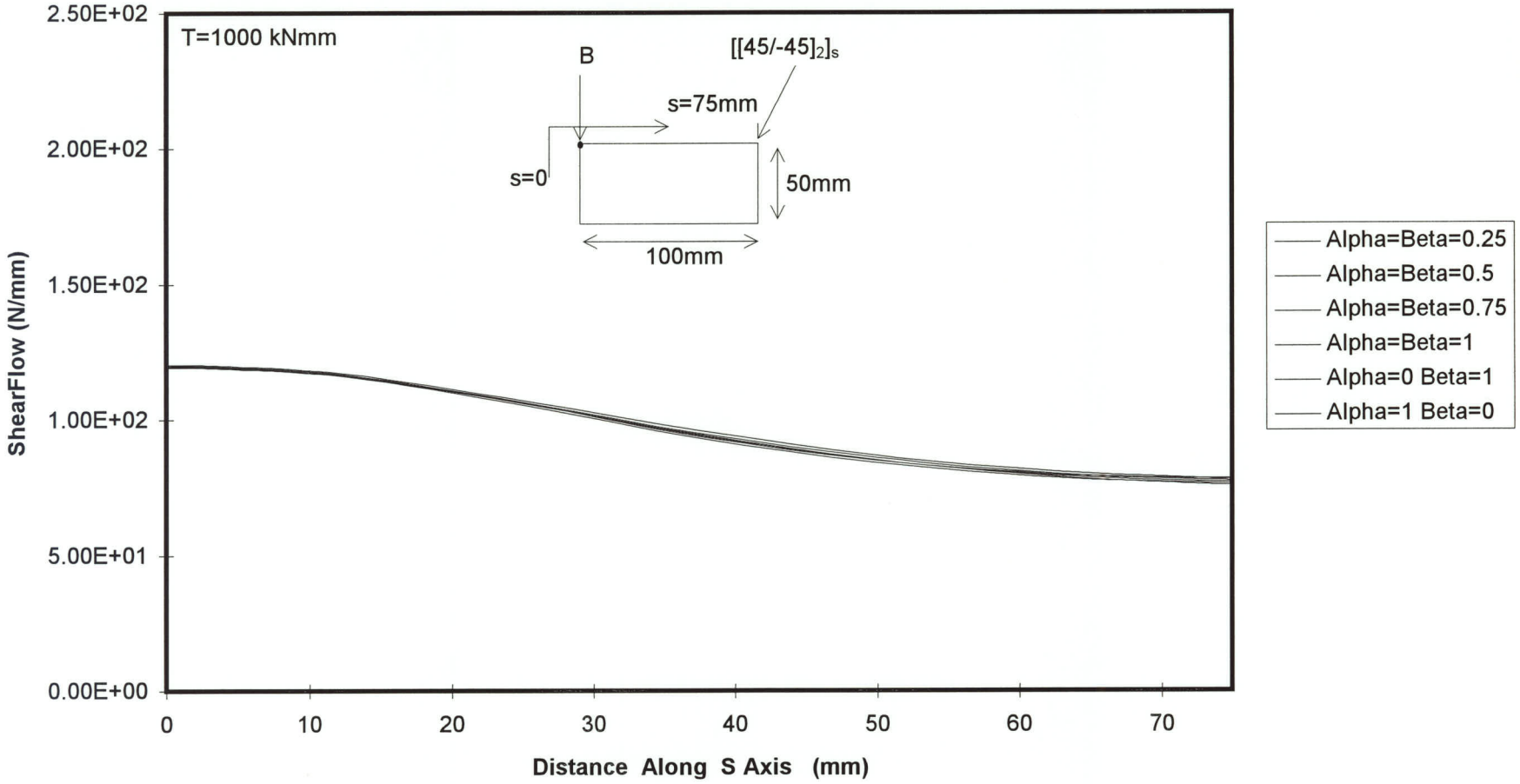

Figure 7.14 TOTAL SHEAR FLOW AROUND BOX AT Z = 20 mm

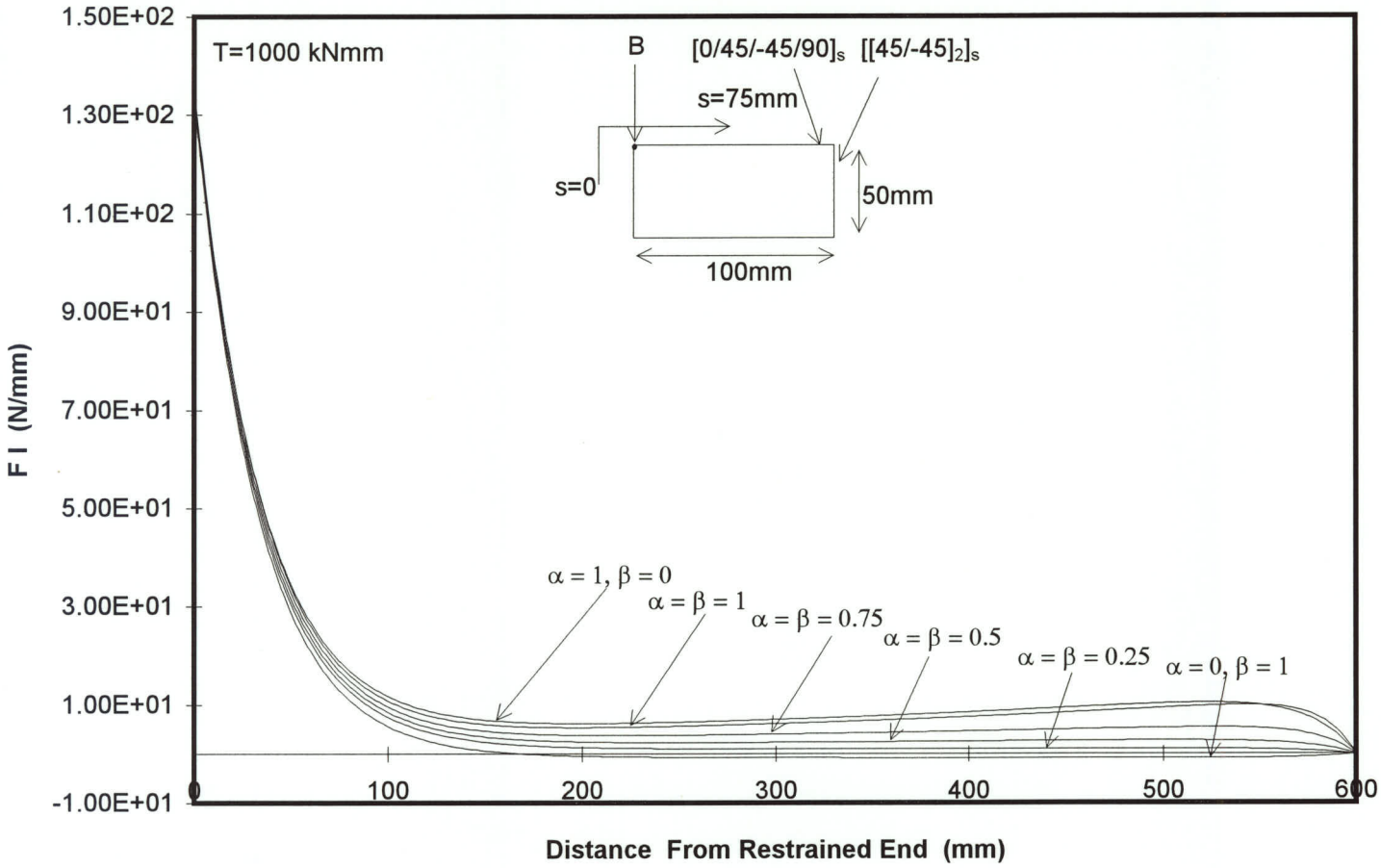

Figure 7.15 FORCE INTENSITY ALONG LENGTH OF BOX AT "B"

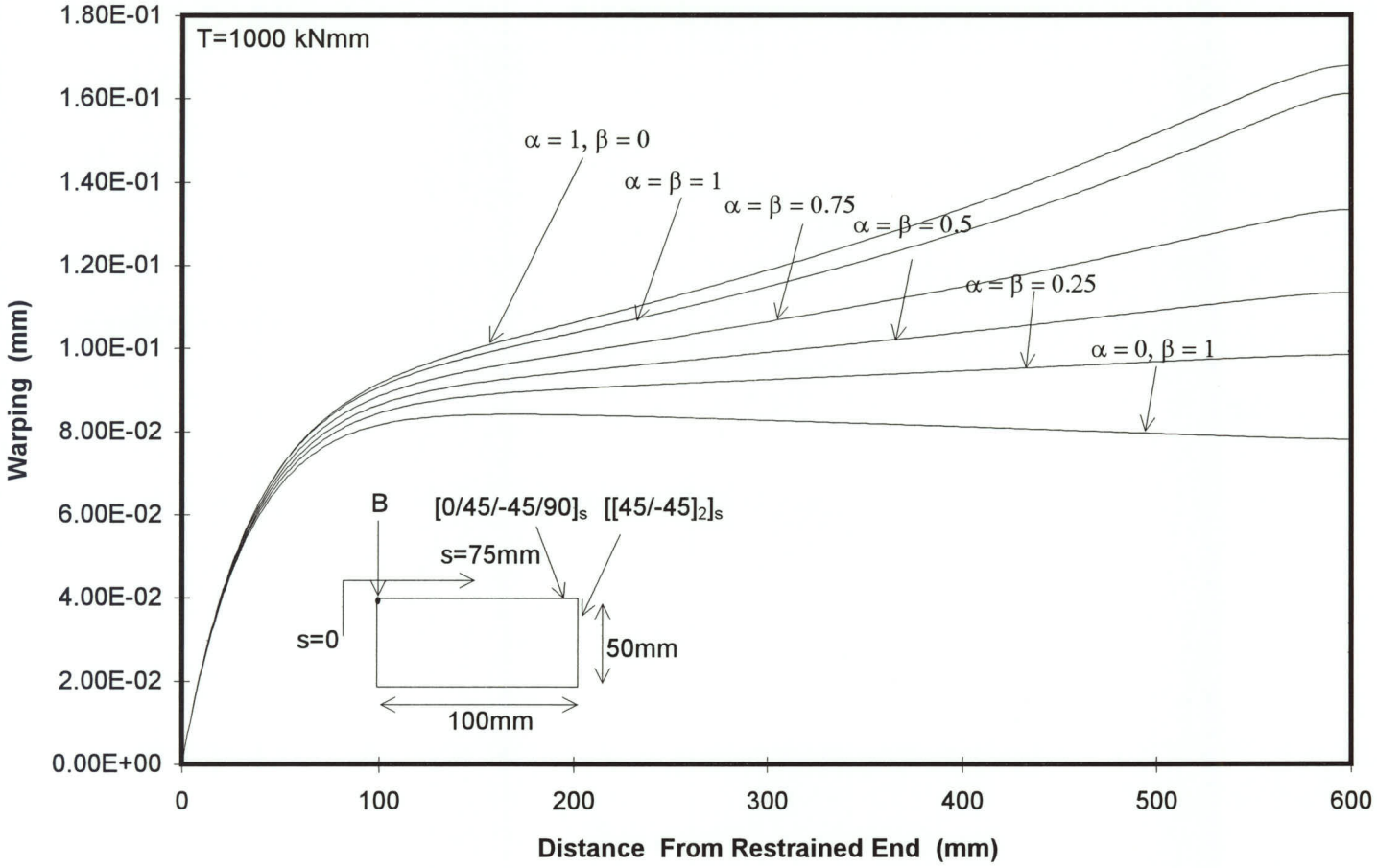

Figure 7.16 WARPING ALONG LENGTH OF BOX AT POINT "B"

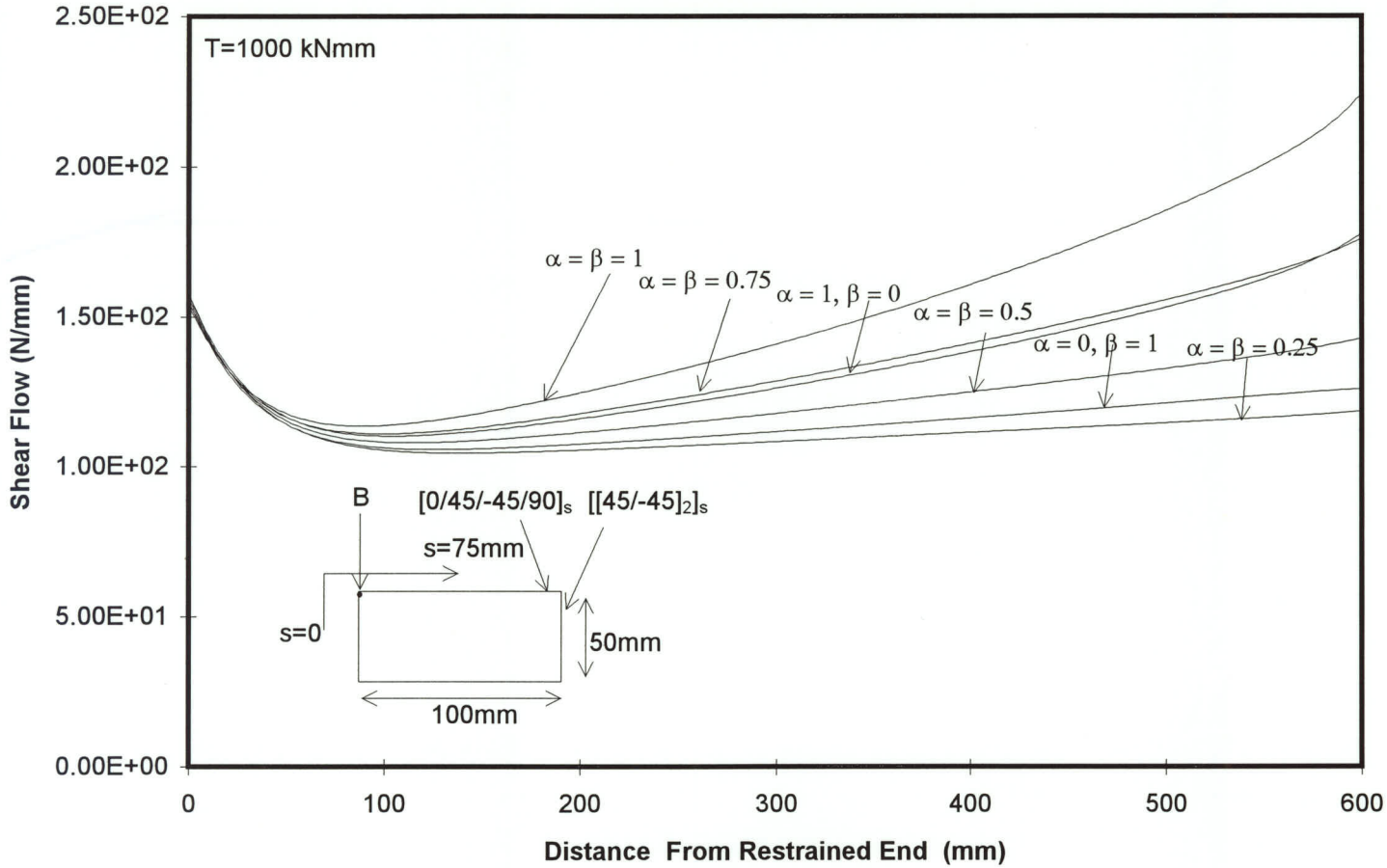

Figure 7.17 SHEAR FLOW ALONG LENGTH OF BOX AT S=0

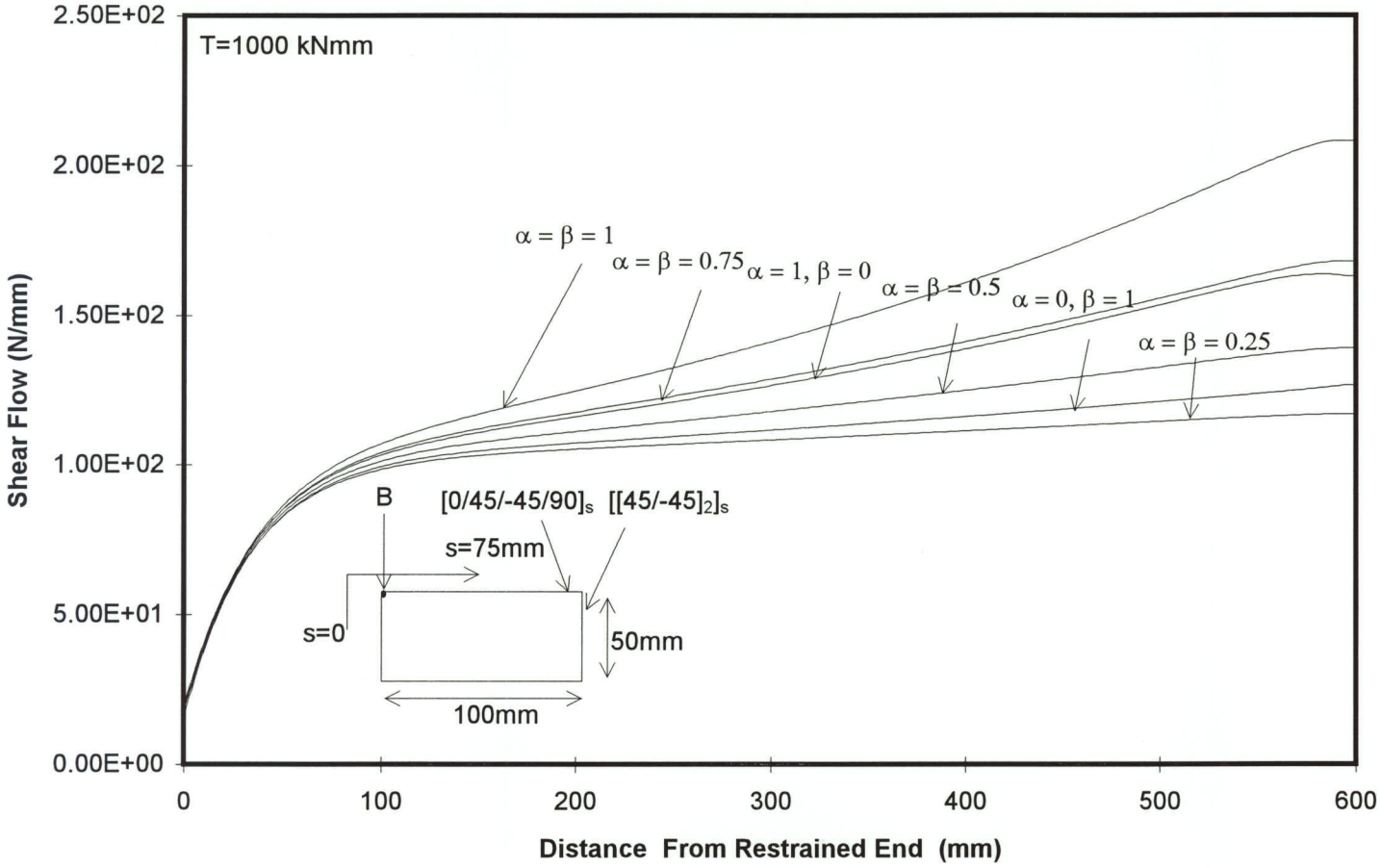

Figure 7.18 SHEAR FLOW ALONG LENGTH OF BOX AT S=75

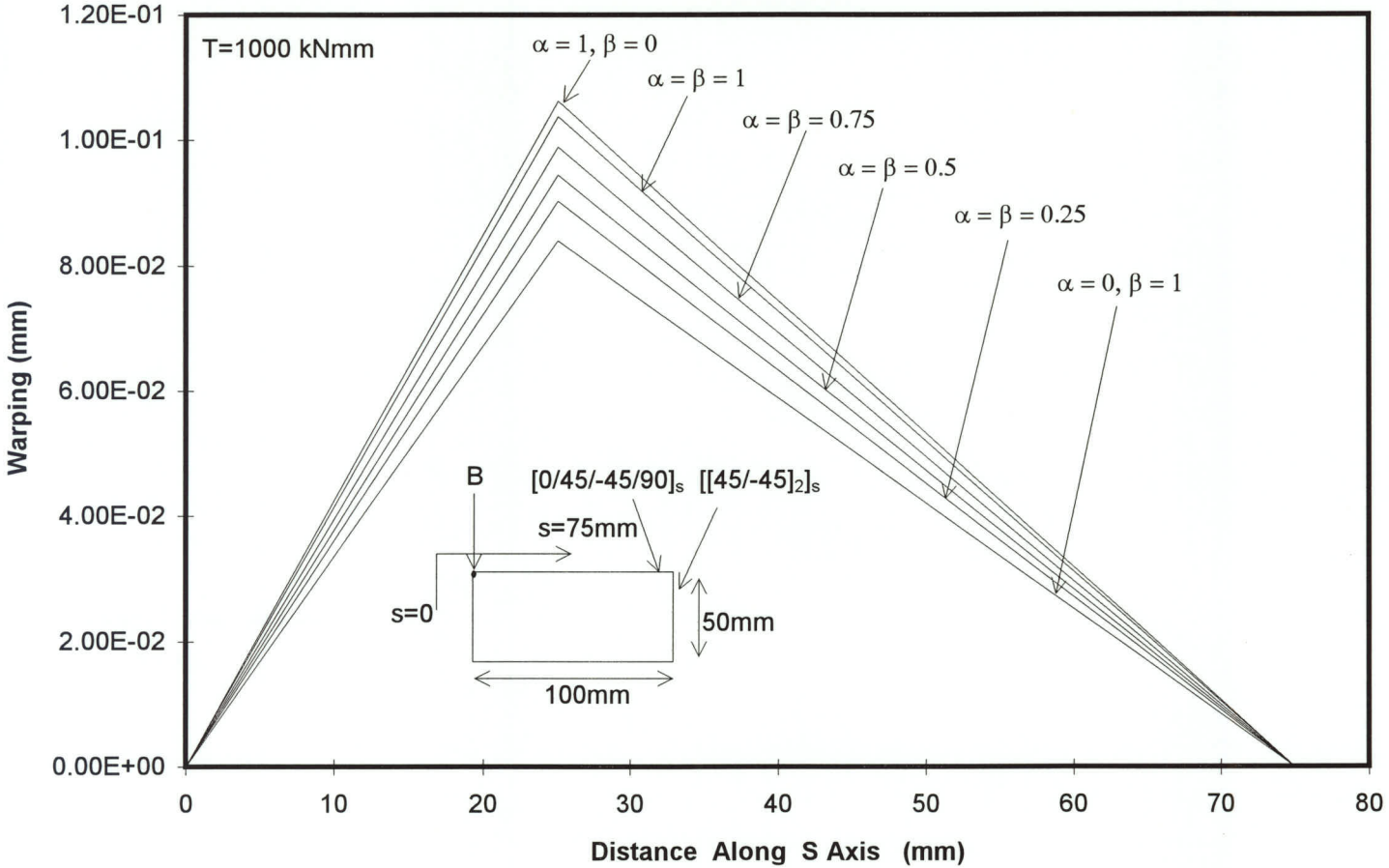

Figure 7.19 WARPING AROUND BOX AT Z = 200 mm

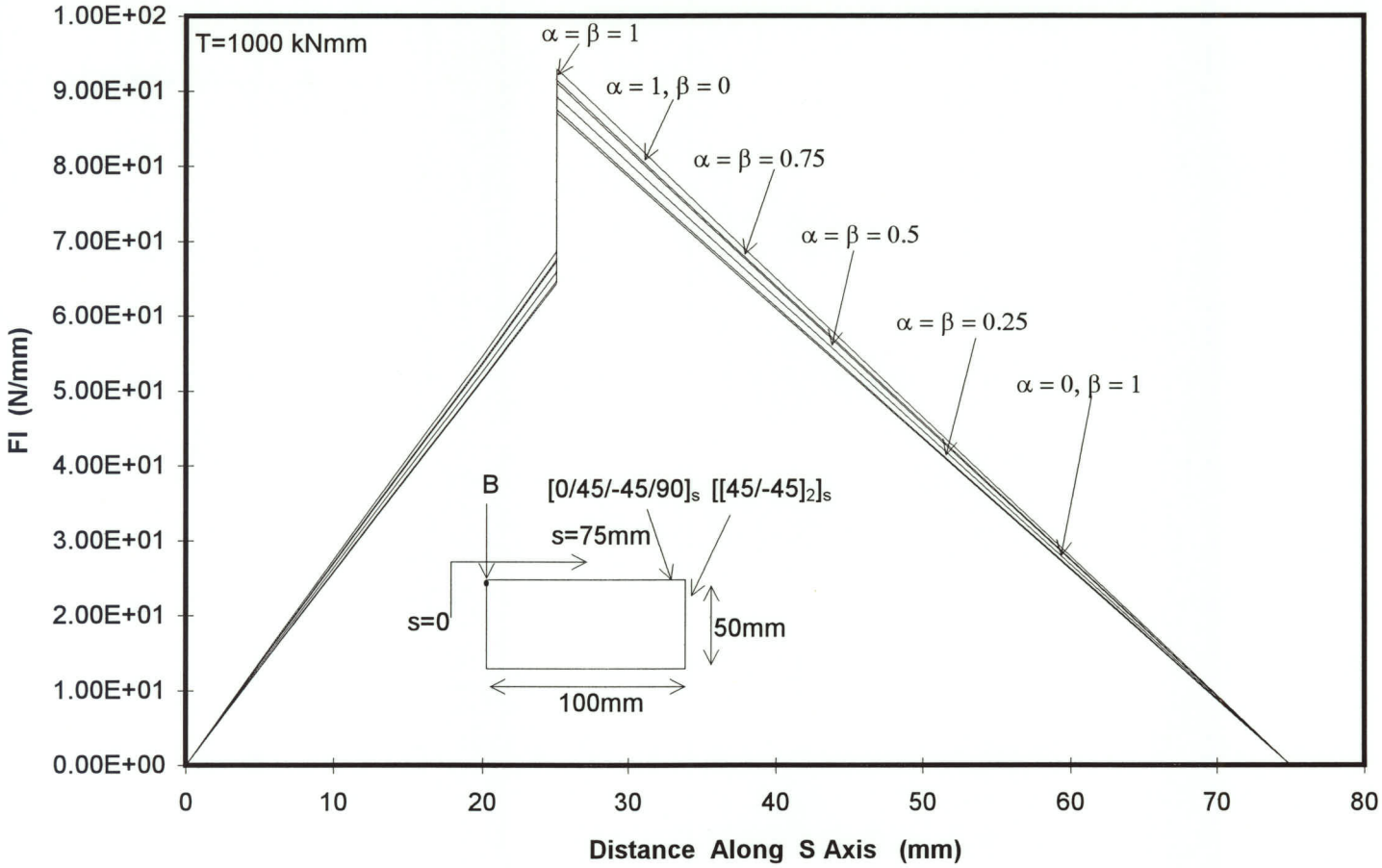

Figure 7.20 F I AROUND BOX AT Z = 20mm

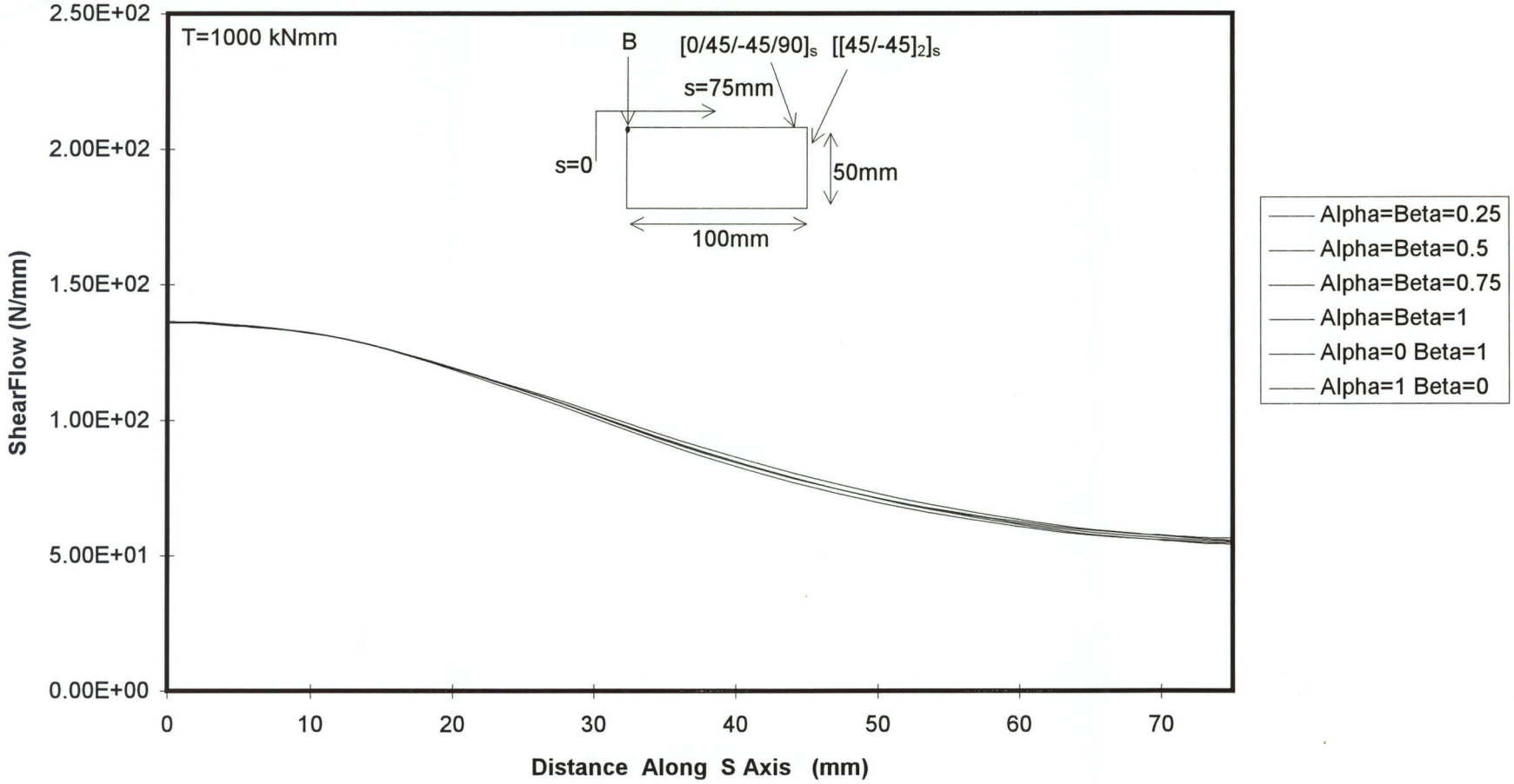

Figure 7.21 TOTAL SHEAR FLOW AROUND BOX AT Z = 20 mm

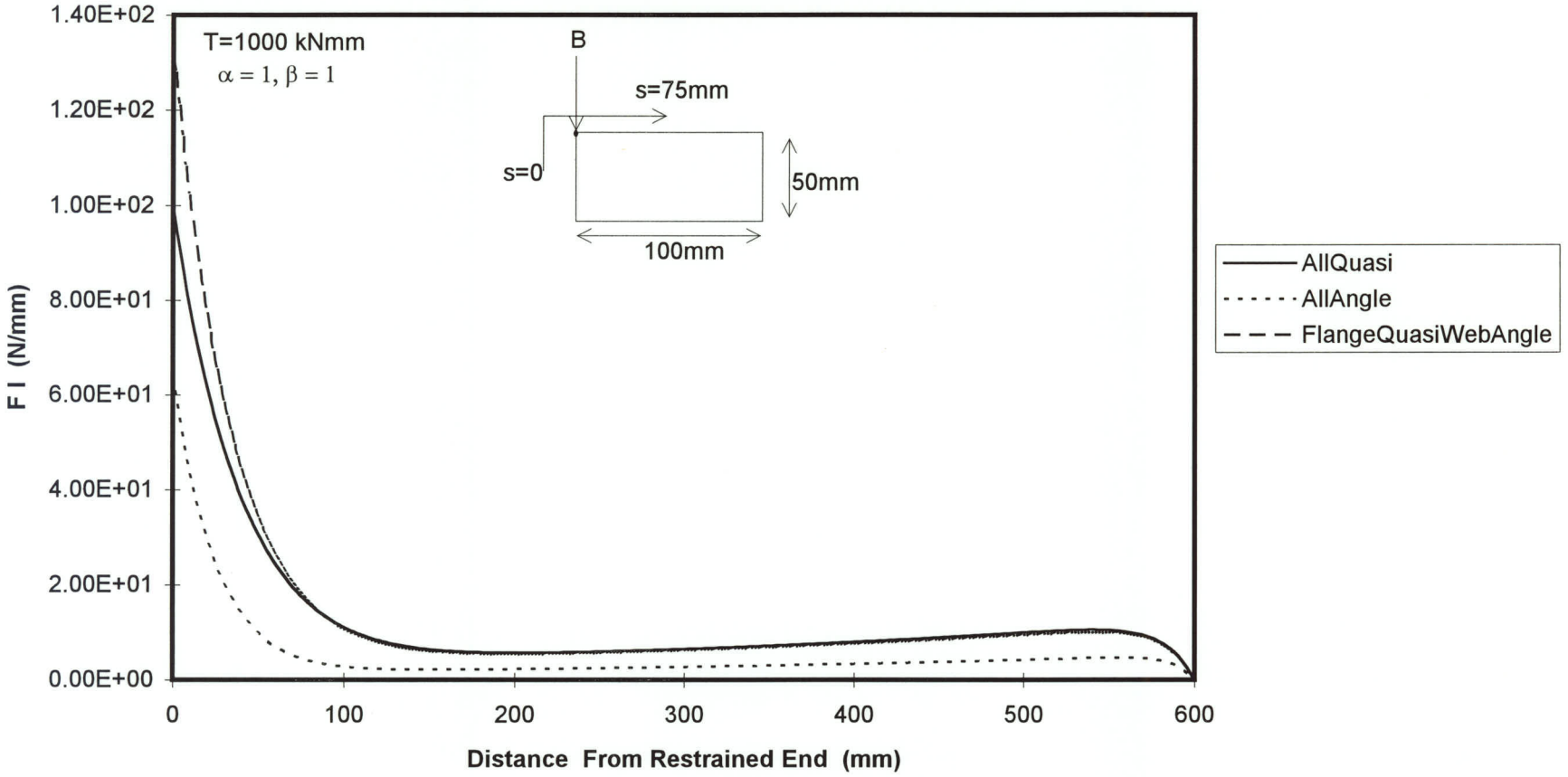

Figure 7.22 FORCE INTENSITY ALONG LENGTH OF BOX AT "B"

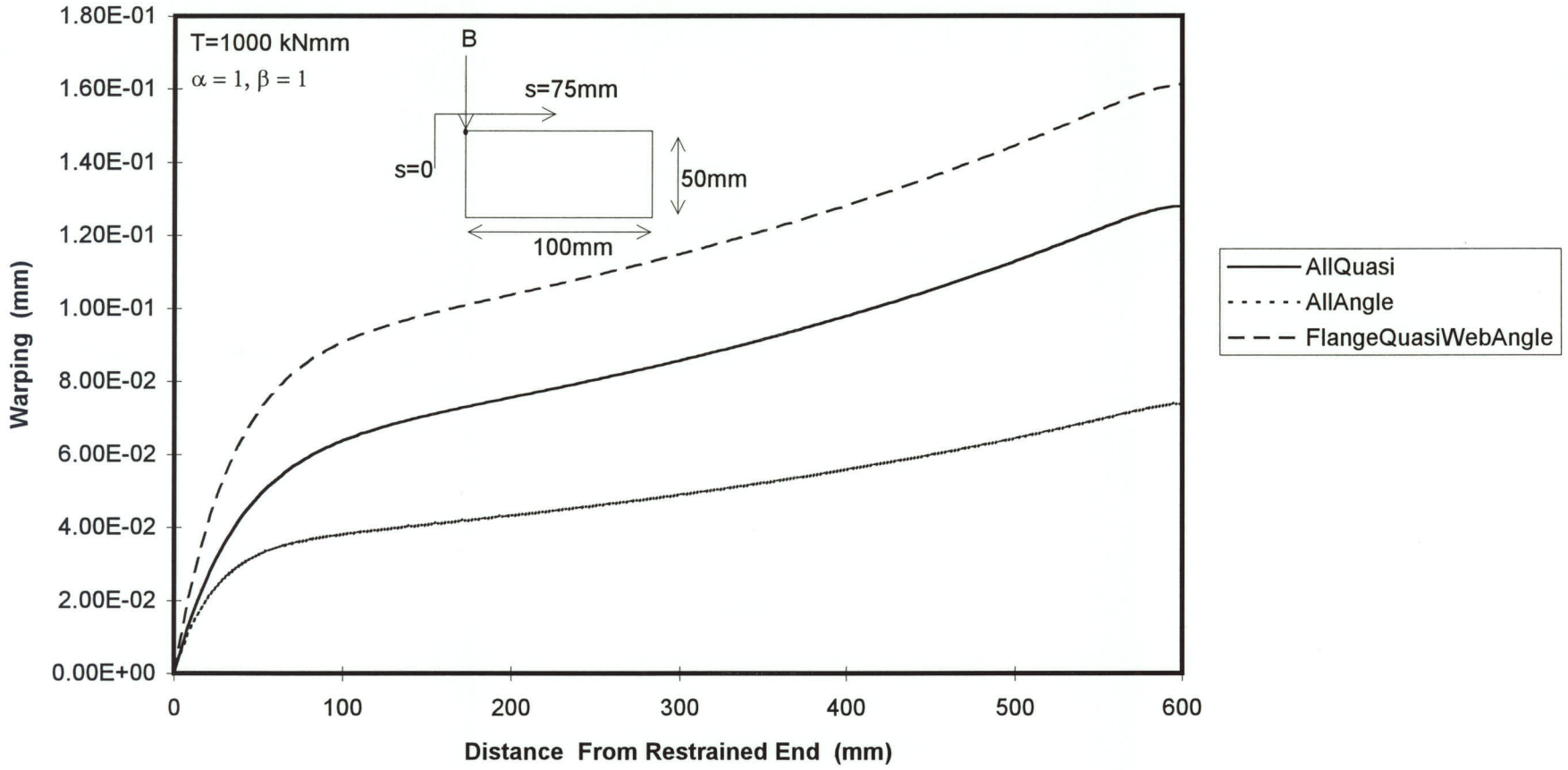

Figure 7.23 WARPING ALONG LENGTH OF BOX AT POINT "B"

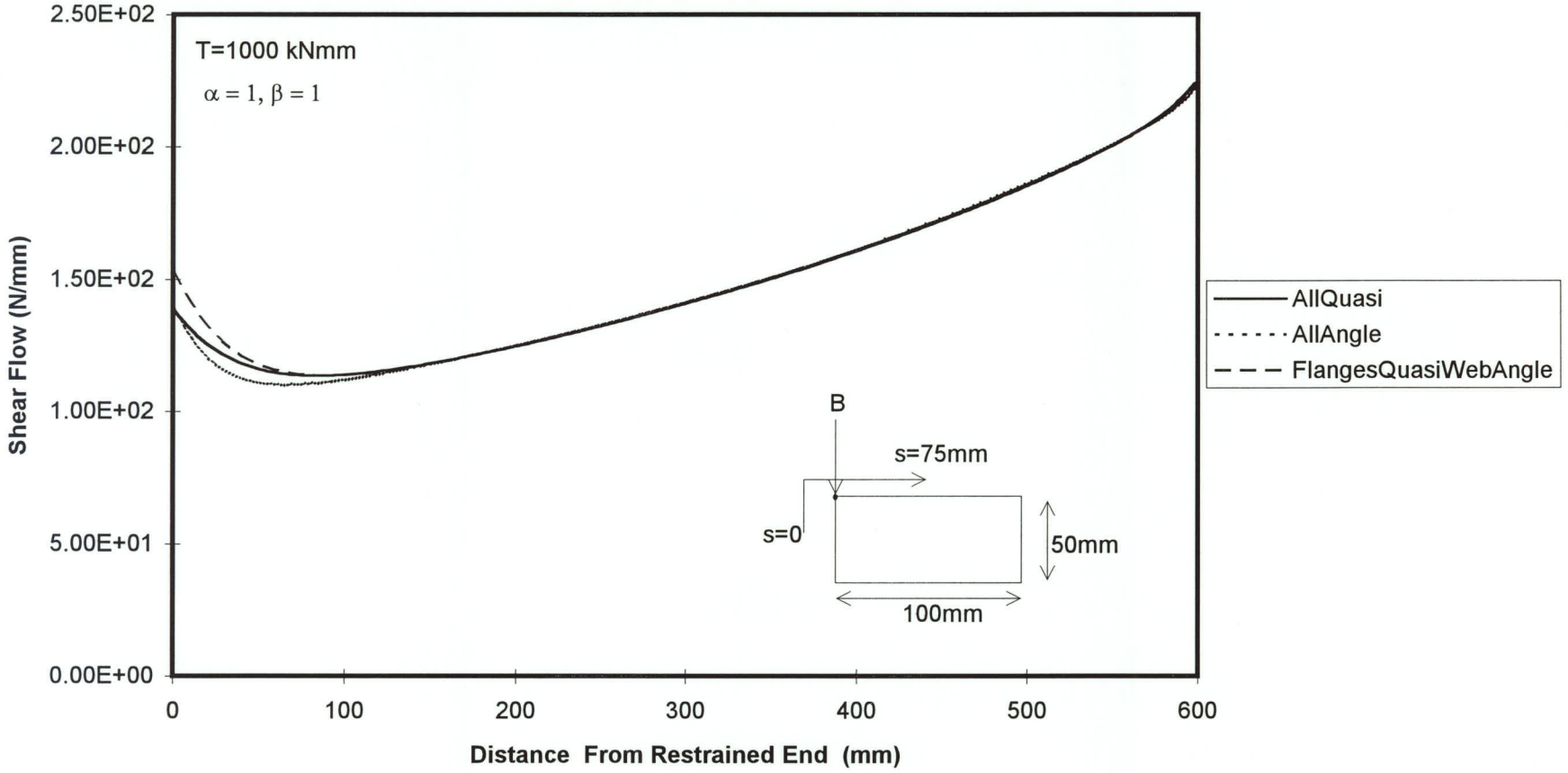

Figure 7.24 SHEAR FLOW ALONG LENGTH OF BOX AT S=0

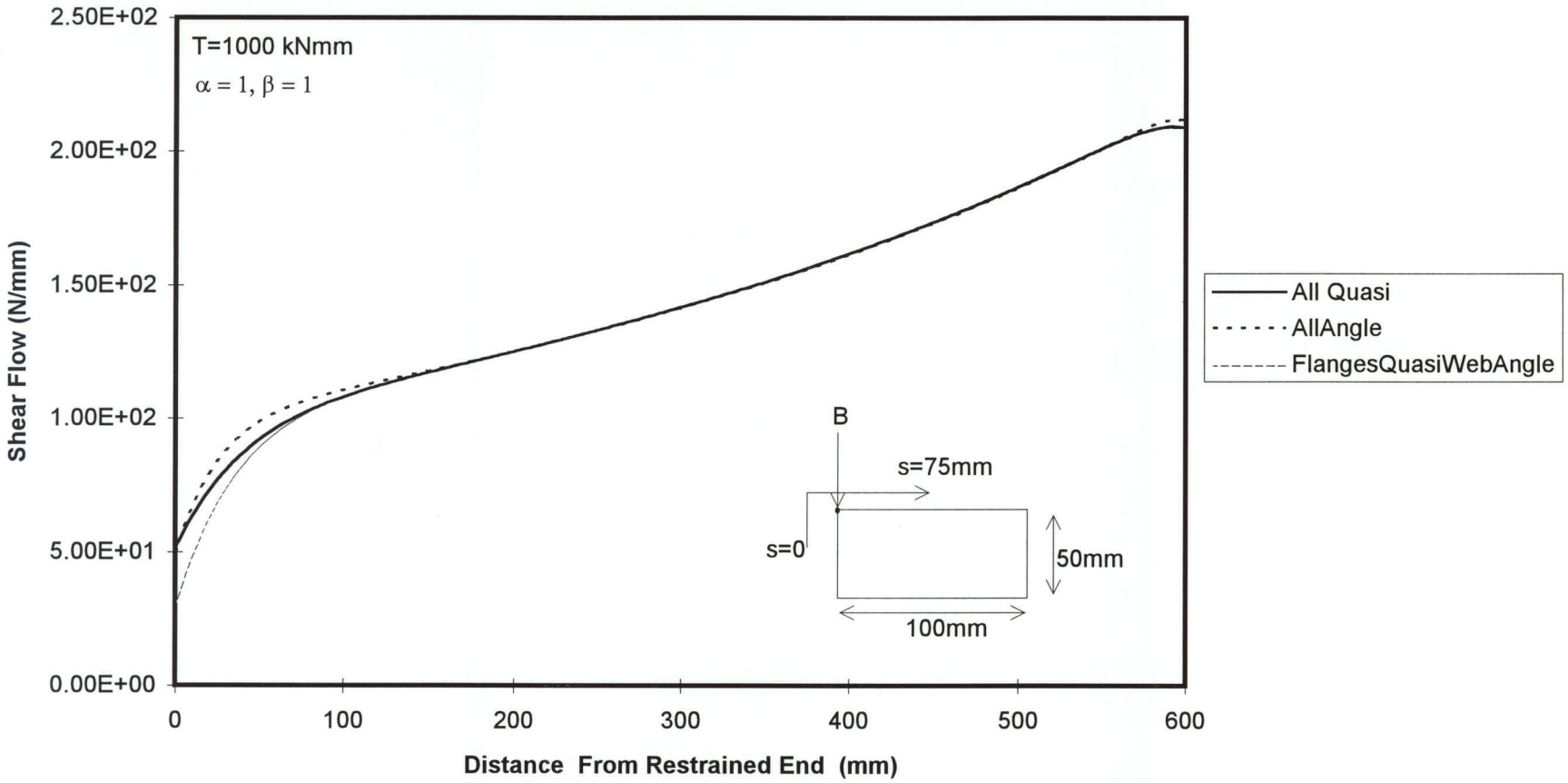

Figure 7.25 SHEAR FLOW ALONG LENGTH OF BOX AT S=75

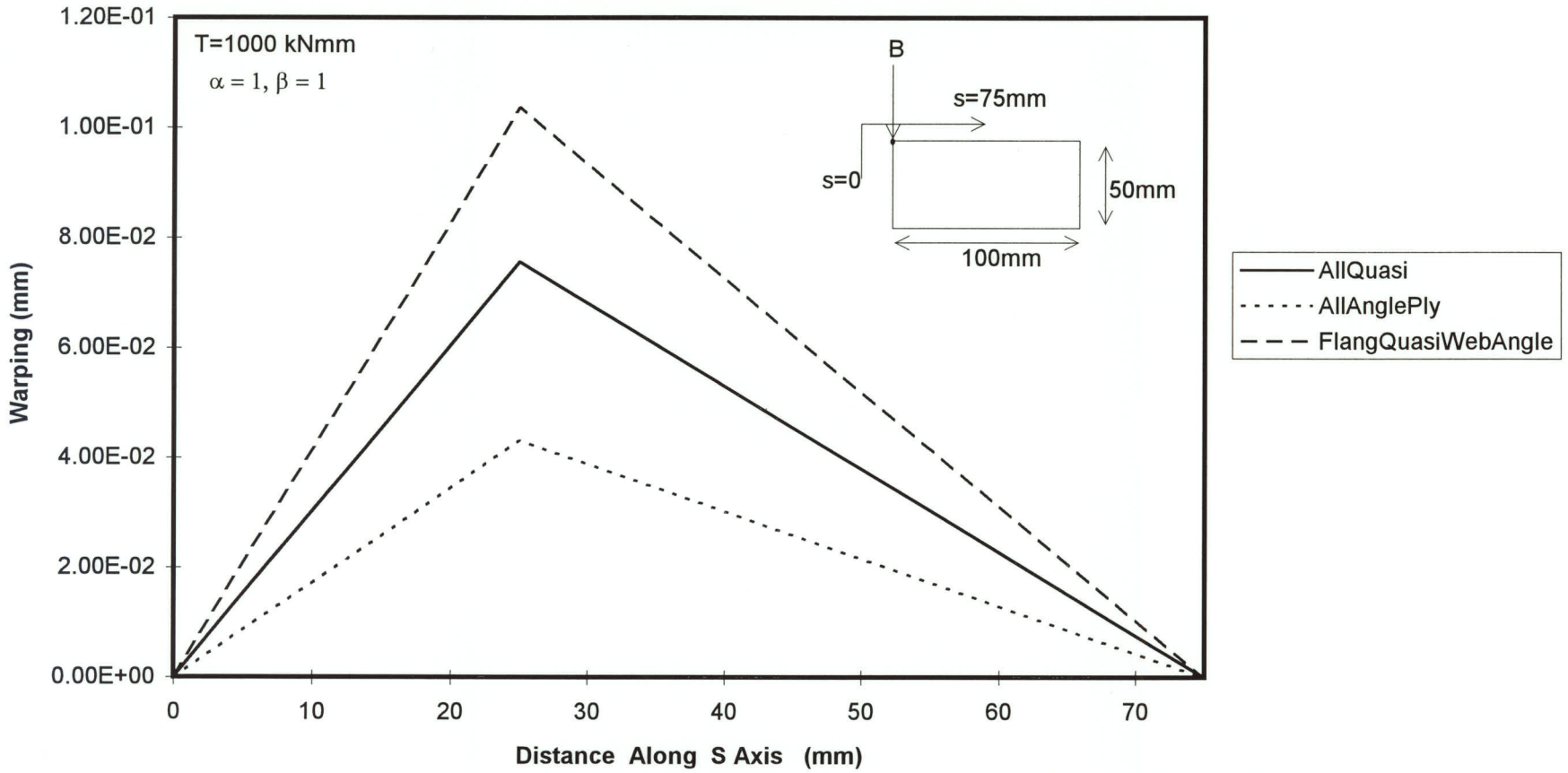

Figure 7.26 WARPING AROUND BOX AT Z = 200 mm

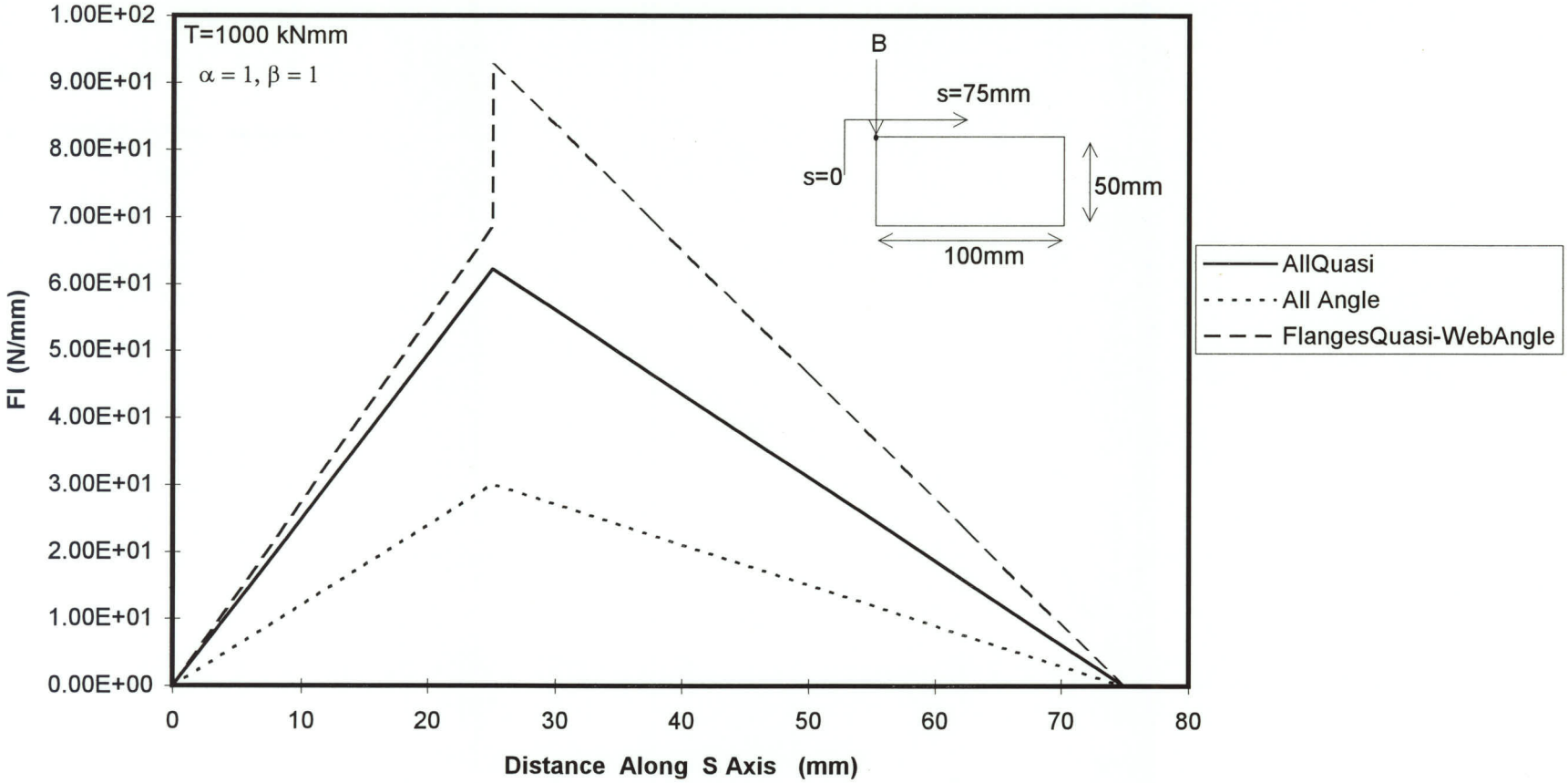

Figure 7.27 F I AROUND BOX AT Z = 20mm

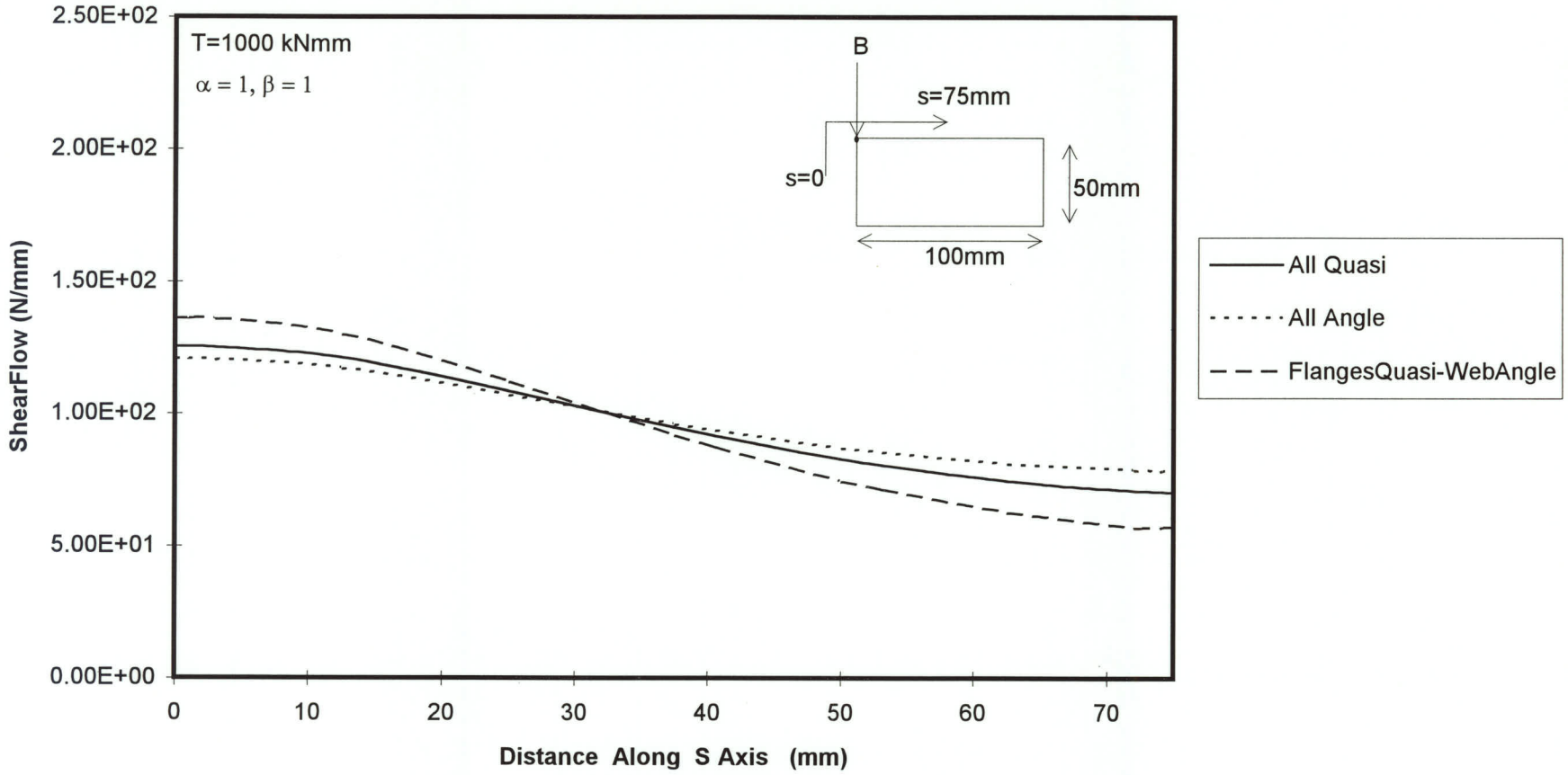

Figure 7.28 TOTAL SHEAR FLOW AROUND BOX AT Z = 20 mm

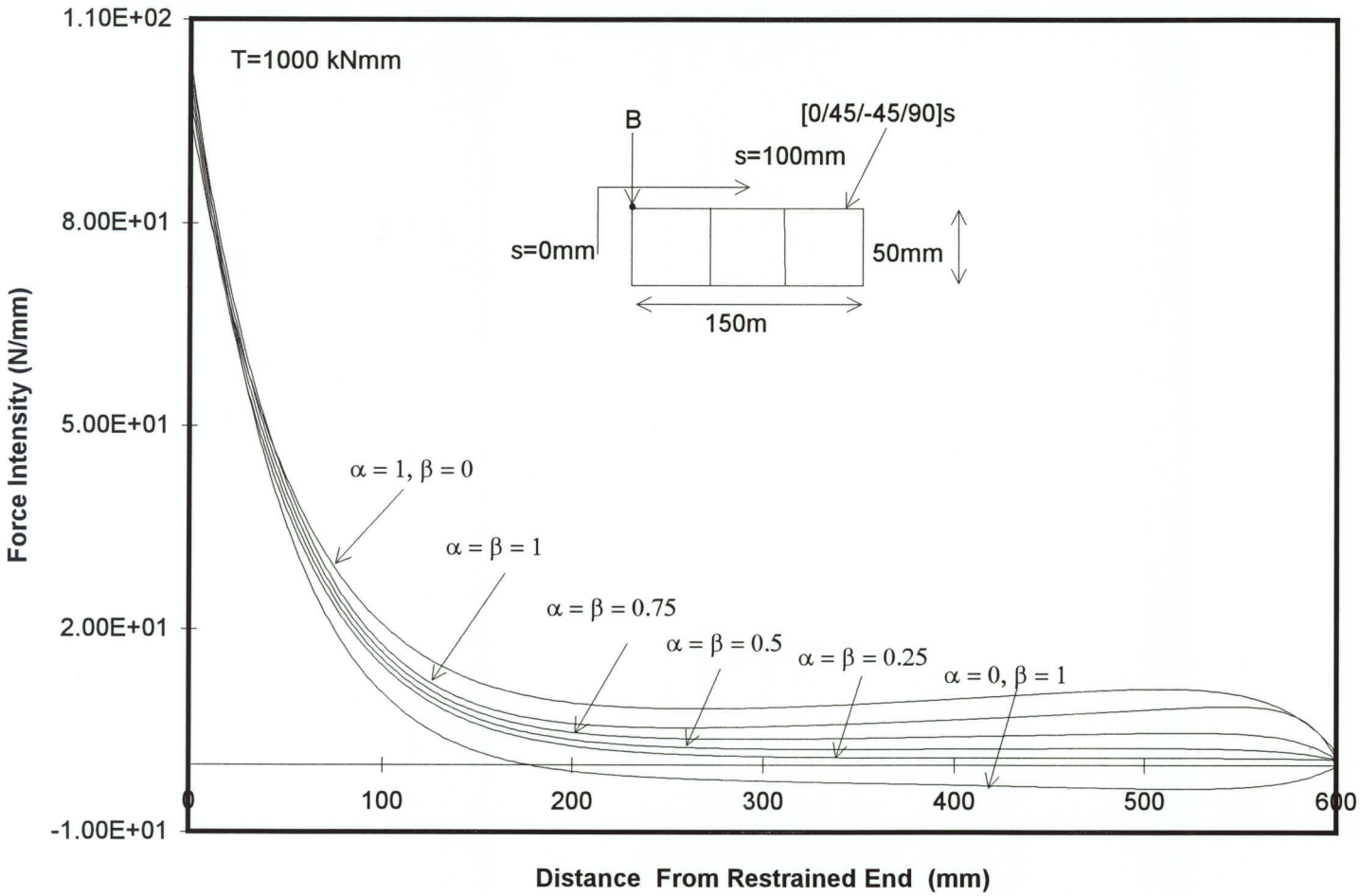

Figure 7.29 FORCE INTENSITY ALONG LENGTH OF BOX AT POINT "B"

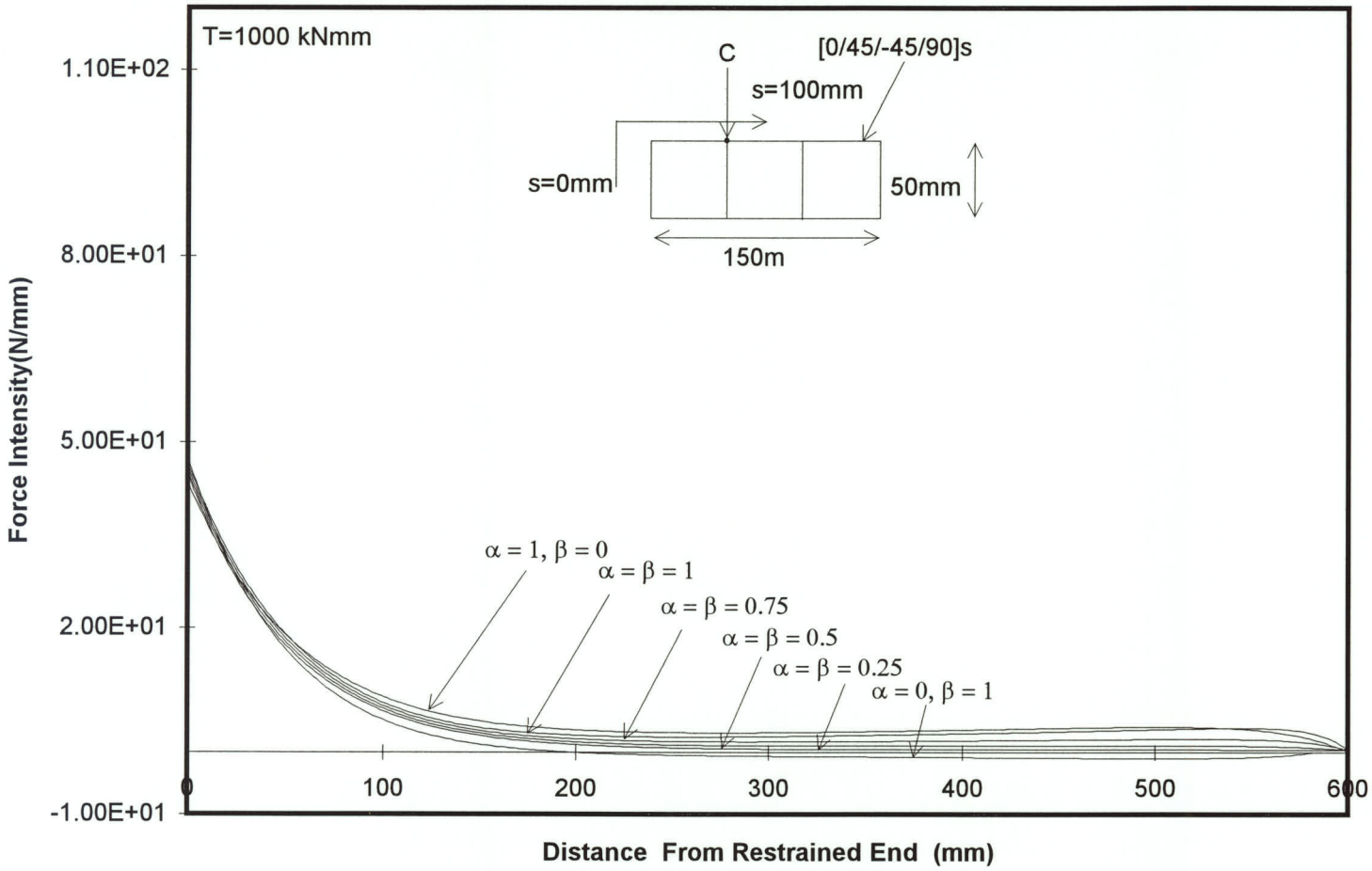

Figure 7.30 FORCE INTENSITY ALONG LENGTH OF BOX AT POINT "C"

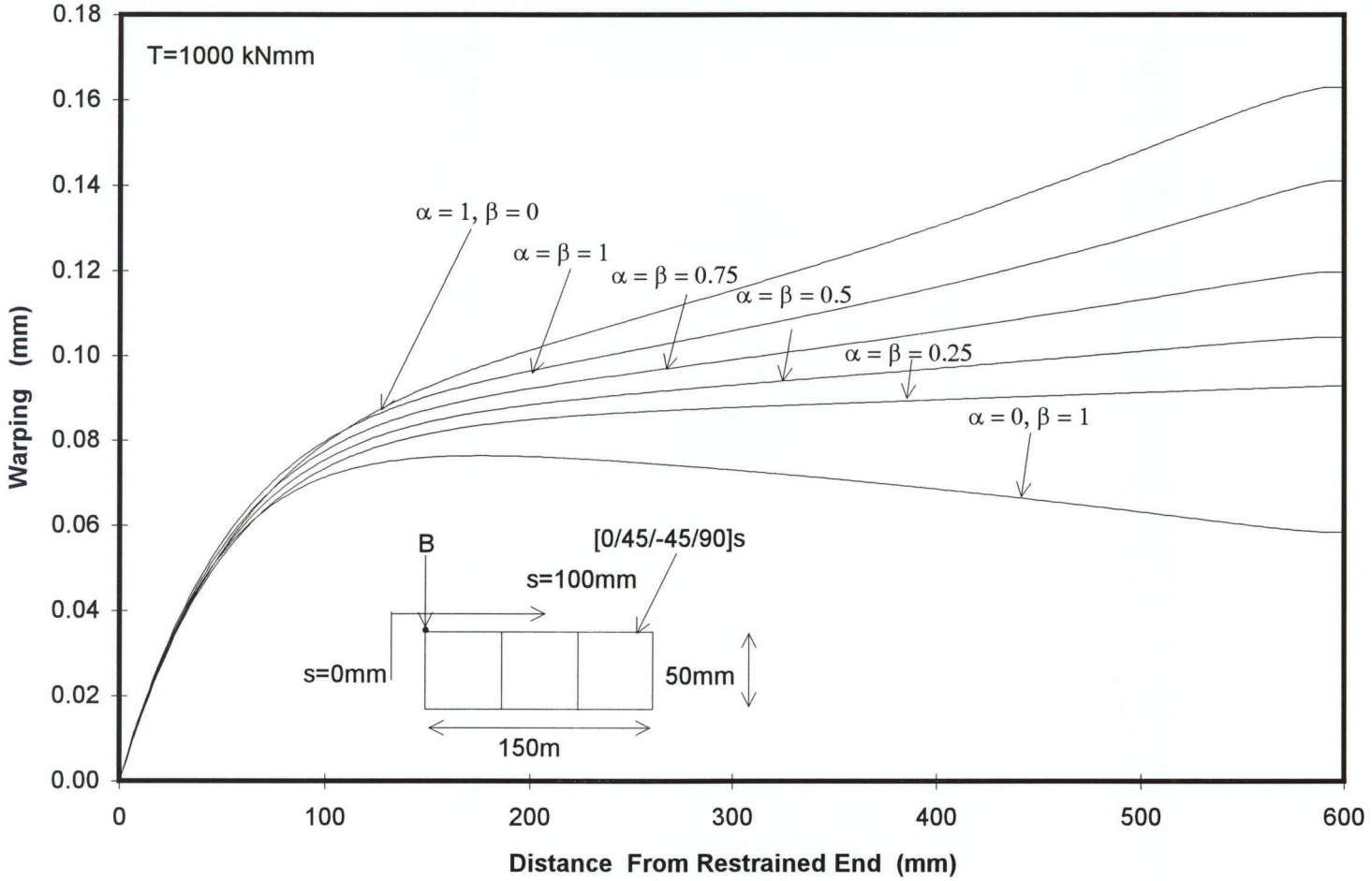

Figure 7.31 WARPING ALONG LENGTH OF BOX AT POINT "B"

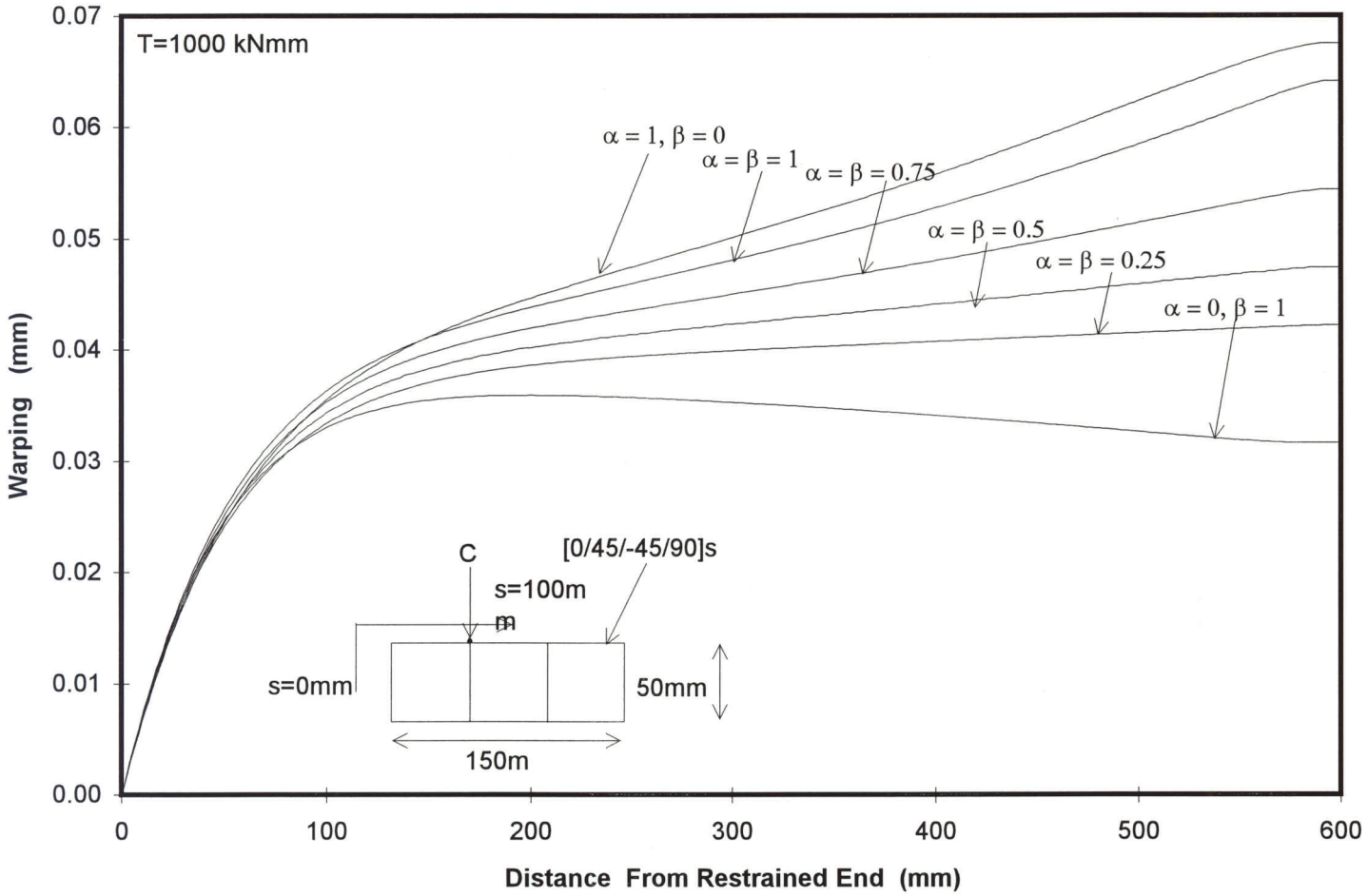

Figure 7.32 WARPING ALONG LENGTH OF BOX AT POINT "C"

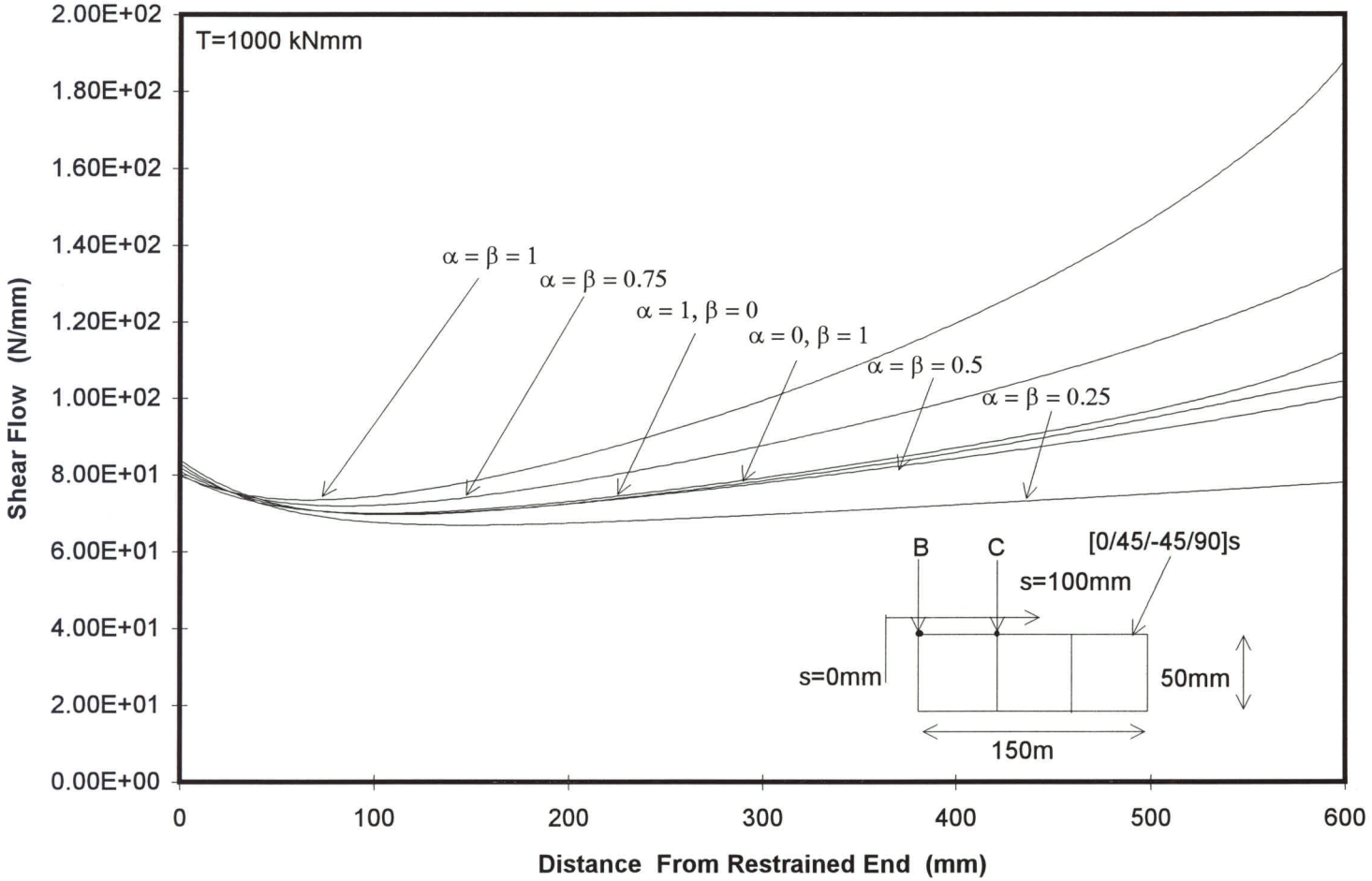

Figure 7.33 SHEAR FLOW ALONG LENGTH OF BOX AT S=0 mm

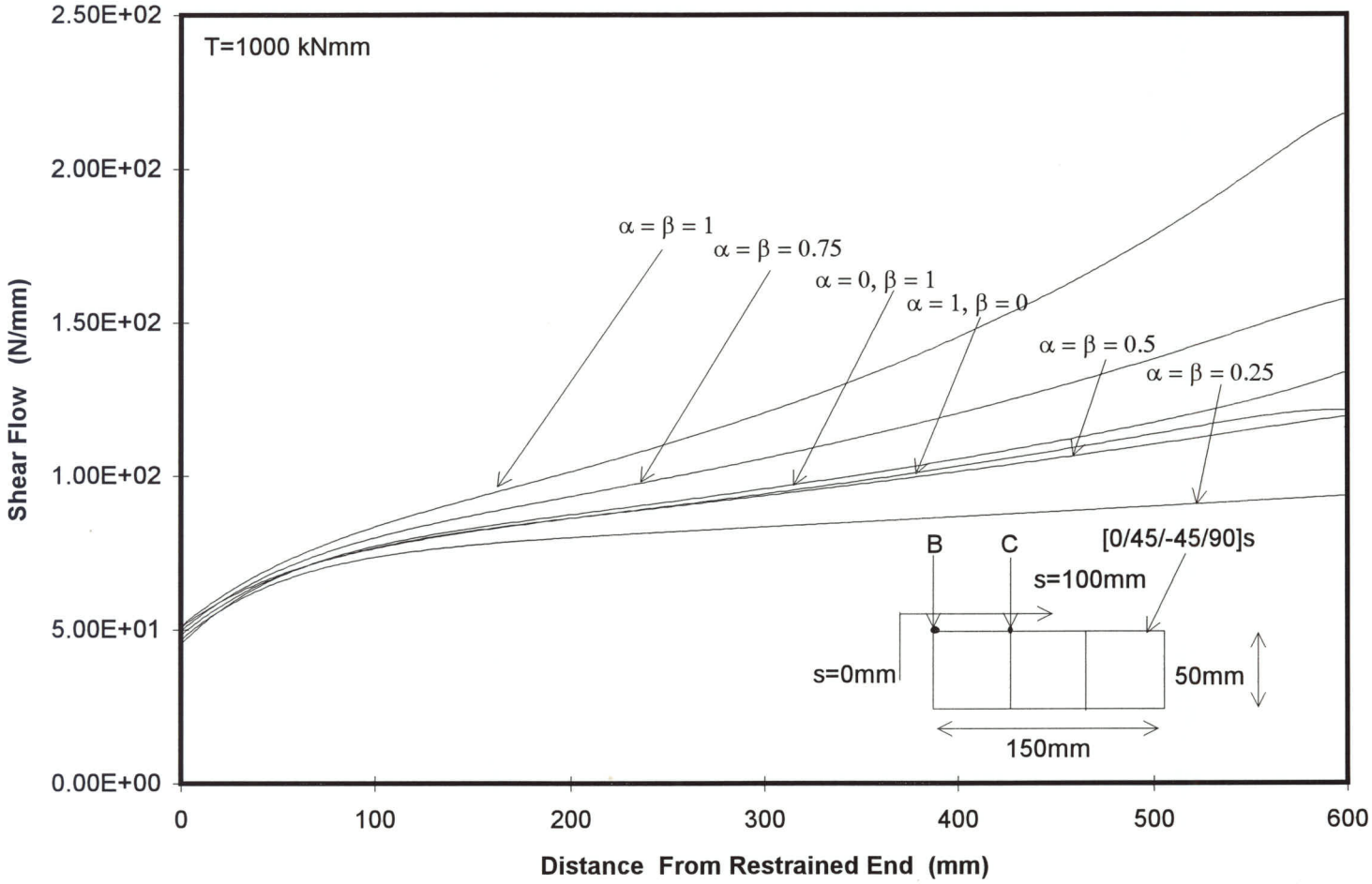

Figure 7.34 SHEAR FLOW ALONG LENGTH OF BOX AT S=100 mm

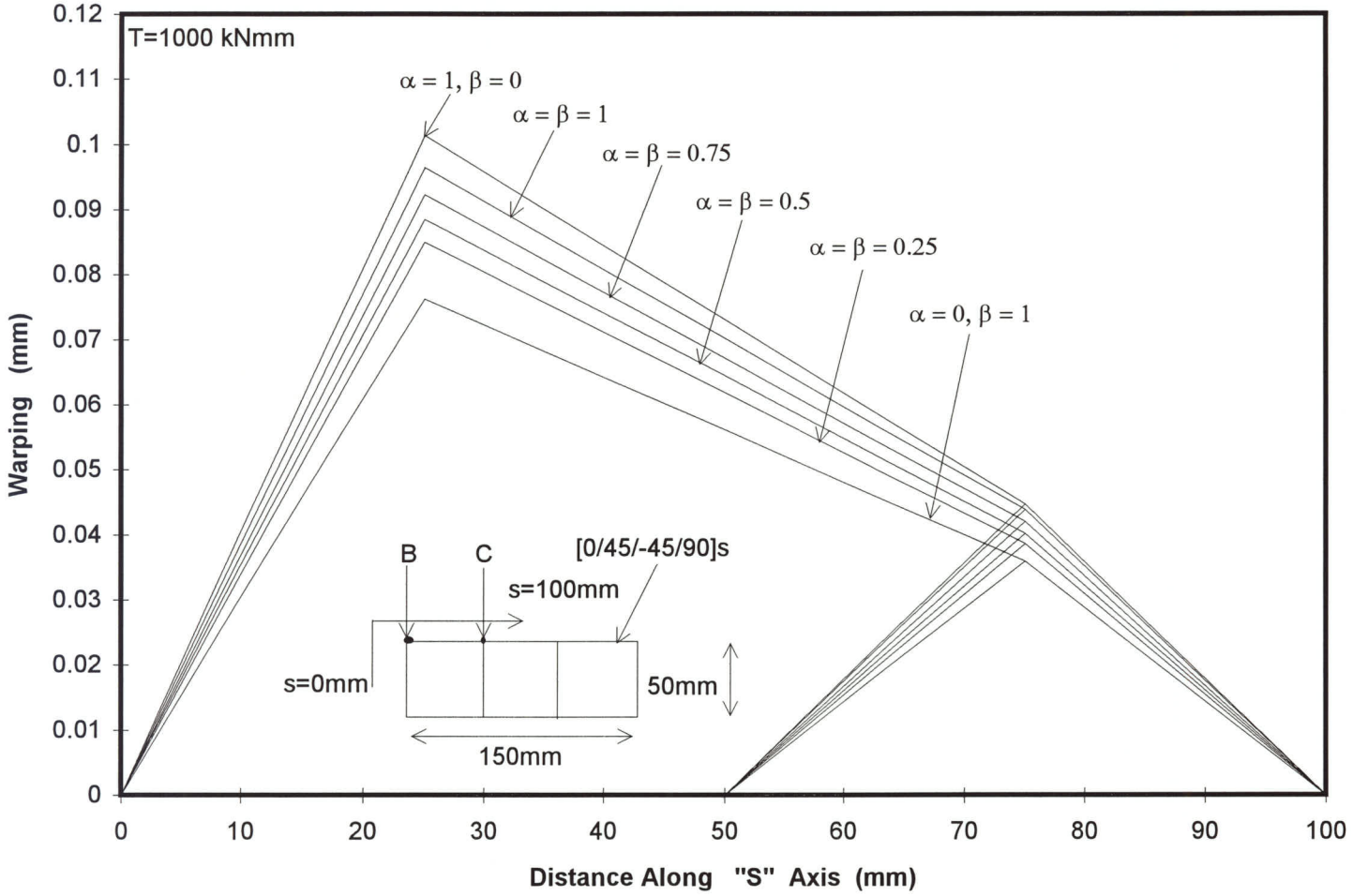

Figure 7.35 WARPING AROUND BOX AT X=200mm

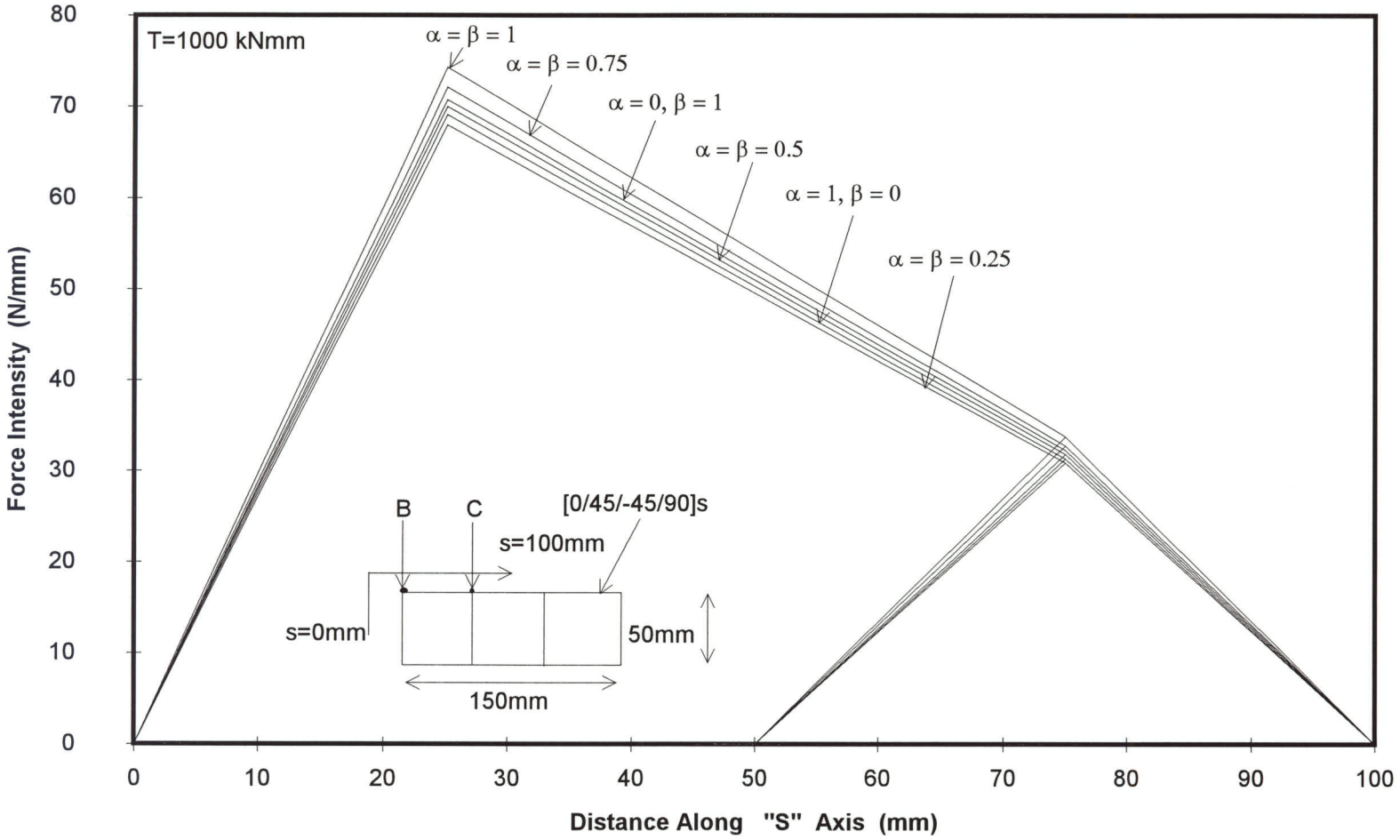

Figure 7.36 FORCE INTENSITY AROUND BOX AT X=20mm

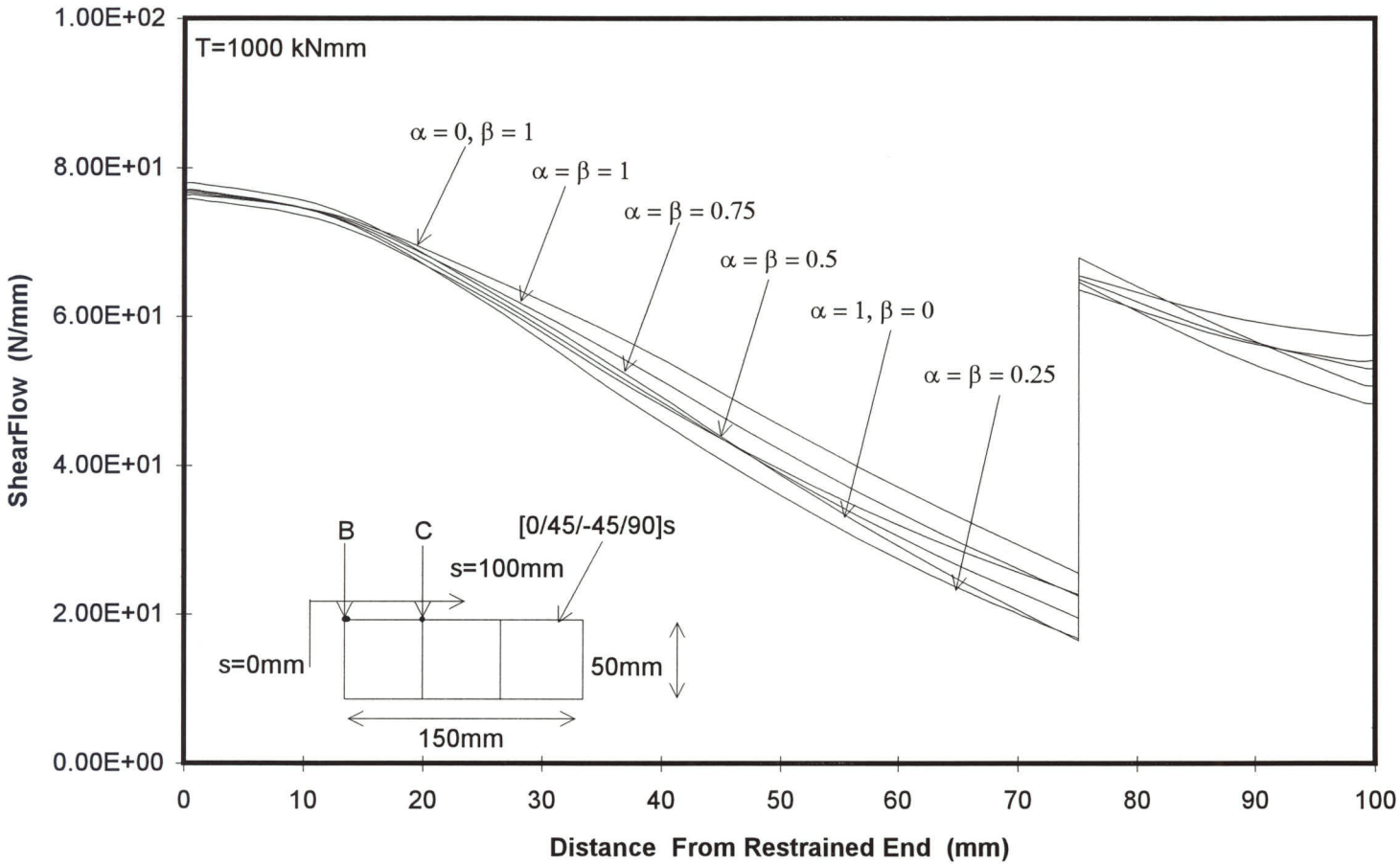

Figure 7.37 SHEAR FLOW AROUND THREE CELL BOX AT Z=20mm

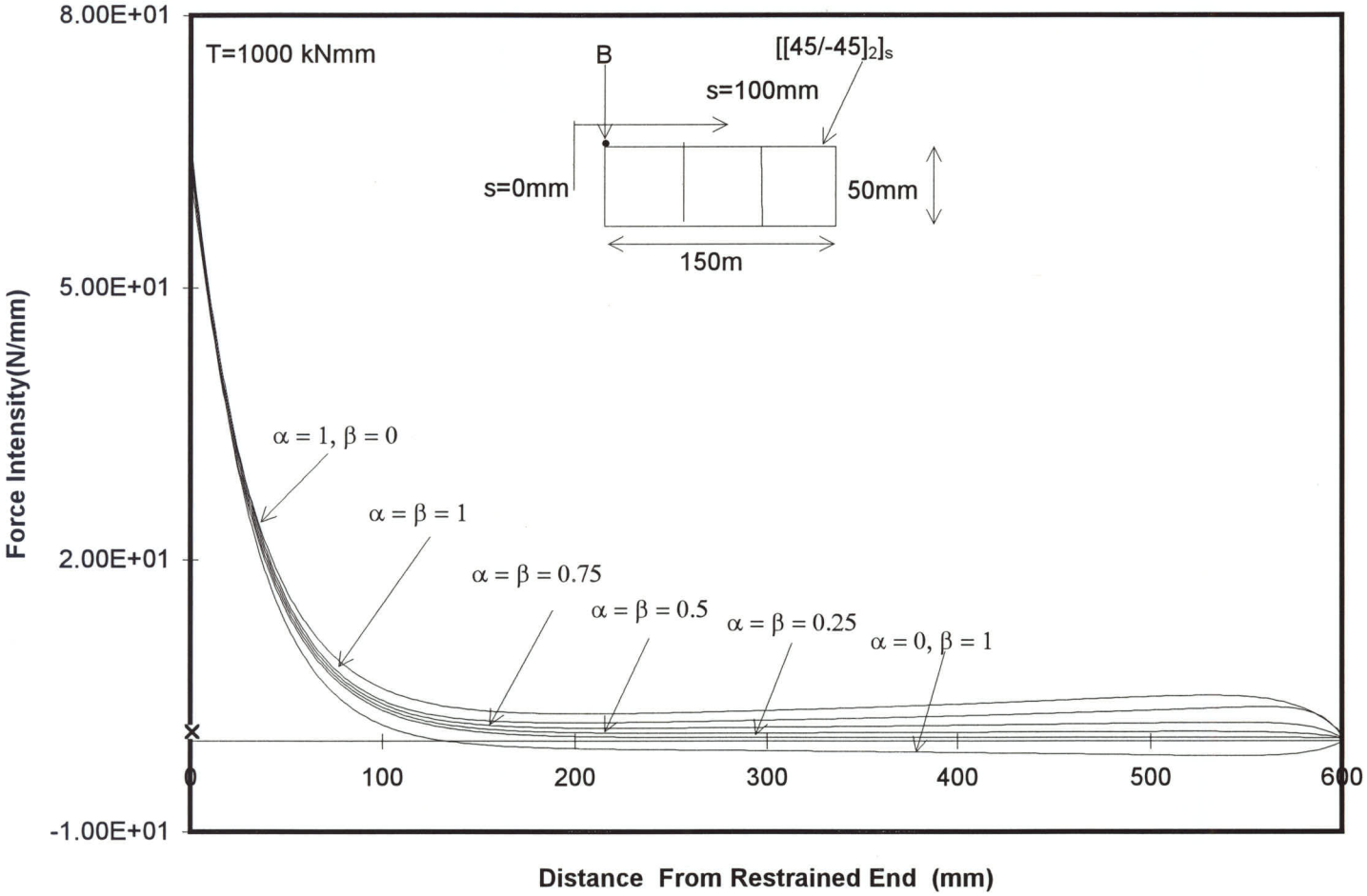

Figure 7.38 FORCE INTENSITY ALONG LENGTH OF BOX AT POINT "B"

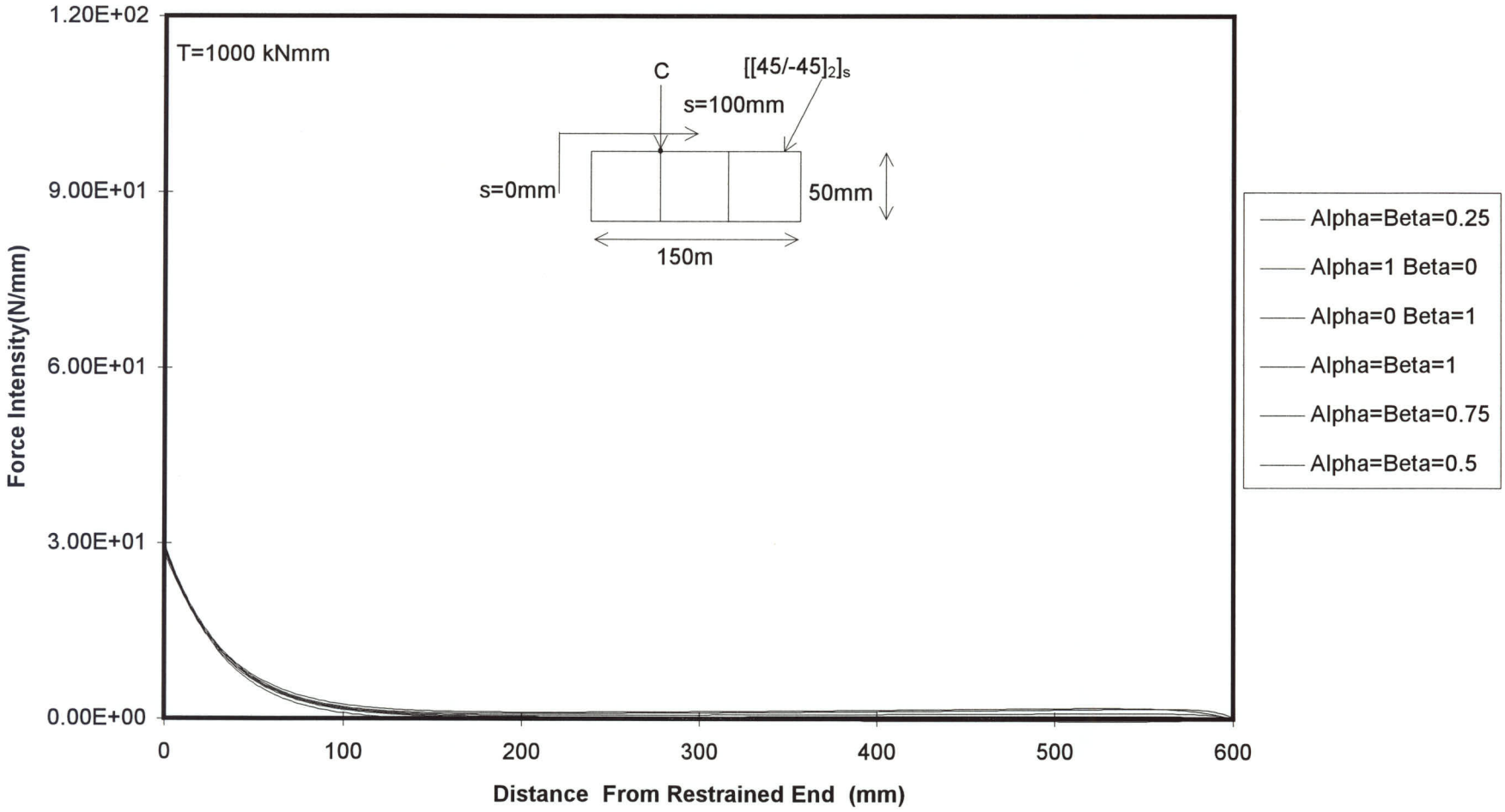

Figure 7.39 FORCE INTENSITY ALONG LENGTH OF BOX AT POINT "C"

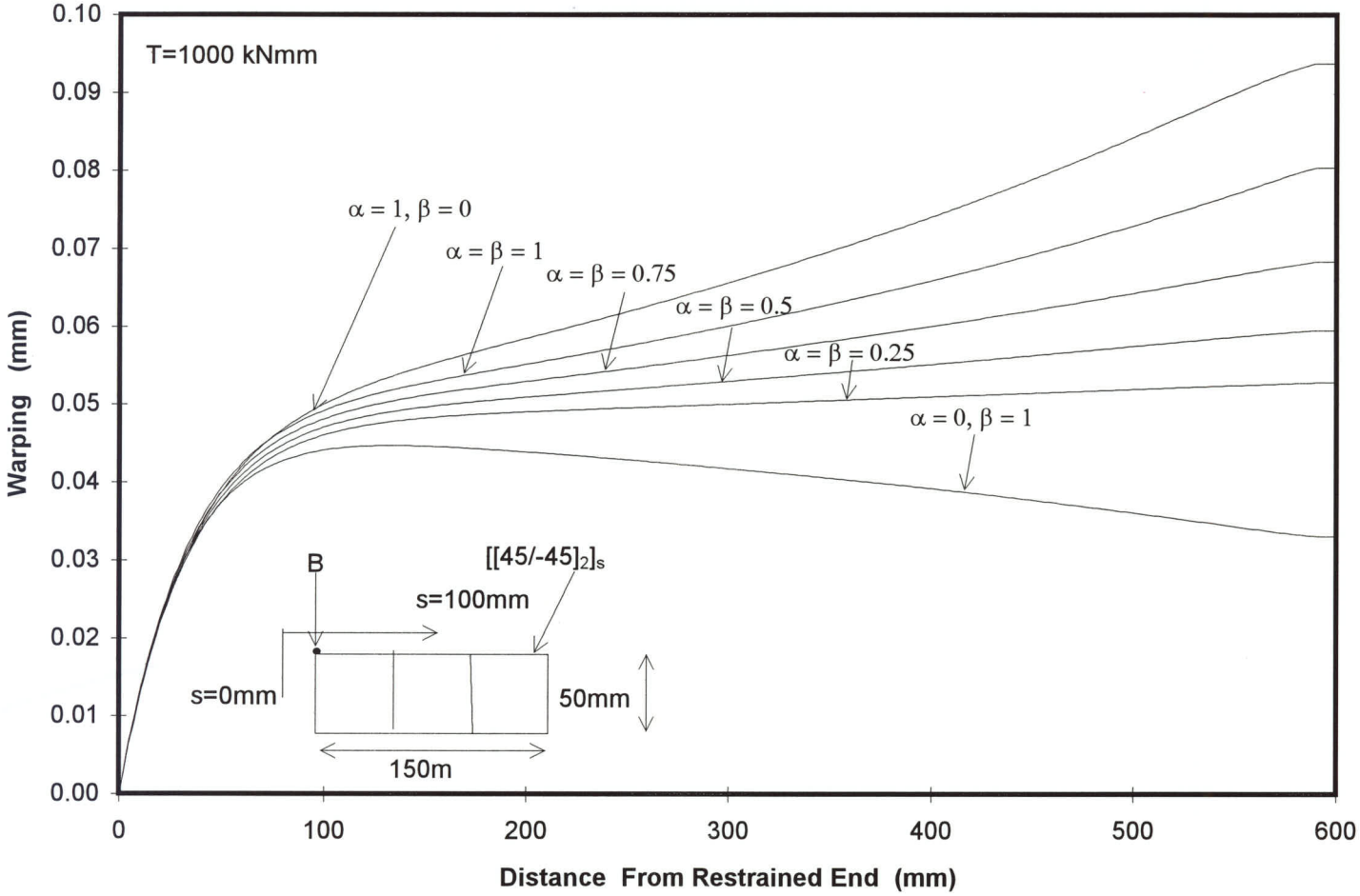

Figure 7.40 WARPING ALONG LENGTH OF BOX AT POINT "B"

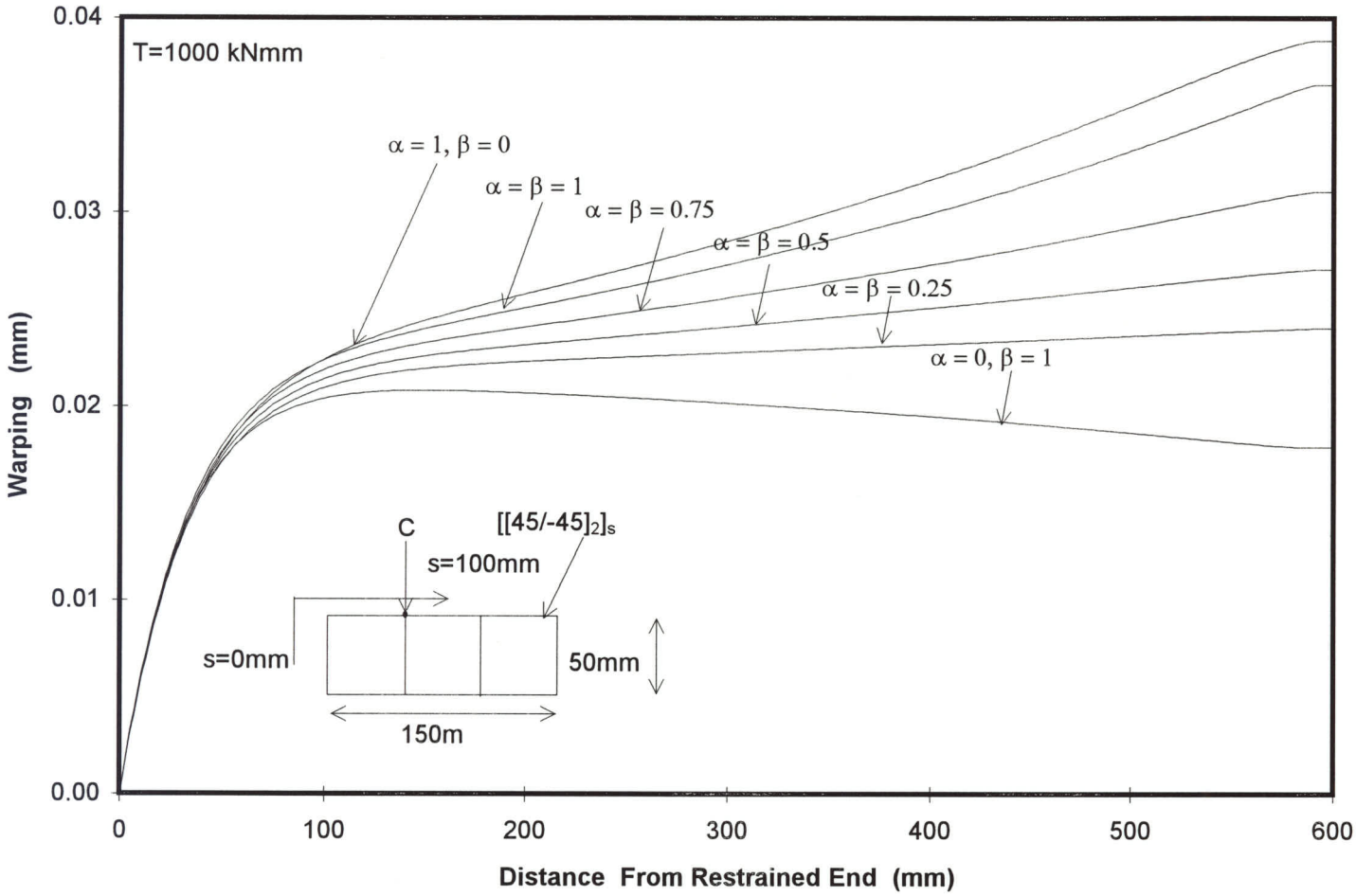

Figure 7.41 WARPING ALONG LENGTH OF BOX AT POINT "C"

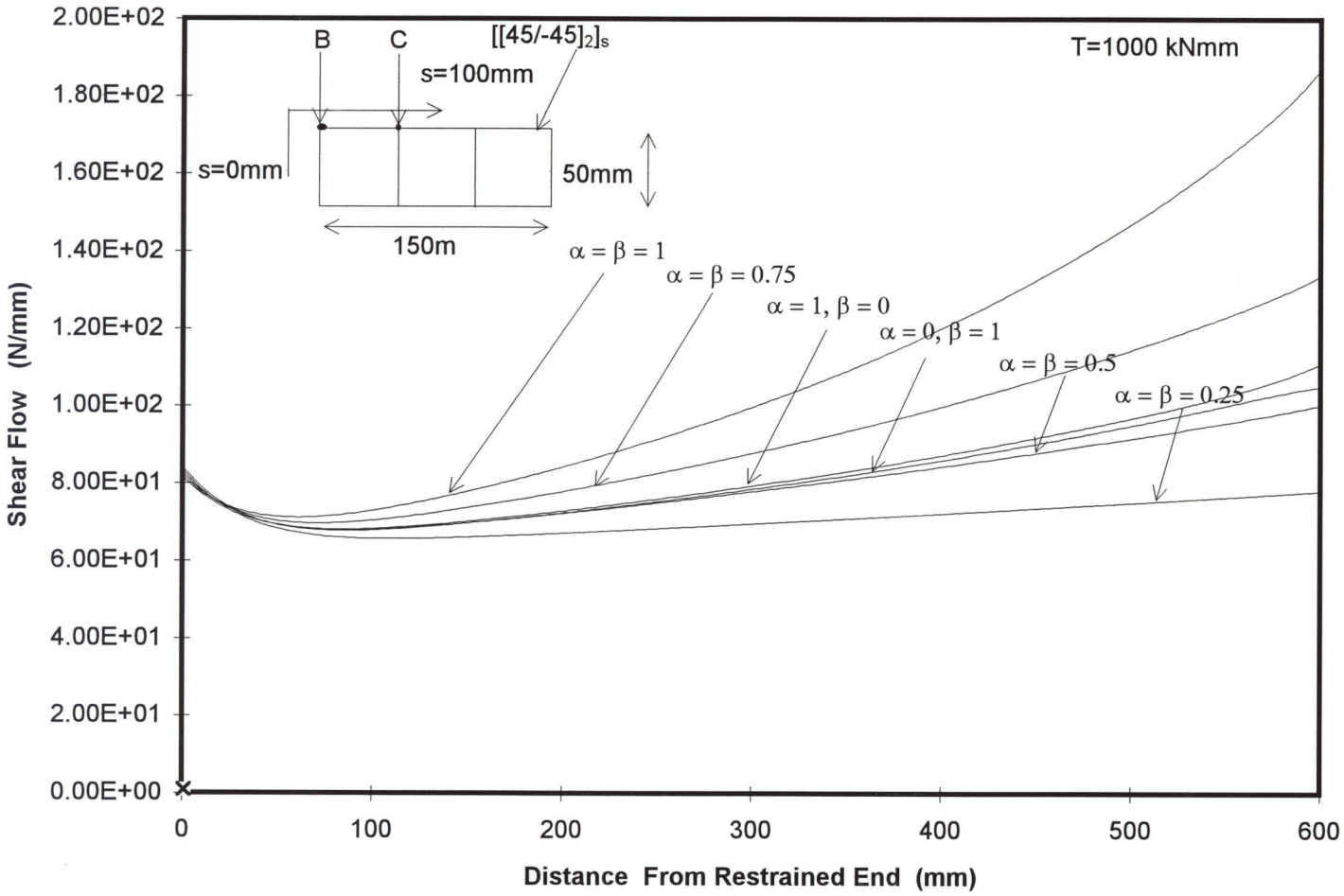

Figure 7.42 SHEAR FLOW ALONG LENGTH OF BOX AT S=0 mm

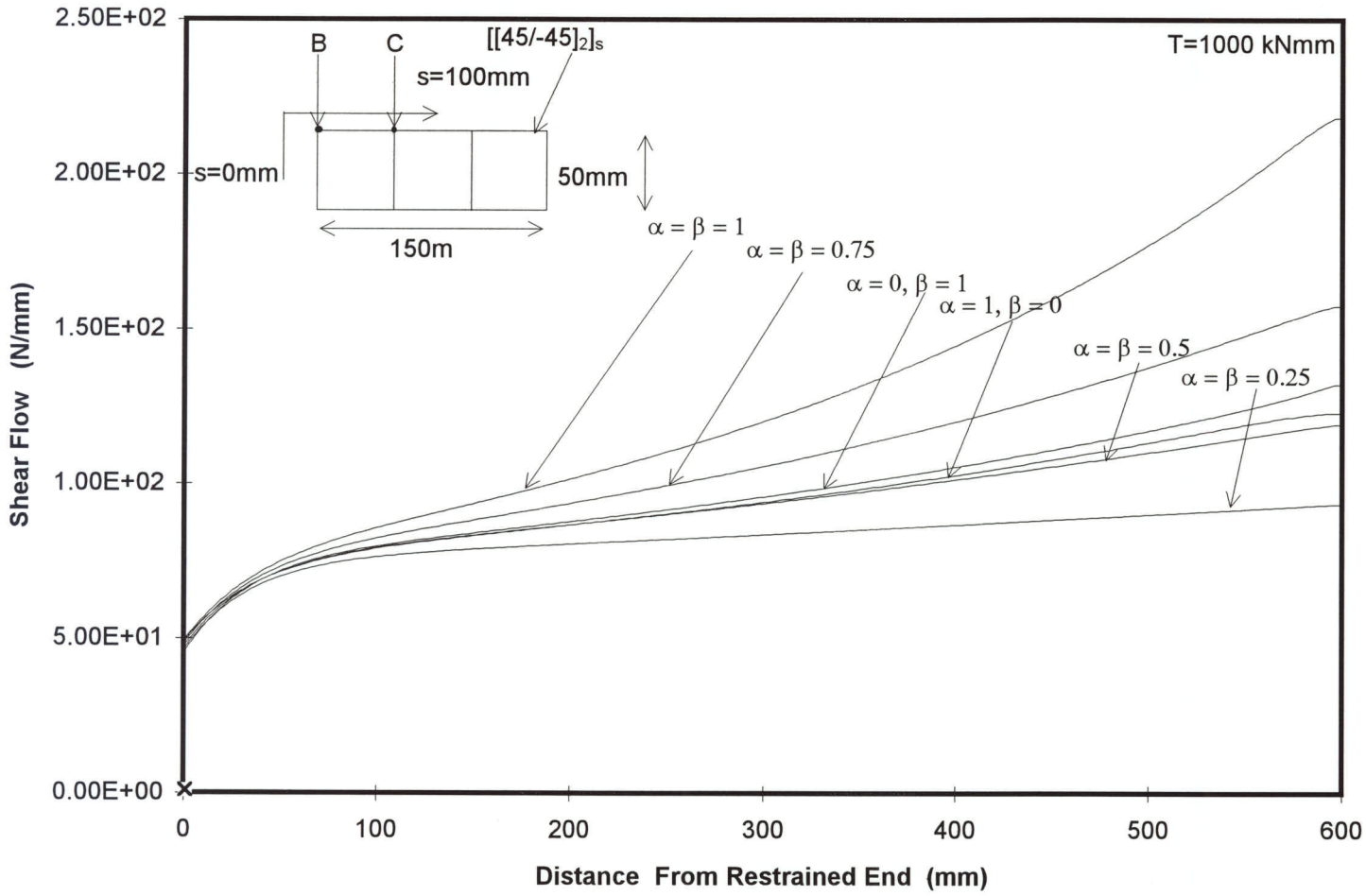

Figure 7.43 SHEAR FLOW ALONG LENGTH OF BOX AT S=100 mm

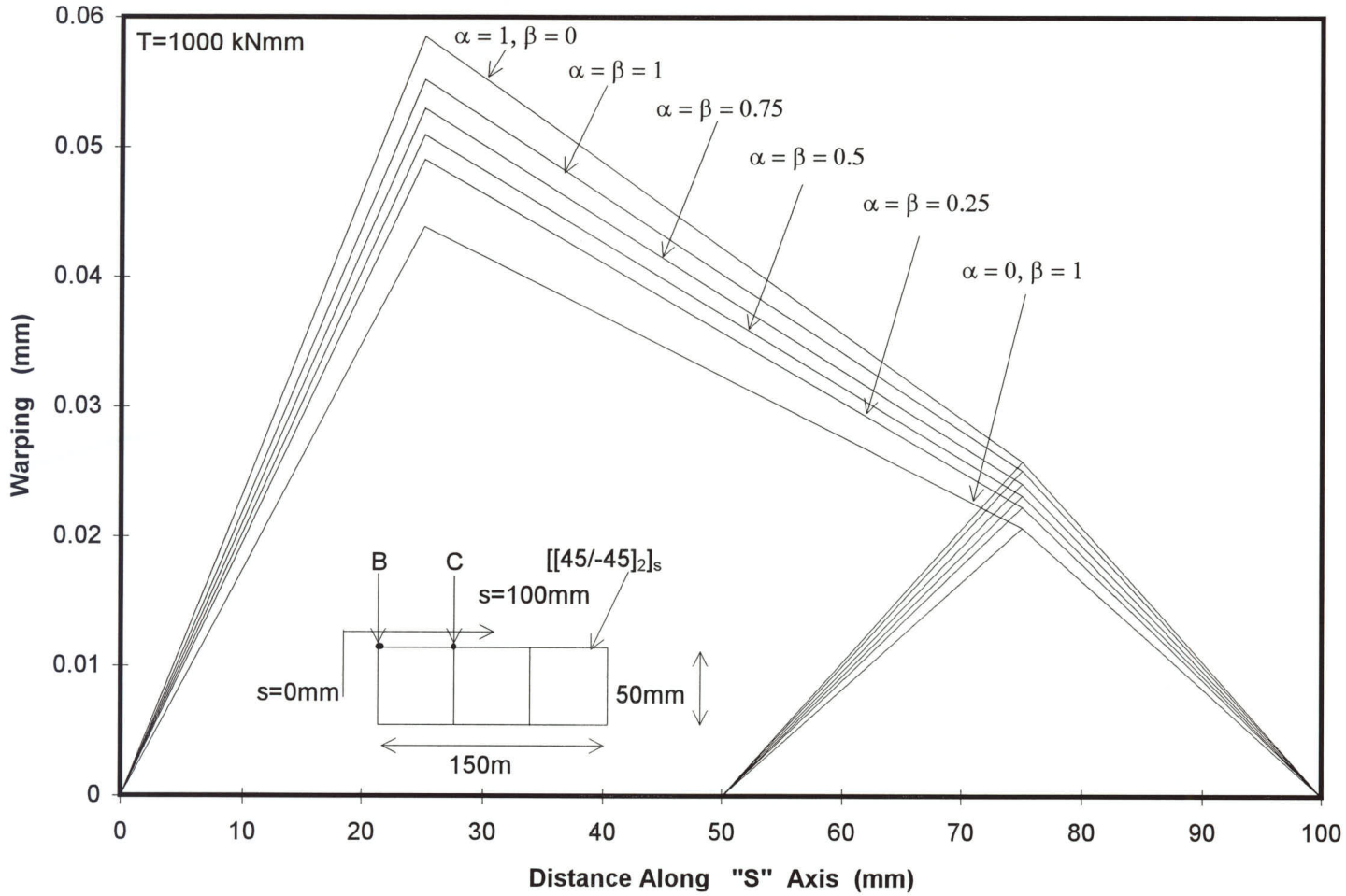

Figure 7.44 WARPING AROUND BOX AT Z=200mm

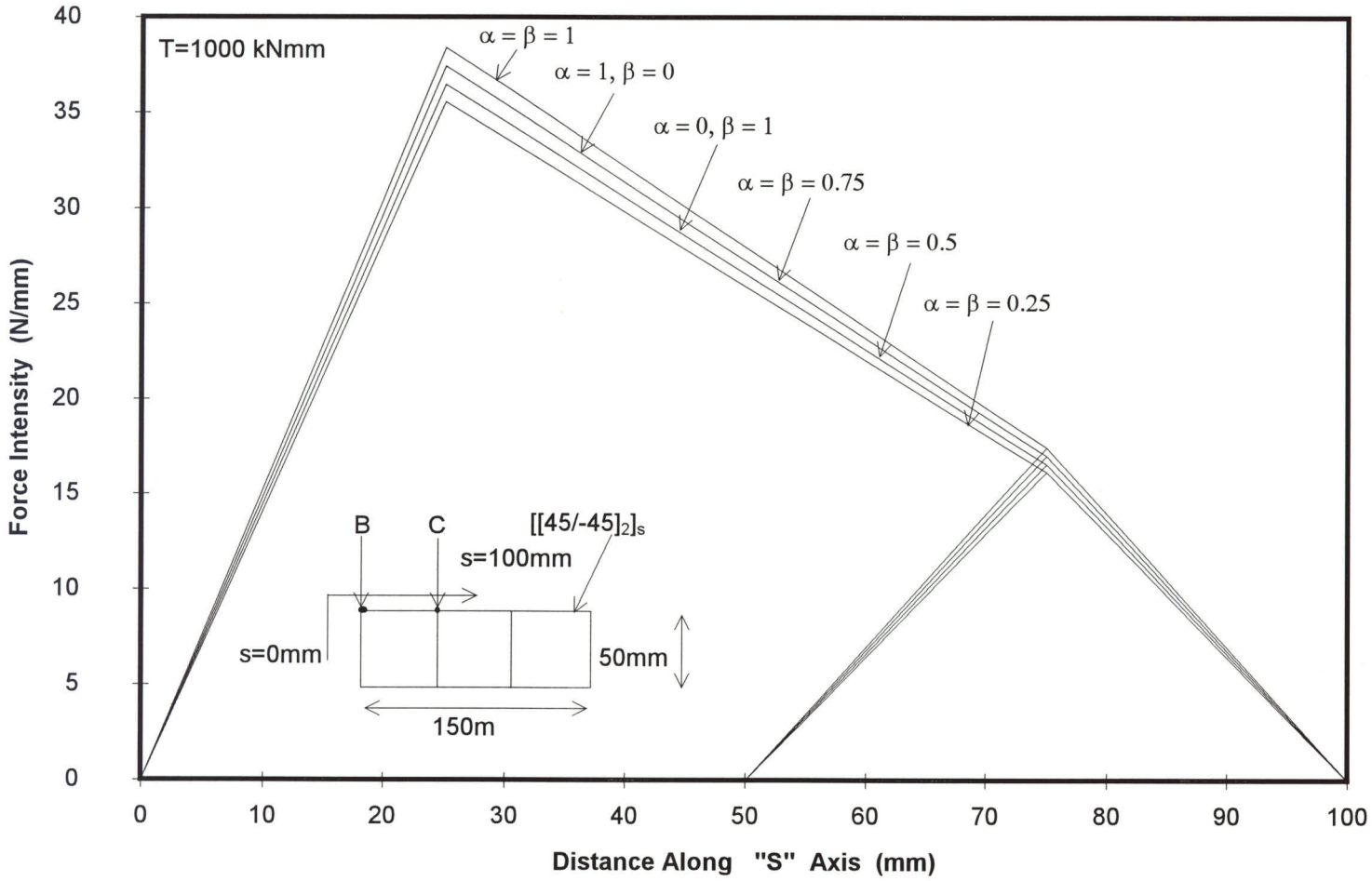

Figure 7.45 FORCE INTENSITY AROUND BOX AT Z=20mm

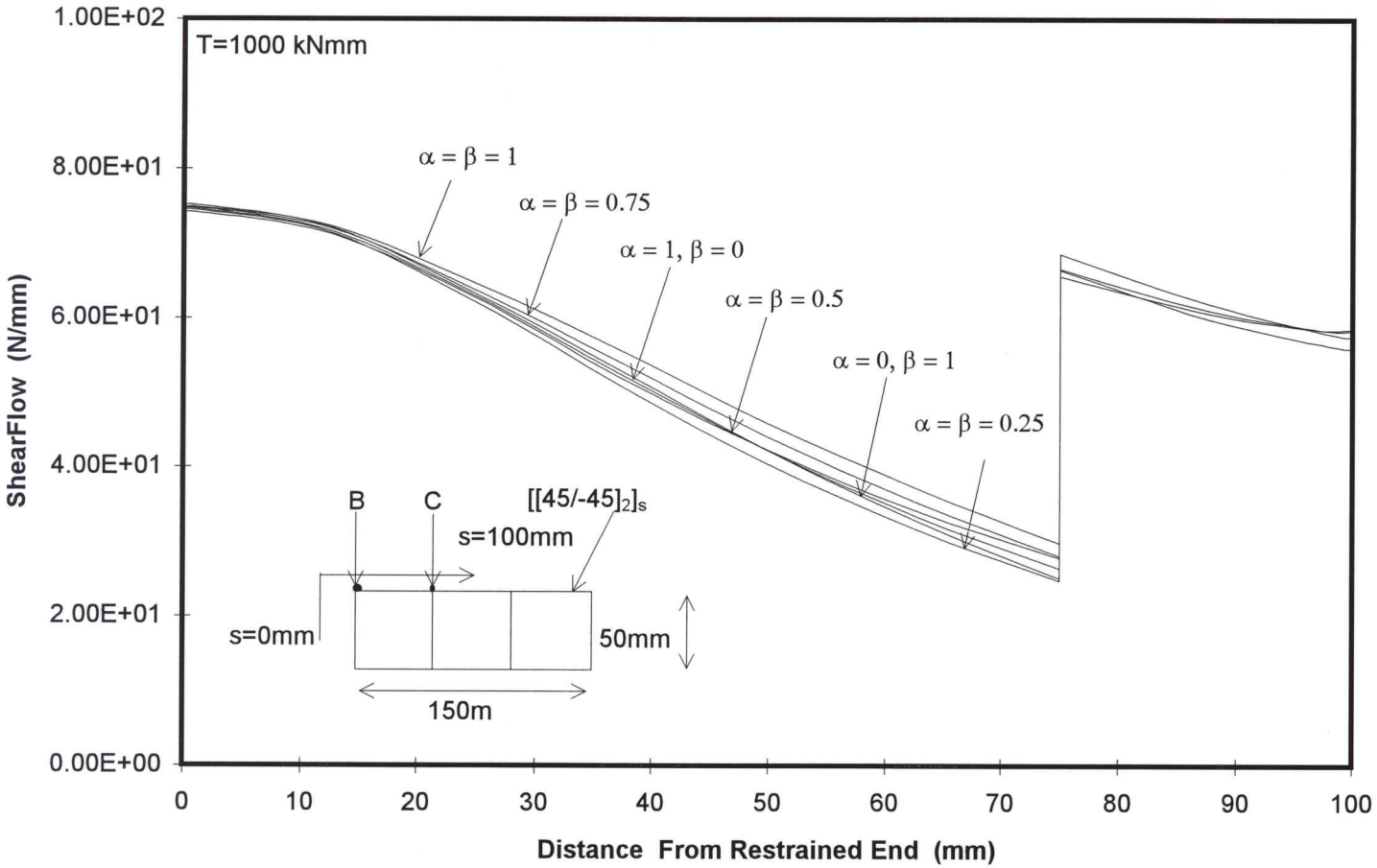

Figure 7.46 SHEAR FLOW AROUND THREE CELL BOX AT Z=20mm

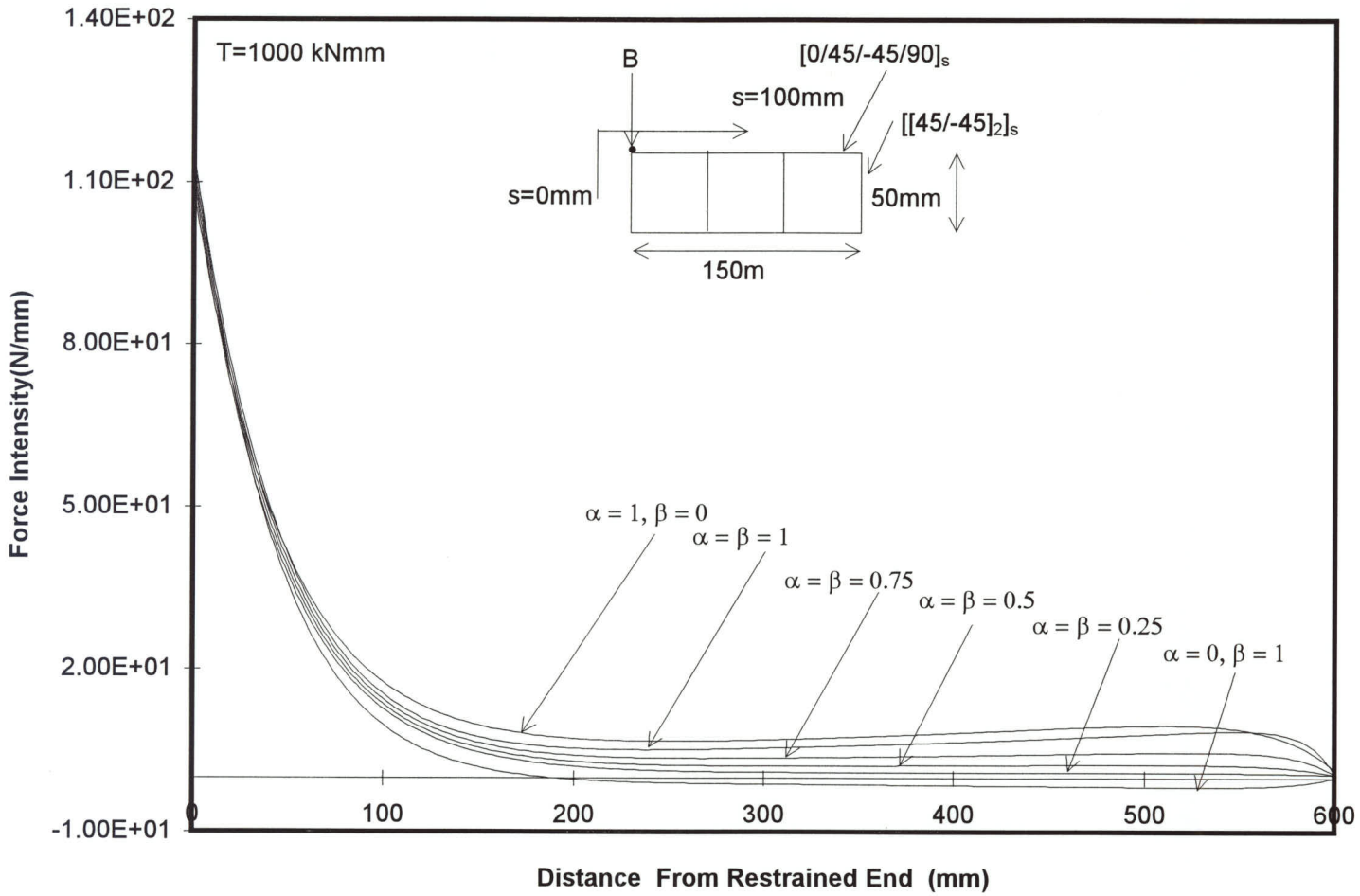

Figure 7.47 FORCE INTENSITY ALONG LENGTH OF BOX AT POINT "B"

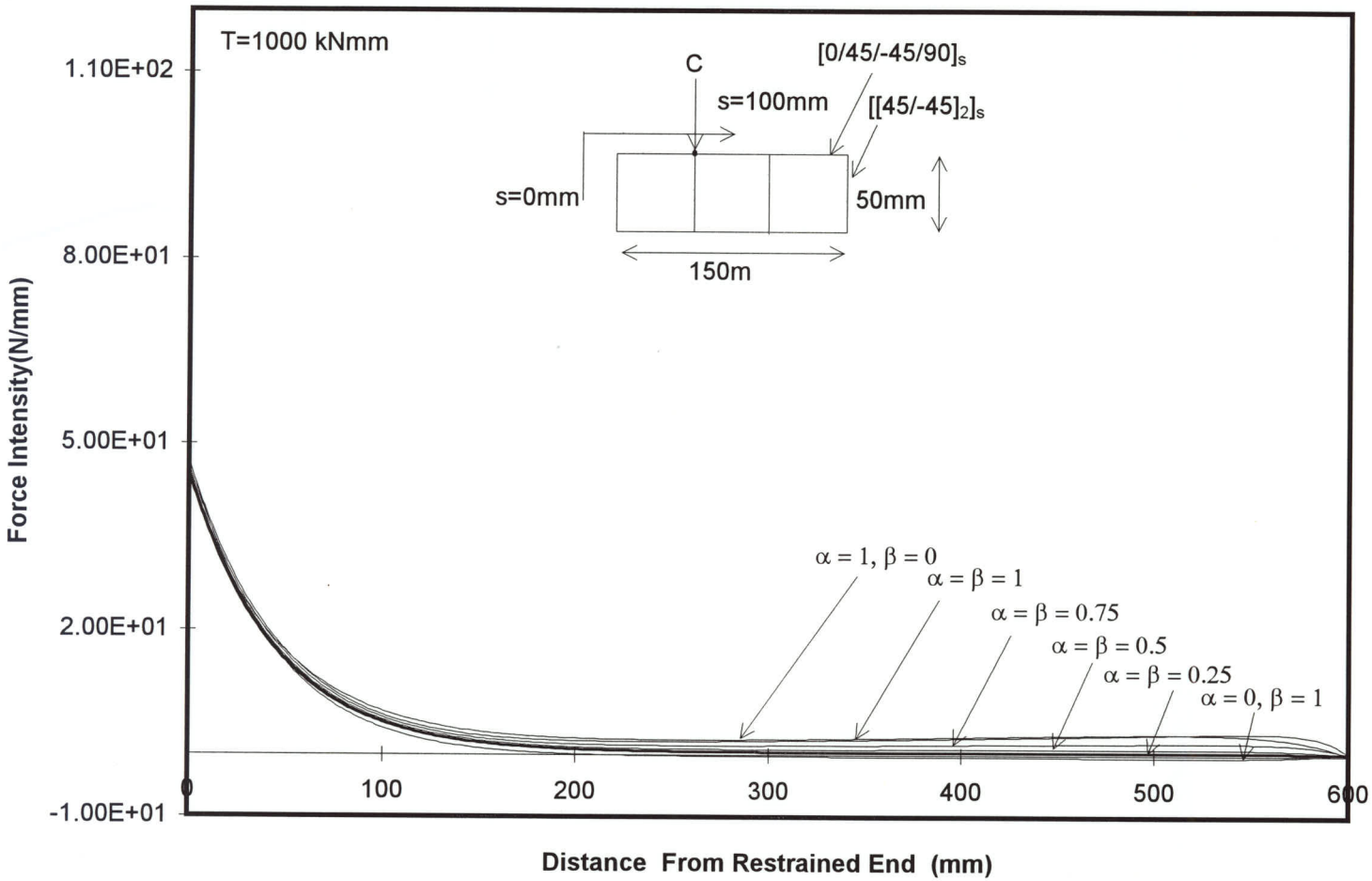

Figure 7.48 FORCE INTENSITY ALONG LENGTH OF BOX AT POINT "C"

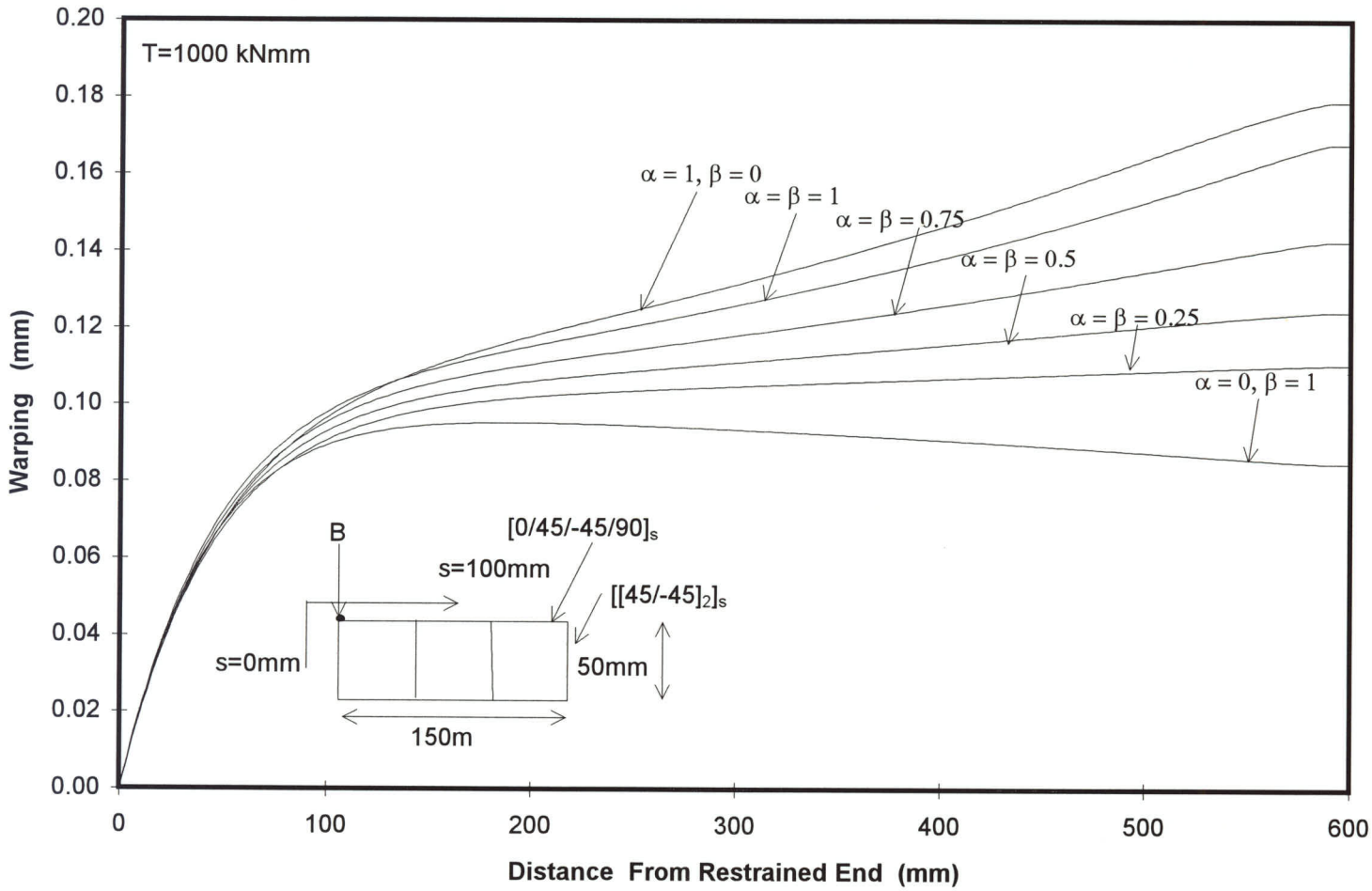

Figure 7.49 WARPING ALONG LENGTH OF BOX AT POINT "B"

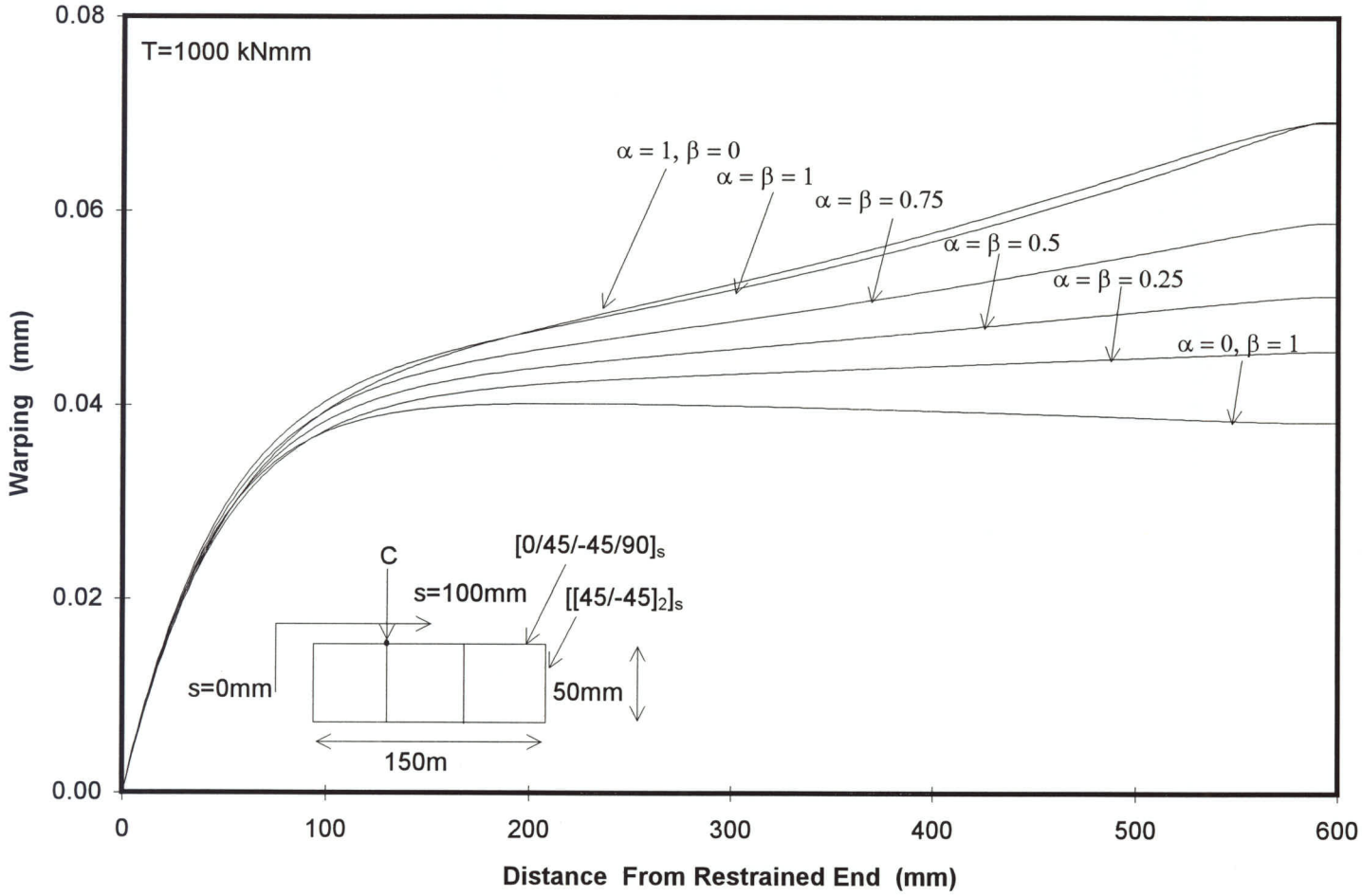

Figure 7.50 WARPING ALONG LENGTH OF BOX AT POINT "C"

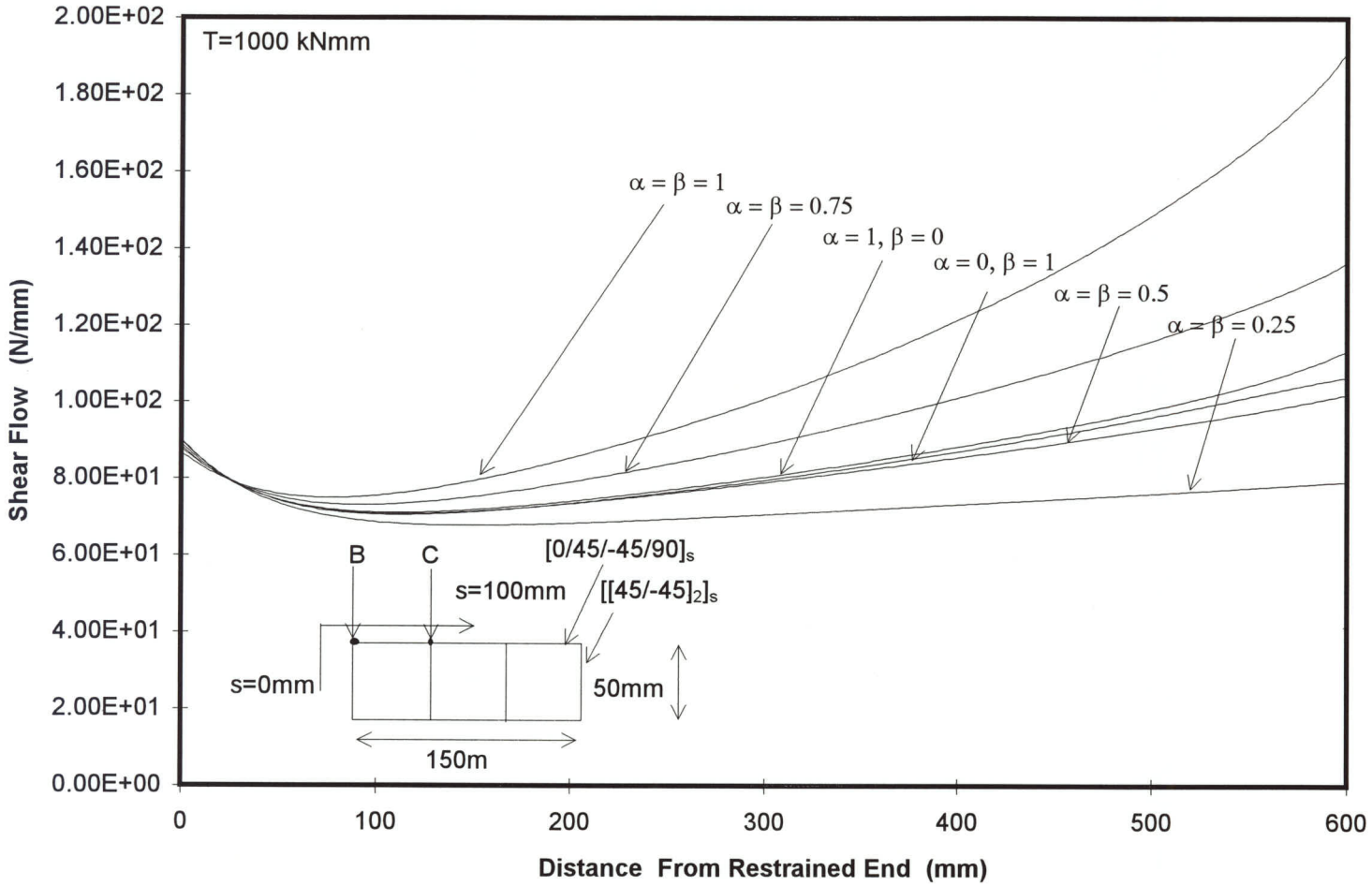

Figure 7.51 SHEAR FLOW ALONG LENGTH OF BOX AT S=0 mm

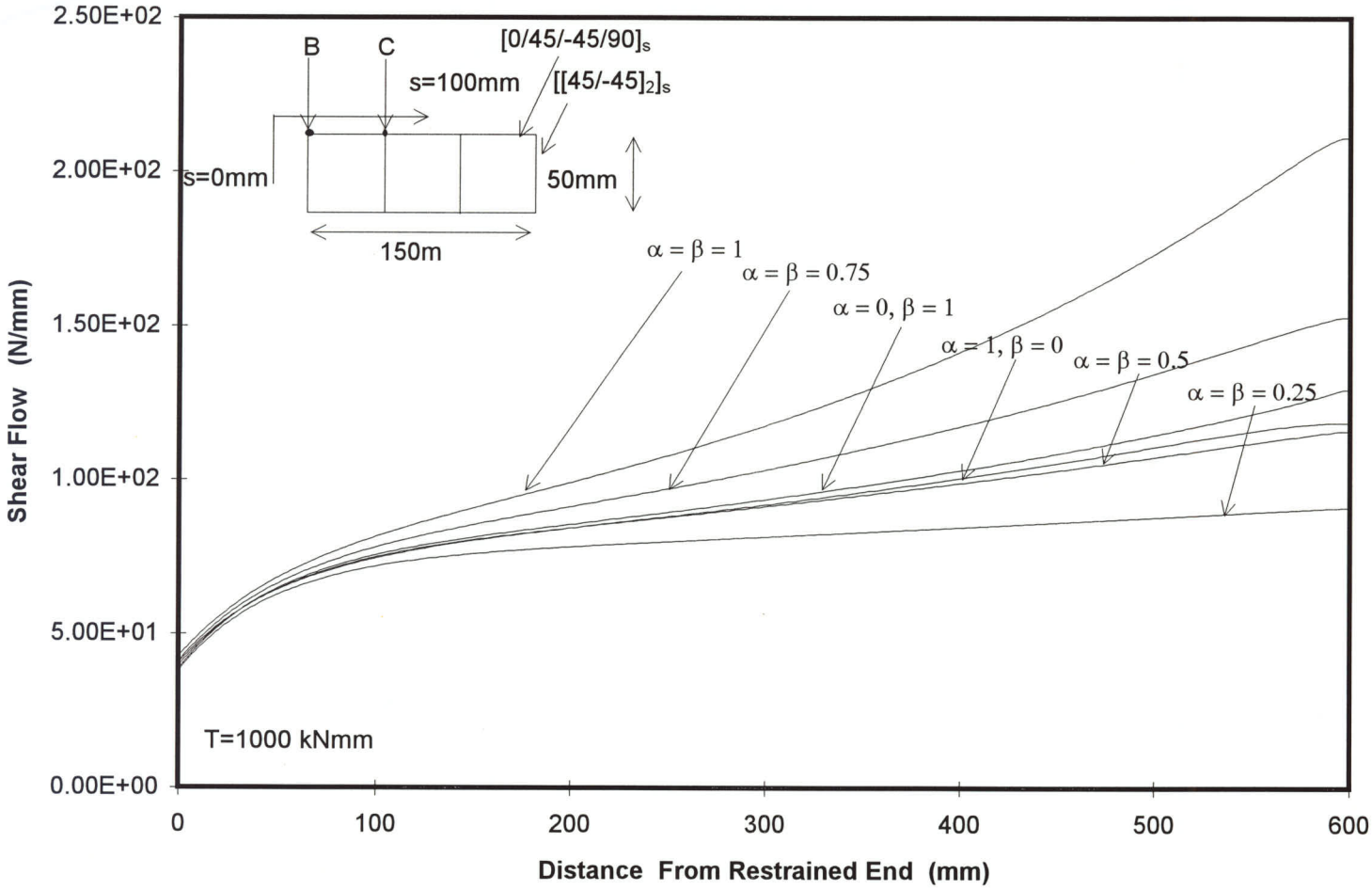

Figure 7.52 SHEAR FLOW ALONG LENGTH OF BOX AT S=100 mm

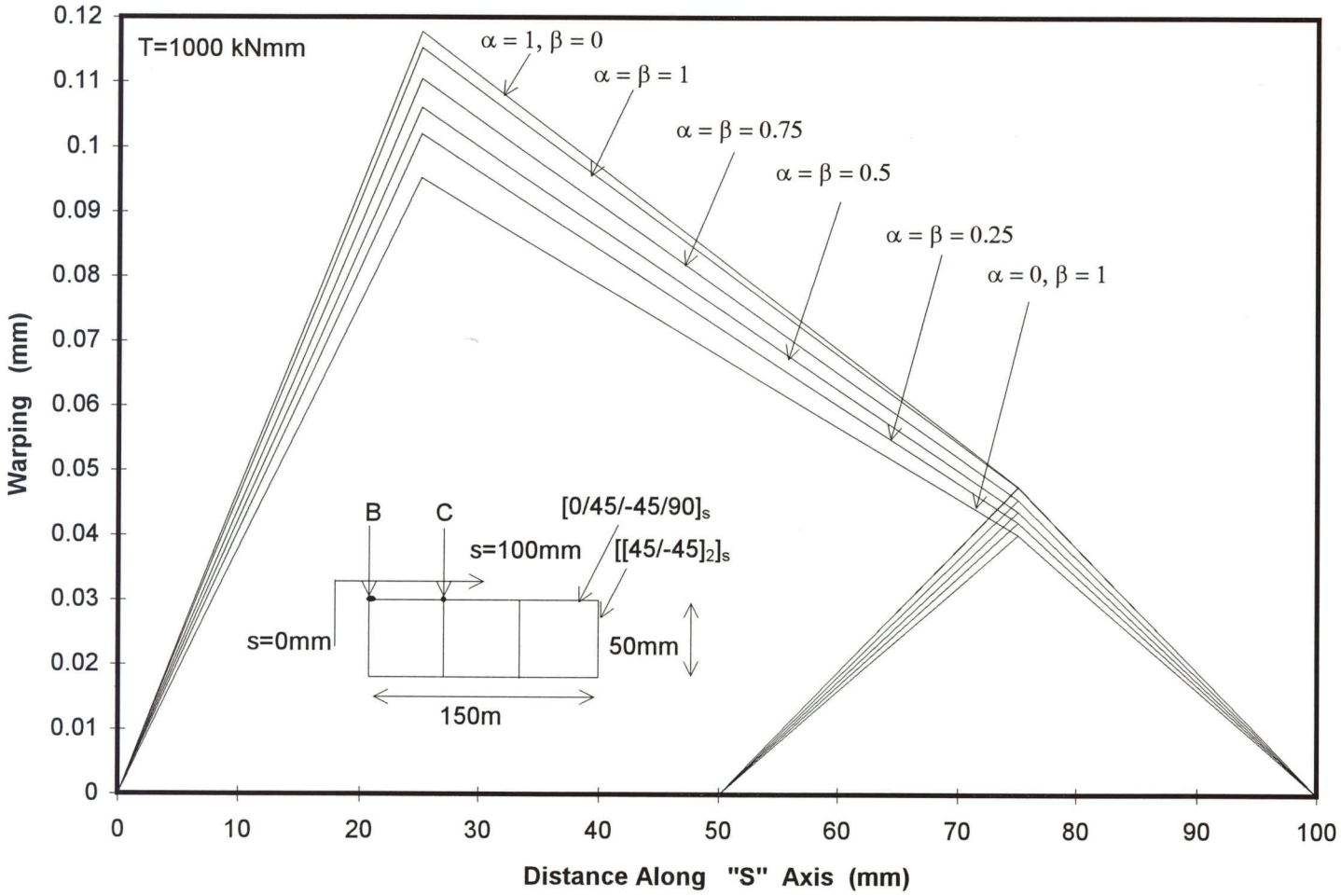

Figure 7.53 WARPING AROUND BOX AT Z=200mm

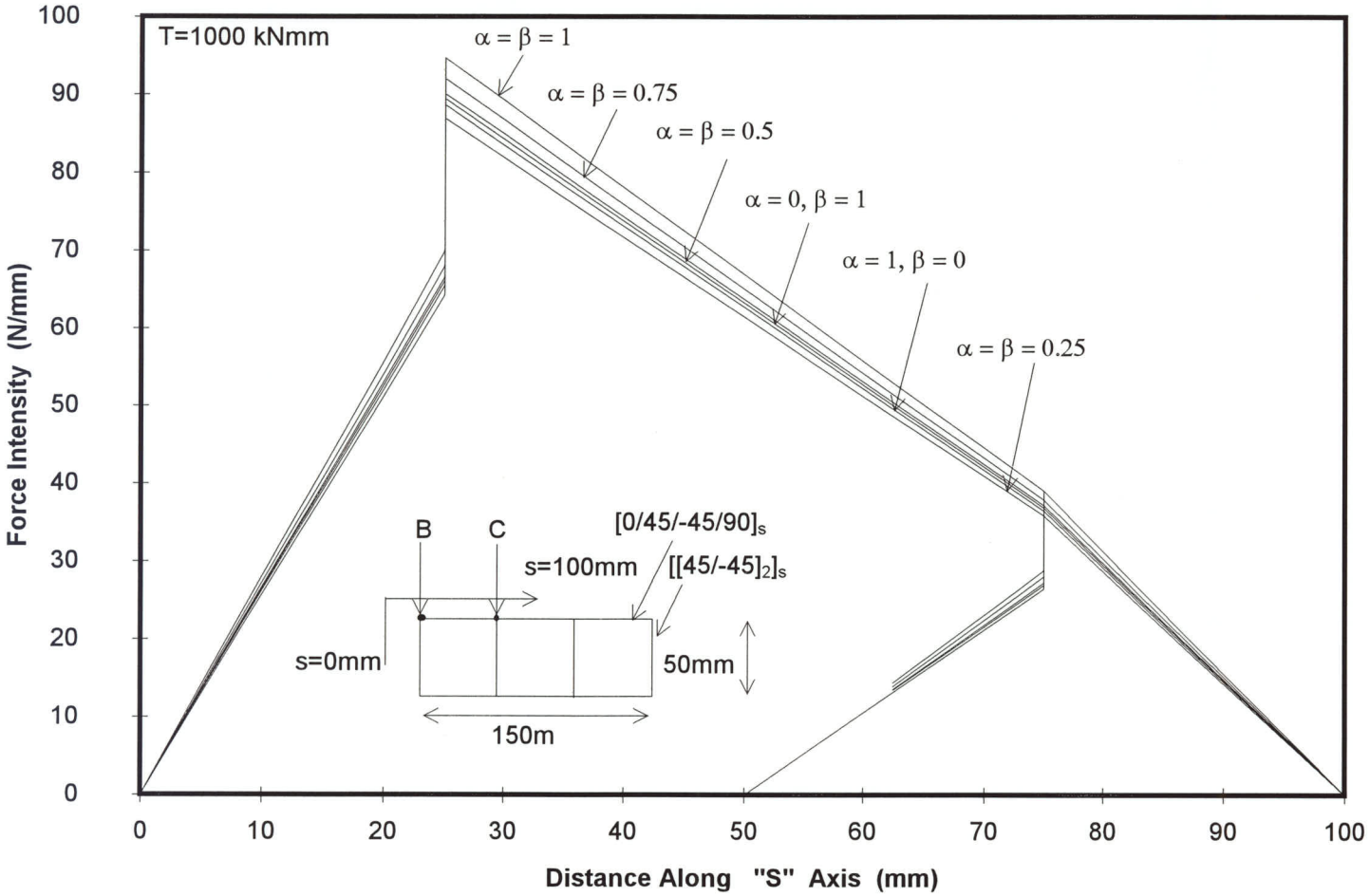

Figure 7.54 FORCE INTENSITY AROUND BOX AT Z=20mm

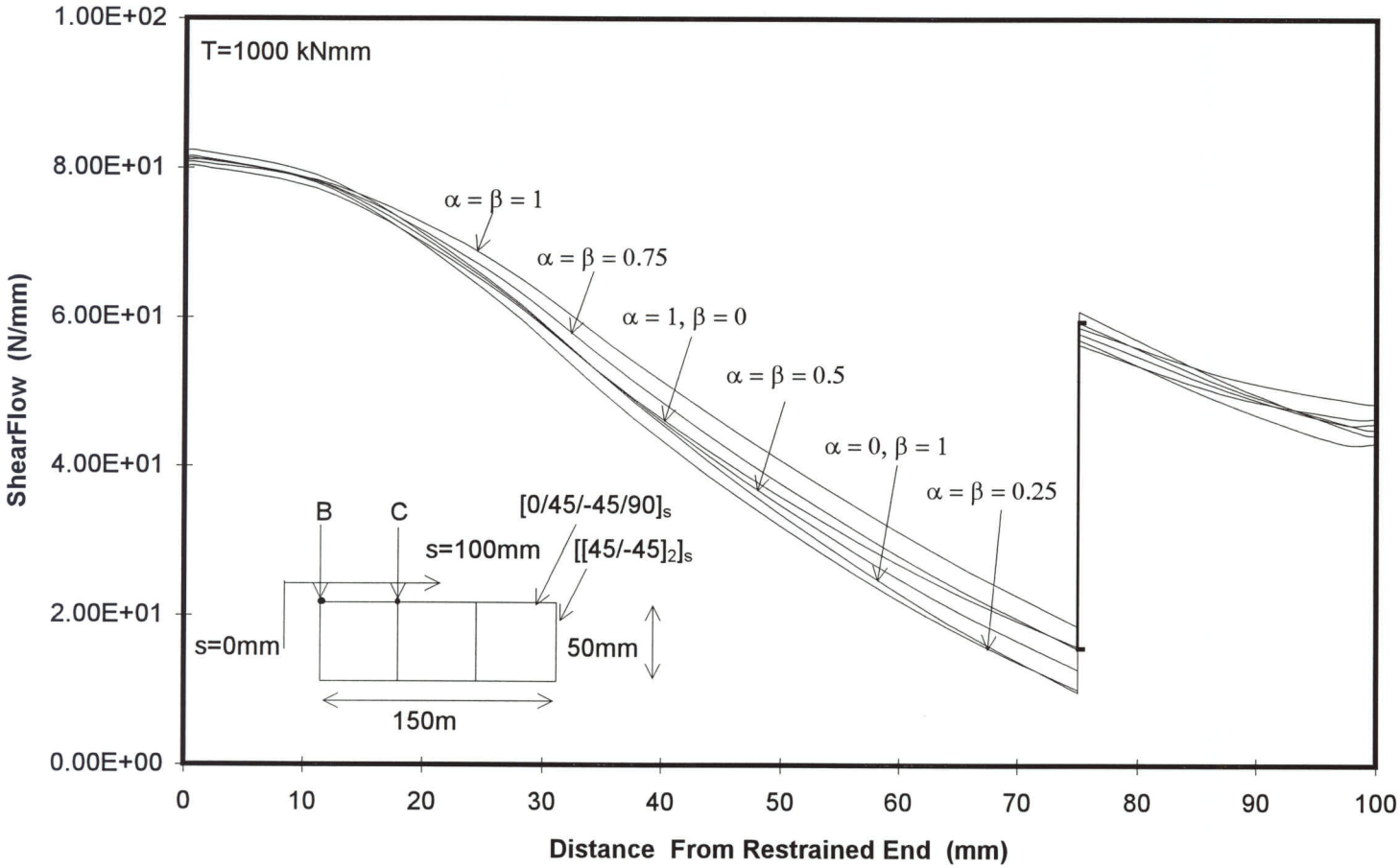

Figure 7.55 SHEAR FLOW AROUND THREE CELL BOX AT Z=20mm

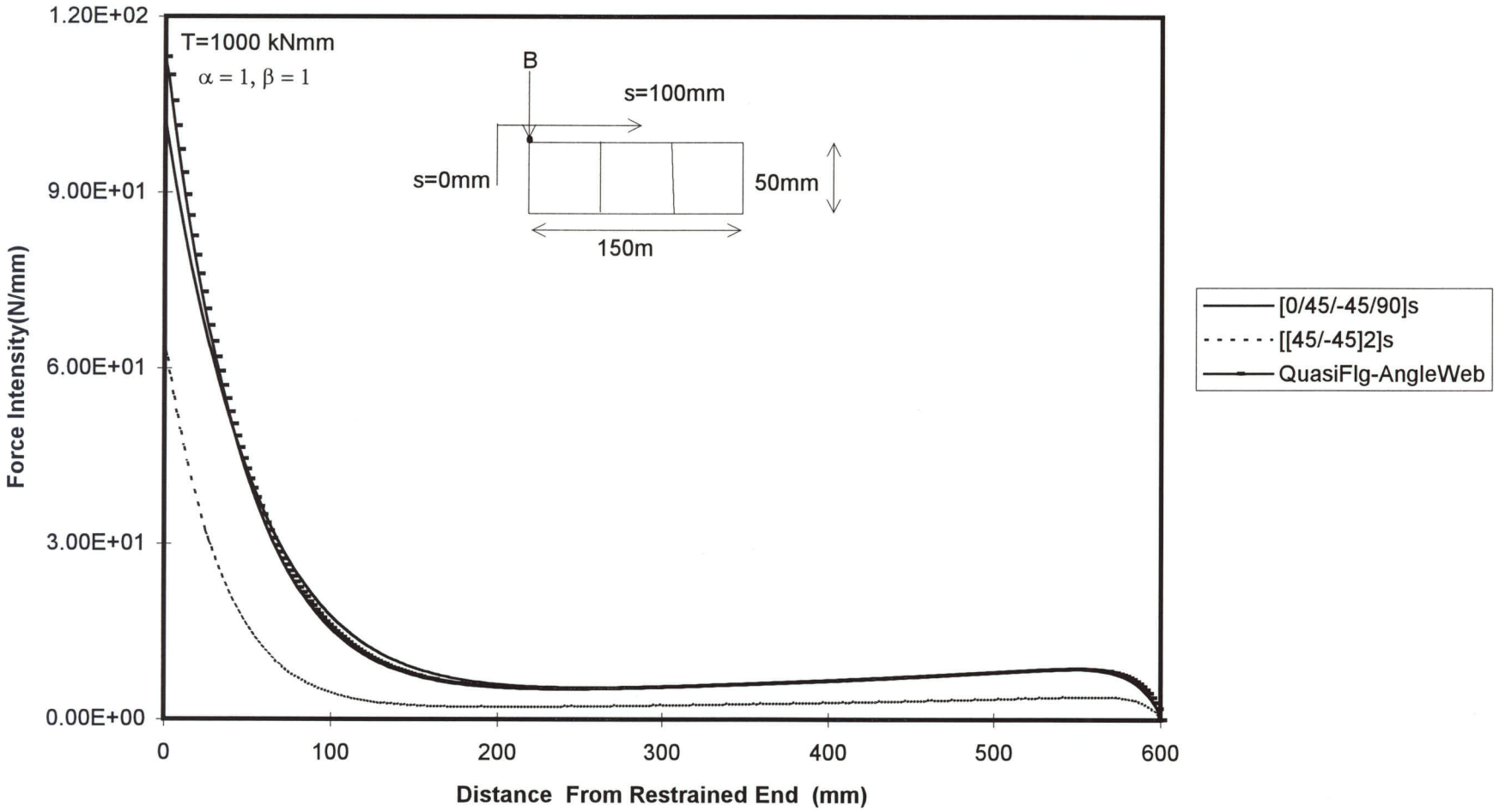

Figure 7.56 FORCE INTENSITY ALONG LENGTH OF BOX AT POINT "B"

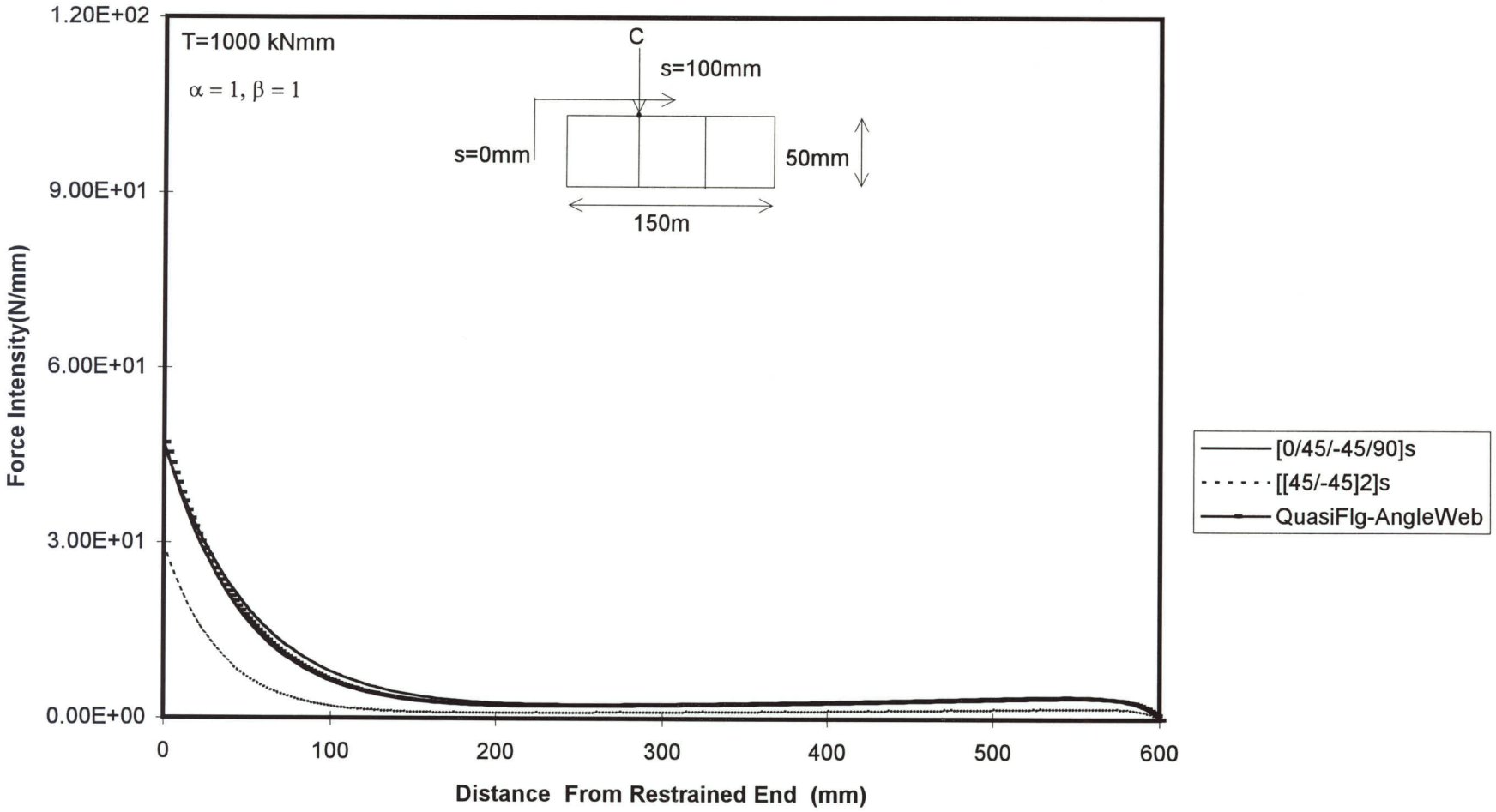

Figure 7.57 FORCE INTENSITY ALONG LENGTH OF BOX AT POINT "C"

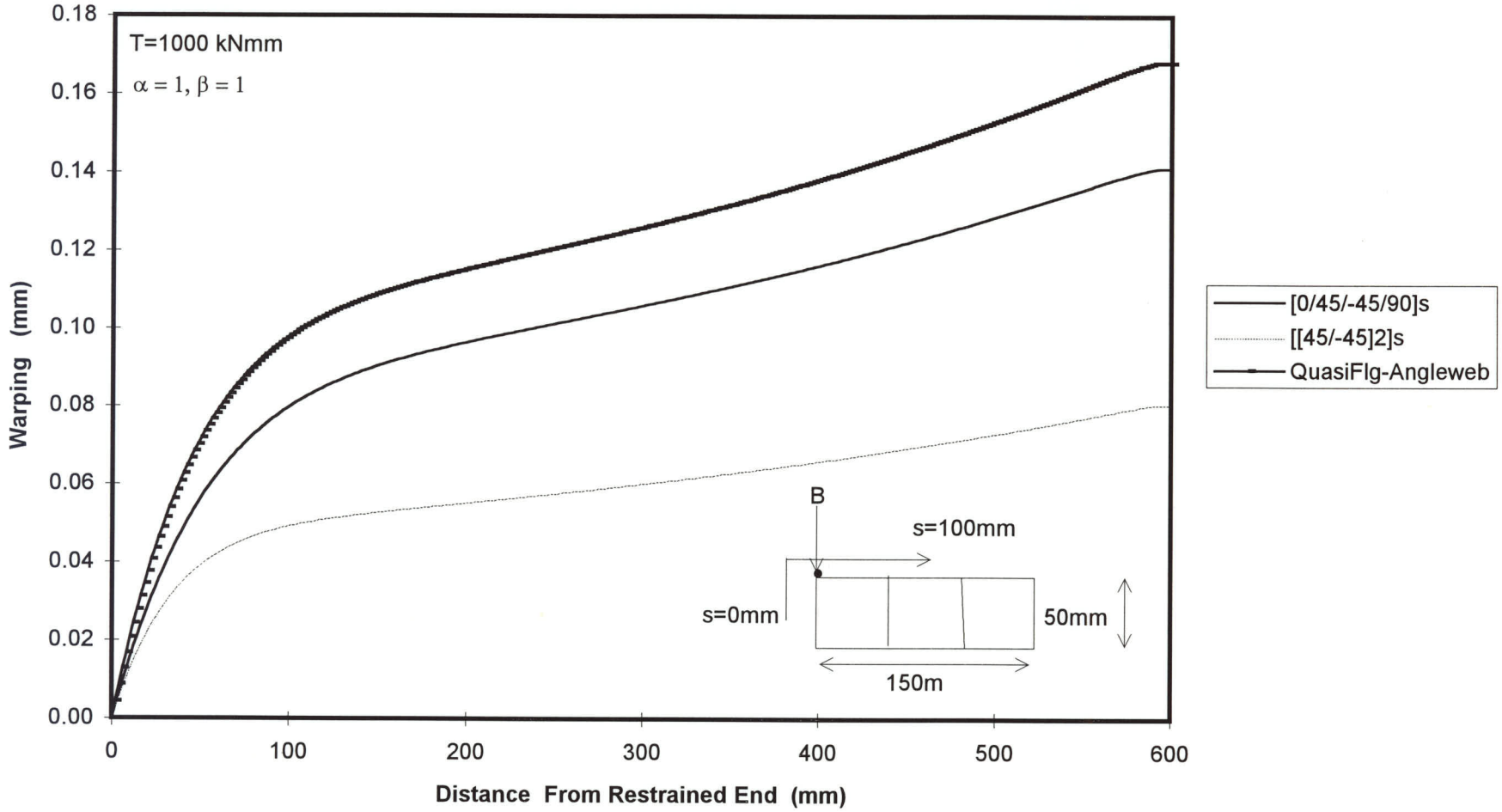

Figure 7.58 WARPING ALONG LENGTH OF BOX AT POINT "B"

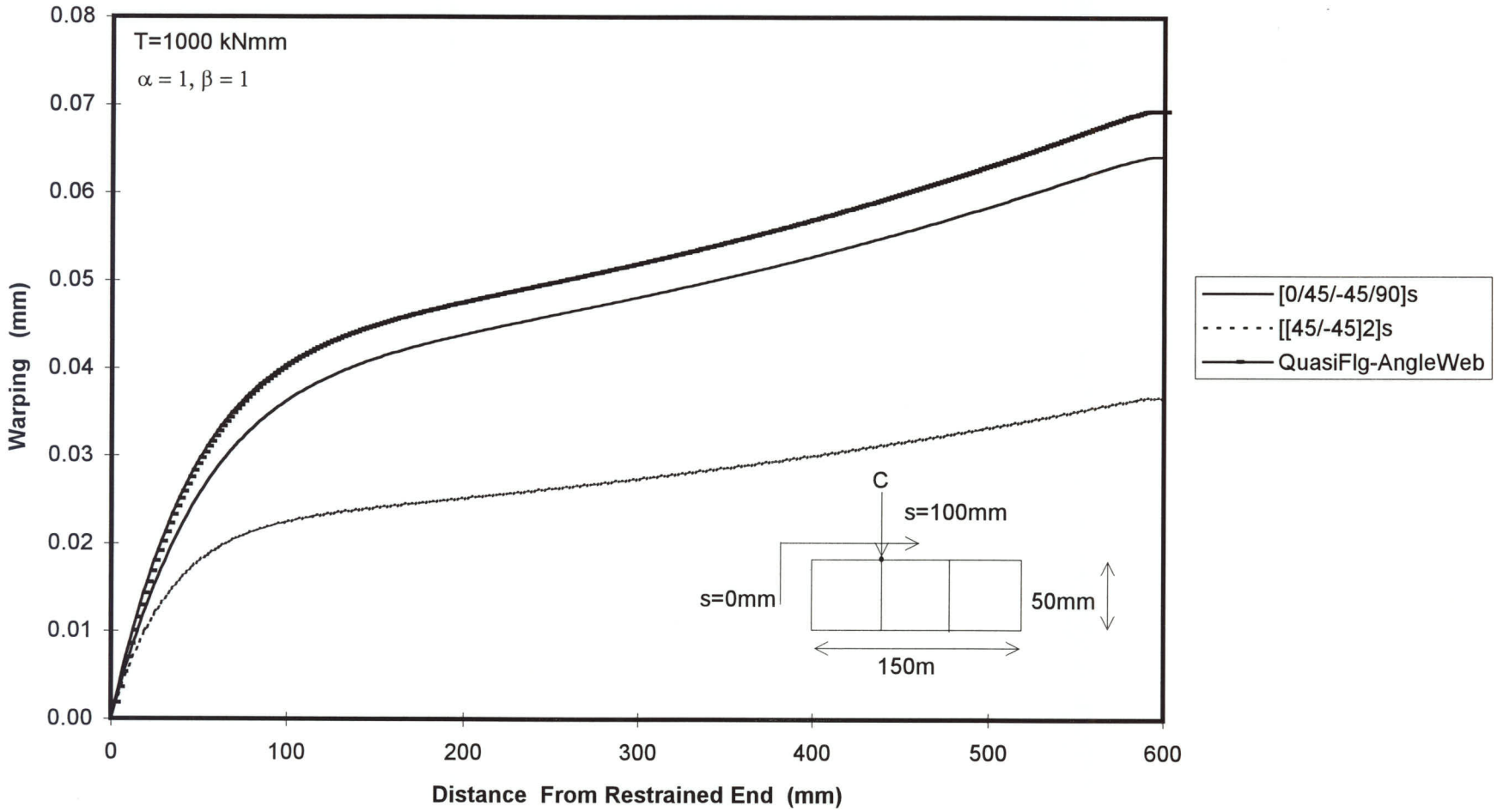

Figure 7.59 WARPING ALONG LENGTH OF BOX AT POINT "C"

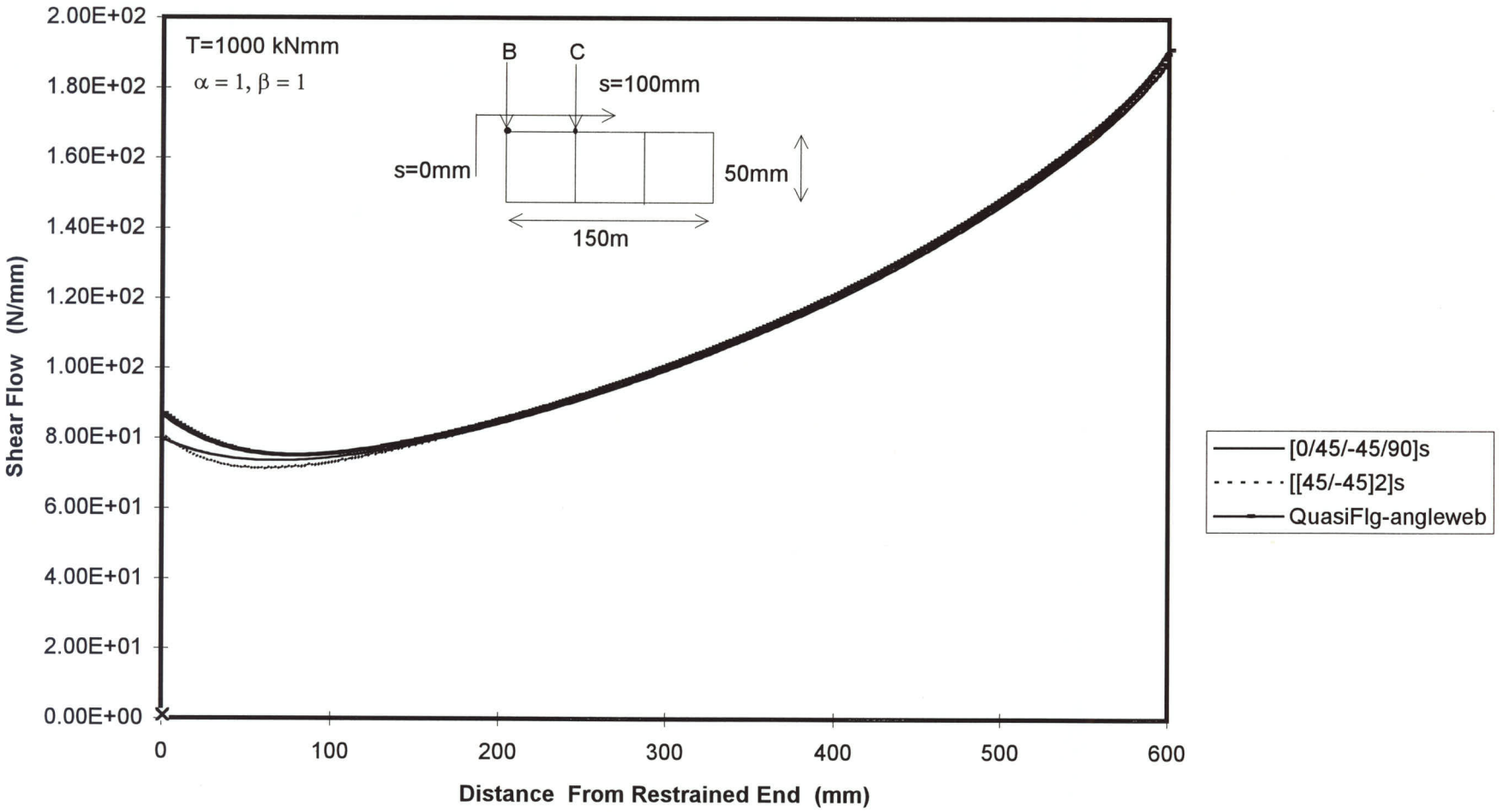

Figure 7.60 SHEAR FLOW ALONG LENGTH OF BOX AT S=0 mm

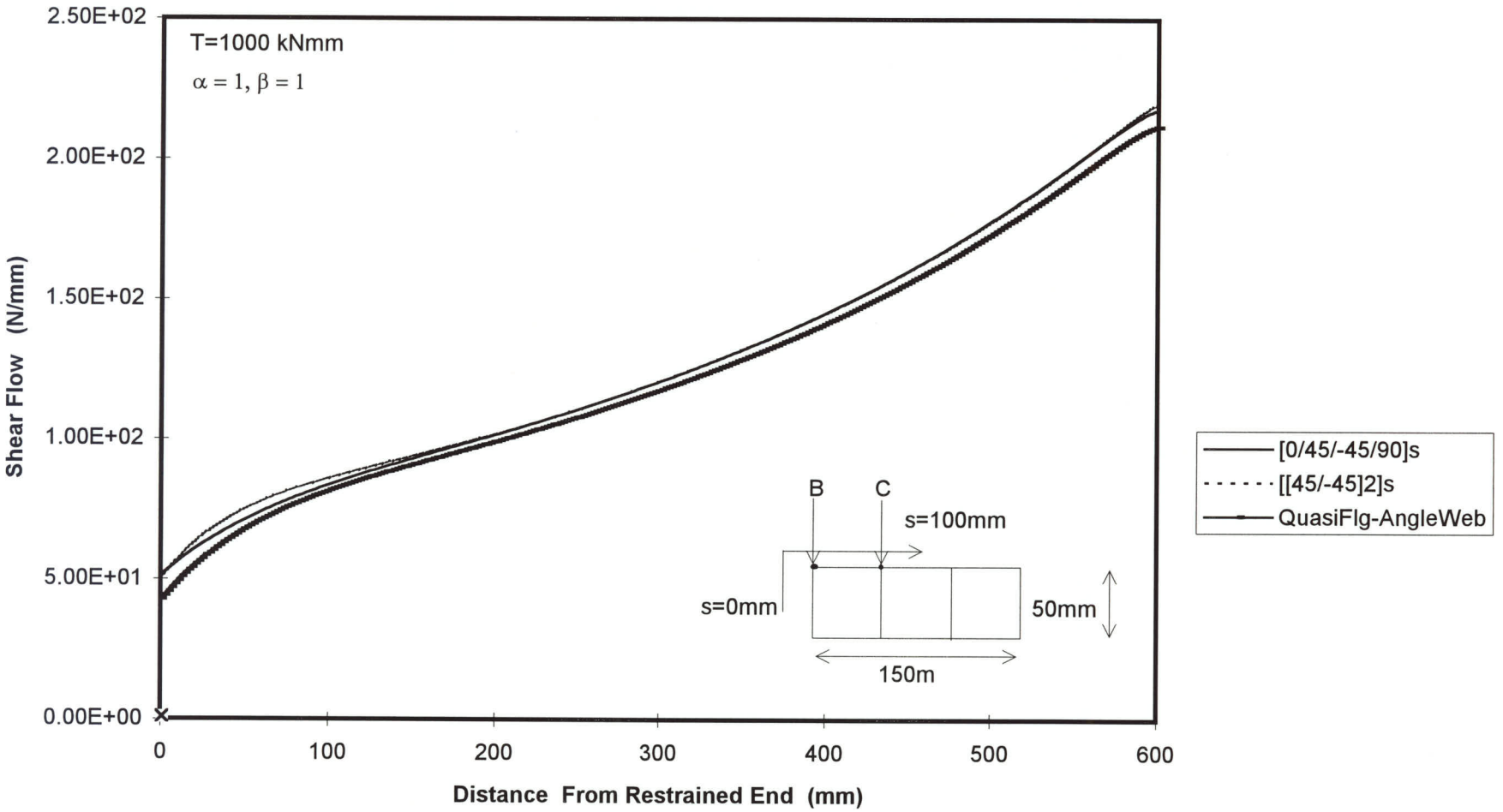

Figure 7.61 SHEAR FLOW ALONG LENGTH OF BOX AT S=100 mm

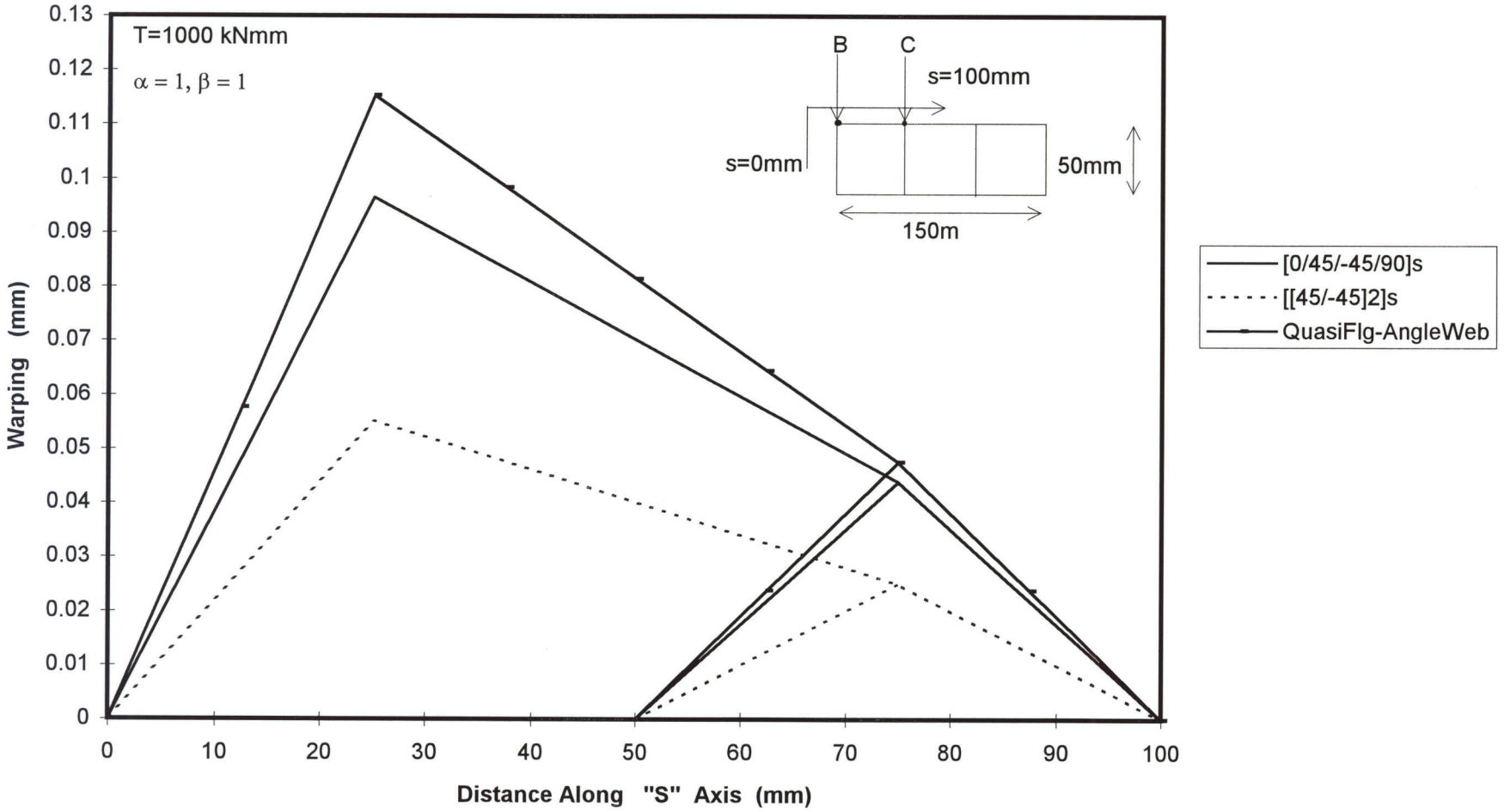

Figfure 7.62 WARPING AROUND BOX AT Z=200mm

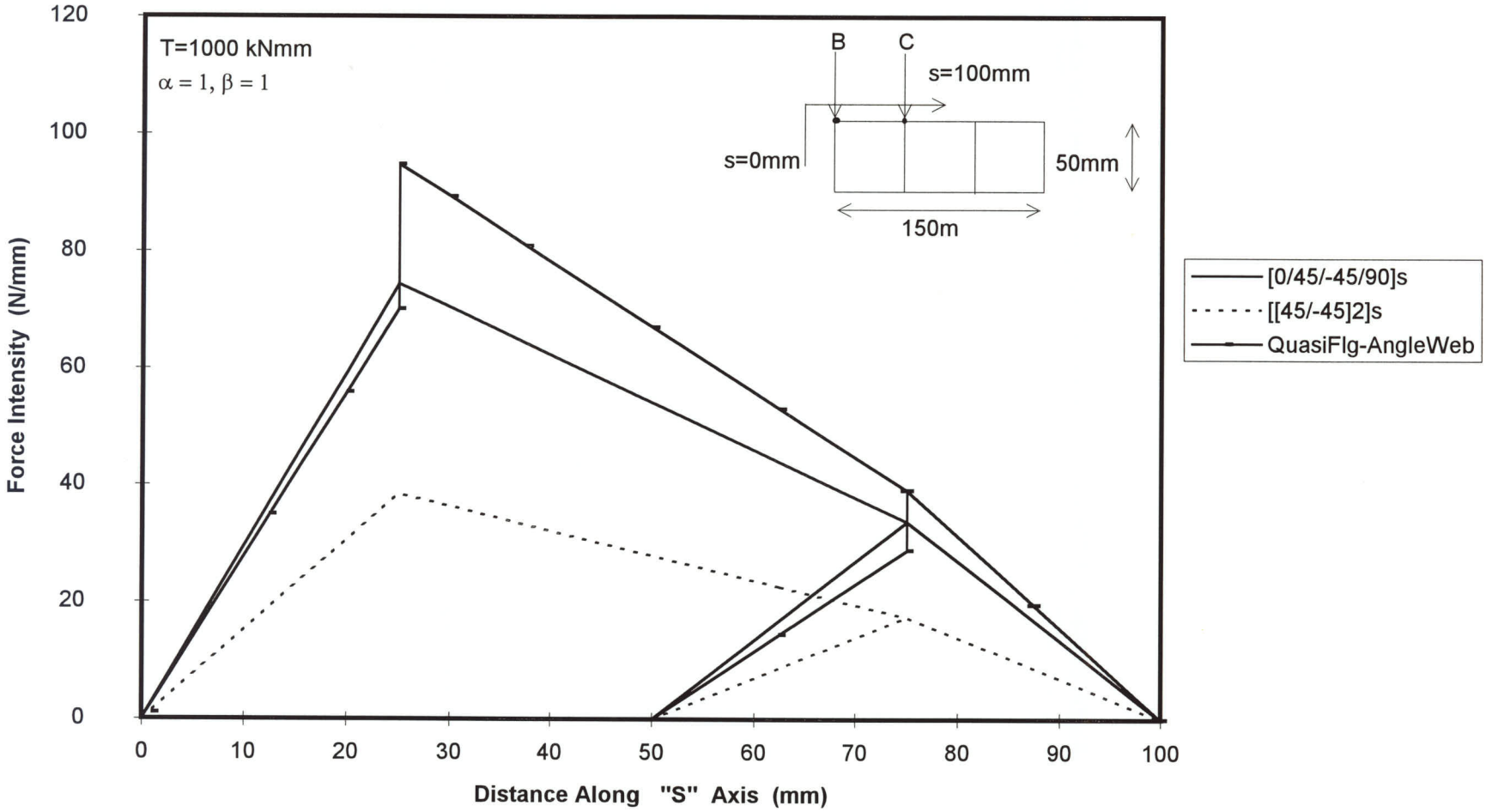

Figure 7.63 FORCE INTENSITY AROUND BOX AT Z=20mm

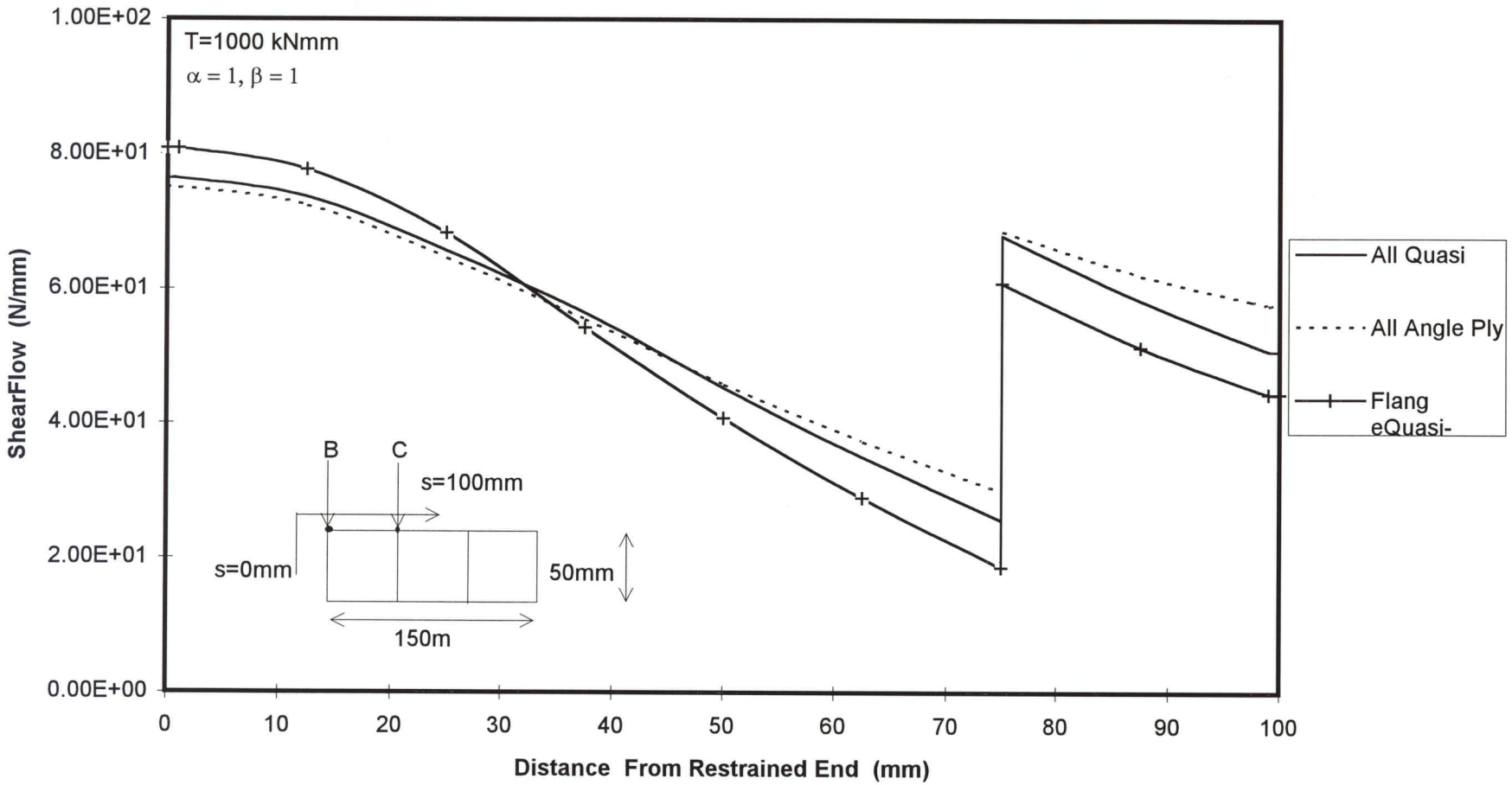

Figure 7.64 SHEAR FLOW AROUND THREE CELL TAPERED BOX AT Z=20mm

8 SUMMARY AND CONCLUSIONS

8.1 GENERAL SUMMARY

The behaviour of thin walled single-cell and multi-cell fibrous composite beams undergoing restrained torsion has been analysed. The analysis is common to the prismatic as well as tapered box beams of single-cell and multi-cell cross sections. Generally speaking classical theories for isotropic beams have been modified to cater for a composite behaviour by defining and using equivalent and effective elastic, geometric and sectorial properties.

8.1.1 MULTI-CELL BOX BEAM

Although the two approaches considered in this study i.e. Von Karman and Christnesen and Benscoter approaches , both have identical governing equations, however the sectorial moment of inertia is modified in case of Benscoter approach by using a Benscoter factor. This modification was necessary due to the fact that Von Karman and Christnesen approach is not accurate as it assumes the shear strains due to warping to be zero. This error was overcome by Benscoter, as he proposed that the sectorial moment of inertia be divided by the Benscoter factor λ to avoid the subject discrepancy.

It is proposed for single and multi-cell box beams that, both the elastic and shear moduli are effective in membrane mode. In case when the laminate configuration of the flanges and the webs are not same, then it is proposed that, the warping displacement distribution around the section is modified since the warping displacement depends upon the shear moduli of the walls. In order to represent this change in warping distribution, an effective thickness is proposed to calculate the sectorial properties of such section based on the relative magnitudes of the shear moduli of the walls.

Bredt Batho shear flow, which is constant along the length (at any particular location around the box section) for any single-cell / multi-cell prismatic box beam due to application of pure torsion is effectively independent of the shear and elastic moduli of the constituent materials. It has same value for any composite lay-up as it has for an isotropic cross-section of same dimensions. Bredt Batho effectively only depends upon the geometry of the cross section and does not get affected by the material constituents of the beam. In case of tapered box beams as the cross-sectional area of the beam decreases when moving away from the restrained end due to the effect of taper angles Alpha and Beta the Bredt Batho shear flow starts to increase accordingly. However for a prismatic box beam with taper angles Alpha and Beta set equal to zero, since the cross-sectional geometry remains constant from the restraint end to the free end, hence the Bredt Batho shear flow remains constant all along the length (at any particular location around the box section) for any single-cell / multi-cell prismatic box beam. It always exists whatever the type of torsion be, whether free torsion or restrained torsion. In restrained torsion the total shear flow is the summation of the Bredt Batho shear flow and the warping shear flows at any location of the cross-section of beam.

The inclusion of the Poisson's effect for the composite theory is important when amending the existing isotropic theory to the composite theory. This is so due to the fact that composites have a higher Poisson's ratio as compared to the isotropic materials. Hence ignoring the Poisson's effect in the isotropic materials although did cause an error, however it was not as grave an error as it is in case of the composite materials. An increase in the beam stiffness is estimated as a result of the Poisson's effect. This increase in stiffness is represented by using active elastic modulus, E^a, instead of the normal E. Moreover it is envisaged that, although an immediate effect of using E^a may not be observed in isotropic beams because of their low Poisson's ratio, a considerable change in behaviour may be expected in composite beams with $\pm 45^0$ fibre orientation, as such laminates have high Poisson's ratio.

Waldron approach is used in determining the sectorial shear function on which the warping related shear flow distribution around the section depends. According to Von Karman and Christnesen and Benscoter approaches, the sectorial shear function is determined via equating the summation of shear flow around the section to zero. On the other hand Waldron approach utilises the fact, that the summation of moments created by the shear forces around the shear centre is zero.

8.1.2 FINITE ELEMENT ANALYSIS

Finite element analysis has been performed on following types of box beams.

- Single-cell prismatic box beam
- Single-cell tapered box beam
- Multi-cell prismatic box beam
- Multi-cell tapered box beams.

The finite element analysis performed on the above box beams was independent of the proposed composite theory due to the reason that isotropic beams were modelled at the start of the analysis and the validity of the model was checked by isotropic theory. When the model was found giving proper results as per the existing isotropic theory than it was considered a correct model. This model was then further used for the composite model box beams, without making any modifications to the finite element model. Only the material properties needed to be changed for each new composite lay up when changing the isotropic finite element model to the composite finite element model.

Due to the nature of the restraint torsion a high stress gradient was expected for all the box beams near the restraint end, thus a refined mesh was used in the first 100 mm of the beam near the restraint end for all the four types of geometry mentioned above. The results from FE matched closely to the proposed composite theory.

8.1.3 COMPUTER PROGRAMME

Two computer programmes ***AHMED-SINGLE , & AHMED-MULTI*** were written in FORTRAN-90 to evaluate the sectorial properties of single-cell prismatic & tapered , isotropic & composite box beams and multi-cell prismatic & tapered , isotropic & composite box beams respectively. A direct method developed by Murray and Attard[52] was used by inclusion of equivalent properties and effective thickness used for the proposed composite theory. In subject computer programme sectorial co-ordinate , sectorial moment of inertia and sectorial shear functions are calculated by solving various numerical equations according to the required boundary conditions at the restraint and free end. The programme for single-cell called ***AHMED-SINGLE*** and the programme for multi-cell called ***AHMED-MULTI*** both differ from each other due to the differences in the geometrical configurations involved between them.

8.2 CONCLUSION

Following conclusions have been arrived at as a result of the comparison of the proposed composite analysis method for single-cell box beams and multi-cell box beams with the FE analysis.

- The elastic and shear moduli, E_m and G_m respectively are to be used during the torsional analysis of single-cell and multi-cell box beams.

- Bredt Batho shear flow remains constant from the root of the box beam at the restrained end to the free end (at any particular location around box beam) in case of single-cell and multi-cell prismatic box beam cross-sections. However Bredt Batho shear flow changes constantly along the length for single cell and multi-cell tapered box beams due to the continuous decrease in the cross-sectional area of the beam affected due to the taper angles Alpha and Beta.

- The total shear flow at any location along the length in single-cell and multi-cell box beam cross-sections undergoing torsional analysis is the summation of the Bredt Batho shear flow and the warping shear flows at that location.

- The active elastic modulus, E^a_m, should always be used instead of the normal elastic modulus, E_m.

- The Poisson's effect is shown to be quite dominant for the composite box beams undergoing restrained torsional analysis.

- Effective Active Elastic modulus E^{a}_{eff} should be used in the evaluation of the torsional analysis results, when the laminate configurations of the flanges and webs are different.

8.3 SUGGESTIONS FOR FUTURE RESEARCH

Following points are suggested for future related research in the field.

- In the present analysis of single-cell and multi-cell composite box beam cross-sections, it has been assumed that , the cross-section of the beam remains undistorted during the application of torsional load. This is practically achieved in most of the applications such as bridges and aircraft wing structures, by using stiffening diaphragms. However it may not be always practically possible to do so. In the absence of stiffening diaphragms , the cross-section of the beam distorts from its original shape and hence modification of the displacements and the stresses occurs. The proposed analysis method may be taken as a starting point to estimate the behaviour of such single cell and multi-cell box beams undergoing distortion during the application of torsional loads.

- The present analysis of single-cell and multi-cell prismatic and tapered composite box beam cross-sections has been verified by using finite element analysis. It is proposed that an experimental analysis be carried out by manufacturing such single-cell and multi-cell prismatic and tapered box beams and then testing them under application of restrained torsional load to compare the results achieved by the proposed theory to the experimental results.

APPENDIX A

EVALUATION OF SECTORIAL PROPERTIES AND THEORETICAL RESULTS FOR SINGLE-CELL & MULTI-CELL PRISMATIC AND TAPERED BOX BEAMS.

The usual way described by Marshal[51] of evaluating the warping properties of a given section involves first establishing an arbitrary set of axes, a parallel shift of the origin to the centroid, a rotation of the axes to the principal directions, the establishment of an arbitrary pole, adjusting the sectorial co-ordinate so that its average value is zero, and finally locating the shear centre. The method has been evolved in this way because of its suitability for hand computation, but, it is tedious and mathematical errors are easily introduced. Also slightly different methods are used depending upon whether the section is open or closed section. In present case since we are dealing with only single-cell and multi-cell closed box beams with prismatic and tapered geometry , therefore we will only take such structures into account. The distribution of warping restraint stresses around the cross-section of a thin-walled beam is defined by a system of sectorial co-ordinates w(s) and several additional geometrical terms, such as, sectorial moment of inertia (or torsion bending constant), Γ , and sectorial shear function, $S_w(s)$.

Two computer programmes ***AHMED-SINGLE , & AHMED-MULTI*** were written in FORTRAN-90 to evaluate the sectorial properties of single-cell prismatic & tapered , isotropic & composite box beams and multi-cell prismatic & tapered , isotropic & composite box beams respectively. A direct method developed by Murray and Attard[52] is used by inclusion of equivalent properties and effective thickness used for the proposed composite theory. In subject computer programme sectorial co-ordinate , sectorial moment of inertia and sectorial shear functions are calculated by solving various numerical equations according to the required boundary conditions at the restraint and

free end. The programme for single-cell called ***AHMED-SINGLE*** and the programme for multi-cell called ***AHMED-MULTI*** both differ from each other due to the differences in the geometrical configurations involved between them.

Figure 1 shows the single-cell box beam with flanges $[0/45/-45/90]_s$ and webs $[(45/45)_2]_s$ and figure 2 shows multi-cell box beam with flanges $[0/45/-45/90]_s$ and webs $[(45/-45)_2]_s$. Single cell box beam has dimensions of 100 mm x 50 mm at the root of the box which then reduce according to the taper angles Alpha and Beta along the length of the box beam and reach their minimum value at the free end. The three cell box beam has two internal webs, each at a distance of 50 mm from the two outer webs. The total dimensions of the flanges are 150 mm and that of webs are 50 mm. The dimensions reduce along the length of the box beam and achieve their minimum value at the free end. However in case of prismatic box beams when the taper angles Alpha and Beta are zero degrees, the dimensions remain same from the restraint end to the free end. Both these programmes are hence capable of providing results for the torsional analysis of prismatic and tapered box beams. The results for prismatic box beams are obtained by putting the values of Alpha and Beta equal to zero.

The theory for the formulation of the computer programme has already been discussed in chapter 3 and chapter 4 for isotropic and composite lay-ups respectively. Hence the repetition of the same here is considered a duplication and is thus being avoided. ***AHMED-SINGLE*** and ***AHMED-MULTI*** are user friendly programmes, and do not require any user manual. The input required is the geometrical dimensions and material properties of the box beam stating the ply lay-ups in flanges and webs. The taper angles Alpha and Beta can be put equal to zero when the analysis is required for a prismatic box beam. All the required sectorial co-ordinates, sectorial moment of inertia and sectorial shear function are calculated numerically according to the theoretical formulas mentioned in previous chapters.

The output file can be given any name as desired by the user, and it can give final outputs as listed below. All the intermediate values used in calculation of following final results can also be included in output file if required. These two programme outputs enable the design engineer to get required results at all the points of interest for the torsional analysis of single-cell and multi-cell prismatic and tapered box beams.

- Sectorial co-ordinate at any location along the beam length
- Sectorial co-ordinate at any location around the box beam
- Sectorial moment of inertia at any location along the beam length
- Sectorial shear function at any location along the beam length
- Sectorial shear function at any location around the box beam
- Warping displacement at any location along the beam length
- Warping displacement at any location around the box beam
- Force Intensity at any location along the beam length
- Force Intensity at any location around the box beam
- Shear Flow at any location along the beam length
- Shear Flow at any location around the box beam

The simple utilisation of these two programmes ***AHMED-SINGLE*** and ***AHMED-MULTI*** thus enables the design engineer to get all the required axial displacements, force Intensities/ stresses and shear flows at any location of interest on the beam surface.
This not only saves valuable time which might take up to many hours of hand calculations in getting different sectorial functions, but also avoids the chances of error which are always associated with the hand calculations .

The sample input files for single-cell box beam and multi-cell box beam are shown in table 1 and table 2 respectively. The sample output files for single-cell box beam and multi-cell box beam are shown in tables 3 and table 4 respectively.

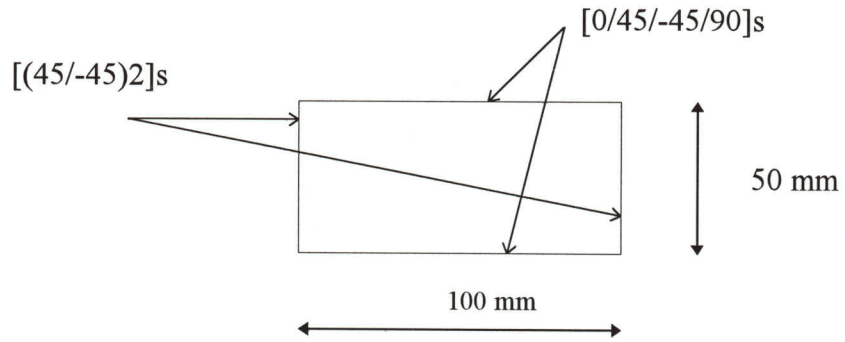

Fig 1 Single Cell Composite Box

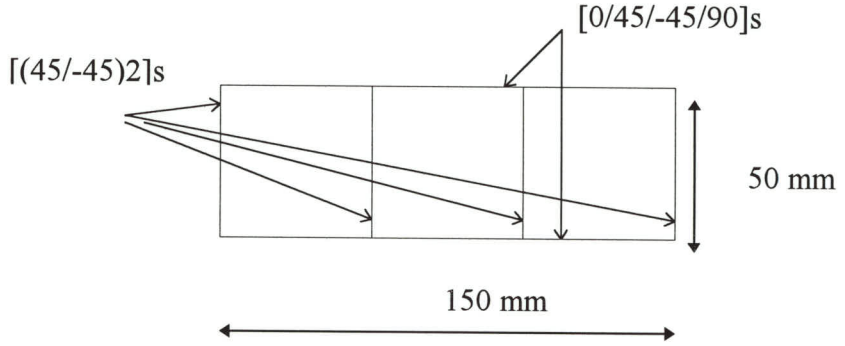

Fig 2 Multi Cell Composite Box

Table 1 Sample Data Input File for Single-cell box beam shown in Figure 1

```
      PROGRAMME AHMED-SINGLE FOR TORSIONAL ANALYSIS OF
      SINGLE-CELL  PRISMATIC AND TAPERED THIN WALLED BOX
      BEAMS    FLANGES  [0/45/-45/90]s        WEBS   [(45/-45)2]s

      ALPHA=1.0D0
      BETA =1.0D0

      F=100-(2*Z*(TAN(BETA*Pi/180.0D0)))
      W=50-(2*Z*(TAN(ALPHA*Pi/180.0D0)))

      AREA=F*W
      PR1=(F/2.0D0)
      PR2=(W/2.0D0)

      NF=2
      NW=2

      L=600.0D0
      TF=1.0D0
      TW=1.0D0
      TORQ=1.0D06

      GF=20616.0D0
      EFLANG=54067.0D0
      NUFLAN=0.3110D0


      GW=36233.0D0
      EWEB=17740.0D0
      NUWEB=0.774D0


      GEFF=(((F/TF)*NF)+((W/TW)*NW))/(((F/(GF*TF))*NF)+
     &  ((W/(GW*TW))*NW))


      TFEFF=(GF*TF)/GEFF

      TWEFF=(GW*TW)/GEFF
```

Table 2 Sample Data Input for Multi-cell section shown in Figure 2

```
      PROGRAMME AHMED-MULTI FOR TORSIONAL ANALYSIS OF
      THREE-CELL  PRISMATIC AND TAPERED THIN WALLED BOX
      BEAMS    FLANGES  [0/45/-45/90]s        WEBS   [(45/-45)2]s


       ALPHA=1.00D0
       BETA =1.00D0

      F=50-(2*Z*(TAN(BETA*Pi/180.0D0)))

      W=50-(2*Z*(TAN(ALPHA*Pi/180.0D0)))

      AREA=(F*W)*3

      PR1=((3*F)/2.0D0)
      PR2=(W/2.0D0)
      PR3=(F/2.0D0)
      PR4=(W/2.0D0)

      NF=6
      NW=4
      L=600.0D0
      TF=1.0D0
      TW=1.0D0
      TORQ=1.0D06

      GF=20616.0D0
      EFLANG=54067.0D0
      NUFLAN=0.3110D0

     GW=36233.0D0
     EWEB=17740.0D0
     NUWEB=0.774D0


      GEFF=(((F/TF)*NF)+((W/TW)*NW))/(((F/(GF*TF))*NF)+
     &  ((W/(GW*TW))*NW))

      TFEFF=(GF*TF)/GEFF

      TWEFF=(GW*TW)/GEFF
```

Table 3 Sample Data Output File for Single-cell box beam

```
Z=,Z=,  600.000000000000   ,  600.000000000000
 S=,WARPO=,  0.000000000000000E+000, -2.934185960349221E-016
 S=,WARPOO=,  12.5000000000000   ,  8.392358420345271E-002
 S=,WARPB=,  25.0000000000000   ,  0.167847168406905
 S=,WARPBB=,  37.5000000000000   ,  0.125885376305179
 S=,WPBBB=,  50.0000000000000   ,  8.392358420345269E-002
 S=,WPBBBB=,  62.5000000000000   ,  4.196179210172638E-002
 S=,WARP00=,  75.0000000000000   ,  0.000000000000000E+000


  Z=,WARPB=,  0.000000000000000E+000, -9.707328210246397E-005
 Z=,WARPB=,  2.00000000000000   ,  5.074934743157303E-003
 Z=,WARPB=,  4.00000000000000   ,  9.962482745162295E-003
 Z=,WARPB=,  6.00000000000000   ,  1.458162340555064E-002
 Z=,WARPB=,  8.00000000000000   ,  1.894751544603184E-002
 Z=,WARPB=,  10.0000000000000   ,  2.307447284759885E-002


  Z=,STRESSB=,  0.000000000000000E+000,  135.43088221071
 Z=,STRESSB=,  2.00000000000000   ,  128.043946286661
 Z=,STRESSB=,  4.00000000000000   ,  121.020876800905
 Z=,STRESSB=,  6.00000000000000   ,  114.393532874580
 Z=,STRESSB=,  8.00000000000000   ,  108.139913650794
 Z=,STRESSB=,  10.0000000000000   ,  102.239227585422


  Z=,TOT0=,  0.000000000000000E+000,  162.7492399933
 Z=,TOT0=,  2.00000000000000   ,  159.304747186596
 Z=,TOT0=,  4.00000000000000   ,  156.065096024041
 Z=,TOT0=,  6.00000000000000   ,  153.016082722078
 Z=,TOT0=,  8.00000000000000   ,  150.147118947895
 Z=,TOT0=,  10.0000000000000   ,  147.448199031312
 Z=,TOT00=,  0.000000000000000E+000,  20.6331940944
 Z=,TOT00=,  2.00000000000000   ,  -24.094550124935
 Z=,TOT00=,  4.00000000000000   ,  28.2856961971020
 Z=,TOT00=,  6.00000000000000   ,  32.4958352583983
 Z=,TOT00=,  8.00000000000000   ,  36.4791058537304
 Z=,TOT00=,  10.0000000000000   ,  40.2480570035097
```

Table 3 Sample Data Output File for Single-cell box beam(Continued)

```
Z=,Z=,  20.0000000000000   ,  20.0000000000000
 S=,AXWEBO=,  0.000000000000000E+000, -1.775759053730743E-013
 S=,AXWEBOO=,  12.5000000000000   ,  33.8033375746357
 S=,AXWEBX=,  20.0000000000000   ,  53.8938535665568
 S=,AXWB=,  25.0000000000000   ,  67.6066751492713
 S=,AXFLGB=,  25.0000000000000   ,  91.4551942198166
 S=,AXFLGXX=,  30.0000000000000   ,  82.3096747978350
 S=,AXFLGBB=,  37.5000000000000   ,  68.5913956648625
 S=,AXFGBBB=,  50.0000000000000   ,  45.7275971099083
 S=,AXFBBBB=,  62.5000000000000   ,  22.8637985549541
 S=,AXFLG00=,  75.0000000000000   ,  0.000000000000000E+000


 SHEAR0=,S=,  0.000000000000000E+000,  -34.7748126611954
 SHEARM=,S=,  1.00000000000000   ,  -34.7335970105128
 SHEARN=,S=,  3.00000000000000   ,  -34.4038718050519
 SHEAROO=,S=,  12.5000000000000   ,  -28.5191895631058
 SHEARB=,S=,  25.0000000000000   ,  -9.38678101233334
 SHEARBB=,S=,  37.5000000000000   ,  13.3554083797523
 SHEARBBB=,S=,  50.0000000000000   ,  30.1857085966076
 SHEARCC=,S=,  62.5000000000000   ,  40.7817933883605
 SHEARNN=,S=,  72.0000000000000   ,  44.6662989149047
 SHEARMM=,S=,  74.0000000000000   ,  45.0253673665383
 SHEAR00=,S=,  75.0000000000000   ,  45.1448588744734


 TOT0=,S=,  0.000000000000000E+000,  136.190993477938
 TOTM=,S=,  1.00000000000000   ,  136.149777827255
 TOTN=,S=,  3.00000000000000   ,  135.820052621794
 TOTOO=,S=,  12.5000000000000   ,  129.935370379848
 TOTB=,S=,  25.0000000000000   ,  110.802961829076
 TOTBB=,S=,  37.5000000000000   ,  88.0607724369902
 TOTBBB=,S=,  50.0000000000000   ,  71.2304722201348
 TOTCC=,S=,  62.5000000000000   ,  60.6343874283820
 TOTNN=,S=,  72.0000000000000   ,  56.7498819018377
 TOTMM=,S=,  74.0000000000000   ,  56.3908134502042
 TOT00=,S=,  75.0000000000000   ,  56.2713219422691
```

Table 4 Sample Data Output File for Multi-cell box beam

```
Z=,Z=,  600.000000000000   ,  600.000000000000
 S=,WARPO=,  0.000000000000000E+000, -7.779340805504458E-017
 S=,WARPOO=,  12.5000000000000   ,  4.200367517541479E-002
 S=,WARPB=,  25.0000000000000   ,  8.400735035082958E-002
 S=,WARPBB=,  37.5000000000000   ,  7.255180257571645E-002
 S=,WPBBB=,  50.0000000000000   ,  6.109625480060332E-002
 S=,WPBBBB=,  62.5000000000000   ,  4.963211321620652E-002
 S=,WARPC=,  75.0000000000000   ,  3.818515925037706E-002
 S=,WPCCCC=,  87.5000000000000   ,  1.909257962518858E-002
 S=,WARP00=,  100.000000000000   ,  0.000000000000000E+000
 S=,WPCCC=,  50.0000000000000   , -3.889670402752229E-017
 S=,WARPCC=,  62.5000000000000   ,  1.909257962518851E-002
 S=,WARPC=,  75.0000000000000   ,  3.818515925037706E-002

Z=,WARPB=,  0.000000000000000E+000,  0.000000000000000E+000
 Z=,WARPB=,  2.00000000000000   ,  3.202224944908923E-003
 Z=,WARPB=,  4.00000000000000   ,  6.281452680510474E-003
 Z=,WARPB=,  6.00000000000000   ,  9.242407521214725E-003
 Z=,WARPB=,  8.00000000000000   ,  1.208963232088715E-002
 Z=,WARPB=,  10.0000000000000   ,  1.482749544273592E-002

Z=,WARPC=,  0.000000000000000E+000,  0.000000000000000E+000
 Z=,WARPC=,  2.00000000000000   ,  1.455556793140419E-003
 Z=,WARPC=,  4.00000000000000   ,  2.855205763868395E-003
 Z=,WARPC=,  6.00000000000000   ,  4.201094327824872E-003
 Z=,WARPC=,  8.00000000000000   ,  5.495287418585062E-003
 Z=,WARPC=,  10.0000000000000   ,  6.739770655789050E-003

Z=,STRESSB=,  0.000000000000000E+000,  96.10409538901
 Z=,STRESSB=,  2.00000000000000   ,  93.9722080927663
 Z=,STRESSB=,  4.00000000000000   ,  90.3627429591305
 Z=,STRESSB=,  6.00000000000000   ,  86.8919171355262
 Z=,STRESSB=,  8.00000000000000   ,  83.5544054969994
 Z=,STRESSB=,  10.0000000000000   ,  80.3450874562856

Z=,STRESSC=,  0.000000000000000E+000,  43.13822517682
 Z=,STRESSC=,  2.00000000000000   ,  42.7146400421665
 Z=,STRESSC=,  4.00000000000000   ,  41.0739740723320
 Z=,STRESSC=,  6.00000000000000   ,  39.4963259706937
 Z=,STRESSC=,  8.00000000000000   ,  37.9792752259088
 Z=,STRESSC=,  10.0000000000000   ,  36.5204942983116
```

```
Z=,Z=,  20.0000000000000    ,  20.0000000000000
 S=,AXWEBO=,  0.000000000000000E+000, -6.116946955879903E-014
 S=,AXWEBOO=,  12.5000000000000    ,  33.0277666737806
 S=,AXWEBX=,  20.0000000000000    ,  52.8444266780490
 S=,AXWB=,  25.0000000000000    ,  66.0555333475612
 S=,AXFLGB=,  25.0000000000000    ,  66.0555333475612
 S=,AXFLGXX=,  30.0000000000000    ,  62.4525042558761
 S=,AXFLGBB=,  37.5000000000000    ,  57.0479606183483
 S=,AXFGBBB=,  50.0000000000000    ,  48.0403878891354
 S=,AXFBBBB=,  62.5000000000000    ,  39.0260577910334
 S=,AXFLGC=,  75.0000000000000    ,  30.0252424307096
 S=,AXWEBC=,  75.0000000000000    ,  30.0252424307096
 S=,AXFCCCC=,  87.5000000000000    ,  15.0126212153549
 S=,AXFLG00=,  100.000000000000    ,  0.000000000000000E+000
 S=,AXWEBCCC=,  50.0000000000000    , -3.058473477939952E-014
 S=,AXWEBCC=,  62.5000000000000    ,  15.0126212153548
 S=,AXWEBC=,  75.0000000000000    ,  30.0252424307096

 SHEAR0=,S=,  0.000000000000000E+000,  -14.6692677987016
 SHEARN=,S=,  1.00000000000000    ,  -14.6433958092585
 SHEAROO=,S=,  12.5000000000000    ,  -10.6267694482096
 SHEARB=,S=,  25.0000000000000    ,  1.50072560326637
 SHEARBB=,S=,  37.5000000000000    ,  16.5682194551002
 SHEARBBB=,S=,  50.0000000000000    ,  29.4307142066656
 SHEARBBBB=,S=,  62.5000000000000    ,  40.0882098579627
 SHEARC11=,S=,  75.0000000000000    ,  48.5407064089914
 SHEARC=,S=,  75.0000000000000    ,  35.8610345640766
 SHEARC22=,S=,  75.0000000000000    ,  12.6796718449148
 SHEARII=,S=,  87.5000000000000    ,  18.1921695955857
 SHEARNN=,S=,  99.0000000000000    ,  20.0179088506078
 SHEAR00=,S=,  100.000000000000    ,  20.0296688458093
 SHEARCCC=,S=,  50.0000000000000    ,  50.5610285658656
 SHEARC=,S=,  75.0000000000000    ,  35.8610345640766

 TOT0=,S=,  0.000000000000000E+000,  77.1692677987016
 TOTN=,S=,  1.00000000000000    ,  77.1433958092585
 TOTOO=,S=,  12.5000000000000    ,  73.1267694482096
 TOTB=,S=,  25.0000000000000    ,  60.9992743967336
 TOTBB=,S=,  37.5000000000000    ,  45.9317805448998
 TOTBBB=,S=,  50.0000000000000    ,  33.0692857933344
 TOTBBBB=,S=,  62.5000000000000    ,  22.4117901420373
 TOTC11=,S=,  75.0000000000000    ,  13.9592935910086
 TOTC22=,S=,  75.0000000000000    ,  62.3203281550852
 TOTII=,S=,  87.5000000000000    ,  56.8078304044143
 TOTNN=,S=,  99.0000000000000    ,  54.9820911493922
 TOT00=,S=,  100.000000000000    ,  54.9703311541907
 TOTCCC=,S=,  50.0000000000000    ,  63.0610285658656
 TOTC=,S=,  75.0000000000000    ,  48.3610345640766

Z=,TOT0=,  0.000000000000000E+000,  84.4954548935
 Z=,TOT0=,  2.00000000000000    ,  83.3688598920317
 Z=,TOT0=,  4.00000000000000    ,  82.5672884087078
 Z=,TOT0=,  6.00000000000000    ,  81.7965052229512
 Z=,TOT0=,  8.00000000000000    ,  81.0553277583412
 Z=,TOT0=,  10.0000000000000    ,  80.3426188611248
Z=,TOT00=,  0.000000000000000E+000,  45.4941829917
 Z=,TOT00=,  2.00000000000000    ,  -46.474553745388
 Z=,TOT00=,  4.00000000000000    ,  47.5997815995056
 Z=,TOT00=,  6.00000000000000    ,  48.6522221285406
 Z=,TOT00=,  8.00000000000000    ,  49.6642385001710
 Z=,TOT00=,  10.0000000000000    ,  50.6373834035566
```

APPENDIX B

EVALUATION OF ANALYTICAL RESULTS FOR SINGLE-CELL & MULTI-CELL PRISMATIC AND TAPERED BOX BEAMS.

Following functions are required to be evaluated analytically in order to solve equations 3.31 and 3.32 as discussed in chapter 3 .

$$\theta_0 = \frac{T}{GI_C}$$

$$f_1 = \frac{d}{dz}(\theta_0)$$

$$f_2 = \frac{d}{dz}(f_1)$$

$$f_5 = (E\Gamma)_{BENSCOTER}$$

$$f_6 = \frac{d}{dz}(f_5)$$

The analytical procedure for evaluating above mentioned functions is outlined below

$$\theta_0 = \frac{T}{GI_C}$$

$$I_c = 2 *[((\frac{3b'}{2})**2) * t_w * d'] + 2 *[((\frac{b'}{2})**2) * t_w * d']$$
$$+ 2 *[((\frac{d'}{2})**2) * t_f * 3 * b']$$

Here b and d are the lengths for flange and web at the root of the restrained box beam and b' and d' are the lengths at any location z from the restrained end, as defined in chapter 3.

$b' = b - 2z\tan\beta$

$d' = d - 2z\tan\alpha$

hence

$$\theta_0 = \frac{T}{GI_C}$$

$$\theta_0 = \frac{2*T}{G*((\ b'**2)\ *\ t_w\ *d'\ +(d'**2)*t_f\ *b')}$$

If for ease of writing we replace b', d', t_w and t_f in above equation by F, W, tw and tf respectively:

Flange = F = b' = b - 2 z tan (β)
Web= W= d' = d - 2 z tan (∝)

Thickness of Web= tw=t_w

Thickness of Flange=tf=t_f

then we have

$$\theta_0 = \frac{2*T}{G*((\ F**2)\ *\ tw\ *W\ +(W**2)*tf\ *F)}$$

Next $f_1 = \frac{d}{dz}(\theta_0)$ and $f_2 = \frac{d}{dz}(f_1)$ are shown below.

```
f1= ( (-2*(T/G)) * ( tw*
((((3*F/2)**2)*(-2*tan(∝))) +
(W*2*(3*F/2)*(-3*tan(β))) ) )
 +
 (2* tf*
((((W/2)**2)*(-2*tan(β))) +
(F*2*(W/2)*(-tan(∝))) ) )
```

```
 +
  ( tw*
( (((F/2)**2)*(-2*tan(∝))) +
 (W*2*(F/2)*(-tan(β)))   ) )
  +
  ( tf*
((((W/2)**2)*(-2*tan(β))) +
 (F*2*(W/2)*(-tan(∝)))   ) )))
          /
     (((tw*((3*F/2)**2)*W*2)+(tf*((W/2)**2)*F*4)
  +(tw*((F/2)**2)*W*2)+(tf*((W/2)**2)*F*2))**2)
```

and $f_2 = \frac{d}{dz}(f_1)$ is defined as

```
  f2= (-2*T/G)*
     ((( (((tw*((3*F/2)**2)*W*2)+(tf*((W/2)**2)*F*4)
 +(tw*((F/2)**2)*W*2)+(tf*((W/2)**2)*F*2))**2))
     *
 ((tw*
 (((2*(-2*tan(∝)))*
 (75-3*Z*tan(β))*(-3*tan(β)))
  +
  ((-3*tan(β))*
  (( ((50-2*Z*tan(∝)))*(-6*tan(β)))
   +
  ((150-6*Z*tan(β))*(-2*tan(∝))) ))))
 +(2*tf*
 ((  (2*(-2*tan(β)))*
 (25-Z*tan(∝))*(-tan(∝)))
  +
  ((-tan(∝))*
  (( ((50-2*Z*tan(β)))*(-2*tan(∝)))
   +
  ((50-2*Z*tan(∝))*(-2*tan(β)))))))
   +(tw*
 (( (2*(-2*tan(∝)))*

 (25-Z*tan(β))*(-tan(β)))
  +
```

```
 ( (-tan(β))*
 (( ((50-2*Z*tan(∝)))*(-2*tan(β)))
  +
 ((50-2*Z*tan(β))*(-2*tan(∝)) ))))
+(tf*
 ( ((2*(-2*tan(β)))*
 (25-Z*tan(∝))*(-tan(∝)))
  +
  ((-tan(∝))*
  (( ((50-2*Z*tan(β)))*(-2*tan(∝)))
   +
  ((50-2*Z*tan(∝))*(-2*tan(β))) ))))))
   -
 ((( tw* (
(((3*F/2)**2)*(-2*tan(∝))) +
(W*2*(3*F/2)*(-3*tan(β)))  ) )
 +
 (2* tf*
( (((W/2)**2)*(-2*tan(β))) +
(F*2*(W/2)*(-tan(∝)))  ) )
 +
 ( tw*
((((F/2)**2)*(-2*tan(∝))) +
(W*2*(F/2)*(-tan(β)))  ) )
 +
 ( tf*
((((W/2)**2)*(-2*tan(β))) +
(F*2*(W/2)*(-tan(∝)))  ) ))
  *
 ( 2*
   ( ((tw*((3*F/2)**2)*W*2)+(tf*((W/2)**2)*F*4)
+(tw*((F/2)**2)*W*2)+(tf*((W/2)**2)*F*2)))
 *
 ((2*tw*
  (((3*F/2)**2)*(-2*tan(∝)))
 +
 (W*
 ((2*(75-3*Z*tan(β)))*(-3*tan(β)))))
        +
( 4*tf*
(((W/2)**2)*(-2*tan(β)))
   +
 (F*
 ((2*(25-Z*tan(∝)))*(-tan(∝)) )))
        +
( 2*tw*
```

```
 (((F/2)**2)*(-2*tan(∝)))
+
(W*
((2*(25-Z*tan(β)))*(-tan(β)))))
+
( 2*tf*
 (((W/2)**2)*(-2*tan(β)))
+
(F*
((2*(25-Z*tan(∝)))*(-tan(∝)))))))))
       /
    (((tw*((3*F/2)**2)*W*2)+(tf*((W/2)**2)*F*4)
+(tw*((F/2)**2)*W*2)+(tf*((W/2)**2)*F*2))**4)
```

Now we shall define E Γ

$$E\Gamma = \frac{1}{3}((2*W*tw*E_w^{/}*w(s)_B^2)+(2*W*tw*E_w^{/}*w(s)_C^2)$$
$$+ (2*F*tf*E_f^{/}*w(s)_C^2)$$
$$+ 4*(F*tf*E_f^{/}*w(s)_B^2) + (w(s)_B*w(s)_C) + (w(s)_C^2))$$

Here $E_W^{/} = \dfrac{EWEB}{1-(NUWEB)**2}$

and

$$E_F^{/} = \frac{EFLANG}{1-(NUFLAN)**2}$$

Since $\eta^2 = 1 - \frac{J}{I_C}$

therefore $(E\Gamma)_{BENSCOTER} = \frac{E\Gamma}{\eta^2}$

$f_5 = (E\Gamma)_{BENSCOTER}$

$f_6 = \frac{d}{dz}(f_5)$

$f_6 = \frac{d}{dz}(\frac{E\Gamma}{\eta^2}) = \eta^2 * \frac{d}{dz}(E\Gamma) - (E\Gamma) * \frac{d}{dz}(\eta^2) / (\eta^2)^{**2}$

$\frac{d}{dz}(E\Gamma)_{BENSCOTER}$ is defined below as f_6

As it can be appreciated that $\frac{d}{dz}(E\Gamma)_{BENSCOTER}$ turns out to be a very large equation and is difficult to write it as a single equation , therefore following few expressions are being defined and then later on f_6 will be expressed in terms of these expressions below.

WY
FY
WSBY
WSCY
EGAMMAY
LAMBDAY

additionally $E\Gamma$ and η^2 have already been defined above as

$$E\Gamma = \frac{1}{3}((2*W*tw*E_w{}'*w(s)_B^2) + (2*W*tw*E_w{}'*w(s)_C^2) + (2*F*tf*E_f{}'*w(s)_C^2) + 4*(F*tf*E_f{}'*w(s)_B^2) + (w(s)_B*w(s)_C) + (w(s)_C^2))$$

and

$$\eta^2 = 1 - \frac{J}{I_C}$$

Hence we define following expressions

WY= (-2*tan(∝))

FY= (-2*tan(β))

F_{i+1} is the Bredt Batho Shear Flow in cell i+1
and θ is the rate of twist for free torsion

WSBY= (0.75*(((F*WY)-(FY*W))-
((1/(θ*G*tw))* F_{i+1} *0.5*WY)))

WSCY= (1.25*(((F*WY)+(FY*W))-
((F_{i+1} / (θ*G))*((0.5/tw)*(WY)+(FY/tf)))))

It may be pointed out here , that in the calculation of EGAMMAY, the differentiation of $w(s)_B$ and $w(s)_C$ needs to be evaluated. This differentiation of $w(s)_B$ and $w(s)_C$ has been defined above as WSBY and WSCY respectively.

In the evaluation of WSBY and WSCY, $(\frac{F_{i+1}}{\theta})$, which is the ratio of the shear flow in cell i+1 to the rate of twist of the multi-cell box beam has been treated as a constant. In fact this ratio is not a constant in itself, rather this ratio has a constant slope i.e.

$$\frac{d}{dz}(\frac{F_{i+1}}{\theta}) = \text{constant}$$

This assumption was made for the ease of calculation. However the good co-relation between theoretical results and the FE analysis has proved that this assumption did not affect the theoretical results adversely.

$\frac{d}{dz}(E\Gamma)$ is defined as the EGAMMAY

and is expressed as shown below

EGAMMAY=0.3333*

(((2* E'_w *tw)

*

((W*(2*$w(s)_B$*WSBY))+($w(s)_B$ **2)*(WY))))

+

((2*E'_w *tw)

*

((W*(2*$w(s)_C$*WSCY))+(($w(s)_C$ **2)*(WY))))

+

((2*E'_f *tf)

*

((F*(2* $w(s)_C$ *WSCY))+(($w(s)_C$ **2)*(FY))))

+

((4*E'_f *tf)

*

((F*((2* $w(s)_B$*WSBY)+ $w(s)_B$ *WSCY+ $w(s)_C$ *WSBY)+(2* $w(s)_C$ *WSCY)))

+

(($w(s)_B$ **2+($w(s)_B$ * $w(s)_C$)+ $w(s)_C$ **2)*FY))))

$\frac{d}{dz}(\eta^2)$ is defined as LAMBDAY and is expressed as shown below.

It is pointed out here that in the calculation of LAMBDAY , η^2 is expressed as

$$\eta^2 = 1 - \frac{J}{I_C}$$

Here J is expressed as

$$J = \frac{4A^2}{\oint \frac{ds}{t}}$$

which is basically the expression for Torsion constant J of single cell box

As torsion constant J for multi-cell section is defined as

$$T = GJ\,\theta \quad , \text{ hence } J = \frac{T}{G\theta}$$

J for multi-cell box section can also be defined as discussed in chapter 3 and shown below

$$J = \sum_{i=1}^{n} F_i\,\Omega_i \quad / \quad \left(- F_{i-1}\,\frac{s_{i-1,i}}{\delta_{i-1,i}} + F_i \oint \frac{ds}{\delta_i} - F_{i+1}\,\frac{s_{i,i+1}}{\delta_{i,i+1}} \right) / \Omega_i \;)$$

However the expression of J which was used in calculation of LAMBDAY is as below

$$J = \frac{4A^2}{\oint \frac{ds}{t}}$$

This expression for J of single cell was used for the evaluation of J for the three cell box by taking the total area of the three cell box in calculating the area "A" , and also taking care of $\oint \frac{ds}{t}$ in the entire circumference of the three cell box . This was done for ease of calculations , however the good co-relation between theoretical results and the FE analysis has proved that this did not affect the theoretical results adversely.

```
LAMBDAY=

((-1*
((G*((4*W/tw)+(6*F/tf)))
*
((4.5*tw*((F**2)*W))+
(0.5*tw*((F**2)*W))+
(1.5*tf*((W**2)*F))))
*
(36*G*(((F**2)*2*W*WY)+((W**2)*2*F*FY))))
+
((36*G*(F**2)*(W**2))
*
(((G*((4*W/tw)+(6*F/tf)))
*
((4.5*tw*(((F**2)*WY)+(W*2*F*FY)))+
(0.5*tw*(((F**2)*WY)+(W*2*F*FY)))+
(1.5*tf*(((W**2)*FY)+(F*2*W*WY)))))
+
(((4.5*tw*((F**2)*W))+
```

```
(0.5*tw*((F**2)*W))+
(1.5*tf*((W**2)*F)))
*
((4*G*WY/tw)+(6*G*FY/tf))))))
/
((G*((4*W/tw)+(6*F/tf)))
*
((4.5*tw*((F**2)*W))+
(0.5*tw*((F**2)*W))+
(1.5*tf*((W**2)*F))))**2
```

Hence f_6 finally can be defined as below

$$f_6 = \frac{d}{dz}\left(\frac{E\Gamma}{\eta^2}\right) = \eta^2 * \frac{d}{dz}(E\Gamma) - (E\Gamma) * \frac{d}{dz}(\eta^2) / (\eta^2)^{**}2$$

Here η^2 is called LAMBDA

$\frac{d}{dz}(\eta^2)$ is called LAMBDAY

$E\Gamma$ is called EGAMMA

$\frac{d}{dz}(E\Gamma)$ is called EGAMMAY

Hence we have f_6 as below

```
f6 = ((LAMBDA*EGAMMAY)-(EGAMMA*LAMBDAY))/(LAMBDA**2)
```

All above mentioned factors are required to be evaluated analytically and then using these factors along with the numerically evaluated factors mentioned in chapter 3 , the required equations 3.22 and 3.23 can be solved and values of C_1 and C_2 obtained.

REFERENCES

1.Waldron, P.
Sectorial Properties of Straight Thin-Walled Beams.
Computers & Structures Vol.24 , No 1, pp.147-156, 1986.

2.Benscoter, S.U.
A Theory of Torsion Bending for Multi-cell Beams.
Journal of Applied Mechanics, Vol. 20, March 1954.

3. M. Fine & Williams, D.
Effect of End Constraint on Thin-Walled Cylinders Subject to Torque.
Aeronautical Research Council, Rep. No. 2223, May 1945

4. Von Karman, T. and Christnesen, N.B.
Methods of Analysis for Torsion with Variable Twist
Journal of Aeronautical Sciences , Vol. 11, April 1944.

5.MSC/NASTRAN Linear Static Analysis Hand-book Version 69
The Mac-Neal Schwendler Corporation 1996

6.J.P Caffrey and J.M.Lee
MSC/NASTRAN Linear Static Analysis- User's Guide Version 69
The Mac-Neal Schwendler Corporation 1996

7. M.Ata
Torsional Analysis of Thin-Walled Fibrous Composite Beams
Phd Thesis Cranfield University Uk 1992

8.G.J.Wooley
Design Analysis of Composite Two Cell Beams
Msc Thesis Cranfield Univesrity 1989

9.Datoo, M.H.
Mechanics of Fibrous Composites
Elsevier Science Publishers Ltd, Essex, England 1991

10.Argyris , J.M.and Dunne , P.C.
The General Theory of Cylindrical and Conical Tubes under Torsion and Bending Loads.
Journal of Royal Aeronautical Society , Parts 1-1V, 1947-49.

11.Vlasov, V.Z.
Thin-Walled Elastic Beams
Israel Programme for Scientific Translations Jerusalem, 1961

12.Zbirohowski-Koscia,K.
Thin -walled Beams
Crosby Lockwood and Son Ltd. London 1967.

13.Wagner-Kappus Torsion Bending Theory for Open Sections
Megson,T.H.G.
Chapter 9 Linear Analysis of Thin-Walled Elastic Structures
Surrey University Press. Uk,1974

14.Oden, J.T. and Ripperger, E.A.
Mechanics of Elastic Structures
McGraw-Hill Book Co. New York, 1967

15.Gjelsvik, A.
The Theory of Thin-Walled Bars
John Wiley and Sons, New York, 1981

16.Timoshenko,S.and Goodier, J.N.
Theory of Elasticity
McGraw-Hill Book co., New York, 1951

17.L.Beskin
Warping and Shear Lag in Closed Cylindrical Shells
Journal of Aeronautical Sciences Vol 15, pp 221-231, 1948

18.Reissner, E. And Tsai, W.T.
Pure Bending, Stretching,and Twisting of Anisotropic Cylindrical Shells
Journal Of Applied Mechanics, March 1972.

19.Mansfield, E.H. and Sobey, A.J.
The Fibre Composite Helicopter Blade ;
Part 1:Stiffness Properties;
Part 2: Prospects for Aeroelastic Tailoring.
Aeronautical Quarterly, May 1979.

20.Hong, Chang-Ho and Chopra,I.
Aeroelastic Stability Analysis of a Composite Blade
Proceedings of 40th Annual Forum of the American Helicopter Society, 1984

21. Hong, Chang-Ho and Chopra,I.
Aeroelastic Stability Analysis of a Bearingless Composite Blade
Presented at the International Conference on Rotorcraft Basic Research,
Feb 1985

22.Panda, B.and Chopra, I.
Dynamics of Composite Rotor Blades in Forward Flight
Vertica,Vol.11 (1/2) ,1987.

23. Rehfield,L.W.
Design Analysis Methodology for Composite Rotor Blade.
Presented at Seventh DoD/NASA Conference on Fibrous Composites in Structural Design, June 1985.

24.Bauchau, O.A.
A Beam Theory for Anisotropic Materials.
Journal of Applied Mechanics, Vol.52, June 1985.

25.Bauchau, O.A.and Hong,C.H.
Nonlinear Composite Beam Theory .
Journal of Applied Mechanics, Vol.55, March 1988.

26.Bicos, A.S. and Springer,G.S.
Design of a Composite Box Beam.
Journal of Composite Materials,Vol.20, January 1986.

27.Chang,S.I. and Libove,C.
Shear Flows, Strains, and Rate of Twist in Single-Cell Thin-Walled Beams with Anisotropic Walls: Simple Theory Compared with Nastran and Experiment.
Presented at the ASME Winter Annual Meeting, 1988.

28.Klang, E.C.and Kuo, T.M.
Component Level Analysis of Composite Box Beams.
Proceedings of the 30th AIAA/ASME/ASCE/AHS/ASC Structures, Structural Dynamics and Materials conference,1989.

29.Minguet, P. And Dugundji, J.
Experiment and Analysis for structurally Coupled Composite Blades
Under Large Deflections, Part 1 Statics, Part 2 Dynamics.
Proceedings of the 30th AIAA/ASME/ASCE/AHS/ASC Structures, Structural Dynamics and Materials conference,1989.

30.Smith,E.C. and Chopra, I.
Formulation and Evaluation of an Analytical Model for Composite Box Beams.
AIAA Paper No: 90-0962-CP, 1990

31.Barrau, J.and Laroze, S.
Torsion of a Composite Box Beam
Proceedings of 2nd International Conference on Composite Structures,
Paisley College of Technology, Scotland, 1983.

32.Jeppe Jonsson
Distortional Warping Functions and Shear Distributions in Thin-Walled Beams
Thin-Walled Structures Vol.33 pp 245-268 , April 1999

33.Jeppe Jonsson
Distortional Theory of Thin-Walled Beams
Thin-Walled Structures Vol.33 pp 269-303 , April 1999

34.Chai Hong Yoo and Samir V Acra
Cross-Sectional Properties of Thin-Walled Multi-Cellular Section
Computers and Structures Vol 22 pp53-61 ,1986

35. Steen Krenk and Bo Jeppesen
Finite Elements for Beam Cross-Sections of Moderate Wall Thickness
Computers and Structures Vol 32 pp1035-1043 ,1989

36.J.Jonsson
Determination of Shear Stress, Warping Functions and Section Properties of Thin-Walled Beams using Finite Elements.
Computers and Structures Vol 68 pp393-410 , 1998

37.J.Loughlan and M.Ata
Variable Twist Torsion Tests on Carbon Fibre Composite Beams
Composite Structures Vol.42 pp 307-327 , 1998

38.J.Loughlan and M.Ata
The Constrained Torsional Characteristics of some Carbon Fibre Composite Box Beams
Thin-Walled Structures Vol.28 pp 233-252 , 1997

39.J.Loughlan and M.Ata
The Analysis of Carbon Fibre Composite Box Beams Subjected to Torsion with Variable Twist.
Computer Methods in Applied Mechanics & Engineering Vol 152 pp 373-391, 1998

40.J.Loughlan and M.Ata
The Behaviour of Open and Closed Section Carbon Fibre Composite Beams Subjected to Constrained Torsion.
Composite Structures Vol.38 pp 631-647 , 1997

41.Grant C
Network Analysis of Thin-Walled Sections in uniform Torsion
Proceedings of Inst. Of Mech. Engg. part C
Journal of Mech. Engg Sciences Vol 209 pp 133-140 , 1995

42. Shakourzadeh, Guo and Batoz

A Torsion Bending Element for Thin-Walled Beams with Open and Closed Cross-Sections.
Computers and Structures Vol.55 pp 1045-1054 , 1995

43.Kaiser, Paracchini and Francescatti
Analysis of Composite Thin-Walled Multi-Celled Beams with Elastic Couplings.
ECCM-8, Proceedings of 8th Europian Conference on Composite Materials pp 173-180, 1998

44.Rodriguez, P.
Design of Multiple-Ply Laminated Composite tapered beams
Report No. NASA-TM-108411; NAS 1.15:108411, 1993

45.Chandra, Alan , Chopra
Thin-Walled Composite Beams Under Bending, Torsional and Extensional Loads.
Journal of Aircraft Vol 27 pp 619-626, 1990

46.Rehfield, Dewey and Atilgan
Some Considerations on the Non-Classical Behaviour of Thin-Walled Composite Beams.
Conference Paper 1988
Proceedings (A89-29451 11-01) American Helicopter Society

47. Bauchau
Composite Box Beam Analysis Theory and Experiments
Journal of Reinforced Plastics & Composites Vol 16 pp 25-35, 1987

48.Wu, Sun
Simplified Theory for Composite Thin walled Beams
AIAA Journal 1992 (ISSN 0001-1452)

49.Chandra , Chopra

Structural Response of Composite Beams and Blades with Elastic Couplings
Journal Article Composite Engineering 1992 (ISSN 0961-9526)

50.Barbero, Massa
A Strength of Materials Formulation for Thin-Walled Beams with Torsion.
Journal of Composite Materials Vol 32, 1998

51. Marshall I. H
Composite Structures 6
Elsevier Science publishers Ltd Essex England 1989.

52.Murray, N.W. and Attard M.M.
A Direct Method of Evaluating the Warping Properties of Thin-Walled Open and Closed Profiles.
Thin-Walled Structures Vol 5, 1987